UNIVERSITY OF CALIFORNIA
RIVERSIDE

Thermochemical and Electrochemical Modulation of the Oxidative Energy Release Profile of Metals, Chemical Hydrides, and Energetic Ionic Liquids as Condensed Phase Fuels

A Dissertation submitted in partial satisfaction
of the requirements for the degree of

Doctor of Philosophy

in

Chemical and Environmental Engineering

by

Prithwish Biswas

June 2023

Dissertation Committee:
Dr. Michael R. Zachariah, Chairperson
Dr. Reza Abbaschian
Dr. Kandis Leslie Abdul-Aziz

The Dissertation of Prithwish Biswas is approved:

_____

_____

_____

Committee Chairperson

University of California, Riverside

Acknowledgements

First and foremost, I want to thank my advisor Dr. Michael R. Zachariah for providing the platform of performing state of the art research, inculcating scholarly abilities, and encouraging independent proposition of new research problems. I am greatly indebted to Dr. George W. Mulholland for mentoring and teaching me fundamental theories on light scattering and particle dynamics in nanofluids, which comprises significant parts of this dissertation. I would also like to thank Dr. Reza Abbaschian and Dr. Kandis Leslie Abdul-Aziz for advising me as members of the dissertation committee. The work presented in this dissertation is a part of collaborative effort and hence I would like to thank all my lab mates and collaborators. I am grateful to the current and former members of Dr. Zachariah's group, Dr. Feiyu Xu, Dr. Pankaj Ghildiyal, Yujie Wang, Dr. Haiyang Wang, Dr. Miles C. Rehwodlt, Dr. Dylan J. Kline, Dr. Yong Yang, Dr. Lucas Algrim, Dr. Zaira Alibay, Dr. William Gibbons, Erik Hagen, Keren Shi, Mahbub Chowdhury, Afrida Anis, Amir Saeidi, Dr. Ashvin K. Vasudevan, and George I. Paul. I also thank my collaborators from other groups, Dr. Steven Herrera, Dr. Reza Abbaschian, Dr. C. Huy Pham, Dr. Hyuna Kwon, Dr. Bryan M. Wong, Joseph Schwan, Brandon Wagner, Dr. Lorenzo Mangolini, Dr. Gregory Young. I also thank the ONR-MURI, DTRA, AFOSR, and MSEE grants and UCR Dean's and Disseration year fellowships for financing my research and stay at UCR. I am also thankful to the CFAMM, ACIF, and Winston Chung Global Energy Center for supporting the microscopic and spectroscopic characterizations involved in this dissertation. I am also thankful to Deanna Vorhees and Adrienne Thomas of CEE department for helping me with material procurement and administrative documentations. Parts of this dissertation have

appeared in previously published primarily self-authored articles and have been reprinted with permission from the publishers, American Chemical Society and Elsevier. I would like to thank my previous research advisors, Dr. Mukta Tripathy and Dr. Rajdip Bandyopadhyaya for encouraging me to pursue an academic career. Lastly I would like to thank my friends, Dr. Nirjhar Sarkar, Dr. Pritam Biswas, Gaurang, Tu, Somchate, Seongbin, Harsh, Daniel, Arun, Prasad, Rito, Durba, Sougata, Kunal, and Debottam for supporting me throughout my academic career and the journey of this dissertation.

To my parents Mita Biswas and Tapan Biswas for constant encouragement and support in pursuing an academic career

ABSTRACT OF THE DISSERTATION

Thermochemical and Electrochemical Modulation of the Oxidative Energy Release Profile of Metals, Chemical Hydrides, and Energetic Ionic Liquids as Condensed Phase Fuels

by

Prithwish Biswas

Doctor of Philosophy, Graduate Program in Chemical and Environmental Engineering
University of California, Riverside, June 2023
Dr. Michael R. Zachariah, Chairperson

Although sustainable thermal energy storage and conversion approaches are becoming increasingly popular, high-power requirements (~10^7 kWh) in certain energy applications such as spacecraft and jet propulsion, can only be accomplished through direct conversion of chemical to thermal energy through combustion. The current research objective in this field is to alleviate the kinetic and mass transfer limitations impeding rapid energy extraction from solid state fuels possessing high energy density. Part of the dissertation focuses on solving such challenges for boron particles and boron containing complexes, as elemental boron has the highest energy density. This dissertation provides mechanistic insights on selectively altering the thermochemical decomposition pathways of boron containing solid-state borane-ammonia complex with the help of a) ammonium-ion based oxidizing salts and b) polymeric carbonyl groups, to facilitate rapid and complete oxidation of boron in the borane-ammonia complex, which otherwise gets kinetically trapped into boron-nitrogen-hydrogen clusters. The dissertation also provides atomic scale

understanding of the manipulation of boron oxide shell by implanting magnesium atoms, as a potential strategy to enhance reactivity of boron particles. Magnesium simultaneously reduces boron oxide creating dangling bonds on boron and induces a net tensile strain on the boron oxide surface, which respectively enhances the adsorption and diffusion rate of oxygen through the boron oxide shell, collectively enhancing the oxidation rate of boron. Significant part of the dissertation also focuses on tuning the reactivity of composites containing aluminum, another high energy density and widely explored solid fuel, by alteration of micro- and meso-structural features, as well as the incorporation of microwave absorbing sensitizers in aluminum-based composites for spatial confinement of the ignition zone when activated using microwave radiation. As a major breakthrough, this dissertation also demonstrates that certain non-flammable condensed phase materials with high energy density such as imidazolinium-ionic liquids can be electrochemically made inflammable and their flame can be dynamically extinguished simply by removing the voltage bias driving the electrochemical reactions. Since most energy dense fuels pose the danger of unintended fire and explosion, this concept paves the path for the development of potentially ‘safe’ fuels, thereby opening multiple avenues for future research.

Table of Contents

List of Figures

List of Tables

1 Introduction

1.1 General overview on energetic materials for propulsion

Thermal energy generation has immense significance in diverse domestic and industrial processes. Approaches involving energy storage and release to generate thermal energy are more sustainable than those based on direct conversion of chemical to thermal energy. Hence, materials for energy storage and conversion, such as electrochemical energy storage in batteries[1,2], fuel (H_2) storage and release in fuel cells[3,4], latent heat storage (phase change materials)[5], and thermochemical energy storage materials with applications in solar and chemical energy harvesting[6], are becoming increasingly popular for thermal energy generation. However, high power demands (~10^7 kWh) in certain energy applications such as spacecraft and jet propulsion, can only be accomplished through direct generation of thermal energy from energy stored in chemical bonds through combustion[7–18]. Combustion is an exothermic process, involving redox reactions generating heat from the oxidation of fuels. Therefore, fuels having high energy density on both gravimetric and volumetric basis are suitable from the standpoint of both economy and energy efficiency.

Fuels used in propulsion systems are typically activated by electric, laser, or plasma discharge driven heating[19,20], in order to raise the temperature of the fuel to the oxidation onset or the ignition point. Ignition is a self-sustaining phenomenon, occurring at a temperature at which the heat release rate from the oxidation of the externally heated sections of the fuel, is sufficient to propagate and oxidize the unheated sections of the fuel, thereby generating a self-sustaining flame. Owing to higher density over liquid and gas fuels, solid fuels are becoming increasingly popular in energetic materials research

focusing on propulsion systems[21,22]. Among the solid-state fuels, metals and chemical hydrides have a much higher oxidative energy density compared to hydrocarbons, which make them attractive to be exploited for energy generation in propulsion systems. Figure 1-1 (a) representing the gravimetric and volumetric energy content of metals and chemical hydrides, shows that metals have a higher energy content on a volumetric basis whereas chemical hydrides have a higher energy content on a gravimetric basis. Hydrocarbons typically have an energy density below 10 kJ/g or cm^{323}, much lower than all chemical hydrides and metals.

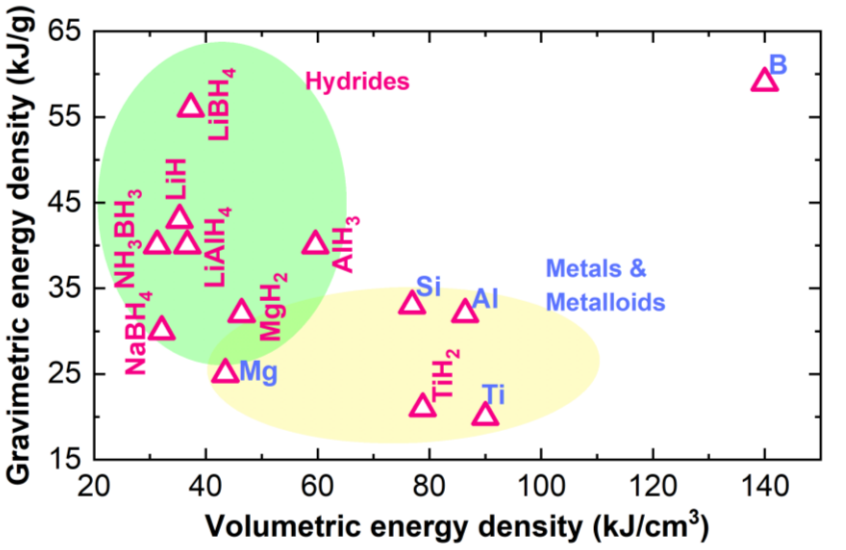

Figure 1-1 Gravimetric and volumetric energy density of metals and chemical hydrides.

From a practical standpoint, to optimize the gravimetric and volumetric energy density of solid-state propellants, one needs to employ hybrid fuel composites comprising of both metals and chemical hydrides. Based on the thermodynamic reaction enthalpies, one can easily propose the design of hybrid propellant systems for use across different

ranges of energy requirements. However, oxidation enthalpy (ΔH) is not the sole factor that the thermal energy release rate depends on, as the major factor that influences the energy release rate is the characteristic reaction time scale (τ). Hence, the energy release rate scales as $\sim\frac{\Delta H}{\tau}$. The reaction time scale depends on intrinsic chemical kinetics and the diffusion rates of reacting species. As species diffusion is slow in solid-state, the τ becomes the major factor impeding the power output. In fact, as the condensed phase reaction and diffusion rates increases exponentially with increasing temperature, τ is interdependent with the energy release rate and has a strong dependence on the heat generation and transfer rate. Thus, a material with a high elemental oxidation enthalpy might demonstrate poor energy release performance, when τ is very high[24–27]. This demonstrates that there are immense opportunities to perform fundamental research to address challenges associated with multiscale and multispecies transport phenomena and reaction propagation in these solid-state fuels for energetic applications. Addressing challenges associated with such phenomena is the broader objective of this dissertation.

1.2 Oxidation and combustion of metal particles

Oxidation and combustion characteristics of particulate metals such as Al, Ti, Mg, and metalloids such as Si and B have been widely explored. As these metals are pyrophoric, after synthesis, small particles of these metals are slowly exposed to air to develop a passivating oxide shell to an equilibrium thickness which can prevent further unintended oxidation or ignition of these particles. The different physical and chemical properties of these metallic cores and the metal oxide shells result in significantly different combustion characteristics. For instance, Al and Mg melt and vaporize at low temperatures whereas

their oxide shell is high temperature resistant[17,28]. On the other hand, the oxide shell of B melts at low temperatures whereas its core remains solid[15]. In the case of Si[21,29] and Ti[30], both the core and the oxide shells are resistant to phase changes till high temperatures.

Both Al and Mg burn in the vapor phase, but there is a subtle difference in the mechanism of initiation of their oxidation and ignition process. Previous studies have found that amorphous alumina shell undergoes polymorphic phase transitions around ~800 K, which creates physical voids or cracks in the shell. The cracks permeate gas phase oxygen diffusion towards the core thereby enabling the oxidation of Al core[31]. Several other studies have also observed that the Al nanoparticle core becomes hollow after its melting, through both electron microscopy (Figure 1-2 (a)) and molecular dynamics simulations[17,32]. Based on these observations, an alternative theory of Al-nanoparticle oxidation has been suggested, according to which, the space charges at the metal-metal oxide interface increase the mobility of molten Al ions and facilitates the outer diffusion of Al through the voids of the oxide shell. Hence, both inward diffusion of oxygen and outward diffusion of Al collectively affect the oxidation process of Al nanoparticles. On the contrary, the magnesium core of magnesium nanoparticles completely vaporizes at low temperatures ~900 K and effuses out through the porous magnesium oxide shell to participate in oxidation reaction (Figure 1-2 (b)), which also leads to their incredibly faster oxidation kinetics compared to Al[28].

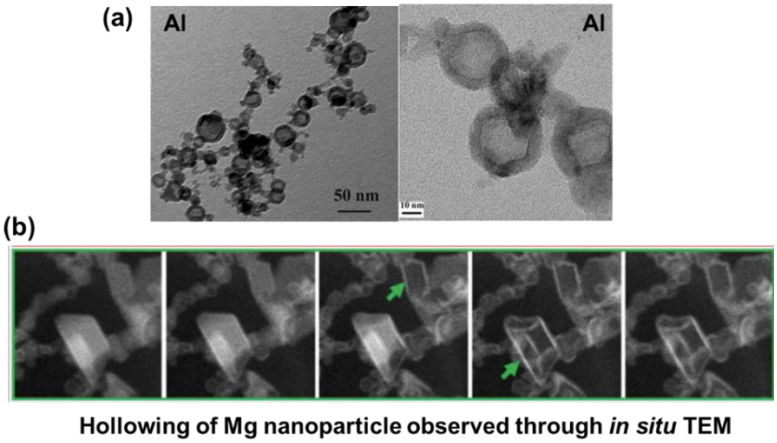

Figure 1-2 (a) Hollowing of Al nanoparticles after oxidation[33]. (b) In situ TEM showing Mg particles become hollow with vaporization of Mg from the particle core[28] (*Reproduced with permission from Taylor & Francis and American Chemical Society*).

The oxidation of B, Ti, and Si occurs in a shrinking core manner where the oxygen diffuses and reacts with the metallic core accompanied with the inward growth of the oxide shell from the surface[21,23]. However, the different physical properties of their oxide shells result in their different oxidation mechanisms. For B, the B_2O_3 shell melts at low temperatures whereas the core remains solid. The molten shell is devoid of any physical voids which develop in the oxide shells of Al or Mg and also the core remains solid and cannot diffuse out like Al or Mg. Hence, the molten B_2O_3 shell prevents any gas phase O_2 diffusion, and the absence of oxygen vacancies results in slow condensed phase diffusion resulting in poor oxidation rates of B[15].

Due to the multiple oxidation states of Ti, its oxide shell consists of high concentrations of oxygen vacancies[34]. This facilitates oxygen diffusion through Ti shell, as a result of which Ti has the lowest ignition temperature in air or with gas phase oxidizers among all of these metals and metalloids. However, it reacts poorly with metal oxides like

CuO, Bi_2O_3 etc. which are condensed phase oxygen ion donors compared to Al and Mg. This is because unlike Al and Mg, the Ti at the core cannot melt or vaporize and diffuse outwards to react with the oxygen ions on the metal oxide surface[23]. Si also oxidizes in the same shrinking core manner as Ti, however its shell has less oxygen vacancies and also melts at relatively lower temperatures, which inhibits the oxidation kinetics of Si nanoparticles. It has been reported that complete oxidation of Si cannot be achieved when its particle size is above ~10 nm[21].

Thus, all of these metals and metalloid particles have different oxidation mechanisms which results in their different energy release rates. Ideally, a mixture of nanoparticles of these different metals or metalloids should be used as fuels in energetic composites, to obtain tunable energy release rates. Additionally, there is a scope to manipulate their oxide shell by pre-stressing of the metal/metal oxide interface or introducing vacancies in the oxide shell to facilitate oxygen diffusion, to lower their oxidation onset or enhance their oxidation kinetics. For instance, it has been shown that pre-stressed Al nanoparticles demonstrate higher reactivity due to faster ion migration through the tensile strained surface[35]. Apart from these, however manipulating the oxide shell of B to enhance oxygen diffusion and reactivity of B particles is still an attractive problem as B has the highest gravimetric and volumetric energy density.

1.3 Metal/metal oxide nanoparticle assemblies in polymer matrices: Effect of binder matrix chemistry and architecture on energy release rate

The combustion of sub-micron or nano-sized metal powders in air is highly inefficient due to their tendency to sinter and agglomerate[36]. When a bed of metal powder is oxidized in air, the metal particles will start to sinter before melting and after melting they will vigorously agglomerate blocking the penetration of gas phase oxygen through the bed. Hence, metal particles are often mixed with sub-micron oxidizer particles (metal oxides, perchlorate/nitrate/iodate salts etc.) particles which can act as local donors of oxygen, to ensure the oxidation occurs faster than the sintering process. However, a physical mixture of loose metal and oxidizer particles does not allow much control on the fuel-oxidizer mixing length which will possibly lead to uncontrollable and irreproducible burning characteristics. Hence, there is considerable interest in assembling these particles into polymer matrices via direct ink writing (3D printing), electrospinning, spray drying, and electro-spraying (Figure 1-3 (a)), to form compact composites with reproducible microstructural features and burning characteristics[37–40].

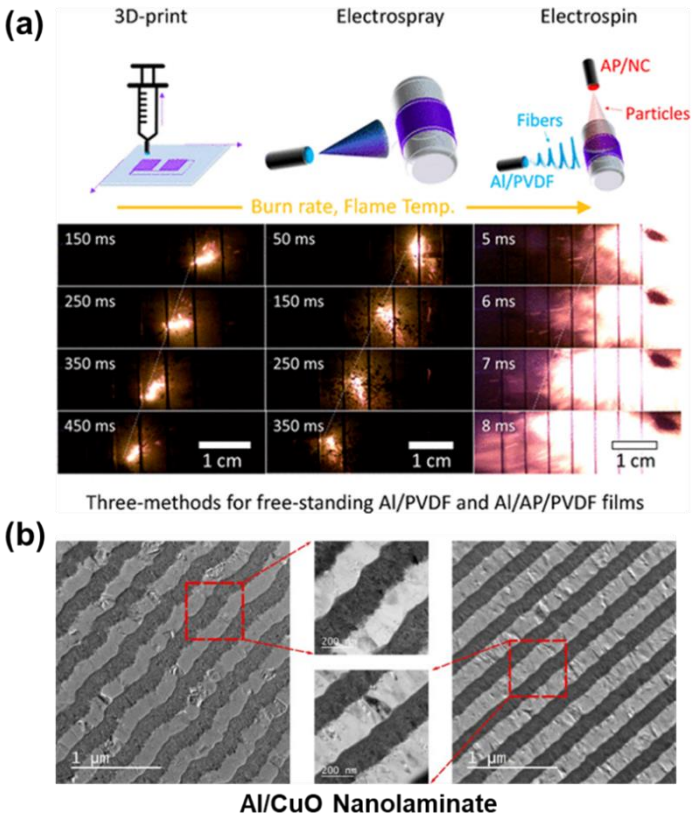

Figure 1-3 (a) Different methods of fabricating polymer composites of metal/metal oxides[41] (b) Sputter deposited Al/CuO nanolaminates[42] (*Reproduced with permission from American Chemical Society and Elsevier*)

Fluorine containing polymer such as polyvinylidene fluoride (PVDF) releases HF gas on decomposition which reacts with Al and Al_2O_3 shell to form AlF_3, thereby enhancing the oxidation rate of Al[43,44]. Hence, the polymer with favorable properties can be chosen as the binder matrix in these composites. As mentioned earlier, metallic fuel and oxidizer particles are often pre-mixed into a composite to ensure that the metal is oxidized prior to sintering. However, even in such pre-mixed composites metal nanoparticles undergo severe sintering and agglomeration losing their nanostructure. With agglomeration and sintering the nanoparticles lose their favorable aspects of having a high surface to

volume ratio and thereby cannot achieve the intended oxidation rate. When Al and CuO have been assembled into mesoscale particles by electro-spraying nitrocellulose as a gas generating energetic binder, the simultaneous gas and heat generation from the nitrocellulose combustion causes volumetric expansion of the medium. This explosively disperses the Al nanoparticles by pushing them apart from each other and thereby preventing their agglomeration and sintering[38].

Using metal oxide particle of different morphologies, it has been shown that metal oxide nanowires can act as pockets preventing the agglomeration and growth of Al particles during combustion[14]. Combustion in a directly ink written solid propellant strand consisting of metal and metal oxide propagates when the heat feedback from the flame is sufficient enough to ignite the unburnt zone. In such a case one would expect that addition of a poor thermal conductor like SiO_2 nanoparticles as an additive in Al based polymer composites will deteriorate the flame propagation rate. Rather an experimental study has shown that the SiO_2 addition increases the flame propagation rate by introducing corrugations in the flame zone, which increases the heat transfer cross-section, therefore enhancing the heat feedback rate[45].

Laminates having several ~nm thick alternate layers of metal and metal oxide have been fabricated by magnetron sputtering or chemical vapor deposition (Figure 1-3 (b)). Such nanolaminates propagate at a much faster rate compared to any metal/metal oxide particulate based polymer films. Additionally, the mixing length between the fuel and oxidizer in these laminate architectures can be easily controlled just by changing the interlayer separation. Increasing the thickness of the oxidizing layer increases the oxygen

diffusion length to the metal thereby reducing the burn-rate. Therefore, energy release rate from such composites can be easily tuned simply by changing the layer thickness. Also, the high reactivity of these composites can be explained by the direct contact between the fuel and oxidizer at nanoscale separation[42,46–49]. However, most propulsion applications require ~mm to ~cm scale composite grains. Thus, sputter deposition techniques are not scalable enough to prepare larger propellants. On the other hand, polymer-based nanoparticle inks can be used for additive manufacturing of large-scale composites. Hence, there is a scope to study whether nanoparticles can be placed in such laminate architecture by direct ink writing and to study combustion characteristics of metal and metal oxide nanoparticles arranged in alternate layers in a laminate architecture. Although, previous studies have already shown that architecture can significantly affect the energy release rate of metal/metal oxide-based composites by controlling particle agglomeration and fuel/oxidizer mixing length, there is a scope to perform multiple fundamental studies to address questions regarding multi-scale transport phenomena and reaction dynamics in metal-metal oxide composites with different architectures.

1.4 Open challenges in energetic materials research

One of the key research interests in the field of energetic materials is to increase the energy density of the propellant composites. To achieve this, the use of high energy density fuels is essential. Boron as a fuel has the highest energy density. However, as mentioned earlier it suffers from slow oxidation kinetics because of the sluggish diffusion of oxygen through its oxide shell. These kinetic limitations cause boron to perform poorly in

comparison with fuels possessing lower energy densities such as Al and Mg. Hence, improving the oxidation kinetics of boron is one of the major challenges in this field.

Metal hydrides or borohydrides consisting of multiple reactive elements and possessing high energy density, have the potential to operate as a gas generating fuel. The gas phase combustion of the released hydrogen should prevent the agglomeration and sintering of the host metal particles by explosively dispersing them, thereby ensuring their rapid and complete oxidation. Several studies have focused on the adsorption and desorption of H_2 as a combustible fuel source from the host metals. However, from the perspective of high energy applications, direct combustion of the solid-state chemical hydrides which involves the oxidation of both the metal and the hydrogen counterparts, is important. This aspect of chemical hydrides has been majorly unexplored and demands further research.

As also mentioned in the previous section, advanced energetic material design by controlling micro and meso-structure of metal and metal oxide nanoparticle assemblies, is becoming increasingly popular, opening up scope for further fundamental and applied research. Another major problem associated with high energy density fuels is that their self-sustaining combustion can lead to united fire and explosion. The prevalent combustion systems extinguish the combustion process by removing the oxidizing source from the combustion zone. However, this strategy may fail under extreme reaction rates and hence methods that can enable rapid control, at the same time as that of the combustion reactions, need to be developed to ensure fuel safety.

1.5 Challenges addressed by this dissertation

1.5.1 Enhancing combustion of boron-the highest energy density fuel

Interest in the development of metal ion batteries has facilitated studies on electrochemically driven solid-state diffusion and redox reactions of metal ions. Decomposition and reaction mechanisms of chemical hydrides have also been widely studied owing to their reversible hydrogen storage capabilities. However, limited studies have been performed on these materials from the perspective of direct chemical to thermal energy conversion associated with thermally driven fast and irreversible oxidation processes. It is evident from Figure 1-1 that elemental boron (B) has the highest gravimetric energy content among all metals and chemical hydrides, and its absolute energy density is significantly higher than all of the other solid fuels. However, the oxide shell on B particles presents unfavorable properties that often hinder the achievement of high energy release rates[15]. This is because, during combustion, the non-volatile boron oxide (B_2O_3) shell melts at a relatively low temperature (~720 K) compared to the solid B-core, resulting in the oxidation of B particles in a shrinking-core manner due to external or oxidative heating[50]. The liquid shell lacks physical voids, which slows down the diffusion of oxygen and thus impedes the B oxidation process. On the other hand, metals with low melting or boiling points like Al and Mg offer higher energetic performance owing to their vapor phase burning capabilities, even though they have a lower energy density than B[31].

In this regard borohydride salts as chemical hydrides are capable of generating gas phase boron in the form of boron-hydrogen clusters alongside hydrogen generation.

Ammonia borane (NH_3BH_3) is one such borohydride which has the highest hydrogen content on a gravimetric basis. Additionally, its covalent character makes it less hygroscopic compared to the other alkali metal (Na^+ / Li^+ /K^+) borohydride salts, which makes it more suitable for practical applications under standard atmosphere as less hygroscopic character preserves the active fuel content[51,52]. However, as one would expect. on heating the dative B-N bond of ammonia borane prevents its disintegration into NH_3 and BH_3 moieties. Rather, it oligomerizes on heating to higher molecular weight boron-nitrogen-hydrogen (BNH_x) clusters such as gaseous borazine and solid-polyborazylene[53]. As chemical resistance increases with molecular weight, the generation of these higher molecular weight BNHx compounds can impede the reactivity and energy generation rate from AB. The oligomerization process is initiated by the formation of an dimeric intermediate, diammoniate of diborane /DADB ($[NH_3BH_2NH_3]^+[BH_4]^-$), as a result of the intermolecular nucleophilic attack of N of one AB molecule on the B of another AB molecule, along with simultaneous hydride transfer from the attacked B to the B attached to the attacking N. The DADB further rearranges and oligomerizes into higher molecular weight BNH_x clusters[54].

The research performed for this dissertation has been able to provide a couple (Chapter 2 and Chapter 3) of solutions to alleviate the issue of AB oligomerization, one of which is by employing NH_4^+ ion based oxidizing salts (Chapter 2). As the nucleophilic attack of N of NH_4^+ on the B of AB molecules, is more favorable than that of N of one AB molecule on the B of another AB molecule, NH_4^+ based oxidizing salt doping results in the formation of a different intermediate, ($[NH_3BH_2NH_3]^+[anion]^-$) in place of DADB. This

alternative intermediate formation inhibits the generation of BNH_x clusters and also results in the complete oxidation of AB, thereby increasing ΔH and reducing τ, hence increasing the overall energy release rate (Figure 1-4 (a))[55].

However, the use of solid-state oxidizers is unattractive for jet propulsion which uses air as an oxidizer. The dissertation provides another alternative solution to the problem of BNH_x cluster generation by showing that the dative B-N bond of AB can be catalytically dissociated by polymeric carbonyl groups, which makes AB also eligible for applications where air is used as an oxidizer (Chapter 3). The dissertation shows by incorporating AB in polymer matrices with carbonyl groups, that the C of carbonyl groups can compete with the B of AB molecules as centers of nucleophilic attack which will eventually result in the dissociation of the B-N bond of AB causing it to disintegrate into smaller NH_3 and B_2H_6 moieties, whereas the carbonyl group along with the other polymer functional groups remain chemically unaltered post AB decomposition and gasification. B_2H_6 having a lower auto ignition temperature than H_2 and NH_3, will spontaneously ignite in air on its release from AB-polymer composites and hence is more attractive as fuel source for air breathing applications (Figure 1-4 (b)). Storage of gas phase B_2H_6 is potentially dangerous owing to its instability and toxicity. This pathway studied through *in situ time-of-flight mass spectrometry* along with supporting spectroscopic characterizations, enables the efficient storage of B_2H_6 in solid state and on demand utilization for energy generation[56].

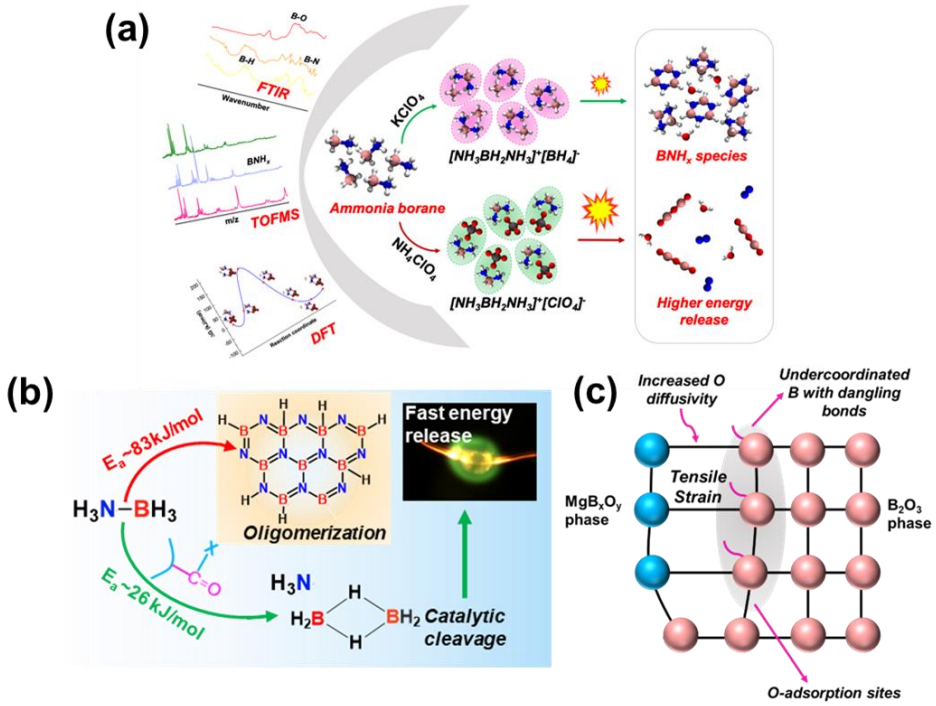

Figure 1-4 Rerouting thermochemical energy release pathways of ammonia borane with NH_4^+ ion-based oxidizers (a)[55] and polymer matrices with carbonyl groups (b)[56]. (c) Enhancing oxidation kinetics of B by manipulating its oxide shell with Mg vapor (*Reproduced with permission from American Chemical Society*).

Another approach to enhance boron combustion is to use an additive that will react with the oxide sell of boron (Figure 1-4 (c)). Several experimental studies have shown that the addition of metals with lower free energy of oxidation such as Mg can reduce the oxide shell of B and enhance the energetic performance of B by ~30-60 %[27,57–62], however the exact underlying mechanism behind the reactivity enhancement is unknown. It has been experimentally proven that when a composite of particulate Mg and B are heated, Mg vaporizes first owing to its high vapor pressure and the Mg vapor interacts with the oxide shell of B. Therefore, I have performed density functional theory tight binding-molecular dynamics (DFTB-MD) simulations to study the reaction of Mg vapor with B_2O_3 surface

(chapter 4), in order to obatin mechanistic understanding of the atomic scale interaction of Mg vapor with the oxide shell of B. I found that the Mg become oxidized on the B_2O_3 surface forming a MgB_xO_y phase, which induces a tensile strain in the B-O bond at the MgB_xO_y-B_2O_3 interface, simultaneously reducing the interfacial B developing dangling bonds. I also found that the there is an overall surface expansion indicating the presence of a net tensile strain on the entire surface as a result of the interfacial bond straining. The interfacial B with dangling bonds can act as active centers for gas phase O_2 adsorption thereby increasing the O adsorption rate. The overall tensile strain on the surface will increase the diffusion flux of adsorbed O through the surface to the particle core. As the overall B particle oxidation rate is dependent on both O adsorption and diffusion rates, the enhancement in both of these rates increases the overall reactivity of B particles. Hence, chapter 2-4 provides mechanistic insights into strategies that can be exploited to enhance the combustion of B.

1.5.2 Micro and mesostructural alterations to tune energy release from other reactive metal nanoparticles

Although B has higher energy density, Al nanoparticles have been the most widely explored metallic fuel for energetic applications as they demonstrate higher energetic performance due to their different physical properties from B. As the boiling point of Al is lower than its adiabatic flame temperature, post-ignition Al nanoparticles mostly undergo combustion in the vapor phase which leads to their high reactivity in absence of any solid state mass transfer limitation. There are two competing theories between the pre-ignition oxidation mechanism of Al nanoparticles. In Al nanoparticles the core Al melts at ~900 K,

whereas the amorphous Al_2O_3 shell also undergoes phase transformation and recrystallization at ~850 K, resulting in the creation of physical voids or cracks in Al_2O_3 shell. One of the theories suggests that the cracking of the shell facilitates the inward diffusion of gas phase oxygen through the pervious oxide shell to the Al core[31]. The alternate theory suggests that the space charges at the Al-AlO_x interface attracts the Al ions from the molten Al core thereby faciliating the outward diffusion of molten Al through the cracks of the oxide shell which can eventually react with an oxidizing source[32]. Given that both of these theories have been supported by experimental findings and mathematical models, the simultaneous occurrence of both of these processes can be expected during Al-nanoparticle. Hence, there is a scope to tune the onset of Al nanoparticle oxidation by manipulating the sequence of these processes. While working on this dissertation, I have found a way to achieve this by in-situ stressing of the Al-AlO_x interface through thermochemical shock, which facilitates condensed phase migration of Al-ions towards the particle surface (chapter 5).

I have coated the surface of Al nanoparticles with tetrammonium copper nitrate/TACN ($Cu(NH_3)_4(NO_3)_2$) which undergoes exothermic decomposition leading to CuO as the final product, in order to exploit the heat generated during the decomposition reaction to manipulate the microsctructure of the Al-AlO_x interface. On heating, molten TACN wets the surface of the Al-nanoparticles simultaneously releasing NH_3 and NO_x gases, along with heating and crystallization of CuO on the Al-nanoparticle surface. The heat generated from the TACN also facilitates such ion migration, resulting in corrugations and non-uniformities in the thickness of the AlO_x shell which also induces a net tensile

strain on the Al-core as observed through transmission electron microscopy and X-ray diffraction analysis (Figure 1-5 (a)). Usually, the reaction between Al and typical metal oxide based oxidzer like CuO is initiated by the decomposition of the oxidizer to gas phase O_2 and then the gas phase O_2 diffuses and reacts with the Al. However, in the case of the TACN coated Al nanoparticles, the non-uniformities in the thickness of the oxide shell, facilitates faster Al-ion migration through the thinner regions of the shell which can diffuse out and react with the crystallized CuO to initiate a condensed phase ignition process[63].

Another way to tune the reactivitity of energetic composites containing metal nanoparticles as fuels and metal oxide nanoparticles as solid-state oxidizers is to arrange the fuel and oxiddizer nanoparticles in separate alternating layers in the form of a laminate architechture (Figure 1-5 (b)). The thickness of the layers can be varied to control the mixing length between the fuel and the oxidizer, which can be used as a module to control the flame propagation rate. With increasing layer thickness, the O_2 diffusion length from metal oxide layer to metal layer increases, thereby reducing the concentration gradient of O_2, eventully decreasing the flame progation rate. In order to demonstrate this concept, I have fabricated free-standing Al/CuO nanoparticle laminates using a direct ink writing approach with the ink consistig of relatively insignificant amount of polymer. Through cross-sectional optical macro- and micro-scopic imaging and pyrometry, it has been shown quantitatively how the burn rate can be altered by changing the layer thicknesses of the fuel and oxidizer in the printed laminates from ~10 to ~100 μm. Numerical simulations of the heat and mass transport processes are able to reproduce the spatio-temporal profile of the reaction fronts. Through the model it has been found that in Al/CuO particle-based

laminates, the lateral O_2 diffusion rate from CuO to the Al layer appears to be rate-limiting. The finger-like profiles appear due to the combined effects from the faster propagation of the interfacial reaction over that of the bulk, as well as the thermal diffusivity differences between the Al/CuO layers. Interestingly there is no evidence of interlayer mixing of particles in the inspected post-combustion product. This is the first attempt on imaging of interface reactions in nanoparticle laminates and it provides a valuable testbed for probing mechanisms and validating models[64].

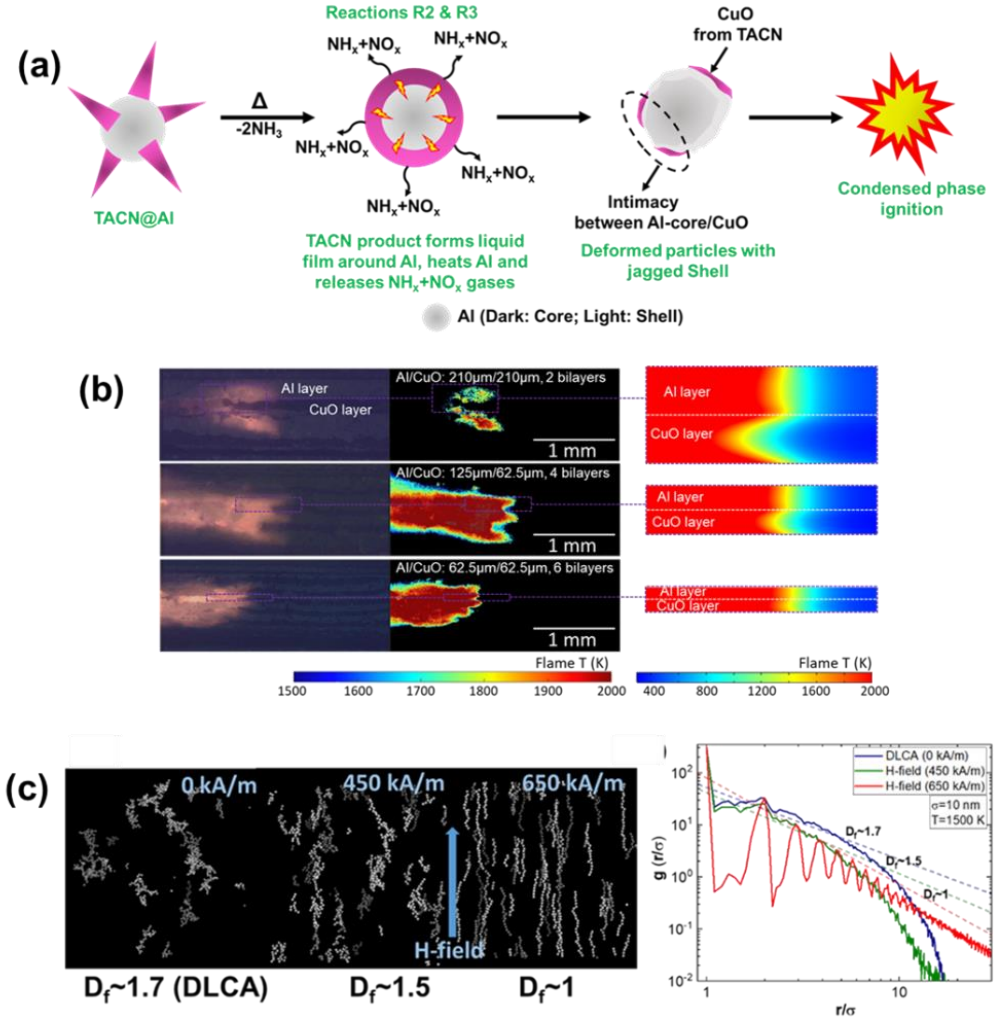

Figure 1-5 (a) *In situ* stressing of Al particles by TACN decomposition on its surface leads to its condensed phase ignition[63]. (b) Direct ink writing of nanoparticulate laminates of Al/CuO for the purpose of architecture driven tuning of elecrgy release rates[64]. (c) Tuning the fractal dimension of superparamagnetic aerosol particle aggregates in free-molecular regime by external magnetic fields[65]. Such nanoparticle aggregates with alternative mesostructural features can be used as precursors for incorporating mesostructure controlled oxide particle aggregates in nanoenergetic composites (*Reproduced with permission from American Chemical Society and Elsevier*)

In a parallel attempt, while synthesizing metal nanoparticles by evaporation and condenstation of metal vapor from an electromagnetically levitated hot metal droplet, I along with my collaborators found that the aggregate structure of ferromagnetic metal nanoparticles (Fe, Ni) is drastically different than that of diamgentic nanoparticles (Cu) obatined by the same method. Unlike liquid phase colloidal assembly, significantly changing the structure of fractal aggregates in the aerosol phase at high temperatures when the particle size is significantly smaller than the medium mean free path is considered impractical. The aggregate structure of the obtained Cu nanoparticles matches with the structure of aerosol difflusion limited cluster aggregates (DLCA) having the universal fractal dimension D_f ~1.8. However, the obatined Fe and Ni particle aggregates had a linear shape with D_f ~1. By perofrming a hybrid ensemble/cluster-cluster aggregation Monte Carlo simulation, I have shown that the aggregate structure transition is dependent on the primary particle sizes, temperature and applied field strength (Figure 1-5 (c)). Both electric and magnetic fields can induce dipole moments in ferroelectic and ferromagentic particles, and such particles with induced dipole moments should interact though directional attractive and repulsive forces, which will lead to their structural transition from DLCA, that form during particle collisions from random directions. However, I have demonstrated that the threshold magnetic field strength required to linearly assemble 10-500 nm particle sizes are practically achievable whereas the electric field required to assemble sub-100 nm particles are beyond the breakdown strength of most gases. A comparison between the simulated coagulation time-scales with the estimated magnetization time-scales of the primary particles along with oscillation time period of the magnetic field shows that sub-

50 nm superparamagnetic primary particles can be magnetized and assembled at any temperature, while below the Curie temperature ferromagnetic particles of all sizes can be magnetized and assembled, given the applied field is higher than the threshold[65]. Since oxides of Fe and Ni are good solid state oxidizers for energetic systems, one can use this technique control the mesoscale architechture of the oxidizer in metal-metal oxide based nanoenergetic composites, and investigate its effect on the reaction and heat generation rate. However, this idea will need more experimental efforts to be realizable for practical applications. Hence, chapters 5-7, presents findings on different methods to alter the nano-micro-meso scale architechture of metal-metal oxide based nanoenergetic composites and the impact of such structural changes on their energy release rates.

1.5.3 External stimuli driven tuning of combustion through electrochemistry and electromagnetic waves

One of the major problems with condensed phase fuels is that their bulk storage and transportation always have the potential to create unintended fire and explosion. Since, combustion is a self-sustaining phenomenon, the combustion of these flammable fuels can only be stopped by the removal of the oxidizing source from the vicinity of the fuel. Chapter 8 presents a potentially seminal contribution, where I have shown that a flammability of an inherently non-flammable condensed phase fuel source can be dynamically manipulated enabling (a) safe storage of the non-flammable fuel source (b) electrochemically generating inflammable gas phase fuel species from the fuel source for combustion and energy generation (c) switch off the genration of the gas phase fuel species to extinguish the flame by removing the applied electrical bias. This approach has been

demonstrated on an imidazolinium based room temperature ionic liquid (RTIL). Although it has a high enthalpy of oxidation, its insignificant volatility makes it non-flammable. Through *in situ time-of-flight mass spectrometry* and high-speed optical imaging, I have demonstrated that the RTIL can be electrolyzed to generate gas phase imidazolinium based free radicals which are released at ~ms time-scales and can participate in the combustion reaction either directly as radicals or as gas phase imidazole dimers. Removing the voltage bias, turns off the generation of these gas phase fuels, hence turning off the combustion (Figure 1-6 (a)). This approach presents a paradigm shift, offering the potential to make a 'safe fuel' and alternatively a simple electrochemically driven fuel metering scheme and hence lot of potential future investigations can be performed on these systems.

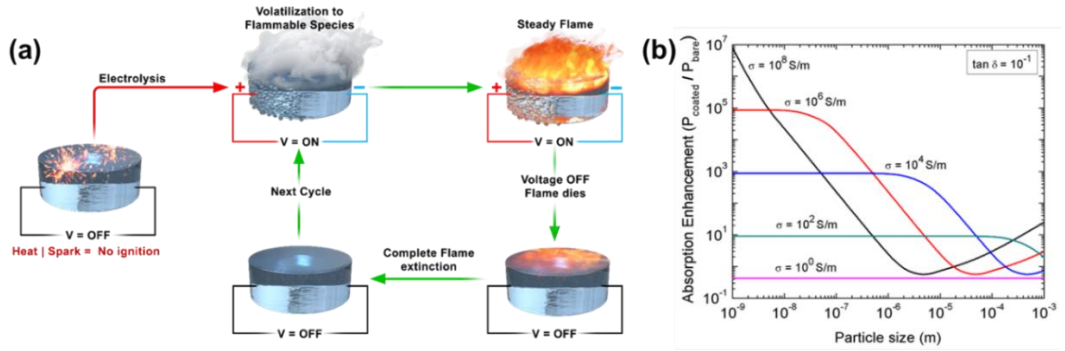

Figure 1-6 (a) Concept of flammability switching of room temperature ionic liquids. (b) Benchmark model for microwave absorption by core-shell metals and metal oxides important as fuel and oxidizers in energetic materials[66] (*Reproduced with permission from Nature and Elsevier*)

Heat delivery and transfer plays a major role in particulate metal based energetic materials for propulsion systems. Microwave frequencies are highly attractive for heat deliverance to energetic materials in two aspects: i) Heat deliverance through physical contact (e.g. joule heated wire), always heats particles from surface to center, leading to

hotter regions near the surface, causing non-uniform heating and hence non-uniform reaction propagation. However, microwave absorption will cause uniform heating of the solid particles making them to uniformly participate in the energetic reaction. ii) For spatially confining the combustion of solid propellants, it is essential to spatially confine the ignition zone by localized heating. As IR frequencies are absorbed by the polymer binder, a localized heating of propellant grains cannot be achieved by IR radiation. However, microwave radiation will only be selectively absorbed by certain metal oxide particles, which can be used as sensitizers for localized heating of the desired regions of the solid-state propellant which can potentially confine the ignition and combustion zones. Hence, chapter 9 presents a Mie light scattering theory-based model to benchmark the microwave absorption by sub-micron metal, metal oxide, and metal core-metal oxide shell particles which are relevant as fuels and oxidizers in energetic materials. Through this model, I have demonstrated that for highly conducting particles coated with a material of low conductivity, the electric field absorption depends only on the optical properties, and the volume fraction of the coating (Figure 1-6 (b)). In contrast, magnetic field absorption depends only on the properties of the core which is the same as that of the bare metal. Another finding is that the power absorbed by coated particles via the electric field is maximized when loss tangent, $\tan\delta \sim 1$. A key result of this study is that a thin layer of lossy coating (~15 % of the particle size) on highly conductive particles will significantly enhance (up to a factor of 10^5) both the power absorbed from the E-field and the total power absorbed[66]. According to these calculations, Ti nanoparticles with an inherent TiO_x shell should absorb ~10^2 times more microwave power compared to Al nanoparticles with AlO_x

shell, owing to the different dielectric properties of the shell. This effect has been clearly demonstrated by testing polyvinylidene fluoride-based films containing ~40 wt. % of either Ti nanoparticles or Al nanoparticles. When the same microwave power is applied at the same frequency ~2.45 GHz, the Ti containing films ignited whereas the Al did not[67]. This shows that significant control can be achieved on the heat transfer in energetic materials by selectively incorporating localized regions of microwave absorbers in different regions of a solid-state propellant.

1.6 References

(1) Sun, H.; Zhu, G.; Xu, X.; Liao, M.; Li, Y. Y.; Angell, M.; Gu, M.; Zhu, Y.; Hung, W. H.; Li, J.; Kuang, Y.; Meng, Y.; Lin, M. C.; Peng, H.; Dai, H. A Safe and Non-Flammable Sodium Metal Battery Based on an Ionic Liquid Electrolyte. *Nature Communications 2019 10:1* **2019**, *10* (1), 1–11. https://doi.org/10.1038/s41467-019-11102-2.

(2) Li, M.; Lu, J.; Chen, Z.; Amine, K. 30 Years of Lithium-Ion Batteries. *Advanced Materials* **2018**, *30* (33), 1800561. https://doi.org/10.1002/ADMA.201800561.

(3) Schlapbach, L.; Züttel, A. Hydrogen Storage Materials for Mobile Applications. *Nature* **2001**, *414* (November), 353–358. https://doi.org/10.1038/35104634.

(4) Demirci, U. B.; Miele, P. Sodium Borohydride versus Ammonia Borane, in Hydrogen Storage and Direct Fuel Cell Applications. *Energy Environ Sci* **2009**, *2* (6), 627–637. https://doi.org/10.1039/b900595a.

(5) Lencer, D.; Salinga, M.; Grabowski, B.; Hickel, T.; Neugebauer, J.; Wuttig, M. A Map for Phase-Change Materials. *Nature Materials 2008 7:12* **2008**, *7* (12), 972–977. https://doi.org/10.1038/nmat2330.

(6) Da, Y.; Xuan, Y.; Teng, L.; Zhang, K.; Liu, X.; Ding, Y. Calcium-Based Composites for Direct Solar-Thermal Conversion and Thermochemical Energy Storage. *Chemical Engineering Journal* **2020**, *382*, 122815. https://doi.org/10.1016/J.CEJ.2019.122815.

(7) Zachariah, M. R. NanoEnergetics: Hype, Reality and Future. *Propellants, Explosives, Pyrotechnics* **2013**, *38* (1), 7. https://doi.org/10.1002/prep.201380131.

(8) Sullivan, K.; Zachariah, M. Simultaneous Pressure and Optical Measurements of Nanoaluminum Thermites: Investigating the Reaction Mechanism. *J Propuls Power* **2010**, *26* (3), 467–472. https://doi.org/10.2514/1.45834.

(9) Wang, H.; Kline, D. J.; Rehwoldt, M. C.; Zachariah, M. R.; Zachariah, M. R. Carbon Fibers Enhance the Propagation of High Loading Nanothermites: In Situ Observation of Microscopic Combustion. *ACS Appl Mater Interfaces* **2021**, *13* (26), 30504–30511. https://doi.org/10.1021/ACSAMI.1C02911/SUPPL_FILE/AM1C02911_SI_003.PDF.

(10) Wang, X.; Wu, T.; Zachariah, M. R. Doped Perovskites to Evaluate the Relationship between Fuel-Oxidizer Thermite Ignition and Bond Energy, Electronegativity, and Oxygen Vacancy. *Journal of Physical Chemistry C* **2017**, *121* (1), 147–152. https://doi.org/10.1021/ACS.JPCC.6B10571/SUPPL_FILE/JP6B10571_SI_001.PDF.

(11) Young, G.; Wang, H.; Zachariah, M. R. Application of Nano-Aluminum/Nitrocellulose Mesoparticles in Composite Solid Rocket Propellants. *Propellants, Explosives, Pyrotechnics* **2015**. https://doi.org/10.1002/prep.201500020.

(12) Young, G.; Wang, H.; Zachariah, M. R. Application of Nano-Aluminum/Nitrocellulose Mesoparticles in Composite Solid Rocket Propellants. *Propellants, Explosives, Pyrotechnics* **2015**, *40* (3), 413–418. https://doi.org/10.1002/prep.201500020.

(13) Yan, S.; Jian, G.; Zachariah, M. R. Electrospun Nanofiber-Based Thermite Textiles and Their Reactive Properties. *ACS Appl Mater Interfaces* **2012**, *4* (12), 6432–6435. https://doi.org/10.1021/am3021125.

(14) Wang, H.; Kline, D. J.; Biswas, P.; Zachariah, M. R. Connecting Agglomeration and Burn Rate in a Thermite Reaction: Role of Oxidizer Morphology. *Combust Flame* **2021**, *231*, 111492. https://doi.org/10.1016/J.COMBUSTFLAME.2021.111492.

(15) Wang, Y.; Wang, H.; Xu, F.; Ghildiyal, P.; Zachariah, M. R. Effect of Alkali Metal Perchlorate and Iodate Type on Boron Ignition: The Role of Oxidizer Phase Change. *Chemical Engineering Journal* **2022**, *446*, 136786. https://doi.org/10.1016/J.CEJ.2022.136786.

(16) Li, X.; Guerieri, P.; Zhou, W.; Huang, C.; Zachariah, M. R. Direct Deposit Laminate Nanocomposites with Enhanced Propellent Properties. *ACS Appl Mater Interfaces* **2015**, *7* (17), 9103–9109. https://doi.org/10.1021/ACSAMI.5B00891/SUPPL_FILE/AM5B00891_SI_001.PDF.

(17) Chowdhury, S.; Sullivan, K.; Piekiel, N.; Zhou, L.; Zachariah, M. R. Diffusive vs Explosive Reaction at the Nanoscale. *The Journal of Physical Chemistry C* **2010**, *114* (20), 9191–9195. https://doi.org/10.1021/jp906613p.

(18) Wagner, B.; Ghildiyal, P.; Biswas, P.; Chowdhury, M.; Zachariah, M. R.; Mangolini, L.; Wagner, B.; Mangolini, L.; Ghildiyal, P.; Biswas, P.; Chowdhury, M.; Zachariah, M. R. In-Flight Synthesis of Core–Shell Mg/Si–SiOx Particles with Greatly Reduced Ignition Temperature. *Adv Funct Mater* **2023**, 2212805. https://doi.org/10.1002/ADFM.202212805.

(19) Jian, G.; Chowdhury, S.; Sullivan, K.; Zachariah, M. R. Nanothermite Reactions: Is Gas Phase Oxygen Generation from the Oxygen Carrier an Essential Prerequisite to Ignition? *Combust Flame* **2013**, *160* (2), 432–437. https://doi.org/10.1016/J.COMBUSTFLAME.2012.09.009.

(20) Granier, J. J.; Pantoya, M. L. Laser Ignition of Nanocomposite Thermites. *Combust Flame* **2004**, *138* (4), 373–383. https://doi.org/10.1016/j.combustflame.2004.05.006.

(21) Ghildiyal, P.; Ke, X.; Biswas, P.; Nava, G.; Schwan, J.; Xu, F.; Kline, D. J.; Wang, H.; Mangolini, L.; Zachariah, M. R. Silicon Nanoparticles for the Reactivity and Energetic Density Enhancement of Energetic-Biocidal Mesoparticle Composites. *ACS Appl Mater Interfaces* **2021**, *13* (1), 458–467. https://doi.org/10.1021/ACSAMI.0C17159/SUPPL_FILE/AM0C17159_SI_001.PDF.

(22) Xu, J.; Tai, Y.; Ru, C.; Dai, J.; Shen, Y.; Ye, Y.; Shen, R.; Fu, S. Characteristic of Energetic Semiconductor Bridge Based on Al/MoOx Energetic Multilayer Nanofilms with Different Modulation Periods. *J Appl Phys* **2017**, *121* (11), 113301. https://doi.org/10.1063/1.4978371/1.4978371.MM.ORIGINAL.V8.MOV.

(23) Rehwoldt, M. C.; Yang, Y.; Wang, H.; Holdren, S.; Zachariah, M. R. Ignition of Nanoscale Titanium/Potassium Perchlorate Pyrotechnic Powder: Reaction Mechanism Study. *Journal of Physical Chemistry C* **2018**, *122* (20), 10792–10800. https://doi.org/10.1021/acs.jpcc.8b03164.

(24) Jiang, Y.; Dincer Yilmaz, N. E.; Barker, K. P.; Baek, J.; Xia, Y.; Zheng, X. Enhancing Mechanical and Combustion Performance of Boron/Polymer Composites via Boron Particle Functionalization. *ACS Appl Mater Interfaces* **2021**, *13* (24), 28908–28915. https://doi.org/10.1021/ACSAMI.1C06727/ASSET/IMAGES/LARGE/AM1C06727_0008.JPEG.

(25) Sun, Y.; Ren, H.; Jiao, Q.; Schoenitz, M.; Dreizin, E. L. Oxidation, Ignition and Combustion Behaviors of Differently Prepared Boron-Magnesium Composites. *Combust Flame* **2020**, *221*, 11–19. https://doi.org/10.1016/J.COMBUSTFLAME.2020.07.022.

(26) Zhao, W.; Wang, H.; Kline, D. J.; Wang, X.; Wu, T.; Xu, J.; Ren, H.; Zachariah, M. R. Influence of Titanium Addition on Performance of Boron-Based Thermites. *Chemical Engineering Journal* **2022**, *438*, 134837. https://doi.org/10.1016/J.CEJ.2022.134837.

(27) Agarwal, P. P. K.; Matsoukas, T. Synthesis and Oxidation Chemistry of Highly Energetic Boron/Aluminum/Magnesium Composites. *FirePhysChem* **2023**. https://doi.org/10.1016/J.FPC.2023.03.001.

(28) Ghildiyal, P.; Biswas, P.; Herrera, S.; Xu, F.; Alibay, Z.; Wang, Y.; Wang, H.; Abbaschian, R.; Zachariah, M. R. Vaporization-Controlled Energy Release Mechanisms Underlying the Exceptional Reactivity of Magnesium Nanoparticles. *ACS Appl Mater Interfaces* **2022**, *14* (15), 17164–17174.

https://doi.org/10.1021/ACSAMI.1C22685/ASSET/IMAGES/MEDIUM/AM1C22685_M002.GIF.

(29) Xu, F.; Nava, G.; Biswas, P.; Dulalia, I.; Wang, H.; Alibay, Z.; Gale, M.; Kline, D. J.; Wagner, B.; Mangolini, L.; Zachariah, M. R. Energetic Characteristics of Hydrogenated Amorphous Silicon Nanoparticles. *Chemical Engineering Journal* **2022**, *430*, 133140. https://doi.org/10.1016/J.CEJ.2021.133140.

(30) Zhao, W.; Wang, X.; Wang, H.; Wu, T.; Kline, D. J.; Rehwoldt, M.; Ren, H.; Zachariah, M. R. Titanium Enhanced Ignition and Combustion of Al/I2O5 Mesoparticle Composites. *Combust Flame* **2020**, *212*, 245–251. https://doi.org/10.1016/J.COMBUSTFLAME.2019.04.049.

(31) Trunov, M. A.; Schoenitz, M.; Zhu, X.; Dreizin, E. L. Effect of Polymorphic Phase Transformations in Al2O3 Film on Oxidation Kinetics of Aluminum Powders. *Combust Flame* **2005**, *140* (4), 310–318. https://doi.org/10.1016/J.COMBUSTFLAME.2004.10.010.

(32) Henz, B. J.; Hawa, T.; Zachariah, M. R. On the Role of Built-in Electric Fields on the Ignition of Oxide Coated Nanoaluminum: Ion Mobility versus Fickian Diffusion. *J Appl Phys* **2010**, *107* (2), 024901. https://doi.org/10.1063/1.3247579.

(33) Rai, A.; Park, K.; Zhou, L.; Zachariah, M. R. Understanding the Mechanism of Aluminium Nanoparticle Oxidation. *http://dx.doi.org/10.1080/13647830600800686* **2010**, *10* (5), 843–859. https://doi.org/10.1080/13647830600800686.

(34) Paidi, V. K.; Lee, B. H.; Ahn, D.; Kim, K. J.; Kim, Y.; Hyeon, T.; Lee, K. S. Oxygen-Vacancy-Driven Orbital Reconstruction at the Surface of TiO2Core-Shell Nanostructures. *Nano Lett* **2021**, *21* (19), 7953–7959. https://doi.org/10.1021/ACS.NANOLETT.1C01995/SUPPL_FILE/NL1C01995_SI_001.PDF.

(35) Jacob, R. J.; Hill, K. J.; Yang, Y.; Pantoya, M. L.; Zachariah, M. R. Pre-Stressing Aluminum Nanoparticles as a Strategy to Enhance Reactivity of Nanothermite Composites. *Combust Flame* **2019**, *205*, 33–40. https://doi.org/10.1016/J.COMBUSTFLAME.2019.03.024.

(36) Sullivan, K. T.; Piekiel, N. W.; Wu, C.; Chowdhury, S.; Kelly, S. T.; Hufnagel, T. C.; Fezzaa, K.; Zachariah, M. R. Reactive Sintering: An Important Component in the Combustion of Nanocomposite Thermites. *Combust Flame* **2012**, *159* (1), 2–15. https://doi.org/10.1016/J.COMBUSTFLAME.2011.07.015.

(37) Wang, H.; Kline, D. J.; Zachariah, M. R. In-Operando High-Speed Microscopy and Thermometry of Reaction Propagation and Sintering in a Nanocomposite. *Nature*

Communications 2019 10:1 **2019**, *10* (1), 1–8. https://doi.org/10.1038/s41467-019-10843-4.

(38) Wang, H.; Jian, G.; Egan, G. C.; Zachariah, M. R. Assembly and Reactive Properties of Al/CuO Based Nanothermite Microparticles. *Combust Flame* **2014**, *161* (8), 2203–2208. https://doi.org/10.1016/J.COMBUSTFLAME.2014.02.003.

(39) Wang, H.; Shen, J.; Kline, D. J.; Eckman, N.; Agrawal, N. R.; Wu, T.; Wang, P.; Zachariah, M. R.; Wang, H.; Zachariah, M. R.; Shen, J.; Kline, D. J.; Eckman, N.; Agrawal, N. R.; Wu, T.; Wang, P. Direct Writing of a 90 Wt% Particle Loading Nanothermite. *Advanced Materials* **2019**, *31* (23), 1806575. https://doi.org/10.1002/ADMA.201806575.

(40) Wang, H.; Rehwoldt, M.; Kline, D. J.; Wu, T.; Wang, P.; Zachariah, M. R. Comparison Study of the Ignition and Combustion Characteristics of Directly-Written Al/PVDF, Al/Viton and Al/THV Composites. *Combust Flame* **2019**, *201*, 181–186. https://doi.org/10.1016/j.combustflame.2018.12.031.

(41) Wang, H.; Kline, D. J.; Rehwoldt, M.; Wu, T.; Zhao, W.; Wang, X.; Zachariah, M. R. Architecture Can Significantly Alter the Energy Release Rate from Nanocomposite Energetics. *ACS Appl Polym Mater* **2019**, *1* (5), 982–989. https://doi.org/10.1021/ACSAPM.9B00016/ASSET/IMAGES/LARGE/AP-2019-00016C_0008.JPEG.

(42) Zapata, J.; Nicollet, A.; Julien, B.; Lahiner, G.; Esteve, A.; Rossi, C. Self-Propagating Combustion of Sputter-Deposited Al/CuO Nanolaminates. *Combust Flame* **2019**, *205*, 389–396. https://doi.org/10.1016/J.COMBUSTFLAME.2019.04.031.

(43) Delisio, J. B.; Hu, X.; Wu, T.; Egan, G. C.; Young, G.; Zachariah, M. R. Probing the Reaction Mechanism of Aluminum/Poly(Vinylidene Fluoride) Composites. *Journal of Physical Chemistry B* **2016**, *120* (24), 5534–5542. https://doi.org/10.1021/ACS.JPCB.6B01100/SUPPL_FILE/JP6B01100_SI_001.PDF.

(44) Rehwoldt, M. C.; Wang, Y.; Xu, F.; Ghildiyal, P.; Zachariah, M. R. High-Temperature Interactions of Metal Oxides and a PVDF Binder. *ACS Appl Mater Interfaces* **2022**, *14* (7), 8938–8946. https://doi.org/10.1021/ACSAMI.1C20938/SUPPL_FILE/AM1C20938_SI_001.PDF.

(45) Kline, D. J.; Rehwoldt, M. C.; Wang, H.; Eckman, N. E.; Zachariah, M. R. Why Does Adding a Poor Thermal Conductor Increase Propagation Rate in Solid Propellants? *Appl Phys Lett* **2019**, *115* (11), 114101. https://doi.org/10.1063/1.5113612.

(46) Rossi, C. Engineering of Al/CuO Reactive Multilayer Thin Films for Tunable Initiation and Actuation. *Propellants, Explosives, Pyrotechnics* **2019**, *44* (1), 94–108. https://doi.org/10.1002/PREP.201800045.

(47) Tichtchenko, E.; Estève, A.; Rossi, C. Modeling the Self-Propagation Reaction in Heterogeneous and Dense Media: Application to Al/CuO Thermite. *Combust Flame* **2021**, *228*, 173–183. https://doi.org/10.1016/J.COMBUSTFLAME.2021.01.040.

(48) Salvagnac, L.; Assie-Souleille, S.; Rossi, C. Layered Al/CuO Thin Films for Tunable Ignition and Actuations. *Nanomaterials* **2020**. https://doi.org/10.3390/nano10102009.

(49) Bahrami, M.; Taton, G.; Conédéra, V.; Salvagnac, L.; Tenailleau, C.; Alphonse, P.; Rossi, C. Magnetron Sputtered Al-CuO Nanolaminates: Effect of Stoichiometry and Layers Thickness on Energy Release and Burning Rate. *Propellants, Explosives, Pyrotechnics* **2014**, *39* (3), 365–373. https://doi.org/10.1002/PREP.201300080.

(50) Young, G.; Sullivan, K.; Zachariah, M. R.; Yu, K. Combustion Characteristics of Boron Nanoparticles. *Combust Flame* **2009**, *156* (2), 322–333. https://doi.org/10.1016/J.COMBUSTFLAME.2008.10.007.

(51) Simagina, V. I.; Vernikovskaya, N. V.; Komova, O. V.; Kayl, N. L.; Netskina, O. V.; Odegova, G. V. Experimental and Modeling Study of Ammonia Borane-Based Hydrogen Storage Systems. *Chemical Engineering Journal* **2017**. https://doi.org/10.1016/j.cej.2017.05.005.

(52) Staubitz, A.; Robertson, A. P. M.; Manners, I. Ammonia-Borane and Related Compounds as Dihydrogen Sources. *Chem Rev* **2010**, *110* (7), 4079–4124. https://doi.org/10.1021/cr100088b.

(53) Stowe, A. C.; Shaw, W. J.; Linehan, J. C.; Schmid, B.; Autrey, T. In Situ Solid State 11B MAS-NMR Studies of the Thermal Decomposition of Ammonia Borane: Mechanistic Studies of the Hydrogen Release Pathways from a Solid State Hydrogen Storage Material. *Physical Chemistry Chemical Physics* **2007**, *9* (15), 1831–1836. https://doi.org/10.1039/b617781f.

(54) Heldebrant, D. J.; Karkamkar, A.; Hess, N. J.; Bowden, M.; Rassat, S.; Feng, Z.; Rappe, K.; Autrey, T. The Effects of Chemical Additives on the Induction Phase in Solid-State Thermal Decomposition of Ammonia Borane. *Chemistry of Materials* **2008**, *20* (16), 5332–5336. https://doi.org/10.1021/cm801253u.

(55) Biswas, P.; Ghildiyal, P.; Kwon, H.; Wang, H.; Alibay, Z.; Xu, F.; Wang, Y.; Wong, B. M.; Zachariah, M. R. Rerouting Pathways of Solid-State Ammonia Borane Energy Release. *The Journal of Physical Chemistry C* **2021**, *126* (1), 48–57. https://doi.org/10.1021/ACS.JPCC.1C08985.

(56) Biswas, P.; Wang, Y.; Herrera, S.; Ghildiyal, P.; Zachariah, M. R. Catalytic Cleavage of the Dative Bond of Ammonia Borane by Polymeric Carbonyl Groups for

Enhanced Energy Generation. *Chemistry of Materials* **2022**, *35*, 963. https://doi.org/10.1021/ACS.CHEMMATER.2C02684/ASSET/IMAGES/LARGE/CM2C02684_0007.JPEG.

(57) Agarwal, P. P. K.; Matsoukas, T. Nanoenergetic Materials: Enhanced Energy Release from Boron by Aluminum Nanoparticle Addition. *ACS Omega* **2022**, *7* (30), 26560–26565. https://doi.org/10.1021/ACSOMEGA.2C02691/ASSET/IMAGES/LARGE/AO2C02691_0006.JPEG.

(58) Agarwal, P. P. K.; Matsoukas, T. Enhanced Energetic Performance of Aluminum Nanoparticles by Plasma Deposition of Perfluorinated Nanofilms. *ACS Appl Mater Interfaces* **2022**, *14* (30), 35255–35264. https://doi.org/10.1021/ACSAMI.2C08300/ASSET/IMAGES/LARGE/AM2C08300_0012.JPEG.

(59) Agarwal, P. P. K.; Matsoukas, T. Low-Temperature Cost-Effective Synthesis of MgB2for Energetic Applications. *ACS Appl Energy Mater* **2022**, *5* (12), 15310–15315. https://doi.org/10.1021/ACSAEM.2C02946/ASSET/IMAGES/LARGE/AE2C02946_0007.JPEG.

(60) Agarwal, P. P. K.; Jensen, D.; Chen, C. H.; Rioux, R. M.; Matsoukas, T. Surface-Functionalized Boron Nanoparticles with Reduced Oxide Content by Nonthermal Plasma Processing for Nanoenergetic Applications. *ACS Appl Mater Interfaces* **2021**, *13* (5), 6844–6853. https://doi.org/10.1021/ACSAMI.0C20825/ASSET/IMAGES/LARGE/AM0C20825_0012.JPEG.

(61) Agarwal, P. P. K.; Jensen, D.; Chen, C.-H.; Rioux, R. M.; Matsoukas, T. Synthesis and Characterization of Magnesium/Boron Solid Solutions for Energetic Applications. *ACS Appl Energy Mater* **2022**, *5* (6), 6716–6723. https://doi.org/10.1021/ACSAEM.2C00312.

(62) Ghildiyal, P.; Xu, F.; Rojas, A.; Wang, Y.; Chowdhury, M.; Biswas, P.; Herrera, S.; Abbaschian, R.; Zachariah, M. R. Magnesium-Enhanced Reactivity of Boron Particles: Role of Mg/B2O3 Exothermic Surface Reactions. *Energy and Fuels* **2022**. https://doi.org/10.1021/ACS.ENERGYFUELS.2C02347/ASSET/IMAGES/LARGE/EF2C02347_0008.JPEG.

(63) Biswas, P.; Xu, F.; Ghildiyal, P.; Zachariah, M. R. In-Situ Thermochemical Shock-Induced Stress at the Metal/Oxide Interface Enhances Reactivity of Aluminum Nanoparticles. *ACS Appl Mater Interfaces* **2022**, *14* (23), 26782–26790. https://doi.org/10.1021/ACSAMI.2C05412.

(64) Wang, H.; Biswas, P.; Zachariah, M. R. Direct Imaging and Simulation of the Interface Reaction of Metal/Metal Oxide Nanoparticle Laminates. *Journal of Physical Chemistry C* **2022**, *126* (20), 8684–8691. https://doi.org/10.1021/ACS.JPCC.2C00156/SUPPL_FILE/JP2C00156_SI_005.MP4.

(65) Biswas, P.; Ghildiyal, P.; Mulholland, G. W.; Zachariah, M. R. Modelling and Simulation of Field Directed Linear Assembly of Aerosol Particles. *J Colloid Interface Sci* **2021**, *592*, 195–204. https://doi.org/10.1016/J.JCIS.2021.02.050.

(66) Biswas, P.; Mulholland, G. W.; Rehwoldt, M. C.; Kline, D. J.; Zachariah, M. R. Microwave Absorption by Small Dielectric and Semi-Conductor Coated Metal Particles. *J Quant Spectrosc Radiat Transf* **2020**, *247*, 106938. https://doi.org/10.1016/j.jqsrt.2020.106938.

(67) Kline, D. J.; Rehwoldt, M. C.; Turner, C. J.; Biswas, P.; Mulholland, G. W.; McDonnell, S. M.; Zachariah, M. R. Spatially Focused Microwave Ignition of Metallized Energetic Materials. *J Appl Phys* **2020**, *127* (5). https://doi.org/10.1063/1.5134089.

2 Experimental and computational methods

2.1 In situ characterization of condensed phase thermochemical and electrochemical reactions through time-of-flight mass spectrometry

A significant part of the research in this dissertation is based on *in situ* time and (or) temperature resolved characterizations of thermochemical and electrochemical reactions of energetic composites. As explained in Figure 2-1, the time-of-flight mass spectrometer consists of a sample probe on which condensed phase sample such as nanoparticles, polymers, and viscous ionic liquids can be coated by drop-casting and the sample coated on the sample probe is vaporized or gasified either by a heating element or electrochemically via application of an electrical bias. The vapor/gas produced are ionized by an electron gun generally operated at ~70 eV. As Figure 2-1 shows, this gasification and ionization is performed in between two charged plates, A1 and A2. Initially, both of the plates are kept at ground. For a time-resolved measurement, a voltage pulse of -200 V is applied on A2 generally at every ~0.1 ms over a period of ~10 ms, so that the generated ions can be sampled at every ~0.1 ms and a spectra can be obtained with the same resolution. The frequency of this pulse and the time period of sampling can be adjusted based on the intended time scale of the measured phenomena. When a negative voltage is applied to A2, A2 attracts the positively charged ions towards itself from the generated ion cloud. A constant -1500 V is maintained at the accelerator plate A3 which applies a constant force on the ions to accelerate through the time-of-flight tube. Since, the ions have different accelerations based on their masses, while moving through the time-of-flight tube they segregate based on their different accelerations causing the smaller ions to move ahead

and reach the detector earlier than the larger fragments. Hence, based on the time-of-flight the mass to charge ratio (m/z) of respective ions can be identified and a spectrum can be obtained. A parabolic calibration curve, $\frac{m}{z} = at^2 + bt + c$, t is the time-of-flight, is used as reference to evaluate the m/z values of the ions generated during the measurement based on their time-of-flight. The constants a,b, and c are obtained by fitting the time-of-flight of ions of known m/z obtained by gasifying and ionizing a mixture of standard samples, that can generate a large number of known ion fragments over a wide m/z range, such as SF_6, I_2O_5, CuO, TiH_2, Bi_2O_3, Ar and background air. The constant liner voltage of -1500 V is maintained along the walls of the time-of-flight tube to restrict the divergence of the beam. Also there are two steering plates aligned perpendicular to the accelerator plate, out of which one is 1600 V more negatively biased than the other is used to optimize the signal by ensuring that the ion beam follows a straight path.

The sample delivery for the characterization of thermochemical reactions (Figure 2-1 (a)) is performed by coating the condensed phase sample on a thin Pt wire (~75 μm). The Pt wire is resistively pulse heated to ~1500 K with a pulse width of ~3ms at a high heating rate of ~10^5 K/s. The pulse width can be adjusted to adjust the heating rate when required. This thermal probe is popularly termed as a T-jump (temperature jump probe). The high heating rate is necessary to simulate the high temperature fast chemistry occurring during combustion events, as high heating rates are required to activate the ignition and combustion reactions. The temperature of the wire is obtained by monitoring the current across the wire through a magnetic field based current probe. All the data acquisition is performed through a Teledyne Lecroy high frequency oscilloscope. Thus the gas phase

species evolving from the sample are identified by the same time-of-flight assembly. Probing the temperature across the wire with time enables both time and temperature resolved characterization of thermochemical reactions.

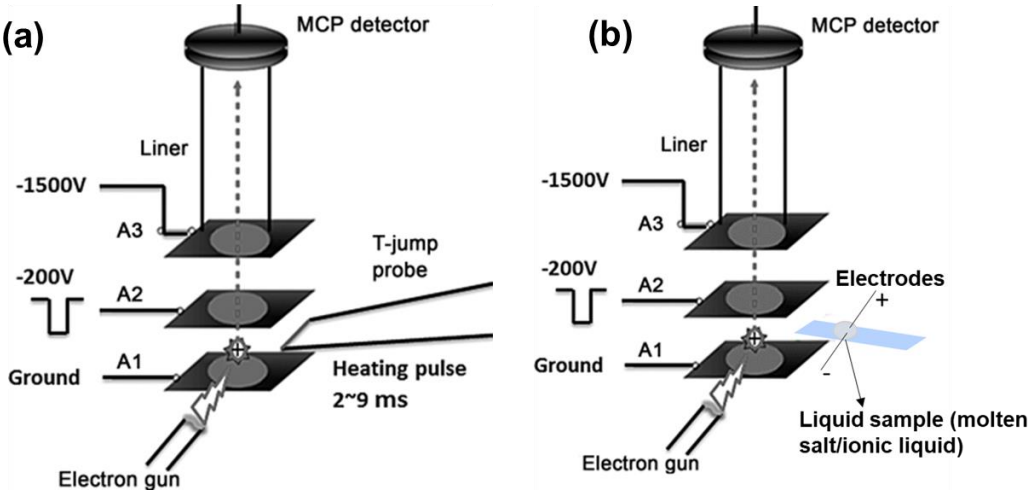

Figure 2-1 In situ characterization of thermochemical (a) and electrochemical (b) reactions through time-of-flight mass spectrometry (*Reproduced in part with permission from Wiley*[1]).

The sample delivery for the characterization of electrochemical reactions is performed by introducing the dropcasted sample coated on a glass coverslip with two Pt wire electrodes (~75 μm) immersed or embedded in the sample as shown in Figure 2-1 (b). The Pt wire electrodes are connected to an external power supply for application of a voltage bias. The cover slip is inserted directly between plates A1 and A2 and the samples are electrochemically stimulated by application of a voltage bias. Time-resolved measurements of the evolving volatile species can be performed using the time-of-flight assembly. The electrochemical component of this system has been primarily developed by me for performing of research involved in this dissertation.

In this regard, it is important to acknowledge the fact that the sample is being directly placed under high vacuum at ~10^{-10} atm. Hence, there are negligible possibilities of secondary gas phase reactions. Additionally, short lived and vapor phase intermediates cannot be detected through other methods such as GC-MS, owing to their rapid condensation rates. Hence, this measurement method enables one to characterize short lived vapor phase intermediates evolving from condensed phase reactions, at ~0.1 ms resolution.

2.2 Ignition temperature measurement

As ignition only occurs at high heating rates, the ignition temperature characterization is performed using the same heating element as that of the T-jump probe described above and the wire temperature is also measured in the same manner. However, in this case, instead of the vacuum chamber of the mass spectrometer, the probe is inserted into a small chamber equipped with gas inlet, purge outlet, and vacuum outlets, which can enable heating of samples under different gaseous environments. When solid state oxidizers are present, typically Ar is used as an inert atmosphere. In absence of oxidizer, a gaseous environment of pure O_2 or air is used. One wall of the chamber is made of quartz, which enables visual observation or optical detection of ignition events. A high-speed Phantom camera is focused on the sample coated on the Pt wire of the T-jump probe through the quartz window. The heating of the Pt wire and the camera are triggered at the same time and the time-delay of the ignition event is obtained from the captured video. Generally, the appearance of more than one bright spot on the sample is denoted as the ignition event, unless otherwise mentioned. From the estimated wire temperature at the

time of the ignition, the ignition temperature can be estimated. In most solid state kinetic or diffusion limited reactions the rate/diffusion constant scales exponentially with temperature (~exp($-\frac{E_a}{k_B T}$). Hence with increase in temperature the overall reaction rate and the exothermic heat generation rate will increase and at a certain temperature the heat generation rate from the reaction will be significantly higher than that of the overall heat dissipation rate. This temperature is basically identified as the ignition temperature and the measurement works on this same principle.

2.3 Combustion cell measurement

The reaction rate measurement during the combustion process requires burn time characterization of a constant mass of sample in a confined volume. Hence, combustion cell or pressure cell measurements are performed to evaluate the combustion reaction rates and the energetic performance of the composites. For the measurement a constant mass of sample is loaded into the cell and the cell is sealed to ensure a constant volume measurement. The cell is equipped with a pressure transducer and an optical cable which measures the pressure and the light intensity over time (Figure 2-2). The cell also has a nichrome wire touching the surface of the sample from top. This wire is resistively heated and the sample is locally ignited from the surface. The locally ignited sample is allowed to self-propagate and the pressure and optical signal during the self-propagating combustion reaction of the sample is acquired over ~ms. The time between the onset to the offset of the optical is registered as the reaction time, whereas the estimated pressure is contributed by both gas generation and also because of vigorous gaseous expansion at high temperatures on heat release from the combustion reactions.

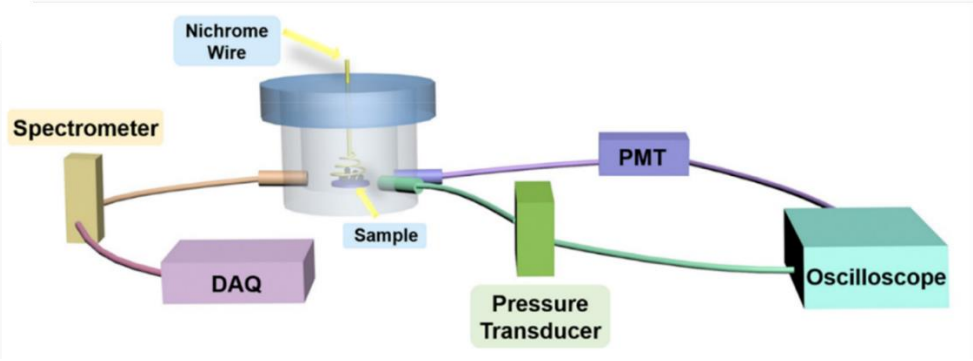

Figure 2-2 Combustion cell setup for pressurization and burn-time measurements (*Reproduced with permission from Elsevier*[2]).

2.4 Off lattice Monte Carlo simulation in Canonical Ensemble to study nanoparticle aggregation in free molecular regime and transition regime

Aerosol nanoparticles typically exist in free-molecular and continuum regime are smaller or comparable to the mean free path of the medium. When the nanoparticles are much smaller than the mean free path of the medium, they follow a ballistic motion travelling in the same direction for longer time-scales. This occurs because they collide with the medium molecules less frequently than when they exist in the transition/continuum regime when they randomly change directions at much shorter time scale, which can be thought of as a random walk model. The random walk model is termed as a diffusive motion (Figure 2-3). In transition regime the transition from ballistic to diffusive motion occurs. The distance by which a nanoparticle will travel before changing direction is known as the persistence length and the probability of the nanoparticle for changing direction is inversely proportional to the persistence length.

Generally, Langevin dynamics simulations are done to simulate these effects assuming for non-interacting hard spheres. Dissipative particle dynamics simulations are used on the other hand for interacting particles. However, such simulations are expensive and are not essential when kinetic information is not required, and the purpose of the simulation is to evaluate the microstructure of nanoparticle aggregates from the most stable microstates. In such cases ensemble-based Monte Carlo simulations with some approximations can be used.

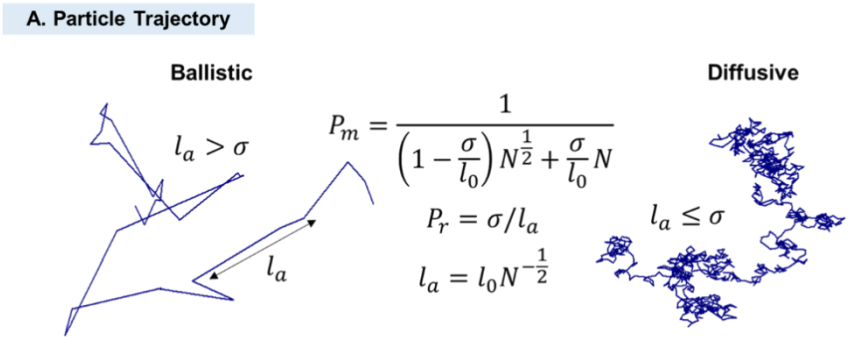

Figure 2-3 Probabilistic equations for simulating ballistic and diffusive trajectories followed by aerosol nanoparticles in free molecular and transition regimes by a Monte Carlo approach (*Reproduced with permission from Elsevier*[3]).

The off-lattice MC simulations for studying nanoparticle aggregation were performed with an initial configuration of N primary particles of size σ placed in a cubic box of size $L = (\frac{N}{10})\sigma$. The simulations initiate with the motion of primary particles in an ensemble. After the appearance of the clusters due to collision and aggregation of the primary particles, movement of the clusters are also included for the remainder of the simulation. At every Monte Carlo step, a particle or an aggregate is chosen at random from the ensemble, and a decision is made on whether the chosen entity will be moved based on

its mobility, imposing the diffusion limitation. The acceptance probability (P_m) of this decision depends inversely on the mobility radius (i.e. smaller aggregates are more likely to move) which is a function of number of primary particles in the aggregate (N) as given by:

$$P_m = \frac{1}{\left(1 - \frac{\sigma}{l_0}\right) N^{\frac{1}{2}} + \frac{\sigma}{l_0} N} \tag{1}$$

The first term in the denominator represents the pure ballistic case when $\sigma \ll l_0$, whereas the second term represents the pure diffusive case when $\sigma = l_0$. The ballistic and diffusive regimes in the trajectory of the moving particle or aggregate is replicated by the fact that the chosen entity will move linearly over a distance of l_a before randomly changing direction under the influence of background gas. This is ensured by making a decision whether the particle or aggregate will keep moving in the same direction or assigned a new direction, determined by the probability $P_r = \sigma / l_a$.

The center of mass of the selected aggregate is displaced by σ in the chosen direction. The move is then accepted or rejected based on an energy test, which compares the total energy due to magnetic interactions in the microstates before and after the move. The system follows the thermodynamics of canonical (NVT) ensemble. Hence, the acceptance probability (P_{NVT}) is:

$$P_{NVT} = \exp\left(-\frac{\Delta U}{k_B T}\right) \tag{2}$$

where $\Delta U = \sum_{final} U_{ij} - \sum_{initial} U_{ij}$, is the difference in net pairwise interaction potentials in the initial and the final states. Once the decision is made to accept the move,

the non-dimensionalized time is incremented by $1/N_t$, where N_t is the total number of entities in the ensemble including both aggregates and isolated primary particles (monomers). The unit of time is given by the characteristic time-scale of m/ξ normalized by the persistence length. When two lone primary particles or primary particles belonging to two different aggregates moves within a center to center distance of $< 1.1\sigma$, they are assumed to have collided and stuck irreversibly. The simulation is run till the number concentration of the monomers decreases to <10 % of the initial value. Periodic boundary conditions with minimum image convention has been considered throughout the simulation.

This simulation has been performed by an in-house C script written by me which treats each cluster as linked-lists for computational efficiency.

2.5 Density functional theory tight binding – molecular dynamics simulations

Density functional theory involves self-consistent charge calculations as the charge density and the energy functional are interdependent on each other. However, solving for large reactive systems by accounting for all the interaction terms comprising the Kohn-Sham energy functional is computationally expensive. Hence, several interatomic potential surfaces such as ReaxFF[4] have been developed over the past decade by empirical fitting of the energy functional to experimental or quantum chemical data, to study reactive systems. However, empirical methods have limited accuracy compared to ab-initio methods and are still computationally expensive. Semi-empirical methods with self-consistent charge calculations such as density functional theory tight binding (DFTB) have relatively higher

accuracy and are also less computationally expensive and can be used for large scale simulation of reactive systems. The energy functional in DFTB is treated in a different manner, in the sense that it is split into three terms (eqn (1)) following a Taylor expansion based on a small perturbation in the charge density $n(r) = n(r) + \delta n$.

$$E_{total} = E_{bandstructure} + E_{Coulombic} + E_{Repulsive} \quad (1)$$

$E_{bandstructure}$ is pre-computed self-consistently from the DFTB Hamiltonian using minimal basis set and represents all the occupied electronic states. The $E_{Coulombic}$ term depends on the long range charge fluctuation and separation of atoms. $E_{Repulsive}$ part containing the ion-ion repulsion and the exchange correlation functional terms which accounts for the bond breaking or formation in the first coordination sphere represents the bonded interactions in the first coordination sphere. Parameters of the $E_{Repulsive}$ part consisting of pairwise and three-body interactions were fitted using the Chebyshev Interaction Polynomial for Efficient Simulation (CHIMES)[4,5] training set. The CHIMES training set is developed by repulsive free computations of the DFTB forces and stress tensor components, which are subtracted from the DFT values of the same. The sum of the squares of the differences in the value of force and stress components calculated from DFT and repulsion free DFTB respectively are used to develop an objective function, from which the parameters for the $E_{Repulsive}$ is obtained. A linear combination of Chebyshev polynomials accounts for pairwise and three-body interactions respectively, is fed to the objective function as an input module to obtain the $E_{Repulsive}$ parameters.

The molecular dynamics simulations were performed in an NVT ensemble using a Nosé-Hoover thermostat. The simulated surface is optimized at 0K first. Periodic boundary conditions are applied to the simulation box, and the box length in the z-direction is kept significantly larger than the thickness of the simulated surface to avoid wall effects on the vapor phase atoms. The optimized surface is annealed at 2000 K to obtain a minimum energy state via a NVT simulation. The vapor phase atoms were introduced in the empty space above the equilibrated surface in the z-direction. The magnitudes of the initial velocities are assigned from the Maxwell-Boltzmann distribution based on the ensemble temperature, whereas the direction of the velocities is assigned randomly. The MD simulation was performed with a time-step of ~0.1 fs and run over several picoseconds to allow the vapor phase atoms to be adsorbed on the simulated surface. The self-consistent charge DFTB calculation is performed to obtain the charge densities of the microstates formed at every MD step. The entire simulation has been performed using the DFTB+ package. The obtained trajectory data have been using in-house scripts and visual molecular dynamics (VMD) has been used to create visual representations of the surface from the trajectory data. All the time-resolved data presented have been moving averaged over ~100 MD steps.

Input scripts and initial coordinate files for DFTB+ have been included in Appendix. Several MATLAB scripts have been written to analyze the trajectory file obtained after simulation through DFTB+ to evaluate pair correlation functions, bond lengths, coordination number and charges.

2.6 References

(1) Jian, G.; Zhou, L.; Piekiel, N. W.; Zachariah, M. R. Low Effective Activation Energies for Oxygen Release from Metal Oxides: Evidence for Mass-Transfer Limits at High Heating Rates. *ChemPhysChem* **2014**, *15* (8), 1666–1672. https://doi.org/10.1002/CPHC.201301148.

(2) Xu, F.; Biswas, P.; Nava, G.; Schwan, J.; Kline, D. J.; Rehwoldt, M. C.; Mangolini, L.; Zachariah, M. R. Tuning the Reactivity and Energy Release Rate of I2O5 Based Ternary Thermite Systems. *Combust Flame* **2021**, *228*, 210–217. https://doi.org/10.1016/J.COMBUSTFLAME.2020.12.047.

(3) Biswas, P.; Ghildiyal, P.; Mulholland, G. W.; Zachariah, M. R. Modelling and Simulation of Field Directed Linear Assembly of Aerosol Particles. *J Colloid Interface Sci* **2021**, *592*, 195–204. https://doi.org/10.1016/J.JCIS.2021.02.050.

(4) Weismiller, M. R.; Duin, A. C. T. V.; Lee, J.; Yetter, R. A. ReaxFF Reactive Force Field Development and Applications for Molecular Dynamics Simulations of Ammonia Borane Dehydrogenation and Combustion. *Journal of Physical Chemistry A* **2010**, *114* (17), 5485–5492. https://doi.org/10.1021/jp100136c.

(5) Lindsey, R. K.; Fried, L. E.; Goldman, N. ChIMES: A Force Matched Potential with Explicit Three-Body Interactions for Molten Carbon. *J Chem Theory Comput* **2017**, *13* (12), 6222–6229. https://doi.org/10.1021/ACS.JCTC.7B00867/ASSET/IMAGES/LARGE/CT-2017-00867G_0006.JPEG.

(6) Goldman, N.; Kweon, K. E.; Sadigh, B.; Heo, T. W.; Lindsey, R. K.; Pham, C. H.; Fried, L. E.; Aradi, B.; Holliday, K.; Jeffries, J. R.; Wood, B. C. Semi-Automated Creation of Density Functional Tight Binding Models through Leveraging Chebyshev Polynomial-Based Force Fields. *J Chem Theory Comput* **2021**, *17* (7), 4435–4448. https://doi.org/10.1021/ACS.JCTC.1C00172/ASSET/IMAGES/LARGE/CT1C00172_0008.JPEG.

3 Rerouting Pathways of Solid State Ammonia Borane Energy Release

3.1 Summary

Ammonia borane (NH_3BH_3, AB) presents a promising energy dense material for hydrogen storage and propulsion, however its energy release mechanisms on oxidation by solid-state oxidizers are not well understood. In this study, through *in-situ* time-of-flight mass spectrometry supported by ATR-FTIR and DFT calculations, I investigate the fundamental reaction mechanisms involved in the energy release from solid-state AB with different chemical oxidizers. I show that the reaction of AB with oxidizer like $KClO_4$ is mediated by $[NH_3BH_2NH_3]^+[BH_4]^-$ (DADB) formation resulting in its kinetic entrapment into low energy BNH_x clusters that are resistant to further oxidation, thus limiting complete energy extraction. In contrast, with an ammonium-based oxidizer such as NH_4ClO_4, the presence of NH_4^+ ions enables AB to follow an alternative reaction pathway forming $[NH_3BH_2NH_3]^+[ClO_4]^-$ rather than DADB, thus inhibiting the formation of BNH_x species, and facilitating its complete oxidation. This alternative reaction route causes the AB/NH_4ClO_4 system to exhibit remarkably higher energy release rates over that of AB/$KClO_4$ (~27x), and the standard Al/NH_4ClO_4 propellant (~7x).

3.2 Introduction

Ammonia borane (AB) and other chemical hydrides[1–7] possess higher enthalpy of oxidation than commonly employed metallic or metalloid fuels in solid-state propellants

such as Al, Ti, Si, and Mg[8–12], on both a gravimetric and molar basis (Figure 3-1). Owing to its high gravimetric hydrogen content (19.6 %), and low hydrogen generation temperature, AB has found considerable interest in the hydrogen storage application communities as has investigation of its dehydrogenation mechanism[13–22]. However, for its application in solid-state propellants, complete oxidation of the constituent boron in addition to hydrogen, is essential to exploit its high energy content.

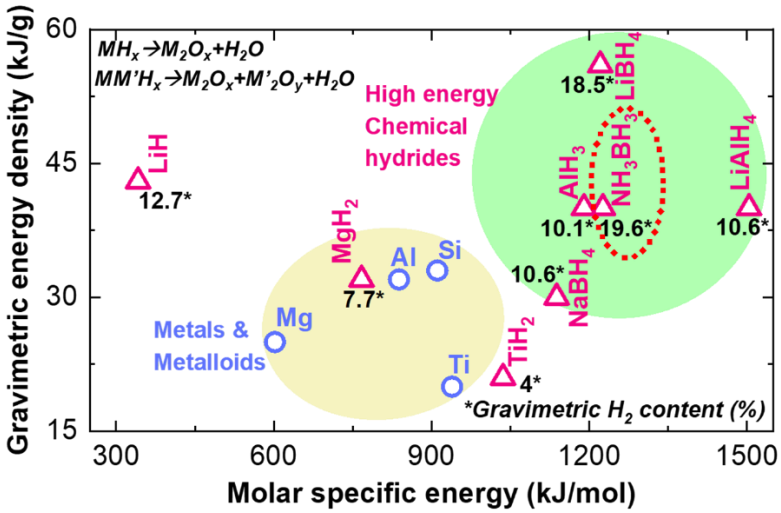

Figure 3-1 Gravimetric energy density hydrogen content, and molar specific energy of chemical hydrides (balanced reactions in FigureS1) showing AB (NH_3BH_3) has a theoretically higher energy content than most metals and metalloids.

Previous studies on AB hypergolic ignition and combustion have only explored its role as an additive in enhancing the combustion kinetics of liquid propellants[23–27]. In liquid propellants, which usually consist of strong oxidizing acids, AB hydrolysis facilitates the formation of borates leading to its complete oxidation and high energy release[25]. However, thermolysis of solid-state AB can result in its oligomerization between ~370-450 K, generating relatively stable boron-nitrogen-hydrogen (BNH_x) compounds such as borazine, poly-aminoboranes (p-AB), poly-iminoboranes (p-IB), poly-borazylene (p-BZ)

and even boron nitride (BN)[28–35]. Most of these BNH_x species being structurally analogous to aromatic hydrocarbons[36], likely have poor combustion kinetics and energy release rates[37–39] than elemental B and H, which may negatively affect the energetic performance of AB based propellants.

In solid propellants, physical and chemical processes occurring in the flame pre-heating zones[40–42], which exist below the ignition temperature, play a significant role in controlling their propagation and energy release rate. The generation of oxidation resistant BNH_x species (~373-450 K) in the pre-heating zone might also affect the energy release profiles of AB based propellants. Studies on AB thermolysis at heating rates of 1-20 K/min have shown that the release of BNH_x varies with increasing heating rates[43–46]. Since, the pre-ignition zone in propellant systems is subjected to much higher heating rates of ~10^5 K/s[47], it is essential to first identify the BNH_x species released from AB at high heating rates, something which has not been studied before. Furthermore, to assess the applicability of AB as a fuel in propellant systems, it is also essential to study the role of the BNH_x species, on the energy release profile of AB with different solid-state oxidizers.

In this study, I provide a mechanistic clarification of the release of BNH_x species and their role in the combustion reaction of AB with different solid-state chemical oxidizers. Using *in-situ* time and temperature-resolved measurements supported with density functional theory computations, I show that the energetic components (boron and hydrogen) of AB gets kinetically trapped into BNH_x species prior to the oxygen evolution from most oxidizers even at high heating rates (~10^5 K/s), resulting in its slower kinetics and lower energy release. Interestingly, I observe that with ammonium perchlorate

/NH_4ClO_4 (AP) as an oxidizer, AB follows a distinctly different energy release pathway, where AB and AP molecules, synergistically form a new intermediate that inhibits the formation of BNH_x species leading to more complete oxidation of AB. This alternative reaction pathway also leads to faster kinetics (~27x) and energy release of AB with AP compared to AB with $KClO_4$ as an oxidizer. This effective rerouting of the thermochemical oxidation pathway of AB with AP, also results in its ~7x faster energy release rates than the standard propellant aluminum (Al/AP) system, thus demonstrating AB as a reactive, primary fuel in solid-state propellant systems.

3.3 Methods

3.3.1 Materials and characterization

Ammonia Borane (~97 %) and hexadecyltrimethylammonium bromide/CTAB (~98 %) were obtained from Sigma-Aldrich and ammonium perchlorate (AP) and potassium perchlorate ($KClO_4$) were procured from Fluka. Solvents (hexane and ethanol) and salts (sodium hydroxide and ammonium chloride) are obtained from Fischer-scientific. The oxidizers particles ($KClO_4$ and AP) were size reduced by spray drying following similar procedures described elsewhere[48,49]. CuO (~50 nm) particles were obtained from US-Research Nanomaterials, and ~90-210 nm Bi_2O_3 were obtained from Sigma Aldrich. 50 nm Aluminum nanoparticles (ALEX) were procured from Argonide Corp. which have similar characteristics as described in previous publications[50].

XRD spectra of different samples were obtained through PANalytical EMPYREAN equipped with Cu-K-αsource (λ=1.543 ˚A). Nova NanoSEM 450 have been used to obtain SEM micrographs of different samples. Thermogravimetric-Differential

Scanning Calorimetry of different samples were performed using Netzsch-TGA/DSC apparatus typically under Ar flow at 10 K/min, unless otherwise mentioned.

Fuel/oxidizer system has been prepared by physically mixing the synthesized solid AB particles (section 2.2) dispersed in hexane, with respective solid oxidizer particles through sonication, in stoichiometric ratios (S.5.1) considering complete oxidation of the fuel. The sonicated dispersion is directly used for sample preparation in T-jump TOFMS (section 2.3) measurements or else vacuum dried at room temperature and used for ATR-FTIR (section 2.4), TGA/DSC, and combustion cell measurements (section 2.5).

3.3.2 Synthesis of size reduced AB

As-received AB particles were dissolved in ethanol (treated with 10^{-5} M NaOH), to make a solution of strength 0.87 M, which is half of the solubility limit of AB in ethanol[30]. CTAB powder is then added to the AB solution in ethanol, such that the final concentration of CTAB in the solution is 0.12 M, which is about half of its critical micellar concentration in ethanol[51]. After the solutes are fully dissolved, the AB/CTAB solution in ethanol is added dropwise to hexane (antisolvent) under vigorous stirring, in a manner such that the ratio of the volume of the solvent to antisolvent in the final mixture is 1:3. The entire process was carried out in a temperature-controlled environment at 40 ^{o}C. The dispersion of particles formed in the solvent-antisolvent mixture is then separated by centrifuging. The separated particles have been washed with anti-solvent for two times, centrifuged and then left for overnight vacuum drying at room temperature. The AB and CTAB concentration have been optimized to obtain the desired particle size and mass fraction of CTAB coating.

3.3.3 T-jump TOFMS and ignition temperature measurements

T-jump Time of flight Mass Spectrometer (T-jump TOFMS) is used for the time and temperature resolved *in-situ* identification of the gas phase species formed during rapid reactions, a detailed description of which can be found elsewhere[52,53]. The sample is loaded by coating on a Pt wire (length~0.8 cm, diameter ~76 µm, Omega Engineering, Inc) and pulse heated to ~1500 K within 3 ms at a heating rate of ~10^5 K/s. The gaseous species generated on heated activation of the sample, are ionized by 70 eV electrons. The positive ions are electrically accelerated through the time-of-flight tube to the multi-channel plate detector and the spectra are obtained for 10 ms at 0.1 ms intervals. The temperature of the wire is monitored by probing the current and voltage across the wire, at 0.1 ms intervals for the entire width of the heating pulse. The ignition measurements, with a detailed description in the references[10,54], consists of the same Pt wire, and the sample is loaded and heated in the same manner, with the same temperature probe. Additionally, in this case the Pt wire is loaded on a different sample holder, which is provisioned to be inserted into a specialized chamber equipped with an inlet and outlet for flowing of gases, an outlet for applying vacuum, a pressure gauge and a wall made of quartz glass for high-speed imaging of the sample on the wire. All ignition measurements were conducted under 1 atm of Ar. The ignition delay time is estimated from the video captured with ~µs resolution by a high-speed camera (Vision Research Phantom V12.1) and correlated with the measured wire temperature to determine the ignition temperature.

3.3.4 ATR-FTIR measurements

ATR-FTIR characterization of solid powders were performed on a Nicolet iS50R spectrometer with a deuterated triglycine sulfate (DTGS) detector. All the spectra were

collected at 4 cm^{-1} resolution. The spectra obtained were averaged every 60 seconds (40 scans/spectrum) and processed using Happ-Genzel apodization, Mertz phase correction, and atmospheric suppression using dry KBr as the reference[55].

3.3.5 Temporal characterization of self-propagating reaction by constant volume combustion cell

Constant volume combustion cell (~20 cm^3) measurements were performed on dry powder mixtures of fuel and oxidizer, for temporal characterization of the self-propagating combustion reaction. Fuel/oxidizer systems have been prepared in the same manner as described in section 2.1 During each combustion cell measurement, 25 mg of the pre-mixed fuel/oxidizer powder was tested under ambient atmospheric pressure. In a typical combustion cell measurement, the powdered sample is placed under a nichrome wire such that the wire only touches the center of the top surface of the powdered sample. The nichrome wire is resistively heated to ignite the sample and the sample is allowed to self-propagate after ignition. The time-dependent pressure signal was obtained using a high-frequency pressure transducer (PCB Piezoelectronics). A photomultiplier tube (Hamamatsu) connected to the combustion cell through an assembly of convex lens and fiber optic cable has been used to measure the optical emission to characterize burn-time. More information on this measurement can be found in an earlier publication[10].

3.3.6 Density functional theory calculations

All the molecules were optimized in periodic 15 x15 x 15 Å-sized unit cells using the ab initio DFT method in the generalized gradient approximation of Perdew-Burke-Ernzerhof (PBE)[56]. Plane-wave basis and projector augmented wave (PAW) pseudopotentials provided by the Vienna ab initio Simulation Package (VASP) have been

used. I only investigated the Γ-point of the Brillouin zone in all the unit cells. I employed the following cut-off values: energy cut-off was 300 eV, force cut-off was 10^{-2} eV/Å, and the energy convergence cut-off was 10^{-6} eV.

After optimizing the structures of each molecule, I performed the climbing image nudged elastic band (CI-NEB) method to find the transition state[57,58]. I used five or seven images to calculate the reaction path. The images in the simulation were relaxed until the forces reduced to the cut-off force, which is 10^{-2} eV/Å. Optimized structures and fractional coordinates are included in sections S.5.2 and S.5.3.

3.4 Results and discussion

3.4.1 Synthesis and characterization of nano-flakes of ammonia borane

Ammonia borane (AB) is synthesized by an anti-solvent crystallization method as described in section 2.2. Since the size of the as-received material is not immediately suitable for our application, I conducted a recrystallization to reduce the particle size. Dropwise addition of an alkaline ethanol-based saturated solution of AB with dissolved hexadecyltrimethylammonium bromide (CTAB) to the antisolvent (hexane) under vigorous stirring (Figure 3-2(b)) leads to the nucleation and growth of AB nano-flakes shown by the SEM images in Figure 3-2 (a). The steric interactions of the cationic surfactant CTAB coupled with enhanced diffusivity of the recrystallizing AB nuclei due to vigorous stirring of the anti-solvent restrict the thickness of the nano-flakes between 75-325 nm (Figure S2(a)), with a modal thickness of ~175 nm, which is drastically lower compared to the agglomerated ~100 μm commercial AB particles (Figure S2(c)).

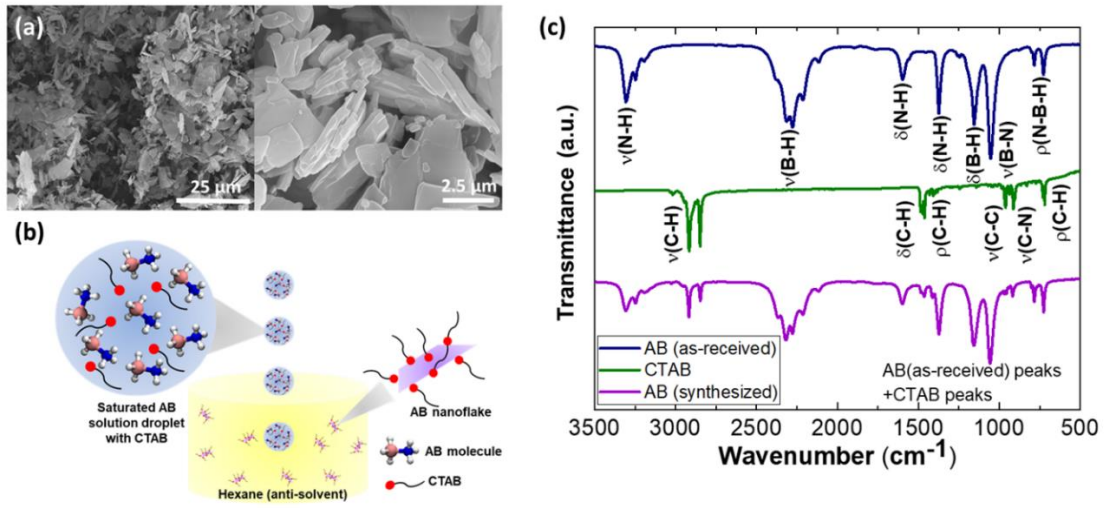

Figure 3-2 (a) SEM images show synthesized ammonia borane particles nano-flakes with thickness 75-325 nm (b) Synthesis of ammonia borane (AB) nano-flakes by anti-solvent crystallization, in the presence of CTAB (c)ATR-FTIR confirms the synthesized material contains both CTAB and ammonia borane.

Figure 3-2(c) shows that the synthesized AB has the FTIR peaks of both AB and CTAB[13], proving the formation of AB particles with CTAB on the surface, as also shown by the XRD spectra (Figure S2(b),supporting information). In TGA/DSC measurement, the synthesized AB shows a similar mass loss (Figure S3(b)) as the as-received AB (Figure S3(a)), indicating that the active content of AB molecules is preserved after recrystallization of the nanoflakes.

3.4.2 Thermolytic Entrapment of AB into BNH_x species

Prior studies on AB thermolysis under an anaerobic environment, have reported that AB molecules tend to oligomerize at high temperatures to form BNH_x species such as borazine, poly-aminoboranes, poly-iminoboranes and poly-borazylene. Scheme 1 shows

one of the widely accepted pathways[28,32] of AB decomposition through diammoniate of diborane (DADB) formation:

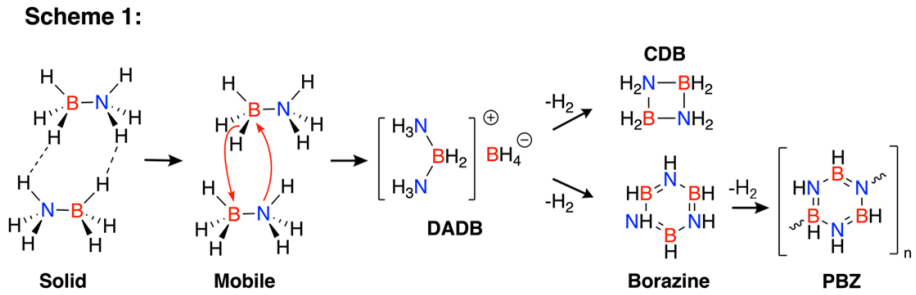

Scheme 1 showing one of the widely accepted pathways of AB decomposition

Strong di-hydrogen bonding exists between the heteropolar hydrogens of AB molecules ($NH^{\delta+} \bullet\bullet {}^{\delta-}HB$) in the solid state. Heating disrupts the di-hydrogen bonds and melting of AB to a mobile phase, in which the interaction between the N and B atoms of different AB molecules leads to the formation of DADB. DADB then rearranges to form gaseous cyclic-diborane (CDB) after releasing H_2 or alternatively reacts with excess AB to form gas-phase borazine and H_2. Borazine can further dehydrogenate and polymerize to form polyborazylene (PBZ) as the final solid-state decomposition product.

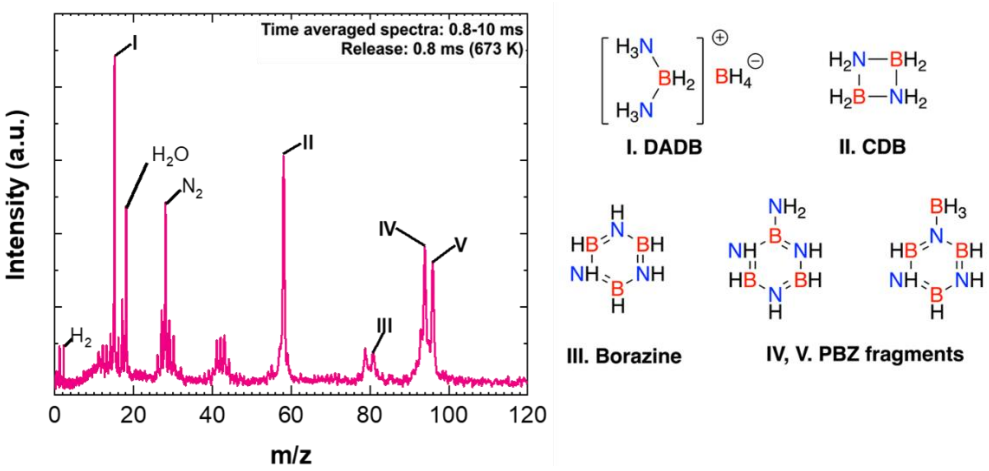

Figure 3-3 Time-averaged T-jump TOFMS spectra (0.8-10 ms) show DADB and different BNH_x species borazine, CDB, and PBZ are released from AB thermolysis at a high heating rate of ~10^5 K/s.

Previous TGA/DSC, FTIR and mass-spectrometric studies on thermal decomposition of AB at different heating rates (1-50 K/min; <1K/s) have reported that the amount of gas phase products increases with an increase in heating rate[43,46]. As high heating rates (~10^5 K/s) are required for the ignition of energetic materials, I performed temperature jump time-of-flight mass spectrometry (T-jump/TOFMS) at ~10^5 K/s, for in-situ time and temperature resolved probing of gas phase species released from AB decomposition, under actual ignition conditions (section 2.3). The sample is shock-heated to 1500 K within 3 ms (~10^5 K/s), and the mass spectra, acquired over 10 ms at an interval of 0.1 ms, show the release of different BNH_x species at ~0.8 ms (623$\pm$6 K) (Figure S4). A time-averaged mass spectra from the release time (~0.8 ms) to 10 ms (Figure 3-3), reveals the release of H_2 (m/z=2) and boron-nitrogen-hydrogen (BNH_x) species such as CDB (m/z=58), borazine (m/z=81), and polyborazylene (PBZ) fragments (m/z=94 and 96), during thermolysis of

AB at 10^5 K/s. The appearance of the strong BH_4 (m/z=15) peak likely indicates the formation of DADB ($[NH_3BH_2NH_3]^+[BH_4]^-$). T-jump TOFMS on standard borohydride salts like $NaBH_4$ show peaks of both cation (Na) and anion (BH_4) (Figure S16 (b)), which appear because of either thermal or electron impact ion dissociation of the salt. Therefore, the m/z=15 peak likely appears due to the BH_4 released from DADB, whereas its cation might have fragmented into smaller species resulting in the small peaks observed between m/z=13-17. Hence, the observation of DADB, CDB, borazine, and PBZ suggests that thermal decomposition of AB at ~10^5 K/s under anaerobic conditions follows scheme 1.

Thus, even at higher heating rates the elemental energetic constituents (B and H) of AB get trapped into BNH_x species, which are analogous to aromatic hydrocarbons. Hence, these species will have poor oxidation and combustion kinetics with low energy release rates. The implications of the release of these species on energy release rates from AB oxidation and combustion, along with a method of chemically overcoming the formation of these species have been studied and discussed in the subsequent sections.

3.4.3 Ignition and self-propagation reaction rates of AB with different oxidizers

Metal oxides like CuO (O_2 release ~ 940 K), Bi_2O_3 (O_2 release ~1220 K), and oxysalts like $KClO_4$ (O_2 release ~870 K), NH_4ClO_4 (O_2 release ~ 670 K) are commonly employed as oxidizers in solid-state energetic formulations[59,60]. The O_2 release temperatures of these oxidizers were also measured by T-jump TOFMS at a heating rate of ~10^5 K/s (Figure S5). To probe the energy release profile of AB, ignition temperature (section 2.3) and constant-volume pressurization (section 2.5) rate measurements have

been performed on ultrasonically mixed powders of AB nanoflakes with respective oxidizer particles in stoichiometric proportions (section 2.1). The ignition temperature measurements were performed under 1 atm of Ar, so that the solid-state oxidizers act as the only oxygen sources.

Figure 3-4(a) compares the pressure and pressurization rates between AB/AP, AB/$KClO_4$, and standard propellant, Al/AP (control system), obtained from constant volume combustion cell measurements. The pressurization rate is estimated from the slope of a linear fit from the pressure rise point to the peak pressure in the acquired pressure signal (Figure S6). AB/AP reaction (peak pressure of ~380 kPa) outperforms the AB/$KClO_4$ reaction (peak pressure ~120 kPa), as well as the standard propellant Al/AP reaction (peak pressure of ~150 kPa). The pressurization rate of AB/AP reaction (76.5 kPa/ms) is ~27 times higher than AB/$KClO_4$ and about ~7 times higher than the standard propellant Al/AP. Figure 3-4(b) shows the burn times characterized by the FWHM of the normalized optical signals (Figure S6) obtained during the same measurement. AB/AP has a burn-time of ~3 ms, which is ~1/5 of AB/$KClO_4$ and ~1/3 of Al/AP. The significantly higher pressurization rates and shorter burn-times indicate the superior reactivity and energy release rate of AB/AP system. No ignition or combustion is observed for AB/CuO and AB/Bi_2O_3 systems, indicating the poor reactivity of AB with CuO and Bi_2O_3.

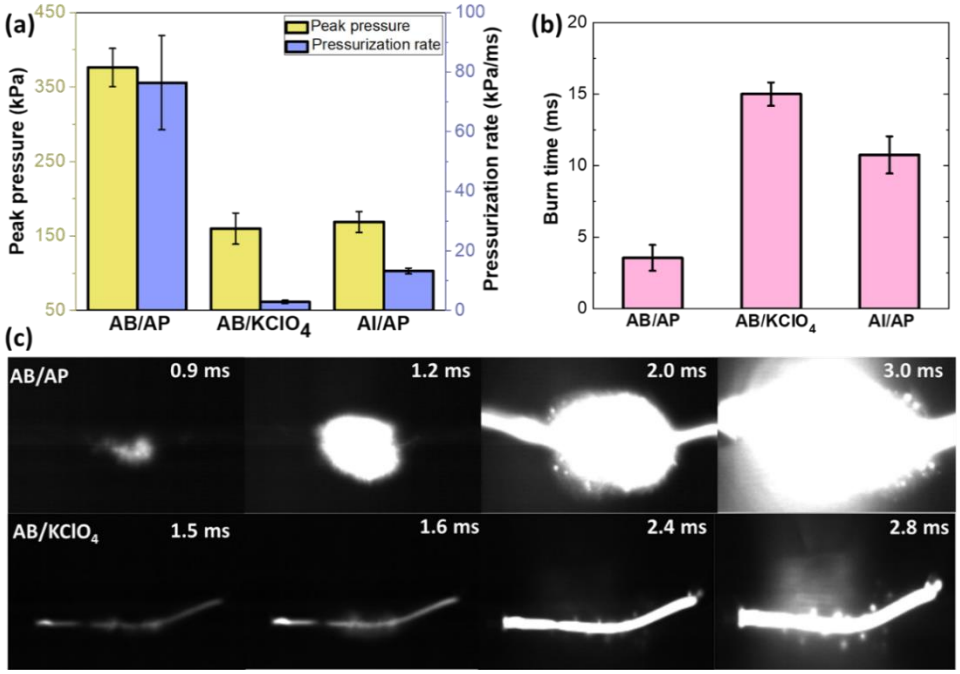

Figure 3-4 Combustion cell experiments showing peak pressure (a) and pressure rise rates (b) of AB/AP is significantly higher than Al/AP and AB/$KClO_4$. (c) Time-resolved snapshot of the ignition process shows AB/AP flame is more violent and brighter than AB/$KClO_4$.

In the time-resolved snapshots from the video obtained during ignition measurement of AB/AP and AB/$KClO_4$ (Figure 3-4(c)), AB/AP flame looks brighter and more violent than AB/$KClO_4$, also qualitatively indicating higher flame-temperature and hence energy release from AB/AP. The measured ignition temperatures of both AB/AP (703$\pm$11 K) and AB/$KClO_4$ (850$\pm$14 K) systems are approximately the same as the O_2 release temperature of the respective oxidizers. As AB already thermolyzes into inert BNH_x species, at much lower temperatures of ~623 K (section 3.2), the lower O_2 release temperature of AP cannot solely explain the much high reactivity of the AB/AP system compared to AB/$KClO_4$. This indicates AB/AP reaction follows an alternative route, rather

than simply getting oxidized by the O_2 released from oxidizer decomposition, the mechanism of which has been investigated and discussed in the subsequent sections.

3.4.4 Absence of BNH_x species in AB/AP reaction

Gas phase species released during the reaction of AB with $KClO_4$ and AP were temporally probed by T-jump TOFMS at the same heating rate of ~10^5 K/s. In Figure 3-5(a), T-jump TOFMS spectra of AB/$KClO_4$ reaction show the release of the same BNH_x species as observed in the case of pristine AB, along with additional peaks for K (m/z=39) and O_2 (m/z=32) from $KClO_4$ decomposition. Hence, during AB/$KClO_4$ reaction, AB thermolyzes into BNH_x species through DADB formation following scheme 1 (section 3.2). Since pristine AP thermally decomposes through the formation of NH_3 and $HClO_4$, gaseous ClO_x species such as $HClO_4$ (m/z=100), ClO_2 (m/z=67), ClO_3 (m/z=93), and ClO (m/z=51), are observed in the T-jump TOFMS spectra of pristine AP (Figure 3-5(b)). Interestingly, during AB/AP reaction (Figure 3-5(b)) both BNH_x species from AB thermolysis and ClO_x species from AP decomposition are absent. The peak of HCl (m/z=36), which can only be released on complete reduction of the perchlorate anion of AP, indicates a redox reaction has occurred between AB and AP.

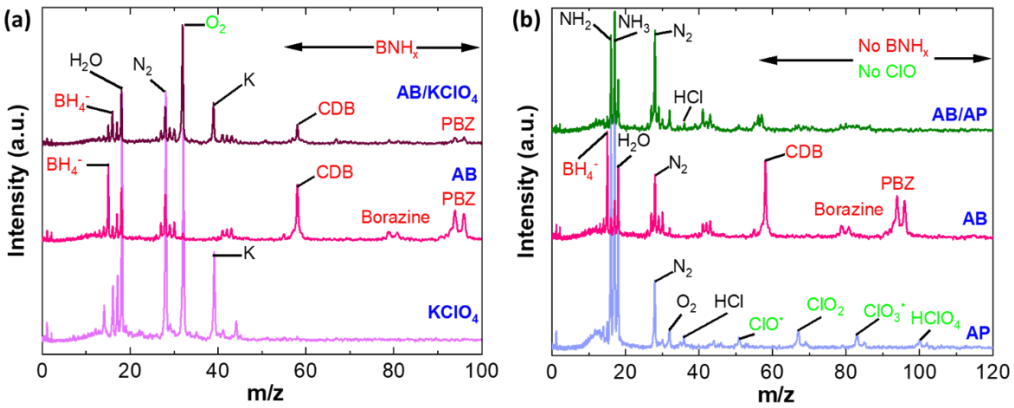

Figure 3-5 (a) T-jump TOFMS shows the evolution of BNH_x, K and O_2 in AB/$KClO_4$ reaction. (b)Both BNH_x and ClO_x species are absent in the T-jump TOFMS spectra of AB/AP reaction, indicating AB/AP redox reaction follows a distinct condensed phase pathway.

Upon complete oxidation, AB should form solid oxides of boron (B_2O_3 or other borates), N_2 (or nitrogen oxides), and H_2O. The BNH_x species observed in the case of AB/$KClO_4$ reaction, implies most of the elements (B,N, and H) of AB got trapped into these species. A small amount of unpolymerized AB or lighter BNH_x species (CDB or borazine) may be oxidized by the O_2 released from $KClO_4$, which led to its ignition and combustion with poor kinetics. The absence of any gas phase species containing B atoms in AB/AP indicates that B is completely oxidized to boron oxides in the condensed phase. Moreover, the absence of any ClO_x species from AP implies that AP is interacting with molten AB to form a different intermediate instead of DADB, which inhibits the formation of BNH_x species and leads to the oxidation of AB in condensed phase.

To further investigate this phenomenon, I performed T-jump TOFMS of AB/AP mixture with excess AB (2:1 by moles). The BNH_x species like CDB and borazine are observed in the spectra of AB/AP mixture with excess AB (Figure S7), indicating that only the amount of AB molecules present in stoichiometric equivalence to AP participates in

the condensed phase redox reaction and the excess AB forms BNH_x species though DADB. This mixture also did not ignite implying poor kinetics and inferior energy release due to BNH_x formation. Previous ^{11}B NMR-study have reported that in presence of NH_4Cl, AB forms $[NH_3BH_2NH_3]^+[Cl]^-$ upon melting, instead of DADB ($[NH_3BH_2NH_3]^+[BH_4]^-$), because of the interaction between the N of the NH_4^+ ion of NH_4Cl and B of the AB molecule[29]. By doing T-jump TOFMS of AB/NH_4Cl mixtures with different molar ratios, I also found that BNH_x species only appear when excess AB is present (Figure S8). Based on these observations, it can be hypothesized that with NH_4ClO_4, AB forms $[NH_3BH_2NH_3]^+[ClO_4]^-$ as described in Scheme 2:

Scheme 2:

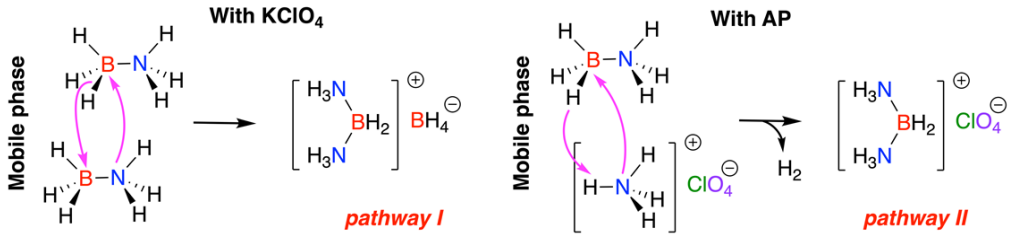

Scheme 2 showing the distinct intermediary pathways followed by AB/KClO4 and AB/AP reactions.

AP is well known to decompose to NH_3 and $HClO_4$[49]. Since, AB decomposes to BNH_x (Figure S4) species at a lower temperature compared to AP (Figure S5), the possibility of alternative pathways through acid-catalyzed hypergolic ignition[25] of AB with $HClO_4$, released on AP decomposition, can be eliminated. The emergence of $[NH_3BH_2NH_3]^+[ClO_4]^-$ in place of DADB not only implies that the formation of BNH_x species is inhibited, however it also indicates that the fuel ($[NH_3BH_2NH_3]^+$) and oxidizer ($[ClO_4]^-$) component are placed into the same molecule. Usually, the reaction kinetics of particulate energetic materials, is limited by the diffusion of oxygen from oxidizer particles

to fuel particles, which in-turn depends on the particle size. However, in intermediates like $[NH_3BH_2NH_3]^+[ClO_4]^-$, molecular level mixing of fuel and oxidizer will drastically decrease the diffusion time-scales, which might also explain the condensed phase initiation (Figure 3-5(b)) and fast kinetics of AB/AP redox reaction (section 3.3). More analysis and discussion on this phenomenon are included in subsequent sections.

3.4.5 Solid-state products of AB oxidation

TGA/DSC measurements of AB in Ar at 10 K/min (Figure S3(b)) show a two-step mass loss out of which the first mass loss step feasibly corresponds to CDB formation, whereas the second mass loss step corresponds to the release of borazine as explained in section S.2.1 (supporting information). ATR-FTIR of the residual post-thermolysis product (~44 % by wt.) shows that it contains bending, stretching and rocking vibration bands from NH, BH, BN and BNH groups indicating the formation of polyborazylene/PBZ (Figure 3-6(a)). The relatively low intensity of BH bands shows that the PBZ formed is deficient in BH bonds compared to NH bonds. These observations are consistent with the BNH_x species including PBZ fragments, observed by T-jump TOFMS (Figure 3-3) at high heating rates (~10^5 K/s). However, precisely the relative amounts of gas phase product species may be higher at high heating rates[43].

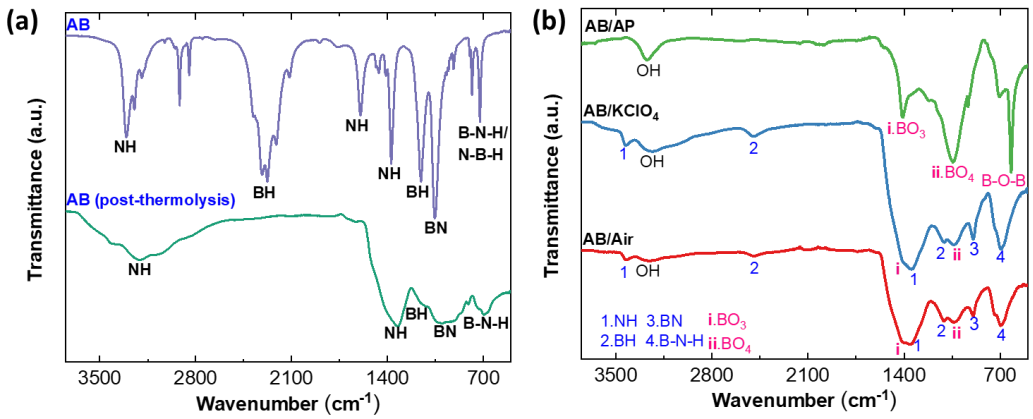

Figure 3-6 ATR-FTIR spectra of, (a) post-thermolysis product of AB in Ar (anaerobic) shows NH, BH, and BN bonds indicating polyborazylene (PBZ) formation, (b) oxidation products of AB/air and AB/$KClO_4$ consist of a mixture of PBZ (NH, BH, and BN peaks) and boron oxides (BO_3 and BO_4 peaks), whereas AB/AP product only contains boron oxides indicating complete AB oxidation with AP.

TGA/DSC of AB in air at 10 K/min shows a ~28 % mass loss in a single-step around the melting point (~383 K) of AB (Figure S9). Ideally, if AB is completely oxidized (Table 2-1), then 1 mole of AB should form 0.5 mole of B_2O_3 resulting in ~12 % mass gain. Hence, heating in air cannot completely oxidize AB and the ~28 % mass loss may be due to gaseous BNH_x species release. TGA/DSC of AB/$KClO_4$ in Ar (Figure S10) at the same heating rate shows similar mass loss (~16 %) between 390-450 K as observed in TGA of pristine AB in Ar (Figure S3(b)), followed by a mass loss around 873 K due to $KClO_4$ decomposition. However, TGA/DSC of AB/AP under the same conditions, completely differs from both pristine AB and AP (Figure S11), as no significant mass loss is observed till 436 K which also indicates that AB/AP reaction proceeds through a distinct intermediate formation in the condensed phase. ATR-FTIR is performed on the residual solid state oxidation products of AB in air, AB/$KClO_4$ and AB/AP obtained from TGA/DSC measurement (Figure 3-6(b)). Both the oxidation products of AB in air and

AB/$KClO_4$ show the presence of NH, BH, BN and BNH groups (Figure 3-6(b)), like pristine AB decomposition in Ar (Figure 3-5(a)) indicating the formation of polyborazylene. Small peaks of BO_3 and BO_4 units are also observed in both cases of AB/air and AB/$KClO_4$ (Figure 3-6(b)), indicating the possible oxidation of some surface AB molecules or low molecular weight BNH_x species. However, the product of AB/AP (Figure 3-6(b)) shows strong peaks from BO_3 and BO_4 units along with rocking vibration from B-O-B units indicating the presence of boron oxides[61,62]. Moreover, NH, BH, BN and BNH groups are also absent in the AB/AP product indicating the absence of polyborazylene.

Hence, it can be inferred from these observations, that AB/AP reaction leads to complete oxidation of B atoms of AB to boron oxides, which is consistent with the observations in section 3.4. The presence of both BO_3 and BO_4 units suggests that the product contains mixed boron oxides[63,64], where BO_3 and B-O-B bands suggest the formation of boric anhydride/B_2O_3 (Figure S12), BO_4 units indicate the formation of cyclic borates and OH groups suggest the formation of some boric acid ($B(OH)_3$). The complete oxidation of AB with AP also explains the superior energy release and combustion kinetics of AB/AP redox reaction compared to AB/$KClO_4$ as observed in section 3.3.

3.4.6 Energetics of AB/AP reaction from DFT and discussion

In section 3.2, I observed that AB thermolysis occurs through DADB ($[NH_3BH_2NH_3]^+[BH_4]^-$) formation which results in its oligomerization into BNH_x species like CDB, borazine and PBZ. With $KClO_4$ and air, AB also undergoes thermolysis to form

DADB, CDB, borazine (section 3.4) and PBZ (section 3.4 and 3.5), additionally forming some boron oxides (section 3.5). With AP, AB possibly forms $[NH_3BH_2NH_3]^+[ClO_4]^-$ (section 3.4) as an intermediate instead of DADB, which results in its complete oxidation to boron oxides (section 3.5). Hence, BNH_x species are absent in AB/AP reaction (section 3.4 and 3.5).

To further evaluate possibility of $[NH_3BH_2NH_3]^+[ClO_4]^-$ formation during AB/AP reaction in place of DADB, the energetics of the formation of DADB and $[NH_3BH_2NH_3]^+[ClO_4]^-$ are evaluated through DFT calculation (section 2.6). Figure 3-7 shows a comparison between the free-energy diagrams of $[NH_3BH_2NH_3]^+[ClO_4]^-$ formation (Figure 3-7(a)) and DADB formation (Figure 3-7(b)). On AB/AP reaction, a negative free energy change (ΔG ~ -57.2 kJ/mol) indicates the higher feasibility of $[NH_3BH_2NH_3]^+[ClO_4]^-$ formation over DADB (ΔG ~ 55.5 kJ/mol). Furthermore, as fuel ($[NH_3BH_2NH_3]^+$) and oxidizer ($[ClO_4]^-$,) are mixed at molecular level in $[NH_3BH_2NH_3]^+[ClO_4]^-$, the rate of its redox decomposition will not be limited by oxygen diffusion. Hence, the intra-molecular redox reaction of $[NH_3BH_2NH_3]^+[ClO_4]^-$ will have extremely fast kinetics.

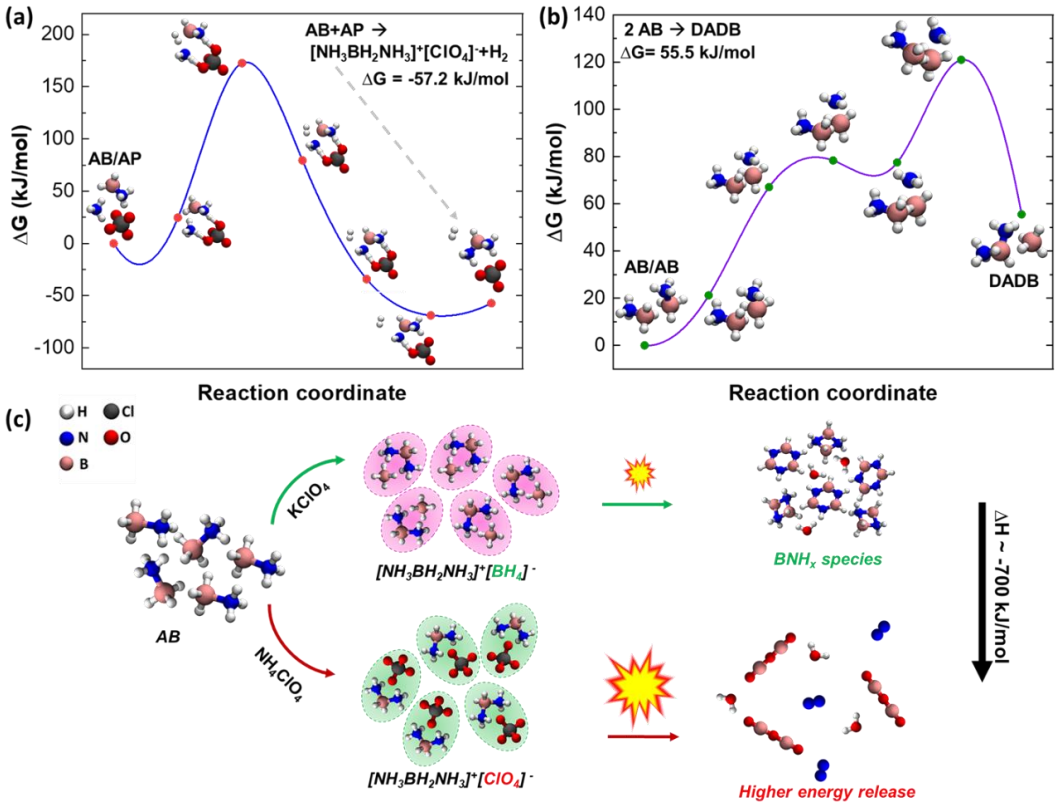

Figure 3-7 Free energy diagram of the $[NH_3BH_2NH_3]^+[ClO_4]^-$ formation (ΔG ~ -57.2 kJ/mol) through AB/AP pathway (a) and DADB formation (ΔG ~ 55.5 kJ/mol) through AB oligomerization (b), demonstrates a higher feasibility of $[NH_3BH_2NH_3]^+[ClO_4]^-$ formation through AB/AP reaction. (c) The schematic summarizes the studied thermochemical oxidation mechanisms of AB, illustrating the alternative AB/AP reaction route leads to complete oxidation of AB and ~700 kJ/mol higher energy release than $AB/KClO_4$.

Thus, with only AP as an oxidizer (Figure 3-7(c)), the formation of $[NH_3BH_2NH_3]^+[ClO_4]^-$ will inhibit the formation of BNH_x species ensuring the complete oxidation of AB resulting in its superior energy release profile. With $KClO_4$ and other oxidizers, the formation of DADB, will trap the elemental constituents of AB (B, N, and H) into BNH_x species, resulting in its incomplete oxidation and inferior energy release profile. Table 2-1, shows borazine formation through the DADB pathway, creates at least ~700 kJ/mol deficit in energy release compared to its complete oxidation through AB/AP

pathway. This energy deficit is much higher than the ~280 kJ/mol difference in total thermodynamic reaction enthalpy between AB/AP and AB/$KClO_4$ (Table 2-1), establishing the significance of alternative pathway on the energy release profile of AB. The higher exothermicity of the AB/AP pathway leads to greater heat generation during the AB/AP combustion reaction, causing a temperature increase, and an accelerated reaction rate. These factors explain the poor combustion kinetics of AB/$KClO_4$ and the non-ignitability of AB with CuO and Bi_2O_3. Additionally, the superior performance of AB/AP compared to the standard Al/AP propellant system, shows that AB can be potentially used as a major fuel component in solid-state propellant systems.

Table 3-1 Reaction enthalpy of 1. DADB pathway (borazine formation), 2. AB/AP pathway (complete oxidation) and the total thermodynamic enthalpy of 3. AB/$KClO_4$ and 4. AB/AP reaction

Reactions	Enthalpy* (kJ/mol of AB)
Reaction enthalpies considering different kinetics:	
1. $3AB(NH_3BH_3) + 3O_2 \rightarrow Borazine(B_3N_3H_6) + 6H_2O$	-522
2. $4AB + 9O_2 \rightarrow 2N_2 + 2B_2O_3 + 12H_2O$	-1226
Total thermodynamic reaction enthalpies:	
3. $8AB + 9KClO_4 \rightarrow 4B_2O_3 + 4N_2 + 24H_2O + 9KCl$	-1233
4: $10AB + 18AP \rightarrow 5B_2O_3 + 14N_2 + 57H_2O + 18HCl$	-1510

**NIST Standard ΔH_f used for all species, except for AB ΔH_f=-133.4 kJ/mol*[65]

At the particle level, molten AB possibly reacts with the surface molecules of NH_4ClO_4 particles forming $[NH_3BH_2NH_3]^+[ClO_4]^-$ following shrinking-core model[66].

When the external temperature ramp causes melting of AP, the rate of formation of $[NH_3BH_2NH_3]^+[ClO_4]^-$ is enhanced. I can hypothesize that with other NH_4^+ based oxidizers, such as, ammonium dinitramide ($NH_4N_3O_4$) and ammonium nitrate (NH_4NO_3), AB will also form $[NH_3BH_2NH_3]^+$[oxidizer anion] as intermediates. Therefore, these oxidizers may also show high reactivity with solid AB. However, since these ammonium salts with different anions have different melting points, the oxidative energy release profile of AB can be further tuned by changing the anions of NH_4^+-based oxidizers, which I plan to investigate in our future studies.

3.5 Conclusions

The current study presents a mechanistic understanding of the distinct thermochemical energy release pathways of AB with different chemical oxidizers in solid-state. Through, in-situ T-jump TOFMS measurements, I have shown that AB thermolyzes to BNH_x species such as CDB, borazine and polyborazylene, through DADB formation, even at high heating rates (~10^5 K/s). With chemical oxidizers like $KClO_4$, T-jump TOFMS shows the formation of same BNH_x species. Additionally, ATR-FTIR confirms that the solid-state AB/$KClO_4$ reaction products contain a mixture of polyborazylene and boron-oxides. However, with AP, complete oxidation of AB to boron oxides is observed in absence of BNH_x species release, which can be attributed to the possible formation of $[NH_3BH_2NH_3]^+[ClO_4]^-$ as an intermediate, instead of DADB. DFT calculations show that $[NH_3BH_2NH_3]^+[ClO_4]^-$ formation (ΔG ~ -57.2 kJ/mol) in AB/AP reaction has a higher feasibility over DADB (ΔG ~ 55.5 kJ/mol). The formation of $[NH_3BH_2NH_3]^+[ClO_4]^-$ also

eliminates oxygen diffusion limitation thereby ensuring faster kinetics. The faster and complete oxidation of AB in the AB/AP pathway explains the higher energy release rate (~27x) of AB/AP compared to AB/$KClO_4$ in combustion cell measurements. Therefore, these mechanistic insights into the energy release profile of solid-state AB, open possibilities for the rational design of materials for hydrogen storage, and propulsion, by exploiting its different reaction pathways to achieve greater control over material properties and reactive characteristics.

3.6 References

(1) Schlapbach, L.; Züttel, A. Hydrogen Storage Materials for Mobile Applications. Nature 2001, 414, 353–358.

(2) Schneemann, A.; White, J. L.; Kang, S.; Jeong, S.; Wan, L. F.; Cho, E. S.; Heo, T. W.; Prendergast, D.; Urban, J. J.; Wood, B. C.; Allendorf, M. D.; Stavila, V. Nanostructured Metal Hydrides for Hydrogen Storage. Chem.Rev. 2018,118,10775-10839

(3) Demirci, U. B.; Miele, P. Sodium Borohydride versus Ammonia Borane, in Hydrogen Storage and Direct Fuel Cell Applications. Energy Environ. Sci. 2009, 2, 627–637.

(4) Aguey-Zinsou, K. F.; Ares-Fernández, J. R. Hydrogen in Magnesium: New Perspectives toward Functional Stores. Energy Environ. Sci. 2010, 3, 526–543.

(5) Zhang, J.; Zhu, Y.; Lin, H.; Liu, Y.; Zhang, Y.; Li, S.; Ma, Z.; Li, L. Metal Hydride Nanoparticles with Ultrahigh Structural Stability and Hydrogen Storage Activity Derived from Microencapsulated Nanoconfinement. Adv. Mater. 2017,29,1700760.

(6) Ngene, P.; Longo, A.; Mooij, L.; Bras, W.; Dam, B. Metal-Hydrogen Systems with an Exceptionally Large and Tunable Thermodynamic Destabilization. Nature Communications 2017, 8 ,1846.

(7) Cao, H.; Georgopanos, P.; Capurso, G.; Pistidda, C.; Weigelt, F.; Chaudhary, A. L.; Filiz, V.; Tseng, J. C.; Wharmby, M. T.; Dornheim, M.; Abetz, V.; Klassen, T. Air-Stable Metal Hydride-Polymer Composites of Mg(NH2)2–LiH and TPXTM. Materials Today Energy 2018,10,98-107.

(8) Salvagnac, L.; Assie-Souleille, S.; Rossi, C. Layered Al/CuO Thin Films for Tunable Ignition and Actuations. Nanomaterials 2020, 10, 2009.

(9) Ghildiyal, P.; Ke, X.; Biswas, P.; Nava, G.; Schwan, J.; Xu, F.; Kline, D. J.; Wang, H.; Mangolini, L.; Zachariah, M. R. Silicon Nanoparticles for the Reactivity and Energetic Density Enhancement of Energetic-Biocidal Mesoparticle Composites. ACS Appl. Mater. Interfaces 2021,13,458-467.

(10) Xu, F.; Biswas, P.; Nava, G.; Schwan, J.; Kline, D. J.; Rehwoldt, M. C.; Mangolini, L.; Zachariah, M. R. Tuning the Reactivity and Energy Release Rate of I2O5 Based Ternary Thermite Systems. Combustion and Flame 2021, 228, 210–217.

(11) Lomba, R.; Bernard, S.; Gillard, P.; Mounaïm-Rousselle, C.; Halter, F.; Chauveau, C.; Tahtouh, T.; Guézet, O. Comparison of Combustion Characteristics of

Magnesium and Aluminum Powders. Combustion Science and Technology 2016,118,1857-1877.

(12) Alibay, Z.; Kline, D. J.; Rehwoldt, M. C.; Biswas, P.; Herrera, S.; Wang, H.; Zachariah, M. R. Mechanism of Microwave-Initiated Ignition of Sensitized Energetic Nanocomposites. Chemical Engineering Journal 2021,415,128657.

(13) Valero-Pedraza, M. J.; Cot, D.; Petit, E.; Aguey-Zinsou, K. F.; Alauzun, J. G.; Demirci, U. B. Ammonia Borane Nanospheres for Hydrogen Storage. ACS Appl. Nano Mater. 2019, 2, 1129–1138.

(14) Wang, C.; Tuninetti, J.; Wang, Z.; Zhang, C.; Ciganda, R.; Salmon, L.; Moya, S.; Ruiz, J.; Astruc, D. Hydrolysis of Ammonia-Borane over Ni/ZIF-8 Nanocatalyst: High Efficiency, Mechanism, and Controlled Hydrogen Release. J. Am. Chem. Soc. 2017, 139, 11610–11615.

(15) Wahab, M. A.; Zhao, H.; Yao, X. D. Nano-Confined Ammonia Borane for Chemical Hydrogen Storage. Frontiers of Chemical Science and Engineering 2012,6,27-33.

(16) Yang, J. B.; Lamsal, J.; Cai, Q.; James, W. J.; Yelon, W. B. Structural Evolution of Ammonia Borane for Hydrogen Storage. Applied Physics Letters 2008,92,091916.

(17) Gao, P.; Huang, Z.; Yu, H. Exploration of the Dehydrogenation Pathways of Ammonia Diborane and Diammoniate of Diborane by Molecular Dynamics Simulations Using Reactive Force Fields. J. Phys. Chem. A 2020, 124, 1698–1704.

(18) Stephens, F. H.; Baker, R. T.; Matus, M. H.; Grant, D. J.; Dixon, D. A. Acid Initiation of Ammonia-Borane Dehydrogenation for Hydrogen Storage. Angew. Chem. Int. Ed. 2007, 46, 746 –749.

(19) Gutowska, A.; Li, L.; Shin, Y.; Wang, C. M.; Li, X. S.; Linehan, J. C.; Smith, R. S.; Kay, B. D.; Schmid, B.; Shaw, W.; Gutowski, M.; Autrey, T. Nanoscaffold Mediates Hydrogen Release and the Reactivity of Ammonia Borane. Angew. Chem. Int. Ed. 2005, 44, 3578-3582.

(20) Lai, Q.; Rawal, A.; Quadir, M. Z.; Cazorla, C.; Demirci, U. B.; Aguey-Zinsou, K. F. Nanosizing Ammonia Borane with Nickel: A Path toward the Direct Hydrogen Release and Uptake of B–N–H Systems. Adv. Sustainable Syst. 2018, 2, 1700122.

(21) Simagina, V. I.; Vernikovskaya, N. V.; Komova, O. V.; Kayl, N. L.; Netskina, O. V.; Odegova, G. V. Experimental and Modeling Study of Ammonia Borane-Based Hydrogen Storage Systems. Chemical Engineering Journal 2017,329,156-164.

(22) Rizzi, V.; Polino, D.; Sicilia, E.; Russo, N.; Parrinello, M. The Onset of Dehydrogenation in Solid Ammonia Borane: An Ab Initio Metadynamics Study. Angew. Chem. Int. Ed. 2019, 58,3976-3980.

(23) Clements, K. A.; Baier, M. J.; Veeraraghavan Ramachandran, P.; Son, S. F. Experimental Study of Factors Affecting Hypergolic Ignition of Ammonia Borane. Journal of Propulsion and Power 2021,37,2.

(24) Baier, M. J.; Ramachandran, P. V.; Son, S. F. Characterization of the Hypergolic Ignition Delay of Ammonia Borane. Journal of Propulsion and Power 2019,35,1.

(25) Baier, M. J.; McDonald, A. J.; Clements, K. A.; Goldenstein, C. S.; Son, S. F. High-Speed Multi-Spectral Imaging of the Hypergolic Ignition of Ammonia Borane. Proceedings of the Combustion Institute 2021,38,4433-4440.

(26) Pfeil, M. A.; Son Prof., S. F.; Anderson Prof., W. E. Influence of Ammonia Borane on the Stability of a Liquid Rocket Combustor. Journal of Propulsion and Power 2014,30,2.

(27) Pfeil, M. A.; Groven, L. J.; Lucht, R. P.; Son, S. F. Effects of Ammonia Borane on the Combustion of an Ethanol Droplet at Atmospheric Pressure. Combustion and Flame 2013,160,2194-2203.

(28) Stowe, A. C.; Shaw, W. J.; Linehan, J. C.; Schmid, B.; Autrey, T. In Situ Solid State 11B MAS-NMR Studies of the Thermal Decomposition of Ammonia Borane: Mechanistic Studies of the Hydrogen Release Pathways from a Solid State Hydrogen Storage Material. Phys. Chem. Chem. Physics. 2007, 9, 1831–1836.

(29) Heldebrant, D. J.; Karkamkar, A.; Hess, N. J.; Bowden, M.; Rassat, S.; Feng, Z.; Rappe, K.; Autrey, T. The Effects of Chemical Additives on the Induction Phase in Solid-State Thermal Decomposition of Ammonia Borane. Chem. Mater. 2008, 20, 5332–5336.

(30) Stephens, F. H.; Pons, V.; Tom Baker, R. Ammonia–Borane: The Hydrogen Source Par Excellence? Journal of the Chemical Society. Dalton Trans. 2007, 2613-2626.

(31) Petit, J. F.; Demirci, U. B. Mechanistic Insights into Dehydrogenation of Partially Deuterated Ammonia Borane NH 3 BD 3 Being Heating to 200 °c. Inorg. Chem. 2019, 58, 489–494.

(32) Demirci, U. B. Mechanistic Insights into the Thermal Decomposition of Ammonia Borane, a Material Studied for Chemical Hydrogen Storage. Inorg. Chem. Front. 2021, 8, 1900–1930.

(33) Petit, J. F.; Demirci, U. B. Discrepancy in the Thermal Decomposition/Dehydrogenation of Ammonia Borane Screened by Thermogravimetric Analysis. International Journal of Hydrogen Energy 2019, 44, 14201–14206.

(34) Bhunya, S.; Zimmerman, P. M.; Paul, A. Unraveling the Crucial Role of Metal-Free Catalysis in Borazine and Polyborazylene Formation in Transition-Metal-Catalyzed Ammonia-Borane Dehydrogenation. ACS Catal. 2015,5,3478-3493.

(35) Bachmann, P.; Düll, F.; Späth, F.; Bauer, U.; Steinrück, H. P.; Papp, C. A HR-XPS Study of the Formation of h-BN on Ni(111) from the Two Precursors, Ammonia Borane and Borazine. J. Chem. Phys. 2018, 149 ,164709.

(36) Yang, P.; Li, J.; Cheng, Z.; Zuo, S. Promoting Effects of Ce and Pt Addition on the Destructive Performances of V2O5/Γ-Al2O3 for Catalytic Combustion of Benzene. Applied Catalysis A: General 2017,542,38-46.

(37) Cofer, C. G.; Economy, J. Oxidative and Hydrolytic Stability of Boron Nitride - A New Approach to Improving the Oxidation Resistance of Carbonaceous Structures. Carbon 1995,33,389-395.

(38) Liu, Z.; Gong, Y.; Zhou, W.; Ma, L.; Yu, J.; Idrobo, J. C.; Jung, J.; Macdonald, A. H.; Vajtai, R.; Lou, J.; Ajayan, P. M. Ultrathin Higherature Oxidation-Resistant Coatings of Hexagonal Boron Nitride. Nature Communications 2013, 4, 2541.

(39) Li, L. H.; Cervenka, J.; Watanabe, K.; Taniguchi, T.; Chen, Y. Strong Oxidation Resistance of Atomically Thin Boron Nitride Nanosheets. ACS Nano 2014, 8, 1457-1462.

(40) Wang, H.; Kline, D. J.; Zachariah, M. R. In-Operando High-Speed Microscopy and Thermometry of Reaction Propagation and Sintering in a Nanocomposite. Nature Communications 2019,10,3032.

(41) Wang, H.; Julien, B.; Kline, D. J.; Alibay, Z.; Rehwoldt, M. C.; Rossi, C.; Zachariah, M. R. Probing the Reaction Zone of Nanolaminates at ∼μs Time and ∼μm Spatial Resolution. J. Phys. Chem. C 2020, 124, 13679–13687.

(42) Chen, B.; Zheng, H.; Riehn, M.; Bok, S.; Gangopadhyay, K.; Maschmann, M. R.; Gangopadhyay, S. In Situ Characterization of Photothermal Nanoenergetic Combustion on a Plasmonic Microchip. ACS Appl. Mater. Interfaces 2018, 10, 427–436.

(43) Weismiller, M. R.; Wang, S. Q.; Chowdhury, A.; Thynell, S. T.; Yetter, R. A. Confined Rapid Thermolysis Studies of Ammonia Borane. Thermochimica Acta 2013, 551, 110–117.

(44) Baitalow, F.; Baumann, J.; Wolf, G.; Jaenicke-Roöβler, K.; Leitner, G. Thermal Decomposition of B-N-H Compounds Investigated by Using Combined Thermoanalytical Methods. Thermochimica Acta 2002,391,159-168.

(45) Baumann, J.; Baitalow, F.; Wolf, G. Thermal Decomposition of Polymeric Aminoborane (H2BNH2)x under Hydrogen Release. Thermochimica Acta 2005,430,9-14.

(46) Chatterjee, T.; Thynell, S. T. Development of a Reaction Mechanism for Liquid-Phase Decomposition of Ammonia Borane. Thermochimica Acta 2019,682,178427.

(47) Mechale, E. T.; von Elbe, G. The Deflagration of Solid Propellant Oxidizers. Combustion Science and Technology 1970,2,227-237.

(48) Zhou, W.; DeLisio, J. B.; Wang, X.; Zachariah, M. R. Reaction Mechanisms of Potassium Oxysalts Based Energetic Composites. Combustion and Flame 2017,177,1-9.

(49) Wang, H.; Rehwoldt, M. C.; Wang, X.; Yang, Y.; Zachariah, M. R. On the Promotion of High Temperature AP Decomposition with Silica Mesoparticles. Combustion and Flame 2019, 200, 296-302.

(50) Jacob, R. J.; Wei, B.; Zachariah, M. R. Quantifying the Enhanced Combustion Characteristics of Electrospray Assembled Aluminum Mesoparticles. Combustion and Flame 2016, 167, 472–480.

(51) Nazir, N.; Ahanger, M. S.; Akbar, A. Micellization of Cationic Surfactant Cetyltrimethylammonium Bromide in Mixed Water-Alcohol Media. Journal of Dispersion Science and Technology 2009,30,51-55.

(52) Jian, G.; Zhou, L.; Piekiel, N. W.; Zachariah, M. R. Low Effective Activation Energies for Oxygen Release from Metal Oxides: Evidence for Mass-Transfer Limits at High Heating Rates. ChemPhysChem 2014, 15 (8), 1666–1672.

(53) DeLisio, J. B.; Huang, C.; Jian, G.; Zachariah, M. R.; Young, G. Ignition and Reaction Analysis of High Loading Nano-Al/Fluoropolymer Energetic Composite Films. 52nd Aerospace Sciences Meeting, National Harbor, Maryland, January 1–8,2014; American Institute of Aeronautics and Astronautics. https://doi.org/10.2514/6.2014-0646.

(54) Zhou, W.; DeLisio, J. B.; Wang, X.; Egan, G. C.; Zachariah, M. R. Evaluating Free vs Bound Oxygen on Ignition of Nano-Aluminum Based Energetics Leads to a Critical Reaction Rate Criterion. Journal of Applied Physics 2015,118,114303.

(55) Holdren, S.; Tsyshevsky, R.; Fears, K.; Owrutsky, J.; Wu, T.; Wang, X.; Eichhorn, B. W.; Kuklja, M. M.; Zachariah, M. R. Adsorption and Destruction of the G-

Series Nerve Agent Simulant Dimethyl Methylphosphonate on Zinc Oxide. ACS Catal. 2019, 9, 902–911.

(56) Perdew, J. P.; Burke, K.; Ernzerhof, M. Generalized Gradient Approximation Made Simple. Phys. Rev. Lett. 1996, 77, 3865.

(57) Vargas-Hernández, R. A. Bayesian Optimization for Calibrating and Selecting Hybrid-Density Functional Models. J. Phys. Chem. A 2020, 124, 4053–4061.

(58) Zarkevich, N. A.; Johnson, D. D. Nudged-Elastic Band Method with Two Climbing Images: Finding Transition States in Complex Energy Landscapes. J. Chem. Phys. 2015,142,024106.

(59) Jian, G.; Chowdhury, S.; Sullivan, K.; Zachariah, M. R. Nanothermite Reactions: Is Gas Phase Oxygen Generation from the Oxygen Carrier an Essential Prerequisite to Ignition? Combustion and Flame 2013, 160, 432–437.

(60) Zhou, W.; Delisio, J. B.; Li, X.; Liu, L.; Zachariah, M. R. Persulfate Salt as an Oxidizer for Biocidal Energetic Nano-Thermites. J. Mater. Chem. A 2015,3, 11838-11846.

(61) Wagh, A.; Raviprakash, Y.; Upadhyaya, V.; Kamath, S. D. Composition Dependent Structural and Optical Properties of PbF2-TeO2-B2O3-Eu2O3 Glasses. Spectrochimica Acta - Part A: Molecular and Biomolecular Spectroscopy 2015, 161, 696-706.

(62) Rao, L. S.; Rao, P. V.; Sharma, M. V. N. V. D.; Veeraiah, N. J-O Parameters versus Photoluminescence Characteristics of 40Li2O-4 MO (MO=Nb2O5, MoO3 and WO3)-55B2O3:1Nd2O3 Glass Systems. Optik 2017, 142, 674-681.

(63) Bødker, M. S.; Mauro, J. C.; Youngman, R. E.; Smedskjaer, M. M. Statistical Mechanical Modeling of Borate Glass Structure and Topology: Prediction of Superstructural Units and Glass Transition Temperature. J. Phys. Chem. B 2019, 123, 5, 1206–1213.

(64) Howes, A. P.; Vedishcheva, N. M.; Samoson, A.; Hanna, J. V.; Smith, M. E.; Holland, D.; Dupree, R. Boron Environments in Pyrex® Glass - A High Resolution, Double-Rotation NMR and Thermodynamic Modelling Study. Phys. Chem. Chem. Phys. 2011,13, 11919-11928.

(65) Kondrat'Ev, Y. V.; Butlak, A. V.; Kazakov, I. V.; Timoshkin, A. Y. Sublimation and Thermal Decomposition of Ammonia Borane: Competitive Processes Controlled by Pressure. Thermochimica Acta 2015,662,64-71.

(66) Lindman, N.; Simonsson, D. On the Application of the Shrinking Core Model to Liquid-Solid Reactions. Chemical Engineering Science 1979,34,31-35.

3.7 Supporting information

S.1 Calculation of oxidative energy content of different hydrides and metlals/metalloids

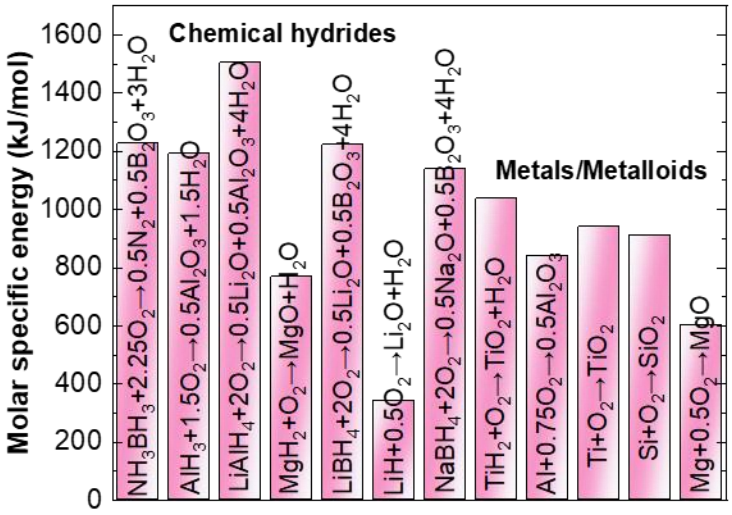

FigureS1 Molar specific energy of chemical hydrides with balanced reactions showing AB (NH_3BH_3) and other chemical hydrides has a theoretically higher oxidative energy content than most metals and metalloids. NIST standard enthalpy of formation have been used for all calculations except that of AB (Thermochimica Acta, Volume 622, 20 December 2015, Pages 64-71), $NaBH_4$, $LiBH_4$ and LiAlH4 (*J. Am. Chem. Soc. 1949, 71, 8, 2775–2781*).

S.2 AB characterization

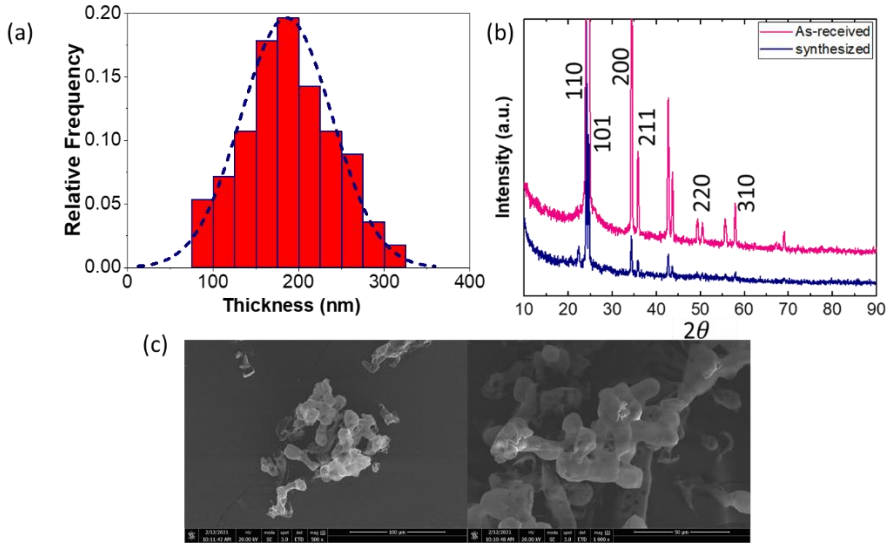

FigureS2 (a) SEM size distribution of synthesized AB (b) XRD comparison of synthesized AB and as-received AB shows synthesized AB is obtained in pure tetragonal phase (c) SEM of as-receeived AB showing agglomerated 100 µm particles.

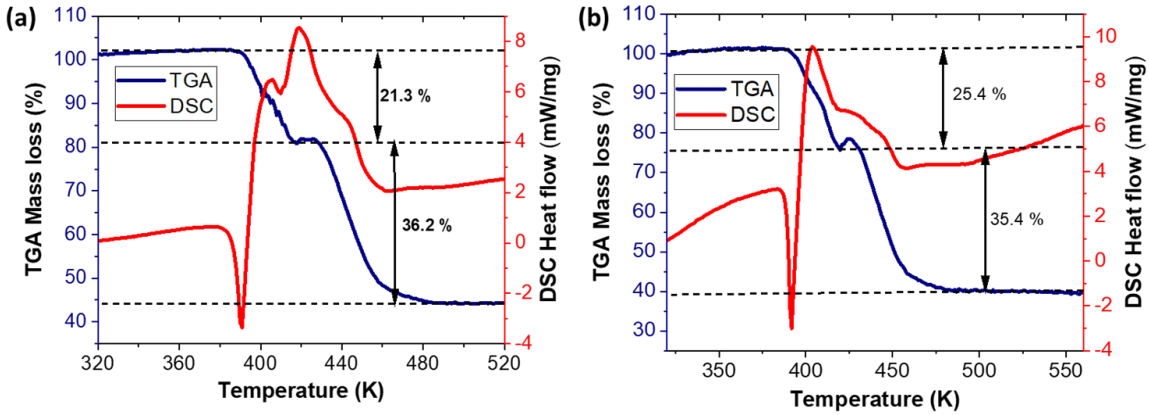

FigureS3 TGA/DSC of (a) commercial AB (b) synthesized AB in Ar with heating rate of 10 K/min shows similar mass loss, indicating the preservation of active after synthesis.

S.2.1 Approximate Estimation of mass loss from detection of BNH_x species in T-jump TOFMS

Balanced equation of formation of the species observed in T-jump TOFMS of AB:

$$2NH_3BH_3(AB) \rightarrow B_2N_2H_8(CDB) + 2H_2$$

$$3NH_3BH_3(AB) \rightarrow B_3N_3H_6(borazine) + 6H_2$$

$$3n\ NH_3BH_3 \rightarrow n[-B_3N_3H_4-]\ (PBZ) + (7n-1)H_2$$

Summing up:

$$(5+3n)NH_3BH_3 \rightarrow B_2N_2H_8 + B_3N_3H_6 + n[-B_3N_3H_4-] + (7n+7)H_2$$

From the balanced equation, the total mass loss from release of gas phase species like $B_2N_2H_8$, $B_3N_3H_6$ and H_2 is ~67%. The first mass loss step of TGA of AB corresponds to chain/cyclic oligomer formation containing B-N single bonds, whereas the second mass loss step of AB corresponds to chain/aromatic species formation containing B=N double bonds (Demirci, Inorg. Chem. Front., 2021, 8, 1900). Hence, CDB and its corresponding hydrogen is released during the first mass loss step and borazine and its corresponding H_2, as well as the H_2 due to PBZ formation are released during the second mass loss step. The mass loss due to CDB and H_2 release in the first step as calculated from the above balanced equation is 25 % which exactly matches the first step mass loss in TGA (FigureS2(b)). The calculated mass loss due to BZ and H_2 formation is 37 % whereas the mass loss due to H_2 release due to PBZ formation is 5 %. Hence, if the observed species exist a maximum ~11.2 % of H_2 can be released from 19.6 % H_2 content of AB. However, this is the maximum possible mass loss during AB thermolysis, as there will be an interconversion between borazine and PBZ, which can reduce the net mass loss under practical conditions. In FigureS2(b), TGA of AB shows 31 % mass loss in the second step, which may be due to the formation of more PBZ compared to borazine.

S.2.2 Comment on CTAB content

According to FigureS3(a), as-received AB shows 21.3 % and 36.2 % mass loss in the first and second step respectively. Figure 3-3(b) shows that the synthesized AB shows 25.4 % and 35.4 % mass loss in the first and second step respectively. The initiation and termination temperatures of both the mass loss steps exactly matches between both the samples. FigureS17 shows TGA/DSC of as-received CTAB. CTAB completely decomposes endothermically between 490-570 K. Hence, it does not have any exothermic effects on the thermal decomposition process of AB. Moreover, TGA curve of synthesised AB in Figure S3(b) shows that its decomposition ends at ~480 K and there is no observable mass loss between 490-570 K. It is possible that CTAB has decomposed earlier owing to the exothermic heat released from the decomposition of AB molecules closer to the surface of the AB particles. In the second decomposition step, the synthesized AB (35.4 %) shows approximately similar mass loss to the as-received AB (36.2 %). Therefore, the higher mass loss in the first step of the synthesized AB (25.4 %) compared to the as-received AB (21.3 %), can be possibly attributed to the earlier decomposition of CTAB. Hence, it can be said that the synthesized AB contains ~4 % CTAB.

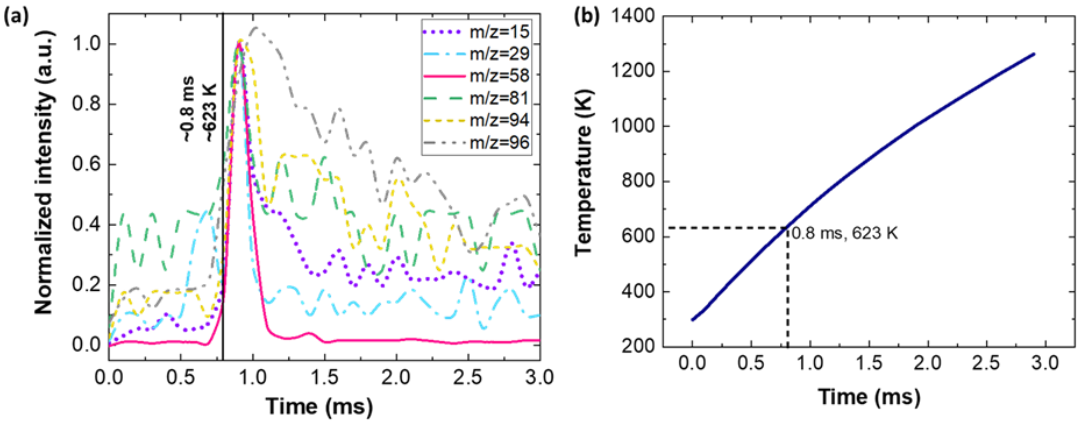

FigureS4 Temporal T-jump TOFMS release profiles of different BNH_x species (m/z=15,29,58,81,94 and 96) showing that these species are released at the same time delay of ~0.8 ms which corresponds to a temperature of ~623 K as obtained from the time-dependent dependent temperature profile of the wire (b).

S.3 Bare oxidizer T-jump

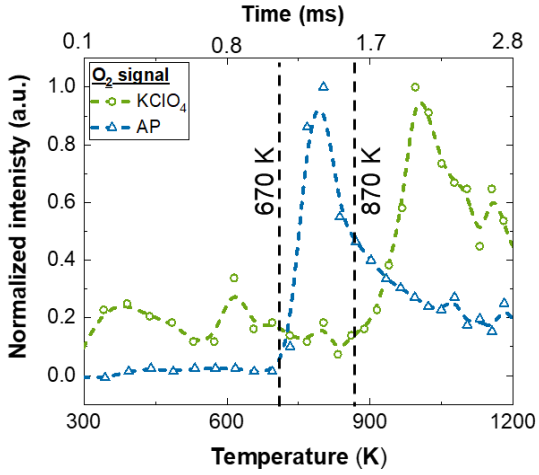

FigureS5 O_2 release temperature of pristine $KClO_4$ (~670 K) and AP (~870 K) in T-jump TOFMS. O2 release temperature from CuO (~940 K) and Bi_2O_3 (~1220 K) has also been detected in the same manner, which has also been presented in previous studies from the group. Since, AB did not ignite with CuO and Bi_2O_3, further characterizations of AB with these two oxidizers have not been performed.

S.4 AB oxidation characterization

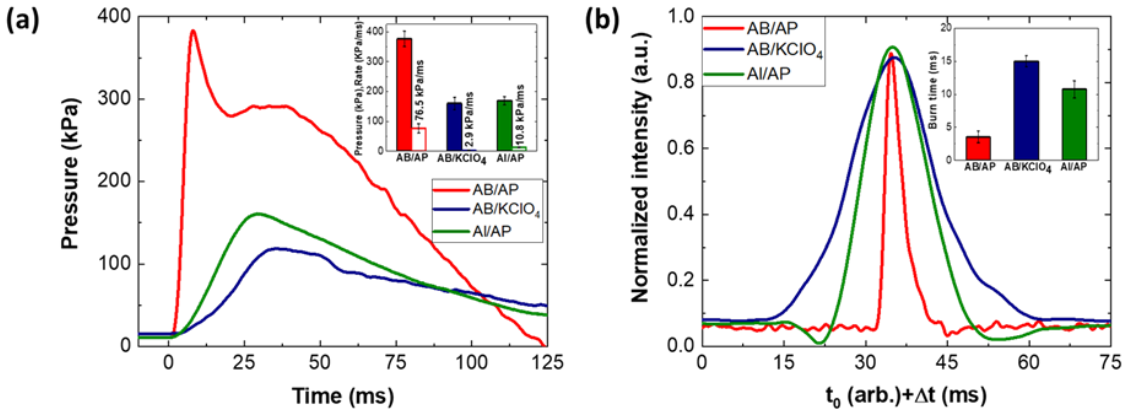

FigureS6 Burn time characterized by the FWHM of the optical signal obtained during combustion cell measurements suggest that AB/AP has shorter burn time than both AB/KClO4 and Al/AP indicating its faster reaction

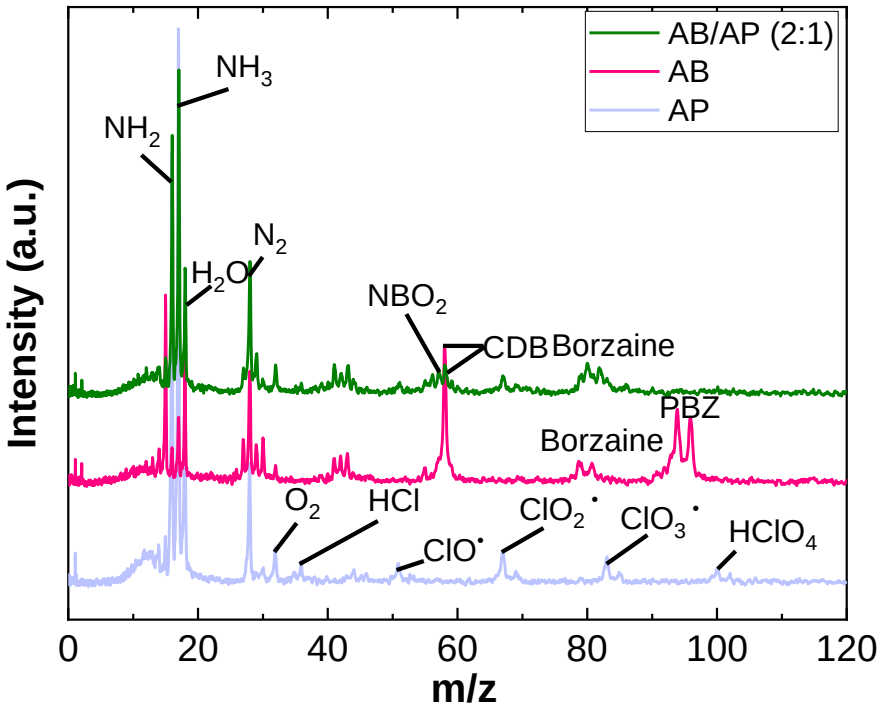

FigureS7 BNH_x (borazine, CDB) form during AB/AP reaction when excess AB is present (AB:AP=2:1) in T-jump TOFMS. This composition also do not ignite.

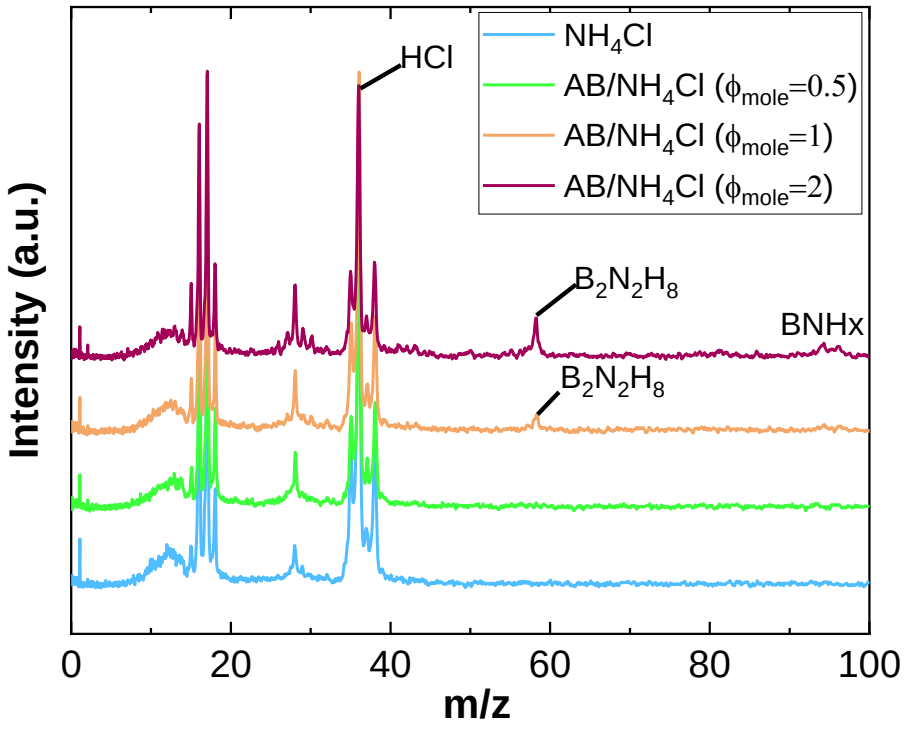

FigureS8 Control experiment with AB/NH_4Cl in T-jump TOFMS, to show that BNH_x are absent in presence of ammonium salts. BNH_x (CDB or $B_2N_2H_8$) species are formed only when excess AB is present and are absent when AB is the leaner constituent with NH_4Cl being in excess.

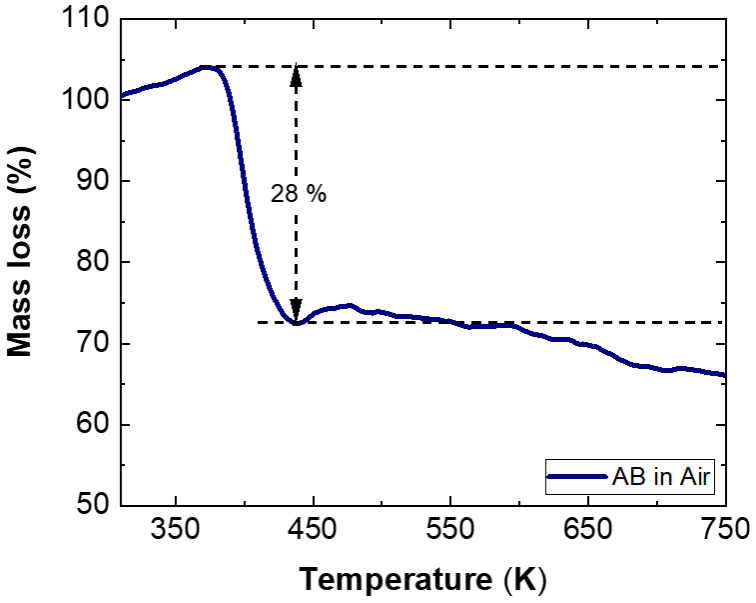

FigureS9 TGA/DSC of AB in air at 10 K/min shows a ~28 % mass loss in a single-step around the melting point of AB (~383 K). Ideally, if AB is completely oxidized, then 1 mole of AB should form 0.5 mole of B_2O_3 resulting in ~12 % mass gain. Hence, heating in air cannot completely oxidize AB and the ~28 % mass loss may be a result of gaseous BNH_x species release.

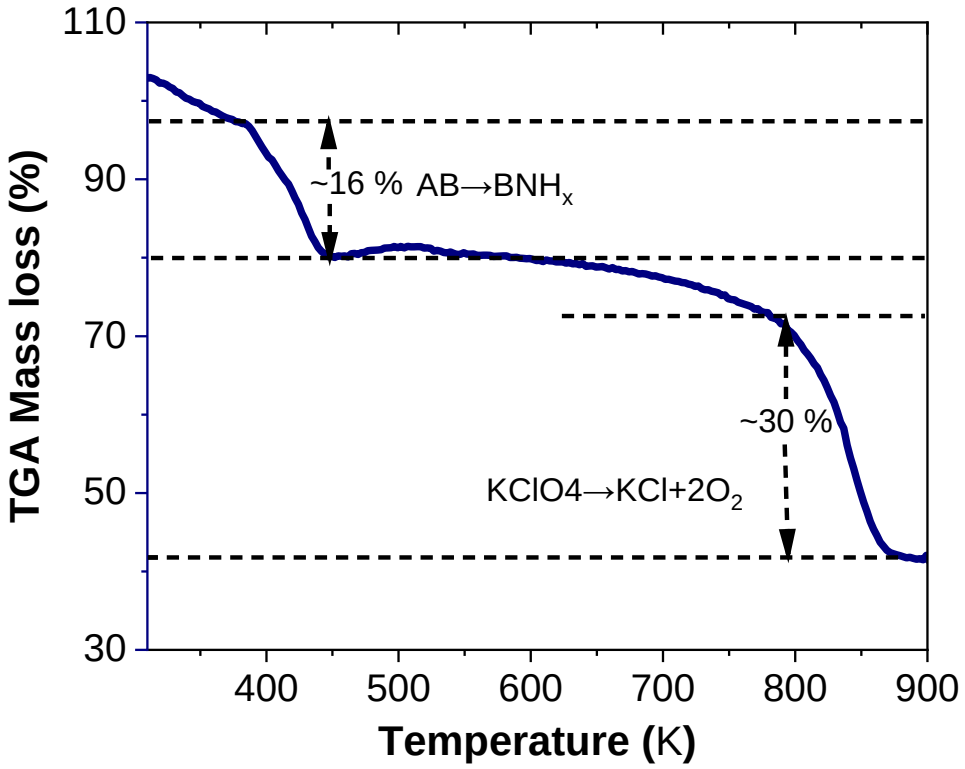

FigureS10 TGA/DSC of AB/$KClO_4$ in Ar at the same heating rate shows similar mass loss between 390-450 K as observed in TGA of pristine AB in Ar, followed by a mass loss around 873 K due to KClO4 decomposition.

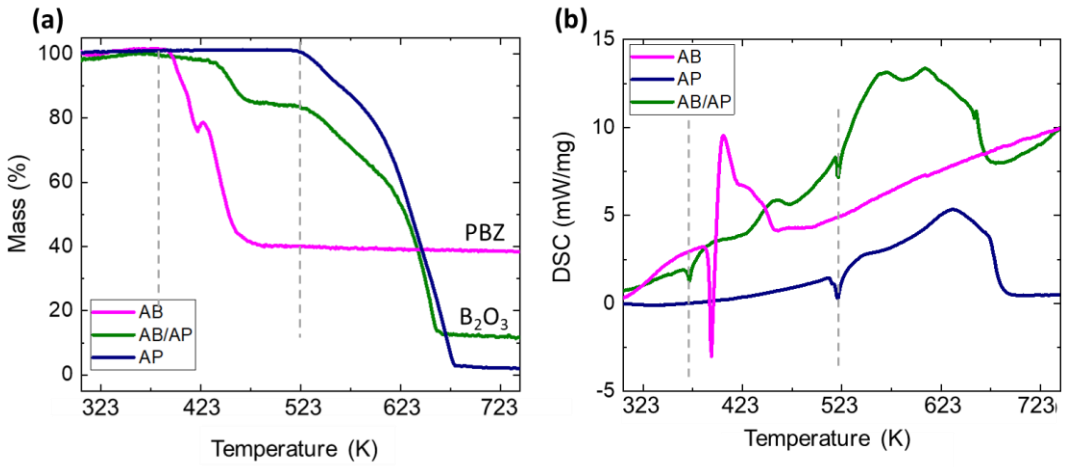

FigureS11 TGA/DSC of AB/AP showing different profile than pristine AB and AP in Ar at a heat rate of 10 K/min.

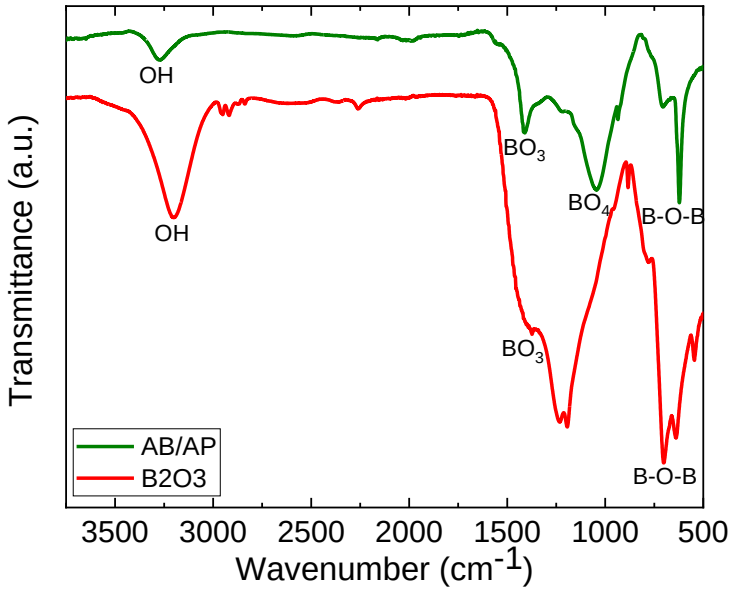

FigureS12 Comparison between ATR-FTIR spectra of AB/AP residue in TGA and commercial B_2O_3 (Sigma Aldrich) for showing that shows that AB/AP reaction product consist of B_2O_3 (BO_3 and B-O-B vibrations) as well as some other borates (BO_4 units).

S.5 Computation of energetics of AB thermolysis,AB/AP, and AB/$KClO_4$ reactions

S.5.1 Balanced stoichiometric reactions considered for mixing AB with $KClO_4$ and AP

$$AB + 1.125KClO_4 \rightarrow 0.5B_2O_3 + 0.5N_2 + 3H_2O + 1.125KCl \qquad (S1)$$

$$\Delta H_{S1} = -1233\ kJ/mol$$

$$AB + 1.8AP \rightarrow 0.5B_2O_3 + 1.4N_2 + 5.7H_2O + 1.8HCl \qquad (S2)$$

$$\Delta H_{S2} = -1510\ kJ/mol$$

S.5.2 Geometries of optimized molecules

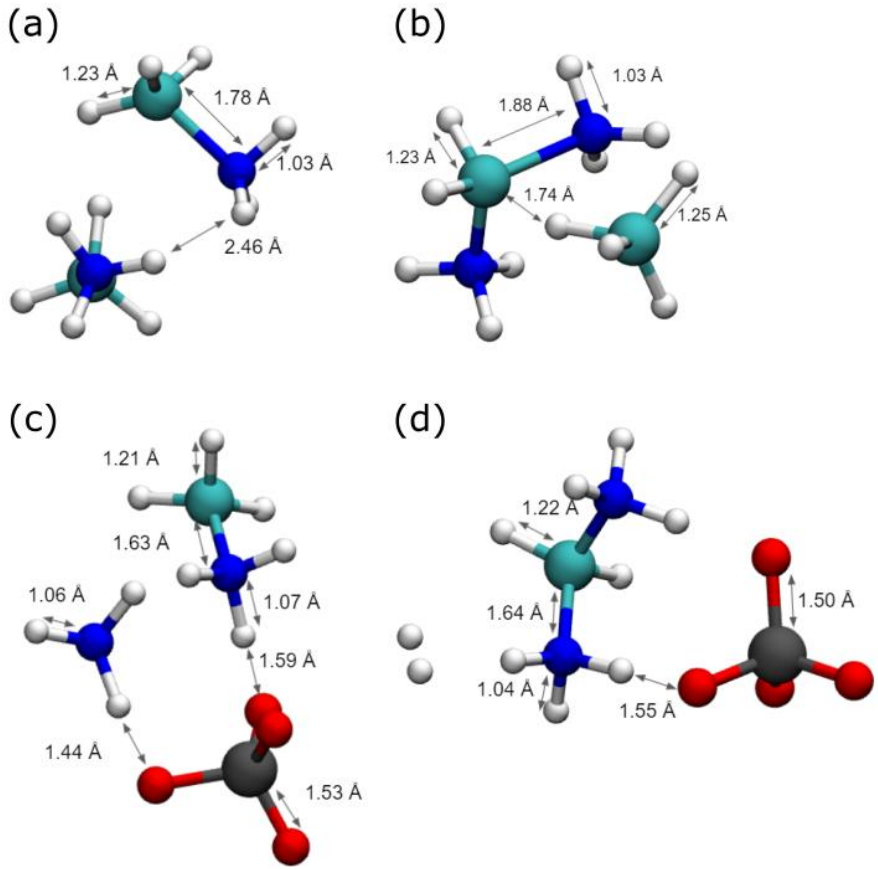

FigureS.13 Optimized structures of (a) reactant and (b) product of AB thermolysis and (c) reactant and (d) product of AB/AP pathway respectively, with bond lengths specified.

S.5.3 Fractional coordinates of optimized geometries

AB/AP (NH_3BH_3 + NH_4ClO_4)

H B N H N Cl O
6 1 1 4 1 1 4 //number of lines for each atom in the given sequence
Direct
0.0455438183040736 0.8863806000273281 0.8314197146603789
0.0632724405693863 0.9742318890501505 0.7248056141973767
0.9472230283624726 0.9620182240486557 0.7799739935675178
0.1416912551144586 0.0164138321648440 0.8451427895387513
0.0686345476123871 0.0973767885115881 0.8365760394734210
0.0721119547990990 0.0322693906083557 0.9289247506983922
0.0283409962966776 0.9570801501895619 0.7956093018644518
0.0760742116863645 0.0323270086415402 0.8576979099132601
0.9236821893081744 0.9896100378560992 0.8768177583741020
0.8935671890984729 0.0319998370334733 0.9877001572664282
0.8334669245300893 0.0551920864976517 0.8872329582612798
0.8335570670409223 0.9506677732378745 0.9284647754458328
0.8705548954967627 0.0078263443905336 0.9201982568950838
0.0107210261052295 0.9970672956838316 0.0862104748429896
0.9273189656762768 0.0550439339390525 0.0744344420503701
0.0829546420515123 0.0402399180933309 0.0342058898968973
0.9906565628656370 0.9092061066318680 0.0482287928714019
0.0336283063809877 0.9948487816292535 0.1785563495500692

$[NH_3BH_2NH_3]^+$ $[ClO_4]^-$+ H_2

H B N H N Cl O
6 1 1 4 1 1 4 //number of lines for each atom in the given sequence
Direct
0.0642743222595489 0.9085016714756258 0.8838856482177962
0.0186212963975965 0.9466543940180335 0.7643310583195763
0.9190983832426810 0.8355778795627936 0.7279901910537867
0.1174763864454948 0.0608701781294612 0.8309827930619501
0.0172561375651839 0.1067296411204574 0.8297946901253967
0.0619718809173625 0.0717315797808863 0.9291339995016675
0.0161179086217736 0.9600960841813105 0.8445185577976743
0.0550341138966974 0.0574899328901540 0.8593462698543022
0.8828258368205724 0.8484151665623160 0.7596704773052458
0.9190859941061645 0.9964307802685533 0.9582854288771437
0.8670263758774381 0.9932412922706942 0.8600834905803114
0.8947385934247614 0.8994303775776543 0.9091231850772231
0.9187972775741698 0.9621308632213841 0.8936526733230959
0.0044287610440065 0.0385283057579320 0.0898522304226000
0.9151751472679911 0.0536664976314163 0.0445406083431814
0.0733663547557005 0.0855205309377943 0.0346884137671330
0.0230696790999063 0.9431887455823881 0.0899512899343131
1.0019806053787876 0.0769137299317201 0.1781141874842245

2x AB ($2xNH_3BH_3$)

H B N H B N
6 1 1 6 1 1 //number of lines for each atom in the given sequence
Direct
0.9479475256260720 0.0998359748795000 1.0114585364199902
1.0079121419528296 0.2149085044558688 0.9794421486679680
0.8724054794895554 0.1936873346796799 0.9504144717284246
0.9371733050457778 0.3123014412740164 0.0488331574280274
0.8596171919378814 0.2723095000166586 0.1184431311288672
0.9641154171924838 0.2500918763156900 0.1367637617464885
0.9368668315750943 0.1795407215024726 -0.0014461397688282
0.9187631861550378 0.2575544689713911 0.0859034642327341
0.7057650309521332 0.1078668907781356 0.0701431237451956
0.7115028315134243 0.2028354541836486 0.1246701893134087
0.6733366307032526 0.1131161068605538 0.1766329553435119
0.8622781002431746 0.1155058074665466 0.0955348660541610
0.8420760686637623 0.1538704457344725 0.2238843427902257
0.8191853711756402 0.0257334991153490 0.1791819425226403
0.8203349581078682 0.1048916181625015 0.1618301056052956
0.7197865643280148 0.1348836841415113 0.1315766261118867

DADB ($[NH_3BH_2NH_3]^+ [BH_4]^-$)

H B N H B N
6 1 1 6 1 1 //number of lines for each atom in the given sequence
Direct
0.9578888749559260 0.0726164458058876 -0.0431566015
0.9848886031162637 0.1987458856276944 -0.01073645671
0.8651166264674927 0.1740092123104593 -0.07135338045
0.9264187278323729 0.2739830735999588 0.0804154870909529
0.8313483088258424 0.2886519323390506 0.1385598914875462
0.9220820522469043 0.2543079393339713 0.1924903161375954
0.9239808517078966 0.1435910838285003 -0.02255133186
0.8875823936749239 0.2499470269573937 0.1330439683539120
0.7200993012831947 0.1248078243801705 0.0675506140622393
0.7180418448698348 0.2167490812585421 0.1291179807725085
0.7003077973090293 0.1202112128184799 0.1782246435736189
0.8834464444472250 0.1211330883878292 0.0482441445439784
0.8447633172962460 0.1577579854621668 0.2342969419292600
0.8547185126662974 0.0555455567108412 0.1548178694143401
0.8406658967801496 0.1359975755059715 0.1552451763109717
0.7377171016693889 0.1507451394030795 0.1291240737564063

S.6 Combustion product size characterization

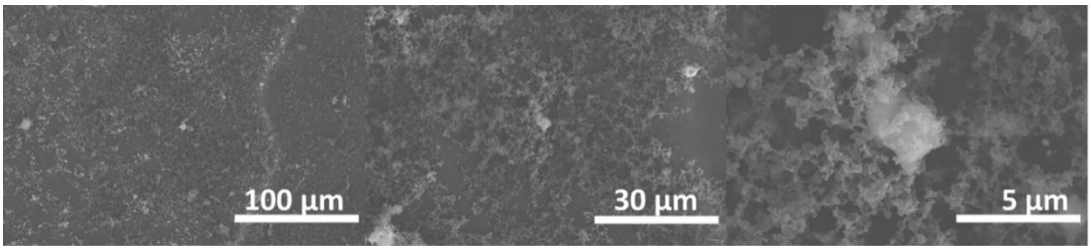

FigureS14 SEM of combustion product of Al/AP reaction contains sub-micron particles

S.7 Bare oxidizer SEM

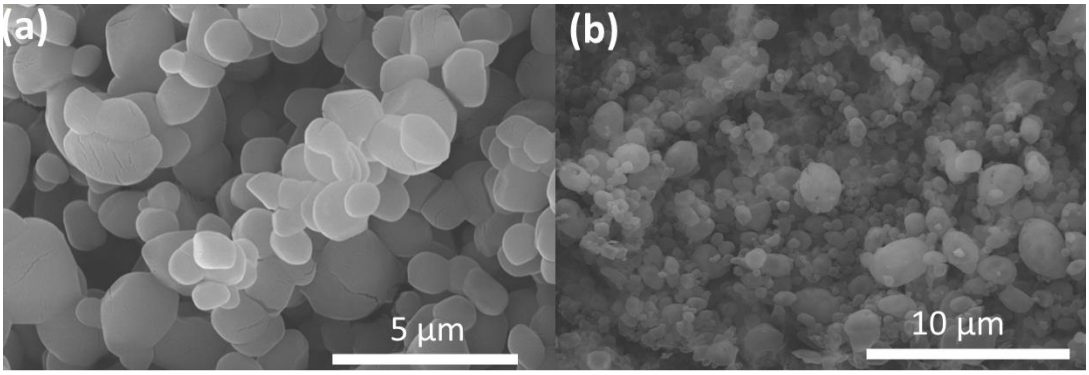

FigureS15 SEM images of bare oxidizers (a) $KClO_4$ (b) AP

S.8 Additional Miscellaneous Characterizations for supporting main results

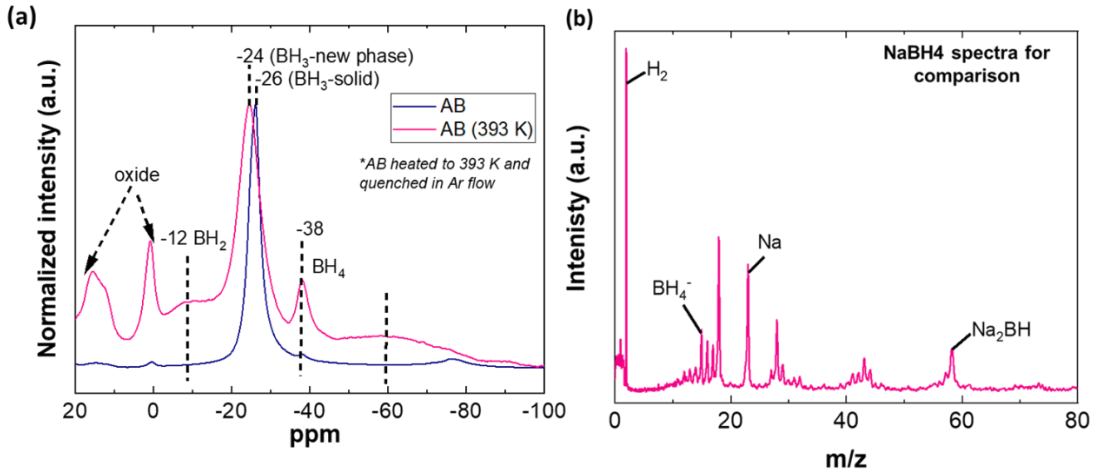

FigureS16 (a) ^{11}B NMR spectra of AB and AB heated to intermediate temperature 393 K (in a tube furnace under Ar flow). The appearance of BH_4 and BH_2 peak in the heated and quenched sample indicates DADB ($[NH_3BH_2NH_3]^+[BH_4]^-$) formation on decomposition of solid-state AB at 393 K. (b) T-jump TOFMS of spectra of $NaBH_4$ shows the separate detection of the cation (Na) and anion (BH_4), which also suggests that the BH_4 observed during the decomposition of AB in T-jump TOFMS likely indicates the formation of DADB.

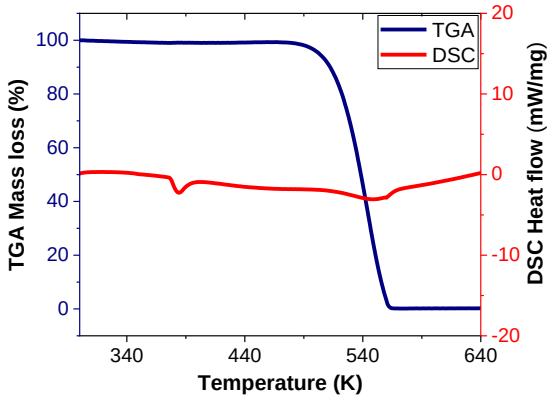

FigureS17 TGA/DSC of as-received CTAB shows its complete endothermic decomposition between 490-570 K

4 Catalytic Cleavage of the Dative Bond of Ammonia Borane by Polymeric Carbonyl Groups for Enhanced Energy Generation

4.1 Summary

Dissociation of the dative (B-N) bond of Ammonia Borane (NH_3BH_3/AB) is essential to prevent its thermochemical oligomerization to chemically resistant BNH_x compounds, for its applicability as a fuel in high energy propulsion systems. I show that when AB is incorporated into polymer matrices containing carbonyl functional groups, thermal activation causes the carbonyl groups to engage in nucleophilic interactions with AB. Such interactions catalyze the lysis of the dative B-N bond resulting in the decomposition of AB to NH_3 and B_2H_6 gases, with no evidence of oligomerization I find the carbonyl groups function as catalysts and do not participate in any net reaction. In-situ high-heating rate (~10^5 K/s) characterizations, demonstrate that facile-synthesized hierarchical (micro/nano) composite particles of AB/carbonyl-based polymers completely gasify to NH_3 and B_2H_6 at ~510 K, followed by spontaneous ignition in air with negligible delay. Thus, the current chemical pathway enables the solid-state storage of reactive fuels, NH_3 and B_2H_6, and their controlled on-demand release for high energy applications.

4.2 Introduction

Chemical hydrides such as ammonia borane (AB/NH_3BH_3) have been widely explored as hydrogen storage mediums for low temperature energy conversion in fuel cells[1–31]. On the other hand, limited efforts have been made[32–35] on investigating the energy generation capability of these compounds for propulsion systems, which demand

extremely high energy release rates [36–44]. Elemental metals and metalloids, particularly boron (B), possess high oxidative energy density and are therefore attractive as fuel components in solid-state energy dense materials for propulsion systems[45]. During the oxidation process of B nanoparticles, a molten oxide shell grows from the surface to the core of the particle, while the core B is still in solid state[46,47]. The liquid oxide shell presents a significant barrier to oxygen diffusion, which severely limits the reactivity of particulate B[48]. Borohydride complexes like ammonia borane (AB) consisting of both of the highest energy dense elements B (~58 kJ/g) and H (~120 kJ/g), are very attractive as fuels for energetic applications. Additionally, such complexes can potentially decompose to gaseous hydrogen and boranes (BH_x), which in principle can react without condensed phase diffusion limitations[49–51].

Unfortunately, the dative B-N bond introduces complications to the thermal decomposition mechanism of AB, as it causes AB molecules to oligomerize to higher molecular weight BNH_x compounds such as gaseous borazine and solid-polyborazylene, instead of forming ammonia or boranes[19,32,52–54]. Solid-polyborazylene is often used as a chassis for regenerating AB to facilitate reversible hydrogen storage in AB[16,19,55]. However, in high energy propulsion systems requiring the oxidation of both B and H elements, these higher molecular weight BNH_x compounds can impede the reactivity and energy generation rate from AB, as chemical resistance increases with molecular weight. Previous studies have employed liquid [34,56–58] and solid-state oxidizers[32] or surrogate exothermic reactions[33] to alter the condensed phase decomposition intermediate of AB, to enhance its energy release rate by inhibiting BNH_x formation. However, this limits the use of AB in

propulsion systems using air as an oxidizer[59,60]. Some studies have reported the interaction with polymer binders can generate NH_3 and H_2 from AB instead of borazine[61–65]. However, those studies are lacking in evidence and discussion on the fate of the boron atoms during AB decomposition.

When neat AB crystals melt, intermolecular hydride transfer between the borons along with subsequent nucleophilic addition of NH_3 moieties to the electrophilic B-centers results in the formation of diammoniate of diborane (DADB/$[NH_3BH_2NH_3]^+[BH_4]^-$) as an intermediate. This activates the oligomerization pathway of AB to BNH_x species [19,32,52]. Herein, I show that the incorporation of AB in matrices of polymers with carbonyl groups such as polymethyl methacrylate (PMMA), polyvinyl pyrrolidone (PVP), and polypropylene carbonate (PPC), can prevent the oligomerization of AB. The carbonyl groups compete with the borons of AB as sites of nucleophilic attack from the NH_3 moieties, thereby resulting in the catalytic cleavage of the dative B-N bond in AB leading to its dissociation into NH_3 and B_2H_6. Using high-heating rate in-situ temperature-jump time-of-flight mass spectrometry (T-jump TOFMS), supported with thermogravimetric analysis and ATR/FTIR characterizations, I show that AB completely gasifies to NH_3 and B_2H_6 before the onset of the decomposition of the polymer, which remains chemically intact post-AB decomposition. The measured activation energy of the AB decomposition pathway to NH_3 and B_2H_6 in the polymer matrix (~26 kJ/mol) is much lower than both the bond-dissociation enthalpy of AB (~194 kJ/mol) and activation energy of DADB formation (~83 kJ/mol), confirming the catalytic effects of the polymeric carbonyl groups.

In order to investigate in-operando performance, I adopted a facile and scalable aerosol route for synthesizing 5-10 μm AB/polymer composite particles containing ~100 nm AB domains. High heating rate measurements revealed that the AB molecules in the composite particles decompose to NH_3 and B_2H_6 at ~510 K, and that the released B_2H_6 spontaneously ignites in air with negligible ignition delay. B_2H_6 with extremely low auto-ignition temperature ~310 K (H_2 ~850 K) is highly desirable for propulsion systems using air as an oxidizer, however the use of B_2H_6 in gaseous form has been limited due to its high instability and toxicity[66,67]. The current study solves this issue, by reporting a novel chemical pathway that facilitates the solid-state storage and controlled on-demand release of B_2H_6 for high energy applications.

4.3 Experimental section

4.3.1 Materials

Ammonia borane (~97 %) powder consisting of ~50-100 μm crystals were purchased from Sigma Aldrich. SEM and XRD of the as-received AB crystals can be found elsewhere[32]. Polymethyl methacrylate (MW~550,000), polyvinyl pyrrolidone (MW~360,000), and polypropylene carbonate (MW~283,000) were obtained from Alfa Aesar, Fisher scientific, and Empower respectively. All solvents used were obtained from Fisher scientific.

4.3.2 AB/polymer composite preparation method for different characterizations

For making AB/polymer composites containing different wt. % of AB, desired amounts of AB and polymers were completely dissolved in an ethanol-dichloromethane

mixture, containing 80 % dichloromethane and 20 % ethanol by volume, to obtain a completely transparent solution. The polymer to solvent ratio is kept constant at 10 mg/ml in all the solutions, and only the AB/polymer ratio has been varied. In case of the AB/PVP composite, only ethanol was used as the solvent. For the T-jump measurements, the composite solvents were directly drop-casted and dried from the solution as a film on the Pt wire sample holder. The coated samples were allowed to stay under high vacuum for ~15 mins, before each measurement, to ensure complete removal of the solvents. For other characterizations like TGA, ATR-FTIR, and XRD, the AB/polymer solutions were dried as solid films on glass petri-dishes in a vacuum oven, and then transferred to the respective sample holders required for the measurements. The AFM imaging was performed on AB/PMMA films spin-coated on glass slides using the same formulation.

4.3.3 **Characterizations on the microstructure, composition, and thermochemical reactions of AB/polymer composites**

ATR-FTIR characterizations has been performed using ThermoFisher Nicolet iS50R, for compositional analysis as well as to characterize the peak splitting due to dihydrogen bonding of AB. X-ray Diffraction has been performed using PANalytical EMPYREAN (Cu Kα source, $\lambda = 1.54$ Å) to identify the composition and degree of crystallinity of AB in polymer matrices. Thermo-gravimetric analysis (TGA) was performed using Netzsch STA 449 F3 to understand the decomposition steps of AB, polymers, and AB/polymer composites at a heating rate of 10 K/min in argon flow. Tapping mode Atomic Force Microscopy (AFM) was performed using Asylum Research

MFP-3D with a 7 nm Si probe to obtain phase retrace images of the AB domains near the surface of the polymer composites, with the assumption that the microstructure near surface of the spin-coated thin-films on glass substrate is identical to that in the bulk. The scanning electron microscope (SEM) micrographs of the meso-particle composites were obtained using FEI NNS450.

4.3.4 In-situ temperature jump time-of-flight mass spectrometry and high-speed imaging

High heating rates attained during fast exothermic reactions, can dramatically influence intrinsic chemical reaction rates and condensed phase diffusivities. Hence, combustion reactions of solid-state fuels need to be probed at high heating rates. Temperature jump probe coupled with a time-of-flight mass spectrometer (T-jump TOFMS) have been used to perform in-situ time and temperature resolved analysis of the gas phase species released on decomposition of AB, polymers, and AB in polymer matrices at high heating rates of ~10^5 K/s. Details about the mass-spectrometer can be found in several of our previous publications[32,45,68,69]. For the measurements, either AB powder was drop-casted from a dispersion in hexane or the dissolved polymer or AB/polymer are drop-casted as films directly from their solutions, on a ~75 μm Pt wire, which is resistively heated to ~1500 K with a ~3 ms voltage pulse, which maintains an average heating rate of ~10^5 K/s. For the Flynn-Wall-Ozawa activation energy measurements, the heating rate was varied by adjusting the pulse width. The thin coating ensures that the sample is at the same instantaneous temperature of the wire and is uniformly heated. The instantaneous

wire temperature is estimated through Callender-Van-Dusen equation by monitoring the current across the wire at every 0.1 ms over the entire 3 ms pulse. The TOFMS assembly samples the gas phase species released at every 0.1 ms over 10 ms. The entire measurement is performed under a high vacuum of ~10^{-9} atm. For the high-speed imaging of the ignition process, the same sample holder and heating assembly is used, the only exception being that the heating of the sample is performed in air. A high-speed Phantom Miro 110 camera triggered by the rising edge of the ~3ms pulse, is used to capture the ignition phenomenon at ~50,000 frames per second with an exposure of ~50 µs.

4.3.5 Synthesis of mesoparticles composites

The hierarchical micro/nano AB/polymer mesoparticles composites were spray dried using a commercial Büchi B-290 Mini Spray Drier. The pre-cursor solution was made using the same procedure used for making the AB/polymer composite films, except the total AB and polymer content in the solution is reduced to 5 mg/ml. The pre-cursor solution was atomized and dried using heated argon gas at ~320 K, to make the composite mesoparticles.

4.4 Results and discussions

4.4.1 High heating rate (~10^5 K/s) decomposition products of AB in PMMA matrix

High heating rates are required for activating the ignition and combustion process of energetic materials (~10^5 K/s). Therefore, the decomposition reactions of crystalline AB and AB in PMMA matrix have been probed in-situ by temperature-jump time-of-flight

mass spectrometry (T-jump TOFMS) at heating rates of ~10^5 K/s under high vacuum (~10^{-9} atm). As mentioned in experimental section, a thin layer of sample coated on a ~75 μm Pt wire is rapidly pulse-heated to ~1500 K within ~3 ms (T-jump), and the gaseous species evolved on decomposition of the sample during the temperature ramp is probed over ~10 ms at an interval of 0.1 ms through the TOFMS technique. Figure 4-1 (a) shows the time-averaged mass spectra of bare AB and 25 wt. %, 50 wt. %, and 75 wt.% of AB in PMMA matrix. The composite samples were coated as a film on the Pt wire by drop-casting of respective AB/PMMA pre-cursor solutions.

At these heating rates, crystalline AB powder melts and AB molecules combine in the condensed phase to form diammoniate of diborane (DADB), as also reported in previous studies [19,25,32,52,70]. The formation of DADB leads to further oligomerization of DADB and AB molecules into higher molecular weight gas phase BNH_x clusters such as cyclic diborane (CDB) and borazine (BZ), simultaneously forming polyborazylene (PBZ) in the condensed phase (Figure 4-1(b)). Signatures of DADB fragments (m/z=15), CDB (m/z=58), BZ (m/z=81), and PBZ fragments (m/z=94 & 96) are observed in the mass-spectra of bare AB shown in Figure 4-1(a). In contrast , BNH_x species are absent in the AB/PMMA composites (Figure 4-1(a)). Rather, AB molecules in AB/PMMA, generate ammonia (NH_3) and diborane (B_2H_6) (Figure 4-1(b)), as evident from the spectra represented in Figure 4-1(a). Thus, AB in PMMA matrix follows an alternative decomposition pathway, possibly because of its interaction with the carbonyl groups, the mechanism of which is systematically investigated and revealed in the rest of the article.

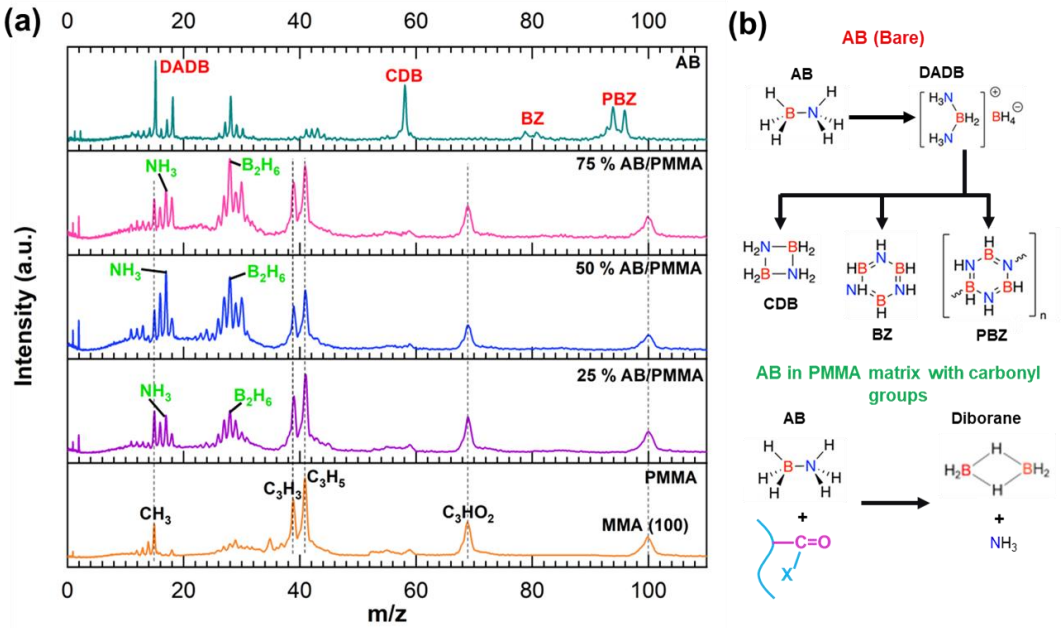

Figure 4-1 (a) T-jump TOFMS spectra shows that bare AB polymerizes to BNH_x species, whereas 25%, 50 %, and 75 % by wt. AB in PMMA matrix decomposes to NH_3 and B_2H_6 when subjected to a temperature ramp (~298-1500 K) within 3 ms at ~10^5 K/s. (b) Schematic explaining the different products formed after decomposition of bare AB and AB in PMMA matrices.

4.4.2 Time and temperature resolved decomposition profiles of AB in PMMA matrix

The time-resolved species and temperature evolution profiles (Figure 4-2(a)) obtained from T-jump TOFMS measurement of 75 % AB/PMMA shows that AB decomposes to gaseous NH_3 and B_2H_6 at ~ 510 K, before PMMA unzips to its monomers [71] at ~660 K. The decomposition temperature remains the same for AB/PMMA composites with lower AB content (25 & 50 wt. %) as shown in Figure S1 (supporting information). Generally higher heating rates have higher reaction onset temperatures[72]. At slow heating rates (10 K/min) of thermogravimetric analysis (TGA) in an argon environment, neat PMMA decomposition initiates at ~460 K (Figure S2), whereas neat AB undergoes a two-stage mass loss between ~380-480 K, leaving ~ 40 % residue (Figure S3) of polyborazylene

(PBZ) [32]. By contrast, a 75 % AB/PMMA composite shows a ~75 % mass loss (Figure 4-2(b)) between ~ 360-450 K, before the onset of PMMA decomposition. This indicates that AB completely decomposes at ~ 450 K (slow-heating rate)/~510 K (high-heating rate), to gas phase species before the initiation of PMMA decomposition. The intermediary stage solid residue collected at ~450 K is devoid of all NH, BH, and BN bands of AB and only shows the IR signatures from PMMA (Figure 4-2(c)). This also confirms that AB has been completely decomposed to gas phase species prior to PMMA decomposition, without leaving any trace of PBZ. Same observation has been made in TGA (Figure S4) and ATR-FTIR (Figure S5) analysis of 25 % AB/PMMA composite. The absence of gas phase PBZ fragments in T-jump TOFMS (Figure 4-1(a)) spectra as well as the absence of its IR signatures in the solid-state intermediate residue (Figure 4-2(c)) of AB/PMMA composites, indicate that PMMA inhibits the polymerization of AB molecules, resulting in its direct decomposition to NH_3 and B_2H_6.

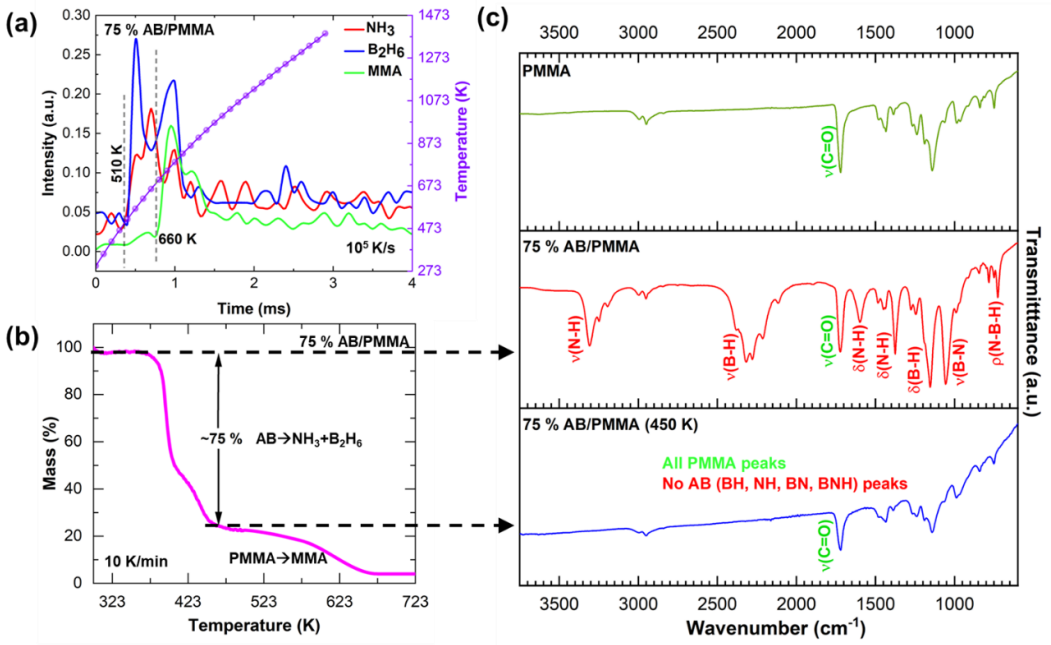

Figure 4-2 (a) T-jump TOFMS (~10^5 K/s) species release profiles show that AB releases NH_3/B_2H_6 (~510 K) before PMMA unzips to MMA (~660 K). (b) TGA (10 K/min) of 75 % AB/PMMA showing that AB completely gasifies to NH_3 and B_2H_6, prior to PMMA decomposition. (c) The TGA residue at 450 K shows all the ATR-FTIR signatures of PMMA, indicating that the chemical composition of the polymer is unaltered post AB decomposition.

4.4.3 Generic Mechanism of AB decomposition with all carbonyl group polymers

T-jump TOFMS spectra presented in Figure 4-3 (a) shows that AB (~75 % by wt.) in matrices of other polymers with carbonyl groups such as polypropylene carbonate (PPC) and polyvinylpyrrolidone (PVP), also decomposes to NH_3 and B_2H_6, rather than polymerizing to BNH_x species. Representative temporal species and temperature evolution profiles of AB in PPC and PVP matrices are shown in Figure S6 and Figure S7 respectively. Interestingly, AB decomposes at the same temperature of ~510 K, with all these carbonyl group polymers (PMMA, PVP, and PPC) regardless of the differing decomposition temperatures of the polymers (Figure 4-3 (b)). Moreover, the decomposition temperature

of AB is lower than the polymer decomposition temperature in all these cases. This suggests that the carbonyl groups of the polymers are solely responsible for altering the decomposition pathway of AB. I also show that in non-carbonyl-based polymer matrix such as poly-vinyl alcohol AB follows the usual DADB pathway forming BNHx species (Figure S8), again proving the necessity of the carbonyl groups for altering the decomposition pathway of AB.

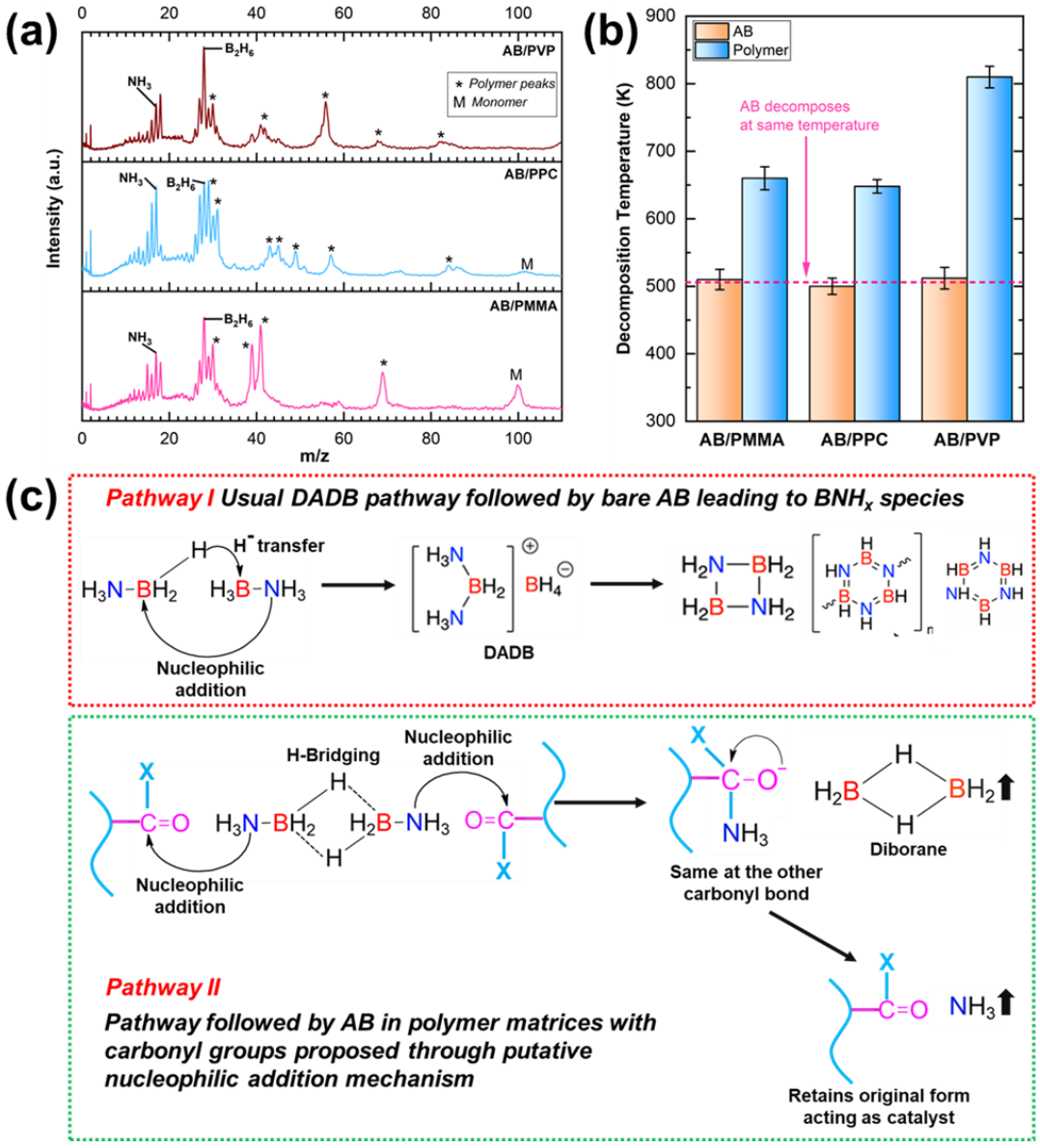

Figure 4-3 (a) T-jump TOFMS spectra shows that AB follows the same pathway releasing NH_3 and B_2H_6 in all polymer matrices with carbonyl groups. (b) The decomposition temperature of AB in all polymer matrices with carbonyl groups is same (~510 K), irrespective of the polymer decomposition temperature. (c) Differences between the DADB pathway followed by bare AB and the NH_3/B_2H_6 pathway followed by AB in PMMA matrix, explained based on putative nucleophilic addition reaction and 3-center 2-electron bridge bond formation mechanisms.

Prior works have shown B and H atoms tend to form 3-center 2-electron bridge or banana bonds, due to the electron deficiency of B and the hydridic nature of the H attached to it [73]. Figure 4-3 (c) shows the interactive behavior of a pair of AB molecules existing in i) the molten phase of bare AB crystals (*Pathway I*) and ii) at the AB/polymer interface when AB is present in the polymer matrix (*Pathway II*), based on putative nucleophilic addition reaction mechanisms[74,75]. In the first case (*Pathway I*), intermolecular bridging interactions between the BH_3 groups of two AB molecules facilitate the nucleophilic addition of the NH_3 moiety of the second molecule to the B-center of the first molecule, resulting in a simultaneous hydride ion transfer from the B-center of the first molecule to that of the second molecule, leading to the formation of DADB. This widely accepted pathway has been reported in several previous studies [19,32,52,70,73], which is also validated by the appearance of DADB and other BNH_x species in the mass spectra of bare AB (Figure 4-1(a)). However, at the AB/polymer interface, the proximity between the NH_3 groups of AB and the carbonyl groups of the polymer, results in the nucleophilic addition of the NH_3 groups to the polymeric carbonyl groups (*Pathway II*), simultaneously leading to a 3-center 2-electron bridge formation between the BH_3 groups. Upon the nucleophilic addition, the oxygen anions will undergo transient bonding with the electron deficient borons, till the BH_3 groups forms the second bridge bond leaving as gaseous diborane (B_2H_6) gas. On the release of B_2H_6, each oxygen anion donates its electron to the carbon to reform the carbonyl bonds, resulting in the release of the attached NH_3. This is also supported by the finding that the carbonyl groups remain intact post AB decomposition (Figure 4-2(c)). Thus, the polymeric carbonyl groups retain their integrity post AB decomposition, acting as catalysts

for the disintegration of the dative B-N bond of AB, thereby generating NH_3 and B_2H_6. This explains the alternative decomposition pathway of the interfacial AB molecules. However, it is still uncertain why the AB molecules at the bulk of the particle phase do not follow the DADB pathway.

4.4.4 Microstructure, dipolar vs dihydrogen bonding: Why the molecules at the core of AB particles do not follow the DADB pathway

The AB molecule possesses an inherent dipole moment due to its dative B-N bond, with nitrogen and boron as the positive and negative poles respectively [18,73]. Moreover, the difference in electronegativities causes the H atoms attached to the boron to be hydridic, whereas those attached to the nitrogen are protic. This leads to intermolecular dihydrogen bonding between the AB molecules, which binds them together in the AB crystal [18,76]. While formation of AB/polymer composites, solvent removal from the AB/polymer solution drives the polymer chains to self-assemble around the nucleating AB particles to form the solid-composite phase. Phase-contrast AFM in tapping mode has been performed on thin AB/PMMA films spin coated on glass-substrates, to image the self-assembled micro-structure of AB/PMMA composites. The AFM measurement can clearly resolve the ~100 nm AB domains (Figure 4-4(a)) embedded near the surface of the 75 % AB/PMMA composite film. By contrast, a single uniform polymer phase is observed in the case of 25 % AB/PMMA indicating that the AB crystals are much smaller and hence the particle phase cannot be resolved. During the self-assembly process, the negative pole (oxygen) of the dipolar carbonyl group [74,75] will have attractive interactions with the acidic protons attached to nitrogen. and therefore, the polymeric carbonyl group will be in contact with

the acidic protons of the interfacial AB molecules after the self-assembly process. Dihydrogen bonding in bare AB splits the IR peaks[64,73] for stretching vibrations of the NH and BH bonds into 3 and 5 peaks respectively (Figure 4-4(b)). The ATR-IR spectra over the entire range of frequencies has been presented in Figure S9. With increasing polymer content, the peaks merge, as the 25 % AB/PMMA only shows 1 peak for the NH band and 4 peaks for the BH band, indicating that the number of dihydrogen bonds decrease with increase in polymer content. Therefore, with increase in polymer content, the particle size decreases, the number of interfacial molecules increases, decreasing the number of dihydrogen bonds. This is also confirmed by the sharpening of the XRD peaks of AB with decreasing polymer content in AB/PMMA composites (Figure S10). Although, the AB molecules at the particle/polymer interface have dipolar interactions with the carbonyl groups of PMMA, those existing at the bulk of the particle phase are bound by dihydrogen bonding as explained in Figure 4-4(c). In the 25 % AB/PMMA composite, AB and MMA are present approximately in a 1:1 molar ratio, which is much lower than the 10:1 AB to MMA molar ratio in 75 % AB/PMMA composite. Thus, the AB in 25 % AB/PMMA is expected to be much smaller having much higher interfacial interaction with the carbonyl groups. However, at lower polymer content (~75 % AB/PMMA) significant number of dihydrogen bonded AB molecules exist at the core of the AB particles, which surprisingly do not oligomerize through the DADB pathway. To explain this phenomenon, I measured the activation energies of the DADB pathway and the NH_3/B_2H_6 pathway, to compare their kinetics.

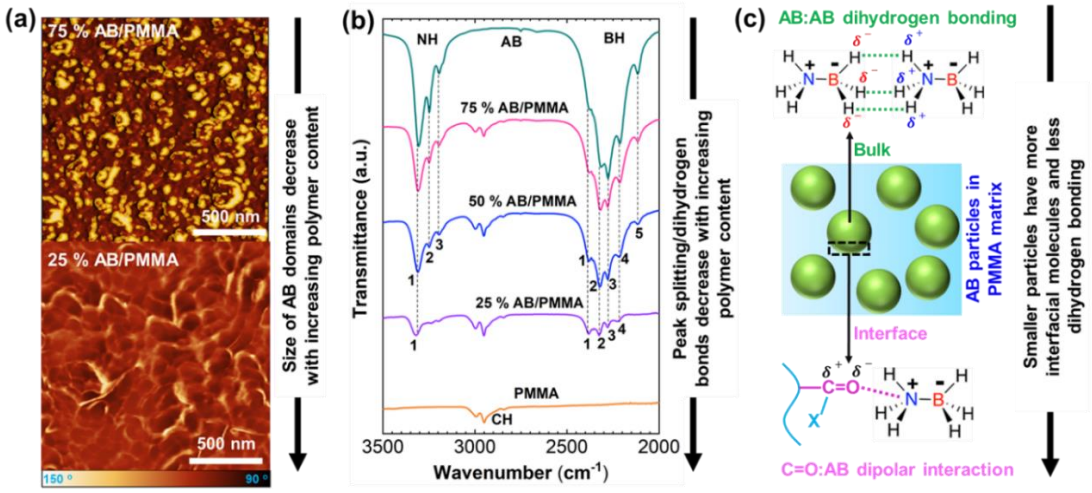

Figure 4-4 (a) AFM phase-retrace micro-graphs of 75 % AB/PMMA composite shows ~100 nm AB domains, whereas the AB domains are small and unresolvable in case of 25 % AB/PMMA. (b) Dihydrogen bonding led IR peak splitting of NH and BH bonds decreases with increase in polymer content. (c) Schematic explaining the dihydrogen bonding between AB molecules at the bulk of the particle phase and the dipolar interaction between AB and polymeric carbonyl groups at the interface.

The activation energy barrier of DADB/BNH_x release from bare AB and NH_3/B_2H_6 release from 75 % AB/PMMA composite have been determined by the Flynn-Wall-Ozawa method [68] from T-jump TOFMS measurements (Figure 4-5 (a)). The Flynn-Wall-Ozawa method relates the activation energy (E_a) and heating rate (β) as $\ln(\beta) = -1.05\frac{E_a}{RT} + const.$, where T is the species release temperature and R is the universal gas constant. The heating pulse-width of the T-jump has been adjusted to vary the heating rates and the species (DADB/B_2H_6) release temperatures at various heating rates have been obtained to make the plot in Figure 4-5 (a), in order to estimate the activation energies. The B-N bond dissociation enthalpy (BDE) of AB, that is the enthalpy of the reaction $AB \rightarrow NH_3 + BH_3$, is ~177 kJ/mol, as calculated using the standard enthalpies of formation of AB [77], NH_3 (Active Thermochemical Tables-Argonne National Laboratory), and BH_3 [78]. The measured

activation energy of bare AB polymerization to BNH_x (Figure 4-5 (a)) is much lower than the BDE of ~177 kJ/mol. This clearly explains why neat AB oligomerizes on thermal activation, rather than breaking its B-N bond. However, the activation energy of AB decomposition in PMMA matrix (~26 kJ/mol) is ~60 kJ/mol lower than that of bare AB (~83 kJ/mol), which makes it favored over the DADB pathway.

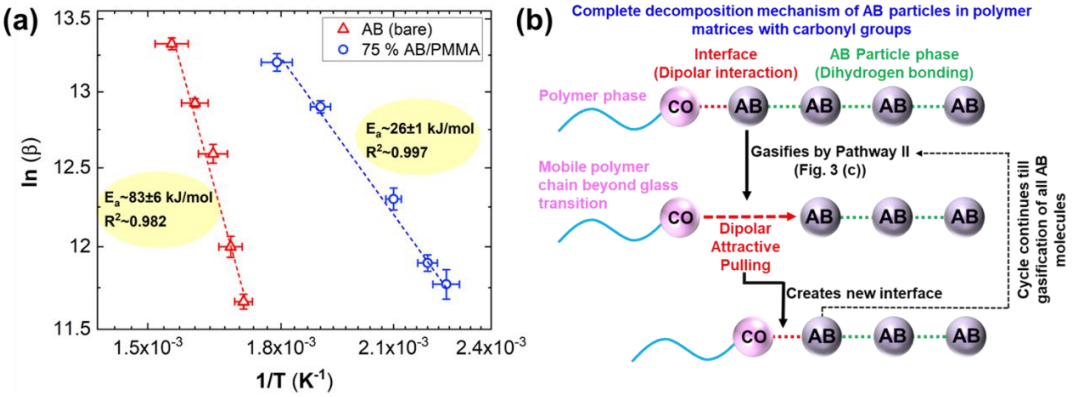

Figure 4-5 (a) Flynn-Wall-Ozawa activation energy of AB decomposition in PMMA matrix, obtained from T-jump TOFMS measurements is ~60 kJ/mol lower than that of the DADB pathway followed by bare AB. (b) Schematic explaining the reason why the AB molecules at the core of the particle phase do not follow the DADB pathway.

Additionally, according to Figure 4-5(a) the decomposition temperature of AB in PMMA matrix is lower than bare AB decomposition temperature at all heating rates. Given that the decomposition temperature of AB/carbonyl polymer composites is independent of the polymer composition (Figure 4-3(b)) and polymer content (Figure S1), it can be assumed that the activation barrier of AB decomposition in all polymer matrices with carbonyl groups will be similar. Based on these facts, an overall decomposition mechanism of the AB particles has been proposed (Figure 4-5(b)). During the temperature ramp, the carbonyl groups will initially catalyze the decomposition of interfacial AB molecules (Figure 4-3(c)). The interfacial molecules will gasify to NH_3 and B_2H_6, exposing the

adjacent underlying layer of AB molecules. As this process is initiated (Figure 4-3(b)) beyond the glass transition temperatures of PMMA/PPC/PVP, the freshly exposed AB layer will attract the mobile polymer chains through dipolar interactions, which can move and fill the angstrom scale gap, creating a new particle/polymer interface. The interfacial AB molecules will decompose again exposing the underlying AB molecular layer which will form a new interface with the polymer. This cycle will continue till all the underlying subsequent layers of AB molecules are gasified to NH_3 and B_2H_6 in a shrinking-core fashion. Since this entire process happens at a lower temperature and at a faster rate (~60 kJ/mol lower E_a) than the DADB pathway, AB particles in polymer matrix containing carbonyl groups will be completely decomposed before the activation of the DADB pathway. Moreover, as the polymers decompose at higher temperatures, the polymers and the carbonyl groups will remain intact till the entire consumption of the AB particles, thereby acting as catalysts for AB decomposition. This explains why the AB molecules at the core of the particle phase do not follow the DADB pathway.

4.4.5 AB/PMMA composites with mesoscopic architectures

The characterizations described so far are performed on AB/polymer composite films formed by evaporation of the solvents from their respective solutions. For practical viability, there is considerable interest in hierarchical assembly of nanoparticles into mesoscale architectures due to ease of processing [79–82]. Hence, for in-operando characterizations I have adopted an aerosol-based approach, to atomize a solution of 75 % AB/PMMA and dry it on-the-fly with heated argon at ~320 K (Figure 4-6(a)), in order to make ~5-10 μm mesoscale composite particles of AB/PMMA, as represented through the

SEM micrographs in Figure 4-6 (b). As 75 wt. % of AB results in ~100 nm AB domains in AB/PMMA composites (Figure 4-4(a)), the spray-dried 75 % AB/PMMA composite particles will likely be a hierarchical assembly of nanoscale AB domains. T-jump TOFMS spectra of the 75 % AB/PMMA composite mesoparticles (Figure S11) matches with that of the 75 % AB/PMMA composite film (Figure 4-1 (a)) and the B_2H_6 release temperature of the mesoparticles remains the same at ~510 K (Figure 4-6 (c)). This indicates that the mesoparticles follow the same chemical decomposition pathway described in the previous sections. The inset of Figure 4-6(c) shows that the first instance of the green BO_2 emission (~0.6 ms) designated as the ignition onset, is observed ~0.2 ms after the initiation of B_2H_6 release (~0.4 ms). The negligible ignition delay (~0.2 ms) indicates that B_2H_6 spontaneously ignites in air on its release, which is expected from its low autoignition temperature (~310 K)[66].

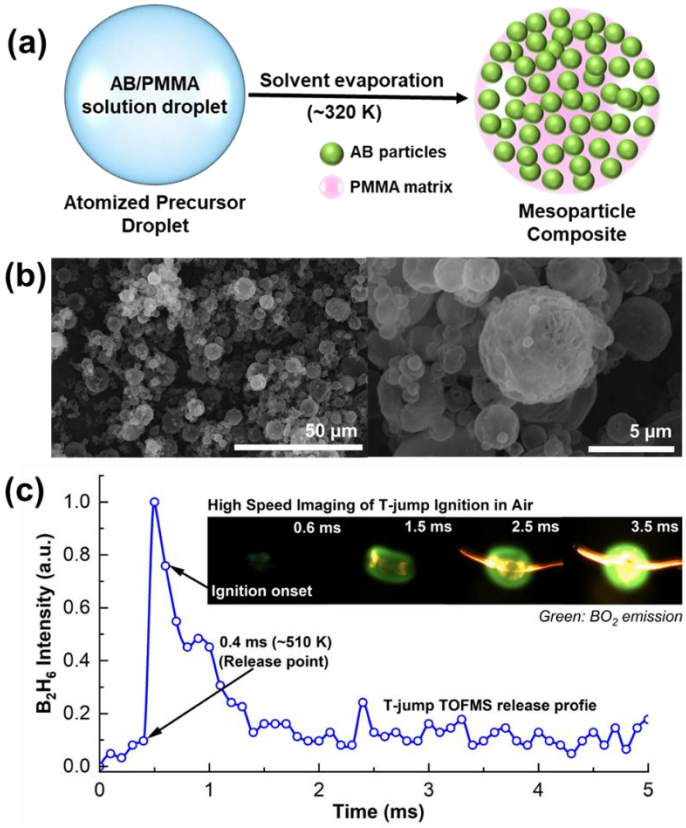

Figure 4-6 (a) Schematic describing the aerosol route for synthesis of mesoscale hierarchical AB/PMMA composite particles. (b) SEM micrographs of the synthesized mesoparticles. (c) T-jump TOFMS B_2H_6 release profile and snapshots of the ignition process of the AB/PMMA mesoparticles composite in air.

Therefore, AB/PMMA composite particles can be used for the generation of reactive gases such as NH_3 and B_2H_6. Polymers with carbonyl groups such as PMMA can be used both as a hydrophobic (~protection from moisture) binding agent as well as a chemical component for altering the decomposition pathway of AB generating lower molecular weight reactive species. The low auto-ignition temperature or high reactivity of B_2H_6 (~310 K) compared to both H_2 (~850 K) and NH_3 (~1000 K) [66,83,84] makes it extremely desirable for processes requiring rapid energy release. As B_2H_6 gas is extremely unstable

and toxic, storing and using it in gaseous form is difficult [67]. However, AB/PMMA composites can serve as solid state B_2H_6 storage materials, which when thermally activated can release B_2H_6, hence producing energy on-demand. As the polymer stays intact post AB decomposition, technologies can be designed to separate the combustion zone of released NH_3 and B_2H_6 from the surface of the polymer, so that the polymer can be recycled. Hence, these fundamental findings will open up multiple possibilities of applied research on making sustainable materials for energy storage.

4.5 Conclusions

In this study I have shown that on thermal activation polymeric carbonyl groups catalyze the dissociation of the dative B-N bond of ammonia borane (AB) through nucleophilic interactions, by generating reactive NH_3 and B_2H_6 gases. This prevents AB to oligomerize to chemically resistant higher molecular weight BNH_x species. The carbonyl groups lower the activation energy of B-N bond dissociation to ~26 kJ/mol which is much lower than the bond dissociation enthalpy (~194 kJ/mol) as well as the activation energy (~83 kJ/mol) of the BNH_x pathway, thereby resulting in the catalytic cleavage of the B-N bond. I have also shown that a facile and scalable aerosol spray drying approach can be employed to synthesize hierarchical (micro/nano) AB/polymer composite particles with AB as the major component (~75 wt. %). Through in-situ high heating rate characterizations, I have shown that the composite particles release NH_3 and B_2H_6 on thermal activation at ~510 K and the released B_2H_6 spontaneously ignites in air with negligible delay. The generation of lower molecular weight reactive species instead of

chemically resistant BNH_x species through this pathway, makes AB suitable as a fuel for high energy applications.

4.6 References

(1) Schlapbach, L.; Züttel, A. Hydrogen Storage Materials for Mobile Applications. *Nature* **2001**, *414*, 353–358.

(2) Ngene, P.; Longo, A.; Mooij, L.; Bras, W.; Dam, B. Metal-Hydrogen Systems with an Exceptionally Large and Tunable Thermodynamic Destabilization. *Nat. Commun.* **2017**, *8*, 1846.

(3) Cao, H.; Georgopanos, P.; Capurso, G.; Pistidda, C.; Weigelt, F.; Chaudhary, A. L.; Filiz, V.; Tseng, J. C.; Wharmby, M. T.; Dornheim, M.; Abetz, V.; Klassen, T. Air-Stable Metal Hydride-Polymer Composites of $Mg(NH_2)_2$–LiH and TPX™. *Mater. Today Energy* **2018**, *10*, 98-107.

(4) Schneemann, A.; White, J. L.; Kang, S.; Jeong, S.; Wan, L. F.; Cho, E. S.; Heo, T. W.; Prendergast, D.; Urban, J. J.; Wood, B. C.; Allendorf, M. D.; Stavila, V. Nanostructured Metal Hydrides for Hydrogen Storage. *Chem. Rev.* **2018**, *118*, 10775-10839.

(5) Ambrosi, A.; Chua, C. K.; Bonanni, A.; Pumera, M. Lithium Aluminum Hydride as Reducing Agent for Chemically Reduced Graphene Oxides. *Chem. Mater.* **2012**, *24*, 2292–2298.

(6) Zhang, J.; Zhu, Y.; Lin, H.; Liu, Y.; Zhang, Y.; Li, S.; Ma, Z.; Li, L. Metal Hydride Nanoparticles with Ultrahigh Structural Stability and Hydrogen Storage Activity Derived from Microencapsulated Nanoconfinement. *Adv. Mater.* **2017**, *29*, 1700760.

(7) Kim, G. J.; Hwang, H. T. Thermal Hydrolysis of Solid-State Sodium Borohydride for Noncatalytic Hydrogen Generation. *Chem. Eng. J.* **2021**, *424*, 130445.

(8) Demirci, U. B.; Miele, P. Sodium Borohydride versus Ammonia Borane, in Hydrogen Storage and Direct Fuel Cell Applications. *Energy Environ. Sci.* **2009**, *2*, 627–637.

(9) Concha, B. M.; Chatenet, M.; Maillard, F.; Ticianelli, E. A.; Lima, F. H. B.; de Lima, R. B. In Situ Infrared (FTIR) Study of the Mechanism of the Borohydride Oxidation Reaction. *Phys. Chem. Chem. Phys.* **2010**, *12*, 11507–11516.

(10) Rostamikia, G.; Janik, M. J. Direct Borohydride Oxidation: Mechanism Determination and Design of Alloy Catalysts Guided by Density Functional Theory. *Energy Environ. Sci.* **2010**, *3*, 1262–1274.

(11) Staubitz, A.; Robertson, A. P. M.; Manners, I. Ammonia-Borane and Related Compounds as Dihydrogen Sources. *Chem. Rev.* **2010**, *110*, 4079–4124.

(12) Simagina, V. I.; Vernikovskaya, N. V.; Komova, O. V.; Kayl, N. L.; Netskina, O. V.; Odegova, G. V. Experimental and Modeling Study of Ammonia Borane-Based Hydrogen Storage Systems. *Chem. Eng. J.* **2017**, *329*, 156-164.

(13) Stephens, F. H.; Baker, R. T.; Matus, M. H.; Grant, D. J.; Dixon, D. A. Acid Initiation of Ammonia-Borane Dehydrogenation for Hydrogen Storage. *Angew. Chem. Int. Ed.* **2007**, *46*, 746-749.

(14) Wang, F.; Planas, O.; Cornella, J. Bi(I)-Catalyzed Transfer-Hydrogenation with Ammonia-Borane. *J. Am. Chem. Soc.* **2019**, *141*, 4235-4240.

(15) Wang, C.; Tuninetti, J.; Wang, Z.; Zhang, C.; Ciganda, R.; Salmon, L.; Moya, S.; Ruiz, J.; Astruc, D. Hydrolysis of Ammonia-Borane over Ni/ZIF-8 Nanocatalyst: High Efficiency, Mechanism, and Controlled Hydrogen Release. *J. Am. Chem. Soc.* **2017**, *139*, 11610-11615.

(16) Demirci, U. B. Ammonia Borane: An Extensively Studied, Though Not yet Implemented, Hydrogen Carrier. *Energies* **2020**, *13*, 3071.

(17) Bhunya, S.; Zimmerman, P. M.; Paul, A. Unraveling the Crucial Role of Metal-Free Catalysis in Borazine and Polyborazylene Formation in Transition-Metal-Catalyzed Ammonia-Borane Dehydrogenation. *ACS Catal.* **2015**, *5*, 3478-3493.

(18) Rizzi, V.; Polino, D.; Sicilia, E.; Russo, N.; Parrinello, M. The Onset of Dehydrogenation in Solid Ammonia Borane: An Ab Initio Metadynamics Study. *Angew. Chem. Int. Ed.* **2019**, *131*, 4016-4020.

(19) Demirci, U. B. Mechanistic Insights into the Thermal Decomposition of Ammonia Borane, a Material Studied for Chemical Hydrogen Storage. *Inorg. Chem. Front.* **2021**, *8*, 1900–1930.

(20) Valero-Pedraza, M. J.; Cot, D.; Petit, E.; Aguey-Zinsou, K. F.; Alauzun, J. G.; Demirci, U. B. Ammonia Borane Nanospheres for Hydrogen Storage. *ACS Appl. Nano Mater.* **2019**, *2*, 1129-1138.

(21) Weismiller, M. R.; Wang, S. Q.; Chowdhury, A.; Thynell, S. T.; Yetter, R. A. Confined Rapid Thermolysis Studies of Ammonia Borane. *Thermochim. Acta* **2013**, *551*, 110–117.

(22) Himmelberger, D. W.; Alden, L. R.; Bluhm, M. E.; Sneddon, L. G. Ammonia Borane Hydrogen Release in Ionic Liquids. *Inorg. Chem.* **2009**, *48*, 9883–9889.

(23) Yang, J. B.; Lamsal, J.; Cai, Q.; James, W. J.; Yelon, W. B. Structural Evolution of Ammonia Borane for Hydrogen Storage. *Appl. Phys. Lett.* **2008**, *92*, 091916.

(24) Wahab, M. A.; Zhao, H.; Yao, X. D. Nano-Confined Ammonia Borane for Chemical Hydrogen Storage. *Front. Chem. Sci. Eng.* **2012**, *6*, 27-33.

(25) Gutowska, A.; Li, L.; Shin, Y.; Wang, C. M.; Li, X. S.; Linehan, J. C.; Smith, R. S.; Kay, B. D.; Schmid, B.; Shaw, W.; Gutowski, M.; Autrey, T. Nanoscaffold Mediates Hydrogen Release and the Reactivity of Ammonia Borane. *Angew. Chem. Int. Ed.* **2005**, *117*, 3644-3648

(26) Yao, Y.; Yong, X.; Tse, J. S.; Greschner, M. J. Dihydrogen Bonding in Compressed Ammonia Borane and Its Roles in Structural Stability. *J. Phys. Chem. C* **2014**, *118*, 29591–29598.

(27) Petit, J. F.; Demirci, U. B. Discrepancy in the Thermal Decomposition/Dehydrogenation of Ammonia Borane Screened by Thermogravimetric Analysis. *Int. J. Hydrogen Energy* **2019**, *44*, 14201–14206.

(28) Chatterjee, T.; Thynell, S. T. Development of a Reaction Mechanism for Liquid-Phase Decomposition of Ammonia Borane. *Thermochim. Acta* **2019**, *682*, 178427.

(29) Kumar, V.; Roy, B.; Sharma, P. Kinetics of Borazine Formation from Ammonia Borane Dehydrocoupling Reaction through Ab Initio Analysis. *Int. J. Hydrogen Energy* **2019**, *44*, 22022–22031.

(30) Yang, Z.; Zhou, D.; Chen, B.; Liu, Z.; Xia, Q.; Zhu, Y.; Xia, Y. Improved Hydrogen Release from Ammonia Borane Confined in Microporous Carbon with Narrow Pore Size Distribution. *J. Mater. Chem. A* **2017**, *5*, 15395–15400.

(31) Umemoto, H.; Miyata, A. Decomposition Processes of Diborane and Borazane (Ammonia-Borane Complex) on Hot Wire Surfaces. *Thin Solid Films* **2015**, *595*, 231–234.

(32) Biswas, P.; Ghildiyal, P.; Kwon, H.; Wang, H.; Alibay, Z.; Xu, F.; Wang, Y.; Wong, B. M.; Zachariah, M. R. Rerouting Pathways of Solid-State Ammonia Borane Energy Release. *J. Phys. Chem. C* **2021**, *126*, 48–57.

(33) Rodriguez, D. A.; Dreizin, E. L.; Shafirovich, E. Hydrogen Generation from Ammonia Borane and Water through Combustion Reactions with Mechanically Alloyed Al·Mg Powder. *Combust. Flame* **2015**, *162*, 1498–1506.

(34) Baier, M. J.; McDonald, A. J.; Clements, K. A.; Goldenstein, C. S.; Son, S. F. High-Speed Multi-Spectral Imaging of the Hypergolic Ignition of Ammonia Borane. *Proc. Combust. Inst.* **2021**, *38*, 4433-4440

(35) Weismiller, M. R.; Duin, A. C. T. V.; Lee, J.; Yetter, R. A. ReaxFF Reactive Force Field Development and Applications for Molecular Dynamics Simulations of Ammonia Borane Dehydrogenation and Combustion. *J. Phys. Chem. A* **2010**, *114*, 5485–5492.

(36) Biswas, P.; Xu, F.; Ghildiyal, P.; Zachariah, M. R. In-Situ Thermochemical Shock-Induced Stress at the Metal/Oxide Interface Enhances Reactivity of Aluminum Nanoparticles. *ACS Appl. Mater. Interfaces* **2022**, *14*, 26782–26790.

(37) Connell, T. L.; Risha, G. A.; Yetter, R. A.; Young, G.; Sundaram, D. S.; Yang, V. Combustion of Alane and Aluminum with Water for Hydrogen and Thermal Energy Generation. *Proc. Combust. Inst.* **2011**, *33*, 1957-1965.

(38) Kline, D. J.; Rehwoldt, M. C.; Wang, H.; Eckman, N. E.; Zachariah, M. R. Why Does Adding a Poor Thermal Conductor Increase Propagation Rate in Solid Propellants? *Appl. Phys. Lett.* **2019**, *115*, 114101.

(39) McClain, M. S.; Gunduz, I. E.; Son, S. F. Additive Manufacturing of Ammonium Perchlorate Composite Propellant with High Solids Loadings. *Proc. Combust. Inst.* **2019**, *37*, 3135–3142.

(40) Wang, H.; Kline, D. J.; Zachariah, M. R. In-Operando High-Speed Microscopy and Thermometry of Reaction Propagation and Sintering in a Nanocomposite. *Nat. Commun.* **2019**, *10* , 3032.

(41) Ma, X.; Li, Y.; Hussain, I.; Shen, R.; Yang, G.; Zhang, K.; Ma, X.; Li, Y.; Hussain, I.; Zhang, K.; Shen, R.; Yang, G. Core–Shell Structured Nanoenergetic Materials: Preparation and Fundamental Properties. *Adv. Mater.* **2020**, *32*, 2001291.

(42) Jiang, Y.; Deng, S.; Hong, S.; Zhao, J.; Huang, S.; Wu, C. C.; Gottfried, J. L.; Nomura, K. I.; Li, Y.; Tiwari, S.; Kalia, R. K.; Vashishta, P.; Nakano, A.; Zheng, X. Energetic Performance of Optically Activated Aluminum/Graphene Oxide Composites. *ACS Nano* **2018**, *12*, 11366–11375.

(43) Jiang, Y.; Deng, S.; Hong, S.; Tiwari, S.; Chen, H.; Nomura, K. I.; Kalia, R. K.; Nakano, A.; Vashishta, P.; Zachariah, M. R.; Zheng, X. Synergistically Chemical and Thermal Coupling between Graphene Oxide and Graphene Fluoride for Enhancing Aluminum Combustion. *ACS Appl. Mater. Interfaces* **2020**, *12*, 7451–7458.

(44) Zhang, Q.; Shreeve, J. M. Energetic Ionic Liquids as Explosives and Propellant Fuels: A New Journey of Ionic Liquid Chemistry. *Chem. Rev.* **2014**, *114*, 10527–10574.

(45) Wang, Y.; Wang, H.; Xu, F.; Ghildiyal, P.; Zachariah, M. R. Effect of Alkali Metal Perchlorate and Iodate Type on Boron Ignition: The Role of Oxidizer Phase Change. *Chem. Eng. J.* **2022**, *446*, 136786.

(46) Chintersingh, K. L.; Schoenitz, M.; Dreizin, E. L. Boron Doped with Iron: Preparation and Combustion in Air. *Combust. Flame* **2019**, *200*, 286–295.

(47) Mursalat, M.; Schoenitz, M.; Dreizin, E. L. Effect of Particle Morphology on Reactivity, Ignition and Combustion of Boron Powders. *Fuel* **2022**, *324*, 124538.

(48) Veith, J.; Pfitzner, M. Combustion of Boron Particles in Premixed Methane/Air Flames. *Propell. Explos. Pyrot.* **2016**, *41* (2), 260–266.

(49) Jeon, E.; Cho, Y. W. Mechanochemical Synthesis and Thermal Decomposition of Zinc Borohydride. *J. Alloys Compd.* **2006**, *422*, 273–275.

(50) Mazaheri, A.; Javadi, M.; Abdi, Y. Chemical Vapor Deposition of Two-Dimensional Boron Sheets by Thermal Decomposition of Diborane. *ACS Appl. Mater. Interfaces* **2021**, *13*, 8844–8850.

(51) Kanth, J. V. B.; Brown, H. C. Improved Procedures for the Generation of Diborane from Sodium Borohydride and Boron Trifluoride. *Inorg. Chem.* **2000**, *39*, 1795–1802.

(52) Stowe, A. C.; Shaw, W. J.; Linehan, J. C.; Schmid, B.; Autrey, T. In Situ Solid State 11B MAS-NMR Studies of the Thermal Decomposition of Ammonia Borane: Mechanistic Studies of the Hydrogen Release Pathways from a Solid State Hydrogen Storage Material. *Phys. Chem. Chem. Phys.* **2007**, *9*, 1831–1836.

(53) Nguyen, V. S.; Matus, M. H.; Nguyen, M. T.; Dixon, D. A. Reactions of Diborane with Ammonia and Ammonia Borane: Catalytic Effects for Multiple Pathways for Hydrogen Release. *J. Phys. Chem. A* **2008**, *112*, 9946–9954.

(54) Nguyen, M.T.; Nguyen, V.S.; Matus, M.H.; Gopakumar, G.; Dixon, D.A. Molecular Mechanism for H_2 Release from BH_3NH_3, Including the Catalytic Role of the Lewis Acid BH3. *J. Phys. Chem . A* **2007**, *111*, 679–690.

(55) Valero-Pedraza, M. J.; Cot, D.; Petit, E.; Aguey-Zinsou, K. F.; Alauzun, J. G.; Demirci, U. B. Ammonia Borane Nanospheres for Hydrogen Storage. *ACS Appl. Nano Mater.* **2019**, *2*, 1129–1138.

(56) Baier, M. J.; Ramachandran, P. V.; Son, S. F. Characterization of the Hypergolic Ignition Delay of Ammonia Borane. *J. Propuls. Power* **2019**, *35*, 182-189.

(57) Clements, K. A.; Baier, M. J.; Veeraraghavan Ramachandran, P.; Son, S. F. Experimental Study of Factors Affecting Hypergolic Ignition of Ammonia Borane. *J. Propuls. Power* **2021**, *37*, 202-210.

(58) Pfeil, M. A.; Groven, L. J.; Lucht, R. P.; Son, S. F. Effects of Ammonia Borane on the Combustion of an Ethanol Droplet at Atmospheric Pressure. *Combust. Flame* **2013**, *160*, 2194-2203.

(59) Gobin, B.; Harvey, N.; Young, G. Combustion Characteristics of Electrically Controlled Solid Propellants Using Polymer Electrolytes. *Combust. Flame* **2022**, *244*, 112291.

(60) Marchioni, F.; Cappelli, M. A. Extended Channel Hall Thruster for Air-Breathing Electric Propulsion. *J. Appl. Phys.* **2021**, *130*, 053306.

(61) Seemaladinne, R.; Pati, S.; Kharel, K.; Bafana, A.; al-Wahish, A.; Wujcik, E. K.; Günaydın-Şen, Ö. Ammonia Borane with Polyvinylpyrrolidone as a Hydrogen Storage Material: Comparison of Different Molecular Weights. *J. Phys. Chem. Solids* **2017**, *110*, 394–400.

(62) Zhao, J.; Shi, J.; Zhang, X.; Cheng, F.; Liang, J.; Tao, Z.; Chen, J. A Soft Hydrogen Storage Material: Poly(Methyl Acrylate)-Confined Ammonia Borane with Controllable Dehydrogenation. *Adv. Mater.* **2010**, *22*, 394–397.

(63) Kharel, K.; Gangineni, R.; Günaydın-Şen, Ö. Low Temperature Phase Transition Studies of Ammonia Borane-Polyacrylamide Composites. *Mater. Chem. Phys.* **2018**, *216*, 354–364.

(64) Ploszajski, A. R.; Billing, M.; Nathanson, A. S.; Vickers, M.; Bennington, S. M. Freeze-Dried Ammonia Borane-Polyethylene Oxide Composites: Phase Behaviour and Hydrogen Release. *Int. J. Hydrogen Energy* **2018**, *43*, 5645–5656.

(65) Li, S. F.; Tang, Z. W.; Tan, Y. B.; Yu, X. B. Polyacrylamide Blending with Ammonia Borane: A Polymer Supported Hydrogen Storage Composite. *J. Phys. Chem. C* **2012**, *116*, 1544–1549.

(66) Savel'ev, A. M.; Kuleshov, P. S.; Lukhovitskii, B. I.; Pelevkin, A. v.; Savel'eva, V. A.; Sharipov, A. S. On the Kinetic Mechanism of Ignition of Diborane Mixtures with Air. *Combust. Explos. Shock Waves* **2020**, *56*, 249–266.

(67) Jones, N. B.; Gibbons, B.; Morris, A. J.; Morris, J. R.; Troya, D. Reversible Dissociation for Effective Storage of Diborane Gas within the UiO-66-NH_2Metal-Organic Framework. *ACS Appl. Mater. Interfaces* **2022**, *14*, 8322–8332.

(68) Jian, G.; Zhou, L.; Piekiel, N. W.; Zachariah, M. R. Low Effective Activation Energies for Oxygen Release from Metal Oxides: Evidence for Mass-Transfer Limits at High Heating Rates. *ChemPhysChem* **2014**, *15*, 1666–1672.

(69) Rehwoldt, M. C.; Wang, Y.; Xu, F.; Ghildiyal, P.; Zachariah, M. R. High-Temperature Interactions of Metal Oxides and a PVDF Binder. *ACS Appl. Mater. Interfaces* **2022**, *14*, 8938–8946.

(70) Heldebrant, D. J.; Karkamkar, A.; Hess, N. J.; Bowden, M.; Rassat, S.; Feng, Z.; Rappe, K.; Autrey, T. The Effects of Chemical Additives on the Induction Phase in Solid-State Thermal Decomposition of Ammonia Borane. *Chem. Mater.* **2008**, *20*, 5332–5336.

(71) Blanchet, G. B.; Fincher, C. R. Laser Induced Unzipping: A Thermal Route to Polymer Ablation. *Appl. Phys. Lett.* **1998**, *65*, 1311.

(72) Xu, F.; Nava, G.; Biswas, P.; Dulalia, I.; Wang, H.; Alibay, Z.; Gale, M.; Kline, D. J.; Wagner, B.; Mangolini, L.; Zachariah, M. R. Energetic Characteristics of Hydrogenated Amorphous Silicon Nanoparticles. *Chem. Eng. J.* **2022**, *430*, 133140.

(73) Lipscomb, W.N. Boron Hydrides; *Dover Publications* **2013**.

(74) Kamer, K. J.; Choudhary, A.; Raines, R. T. Intimate Interactions with Carbonyl Groups: Dipole-Dipole or n →π*? *J. Org. Chem.* **2013**, *78* (5), 2099–2103.

(75) Newberry, R. W.; Raines, R. T. The N→π∗ Interaction. *Acc. Chem. Res.* **2017**, *50*, 1838–1846.

(76) Klooster, W. T.; Koetzle, T. F.; Siegbahn, P. E. M.; Richardson, T. B.; Crabtree, R. H. Study of the N-H···H-B Dihydrogen Bond Including the Crystal Structure of BH3NH3 by Neutron Diffraction. *J. Am. Chem. Soc.* **1999**, *121*, 6337–6343.

(77) Kondrat'Ev, Y. V.; Butlak, A. V.; Kazakov, I. V.; Timoshkin, A. Y. Sublimation and Thermal Decomposition of Ammonia Borane: Competitive Processes Controlled by Pressure. *Thermochim. Acta* **2015**, *622*, 64–71.

(78) Yu, C. L.; Bauer, S. H. Thermochemistry of the Boranes. *J. Phys. Chem. Ref. Data* **2009**, *27*, 807.

(79) Yao, H. bin; Fang, H. Y.; Wang, X. H.; Yu, S. H. Hierarchical Assembly of Micro-/Nano-Building Blocks: Bio-Inspired Rigid Structural Functional Materials. *Chem. Soc. Rev.* **2011**, *40*, 3764–3785.

(80) Qiu, W.; Li, G.; Luo, D.; Zhang, Y.; Zhao, Y.; Zhou, G.; Shui, L.; Wang, X.; Chen, Z. Hierarchical Micro-Nanoclusters of Bimetallic Layered Hydroxide Polyhedrons

as Advanced Sulfur Reservoir for High-Performance Lithium–Sulfur Batteries. *Adv. Sci.* **2021**, *8*, 2003400.

(81) Lu, Y.; Fan, H.; Stump, A.; Ward, T. L.; Rieker, T.; Brinker, C. J. Aerosol-Assisted Self-Assembly of Mesostructured Spherical Nanoparticles. *Nature* **1999**, *398*, 223–226.

(82) Jia, X.; Chen, Z.; Cui, X.; Peng, Y.; Wang, X.; Wang, G.; Wei, F.; Lu, Y. Building Robust Architectures of Carbon and Metal Oxide Nanocrystals toward High-Performance Anodes for Lithium-Ion Batteries. *ACS Nano* **2012**, *6*, 9911–9919.

(83) He, X.; Shu, B.; Nascimento, D.; Moshammer, K.; Costa, M.; Fernandes, R. X. Auto-Ignition Kinetics of Ammonia and Ammonia/Hydrogen Mixtures at Intermediate Temperatures and High Pressures. *Combust. Flame* **2019**, *206*, 189–200.

(84) Chen, J.; Jiang, X.; Qin, X.; Huang, Z. Effect of Hydrogen Blending on the High Temperature Auto-Ignition of Ammonia at Elevated Pressure. *Fuel* **2021**, *287*, 119563.

4.7 Supporting information

S.1 In-situ time/temperature resolved decomposition characterization of AB/PMMA

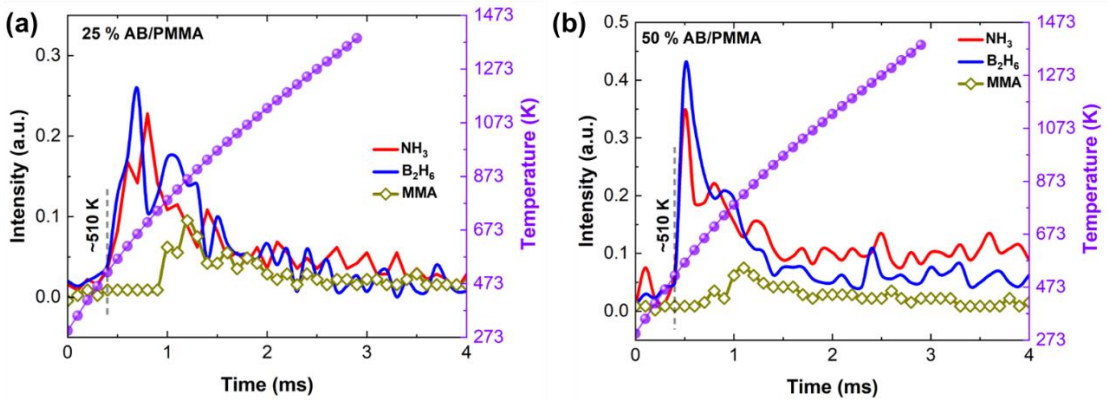

Figure S1 Time/temperature resolved evolution of NH_3, B_2H_6 and PMMA-monomers from 25 % (a) and 50 % (b) AB/PMMA composites, showing that the release temperatures of these species do not vary with the variation in the AB to polymer ratio. **S.2 Ex-situ time/temperature resolved decomposition characterization of AB/PMMA**

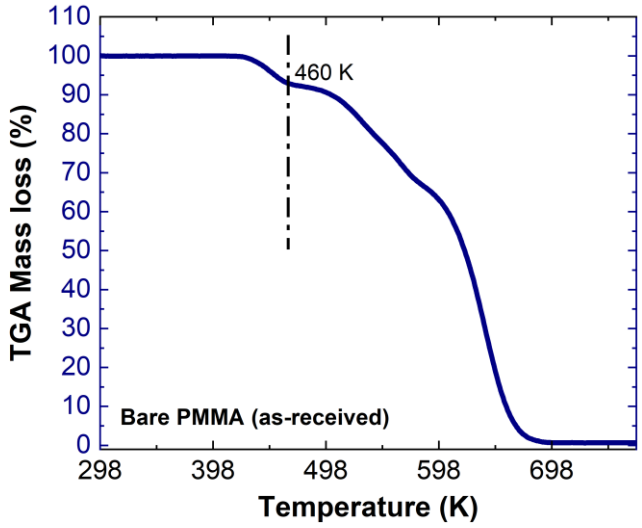

Figure S2 Decomposition of as-received PMMA powder showing that decomposition of bare-PMMA initiates at ~460 K.

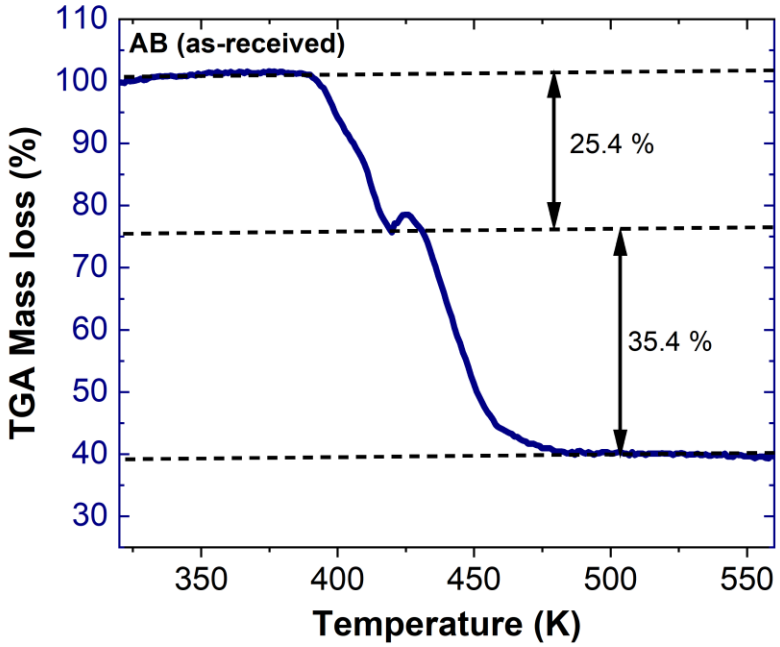

Figure S3 TGA of bare AB showing a two stage mass loss between ~380-480 K, leaving a final solid state residual mass of ~40 %.

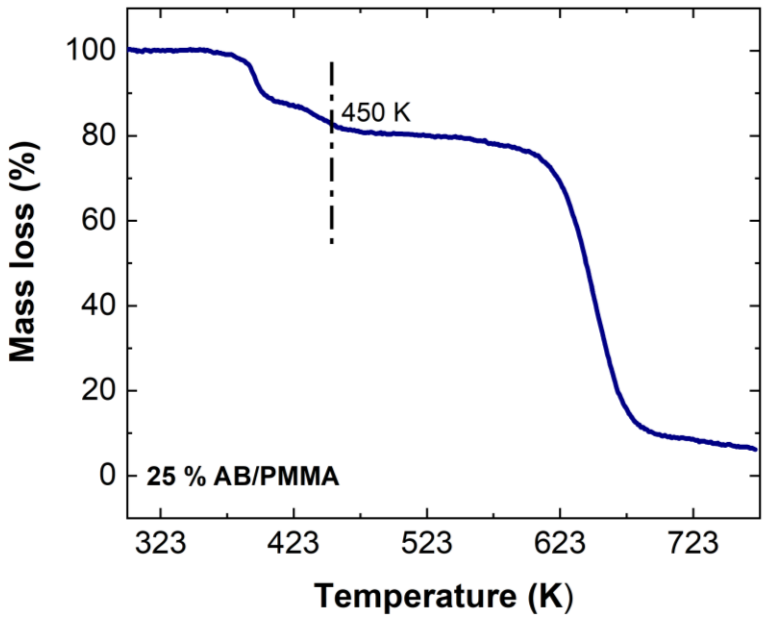

Figure S4 TGA of 25 % AB/PMMA shows at 25 % mass loss due to the gasification of AB before the onset of the decomposition of PMMA at ~460 K.

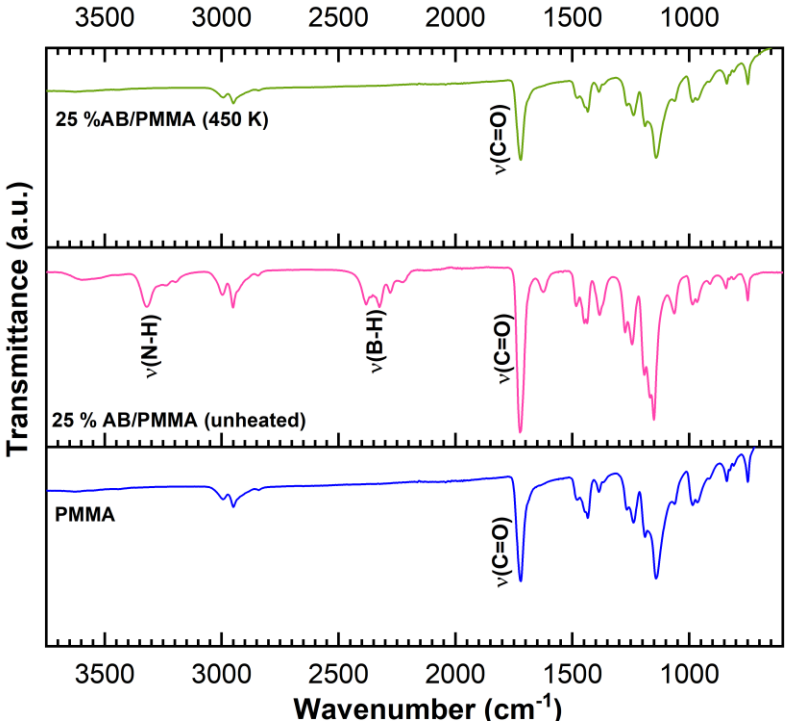

Figure S5 ATR-FTIR of the intermediate residue collected on heating 25 % AB/PMMA in TGA to 450 K, shows no signatures of AB, whereas the C=O bond along with the other bonds of the polymer remains intact post AB decomposition.

S.3 In-situ characterization of AB in other carbonyl-based polymer matrices like PPC and PVP

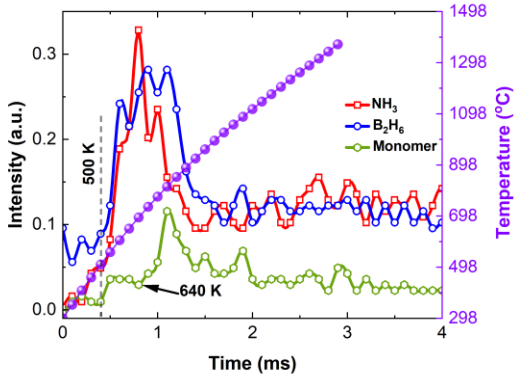

Figure S6 Time/temperature resolved evolution of NH_3, B_2H_6 and PPC-monomers from 75 % AB/PPC composites, showing that the decomposition temperature of AB remains same across all polymer matrices with carbonyl groups.

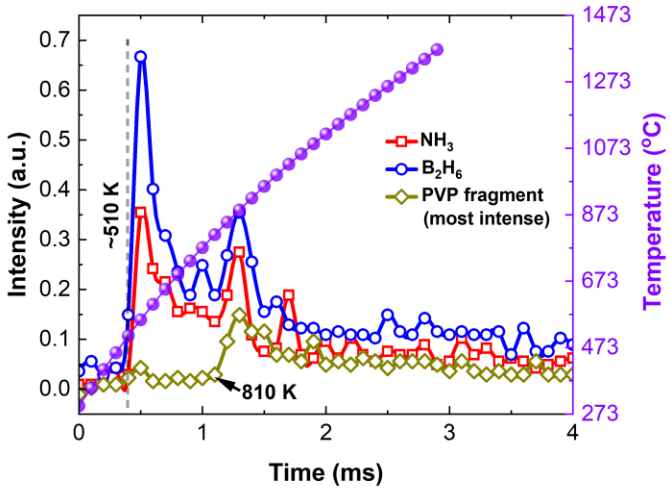

Figure S7 Time/temperature resolved evolution of NH_3, B_2H_6 and PVP-fragments (released with the intensity) from 75 % AB/PVP composites, showing that the decomposition temperature of AB remains same across all polymer matrices with carbonyl groups.

S.4 In-situ characterization of AB in non-carbonyl-based polymer matrix such as poly-vinyl alcohol

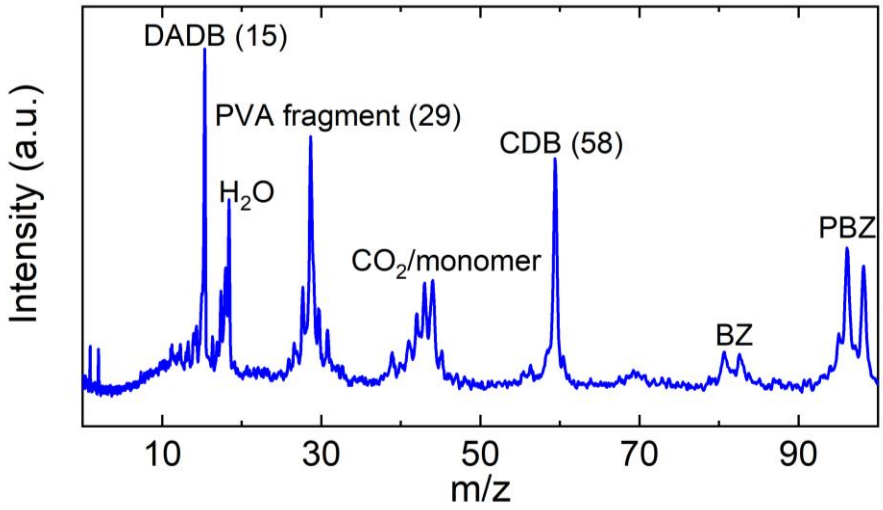

Figure S8 AB follows the usual DADB pathway forming BNHx species in non-carbonyl based polymer matrices such as PVA.

S.5 Effects of AB concentration on IR and XRD signatures in AB/polymer composites

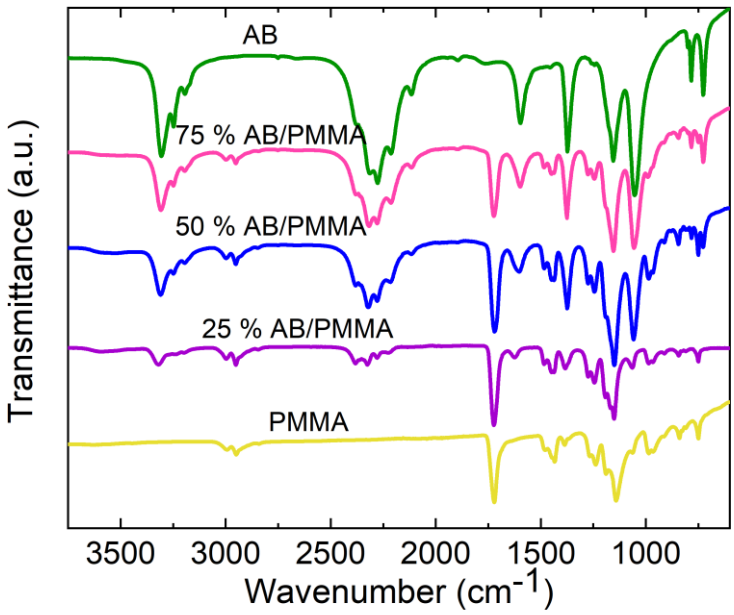

Figure S9 IR spectra of AB/PMMA composites over the entire wavelength range

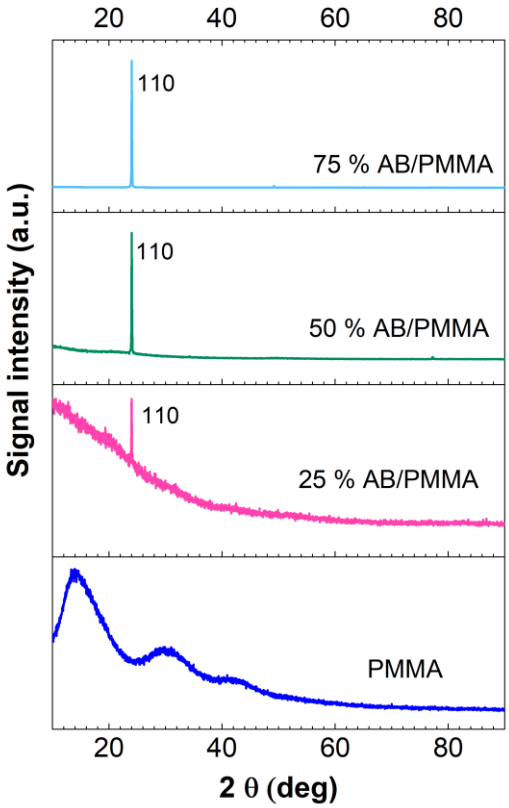

Figure S10 XRD spectra of AB/PMMA composites containing different wt. % of AB.

S.6 In-situ characterization of hierarchical mesoparticles

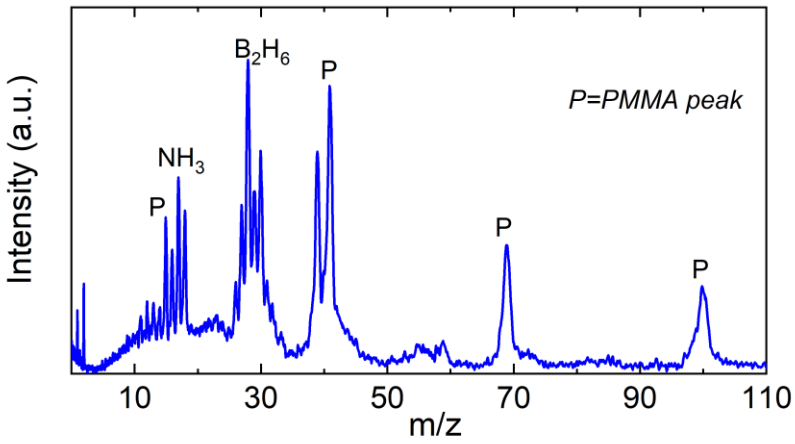

FigureS11 T-jump TOFMS average spectra of mesoparticles composites

5 Magnesium Induced Strain and Immobilized Radical Generation on Boron Oxide Surface Enhances Oxidation Rate of Boron Particles: A DFTB-MD Study

5.1 Summary

Despite its high gravimetric and volumetric energy densities, boron (B) particles suffer from poor oxidative energy release rates as the boron oxide (B_2O_3) impedes the diffusivity of O_2 to the particle interior. Recent experiemental studies have shown that the addition of metals with lower free energy of oxidation such as Mg can reduce the oxide shell of B and enhance the energetic performance of B by ~30-60 %, however the exact underlying mechanism behind the reactivity enhancement is unknown. Here, I have performed DFTB-MD simulations to study the reaction of Mg vapor with a B_2O_3 surface. I found that the Mg become oxidized on the B_2O_3 surface forming a MgB_xO_y phase, which induces a tensile strain in the B-O bond at the MgB_xO_y-B_2O_3 interface, simultaneously reducing the interfacial B, developing dangling bonds. The interfacial bond straining creates an overall surface expansion indicating the presence of a net tensile strain on the entire surface. The B with dangling bonds can act as active centers for gas phase O_2 adsorption thereby increasing the adsorption rate and the overall tensile strain on the surface will increase the diffusion flux of adsorbed O through the surface to the particle core. As the overall B particle oxidation rate is dependent on both O adsorption and diffusion rates, the enhancement in both of these rates increases the overall reactivity of B particles.

5.2 Introduction

With the highest oxidative energy density on both gravimetric and volumetric basis, boron (B) is extremenly attractive as a fuel component in propulsion systems requiring maximal energy release rates[1–5]. In practice however, achieving high energy release rates from B is often impeded by the unfavorable properties of the oxide shell on B particles[6–9]. B particles oxidize in a shrinking-core manner. On external or oxidative heating, the boron oxide (B_2O_3) shell melts into a non-volatile liquid, at a relatively low temperature (~720 K) compared to the B-core, which remains solid during combustion [10–13]. The liquid shell being devoid of any physical voids impedes the diffusivity of oxygen and hence the B oxidation process[1–4,6,10,14].By contrast , metals with low melting or boiling points such as Al[15–18] and Mg[19–21] provide higher energetic performance, although having an inferior energy density compared to B, as they burn in the vapor phase [15,17,22–24].

One of the strategies to overcome the liquid phase mass transfer limitation has been to use solid-state borohydrides such as ammonia borane that can generate gas phase boron and hydrogen containing moeities[25,26]. Another approach to circumvent this limitation is to use an additive that will react with the oxide sell of boron. From a thermochemical perspective, the free energy of oxidation of metals such as Mg and Al are much lower than that of B[27], which implies that metals such as Mg and Al can reduce B_2O_3 to elemental B. However, in the solid state the complete reduction of B_2O_3 will be inhibited by slow diffusion processes, and hence it is likely that Mg and Al will form mixed oxide phases with B on reacting with B_2O_3[28]. Recent studies on the energetic performance of Al/B and Mg/B composites prepared through ball-milling, plasma deposition, or physical mixing

have reported ~30-60 % enhancement (Figure 5-1(a)) in the reactivity of B on addition of Al and Mg as a minor component[28–34]. The percent enhancement presented in Figure 5-1 (a) is obtained from calorimetry, pressurization rate, burn-time or ignition delay measurements. In one of these studies, the highest enhancement in reactivity ~60 % have been reported for a 10 wt. % Mg/B physically mixed nanoparticulate system[34]. A conjecture have been made that the Mg vapor (Figure 5-1(b)) generated from the Mg nanoparticle on heating, reacts with the B_2O_3 shell to form a mixed Mg-B-O oxide phase having different physical properties than B_2O_3, which somehow enhances the rate of oxidation of B. However, experimentally probing the actual composition of the mixed oxide phase along with the exact atomic scale mechanism behind the reactivity enhancement of B is nearly impossible. Hence, atomistic simulations are essential to address these questions.

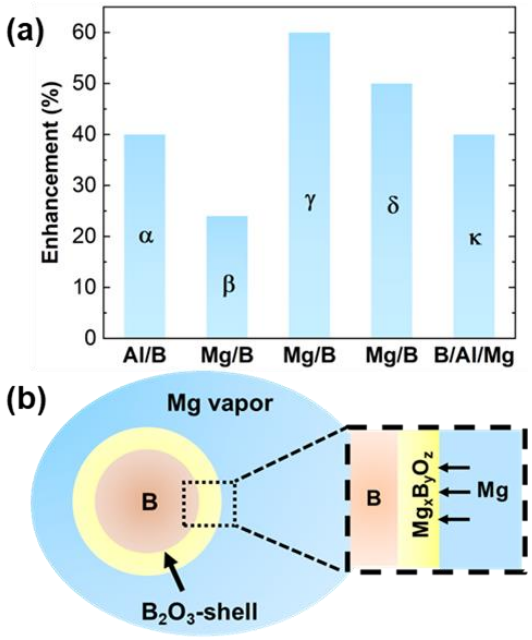

Figure 5-1 (a) Enhancement of the energy release rate of B with Al and Mg addition as reported by previous experimental studies (α[29], *β*[33],γ[34], *δ*[28], κ[31]). (b) Schematic on how Mg vapor might manipulate the oxide shell of B making Mg/B composite the highest performing system.

In this study, I have investigated the reaction of vapor phase Mg atoms with a B_2O_3 surface, through density functional theory tight binding[35–37] - molecular dynamics simulations (DFTB-MD), employing three-body interatomic interactions based on the Chebyshev Interaction Model for Efficient Simulation (CHIMES) framework[38,39]. DFTB being a semiempirical model is already less computationally expensive than DFT[35]. The CHIMES framework where the repulsive part of the DFTB energy functional is fitted to training data by a linear combination of Chebyshev polynomials further increases the computational efficiency of simulations of reactive systems having three body interactions. [38].

Based on our simulation results, I show that Mg binds with O-atoms on the B_2O_3 surface to form MgB_xO_y phases. This results in tensile straining of the O-B bond at the developing MgB_xO_y-B_2O_3 interface The excess volume created by the bond length extension, which is accomodated by an overal surface expansion. I also found that interfacial boron is reduced and the undercoordinated B should develop dangling bonds, making it available to particpate in subsquent reaction with external oxygen. The net tensile strain on the surface will enhance the diffusion flux of adsorbed oxygen through the B_2O_3 shell. As the rate of oxidation of the B particles depends on the sum of the rate of O_2 adsortion to its surface and the rate of adsorbed O-ion diffusion through its shell, the simultaneous enhancement of both of these factors should enhance the overall oxidation rate of boron.

5.3 Computational details

Semi-empirical DFTB with self-consistent charge calculations have been described elsewhere[38,39]. The tight binding model assumes that electron densities are localized around the atom centers and the density drops to zero at larger distances from the nuclei. Assuming a small perturbation in the charge density $n(r) = n(r) + \delta n$, Taylor expansion of the charge density dependent Kohn Sham total energy functional yields an energy expression which can be broadly divided into three terms as represented by eq1:

$$E_{total} = E_{bandstructure} + E_{Coulombic} + E_{Repulsive} \quad (1)$$

$E_{bandstructure}$ represents all the occupied electronic states and is evaluated from the DFTB Hamiltonian. The $E_{Coulombic}$ contains the second order and third order long range charge density fluctuation terms and are self-consistently evaluated from pre-computed Hubbard

U values of each atom. $E_{Repulsive}$ part containing the ion-ion repulsion and the exchange correlation functional terms represent the bonded interactions in the first coordination sphere. Parameters of the $E_{Repulsive}$ part consisting of pairwise and three-body interactions were fitted using the CHIMES training set. The CHIMES training set is developed by repulsive free computations of the DFTB forces and stress tensor components, which are subtracted from the DFT values of the same. The sum of the squares of the differences in the value of force and stress components calculated from DFT and repulsion free DFTB respectively are used to develop an objective function, from which the parameters for the $E_{Repulsive}$ is obtained. A linear combination of Chebyshev polynomials accounts for pairwise and three-body interactions respectively, is fed to the objective function as an input module to obtain the $E_{Repulsive}$ parameters.

The molecular dynamics simulations were performed in an NVT ensemble using a Nosé-Hoover thermostat[40]. I used a B_2O_3 – (001) surface (17.7x15.3 Å) created with total 320 (B+O) atoms using the coordinates reported by a previous study[41] and optimized at 0 K. Periodic boundary conditions are applied to the simulation box, and the box length in the z-direction 3x larger than the thickness of the simulated surface to avoid wall effects on the vapor phase atoms. The optimized surface is annealed at 2000 K to obtain a minimum energy state via a NVT simulation. The Mg atoms were introduced as Mg vapor in the empty space above the equilibrated surface in the z-direction. The magnitudes of the initial velocities are assigned from the Maxwell-Boltzmann distribution based on the ensemble temperature, whereas the direction of the velocities is assigned randomly. The MD simulation was performed with a time-step of ~0.1 fs, and run over ~ 3ps to allow the

Mg to be adsorbed on the B_2O_3 surface. The self-consistent charge DFTB calculation is performed to obtain the charge densities of the microstates formed at every MD step. The entire simulation has been performed using the DFTB+ package[42]. The obtained trajectory data have been using in-house scripts and visual molecular dynamics (VMD) has been used to create visual representations of the surface from the trajectory data. All the time-resolved data presented have been moving averaged over ~100 MD steps.

5.4 Results and discussions

5.4.1 Surface optimization, equilibration, and Mg introduction

The B_2O_3 (001) surface optimized at 0 K (Figure 5-2(a)), was equilibrated at the simulation temperature (2000 K) by running a MD simulation in a NVT ensemble. After the energy minimization (Figure S1), one of the equal energy microstates (~1.1 ps) is chosen as the relaxed surface, and free Mg atoms are introduced above the surface (Figure 4-2(c)), with initial velocities assigned from the Maxwell-Boltzmann distribution based on the simulation temperature. The snapshot of the relaxed surface (Figure 5-2(a)) shows considerable restructuring significantly altered the ordering and distances between the B and O atoms. It is evident from the visual representations that there is no long-range order in the relaxed surface. The radial distribution function (Figure 5-2(b)) of pairwise distances between B and O at 0 K consists of two strong peaks at 1.3 Å and 3 Å, corresponding to the B-O bond distance and the distance of the B from the O attached to the neighboring B respectively (Figure 5-2(a)). No other peaks exist between 1.4-2.9 Å, indicating the presence of long-range order in the system as evident from the visual snapshots. Multiple

peaks emerge between 1.3-3 Å in the pair-correlation function of the B_2O_3 surface equilibrated to 2000 K indicating the absence of any long-range order. The absence of long-range ordering in the surface equilibrated to 2000 K makes it an ideal replica of the realistic B_2O_3 shell under reaction conditions, which exists in an amorphous state at room temperature and melts at ~720 K[1,43].

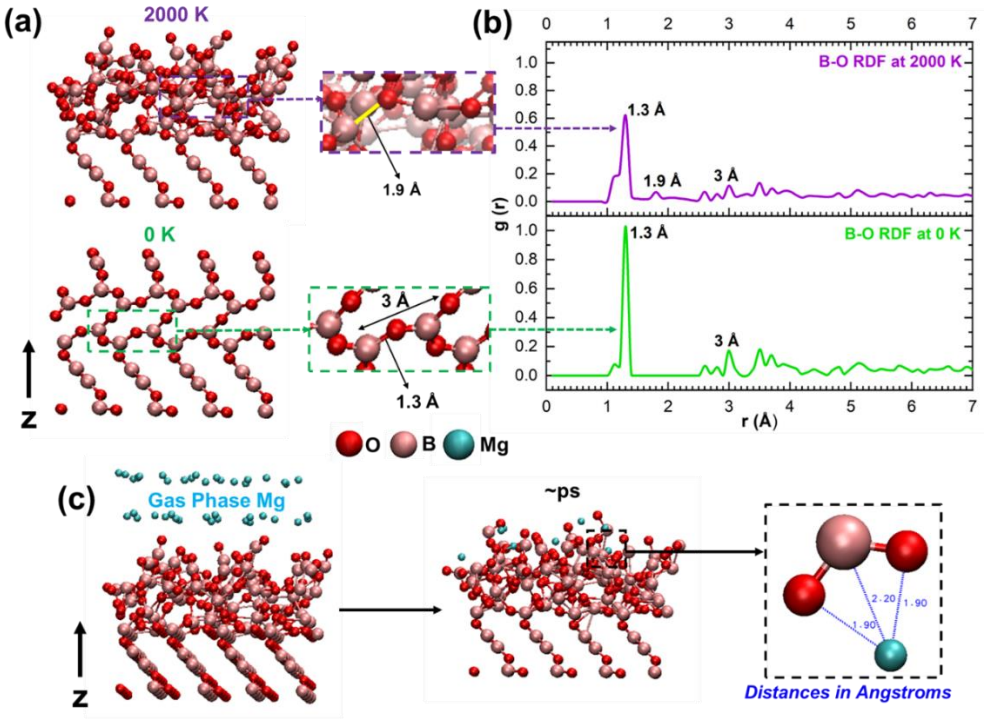

Figure 5-2 (a) Visual representation of the B_2O_3 (001) surface and B-O bond lengths, optimized at 0 K and after equilibration at 2000 K with the (b) corresponding radial distribution functions. (c) Visual representation of gas phase Mg above the surface equilibrated at 2000 K, the surface post-Mg adsorption, and representative illustration of the Mg-O and Mg-B bond lengths.

The simulations with the Mg were run for ~3 ps, which was sufficient to study the bond breakage/formation on Mg attachment to the surface. Figure 5-2(c) shows the

representative snapshot of a microstate formed by the surface with adsorbed Mg at picoseconds timescales. Analysis for one particular Mg from the particular microstate shows that the Mg-O bond length is 1.9 Å and the Mg-B bond distance is 2.2 Å. Figure S2 contains the visual representation of the optimized surface, equilibrated surface, and surface with adsorbed Mg from different angles. For better statistical interpretation, an analysis over all the microstates and the surroundings of all the adsorbed Mg has been analyzed and presented in the rest of the paper.

5.4.2 Mg oxidation and formation of Mg-B-O phase

The radial distribution functions representing the pairwise distances between Mg-O and Mg-B (Figure 5-3(a)) shows that the mode of the bond distance between Mg-O is at 1.8 Å whereas 2.2 Å for Mg-B. This suggests that the Mg prefers proximity to the O-sites over that of the B-sites, as expected from electronegativity differences Figure 5-3(b) shows the time-evolution of the occupancy of the nearest neighboring sites of Mg by B and O. The average coordination of O (~2.7) surrounding Mg is higher than the average of B (~2.2) surrounding the Mg, which also indicates that Mg atoms prefer to be in the vicinity of O over that of B. The nearest neighbor distribution also suggests that Mg tends to form $MgB_{2.2}O_{2.7}$ phase after reaction with the B_2O_3 surface.

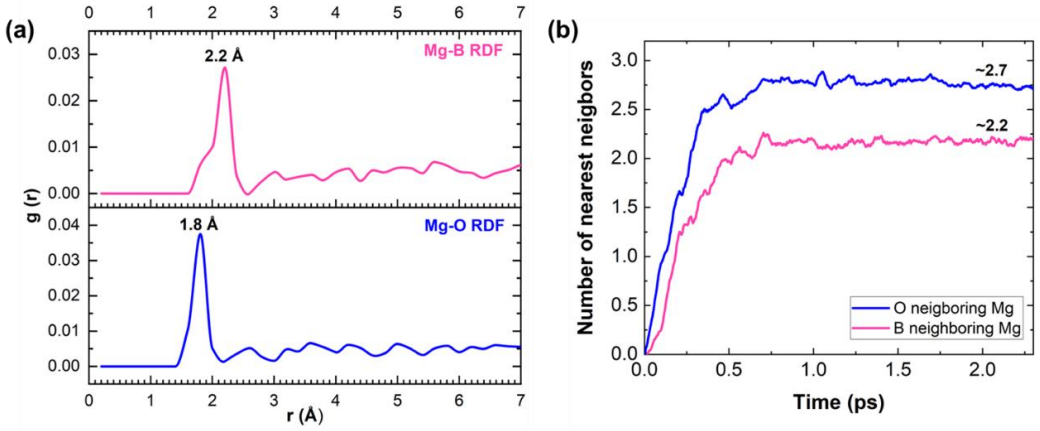

Figure 5-3 (a) Radial distribution function of pairwise of Mg-O and Mg-B distances showing that the average Mg-O bond length is 1.8 Å and the average Mg-B bond length is 2.2 Å. (b) The average number of B and O occupying the nearest neighboring sites of Mg are ~2.2 and ~2.7 respectively, indication the formation of $MgB_{2.2}O_{2.7}$ phase.

Figure 5-4 shows the temporal evolution of the average z-coordinate value and the relative change in the oxidation state of Mg which eventually get adsorbed on the B_2O_3 surface. The Mg move to positions with lower z-coordinates as they approach the surface from the vapor phase, and the value of z-coordinate becomes constant indicating their adsorption on the B_2O_3 surface. The average oxidation state of the adsorbed Mg atoms simultaneously increases by +1, which signifies that the Mg atoms have been oxidized on the B_2O_3 surface. According to the Mg-B-O phase diagram [44], different mixed oxide phases such as MgB_4O_7, $Mg_2B_2O_5$, and $Mg_3B_2O_6$ can form on reaction of Mg with B_2O_3. In all of these oxide phases Mg is bonded to O with an average bond distance between ~1.7-1.9 Å. Thus, Figure 5-3 and 5-4 confirms that the adsorbed Mg are indeed oxidized on B_2O_3, with the average bond length being ~1.8 Å. Mg lean systems, upon complete reaction should form a MgB_4O_7 phase. Since, the simulated system is Mg lean, it tends to form

$MgB_{2.2}O_{2.7}$ which can potentially evolve into MgB_4O_7 on reaction completion at longer timescales.

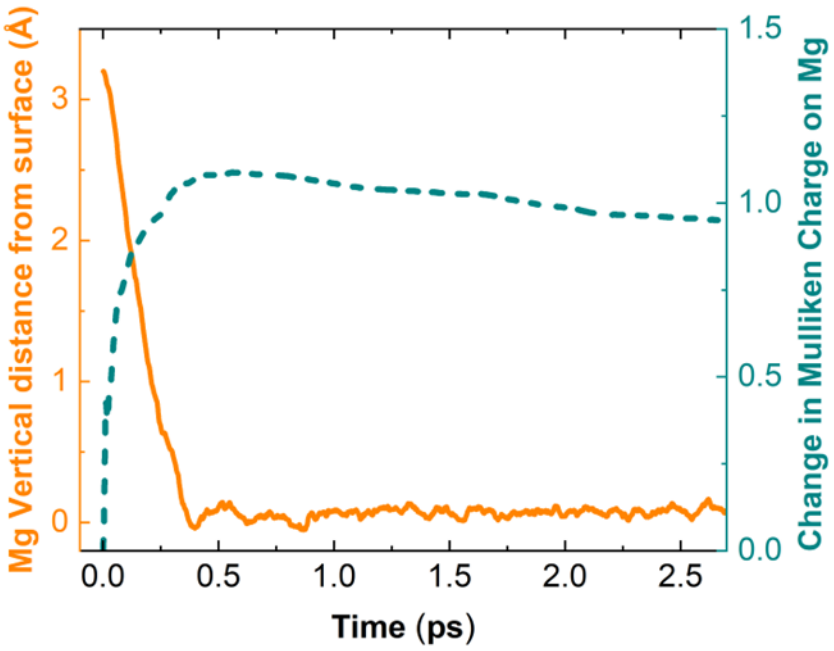

Figure 5-4 Decrease in the average z-coordinate value and increase in the Mulliken Charge of adsorbed Mg indicates the oxidation of the adsorbed Mg-atoms on the B_2O_3 surface.

5.4.3 Rearrangement of B and O in the MgB_xO_y phase

To understand the rearrangement of the O and B surrounding Mg during Mg-O bond formation, the displacement of the O and B atoms with respect to Mg is temporally tracked. Figure 5-5 shows the of displacement, $\Delta r = r(t) - r(0)$of either B or O with respect to Mg as a function of time. Figure 5-5(a) shows a schematic representing the physical meaning of Δr. A positive Δr indicates a displacement away from Mg whereas a negative Δr indicates a displacement towards Mg. Figure 5-5(b) shows that on average the Bare displaced away from Mg, whereas there is a net displacement of the O towards Mg

by approximately the same extent. Thus, Mg displaces B from its previously occupied sites and attracts the O-atoms to form the Mg-O bond in the Mg-B-O mixed oxide phase. The magnitude of the displacement of the neighboring O and B atoms towards or away from Mg are comparable to the ensemble averaged displacement of all atoms (Figure S3), indicating that there is a significant extent of directional displacement of O and B atoms towards or away from Mg.

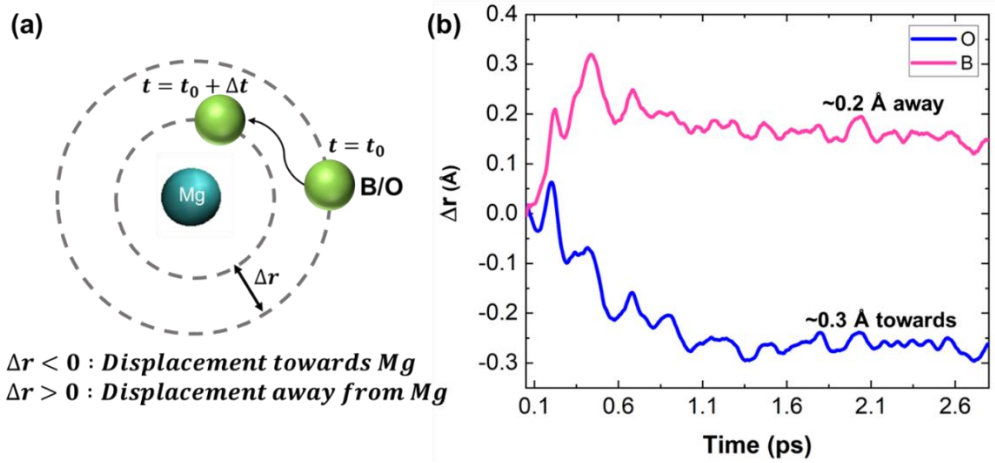

Figure 5-5 (a) Schematic explaining the significance of the evolution of Δr as a parameter to understand the directional displacement of B and O atoms towards or away from Mg. (b) Time-evolution of Δr of B and O surrounding Mg shows that the B-atoms are displaced away from Mg whereas the O atoms move towards Mg.

5.4.4 Bond strain, and reduction of B at the MgB_xO_y-B_2O_3 interface

It is essential to analyze the evolution of the oxidation state and the distance of the B initially bonded with O that formed the Mg-O bond, to understand the migration of atoms across the MgB_xO_y-B_2O_3 interface. Figure 5-6 shows that the aforementioned average O-B bond distance increases from ~1.4 Å to 2 Å, resulting in a ~40 % bond strain, whereas the oxidation state of the corresponding B decreases by 0.4 . Figure S4 shows the oxidation states of B, Mg, and O with increasing z-coordinate, at the initial state, and after ~3 ps,

which clearly shows that the oxidation state of B near the surface where Mg is adsorbed decreases by ~0.4 implying that boron is getting reduced at the surface. Hence, the interfacial B are undercoordinated and exist as immobilized free radicals (i.e. dangling bonds) ready to participate in surface reactions.

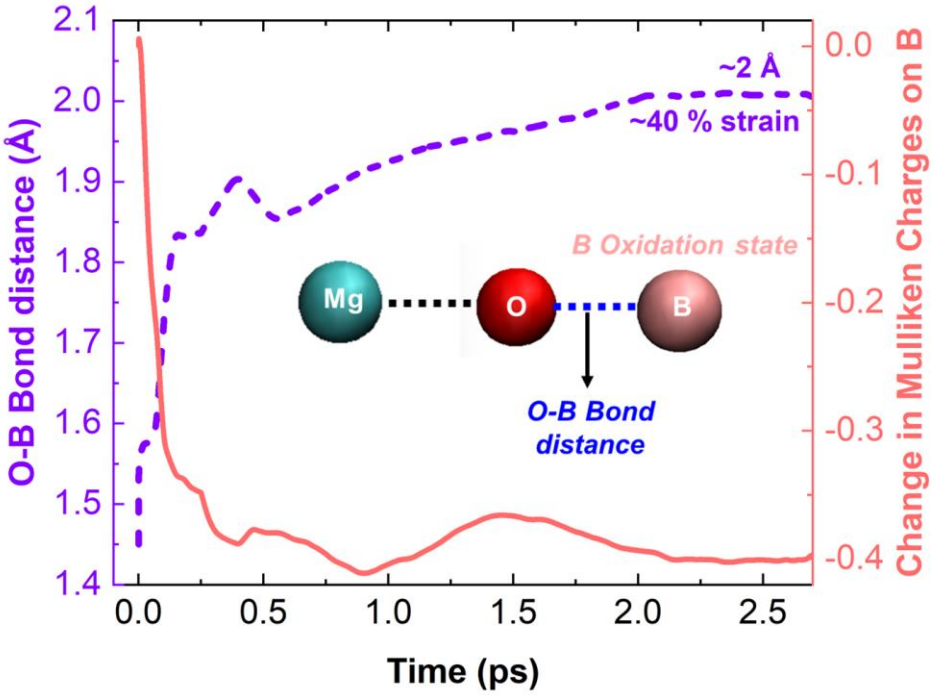

Figure 5-6 Time evolution of the O-B bond length at the MgB_xO_y-B_2O_3 interface, where the O is bonded to Mg, and the relative change in Mulliken Charge of the respective B, showing that the O-B bond length extends with time and the attached B is reduced.

The tensile strain in the evolving O-B bond should result in an excess volume of ~20 $Å^3$. The excess volume can be either accommodated by formation of regions of compressive strain in other locations in of the lattice, or by the expansion of the entire surface [46]. In this case I observe that the minimum B-O bond distance is ~1.3 Å, which is the equilibrium B-O bond distance [47] and hence the possibility of the existence of compressive strains can be eliminated. Since the simulated surface is periodic in the x and

y directions, a surface expansion can only be registered in the z-direction. From Figure 5-7(a) it is evident that the surface expands in the z-direction by ~0.4 Å, which is approximately the same as that of the O-B bond length extension (~0.6 Å). Thus, the excess volume created by tensile straining of the interfacial O-B bond, is accommodated by the overall surface expansion, which implies that there is an overall tensile strain on the B_2O_3 surface. The expansion of the interstitial voids due to the overall tensile strain on the surface should imply an increase in the diffusivity of adsorbed species through the surface.

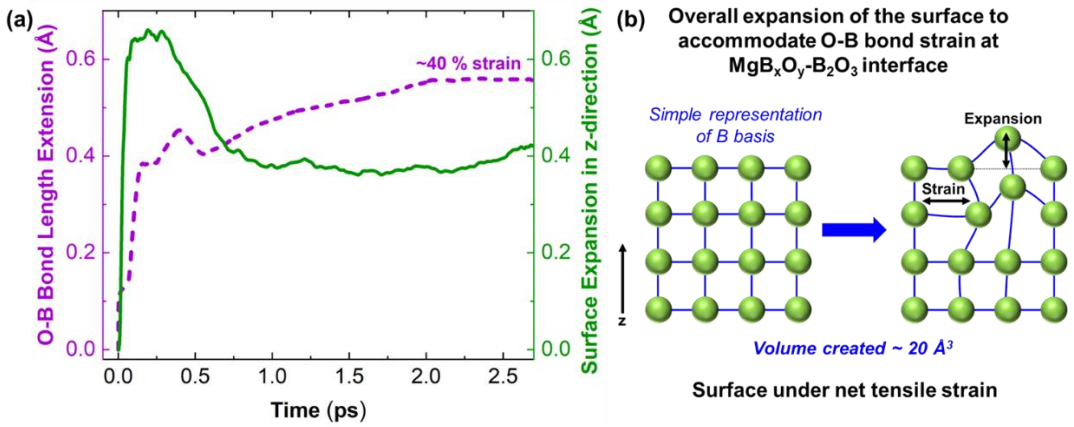

Figure 5-7 (a) Time evolution of the O-B bond length extension at the MgB_xO_y-B_2O_3 interface, where the O is bonded to Mg and the linear expansion of the surface in z-direction. (b) Schematic explaining how the surface expands to accommodate the excess volume created by the extension in the O-B bond length which results in an overall tensile strain on the entire surface.

5.4.5 Effect on the oxidation rate of B particles

To summarize, Mg adsorption on the B_2O_3 surface results in the formation of Mg lean MgB_xO_y phases, which causes a rearrangement of the B and O-atoms surrounding the adsorbed Mg. The oxygen exchange reaction leading to the Mg-O bond, strains the remnant

B-O bond, leading to simultaneous reduction of the oxidation state of B (i.e. dangling bond formation). The O-B bond distance increase results in a tensile strain, the excess volume created is accommodated by a net expansion of the surface. The B-atoms with dangling bonds are active sites for gas phase species adsorption. The net tensile strain on the surface should enhance the diffusivity of species from surface to the bulk as explained by the schematic in Figure 5-8(a).

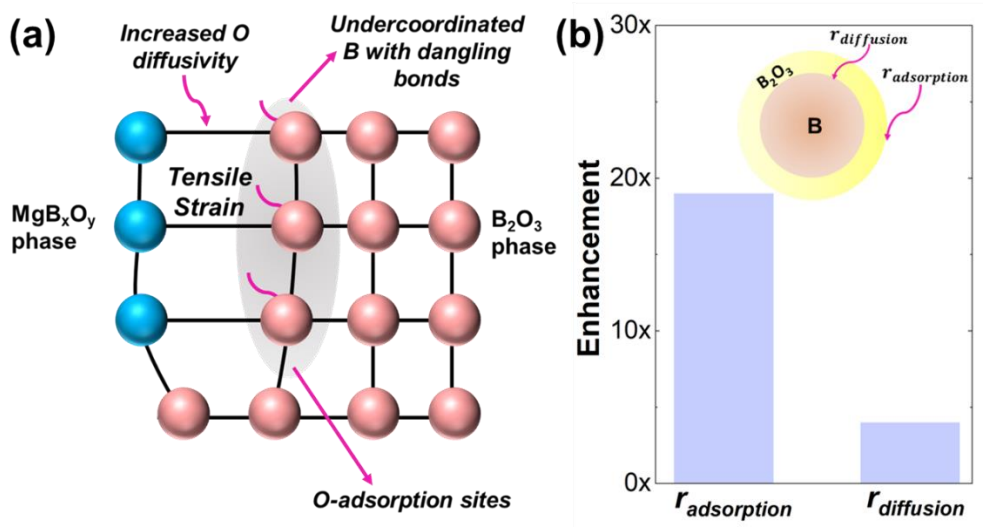

Figure 5-8 (a) Schematic showing the undercoordinated B existing at the MgB_xO_y-B2O3 interface possess dangling bonds which can act as active centers for O_2 adsorption as well as the straining of the interfacial B-O bond which will result in enhanced diffusion flux of adsorbed O. (b) Estimated enhancements in the rate of adsorption and diffusion of O to the B-particle interior based on simple continuum adsorption and diffusion models.

According to Langmuir adsorption model [48], the rate of adsorption of gases on a surface depends on the fraction of surface coverage as $r_{ads} = k_{ads}P(1-\theta)$ where k_{ads} is the adsorption rate constant, P is the partial pressure of the gas phase reactant, and θ is the fraction of surface coverage. For a fully oxidized B_2O_3 surface, θ should be ideally 1, and

hence the rate of adsorption of gas phase O_2 should be null. However, practically a B_2O_3 surface cannot exist as a pure B_2O_3 phase, as surface reconstruction (Figure 5-2 (a)) always leads to uncoordinated atoms. For the sake practical clarity let us assume that a B_2O_3 surface has 99 % O coverage. Consider a case with 10% (by number) adsorbed Mg. Given the Mg forms an MgB_4O_7 phase on complete reaction, then each Mg should pull one O out of the B_2O_3 phase, resulting in a ~18.5 % reduction in the number of O atoms in the B_2O_3 phase. This will create dangling bonds for ~19.4 % of B, thereby reducing θ to 0.81. In principle this could provide an enhancement of ~19x in the O_2 adsorption rate. (Figure 5-8(b)). It is well known that the interstitial diffusional flux (J) of a particular species scale linearly with the product of the diffusivity (D) and the interstitial volume increment relative to the volume of the diffusing atom (v_0), $J \sim Dv_0$ given the gradient in strain remains constant [46]. Neglecting the fact that the D is also influenced by the lattice strain to avoid complication, a bond length extension from 1.3 Å to 2.0 Å resulting in ~20 $Å^3$ volume increment should increase the flux O-atoms (radius~152 pm [49]) by 4x. Apart from the intrinsic reaction kinetics, the rate of oxidation of solid particles in gas phase oxygen depends on i) rate of adsorption of gas phase oxygen to the particle surface ii) rate of diffusion of the adsorbed oxygen through the oxide shell to the particle interior[50]. Hence, for a B-particle with a B_2O_3 shell, exposure to Mg vapor will result in the creation of immobilized B radicals at the surface of the oxide shell which will act as active centers for gas phase O_2 adsorption, thereby increasing the rate of O_2 adsorption. Additionally, the Mg incorporation also results in a net tensile strain on the B_2O_3 surface leading to an

enhancement in the diffusivity of adsorbed O through the oxide shell. The combination of these two factors will simultaneously increase the rate of oxidation of the B particles.

5.5 Conclusion

I have computationally explored the reaction of vapor phase Mg with B_2O_3 surface using DFTB-MD simulations based on CHIMES framework. I found that Mg become oxidized on the B_2O_3 surface to form the $MgB_{2.2}O_{2.7}$ phase, with Mg-O bond length being 1.8 Å, which can potentially evolve into stoichiometric MgB_4O_7 on complete reaction. During the formation of the MgB_xO_y phase, there is a net displacement of B-atoms away from Mg and O-atoms towards Mg. As the Mg atoms pull the O-atoms from B across the MgB_xO_y-B_2O_3 interface, a tensile strain develops in the B-O bond and the bond length extends by ~0.6 Å. I found that the surface expands along the z-direction by ~0.4 Å, to accommodate the excess volume created by the straining of the interfacial bond, indicating that there is a net tensile strain on the entire surface. Simultaneously, B-atoms at the interface are reduced to immobilized free radicals with dangling bonds which can act as active centers for gaseous O_2 adsorption, leading to an enhancement in the oxygen adsorption rate on the surface. The tensile strain on the surface will increase the diffusion flux of adsorbed O-atoms through the surface. As the rate of B-particle oxidation depends on both oxygen adsorption rate and oxygen diffusion flux through the boron oxide shell, the enhancement of both of these rates will increase the overall oxidation rate of B-particles. Hence, our findings provide sufficient mechanistic understanding of the enhancement in the oxidative energy release rates from B in presence of Mg, observed by previous experimental studies.

5.6 References

(1) Wang, Y.; Wang, H.; Xu, F.; Ghildiyal, P.; Zachariah, M. R. Effect of Alkali Metal Perchlorate and Iodate Type on Boron Ignition: The Role of Oxidizer Phase Change. *Chemical Engineering Journal* **2022**, *446*, 136786. https://doi.org/10.1016/J.CEJ.2022.136786.

(2) Mursalat, M.; Schoenitz, M.; Dreizin, E. L. Effect of Particle Morphology on Reactivity, Ignition and Combustion of Boron Powders. *Fuel* **2022**, *324*, 124538. https://doi.org/10.1016/J.FUEL.2022.124538.

(3) Veith, J.; Pfitzner, M.; Veith,] J; Pfitzner, M. Combustion of Boron Particles in Premixed Methane/Air Flames. *Propellants, Explosives, Pyrotechnics* **2016**, *41* (2), 260–266. https://doi.org/10.1002/PREP.201500069.

(4) Chintersingh, K. L.; Schoenitz, M.; Dreizin, E. L. Boron Doped with Iron: Preparation and Combustion in Air. *Combust Flame* **2019**, *200*, 286–295. https://doi.org/10.1016/J.COMBUSTFLAME.2018.11.031.

(5) Gottfried, J. L.; Wainwright, E. R.; Huang, S.; Jiang, Y.; Zheng, X. Probing Boron Thermite Energy Release at Rapid Heating Rates. *Combust Flame* **2021**, *231*, 111491. https://doi.org/10.1016/J.COMBUSTFLAME.2021.111491.

(6) Chintersingh, K. L.; Schoenitz, M.; Dreizin, E. L. Oxidation Kinetics and Combustion of Boron Particles with Modified Surface. *Combust Flame* **2016**, *173*, 288–295. https://doi.org/10.1016/J.COMBUSTFLAME.2016.08.027.

(7) Baek, J.; Jiang, Y.; Demko, A. R.; Jimenez-Thomas, A. R.; Vallez, L.; Ka, D.; Xia, Y.; Zheng, X. Effect of Fluoroalkylsilane Surface Functionalization on Boron Combustion. *ACS Appl Mater Interfaces* **2022**, *14* (17), 20190–20196. https://doi.org/10.1021/ACSAMI.2C00347/SUPPL_FILE/AM2C00347_SI_005.AVI.

(8) Huang, S.; Deng, S.; Jiang, Y.; Zheng, X. Experimental Effective Metal Oxides to Enhance Boron Combustion. *Combust Flame* **2019**, *205*, 278–285. https://doi.org/10.1016/J.COMBUSTFLAME.2019.04.018.

(9) Jiang, Y.; Dincer Yilmaz, N. E.; Barker, K. P.; Baek, J.; Xia, Y.; Zheng, X. Enhancing Mechanical and Combustion Performance of Boron/Polymer Composites via Boron Particle Functionalization. *ACS Appl Mater Interfaces* **2021**, *13* (24), 28908–28915. https://doi.org/10.1021/ACSAMI.1C06727/ASSET/IMAGES/LARGE/AM1C06727_0008.JPEG.

(10) Chintersingh, K. L.; Schoenitz, M.; Dreizin, E. L. Transition Metal Catalysts for Boron Combustion. *Combustion Science and Technology* **2021**, *193* (8), 1400–1424. https://doi.org/10.1080/00102202.2019.1696317/SUPPL_FILE/GCST_A_1696317_SM6598.DOCX.

(11) Young, G.; Sullivan, K.; Zachariah, M. R.; Yu, K. Combustion Characteristics of Boron Nanoparticles. *Combust Flame* **2009**, *156* (2), 322–333. https://doi.org/10.1016/J.COMBUSTFLAME.2008.10.007.

(12) Zhao, W.; Wang, X.; Wang, H.; Wu, T.; Kline, D. J.; Rehwoldt, M.; Ren, H.; Zachariah, M. R. Titanium Enhanced Ignition and Combustion of Al/I2O5 Mesoparticle Composites. *Combust Flame* **2020**, *212*, 245–251. https://doi.org/10.1016/J.COMBUSTFLAME.2019.04.049.

(13) Zhao, W.; Wang, H.; Kline, D. J.; Wang, X.; Wu, T.; Xu, J.; Ren, H.; Zachariah, M. R. Influence of Titanium Addition on Performance of Boron-Based Thermites. *Chemical Engineering Journal* **2022**, *438*, 134837. https://doi.org/10.1016/J.CEJ.2022.134837.

(14) Yeh, C. L.; Kuo, K. K. Ignition and Combustion of Boron Particles. *Prog Energy Combust Sci* **1996**, *22* (6), 511–541. https://doi.org/10.1016/S0360-1285(96)00012-3.

(15) Henz, B. J.; Hawa, T.; Zachariah, M. R. On the Role of Built-in Electric Fields on the Ignition of Oxide Coated Nanoaluminum: Ion Mobility versus Fickian Diffusion. *J Appl Phys* **2010**, *107* (2), 024901. https://doi.org/10.1063/1.3247579.

(16) Trunov, M. A.; Umbrajkar, S. M.; Schoenitz, M.; Mang, J. T.; Dreizin, E. L. Oxidation and Melting of Aluminum Nanopowders. *Journal of Physical Chemistry B* **2006**, *110* (26), 13094–13099. https://doi.org/10.1021/JP0614188.

(17) Firmansyah, D. A.; Sullivan, K.; Lee, K. S.; Kim, Y. H.; Zahaf, R.; Zachariah, M. R.; Lee, D. Microstructural Behavior of the Alumina Shell and Aluminum Core before and after Melting of Aluminum Nanoparticles. *Journal of Physical Chemistry C* **2012**, *116* (1), 404–411. https://doi.org/10.1021/JP2095483/ASSET/IMAGES/JP2095483.SOCIAL.JPEG_V03.

(18) Huang, S.; Hong, S.; Su, Y.; Jiang, Y.; Fukushima, S.; Gill, T. M.; Yilmaz, N. E. D.; Tiwari, S.; Nomura, K. ichi; Kalia, R. K.; Nakano, A.; Shimojo, F.; Vashishta, P.; Chen, M.; Zheng, X. Enhancing Combustion Performance of Nano-Al/PVDF Composites with β-PVDF. *Combust Flame* **2020**, *219*, 467–477. https://doi.org/10.1016/J.COMBUSTFLAME.2020.06.011.

(19) Nie, H.; Schoenitz, M.; Dreizin, E. L. Oxidation of Magnesium: Implication for Aging and Ignition. *Journal of Physical Chemistry C* **2016**, *120* (2), 974–983.

https://doi.org/10.1021/ACS.JPCC.5B08848/ASSET/IMAGES/LARGE/JP-2015-08848M_0022.JPEG.

(20) Ghildiyal, P.; Biswas, P.; Herrera, S.; Xu, F.; Alibay, Z.; Wang, Y.; Wang, H.; Abbaschian, R.; Zachariah, M. R. Vaporization-Controlled Energy Release Mechanisms Underlying the Exceptional Reactivity of Magnesium Nanoparticles. *ACS Appl Mater Interfaces* **2022**, *14* (15), 17164–17174. https://doi.org/10.1021/ACSAMI.1C22685/ASSET/IMAGES/MEDIUM/AM1C22685_M002.GIF.

(21) Wagner, B.; Ghildiyal, P.; Biswas, P.; Chowdhury, M.; Zachariah, M. R.; Mangolini, L.; Wagner, B.; Mangolini, L.; Ghildiyal, P.; Biswas, P.; Chowdhury, M.; Zachariah, M. R. In-Flight Synthesis of Core–Shell Mg/Si–SiOx Particles with Greatly Reduced Ignition Temperature. *Adv Funct Mater* **2023**, 2212805. https://doi.org/10.1002/ADFM.202212805.

(22) Bazyn, T.; Krier, H.; Glumac, N. Evidence for the Transition from the Diffusion-Limit in Aluminum Particle Combustion. *Proceedings of the Combustion Institute* **2007**, *31* (2), 2021–2028. https://doi.org/10.1016/J.PROCI.2006.07.161.

(23) Law, C. K. A Simplified Theoretical Model for the Vapor-Phase Combustion of Metal Particles†. *http://dx.doi.org/10.1080/00102207308952359* **2007**, *7* (5), 197–212. https://doi.org/10.1080/00102207308952359.

(24) Mohan, S.; Trunov, M. A.; Dreizin, E. L. On Possibility of Vapor-Phase Combustion for Fine Aluminum Particles. *Combust Flame* **2009**, *156* (11), 2213–2216. https://doi.org/10.1016/J.COMBUSTFLAME.2009.08.007.

(25) Biswas, P.; Ghildiyal, P.; Kwon, H.; Wang, H.; Alibay, Z.; Xu, F.; Wang, Y.; Wong, B. M.; Zachariah, M. R. Rerouting Pathways of Solid-State Ammonia Borane Energy Release. *The Journal of Physical Chemistry C* **2021**, *126* (1), 48–57. https://doi.org/10.1021/ACS.JPCC.1C08985.

(26) Biswas, P.; Wang, Y.; Herrera, S.; Ghildiyal, P.; Zachariah, M. R. Catalytic Cleavage of the Dative Bond of Ammonia Borane by Polymeric Carbonyl Groups for Enhanced Energy Generation. *Chemistry of Materials* **2022**, *35*, 963. https://doi.org/10.1021/ACS.CHEMMATER.2C02684/ASSET/IMAGES/LARGE/CM2C02684_0007.JPEG.

(27) Balart, M. J.; Patel, J. B.; Gao, F.; Fan, Z. Grain Refinement of Deoxidized Copper. *Metall Mater Trans A Phys Metall Mater Sci* **2016**, *47* (10), 4988–5011. https://doi.org/10.1007/S11661-016-3671-8/TABLES/5.

(28) Sun, Y.; Ren, H.; Jiao, Q.; Schoenitz, M.; Dreizin, E. L. Oxidation, Ignition and Combustion Behaviors of Differently Prepared Boron-Magnesium Composites. *Combust Flame* **2020**, *221*, 11–19. https://doi.org/10.1016/J.COMBUSTFLAME.2020.07.022.

(29) Agarwal, P. P. K.; Matsoukas, T. Nanoenergetic Materials: Enhanced Energy Release from Boron by Aluminum Nanoparticle Addition. *ACS Omega* **2022**, *7* (30), 26560–26565. https://doi.org/10.1021/ACSOMEGA.2C02691/ASSET/IMAGES/LARGE/AO2C02691_0006.JPEG.

(30) Agarwal, P. P. K.; Matsoukas, T. Low-Temperature Cost-Effective Synthesis of MgB2for Energetic Applications. *ACS Appl Energy Mater* **2022**, *5* (12), 15310–15315. https://doi.org/10.1021/ACSAEM.2C02946/ASSET/IMAGES/LARGE/AE2C02946_0007.JPEG.

(31) Agarwal, P. P. K.; Matsoukas, T. Synthesis and Oxidation Chemistry of Highly Energetic Boron/Aluminum/Magnesium Composites. *FirePhysChem* **2023**. https://doi.org/10.1016/J.FPC.2023.03.001.

(32) Agarwal, P. P. K.; Jensen, D.; Chen, C. H.; Rioux, R. M.; Matsoukas, T. Surface-Functionalized Boron Nanoparticles with Reduced Oxide Content by Nonthermal Plasma Processing for Nanoenergetic Applications. *ACS Appl Mater Interfaces* **2021**, *13* (5), 6844–6853. https://doi.org/10.1021/ACSAMI.0C20825/ASSET/IMAGES/LARGE/AM0C20825_0012.JPEG.

(33) Agarwal, P. P. K.; Jensen, D.; Chen, C.-H.; Rioux, R. M.; Matsoukas, T. Synthesis and Characterization of Magnesium/Boron Solid Solutions for Energetic Applications. *ACS Appl Energy Mater* **2022**, *5* (6), 6716–6723. https://doi.org/10.1021/ACSAEM.2C00312.

(34) Ghildiyal, P.; Xu, F.; Rojas, A.; Wang, Y.; Chowdhury, M.; Biswas, P.; Herrera, S.; Abbaschian, R.; Zachariah, M. R. Magnesium-Enhanced Reactivity of Boron Particles: Role of Mg/B2O3 Exothermic Surface Reactions. *Energy and Fuels* **2022**. https://doi.org/10.1021/ACS.ENERGYFUELS.2C02347/ASSET/IMAGES/LARGE/EF2C02347_0008.JPEG.

(35) Foulkes, W. M. C.; Haydock, R. Tight-Binding Models and Density-Functional Theory. *Phys Rev B* **1989**, *39* (17), 12520. https://doi.org/10.1103/PhysRevB.39.12520.

(36) Seifert, G. Tight-Binding Density Functional Theory: An Approximate Kohn-Sham DFT Scheme. *Journal of Physical Chemistry A* **2007**, *111* (26), 5609–5613. https://doi.org/10.1021/JP069056R/ASSET/IMAGES/LARGE/JP069056RF00005.JPEG.

(37) Spiegelman, F.; Tarrat, N.; Cuny, J.; Dontot, L.; Posenitskiy, E.; Martí, C.; Simon, A.; Rapacioli, M. Density-Functional Tight-Binding: Basic Concepts and Applications to Molecules and Clusters. *https://doi.org/10.1080/23746149.2019.1710252* **2020**, *5* (1), 1710252. https://doi.org/10.1080/23746149.2019.1710252.

(38) Goldman, N.; Kweon, K. E.; Sadigh, B.; Heo, T. W.; Lindsey, R. K.; Pham, C. H.; Fried, L. E.; Aradi, B.; Holliday, K.; Jeffries, J. R.; Wood, B. C. Semi-Automated Creation of Density Functional Tight Binding Models through Leveraging Chebyshev Polynomial-Based Force Fields. *J Chem Theory Comput* **2021**, *17* (7), 4435–4448. https://doi.org/10.1021/ACS.JCTC.1C00172/ASSET/IMAGES/LARGE/CT1C00172_0008.JPEG.

(39) Lindsey, R. K.; Fried, L. E.; Goldman, N. ChIMES: A Force Matched Potential with Explicit Three-Body Interactions for Molten Carbon. *J Chem Theory Comput* **2017**, *13* (12), 6222–6229. https://doi.org/10.1021/ACS.JCTC.7B00867/ASSET/IMAGES/LARGE/CT-2017-00867G_0006.JPEG.

(40) Evans, D. J.; Holian, B. L. The Nose–Hoover Thermostat. *J Chem Phys* **1998**, *83* (8), 4069. https://doi.org/10.1063/1.449071.

(41) Assaf, N. W.; De La Pierre, M.; Altarawneh, M. K.; Radny, M. W.; Jiang, Z. T.; Dlugogorski, B. Z. Structure, Stability, and (Non)Reactivity of the Low-Index Surfaces of Crystalline B2O3-I. *Journal of Physical Chemistry C* **2017**, *121* (21), 11346–11352. https://doi.org/10.1021/ACS.JPCC.7B01347/ASSET/IMAGES/LARGE/JP-2017-013476_0007.JPEG.

(42) Hourahine, B.; Aradi, B.; Blum, V.; Bonafé, F.; Buccheri, A.; Camacho, C.; Cevallos, C.; Deshaye, M. Y.; Dumitric, T.; Dominguez, A.; Ehlert, S.; Elstner, M.; Van Der Heide, T.; Hermann, J.; Irle, S.; Kranz, J. J.; Köhler, C.; Kowalczyk, T.; Kubař, T.; Lee, I. S.; Lutsker, V.; Maurer, R. J.; Min, S. K.; Mitchell, I.; Negre, C.; Niehaus, T. A.; Niklasson, A. M. N.; Page, A. J.; Pecchia, A.; Penazzi, G.; Persson, M. P.; Řezáč, J.; Sánchez, C. G.; Sternberg, M.; Stöhr, M.; Stuckenberg, F.; Tkatchenko, A.; Yu, V. W. Z.; Frauenheim, T. DFTB+, a Software Package for Efficient Approximate Density Functional Theory Based Atomistic Simulations. *Journal of Chemical Physics* **2020**, *152* (12). https://doi.org/10.1063/1.5143190.

(43) Sdiri, N.; Elhouichet, H.; Elakermi, E.; Dhifallah, A.; Ferid, M. Structural Investigation of Amorphous Na2O–P2O5–B2O3 Correlated with Its Ionic Conductivity. *J Non Cryst Solids* **2015**, *409*, 34–42. https://doi.org/10.1016/J.JNONCRYSOL.2014.11.009.

(44) MUTLUER, T.; TIMUCIN, M. Phase Equilibria in the System MgO-B2O3. *Journal of the American Ceramic Society* **1975**, *58* (5–6), 196–197. https://doi.org/10.1111/J.1151-2916.1975.TB11442.X.

(45) Kuzuya, M.; Ishikawa, M.; Noguchi, A.; Ito, H.; Kamiya, K.; Kawaguchi, T. Nature of Dangling-Bond Sites in Native Plasma-Polymerized Films of Unsaturated Hydrocarbons, and Electron Paramagnetic Resonance Kinetics on Heat Treatment of the Films. *J Mater Chem* **1991**, *1* (3), 387–391. https://doi.org/10.1039/JM9910100387.

(46) Grönbeck, H.; Zhdanov, V. P. Effect of Lattice Strain on Hydrogen Diffusion in Pd: A Density Functional Theory Study. *Phys Rev B Condens Matter Mater Phys* **2011**, *84* (5), 052301. https://doi.org/10.1103/PHYSREVB.84.052301/FIGURES/3/MEDIUM.

(47) Albert, B.; Hillebrecht, H. Boron: Elementary Challenge for Experimenters and Theoreticians. *Angewandte Chemie International Edition* **2009**, *48* (46), 8640–8668. https://doi.org/10.1002/ANIE.200903246.

(48) Myong, R. S. Gaseous Slip Models Based on the Langmuir Adsorption Isotherm. *Physics of Fluids* **2003**, *16* (1), 104. https://doi.org/10.1063/1.1630799.

(49) Rivera Rocabado, D. S.; Nanba, Y.; Koyama, M. Density Functional Theory and Machine Learning Description and Prediction of Oxygen Atom Chemisorption on Platinum Surfaces and Nanoparticles. *ACS Omega* **2021**, *6* (27), 17424–17432. https://doi.org/10.1021/ACSOMEGA.1C01726/ASSET/IMAGES/MEDIUM/AO1C01726_M005.GIF.

(50) Park, K.; Lee, D.; Rai, A.; Mukherjee, D.; Zachariah, M. R. Size-Resolved Kinetic Measurements of Aluminum Nanoparticle Oxidation with Single Particle Mass Spectrometry. *Journal of Physical Chemistry B* **2005**, *109* (15), 7290–7299. https://doi.org/10.1021/JP048041V/ASSET/IMAGES/MEDIUM/JP048041VE00008.GIF.

5.7 Supporting information

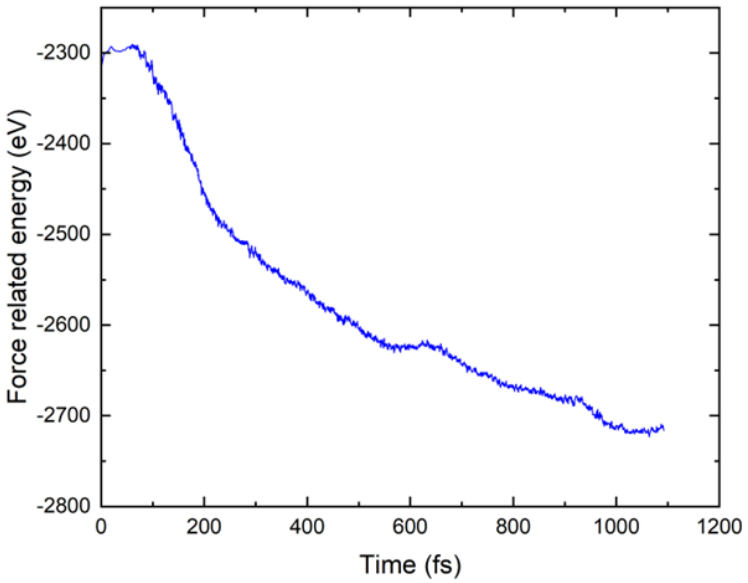

Figure S1 Annealing of the 0 K surface at 2000 K for equilibration.

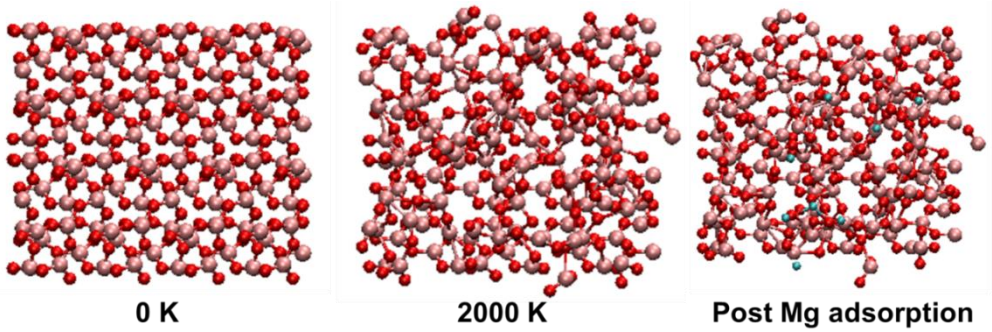

Figure S2 Top down view of the surfaces.

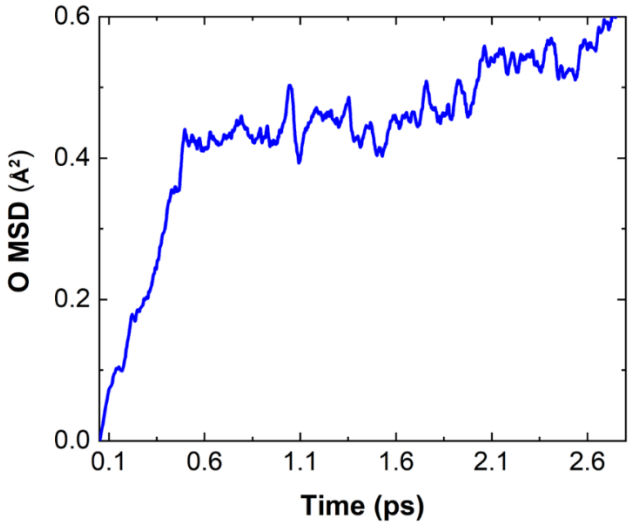

Figure S3 Mean squared displacement of all O atoms in the ensemble.

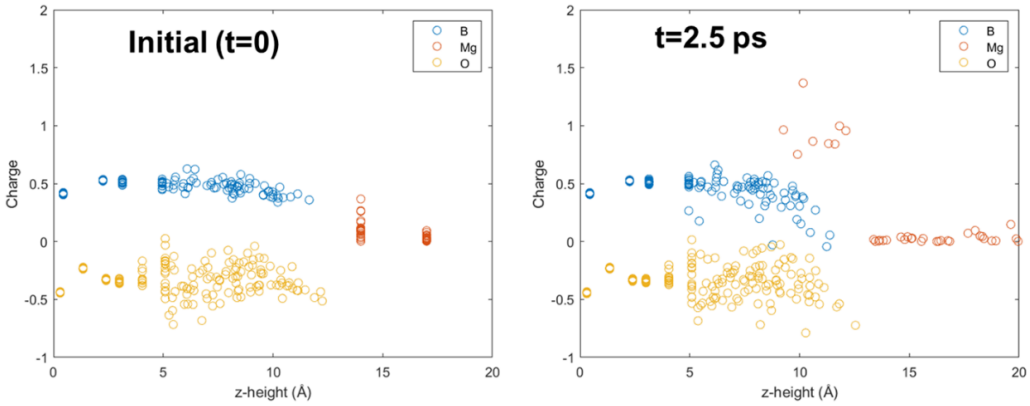

Figure S4 Charge on B, Mg, O along z direction.

6 In-situ Thermochemical Shock Induced Stress at the Metal/Oxide Interface Enhances Reactivity of Aluminum Nanoparticles

6.1 Summary

Although aluminum (Al) nanoparticles have been widely explored as a fuel in energetic applications, researchers are still exploring approaches for tuning their energy release profile via microstructural alteration. In this study, I show that a nanocomposite (~70 nm) of metal ammine complex such as tetramine copper nitrate ($Cu(NH_3)_4(NO_3)_2$/TACN) coated Al containing only 10 % TACN (by mass), demonstrates a ~200 K lower reaction initiation temperature coupled with an order of magnitude enhancement in reaction rate. Through time/temperature resolved mass-spectrometry and ignition measurements at high heating rates, I show that the ignition occurs due to a condensed phase reaction between Al and copper oxide (CuO) crystallized on TACN decomposition. TEM and XRD analysis on the particles at an intermediate stage, show that the rapid heat release from TACN decomposition, in-situ enhances the strain on the Al-core with induction of non-uniformities in the thickness of its shell. The thinner region of the non-uniform shell enables rapid mass transfer of Al-ions to the crystallized CuO enabling their condensed phase ignition. Hence, the thermochemical shock from TACN coating induces stresses at the Al/AlO_x interface, which effectively switches the usual gas phase O_2 diffusion limited ignition process of Al nanoparticles to become condensed phase Al-ion transfer controlled, thereby enhancing their reactivity.

6.2 Introduction

Among the nanometallic fuels used in energetic materials for propulsion and pyrotechnics [1–3], Al is the most commonly employed fuel due to its high gravimetric (~32 kJ/g) and volumetric combustion enthalpy (~86 kJ/cm^3) [4–12]. Extensive efforts have been employed in modulating the energy release profile of Al nanoparticles in fuel/oxidizer

composites by altering the ionic conductivity of oxidizers [13–15], oxidizer morphology [16–18], and utilization of additives [19–21] to improve reactivity.

Several studies have focused on improving the reactivity of Al nanoparticles by their microstructural alteration, through induction of thermomechanical stresses [22–32]. The core of the Al nanoparticles nominally exists under tensile stress at room temperature, which attains a zero-strain state when heated to ~673 K [33]. It has been observed that pre-annealing of Al nanoparticles at around ~673 K for several minutes followed by fast quenching, induces dilatational lattice strain on the core, which appears to enhance Al transport through the shell. [22–32]. Additionally, an investigation on aging behavior of nanothermite composites of Al with oxidizers such as CuO, Fe_2O_3, and Co_3O_4, by annealing of the mixtures at ~473 K for 15 days, showed that the alumina shell became non-uniform in thickness [34]. The non-uniformity in the thickness of the shell led to higher mass transport rate of Al through the thinner regions, resulting in an unexpectedly high reactivity of the annealed nanothermite composites.

In this regard, Werner type metal ammine complexes [35–39] such as tetraamine copper nitrate ($Cu(NH_3)_4(NO_3)_2$/TACN) can be used with Al nanoparticles for two potential benefits. First, it can act as a reactive gas generator, by exothermically ($\Delta H \sim -644\ kJ/mol$) [37] decomposing to NH_x and NO_x gases, leaving residual CuO to participate in a redox reaction with Al. This has important implications with respect to Al combustion as the phase transformation of Al during high temperature oxidation processes together with the high mobility of Al-ions through its oxide shell, results in rapid sintering and agglomeration of Al nanoparticles, thereby impeding the progress of the energetic reaction

[9,33,40–43]. In-situ gas generation through polymeric additives has been effective in mitigating this problem, as gas generation during high temperature decomposition of these polymers reduces sintering and agglomeration by pushing particles away from each other [44]. Therefore, TACN can be potentially used for in-situ gas generation for mitigating similar challenges. Secondarily, as pre-stressing has been shown to improve the reactivity of Al, the rapid energy released during TACN decomposition ($\Delta H \sim -644\ kJ/mol$), can be potentially employed to shock-heat and induce strain in the Al-nanoparticles. Hence, this approach may be able to mitigate the preprocessing steps associated with the annealing [22–32]. Previous explorations have shown that the use of super-micron TACN particles as gas generating additives, can significantly improve the reactivity of Al/CuO composites [45–47]. However, the application of nanoscale TACN for in-situ stress induction in Al nanoparticles has not been explored.

In this study, I have synthesized ~70 nm particles of TACN coated Al (TACN@Al) by a heterogeneous crystallization method. Synthesis of bare TACN crystals in the absence of Al nanoparticles as seed led to the formation of ~4 μm TACN particles. Using in-situ T-jump ignition, T-jump time-of-flight mass spectrometry (T-jump TOFMS), and TGA/DSC analysis, I show that the heat released on decomposition of TACN in TACN@Al into NH_x and NO_x species, is absorbed by Al nanoparticles resulting in their early oxidation and condensed phase ignition. Through XRD and TEM, I have shown that the released heat collectively deforms the Al particles, enhances strain on the Al-core, and induces non-uniformity in the thickness of the alumina shell. The thinner regions of the non-uniform shell having shorter diffusion length, enables the Al-ions to diffuse across the

shell and initiate a condensed phase reaction with the oxidizer, thereby lowering the oxidation and ignition onsets. Such an effect was not observed in the case of physically mixed Al with micron TACN, as the processes of TACN decomposition and Al oxidation, occurred independently.

6.3 Experimental

6.3.1 Materials

Aluminum nanoparticles (ALEX) with a mean size of ~50 nm and having an Al content of ~67 % by mass was procured from Argonide Corp. The copper nitrate trihydrate ($Cu(NO_3)_2.3H_2O$) salt was obtained from Sigma Aldrich. 30 % NH_4OH and ethanol were procured from Fischer-scientific. The CuO nanoparticles (~50 nm) were obtained from US Research nanomaterials.

6.3.2 Synthesis of TACN coated Al composites

Previous studies have synthesized TACN crystals by a precipitation reaction between dissolved $Cu(NO_3)_2$ and NH_4OH [45]. To make TACN coated Al composites (TACN@Al) I prepared various strengths (0.2 mM, 0.4 mM, 0.8 mM, and 1.6 mM) of copper nitrate trihydrate ($Cu(NO_3)_2.3H_2O$) solutions in ethanol. Equal amounts of Al nanoparticles (~50 nm) were ultrasonically dispersed in all of the $Cu(NO_3)_2$ solutions, such that the mass concentration of Al in each solution is 0.5 mg/ml. The concentration of $Cu(NO_3)_2$ was varied with the goal to make different TACN@Al composites with TACN content varying between 5-20 % (by mass). The $Cu(NO_3)_2$ solutions with dispersed Al nanoparticles were magnetically stirred for ~10 minutes. Then 30 % NH_4OH was added

dropwise to each of the $Cu(NO_3)_2$ solutions with dispersed Al nanoparticles, under vigorous magnetic stirring. As 4 moles of NH_3 needs to be inserted into 1 mole of $Cu(NO_3)_2$ to make TACN, the total amount of NH_4OH added to each solution was varied to ensure that the final NH_4OH concentration is four times the concentration of dissolved $Cu(NO_3)_2$. After NH_4OH addition, each solution was kept under magnetic stirring for ~1 hour. Then each solution was centrifuged and washed (10,000 rpm, 10 minutes) with blank solvents for two times. The washed powders were dried overnight in a vacuum oven at room temperature. For the synthesis of the bare TACN crystals, I started with a 0.8 mM $Cu(NO_3)_2.3H_2O$ solution and followed the exact same procedure except the addition of Al nanoparticles.

6.3.3 Ex-situ characterizations on composition and material properties

Particle sizes and morphologies of TACN and TACN@Al were characterized by FEI NNS450 scanning electron microscope (SEM) and FEI Tecnail 12 transmission electron microscope (TEM). X-ray Diffraction (XRD), performed using PANalytical EMPYREAN (Cu Kα source, $\lambda = 1.54$ Å), was used to characterize the composition, lattice strain and crystallite size of the TACN@Al crystals. Thermo-gravimetric analysis (TGA)/Differential scanning calorimetry (DSC), performed using SDT-Q600 (TA instruments) were used to characterize the decomposition steps of TACN and the oxidation onset of Al, at a heating rate of 10 K/min. The TACN content of each sample was also identified through TGA.

6.3.4 In-situ time and temperature resolved characterization on ignition and combustion

Temperature jump time-of-flight mass spectrometry (T-jump TOFMS) was used for in-situ time and temperature resolved identification of the gas phase species released during the pre-ignition and combustion reactions. Details about the mass-spectrometer can be found in several of our previous publications [3,48,49]. For this measurement, a thin Pt wire (~75 µm) is used as the sample holder, on which thin layers of solid nano-powder samples are coated by drop casting through micro-pipettes. During the measurement, the Pt wire is resistively heated to ~1500 K by applying a voltage pulse of width ~3 ms, which leads to an average heating rate of ~10^5 K/s. The thin coating of the sample ensures that the sample is at the same instantaneous temperature as that of the wire and that it is uniformly heated at the same heating rate. Through a probe, the current across the wire is monitored at every 0.1 ms, and Callender-Van Dusen equations is used to estimate the instantaneous wire temperature at every 0.1 ms over the 3 ms pulse. The gas phase species released on thermal activation of the reactions, are sampled and identified over 10 ms at an interval of 0.1 ms by the time-of-flight mass spectrometric process. This measurement is performed under a high vacuum of ~10^{-10} atm.

The ignition temperature of each sample was measured using a similar Temperature jump process (T-jump ignition). The sample holder and the sample delivery, heating and temperature estimation methods of this measurement is exactly same as that of T-jump TOFMS. However, instead of vacuum, this measurement is performed by inserting the sample holder into a specialized chamber equipped with several ports for flowing gases

and applying vacuum, along with a pressure gauge and a quartz glass wall for high-speed imaging of the ignition event, which is filled with Ar at ~1 atm. A high-speed camera (Vision Research Phantom V12.1) is used to track the delay-time of the ignition event with ~μs resolution. The temperature of the wire at this time is estimated to be the ignition temperature. More details about this measurement can be found in our previous papers [3,50]. The T-jump ignition and TOFMS characterizations cannot be performed on the super-micron bare TACN crystals and PM-TACN/Al, as those particle sizes are comparable to the thickness of the Pt wire sample holder as described in section, which leads to non-uniform coatings resulting in inconsistencies in the temperature measurement.

Constant volume combustion cell measurements were performed to characterize the pressurization rate and burn-time of the self-propagating combustion reaction. A charge of 25 mg is used for every measurement in the ~20 cm^3 cell. The powdered sample is ignited at the center by the tip of a resistively heated nichrome wire which touches only the surface sample. During the progress of the reaction, the time-dependent pressure and optical signal is monitored by a high frequency pressure transducer (PCB electronics) and a photomultiplier tube (Hamamatsu) respectively. More details about the measurement can be found elsewhere [3,19].

6.4 Results and discussions

6.4.1 Synthesis of TACN coated Al nanocomposites

TACN coated Al nanoparticles are synthesized by a heterogeneous crystallization (Figure 6-1(a)) process as described in section 2.1. Representative TEM images (Figure 6-1 (b)) of 10 % TACN@Al (by mass), clearly shows the growth of needle like TACN

crystals on the surface of Al particles. The mass percentages of TACN in the TACN@Al composites have been estimated through TGA as presented in the next section (section 3.2). By varying the $Cu(NO_3)_2.3H_2O$ precursor concentration relative to Al nanoparticle concentration (5-50 %), I have synthesized TACN@Al composites containing various mass fractions of TACN. In the final composite, different initial precursor concentrations of 0.2 mM, 0.4 mM, 0.8 mM, and 1.6 mM resulted in a TACN content of 4%, 12%, 21%, and 48 % respectively (by mass), as listed in Table S1 (supporting information). For the sake of simplicity, I have designated the TACN@Al composites with TACN contents of 4%, 12%, 21%, and 48 % as 5 % TACN@Al, 10% TACN@Al, 20% TACN@Al, and 50 % TACN@Al respectively, in the rest of the manuscript.

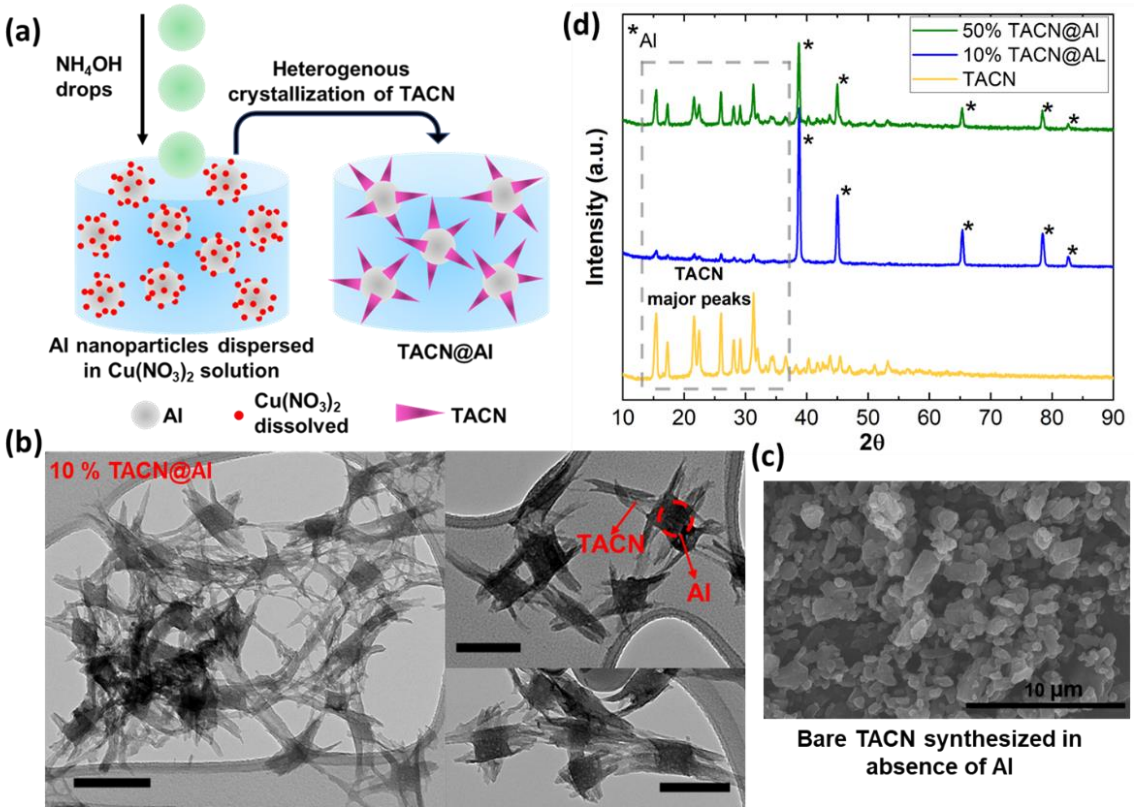

Figure 6-1 (a) Schematic showing the preparation of TACN@Al nanocomposite by heterogeneous crystallization method. (b) Representative TEM images of synthesized TACN@Al composites showing the growth of needle like TACN crystals on Al particles *(scalebar: 100 nm).* (c) SEM images of super-micron TACN crystals synthesized by homogeneous crystallization method in absence of Al seeds. (d) XRD spectra confirms the presence of TACN and Al in the nanocomposites, also clearly showing an increase in the intensity of TACN peaks relative to that of Al with increase in TACN content.

Drop wise addition of NH_4OH to Al nanoparticles dispersed in $Cu(NO_3)_2.3H_2O$, results in the heterogenous nucleation and growth of TACN crystals, leading to the formation of core-shell TACN@Al (Figure 6-1(a)). Dropwise addition maintains a low concentration of NH_4OH in the solution, thereby limiting homogeneous nucleation of TACN, and restricting the size of TACN@Al to ~70 nm (Figure 6-1(b) & Figure S1(a)). For the purpose of preparing physically mixed Al/TACN control samples, bare TACN has

been synthesized by precipitation in absence of Al nanoparticles, keeping the rest of the procedure same (section 2.1). SEM micrographs (Figure 6-1(c)) of bare TACN shows the formation of ~4 μm crystals (Figure S2(b)). Larger crystal sizes maybe attributed to slower homogeneous nucleation process. Figure 6-1(d) representing the XRD spectra of bare TACN, 10% TACN@Al, and 50 %TACN@Al, shows a clear variation between the relative peak intensities of Al and TACN, confirming the presence of different concentrations of TACN in different formulations of the composite.

6.4.2 Influence of the thermochemical decomposition of TACN on Al oxidation under slow heating rates

Previous studies[35,45] have shown that the thermochemical decomposition of TACN/$Cu(NH_3)_4(NO_3)_2$ occurs in the following three major steps, (i) endothermic release of two moles of NH_3 attached as a ligand, to form $Cu(NH_3)_2(NO_3)_2$:

$$Cu(NH_3)_4(NO_3)_2 \rightarrow Cu(NH_3)_2(NO_3)_2(s) + 2NH_3(g)\ (\sim 87\ \%\ residue) \qquad \text{R1}$$

(ii) solid to liquid phase transformation of $Cu(NH_3)_2(NO_3)_2$:

$$Cu(NH_3)_2(NO_3)_2(s) \rightarrow Cu(NH_3)_2(NO_3)_2(l) \qquad \text{R2}$$

(iii) simultaneous exothermic formation of CuO and NH_x+NOx species:

$$Cu(NH_3)_2(NO_3)_2 \rightarrow CuO(s) + (NH_x + NO_x)_{products}(g)\ (\sim 31\ \%\ residue) \qquad \text{R3}$$

I also observed all of the three aforementioned steps during the TGA/DSC characterization of bare TACN in air. The TGA curve of bare TACN (Figure 6-2(a)), shows two mass loss steps terminating at ~423 K (~87 % residue) and ~533 K (~32 % residue) corresponding to the chemical reactions presented in eqn(R1) and eqn(R3) respectively. The simultaneous DSC profile of bare TACN obtained during the same measurement

shows two endotherms at ~423 K and ~493 K corresponding to eqn(R1) and eqn(R2) respectively, followed by an exotherm associated with the second mass loss step corresponding to eqn(R3).

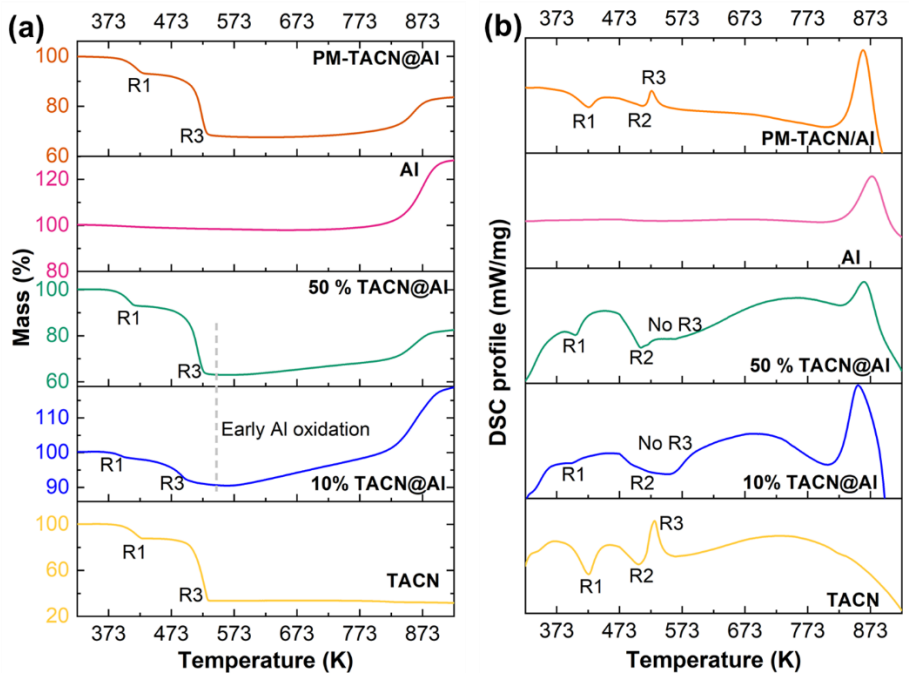

Figure 6-2 (a) TGA shows the decomposition of TACN in bare TACN, TACN@Al, and PM-TACN/Al occurs in two mass loss steps, however the Al in TACN@Al shows an early oxidation onset initiating exactly after TACN decomposition. (b) DSC shows the decomposition of TACN in bare TACN and PM-TACN/Al has two endothermic peaks (R1-R2) and one exothermic peak (R3), whereas the exothermic peak disappears in the case of TACN@Al.

It is well known that the oxidation onset of Al nanoparticles in air (~833 K) at low heating rates, is governed by the formation of voids due to the crystallization of the nativeAl_2O_3 shell [4]. TGA/DSC on bare Al nanoparticles and physically mixed bare-Al/bare-TACN particles (PM-Al/TACN), shows that Al nanoparticles in PM-Al/TACN have the same oxidation onset (~833 K) as that of bare Al nanoparticles (Figure 6-2(a) & (b)). The TGA profile (Figure 6-2(a)) of PM-Al/TACN clearly show the two stage mass

loss [eqn(R1 & R3)] during thermolysis of TACN and the mass gain on oxidation of Al occur independently, with the former phenomenon terminating at ~533 K and the later reaction initiating at ~833 K. The DSC profile (Figure 6-2(b)) of PM-Al/TACN shows all the three peaks corresponding to eqn (R1, R2, & R3) similar to that of bare TACN with the Al oxidation exothermic peak arising at ~833 K, also confirming that the TACN decomposition and Al oxidation occur separately.

However, in the case of the TACN coated Al composites, both 10% TACN@Al and 50 % TACN@Al, a gradual mass gain is observed right after the termination of the TACN decomposition at ~533 K (Figure 6-2(a)). Additionally, only the two endothermic peaks corresponding to chemical eqns (R1 & R2) are observed in the DSC of both of these samples (Figure 6-2(b)) whereas the exothermic peak that is observed in the case of bare TACN due to the reaction in eqn(R3) is absent. Instead, a gradually rising exotherm is observed post ~533 K concomitant with the gradual mass gain in TGA at the same temperature. The gradual mass gain and heat release initiating at ~533 K is most likely due to the oxidation of Al, indicating that the Al in the pre-assembled TACN@Al samples have incurred an early oxidation onset. The absence of the exothermic peak corresponding to eqn(R3) implies that the heat release associated with this step has been absorbed by some parallel occurring endothermic process that is possibly contributing to the early oxidation of Al. Therefore, it is evident that the decomposition and energy release profile of the nanoscale TACN@Al composite differs significantly from that of both super-micron PM-TACN/Al formulation as well as bare Al, the underlying mechanism of which is investigated in the subsequent sections.

6.4.3 Ignition and combustion reaction of TACN@Al at high heating rates

In-situ temperature resolved time-of-flight mass spectrometry (T-jump TOFMS) is used to probe the reaction mechanism during the ignition and combustion of TACN@Al, on activating at a high heating rate of ~10^5 K/s. The inset of Figure 6-3(a) presenting the T-jump TOFMS time-averaged spectra of 10 % TACN@Al, shows the release of gaseous NH_3 and NO_x species such as N_2O, NO, and NO_2. On comparing the temporal intensity and temperature profiles of these species (Figure 6-3(a)), their release temperature has been estimated to be ~470 K. T-jump TOFMS spectra of all other TACN@Al composites also show the release of these species regardless of the TACN content (Figure S3). The NO_x species are generated either from the decomposition of the NO_3 group or from the reaction between NH_3 and NO_x groups, with CuO being the residual solid-state product as described in section 3.2. This indicates that the decomposition of TACN at high heating rates also occurs through the reactions presented in eqn(R1, R2, and R3) in section 3.2. Figure 6-3(b) shows that the release of all the gaseous species occurs around ~470 K, for all TACN@Al composites, regardless of TACN content. The single step release of these gaseous species in contrast to the two stage TGA mass loss, can be attributed to the faster reaction kinetics at high heating rates in T-jump TOFMS, which makes it difficult to resolve multiple reaction steps involved.

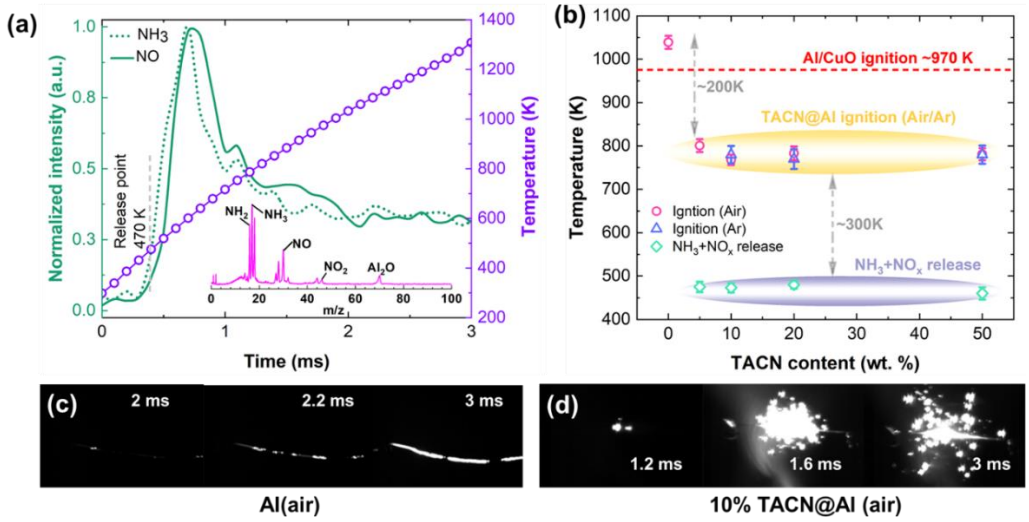

Figure 6-3 (a) T-jump TOFMS release profiles of NH_3 and NO species from 10% TACN@Al, shows that TACN decomposes at ~470 K, at high heating rates (~10^5 K/s). The inset containing time-averaged mass spectra of 10 % TACN@Al shows the release of different NH_x and NO_x species. (b) Ignition temperatures of Al(air), Al/CuO, and TACN@Al composites with different TACN content in Air and Ar, show that all TACN@Al composites ignite at a ~200 K lower temperature. The ignition of 10 % TACN@Al (d) with a small oxidizer content is unexpectedly more violent than that of Al in air (c).

T-jump ignition measurements performed in Air and Ar environments (~1 atm), reveal that all the TACN@Al composites ignite at ~ 770 K (Figure 6-3(b)). This ignition temperature is much lower compared to the ignition temperature of Al in air (by ~270 K) and Al/CuO (by ~200 K) as shown in Figure 6-3(b). The snapshots from the high-speed imaging of the ignition events of bare Al and 10 % TACN@Al in air are shown in Figure 6-3 (c) & Figure 6-3 (d) respectively. These images clearly show that the ignition event of bare-Al is very mild with no particle ejections from the wire, indicating that the ignition event is not associated with intense gaseous expansion due to low energy release during the oxidation process. In contrast, the ignition event of 10 % TACN@Al is associated with intense gas generation and expansion causing particle ejections, leading to a brighter and

bigger flame. Representative snapshots of the flames of different TACN@Al obtained during the T-jump ignition measurements, can be found in Figure S4. Combustion cell measurements obtained with TACN@Al samples with different compositions of TACN, physically mixed with nano CuO in stoichiometric amounts, shows that 10 % TACN@Al has the highest peak pressure (~2x), pressurization rate (~10x), and the shortest burn time (~50 ms less) among all TACN@Al samples (Figure S5, supporting information). The reactivity of these composites initially increases with the increase in TACN content up to ~10 % due to hot gas generation, and then it decreases with further increase in TACN content, as TACN with high molar mass reduces the gravimetric energy density of the TACN@Al composites. Although the trend of the measured pressurization rates is qualitatively similar to that of the observations made by Wu et al. [45], an order of magnitude enhancement in pressurization rates has not been observed for physically mixed micron-TACN, Al and CuO. A ~200 K lowering of ignition temperature, along with an order of magnitude enhancement in reactivity, on application of only 10 % by mass of coating is unexpected.

As most of the NO_x species are released at a lower temperature (~470 K), much earlier than the ignition event (~770 K), the possibility of Al/NO_x being the source of ignition can be eliminated. Moreover, the higher ignition temperature of Al in air (~1050 K) and the similarity of the ignition temperature of TACN@Al composites in air and argon environments, implies that the Al is not reacting with atmospheric oxygen prior to ~770 K. This implies that the ignition is possibly initiated by the reaction between Al and the condensed CuO formed after decomposition of TACN. Usually, physically mixed Al/CuO

nano-thermites ignite at 993 K, post O_2 release from CuO (~930 K) (Figure S6 & S7) [51], due to the heterogeneous reaction between gas phase O_2 with condensed Al. It is still uncertain why TACN@Al composites initiates primarily in the condensed phase and ignite at a ~200 K lower temperature than Al/CuO, prior to the release of O_2 from CuO. The heat released during the TACN decomposition (R3) may have some contribution to the transition from gas phase initiation to condensed phase initiation, as it has been already observed in section 3.2 that the exothermic peak associated with this reaction during bare TACN decomposition disappears during the reaction of TACN@Al, indicating the released heat might be absorbed in activating some parallel occurring interactions. This uncertainty has been addressed with the depiction of the underlying reaction mechanisms in the subsequent sections.

6.4.4 Intermediate product analysis revealing in-situ stress induction in Al core

In order to characterize the morphology and composition of the intermediate state of the Al particles post TACN decomposition using ex-situ TEM/XRD, I heated the 10 % TACN@Al particles, to the decomposition termination temperature of TACN (~533 K) using the same TGA/DSC apparatus and cooled them under ambient conditions. XRD spectra (Figure 5-4(b)) of the heated 10 % TACN@Al clearly show that the diffraction peaks belonging to TACN have disappeared and the heated intermediate state only contains peaks of Al and CuO. TEM images of the heated 10 % TACN@Al particles, show non-spherical and deformed Al particles with corrugations near the surface (Figure 6-4(a)). Similar Al particles with rough surfaces have been also observed by Wu et al. [34] when they thermally annealed/aged a nanothermite mixture of Al/CuO at ~473 K for 15 days. They

observed that the thickness of the alumina shell became non-uniform on annealing owing to thermally induced stresses causing it to become jagged and claimed that the faster outward diffusion of Al through the thinner regions of the shell enhanced the reactivity of the annealed Al/CuO mixture. Independently, several other studies [22–32] have shown that annealing (473-573 K) of Al-nano/microparticles with native oxide shells enhances the lattice strain on the Al-core thereby reducing the hardness of the particles leading to their higher reactivity. However, the jagging of the shell in the current scenario might be due to a combination of several different factors, as systematically explained later.

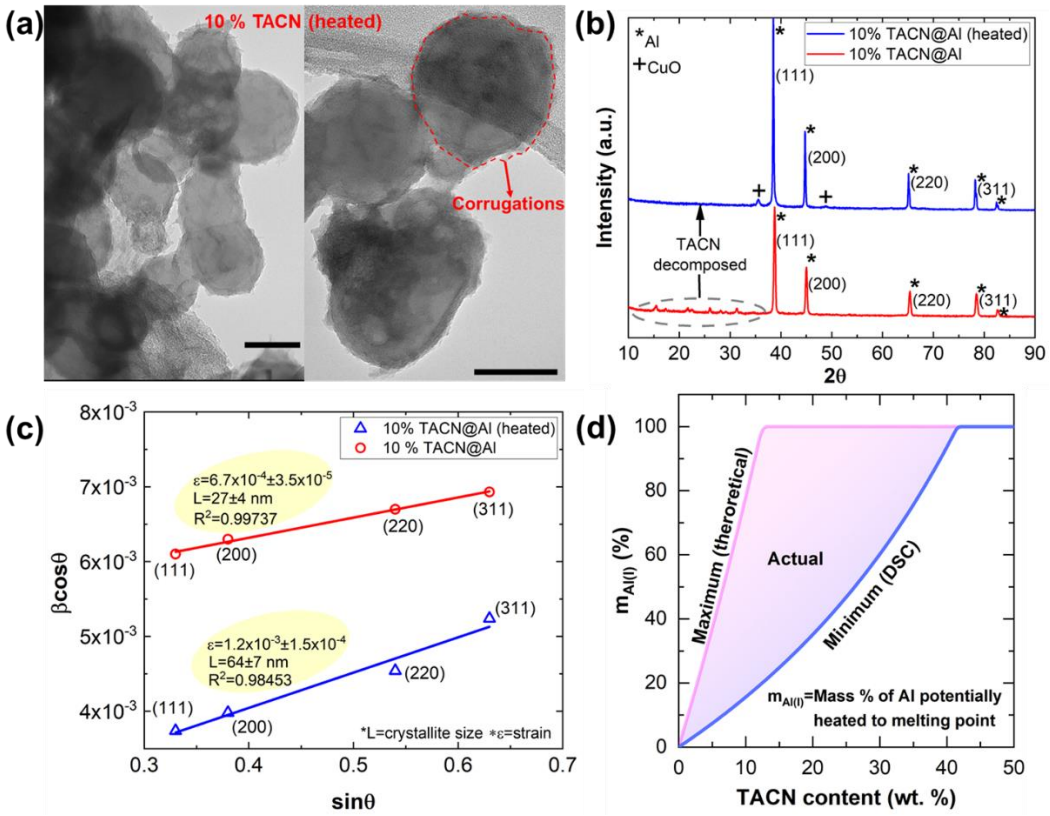

Figure 6-4 TEM images of heated 10 % TACN@Al show that Al particles deform, and their shells become corrugated, post TACN decomposition (~523 K) (scalebar: 100 nm). (b) XRD of the same particles show confirm that the TACN peaks have disappeared on heating and the heated particle only contains Al and CuO. (c)Williamson-Hall analysis of the XRD peaks show that he heated Al-core in the heated particles possesses higher strain and crystallite size. (d) Estimated maximum and minimum mass percentages of Al that can be potentially melted by considering maximum (theroretical) and minimum (DSC) heat release from TACN respectively.

Through a combination of in-situ XRD and TEM characterizations, Firmansyah et al. [33] have shown that the core of Al nanoparticles are already under tensile stress at room temperature. I performed the Williamson-Hall analysis [52] (section S.3) on the XRD peaks (Figure 6-4(b)) of the as-synthesized and heated 10% TACN@Al, to estimate the lattice strain on the core before and after heating. The Williamson-Hall plot presented in Figure 6-4(c) shows that the heated sample possesses a higher lattice strain ($\varepsilon=1x10^{-3}$) and

crystallite size (L=64 nm) compared to the unheated (ε=6x10^{-4}; L=27 nm). The disappearance of the exothermic DSC peak (Figure 6-2(b)) associated with reaction in eqn(R3) in for TACN@Al, implies that the heat released is possibly absorbed by simultaneous melting of Al. Although the area of the DSC exotherm, underestimates the heat release associated with a gas generating reaction, in this case it is an indicator of the minimum heat delivered (~128 kJ/mol) to Al from TACN decomposition, whereas the maximum heat is limited by the calculated enthalpy of decomposition of TACN ($\Delta H = -644\ kJ/mol$). Based on these two estimates, Figure 6-4 (d) shows the comparison between the maximum and minimum mass percentages of Al (section S.4), enthalpy of which can be raised to its melting point (~923 K), by the heat released from TACN. According to this estimate, a 10 % TACN coating can potentially melt ~16-80 % mass of Al. As TACN forms a liquid film followed by successive gas and heat generation through reactions in eqn (R2 & R3), formation of gas bubbles might lead to inhomogeneous temperature distribution across the liquid film which will result in inhomogeneous heat transfer flux across the Al/AlO_x interface causing localized overheating and hot-spot formation [53,54]. Such localized hotspots might lead to partial melting of Al and the expansion associated with the melting process causes molten Al to flow out of the imperfections in the shell inducing non-uniformity in the shell thickness creating the jagged shape [28,33,34]. The inhomogeneous melting might explain the increase in the strain and the crystallite size of the core [30,55]. The non-uniformity in the thickness of the shell may also be enhanced by the localized swelling caused by high temperature diffusion of Al-cations into the interstices of the AlO_x shell [33]. Table 5-1 presents a comparison of the

microstructural evolution mechanisms of Al nanoparticles under thermally induced stresses observed by the current study to previous literatures.

Table 6-1 Comparison of microstructural evolution of Al nanoparticles under thermo-mechanical stresses

Reference	Material	Treatment	Finding
Wu et al. [34]	Al/CuO-nanothermite	Annealing (473 K, 15 days)	Jagging of shell; Enhanced mass transfer; Enhanced reactivity
Jacob et al. [28]	Al nanoparticle	Annealing (573 K, 15 minutes)	Enhanced strain on Al-core softens shell; No morphology change; Enhanced reactivity
Firmansyah et al. [33]	Al nanoparticle	In-situ heating (10 K/min; ~10^5 K/s)	Existing tensile strain on Al-core at ~298 K; No morphology changes till ~873 K; Swelling of shell on interstitial diffusion of Al-ions
Current study	TACN@Al	In-situ heating (10 K/min; ~10^5 K/s)	Jagging of shell leading to lower oxidation and ignition onset

Overall, the heat generated during the exothermic decomposition of TACN induces strain on the Al-core simultaneously causing the surrounding AlO_x shell to become rough. Due to non-uniformity in the thickness of the surrounding shell, certain regions of the Al-particle surface will have a thinner shell thereby placing the Al-core closer to the CuO crystallized from TACN decomposition. A thinner diffusion barrier enables the interstitial mass transfer of Al cations across the shell initiating a condensed phase reaction between Al and CuO, which leads to the lower ignition onset (~770 K). Additionally, previous studies [22–32] have also reported that pre-stressing reduces the hardness of the Al particles causing the faster expulsion of molten Al and thereby enhancing its reactivity. In the current case, the thermo-mechanical shock induced stress applied by TACN

decomposition, should also soften the Al nanoparticles thereby enhancing their reactivity. [Figure 6-4(b-d) & Figure S5]. In physically mixed PM-Al/TACN powder, the contact area for heat transfer between the Al and TACN is much lower compared to the core-shell architecture. Hence, the oxidation of Al is not lowered in the case of PM-Al/TACN as observed in section 3.2.

6.4.5 Discussion on overall mechanism

Figure 6-5 summarizes the overall reaction mechanism of TACN@Al, based on the aforementioned observations and inferences. On heating of TACN@Al, two moles of NH_3 are released from the decomposition of TACN through eqn (R1), followed by a phase transformation of the intermediate product $Cu(NH_3)_2(NO_3)_2$. The molten $Cu(NH_3)_2(NO_3)_2$ wets the surface of the Al-nanoparticles forming a liquid film. Exothermic decomposition (R3) of $Cu(NH_3)_2(NO_3)_2$ to solid CuO and NH_x+NO_x gases, shock heats the Al particles over the short reaction time-scale. This shock-heating leads to partial liquefaction (expansion), causing some Al to leak into the inhomogeneous shell, followed by re-solidification (contraction) of the Al-core, thereby causing deformation of the particles and simultaneously resulting in corrugations at the Al-core/AlO_X-shell interface. Because of the corrugations, the shell has non-uniform thickness with localized thinner regions, which increases the intimacy between the Al-core and the CuO crystallized from (R3). The reduced interstitial diffusion length enables the Al ions to diffuse to the surface CuO, thereby initiating the condensed phase reaction and ignition process. Thus, heat generated from TACN decomposition causes in-situ stressing of Al nanoparticles which leads to their condensed phase ignition.

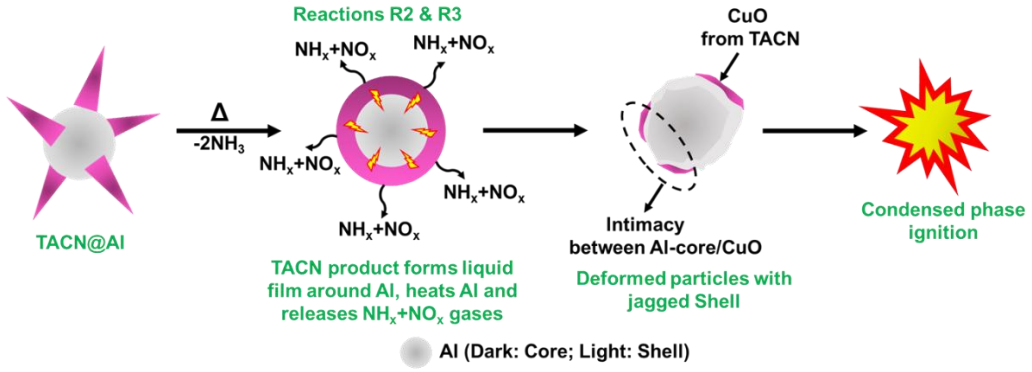

Figure 6-5 Schematic showing the overall reaction mechanism of TACN@Al nanocomposites.

However, in the case of the physically mixed sample (PM-Al/TACN), the molten $Cu(NH_3)_2(NO_3)_2$ is unable to completely wet the surface of the Al-nanoparticles thereby reducing the heat transfer area. Therefore, the oxidation onset of Al in PM-Al/TACN is not lowered and the decomposition of TACN and oxidation of Al occur separately (section 3.2). Although the TACN@Al composites are fuel lean, the in-situ stress induction and the condensed phase ignition process will shorten the timescale of the extraction of oxidative energy from the Al-core in presence of adequate amount of oxygen sources. The higher reactivity of the TACN@Al in air and with CuO observed in ignition and combustion cell measurements, also confirms the same. For the purpose of qualitative visual depiction of the decomposition and ignition process, optical snapshots of flash-heated TACN powder decomposition and 10% TACN@Al ignition captured using a high-speed camera, have been presented in Figure S8 and Figure S9. Figure S8 clearly shows the melting of bare TACN powder (R2) forming a liquid droplet, which bubbles and releases gaseous fumes (NH_x+NO_x) indicating the occurrence of reactions in eqn(R2 and R3). Figure S9 confirms

that the fumes are released ahead of the ignition process. These images also qualitatively support the above-mentioned mechanisms.

6.5 Conclusion

In this study I show that, despite having the same fuel and oxidizer combination tetraamine copper nitrate complex (TACN) coated Al nanocomposites (TACN@Al) synthesized by a heterogeneous crystallization method, demonstrate unexpectedly lower ignition onset (by ~200 K) and higher reactivity (~10x) compared to benchmark nanothermite mixture of Al/CuO. T-jump TOFMS reveals that TACN@Al releases NO_x gases on decomposition of TACN, at a ~300 K lower temperature than their ignition temperature. Hence, the released NO_x cannot initiate the ignition process acting as an oxidizer for Al. However, through TEM and XRD analysis, I show that the heat released on TACN decomposition shock-heats the Al particles thereby enhancing the strain on the Al core, successively deforming the particles, and inducing non-uniformity in the thickness of their inherent oxide shell. The thinner regions of the jagged oxide shell with non-uniform thickness, reduce the mass transfer barrier of Al-ions, enabling them to diffuse across the shell and initiate a condensed phase reaction with the CuO crystallized as a product of TACN decomposition, thereby lowering the ignition onset. These effects were not observed during the reaction of physically mixed nano-Al/micron TACN powder, as in that case the decomposition of TACN and oxidation of Al occurred independently, owing to the smaller contact area for heat transfer between TACN and Al. Hence, the thermo-mechanical shock provided to the Al nanoparticles on TACN decomposition, plays major role in enhancing the reactivity of TACN@Al composites.

6.6 References

(1) Hastings, D.; Rodriguez, N.; McCann, H.; Schoenitz, M.; Dreizin, E. L. Titanium-Boron Reactive Composite Powders with Variable Morphology Prepared by Arrested Reactive Milling. *Fuel* **2022**, *310*, 122313.

(2) Xu, F.; Nava, G.; Biswas, P.; Dulalia, I.; Wang, H.; Alibay, Z.; Gale, M.; Kline, D. J.; Wagner, B.; Mangolini, L.; et al. Energetic Characteristics of Hydrogenated Amorphous Silicon Nanoparticles. *Chem. Eng. J.* **2022**, *430*, 133140.

(3) Biswas, P.; Ghildiyal, P.; Kwon, H.; Wang, H.; Alibay, Z.; Xu, F.; Wang, Y.; Wong, B. M.; Zachariah, M. R. Rerouting Pathways of Solid-State Ammonia Borane Energy Release. *J. Phys. Chem. C* **2021**, *126*, 48–57.

(4) Trunov, M. A.; Schoenitz, M.; Zhu, X.; Dreizin, E. L. Effect of Polymorphic Phase Transformations in Al_2O_3 Film on Oxidation Kinetics of Aluminum Powders. *Combust. Flame* **2005**, *140*, 310–318.

(5) Trunov, M. A.; Umbrajkar, S. M.; Schoenitz, M.; Mang, J. T.; Dreizin, E. L. Oxidation and Melting of Aluminum Nanopowders. *J. Phys. Chem. B* **2006**, *110*, 13094–13099.

(6) Senyurt, E. I.; Dreizin, E. L. At What Ambient Temperature Can Thermal Runaway of a Burning Metal Particle Occur? *Combust. Flame* **2022**, *236*, 111800.

(7) Mursalat, M.; Huang, C.; Julien, B.; Schoenitz, M.; Esteve, A.; Rossi, C.; Dreizin, E. L. Low-Temperature Exothermic Reactions in Al/CuO Nanothermites Producing Copper Nanodots and Accelerating Combustion. *ACS Appl. Nano Mater.* **2021**, *4*, 3811–3820.

(8) Hastings, D.; Schoenitz, M.; Dreizin, E. L. Highly Reactive Spheroidal Milled Aluminum. *Materialia* **2021**, *15*, 100959.

(9) Henz, B. J.; Hawa, T.; Zachariah, M. R. On the Role of Built-in Electric Fields on the Ignition of Oxide Coated Nanoaluminum: Ion Mobility versus Fickian Diffusion. *J. Appl. Phys.* **2010**, *107*, 024901.

(10) Jiang, Y.; Deng, S.; Hong, S.; Zhao, J.; Huang, S.; Wu, C. C.; Gottfried, J. L.; Nomura, K. I.; Li, Y.; Tiwari, S.; et al. Energetic Performance of Optically Activated Aluminum/Graphene Oxide Composites. *ACS Nano* **2018**, *12*, 11366–11375.

(11) Jiang, Y.; Deng, S.; Hong, S.; Tiwari, S.; Chen, H.; Nomura, K. I.; Kalia, R. K.; Nakano, A.; Vashishta, P.; Zachariah, M. R.; et al. Synergistically Chemical and Thermal

Coupling between Graphene Oxide and Graphene Fluoride for Enhancing Aluminum Combustion. *ACS Appl. Mater. Interfaces* **2020**, *12*, 7451–7458.

(12) Séverac, F.; Alphonse, P.; Estève, A.; Bancaud, A.; Rossi, C. High-Energy Al/CuO Nanocomposites Obtained by DNA-Directed Assembly. *Adv. Funct. Mater* **2012**, *22*, 323–329.

(13) Wang, X.; Zhou, W.; Delisio, J. B.; Egan, G. C.; Zachariah, M. R. Doped δ-Bismuth Oxides to Investigate Oxygen Ion Transport as a Metric for Condensed Phase Thermite Ignition. *Phys. Chem. Chem. Phys.* **2017**, *19*, 12749–12758.

(14) Wang, X.; Wu, T.; Zachariah, M. R. Doped Perovskites to Evaluate the Relationship between Fuel-Oxidizer Thermite Ignition and Bond Energy, Electronegativity, and Oxygen Vacancy. *J. Phys. Chem. C* **2017**, *121*, 147–152.

(15) Xu, F.; Hirt, B.; Biswas, P.; Kline, D. J.; Yang, Y.; Wang, H.; Sehirlioglu, A.; Zachariah, M. R. Superior Reactivity of Ferroelectric Bi2WO6/Aluminum Metastable Intermolecular Composite. *Chem. Eng. Sci.* **2022**, *247*, 116898.

(16) Chen, Y.; Ren, W.; Zheng, Z.; Wu, G.; Hu, B.; Chen, J.; Wang, J.; Yu, C.; Ma, K.; Zhou, X.; et al. Reactivity Adjustment from the Contact Extent between CuO and Al Phases in Nanothermites. *Chem. Eng. J.* **2020**, *402*, 126288.

(17) Wang, H.; Kline, D. J.; Biswas, P.; Zachariah, M. R. Connecting Agglomeration and Burn Rate in a Thermite Reaction: Role of Oxidizer Morphology. *Combust. Flame* **2021**, *231*, 111492.

(18) Wang, W.; Li, H.; Zhang, M.; Zhao, F.; Xu, S.; Wang, C.; Qin, Z.; An, T.; Xu, K. Effects of Oxidizer and Architecture on the Thermochemical Reactivity, Laser Ignition and Combustion Properties of Nanothermite. *Fuel* **2022**, *314*, 123141.

(19) Xu, F.; Biswas, P.; Nava, G.; Schwan, J.; Kline, D. J.; Rehwoldt, M. C.; Mangolini, L.; Zachariah, M. R. Tuning the Reactivity and Energy Release Rate of I2O5 Based Ternary Thermite Systems. *Combust. Flame* **2021**, *228*, 210–217.

(20) Ghildiyal, P.; Ke, X.; Biswas, P.; Nava, G.; Schwan, J.; Xu, F.; Kline, D. J.; Wang, H.; Mangolini, L.; et al. Silicon Nanoparticles for the Reactivity and Energetic Density Enhancement of Energetic-Biocidal Mesoparticle Composites. *ACS Appl. Mater. Interfaces* **2021**, *13*, 458–467.

(21) Zhu, Y.; Zhou, X.; Xu, J.; Ma, X.; Ye, Y.; Yang, G.; Zhang, K. In Situ Preparation of Explosive Embedded CuO/Al/CL20 Nanoenergetic Composite with Enhanced Reactivity. *Chem. Eng. J.* **2018**, *354*, 885–895.

(22) Hill, K. J.; Pantoya, M. L.; Washburn, E.; Kalman, J. Single Particle Combustion of Pre-Stressed Aluminum. *Materials* **2019**, *12*, 1737.

(23) Hill, K. J.; Warzywoda, J.; Pantoya, M. L.; Levitas, V. I. Dropping the Hammer: Examining Impact Ignition and Combustion Using Pre-Stressed Aluminum Powder. *J. Appl. Phys.* **2017**, *122*, 125102.

(24) Hill, K. J.; Tamura, N.; Levitas, V. I.; Pantoya, M. L. Impact Ignition and Combustion of Micron-Scale Aluminum Particles Pre-Stressed with Different Quenching Rates. *J. Appl. Phys.* **2018**, *124*, 115903.

(25) Williams, A.; Shancita, I.; Vaz, N. G.; Tran-Ngo, T.; Demko, A.; Altman, I.; Hill, K. J.; Tunega, D.; Aquino, A. J. A.; Pantoya, M. L. Stress-Altered Aluminum Powder Dust Combustion. *J. Appl. Phys.* **2020**, *127*, 175110.

(26) Altman, I.; Demko, A.; Hill, K.; Pantoya, M. On the Possible Coexistence of Two Different Regimes of Metal Particle Combustion. *Combust. Flame* **2020**, *221*, 416–419.

(27) Bello, M. N.; Williams, A. M.; Levitas, V. I.; Tamura, N.; Unruh, D. K.; Warzywoda, J.; Pantoya, M. L. Highly Reactive Energetic Films by Pre-Stressing Nano-Aluminum Particles. *RSC Adv.* **2019**, *9*, 40607–40617.

(28) Jacob, R. J.; Hill, K. J.; Yang, Y.; Pantoya, M. L.; Zachariah, M. R. Pre-Stressing Aluminum Nanoparticles as a Strategy to Enhance Reactivity of Nanothermite Composites. *Combust. Flame* **2019**, *205*, 33–40.

(29) Bello, M. N.; Williams, A.; Shancita, I.; Hoque, M. N.; Christopher, G.; Aquino, A. J. A.; Tunega, D.; Pantoya, M. L. Synthesis and Characterization of Polymeric Films with Stress-Altered Aluminum Particle Fillers. *J. Mater. Sci.* **2020**, *55*, 14229–14242.

(30) McCollum, J.; Smith, D. K.; Hill, K. J.; Pantoya, M. L.; Warzywoda, J.; Tamura, N. A Slice of an Aluminum Particle: Examining Grains, Strain and Reactivity. *Combust. Flame* **2016**, *173*, 229–234.

(31) Lucas, M.; Brotton, S. J.; Min, A.; Woodruff, C.; Pantoya, M. L.; Kaiser, R. I. Effects of Size and Prestressing of Aluminum Particles on the Oxidation of Levitated Exo-Tetrahydrodicyclopentadiene Droplets. *J. Phys. Chem. A* **2020**, *124*, 1489–1507.

(32) Dikici, B.; Pantoya, M. L.; Levitas, V. The Effect of Pre-Heating on Flame Propagation in Nanocomposite Thermites. *Combust. Flame* **2010**, *157*, 1581–1585.

(33) Firmansyah, D. A.; Sullivan, K.; Lee, K. S.; Kim, Y. H.; Zahaf, R.; Zachariah, M. R.; Lee, D. Microstructural Behavior of the Alumina Shell and Aluminum Core before and after Melting of Aluminum Nanoparticles. *J. Phys. Chem. C* **2012**, *116*, 404–411.

(34) Wu, T.; Lahiner, G.; Tenailleau, C.; Reig, B.; Hungria, T.; Esteve, A.; Rossi, C. Unexpected Enhanced Reactivity of Aluminized Nanothermites by Accelerated Aging. *Chem. Eng. J.* **2021**, *418*, 129432.

(35) Southern, T. M.; Wendlandt, W. W. The Thermal Decomposition of Metal Complexes—XX: Some Amine Copper(II) Nitrate Complexes. *J. Inorg. Nucl. Chem.* **1970**, *32*, 3783–3792.

(36) Mathew, S.; Nair, C. G. R.; Ninan, K. N. Thermal Decomposition Studies on Amine Complexes of Copper(II) Nitrate in Solid State. *B. Chem. Soc. Jpn.* **2006**, *64*, 3207–3209.

(37) Künzel, M.; Vodochodský, O.; Matyáš, R.; Jalový, Z.; Pachman, J.; Maixner, J. Tetraamminecopper(II) Nitrate and Its Effects on Ammonium Nitrate(V). *Cent. Eur. J. Energ. Mat.* **2017**, *14*, 169–183.

(38) Liszka-Skoczylas, M.; Mikuli, E.; Szklarzewicz, J.; Hetmańczyk, J. Thermal Behaviour, Phase Transition and Molecular Motions in $[Co(NH_3)_6](NO_3)_2$. *Thermochim. Acta* **2009**, *496*, 38–44.

(39) Pradère, C.; Suhard, S.; Vendier, L.; Jacob, G.; Chaudret, B.; Sabo-Etienne, S. Heterometallic Werner Complexes as Energetic Materials. *Dalton T.* **2008**, 2725–2731.

(40) Sullivan, K. T.; Piekiel, N. W.; Wu, C.; Chowdhury, S.; Kelly, S. T.; Hufnagel, T. C.; Fezzaa, K.; Zachariah, M. R. Reactive Sintering: An Important Component in the Combustion of Nanocomposite Thermites. *Combust. Flame* **2012**, *159*, 2–15.

(41) Wang, H.; Kline, D. J.; Zachariah, M. R. In-Operando High-Speed Microscopy and Thermometry of Reaction Propagation and Sintering in a Nanocomposite. *Nat. Commun. 2019 10:1* **2019**, *10*, 3032.

(42) Egan, G. C.; Lagrange, T.; Zachariah, M. R. Time-Resolved Nanosecond Imaging of Nanoscale Condensed Phase Reaction. *J. Phys. Chem. C* **2015**, *119*, 2792–2797.

(43) Brotman, S.; Rouhani, M. D.; Rossi, C.; Estève, A. A Condensed Phase Model of the Initial Al/CuO Reaction Stage to Interpret Experimental Findings. *J. Appl. Phys.* **2019**, *125*, 035102.

(44) Wang, H.; Jian, G.; Egan, G. C.; Zachariah, M. R. Assembly and Reactive Properties of Al/CuO Based Nanothermite Microparticles. *Combust. Flame* **2014**, *161*, 2203–2208.

(45) Wu, T.; Sevely, F.; Julien, B.; Sodre, F.; Cure, J.; Tenailleau, C.; Esteve, A.; Rossi, C. New Coordination Complexes-Based Gas-Generating Energetic Composites. *Combust. Flame* **2020**, *219*, 478–487.

(46) Sevely, F.; Liu, X.; Wu, T.; Mesnilgrente, F.; Franc, B.; Assie-Souleille, S.; Dollat, X.; Rossi, C. Effect of Process Parameters on the Properties of Direct Written Gas-Generating Reactive Layers. *ACS Appl. Polym. Mater.* **2021**, *3*, 3972–3980.

(47) Wu, T.; Sevely, F.; Pelloquin, S.; Assié-Souleille, S.; Estève, A.; Rossi, C. Enhanced Reactivity of Copper Complex-Based Reactive Materials via Mechanical Milling. *Combust. Flame* **2021**, *233*, 111598.

(48) Jian, G.; Zhou, L.; Piekiel, N. W.; Zachariah, M. R. Low Effective Activation Energies for Oxygen Release from Metal Oxides: Evidence for Mass-Transfer Limits at High Heating Rates. *ChemPhysChem* **2014**, *15*, 1666–1672.

(49) Rehwoldt, M. C.; Wang, Y.; Xu, F.; Ghildiyal, P.; Zachariah, M. R. High-Temperature Interactions of Metal Oxides and a PVDF Binder. *ACS Appl. Mater. Interfaces* **2022**, *14*, 8938–8946.

(50) Zhou, W.; DeLisio, J. B.; Wang, X.; Egan, G. C.; Zachariah, M. R. Evaluating Free vs Bound Oxygen on Ignition of Nano-Aluminum Based Energetics Leads to a Critical Reaction Rate Criterion. *J. Appl. Phys.* **2015**, *118*, 114303.

(51) Jian, G.; Chowdhury, S.; Sullivan, K.; Zachariah, M. R. Nanothermite Reactions: Is Gas Phase Oxygen Generation from the Oxygen Carrier an Essential Prerequisite to Ignition? *Combust. Flame* **2013**, *160*, 432–437.

(52) Kunka, C.; Boyce, B. L.; Foiles, S. M.; Dingreville, R. Revealing Inconsistencies in X-Ray Width Methods for Nanomaterials. *Nanoscale* **2019**, *11*, 22456–22466.

(53) Fedorchenko, A. I.; Hruby, J. On Formation of Dry Spots in Heated Liquid Films. *Phys. Fluids* **2021**, *33*, 023601.

(54) Tenzer, F. M.; Roisman, I. v.; Tropea, C. Fast Transient Spray Cooling of a Hot Thick Target. *J. Fluid Mech.* **2019**, *881*, 84–103.

(55) Levitas, V. I.; Samani, K. Size and Mechanics Effects in Surface-Induced Melting of Nanoparticles. *Nat. Commun.* **2011**, *2*, 284.

6.7 Supporting information

S.1 Information about content, size and morphology of TACN@Al

Table S1 TACN content in TACN@Al samples as measured in TGA

Sample name	Initial $Cu(NO_3)_2.3H_2O$ concentration (mM)	Actual TACN content (wt. %) from TGA
5% TACN@Al	0.2	4
10% TACN@Al	0.4	12
20 % TACN@Al	0.8	21
50 % TACN@Al	1.6	48

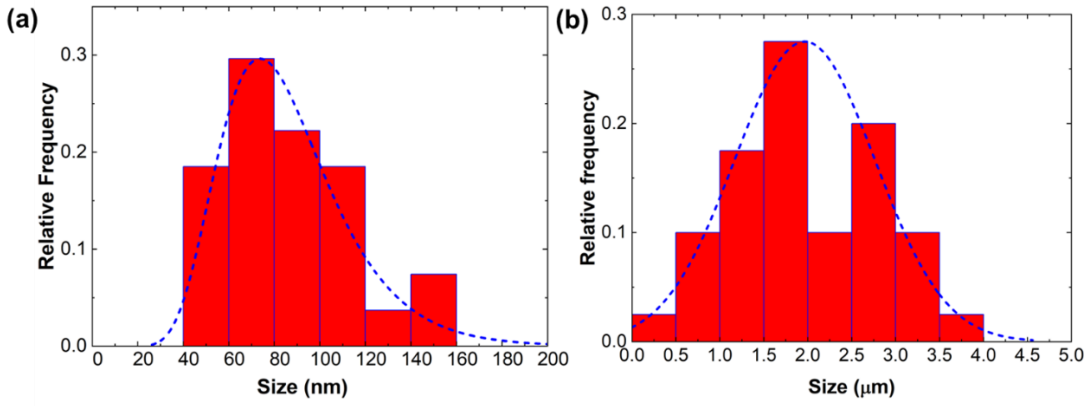

Figure S2 (a) Size distribution of 10 % TACN@Al (accounted by measuring the regions with darker contrast); (b) Size distribution of bare TACN (accounted by measuring the length of the highest dimension).

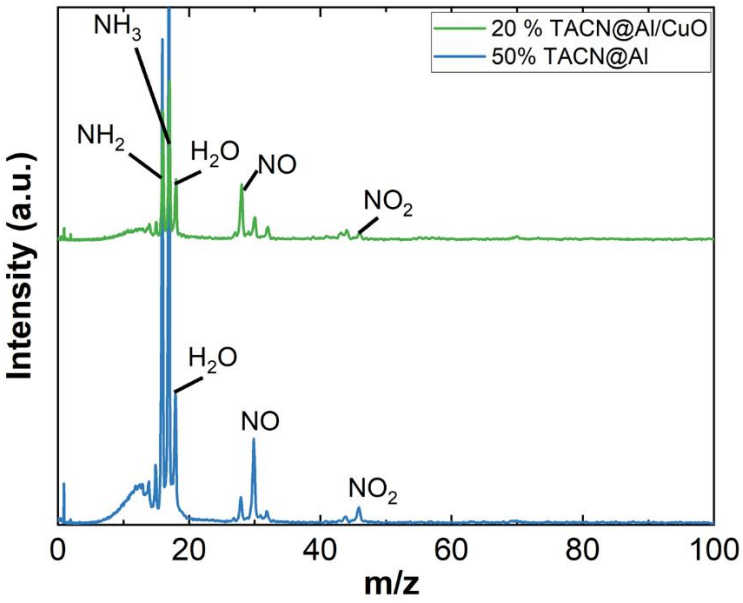

Figure S3 T-jump TOFMS time-averaged spectra of 20 % and 50 % TACN@Al shows the release of same species as that of 10 % as shown in the inset of Figure3(a).

S.2 Ignition and Combustion of TACN@Al

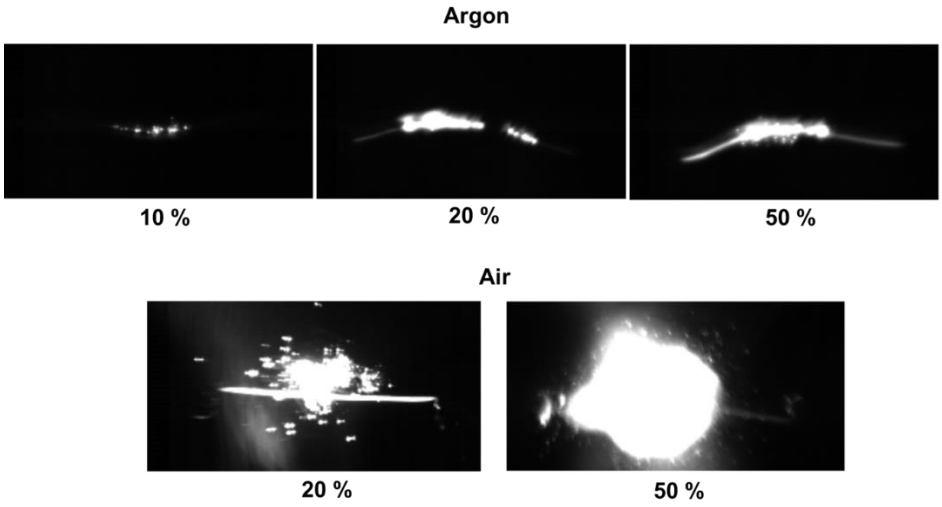

Figure S4 Snapshots of the flame of different TACN@Al in Air and Ar taken during the T-jump Ignition measurement. The frame when the flame is largest and brightest is presented here.

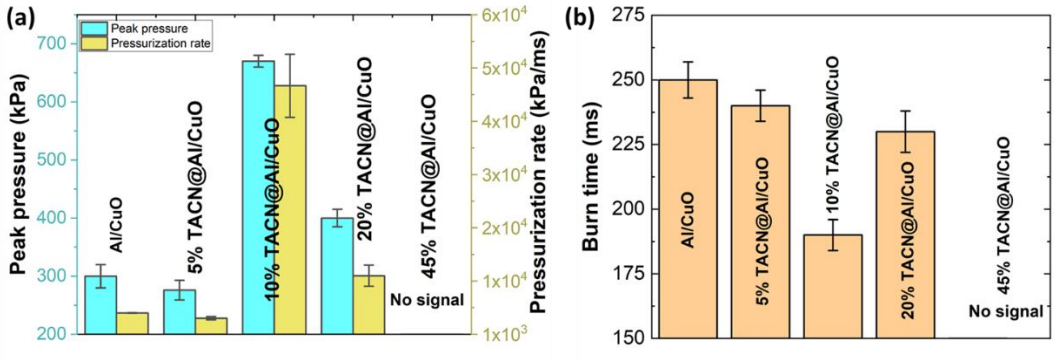

Figure S5 Pressure, pressurization rate and burn time estimated during the combustion cell measurements show that 10 %TACN@Al have ~2x peak pressure, ~10x pressurization rate and with ~50 ms shorter burn time. The reactivity (lower pressurization rate and higher burn time) decreases with further increase in TACN, because the high molar mass of TACN reduces the overall gravimetric energy density of the composites.

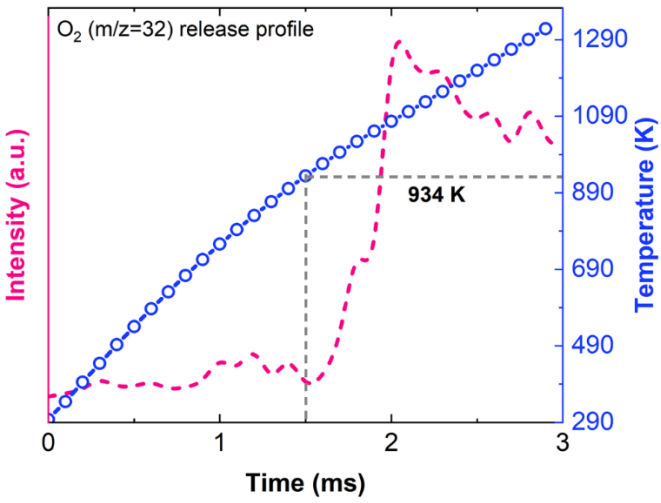

Figure S6 T-jump TOFMS of bare CuO showing its O_2 release profile and temperature.

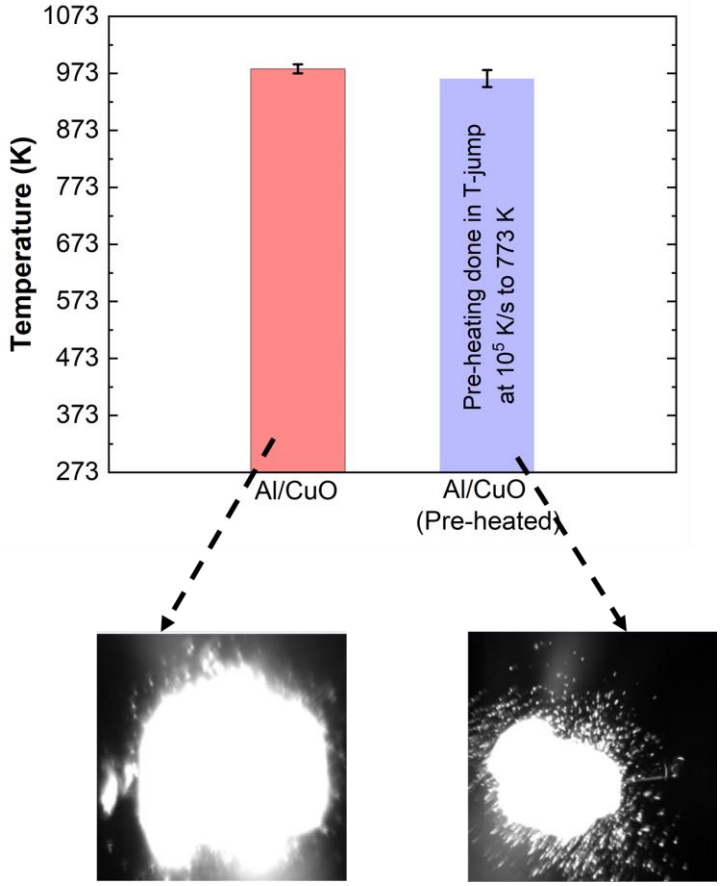

Figure S7 Comparison of ignition temperatures of physically mixed Al/CuO and physically mixed annealed Al/CuO (~10^5 K/s, to 773 K), showing that annealing a mixture of Al/CuO at this heating rate does not affect its ignition.

S.3 Details about Williamson-Hall analysis

XRD peak broadening can be an indicator of two parameters i) lattice strain in the sample ii) crystallite size. To isolate the effect of these two parameters on the XRD peak, Williamson-Hall analysis is performed. Williamson-Hall plot is a semi-quantitative analysis which expresses the peak broadening (FWHM) in terms of the lattice strain and crystallite size through the following expression:

$$\beta cos\theta = C\varepsilon sin\theta + \frac{K\lambda}{L}$$

Where C is a constant generally equals to 4; K=constant=0.9; λ=wavelength=1.54 Å; *L*=crystallite size; ε=strain. Hence, when I plot $\beta cos\theta$ vs $sin\theta$ from the obtained XRD spectra for all diffraction planes, and perform a linear fit, the slope of the fit will give us the lattice strain ε whereas the intercept will give us the crystallite size *L*.

S.4 Calculation of mass percentage of Al potentially heated to melting point

Let there be x% TACN; specific heat of Al~Al_2O_3~890 J/kg-K. Theoretical energy release from TACN is ~644 kJ/mol or 2500 J/g. DSC heat release from TACN is 128 kJ/mol or ~500 J/g. The mass percentage of Al, enthalpy of which can be changed from 523 K to 923 K, can be then given by the following equation (considering a total of 100 g of sample)

$$m_{Al} = \frac{(Heat\ released)(\frac{J}{g}) * x\ (g)}{0.89\ (\frac{J}{g.K}) * (923 - 523)K} * \frac{1}{100(g) - x(g)} * 100\ \%$$

S.5 Visualization through high speed camera

TACN and TACN@Al samples where flash heated by a wide-bandwidth lamp radiating across the whole UV-IR range, with the only goal to visually demonstrate the various steps associated with the reactions, by capturing with a high speed camera (Phantom Miro 110).

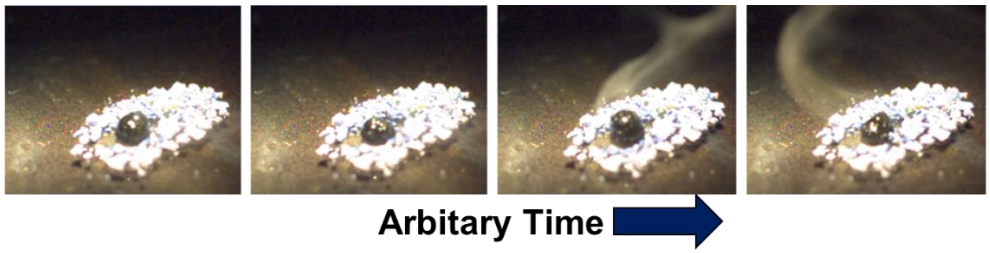

Figure S8 The set of images clearly show that bare TACN forms a liquid bubble through the reaction in eqn (R2) (main text) when heated and the liquid bubble expands and contracts releasing gaseous fumes of NH_x+NO_x through reaction in eqn (R3).

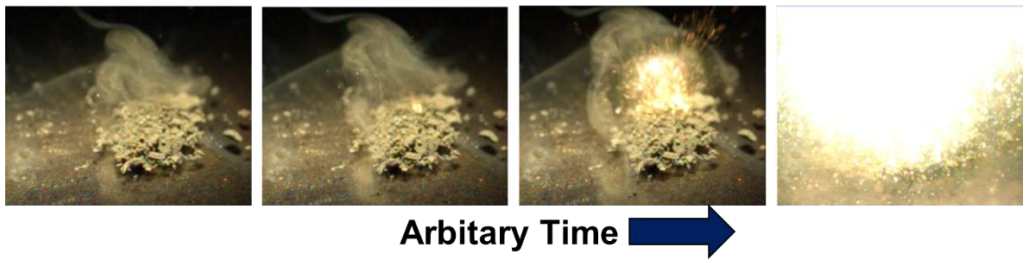

Figure S9 The set of images clearly show that for 10% TACN@Al, the fumes are released before the ignition process also supporting the fact that ignition happens after the completion of TACN decomposition.

7 Direct Imaging and Simulation of the Interface Reaction of Metal/Metal Oxide Nanoparticle Laminates

7.1 Summary

One of the difficulties in understanding how powder composites of reactive fuel/oxidizer systems behave is the lack of control of the mixing length. In this study, I have prepared Al/CuO particle laminates using a direct writing approach. With as little as 10 wt% polymers I were able to obtain free-standing microscale particle-based laminates. Using these composites, I were able to image the cross-section of the laminates to directly probe the interface reaction with high-speed microscopic imaging and pyrometry. I show quantitatively how the burn rate can be altered by changing the layer thicknesses of the printed laminates and under high-speed microscopy imaging asymmetry heat transfer resulting in fingering in the temperature profiles in the reaction front. Numerical simulations of the heat and mass transport processes are able to reproduce the finger-structured reaction fronts. I find that for Al/CuO particle-based laminates the lateral O_2 diffusion rate from CuO to the Al layer appears to be rate-limiting. The finger-like profiles appear due to the combined effects from the faster propagation of the interfacial reaction over the bulk, and the thermal diffusivity differences between the Al/CuO layers. Interestingly I see no evidence of layer intermixing even on post-combustion inspection. These results are to our knowledge the first imaging of interface reactions between particle composites and provide a valuable testbed for probing mechanisms and validating models.

7.2 Introduction

One of the difficulties in understanding how powder composites of reactive fuel/oxidizer [1–6]systems behave is the lack of control of the mixing length. On the other hand, there is a considerable body of work on the formation of nanolaminate structures with alternating reactive layers typically created by sputter deposition. These sputter-deposited reactive nanolaminates consisting of sequential layers of fuel and oxidizers with high energy density have attracted particular attention due to their precisely tunable energy release rate that can be attributed to their highly controllable architecture [7–12] . In addition to the utility in probing of nanothermite reactions, these configurations have also been explored as a method to probe the energy release from binary alloying reactions of Al/Ni [13,14], Al/Zr [15], and Al/Pt [16]. Previous studies have observed that the energy release rate of Al/CuO nanolaminates could be easily adjusted via bilayer thicknesses [17], equivalence ratios [18], tertiary interfacial layer insertion [19–21], sample width [22], and altering oxidation state of oxidizers [23].

Energetic particulate composites have been extensively investigated through macroscopic characterization approaches to characterize temperature, burn rates, and thermal decomposition properties [1-22] However, characterization at the microscopic scale has been less readily available. Given that the composition of these composites consists of nano or micro-sized reactants, observation at smaller length scales is needed to better understand the role of mass and heat transfer [2,24–28]. Previously, I employed a recently developed microscopic dynamic imaging system to probe the reaction zone of sputter-deposited Al/CuO nanolaminates with μs and μm temporal and spatial resolution

respectively, which is more comparable to the reactant dimensions and reaction timescales [29]. Through this technique, I obtained detailed images and temperature profiles across the Al/CuO nanolaminates reaction front. However, this system never enabled us to probe and image the cross-section which meant I could never directly observe the interface reaction.

The objective of this paper is twofold. A) Fabricate microscale particulate laminates with controlled bilayer spacing and sufficient mechanical integrity by direct writing deposition of high loading nanothermite inks. To accomplish this, I explore the utility of 3-D printing for fabrication based on our prior capabilities and the fact that I have been able to prepare similar structures using electrospray deposition[30]. B) Image the cross-sectional interface *in-operando* of the particulate laminates to provide data for benchmark modeling. This then enables us to ask the fundamental questions related to the role of heat and mass transfer on flame propagation of energetic nanocomposites (**Scheme 1**).

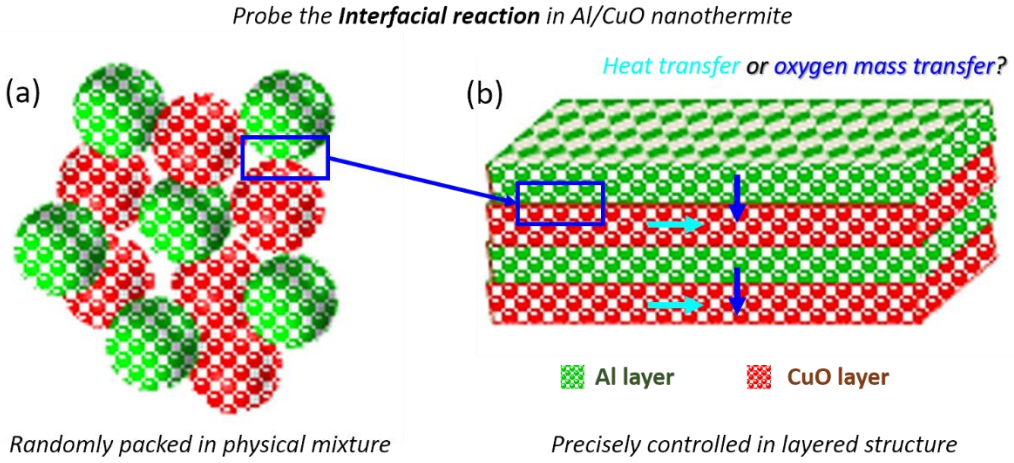

Scheme 1. *Concept of this study: Imaging the cross-section of a particle-based laminate structure during propagation to deduce the controlling effects of heat and oxygen mass transfer.*

In this study, I prepared Al/CuO particle laminates using a recently developed direct writing approach. Through first-ever microscopic imaging of the cross-section during reaction I observed the development of unusual finger-like temperature profiles near the flame front. Macroscopic burn-rate characterizations revealed that the burn rate can be altered by changing the layer thicknesses of the printed laminates, indicating strong effects from oxygen transport between the fuel and oxidizer layer. Using a numerical model of the heat and mass transport during the flame propagation, I have shown that the development of such a finger-shaped profile can be attributed to a combination of i) faster interfacial reaction than flame propagation in the bulk and ii) difference in thermal diffusivities between the fuel layer and the oxidizer layer. Both the experiment and model confirmed that O_2 transport is the rate-limiting factor in the reaction propagation of printed laminates. These fundamental insights into the interfacial reaction propagation in energetic laminates, are extremely important to validate mechanisms and models.

7.3 Methods

7.3.1 Materials

Aluminum nanoparticles (Al NPs, 67 wt. % active, 81 nm) and CuO nanoparticles (CuO NPs, ~40 nm) are purchased from Novacentrix Inc. and US Research Nanomaterials, respectively. METHOCEL™ F4M Hydroxypropyl Methylcellulose (HPMC) and Polyvinylidene Fluoride (PVDF, M_w ~534,000) are obtained from Dow Chemical

Company and Sigma-Aldrich, respectively. N, N dimethylformamide (DMF, 99.8%) is purchased from Sigma-Aldrich and used as a solvent to dissolve the above polymers.

7.3.2 Ink preparation and direct writing approach

Typically, 750 mg Al or CuO, 50 mg HPMC, and 33 mg PVDF, and DMF (5 mL and 4 mL DMF for Al and CuO, respectively) are used for each ink formulation. When preparing the inks, polymer mixtures of HPMC and PVDF in a mass ratio of 3:2 is first added and dissolved in DMF. Then, the weighed CuO NPs or Al NPs are added to form a slurry. A 30 mins ultra-sonication step is used to break up nanoparticle aggregates. Then the slurries are magnetically stirred (300 rpm) for 24 hours to achieve homogenization prior to printing.

In a typical printing process, the inks are extruded through a 16-gauge needle (ID: 1.35 mm) at a feed rate of 3 mL/h and printed into Gcode-patterned square pads (2 cm × 2 cm) on a pre-heated substrate (75 ^{o}C) at a writing speed of 22 cm/min (moving speed of the nozzle). At this rate, the print is completely dry before depositing another layer. All the laminates have a total thickness of 0.65-0.75 mm but with different bilayer thicknesses of Al/CuO. When printing Al/CuO laminates, Al layers are always printed first on the pre-heated substrate, followed by the CuO layer, and so on. After printing, the samples are left on the heated substrate (kept at ~75 ^{o}C) for 30 mins to further evaporate any remaining solvent. Finally, the pads are peeled off from the substrate and cut into ~2 mm wide sticks for combustion characterization. The porosity of all laminates is estimated as ~65% based on our previous studies[2,27–29.]

7.3.3 Macroscopic and microscopic imaging of the combustion

The experimental setup used in this study is shown in Figure S1. The samples are free-standing sticks (1.5 cm long, ~2 mm wide, ~1 mm thick), which are sandwiched by two thin glass slides (22 mm × 22 mm, 1 mm thick) to avoid vibration during the microscopic combustion observation. The sample is confined in a 0.5 L box to enable an inert gas environment of argon. (1 atm) and ignited by a nichrome wire. Two camera systems with macroscopic and microscopic magnifications are triggered simultaneously to obtain videos for a single combustion event. The macroscopic imaging high-speed camera (80 μm/pixel, Vision Research Phantom Miro M110) captures the whole burning event of the stick at a sample rate of 13,000 frames/s (640×200 pixels) to obtain the burn rate and flame temperature, while the microscopic imaging system (2 μm/pixel, Vision Research Phantom VEO710L coupled to Infinity Photo-Optical Model K2 DistaMax) captures the local flame front at a sample rate of 24,000 frames/s (512×512 pixels). The details of using the color filters to obtain temperature maps by pyrometry can be found in our previous studies [31,32]. Briefly, three-channel intensity (red, green, blue) ratios (calibrated from a Mikron M390 blackbody source) are extracted to obtain the reaction flame temperature both temporally and spatially from the video images. The threshold errors for data acceptance and false-color temperature assignment are set nominally to ~200-300 K. The morphologies and compositions of the 3D-printed Al/CuO laminates and their combustion products are characterized by scanning electron microscope (SEM, Thermo-Fisher Scientific NNS450) coupled with energy-dispersive X-ray spectroscopy (EDS).

7.3.4 Simulation of Reaction Propagation in Particle Laminates

In order to model the energy and mass transfer processes leading to reaction propagation in the particle laminates, I have considered a 2-D single bi-layer of Al/CuO particles as a solution domain (Figure S2). Periodic boundary conditions have been considered in the z-direction such that the energy and mass fluxes exiting across the top boundary of the Al layer, enters through the bottom boundary of the CuO-layer and conversely those exiting through the bottom of CuO layer enters the Al layer from the top. These conditions ensure the elimination of edge effects, thereby representing the case of a laminate containing multiple bilayers. Energy transfer and the temperature profile (T) of the laminates have been modeled by the 2-D temporal reaction-diffusion energy equation Eq. (1):

$$\alpha_i \left(\frac{\partial^2 T}{\partial x^2} + \frac{\partial^2 T}{\partial z^2} \right) + \left(\frac{-r_i''' \Delta H_i}{\rho_i C_{p_i}} \right) = \frac{\partial T}{\partial t} \; ; [i = Al, CuO] \tag{1}$$

where the source term is either heat generation due to Al-oxidation ($\Delta H = -838\ kJ/mol$) in the Al layer or heat dissipation due to endothermic CuO decomposition in the CuO-layer ($\Delta H = 156\ kJ/mol$). r_i''' is the volumetric consumption rate ($mol/m^3 s$) of either Al or CuO due to oxidation or decomposition respectively and the negative sign treats the inverse relation between the sign of enthalpy (ΔH_i) and heat generation. For simplicity, density (ρ_i) and mass-specific heat (C_{p_i}) of bulk Al (~2700 kg/m^3 and 890 J/kg-K) and CuO (~6310 kg/m^3 and 695 J/kg-K) has been used for the corresponding layers, while thermal diffusivity (α_i) has been used as a free-parameter and optimized based on experimental data. Although, the thermal diffusivities have been varied as a free-parameter,

the ratio of thermal diffusivities between the Al and CuO layer have been kept constant at 10:1, corresponding to bulk Al and CuO. As the Al-oxidation rate is dependent on availability of oxygen in the Al layer, the mass-transfer and concentration profile (C_{O_2}) of oxygen has been modeled by Eq. (2):

$$D_i\left(\frac{\partial^2 C_{O_2}}{\partial x^2}+\frac{\partial^2 C_{O_2}}{\partial z^2}\right)+r'''_{O_{2i}}=\frac{\partial C_{O_2}}{\partial t}\ ;[i=Al,CuO] \tag{2}$$

where the D_i is O_2 diffusivity in either Al or CuO layer and $r_{O_{2i}}'''$ is the volumetric O_2 generation/dissipation rate in either CuO or Al layer. I have assumed that the initial free concentration of O_2 is null and the O_2 generated from the decomposition of CuO only diffuses through the pores in the CuO layer having a porosity (ϵ) of 0.65. Therefore, I estimated an effective O_2 diffusivity in the CuO layer, $D_{eff}=\frac{\epsilon}{\epsilon^{-\frac{1}{3}}}D_{O_2}$, through the Millington-Quirk tortuosity model [33], where D_{O_2} ~ 2x10^{-5} m^2/s is the molecular diffusivity of O_2 at standard temperature and pressure (NIST) and a $D_{O_2}=D_{O_2}(\frac{T}{298})^{1.5}$ temperature dependance. The diffusivity value of O_2 (~10^{-18} m^2/s) in solid Al_2O_3 [34] has been used for solving Eq. (2) in the Al layer.

Whenever, C_{O_2} is non-zero in the Al layer, Al is assumed to oxidize at a critical reaction rate, r_{Al}'''~6x10^6 mol/m^{3}s, obtained from the critical rate determined from a previous study [35] assuming a particle size of 50 nm. The CuO decomposition has been assumed to follow a zero-order rate law, $r'''_{CuO}=k_0\exp(-\frac{E_a}{RT})$ mol/m^{3}s, with the Arrhenius pre-exponential factor (k_0) the same as r_{Al}''' with an activation energy (E_a) of ~125 kJ/mol

[36]. Hence, the rate of O_2 generation in the CuO layer is $r'''_{O_2{}_{CuO}} = 0.5r'''_{CuO}$, whereas the rate of O_2 dissipation in the Al layer is $r'''_{O_2{}_{Al}} = -0.75r'''_{Al}$, by accounting for the stoichiometries of the respective reactions. For simplicity, both the CuO decomposition (high heating rate O_2 release~940 K) [36]and Al-oxidation are assumed to initiate at *T=923 K*, which is the melting point of Al. The left boundary condition for the energy equation (Eq. (1)) has been assumed to be a constant temperature of *T=2100 K*, which is experimentally observed average flame temperature. A constant convective heat flux to the ambient at *T=298 K* with *h=1 W/K*, has been imposed as the right boundary condition of Eq. (1). No-flux conditions has been imposed on both left and right boundaries for solution of Eq. (2). *T=298 K* and $C_{O_2} = 0$ has been used as initial conditions for solving Eq. (1) and Eq. (2) respectively. The coupled Eq. (1) and Eq. (2) with the above parameters and boundary conditions was solved using COMSOL.

7.4 Results and discussion

7.4.1 Microscale Al/CuO particle laminates

Figure 7-1(a) shows the direct writing approach, which is formulated based on our previous studies[2,27–29]. The only difference is that I used two syringes/nozzles to alternatively deposit Al or CuO on the pre-heated substrate. Inks in both the syringes contain 10 wt% polymer mixtures of HPMC and PVDF, and 90 wt% nanoparticles of Al or CuO. The typical optical, SEM and EDS images of the resulting Al/CuO laminates with a different bilayer thickness of 125 μm and 32 μm are shown in Figure 7-1(b) and 7-1(c), respectively. A more zoomed-in view of the thinnest bilayer (32 μm) of Al/CuO particle

laminate is shown in Figure 7-1(d). These images demonstrate that well-layered Al and CuO particle laminates can be prepared, and the interface between Al and CuO layers is clear and do not show overlap between the layers.

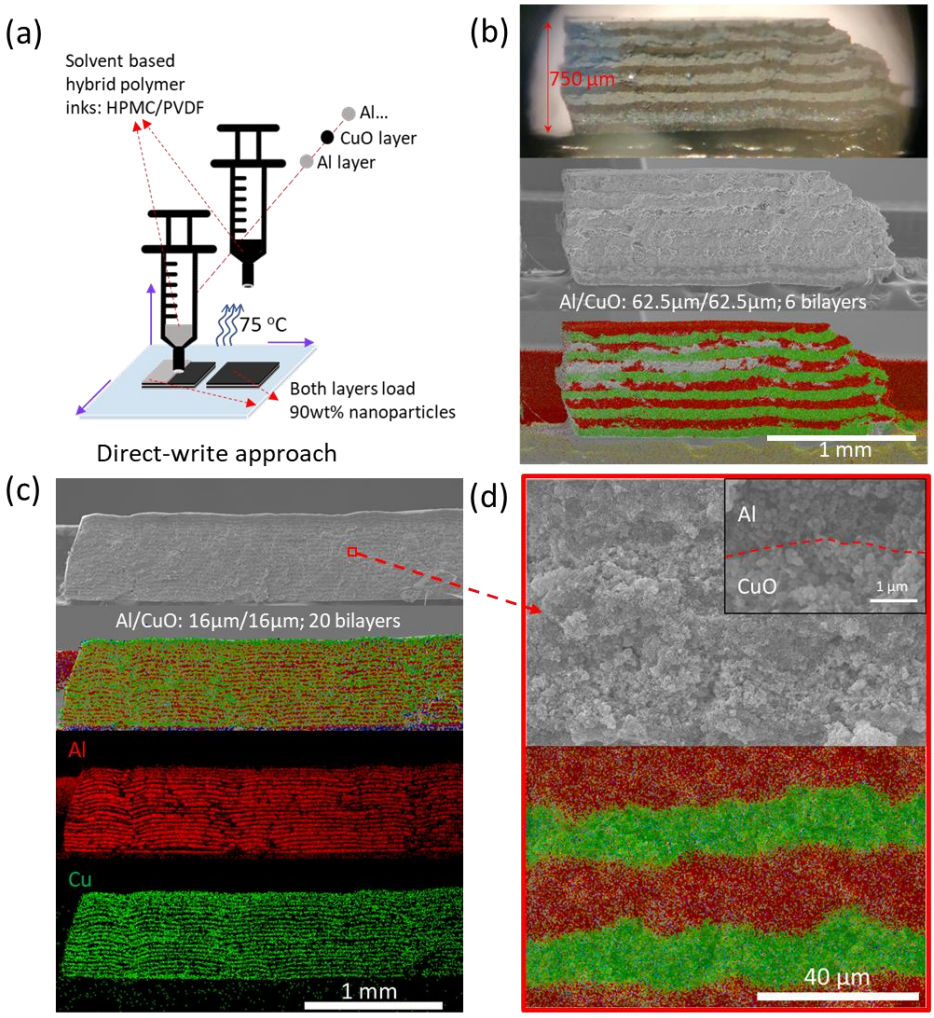

Figure 7-1 Direct-write approach of Al/CuO high loading particle laminates (a); optical, SEM and EDS images of Al/CuO particle laminates with bilayer thickness of 125µm (b); low (c) and higher (d) magnification SEM and EDS images with bilayer thickness of 32µm. Note: image of Al/CuO laminate with bilayer thickness of 187.5µm is shown in Figure S3. The total laminate thickness for 20 bilayers of Al/CuO (bilayer thickness: 32µm) is ~650µm.

The burn rate and flame temperature of the Al/CuO laminates are obtained from macroscopic burning of the composite sticks with different bilayer thickness (Figure 7-2(a)), more details in supporting videos 1). With the increase of bilayer thickness, both the burn rate and flame temperature decrease monotonically. Burn rate reduces by a factor of 3 when bilayer thickness changes from 32μm (2.3cm/s) to 420μm (0.7cm/s). Over this range the flame temperature drops from 2500K to 1500K. Considering the density is roughly the same for all the laminates, the normalized energy release rate (Figure 7-2 (b)) also decreases with increasing bilayer thickness. Details about the burn behavior of pre-mixed films can be found in our previous work [37].

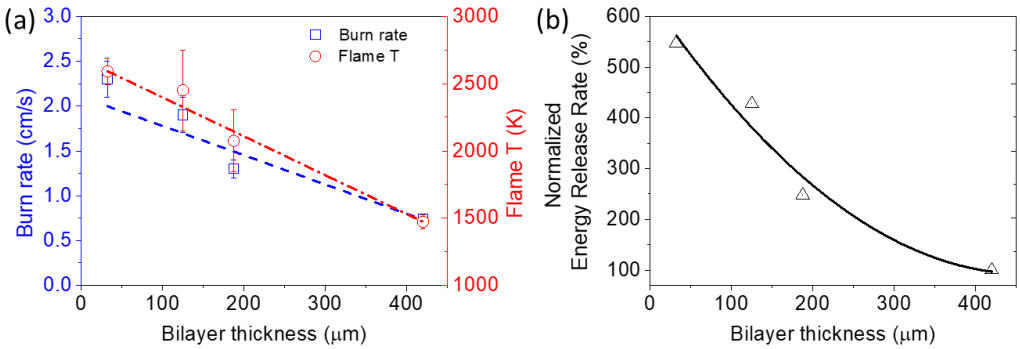

Figure 7-2 Burn rate, flame T (a) and energy release rate (b) changing with bilayer thickness

7.4.2 Temperature distribution from experiments and simulation

A typical microscopic image and its temperature map of the cross-section (bilayer thickness of 420, 187.5, and 125 μm) is shown in Figure 7-3 (a) to 7-3 (c) (supporting video 2). The snapshots clearly show a "finger" like structure in the flame front, with the Al layer proceeding ahead of the CuO layer. The reason for the lagging effects of the CuO layer on

the flame front is that the heat generated from the interface reaction conducts differently into the Al and CuO layers. Since the CuO layer undergoes a latent decomposition process, the temperature will lag as it first decomposes before energy can go into the sensible heating.

The numerical model (section 2.4) as outlined above was solved over 100 ms, to obtain a spatiotemporal temperature profile. Figures 7-3 (d) to 7-3 (f) show the spatial temperature distribution with different bilayer thicknesses after 40 ms of propagation. The computed (Figure 7-3) reaction front in the CuO-layer lags the reaction front in the Al layer giving rise to a finger-like profile, consistent with the experimental flame front. Figure 7-3 (g) shows both experimental and calculated burn rates from Al/CuO laminates with different bilayer thicknesses, and shows experimental data matches well with the calculation. The computed burn rate decreases linearly with increasing bilayer thicknesses, showing the same trend as observed in experiments. In the numerical solution, the absolute values of thermal diffusivities of the Al and CuO layers (preserving the 10:1 ratio) have been optimized (α_{Al}~5.1x10^{-6} m^2/s) to match the computed burn-rate with experimental burn-rates. The sensitivity of the computed burn rate to the thermal diffusivity has been analyzed later. With increasing bilayer thickness, the O_2 diffusion rate from the CuO layer to the Al layer decreases correspondingly, thereby possibly reducing the rate of mixing between the fuel and oxidizer. The role of this diffusion limitation as a major controlling factor on the overall reaction rate is further evaluated in the subsequent sections.

The characteristic “finger” is also observed in both the microscopic experiment and computational results. Generally, the thicker bilayers show slow burning rate and enhanced

finger-like profile. When the bilayer thickness is as small as 30 μm, I barely see any finger structures on the flame front (Figure S4). The finger-like profile may appear as a result of i) difference in reaction propagation rates at the interface and the bulk ii) thermal diffusivity difference (10x) between the layer, the mechanism of which is analyzed in the next section.

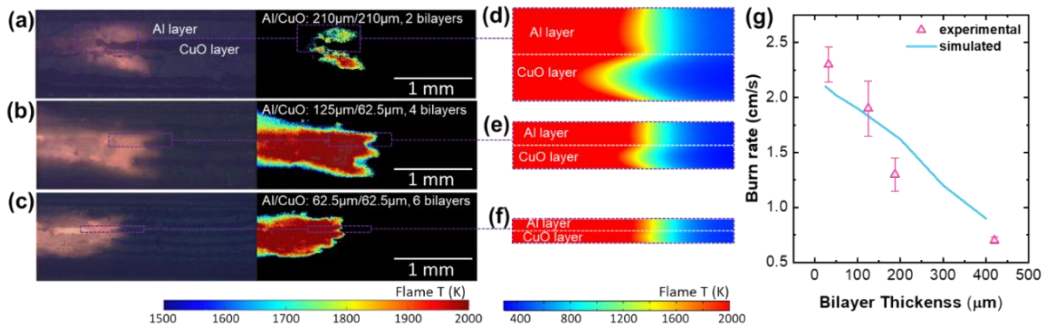

Figure 7-3 Typical microscopic snapshots and their corresponding temperature maps (a-c) indicate the "finger" structures of the flame front 2 (a), 4(b), and 6 (c) bilayers (bilayer thickness is 420μm, 187.5μm, and 125μm, respectively). Numerical computations (d, e, and f) reveal a similar "finger" structure of the flame propagation with a similar bilayer thickness of 400μm (d), 200μm (e), and 100μm (f). Experimental and simulated burn rates change with increasing bilayer thickness (g).

7.4.3 O_2 diffusion and interface reaction

I now turn to a mechanistic interpretation to further explain our observations. The computationally determined time-resolved O_2 concentration and temperature profiles obtained from the numerical solution are shown in Figure 7-4 (a) and 7-4 (b) respectively. Figure 7-4 (a) shows the concentration profile of O_2 in the 400 μm bilayers case, at different times. During the reaction, a maximum in O_2 concentration is observed at the center of the CuO layer (Figure 7-4 (a) & supporting video 3) and is depleted towards the interfacial boundary. This implies that O_2 consumption by Al is faster than can be replenished by the center of the CuO layer. This effect can be also be observed in the computed temperature

distribution (Figure 7-4 (b) & supporting video 4). Three distinct features are observed on the temperature profile of the flame front: i) short projections (~10 μm) near the Al/CuO interfacial boundary, which propagate ahead of the rest of the reaction front ii) reaction front in the Al layer which lags a little (~10 μm) behind the interfacial front giving rise to the finger like profile observed experimentally iii) the CuO front which lags far behind the Al front (~100 μm).

By simulating an ideal but unrealistic case where the thermal diffusivity is the same everywhere, but keeping the other mass transfer parameters the same, I find that small projections from the propagation front still appear at the interfacial boundary (Figure S5). This implies that the smaller projections appear due to the faster reaction propagation at the interfacial boundary. Hence, during the combustion of particulate laminates, the reaction is initiate at the interfacial boundary of the fuel-oxidizer layers. The higher (~10x) thermal diffusivity of the Al layer propagates the heat generated at the interface faster across the bulk of the layer causing the Al front to propagate ahead of the CuO front creating a finger like profile. In fully dense nanolaminates, these fingering flame fronts have not been experimentally observed, since the propagation is not diffusion-limited due to short distances (nanoscale) between fuel and oxidizer. Rather it is the decomposition rate of CuO as rate controlling [38]. In our case, the particulate laminates have relatively long diffusion distance between Al and CuO layers, making the decomposition characteristic time negligible compared to the time of diffusion.

An optical image of the post combustion laminate (Figure 7-4 (c) (i)) along with its EDS mapping results (Figure 7-4 (c) (ii and iii)) indicate that upon burning, the Al and

CuO layer become Al_xO_y and Cu layer respectively, retaining their respective positions in the laminate architecture without mixing. This implies that during the combustion CuO decomposes and the released O_2 diffuses to the Al layer initiating the oxidation process. In the model, the absence of O_2 in the Al layer (Figure 7-4 (a)), suggest that the oxidation occurs more rapidly than the mass transfer of O_2 to the Al layer. Therefore, I may conclude that the combustion rate of Al/CuO particle laminates is limited by O_2 diffusion rate. Hence, with increasing bilayer thickness, the increased O_2 diffusion distance reduces the overall burn-rate, as observed in section 2.2. An EDS image of the interface (Figure S6) shows that the condensed phase mixing between Al and CuO is only limited to a short distance <10 µm from the interface for a bilayer thickness of ~188 µm (5 % of bilayer thickness) and thereby has negligible impact on the overall reaction propagation. This justifies having neglected interfacial mixing in our simulation.

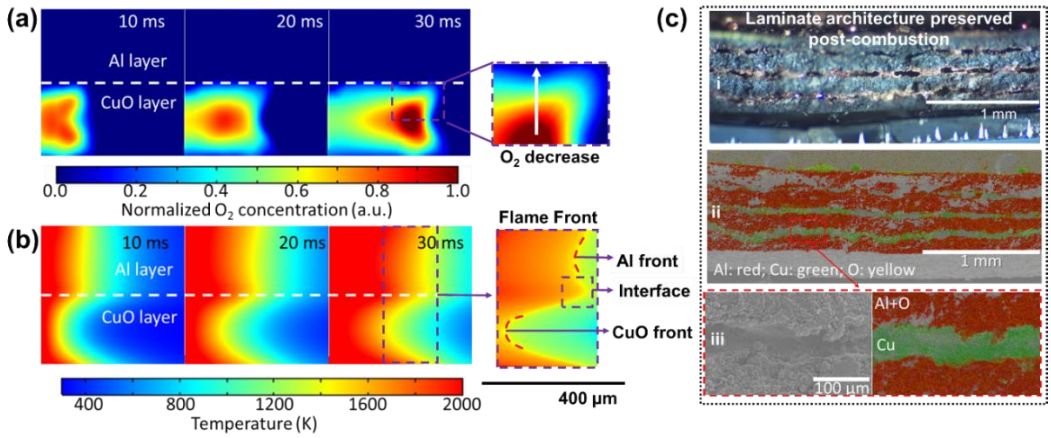

Figure 7-4 (a) Computed time resolved O_2 concentration showing a decrease in its concentration from the center of the CuO layer to the interface; (b) Computed temperature map showing the different features of the flame front at the Al-layer, CuO-layer, and the interface (c) Optical image after combustion (i) and its EDS mapping result (ii,iii) shows that the laminate architecture (187 µm bilayer) is preserved post-combustion and the products AlO_x and Cu remain in separate layers.

7.4.4 Sensitivity of burn rate to heat transfer and O_2 diffusion

The numerical solution of the burn-rate is dependent on various parameters such as thermal diffusivity of Al layer (α_{Al}), thermal diffusivity of CuO layer (α_{CuO}), O_2 diffusivity in CuO layer, O_2 diffusivity in Al layer, decomposition rate of CuO, and oxidation rate of Al. Values obtained from in-situ measurements as reported in previous studies[35,36] have been used for these parameters, whereas the thermal diffusivities have been adjusted to match the numerical results with experiments (Section 3.2). Figure S7 (a) shows the burn-rates obtained for various bilayer thicknesses when the thermal diffusivity of the Al layer is perturbed to 0.68x and 0.1x times its optimized value (best fit to experimental results). A significant difference is observed in the burn-rates of all the bilayer thicknesses on changing of this parameter. However, Figure S7 (b) shows that the O_2 diffusion coefficient in the CuO layer does not have a significant effect on the absolute burn-rate value, indicating that the mass transfer rate of O_2 from CuO to Al layer is mostly dependent on the length of the diffusion barrier.

To quantitatively identify the sensitivity of the burn-rates at different bi-layer thicknesses, I have computed a sensitivity coefficient for the thermal diffusivity, $S_\alpha = \frac{dlnv}{dln\alpha}$, where v and α are the burn-velocity and thermal diffusivity respectively. The evaluated sensitivity coefficient obtained from linear fitting (R^2>0.99) of the values in Figure S7a is shown in Figure 7-5 (a). According to laminar pre-mixed flame theory, $v \sim \sqrt{\alpha}$ and hence the sensitivity coefficient, $S_\alpha = \frac{dlnv}{dln\alpha} \sim 0.5$. However, Figure 7-5 (a) shows that the burn rate of the laminates scales with thermal diffusivity as $v \sim \alpha^x$, where x increases (~0.4 to

1.1) with increase in bilayer thickness. This indicates that the sensitivity of the burn-rate to thermal diffusivity increases with increasing bilayer thickness.

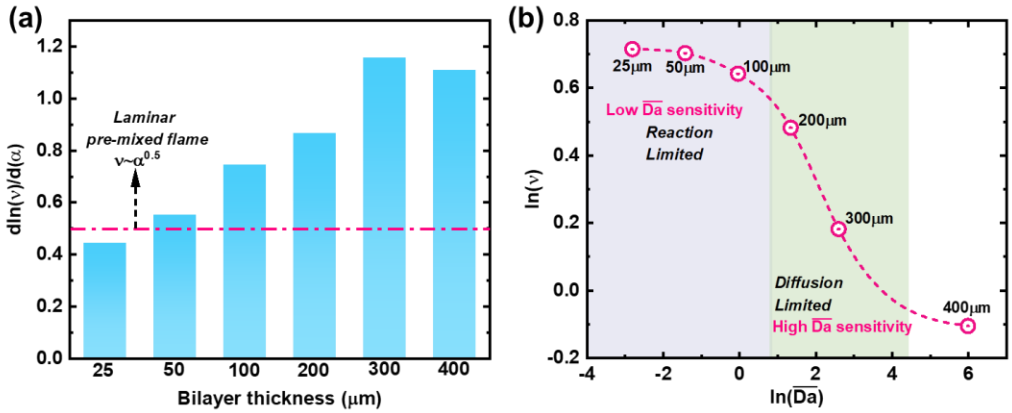

Figure 7-5 (a) Sensitivity of burn rate to thermal diffusivity increases with increase in bilayer thickness (b) Sensitivity of the burn-rate to Damköhler number shows a clear transition from reaction limitation to diffusion limitation with increase in bilayer thickness.

Since the propagation is limited by O_2 diffusion, the rate of O_2 transport to the Al layer and the rate of O_2 uptake in Al layer (or oxidation rate) will have major influence on the burn rate. Here I express this in the form of an average *Damköhler* number, $\overline{Da} = \frac{r'''_{O_2 Al} t_z^2}{D_{O_2 CuO} C_0}$, based on the ratio of these two rates, for various bi-layer thicknesses (details in SI). Here, $r'''_{O_2 Al}$, t_z, $D_{O_2 CuO}$, and C_0, implies Al oxidation rate, bilayer-thicknesses, O_2 diffusivity in the CuO layer and maximum O_2 concentration in the center of CuO layer respectively. As there is a non-linear dependence of burn rate on $\overline{Da}$, to perform a sensitivity analysis, I present the results in terms of the natural logarithms in Figure 7-5 (b). The derivative of this sigmoidal curve is of course the sensitivity of the burn rate to the *Damköhler number. The slope of the curve increases with bilayer thickness, indicating an increasing sensitivity of burn-rate to the Damköhler number in the high Damköhler number*

or mass-transfer limited regime. For bilayer thicknesses of 25-100 μm,the $\overline{Da} \ll 1$, indicating reaction limitation, whereas bilayer thicknesses >100 μm with $\overline{Da} \gg 1$, are limited by diffusion of O_2 to the Al layer. Hence, with increase in bi-layer thickness, mass transfer control increases, and the flame propagation behavior deviates from that of laminar pre-mixed flames. The sensitivity of the burn-rate to the $\overline{Da}$ shows a dip at 400 μm bilayer, which maybe a mathematical artefact due to the low burn-rate there. Since, the absolute value of the burn-rate is small, the relative change in the burn-rate value on changing of $\overline{Da}$ is also small. Hence, the efficient working range of this sensitivity analysis is limited to bilayer thicknesses of less than 300 μm.

As mentioned previously, Al/CuO sputter deposited nanolaminates have attracted considerable study owing to their precisely adjustable reactivity through the bilayer thickness. [2,24–28], I now compare our particle laminates with those prior studies. Figure 7-6 summarizes the burn rate and energy release rate (normalized based on the burn rate × density × flame temperature) with different bilayer thickness range from 0.15μm to 420μm. Figure 7-6 shows both burn rate and energy release rate can be fit over 3 orders of magnitude in bilayer thickness, leading to a 5-order of magnitude change in burn and energy release rate. The slope for energy release rate is higher than that of burn rate mainly owing to the higher density of Al/CuO nanolaminates (4x) compared to porous particulate laminates in this study. The results further confirm that the mass transfer from oxidizer to fuel layer is dominating the reaction and flame propagation of the reactive laminates. The differences between the nanolaminates and particulate laminates are the mass transfer

mechanism, while the former is controlled by diffusion of condensed phase oxygen ions [17], the latter is controlled by gas phase O_2 diffusion.

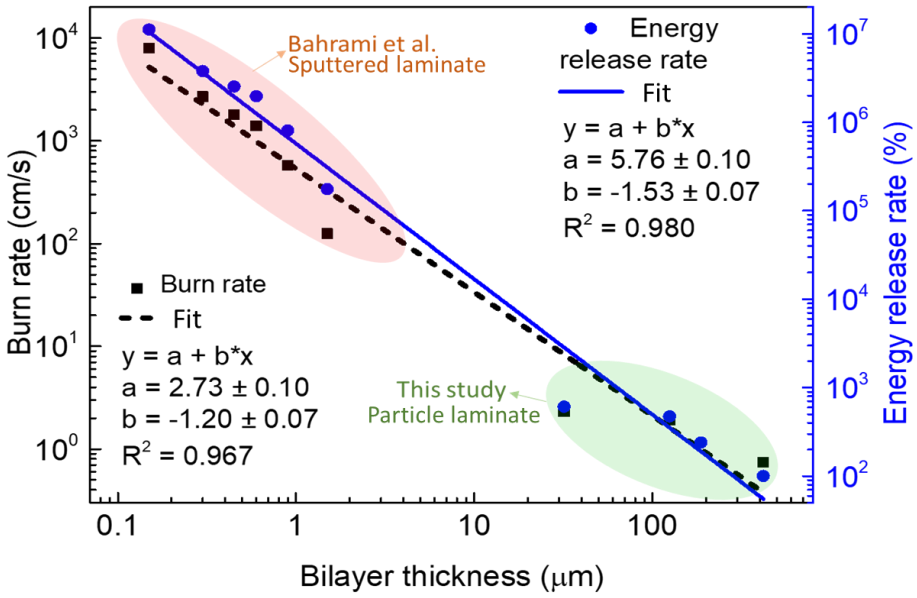

Figure 7-6 Burn rate and normalized energy release rate as a function of bilayer thickness from nano to micro. The data points of Al/CuO sputter deposited nanolaminates are from Bahrami et al. [18], while this study examines particle-based laminates.

7.5 Conclusions

In this study, I prepared free-standing microscale Al/CuO particle laminates with precise control of interfacial contact between fuel and oxidizer using a simple direct writing approach. With small (10 wt%) polymer additions in each layer of the laminates, I obtain free-standing microscale laminates with burn rates on the order of ~cm/s, making it easier to observe the Cross-section of the flame front at the Al/CuO interface. I find that the burn-rate can be altered by changing the layer thicknesses of the printed laminates, indicating effects from oxygen transport between the fuel and oxidizer layer, the evidence of which is also observed in post-combustion materials. Through microscopic imaging of the flame

propagation in 3D printed Al/CuO laminates as a typical model system, I observed the development of unusual finger-like temperature profiles near the flame front. Through a numerical model of the heat and mass transport processes during the flame propagation in laminates, I have successfully reconstructed these finger-structured flame fronts. I conclude that such finger-shaped profile can be attributed to a combination of i) faster propagation of the interfacial reaction than the bulk and ii) difference in thermal diffusivities of the fuel-oxidizer layers, which has been also confirmed by ex-situ analysis of combustion products. Both the experiment and model confirmed that O_2 transport is the rate limiting factor in the reaction propagation of printed laminates.

7.6 References

(1) Wang, H.; Jian, G.; Egan, G. C.; Zachariah, M. R. Assembly and Reactive Properties of Al/CuO Based Nanothermite Microparticles. *Combust. Flame* **2014**, *161* , 2203–2208.

(2) Wang, H.; Kline, D. J.; Biswas, P.; Zachariah, M. R. Connecting Agglomeration and Burn Rate in a Thermite Reaction: Role of Oxidizer Morphology. *Combust. Flame* **2021**, *231*, 111492.

(3) Ghildiyal, P.; Ke, X.; Biswas, P.; Nava, G.; Schwan, J.; Xu, F.; Kline, D. J.; Wang, H.; Mangolini, L. et al. Silicon Nanoparticles for the Reactivity and Energetic Density Enhancement of Energetic-Biocidal Mesoparticle Composites. *ACS Appl. Mater. Interfaces* **2021**, *13* , 458–467.

(4) Xu, F.; Nava, G.; Biswas, P.; Dulalia, I.; Wang, H.; Alibay, Z.; Gale, M.; Kline, D. J.; Wagner, B.; Mangolini, L.; Zachariah, M. R. Energetic Characteristics of Hydrogenated Amorphous Silicon Nanoparticles. *Chem. Eng. J.* **2022**, *430*, 133140.

(5) Xu, F.; Hirt, B.; Biswas, P.; Kline, D. J.; Yang, Y.; Wang, H.; Sehirlioglu, A.; Zachariah, M. R. Superior Reactivity of Ferroelectric Bi2WO6/Aluminum Metastable Intermolecular Composite. *Chem. Eng. Sci.* **2022**, *247*, 116898.

(6) Biswas, P.; Ghildiyal, P.; Kwon, H.; Wang, H.; Alibay, Z.; Xu, F.; Wang, Y.; Wong, B. M.; Zachariah, M. R. Rerouting Pathways of Solid-State Ammonia Borane Energy Release. *J.Phys.Chem.C* **2021**, 126, 1, 48–57.

(7) Rossi, C. Engineering of Al/CuO Reactive Multilayer Thin Films for Tunable Initiation and Actuation. *Propellants, Explos., Pyrotech.*, **2019**, *44* , 94–108.

(8) Zapata, J.; Nicollet, A.; Julien, B.; Lahiner, G.; Esteve, A.; Rossi, C. Self-Propagating Combustion of Sputter-Deposited Al/CuO Nanolaminates. *Combust. Flame* **2019**, *205*, 389–396.

(9) Egan, G. C.; Mily, E. J.; Maria, J. P.; Zachariah, M. R. Probing the Reaction Dynamics of Thermite Nanolaminates. *J.Phys.Chem.C* **2015**, *119* , 20401–20408.

(10) Tai, Y.; Xu, J.; Wang, F.; Dai, J.; Zhang, W.; Ye, Y.; Shen, R. Experimental and Modeling Investigation on the Self-Propagating Combustion Behavior of Al-MoO3 Reactive Multilayer Films. *J.Appl.Phys.* **2018**, *123* , 235302.

(11) Xu, J.; Shen, Y.; Wang, C.; Dai, J.; Tai, Y.; Ye, Y.; Shen, R.; Wang, H.; Zachariah, M. R. Controlling the Energetic Characteristics of Micro Energy Storage

Device by in Situ Deposition Al/MoO3 Nanolaminates with Varying Internal Structure. *Chem. Eng. J.* **2019**, *373*, 345–354.

(12) Adams, D. P. Reactive Multilayers Fabricated by Vapor Deposition: A Critical Review. *Thin Solid Films* **2015**, *576*, 98–128.

(13) Grapes, M. D.; Weihs, T. P. Exploring the Reaction Mechanism in Self-Propagating Al/Ni Multilayers by Adding Inert Material. *Combust. Flame* **2016**, *172*, 105–115.

(14) Kim, J. S.; Lagrange, T.; Reed, B. W.; Knepper, R.; Weihs, T. P.; Browning, N. D.; Campbell, G. H. Direct Characterization of Phase Transformations and Morphologies in Moving Reaction Zones in Al/Ni Nanolaminates Using Dynamic Transmission Electron Microscopy. *Acta Materialia* **2011**, *59*, 3571–3580.

(15) Overdeep, K. R.; Schmauss, T. A.; Panigrahi, A.; Weihs, T. P. The Influence of Sample Thickness on the Combustion of Al:Zr and Al-8Mg:Zr Nanolaminate Foils. *Combust. Flame* **2018**, *196*, 88–98.

(16) Abere, M. J.; Yarrington, C. D.; Adams, D. P. Heating Rate Dependent Ignition of Al/Pt Nanolaminates through Pulsed Laser Irradiation. *J. Appl. Phys.* **2018**, *123* , 235304.

(17) Lahiner, G.; Nicollet, A.; Zapata, J.; Marín, L.; Richard, N.; Rouhani, M. D.; Rossi, C.; Estève, A. A Diffusion–Reaction Scheme for Modeling Ignition and Self-Propagating Reactions in Al/CuO Multilayered Thin Films. *J. Appl. Phys.* **2017**, *122* , 155105.

(18) Bahrami, M.; Taton, G.; Conédéra, V.; Salvagnac, L.; Tenailleau, C.; Alphonse, P.; Rossi, C. Magnetron Sputtered Al-CuO Nanolaminates: Effect of Stoichiometry and Layers Thickness on Energy Release and Burning Rate. *Propellants, Explos., Pyrotech.* **2014**, *39*, 365–373.

(19) Marín, L.; Nanayakkara, C. E.; Veyan, J. F.; Warot-Fonrose, B.; Joulie, S.; Esteìve, A.; Tenailleau, C.; Chabal, Y. J.; Rossi, C. Enhancing the Reactivity of Al/CuO Nanolaminates by Cu Incorporation at the Interfaces. *ACS Appl. Mater. Interfaces* **2015**, *7* , 11713–11718.

(20) Marín, L.; Warot-Fonrose, B.; Estève, A.; Chabal, Y. J.; Alfredo Rodriguez, L.; Rossi, C. Self-Organized Al2Cu Nanocrystals at the Interface of Aluminum-Based Reactive Nanolaminates to Lower Reaction Onset Temperature. *ACS Appl. Mater. Interfaces* **2016**, *8* , 13104–13113.

(21) Lanthony, C.; Guiltat, M.; Ducéré, J. M.; Verdier, A.; Hémeryck, A.; Djafari-Rouhani, M.; Rossi, C.; Chabal, Y. J.; Estève, A. Elementary Surface Chemistry during

CuO/Al Nanolaminate-Thermite Synthesis: Copper and Oxygen Deposition on Aluminum (111) Surfaces. *ACS Appl. Mater. Interfaces* **2014**, *6* , 15086–15087.

(22) Xu, J.; Tai, Y.; Ru, C.; Dai, J.; Shen, Y.; Ye, Y.; Shen, R.; Fu, S. Characteristic of Energetic Semiconductor Bridge Based on Al/MoOx Energetic Multilayer Nanofilms with Different Modulation Periods. *J. Appl. Phys.* **2017**, *121* , 113301.

(23) Blobaum, K. J.; Reiss, M. E.; Plitzko Lawrence, J. M.; Weihs, T. P. Deposition and Characterization of a Self-Propagating CuOx/Al Thermite Reaction in a Multilayer Foil Geometry. *J. Appl. Phys.* **2003**, *94* , 2915.

(24) Grapes, M. D.; Lagrange, T.; Friedman, L. H.; Reed, B. W.; Campbell, G. H.; Weihs, T. P.; Lavan, D. A. Combining Nanocalorimetry and Dynamic Transmission Electron Microscopy for in Situ Characterization of Materials Processes under Rapid Heating and Cooling. *Rev. Sci. Instrum.* **2014**, *85* , 084902.

(25) Santala, M. K.; Grapes, M. D.; Weihs, T. P.; Reed, B. W.; Lagrange, T.; Campbell, G. H. Imaging Unsteady Propagation of Reaction Fronts in Reactive Multilayer Foils with Multi-Frame Dynamic TEM. *Micros. Microanal.* **2014**, *20* , 1584–1585.

(26) Pauls, J. M.; Shuck, C. E.; Genç, A.; Rouvimov, S.; Mukasyan, A. S. In-Situ Transmission Electron Microscopy Determination of Solid-State Diffusion in the Aluminum-Nickel System. *J. Sol. Stat. Chem.* **2019**, *276*, 114–121.

(27) Wang, H.; Kline, D. J.; Zachariah, M. R. In-Operando High-Speed Microscopy and Thermometry of Reaction Propagation and Sintering in a Nanocomposite. *Nat. Commun.* **2019**, *10*, 3032.

(28) Wang, H.; Kline, D. J.; Rehwoldt, M. C.; Zachariah, M. R.; Zachariah, M. R. Carbon Fibers Enhance the Propagation of High Loading Nanothermites: In Situ Observation of Microscopic Combustion. *ACS Appl. Mater. Interfaces* **2021**, *13* , 30504–30511.

(29) Wang, H.; Julien, B.; Kline, D. J.; Alibay, Z.; Rehwoldt, M. C.; Rossi, C.; Zachariah, M. R. Probing the Reaction Zone of Nanolaminates at ∼μs Time and ∼μm Spatial Resolution. *J. Phys. Chem. C* **2020**, *124*, 13679–13687.

(30) Li, X.; Guerieri, P.; Zhou, W.; Huang, C.; Zachariah, M. R. Direct Deposit Laminate Nanocomposites with Enhanced Propellent Properties. *ACS Appl. Mater. Interfaces* **2015**, *7* , 9103–9109.

(31) Jacob, R. J.; Kline, D. J.; Zachariah, M. R. High Speed 2-Dimensional Temperature Measurements of Nanothermite Composites: Probing Thermal vs. Gas Generation Effects. *J. Appl. Phys.* **2018**, *123*, 115902.

(32) Kline, D. J.; Rehwoldt, M. C.; Wang, H.; Eckman, N. E.; Zachariah, M. R. Why Does Adding a Poor Thermal Conductor Increase Propagation Rate in Solid Propellants? *Appl. Phys. Lett.* **2019**, *115* , 114101.

(33) Millington, R. J.; Quirk, J. P. Permeability of Porous Solids. *Trans. Faraday Soc.* **1961**, 57, 1200-1207.

(34) Lee, K.; Stewart, D. S. Modeling Aluminum Combustion in Oxidizing Environment with the Gibbs Formulation. *Combust. Flame* **2020**, *220*, 92–106.

(35) Jian, G.; Zhou, L.; Piekiel, N. W.; Zachariah, M. R. Low Effective Activation Energies for Oxygen Release from Metal Oxides: Evidence for Mass-Transfer Limits at High Heating Rates. *ChemPhysChem* **2014**, *15* , 1666–1672.

(36) Zhou, W.; DeLisio, J. B.; Wang, X.; Egan, G. C.; Zachariah, M. R. Evaluating Free vs Bound Oxygen on Ignition of Nano-Aluminum Based Energetics Leads to a Critical Reaction Rate Criterion. *J. Appl. Phys.* **2015**, 118, 114303.

(37) Wang, H.; Shen, J.; Kline, D. J.; Eckman, N.; Agrawal, N. R.; Wu, T.; Wang, P.; Zachariah, M. R.; Wang, H.; Zachariah, M. R.; Shen, J.; Kline, D. J.; Eckman, N.; Agrawal, N. R.; Wu, T.; Wang, P. Direct Writing of a 90 Wt% Particle Loading Nanothermite. *Adv. Mater.* **2019**, *31*, 1806575.

(38) Tichtchenko, E.; Estève, A.; Rossi, C. Modeling the Self-Propagation Reaction in Heterogeneous and Dense Media: Application to Al/CuO Thermite. *Combust. Flame* **2021**, *228*, 173–183.

7.7 Supporting information

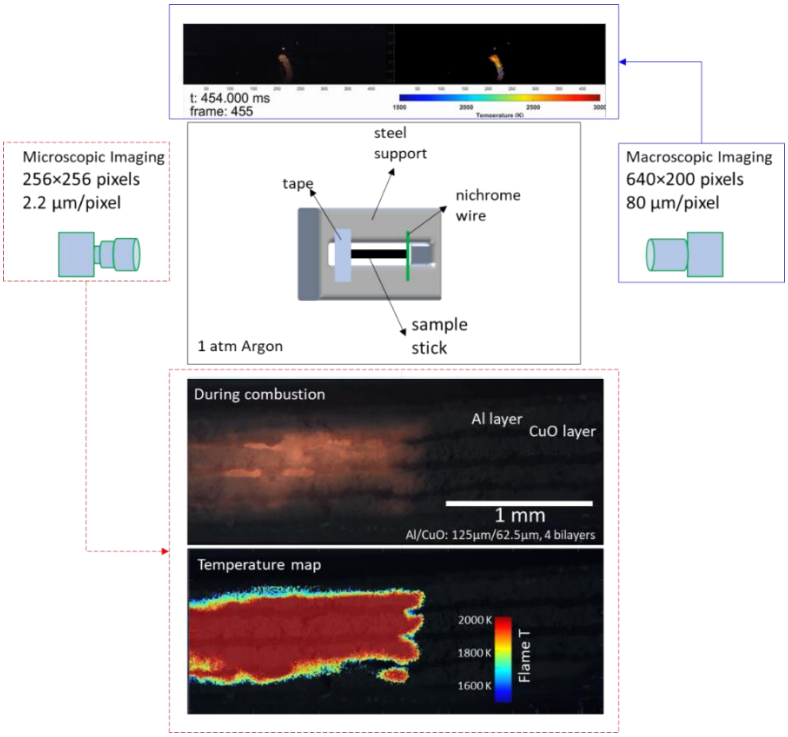

Figure S1. *Schematic showing of microscopic and macroscopic imaging of microscale Al/CuO laminates.*

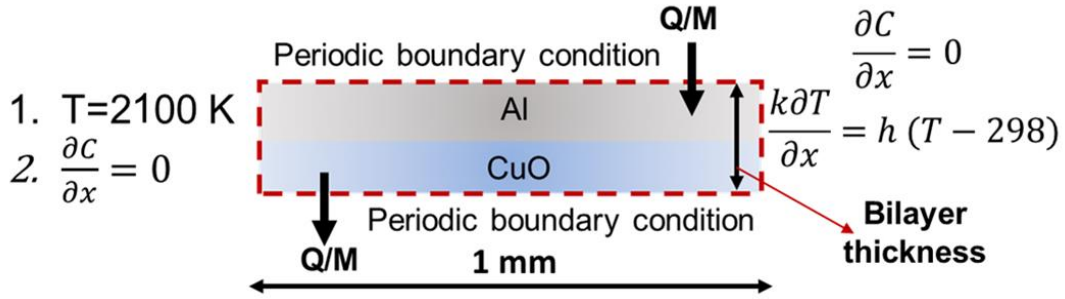

Figure S2*. Schematic of geometry of the solution domain with boundary conditions*

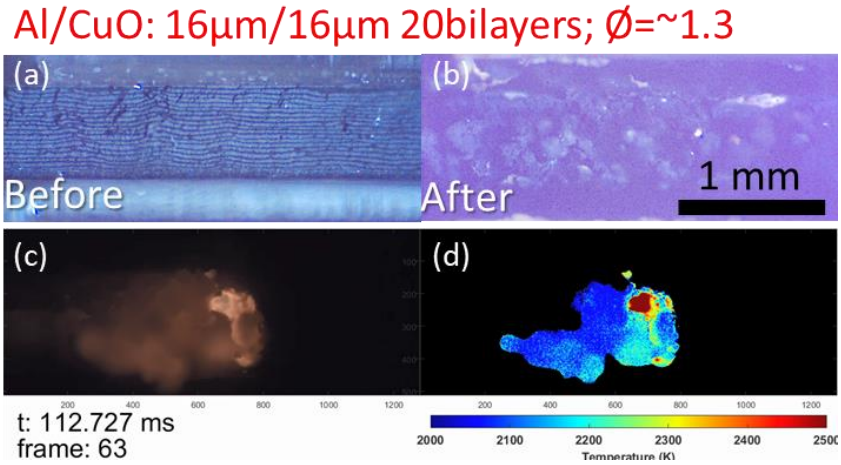

Figure S3. *Optical images (a and b) of Al/CuO laminates with a bilayer thickens of 32 µm before (a) and after (b) combustion; The microscopic combustion imaging (c) and its corresponding temperature map (d) of the above laminate.*

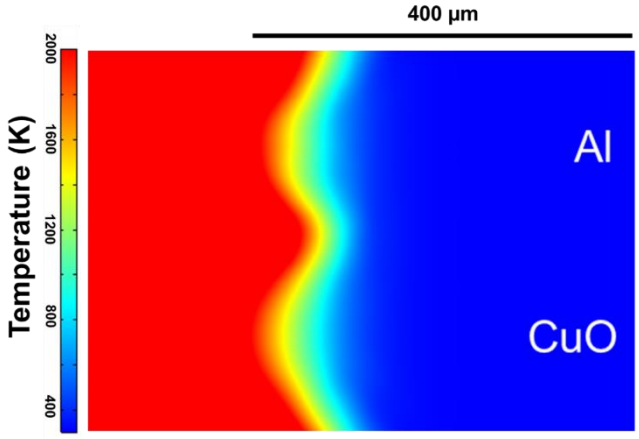

Figure S4. *Small finger like projections appear at the interfaces, even when thermal diffusivity of both the layers are made equal, due to the faster interfacial reaction rate than the bulk.*

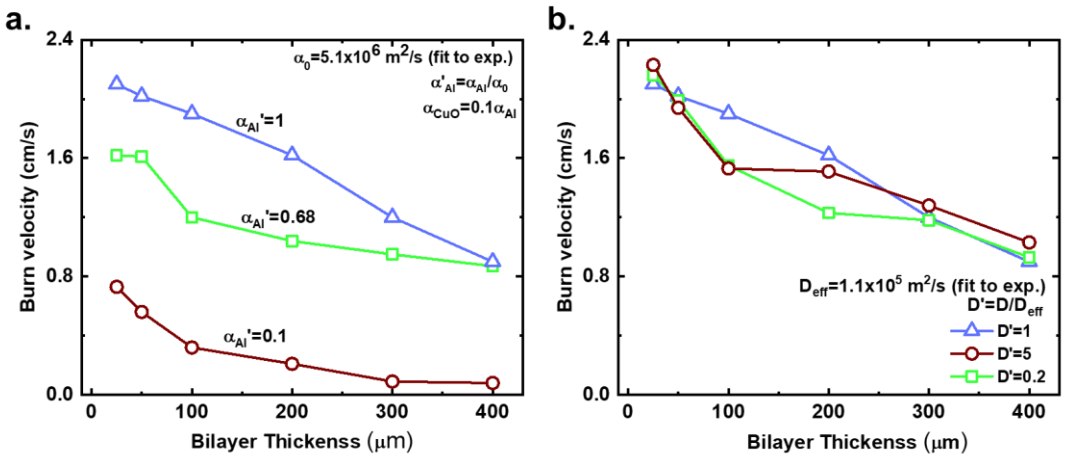

FigureS5 Relationship between burn-rate and bilayer thicknesses for different (a) thermal diffusivities (a) and O2 diffusivities (b) showing that the absolute burn-rate is more sensitive to perturbations in the thermal diffusivity in the Al layer than O_2 diffusivity in the CuO layer.

S.1 *Damköhler number calculation*

The *Damköhler* number has been calculated by taking ratio of the rate of Al oxidation and the average rate of O_2 transport from the middle of the CuO layer to the middle of the Al layer.

Rate of Al oxidation (mol/s) = $r'''_{O_2 Al} A t_z$ where A=interfacial area of the layers

Rate of O2 transport (mol/s) = $\frac{D_{O_2} A C_0}{t_z}$ where C_0 is the maximum concentration of O_2, which occurs in the middle of the CuO layer. The value of all these parameters can be found in section 2.4.

This gives the $\overline{Da} = \frac{r'''_{O_2 Al} t_z^2}{D_{O_2 CuO} C_0}$.

Table S1 Values of $\overline{Da}$ for different bilayer thicknesses:

Bilayer thickness	$\overline{Da}$
25	0.06
50	0.24
100	0.96
200	3.83
300	8.63
400	15.33

8 Modelling and Simulation of Field Directed Linear Assembly of Aerosol Particles

8.1 Summary

Unlike liquid phase colloidal assembly, changing the structure of fractal aggregates in the aerosol phase significantly, is considered impractical. In this study, I discuss the possibility of applying external magnetic and electric fields, to tune the structure and fractal dimension (D_f) of aggregates grown in the aerosol phase. I show that external fields can be used to induce dipole moments in primary nanoparticles. I found that an ensemble of particles with induced dipole moments will interact through directional attractive and repulsive forces, leading to the formation of linear, chain-like aggregates with D_f~1. The aggregate structure transition is dependent on the primary particle sizes, temperature and applied field strength which was evaluated by performing a hybrid ensemble/cluster-cluster aggregation Monte Carlo simulation. I demonstrate that the threshold magnetic field strength required to linearly assemble 10-500 nm particle sizes are practically achievable whereas the electric field required to assemble sub-100 nm particles are beyond the breakdown strength of most gases. To theoretically account for the enhanced coagulation rates due to attractive interactions, I have also derived a correction factor to both free molecular and transition regime coagulation kernel, based on magnetic dipolar interactions. A comparison has been made between the coagulation time-scales estimated by theory and simulation, with the estimated magnetization time-scales of the primary particles along with oscillation time period of the magnetic field, to demonstrate that sub-50 nm superparamagnetic primary particles can be magnetized and assembled at any temperature,

while below the Curie temperature ferromagnetic particles of all sizes can be magnetized and assembled, given the applied field is higher than the threshold.

8.2 Introduction

Aerosol routes comprise one of the primary approaches to sub-micron particle production at the industrial scale[1]. However, considerable research has been expended in modification to common aerosol routes, such as laser ablation[2], sputtering[3], vapor phase decomposition[1] in an a effort to better control and affect chemistry, crystallinity and size distribution. [4–7] However, most of these commonly used aerosol routes result in considerable aggregation at practical particle densities, leading to close compact aggregates, resulting from rapid Brownian motion [8].

During the formation of sub-micron particles by nucleation, the aerosol typically transitions from free-molecule transport to the continuum. This is in contrast with liquid-phase synthesis techniques which are always in the continuum regime, and Brownian dynamics are orders of magnitude slower. Furthermore, in the liquid phase surface charges or polymer coatings are often employed to manipulate colloidal stability to enable manipulation of particle assembly[9] In contrast and unfortunately, irreversible sticking of particles in the aerosol phase, due to short range inter-particle attractive forces (commonly represented by hard-sphere Hamaker forces) [10], offer little ability to slow down coagulation. The resulting coagulation in the gas phase leads to a self-similar aggregate structure, which is commonly quantified by the universal fractal dimension (D_f) of ~1.8[11]. To manipulate or otherwise slow coagulation, researchers have explored repulsive

interactions such as unipolar charging, however this is quite challenging as uniform charging is typically inefficient, and very size dependent [12–14].

Relatively little work has been done to manipulate the fractal character of aggregates. In liquids dipolar interactions between particles can induce directional control of attractive and repulsive forces, which has been shown to form linear low-dimensional aggregates[15]. Through both experiments and simulations, it has been shown that liquid phase particles can be assembled into linear chains through induction of electric and magnetic dipolar interactions[15–18]. Apart from conservation of surface area, the linear assembly of particles have several applications in materials processing and design for mechanical and electromagnetic applications[19–21]. To our knowledge no previous experimental attempts have been made to assemble nanoparticles in aerosol phase which are in the free molecular regime. Also, the possibility of such an assembly in the aerosol phase have not been justified through theory or simulation before. Recently, our group has been able to synthesize nanoparticles (~10-20 nm) of ferromagnetic materials, Fe and Ni, from an electromagnetically levitated metal droplet and found that the magnetic field used for levitation, can be also be used to assemble any ferromagnetic particles into linear aggregates [22].

In this study I have combined the theories on Langevin dynamics of aerosol particles with the thermodynamics of ensemble of interacting particles, to perform a hybrid ensemble/cluster-cluster aggregation Monte Carlo simulation, of the aggregation and assembly of ferromagnetic particles in an applied magnetic field. I have considered different primary particle sizes in the range 5-500 nm, at various temperatures 300-1500

K, which cover both free molecular and transition regimes. I have shown that if the magnetic field is higher than a critical threshold, aggregate structure transitions from $D_f \sim 1.8$ to $D_f \sim 1$. As the assembly is heavily dependent on the particle size and temperature, the range of size and temperature for successful assembly have been evaluated along with the threshold magnetic field. Doing similar simulations with electric dipoles in electric field, a comparison has been drawn between the practical achievability of the threshold fields required in both cases. Time scales of magnetization of the primary particles of different sizes have been estimated to determine the sizes for which the induced magnetic dipolar alignment will be in equilibrium with the applied field, a condition which will ensure uniform interactions, and hence tunable assembly.

8.3 Theory, model and simulation procedure

8.3.1 Langevin Equation in an ensemble of magnetic dipoles

The Langevin equation of motion has been shown to accurately explain the dynamics of small aerosol particles and aggregates in both ballistic and diffusive time scales in the free molecular and transition regime [23,24] . Several studies have also employed this equation to develop collision kernel by simulation of coagulation [25–29] and charging processes [12–14,26,30,31] of fractal aggregates in the aerosol phase which have also been experimentally validated [32,33]. The situation of interest to us, the presence of an external magnetic field (H-field), ferromagnetic particles and aggregates have a net magnetic anisotropy along the direction of the magnetic field. As a result of the field induced anisotropy, the particle and particle aggregates behave as magnetic dipoles, and interact with each other through dipole-dipole interactions. The Langevin equation of 1-D motion

of particles and aggregates moving in an ensemble with other similar entities can be represented by:

$$m\frac{d^2x}{dt^2} = -\xi\frac{dx}{dt} + \tilde{F}(t) + F_H \qquad (1)$$

where m is the mass of the entity, ξ is the drag co-efficient, $\tilde{F}(t)$ is the random Brownian force acting on the entity which satisfies $\langle\tilde{F}(t)\rangle = 0$ and $\langle\tilde{F}(t)\tilde{F}(t')\rangle = 2\xi k_B T\delta(t-t')$ [34]. F_H, which is not present in the original Langevin equation for non-interacting particles, is the force on the entity due to dipolar interactions with other entities in the ensemble. As the dipolar interactions are short-ranged compared to the mean-displacement of the particles, F_H insignificantly affects the overall kinetics of the ensemble and can be ignored. However, it has a significant effect on the stability and structure of the aggregates. Hence, I have derived the expressions of the kinetic variables in the simulation solely based on the Brownian dynamics, by dropping the F_H term and only considering $\tilde{F}(t)$. The thermodynamics of the magnetic interactions have been dealt with by assuming the particles to be in a canonical (constant temperature) ensemble, which implies the average kinetic energy of the overall ensemble is conserved. After neglecting F_H, and by multiplying *x* on both sides of eqn(1), doing a derivative transformation, applying the equipartition theorem ($m\langle v^2\rangle = k_B T$) and taking ensemble averages of the variables, (section S.1, supplemental) I arrive at the time dependent solution of the mean square displacement, $\langle x^2(t)\rangle$ as given by eqn(2)[35],

$$\langle x^2(t)\rangle = \frac{2k_B T}{\xi}\left(t - \frac{m}{\xi} + \frac{m}{\xi}e^{-\frac{\xi t}{m}}\right) \qquad (2)$$

For the ballistic limit, $t \ll \frac{m}{\xi}$, I can approximate the exponential term in eqn(2) by a third order series expansion, so that $\langle x^2(t)\rangle$ is given by $\langle x^2(t)\rangle = \frac{k_B T}{m} t^2$, which implies that the 3-D root-mean-squared displacement over the characteristic time scale $\frac{m}{\xi}$, also known as the persistence length (l_a) will be given, by:

$$l_a = \frac{\sqrt{3k_B T m}}{\xi} \tag{3}$$

In the free molecular regime ξ is given by: [23],

$$\xi = 4\pi\delta P \sqrt{\frac{m_g}{3k_b T}} r_p^2 N \tag{4}$$

where m_g is the mass of the ambient gas molecule, P is the ambient pressure (1 atm), δ is the accommodation coefficient (1.44 assuming N_2)[36], r_p is the radius of the primary particle, and N is the number of primary particles in the aggregate. In eqn(3) m scales with the mobility radius (R_m) of the aggregate. It is known that R_m of aggregates formed by cluster-cluster aggregates scales with N as, $R_m \sim N^{\frac{1}{2}}$ [37], and the aggregate mass, $m = m_p N$, m_p being the mass of primary particle in the aggregate. Substituting for m and ξ from eqn(4) into eqn(3), the persistence length is given given by:

$$l_a = \frac{3k_B T}{4\pi\delta P} \sqrt{\frac{m_p}{m_g}} r_p^{-2} N^{-\frac{1}{2}} \tag{5}$$

The special case of $N=1$, is the persistence length of a monomer (l_0)[23]. Physically, the persistence length signifies the length scale of ballistic linear motion of the primary

particles or aggregates, as depicted in the schematic in Figure 8-1. For small nanoparticles ~10 nm, in the free molecular regime, ballistic motion dominates the trajectory, and the persistence length is several times the diameter which implies that the particles will move several diameters without changing direction as shown by a representative trajectory in Figure 8-1. In the diffusive limit, $t \gg \frac{m}{\xi}$ the 3-D mean squared displacement is equal to $\frac{6k_BT}{\xi}$, as given by the Einstein model[35]. For the diffusive limit, the persistence length is smaller, or on the order of the particle diameter, and the particle changes direction randomly, also shown in Figure 8-1. For simulating aggregation of small particles in aerosol phase at high temperatures, accurately mimicking the ballistic limit is crucial.

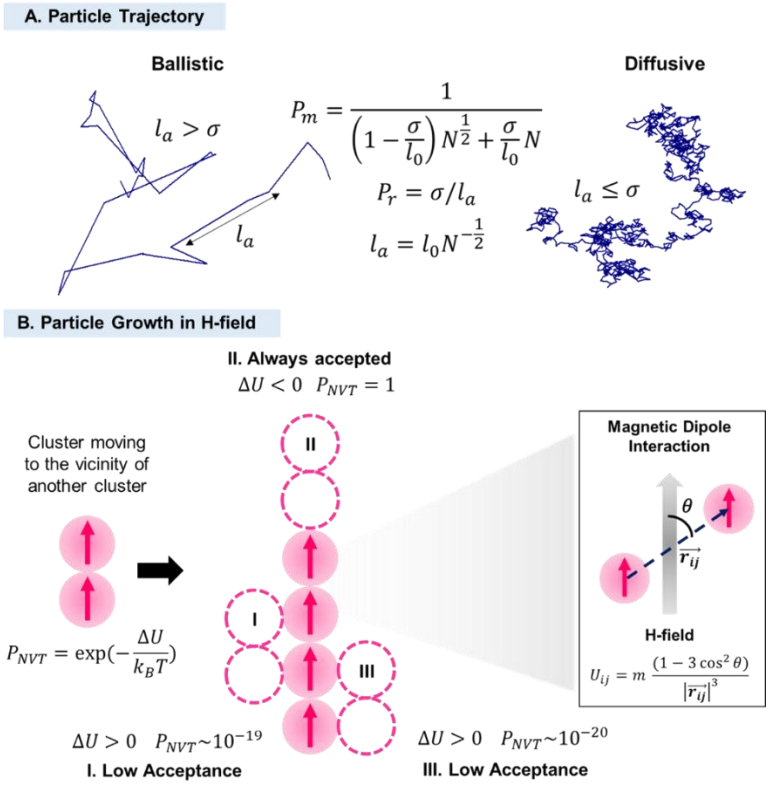

Figure 8-1 Graphical representation of the simulation method, the movement trajectories (A), aggregate growth (B) and the magnetic dipolar interactions

8.3.2 Pairwise dipolar interaction potential in H-field

The potential energy (U_{ij}) of pairwise interaction between two spherical particles with magnetic dipoles with dipole moments $\vec{\boldsymbol{p}}_i$and $\vec{\boldsymbol{p}}_j$is given by:[16],

$$U_{ij} = \frac{1}{4\pi\mu_0\left|\vec{\boldsymbol{r}}_{\boldsymbol{ij}}\right|^{\mathbf{3}}}\left[\vec{\boldsymbol{p}}_i.\vec{\boldsymbol{p}}_j - \frac{3\left(\vec{\boldsymbol{p}}_i.\vec{\boldsymbol{r}}_{\boldsymbol{ij}}\right)\left(\vec{\boldsymbol{p}}_j.\vec{\boldsymbol{r}}_{\boldsymbol{ij}}\right)}{\left|\vec{\boldsymbol{r}}_{\boldsymbol{ij}}\right|^{\mathbf{2}}}\right] \tag{6}$$

When the magnitude of both dipoles are equivalent and aligned in the same direction as H-field, U_{ij} can be represented in scalar form as:

$$U_{ij} = \frac{p^2(1-3\cos^2\theta)}{4\pi\mu_0\left|\vec{\boldsymbol{r}}_{\boldsymbol{ij}}\right|^{\mathbf{3}}} \tag{7}$$

where μ_0 is the permeability of free space, p is the magnitude of the dipoles, θ is the angle between $\vec{\boldsymbol{r}}_{\boldsymbol{ij}}$ and the H-field, a graphical representation of which has been shown in the schematic in Figure 8-1. Both eqn(6) and (7), are for the $\left|\vec{\boldsymbol{r}}_{\boldsymbol{ij}}\right| \geq \boldsymbol{\sigma}$**.** The magnitude of the dipole moment is related to both material properties, and the strength of H-field, by $p = \alpha\sigma^3 H$, where σ is the spherical particle diameter, H is the strength of the applied magnetic field, and α is the polarizability. The polarizability is related to the relative permeability (μ_r) of the material by:

$$\alpha = 4\pi\mu_0\left(\frac{\mu_r - 1}{\mu_r + 2}\right) \tag{8}$$

For ferromagnetic materials (Fe, Co, Ni etc.) in presence of an applied magnetic field, μ_r is large and ranges between ~10^2-10^3 [38–40]. Hence for ferromagnetic materials since $\mu_r >> 1$, $\left(\frac{\mu_r-1}{\mu_r+2}\right) \sim 1$, makes $\alpha \sim 4\pi\mu_0$ a constant for all ferromagnetic materials. For

paramagnetic materials, $\mu_r = 1$, which makes $\alpha = 0$, and hence there is no magnetic dipolar interactions. Since, α is a constant for ferromagnetic materials, the dipole moment is only a function of σ and H. To non-dimensionalize the interaction potential for simulation purposes, σ is used as the unit of length and $k_B T_0$ (T_0=300 K) as the unit of energy. In non-dimensionalized form, eqn(7) will become $U_{ij} = \frac{q(1-3\cos^2\theta)}{r_{ij}^3}$, where r_{ij} is the non-dimensionalized radial distance between two particles and $q = \frac{p^2}{4\pi\mu_0\sigma^3 k_B T_0}$ having dimension of energy. This implies the pairwise interaction energy which depends on $q \sim \sigma^3 H^2$, can be tuned by both particle size and strength of the magnetic field.

8.3.3 Hybrid Canonical Ensemble/Cluster-Cluster Aggregation Monte Carlo simulation of Magnetic dipoles

The off-lattice MC simulation is performed with an initial configuration of 1000 primary particles of size σ placed in a cubic box of size $L = 60\sigma$. The simulations initiate with the motion of primary particles in an ensemble. After the appearance of the clusters due to collision and aggregation of the primary particles, movement of the clusters are also included for the remainder of the simulation. At every Monte Carlo step, a particle or an aggregate is chosen at random from the ensemble, and a decision is made on whether the chosen entity will be moved based on its mobility, imposing the diffusion limitation. The acceptance probability (P_m) of this decision depends inversely with the mobility radius (i.e. smaller aggregates are more likely to move) which is a function of number of primary particles in the aggregate (N) as given by:

$$P_m = \frac{1}{\left(1 - \frac{\sigma}{l_0}\right) N^{\frac{1}{2}} + \frac{\sigma}{l_0} N} \quad (9)$$

The first term in the denominator represents the pure ballistic case when $\sigma \ll l_0$, whereas the second term represents the pure diffusive case when $\sigma = l_0$. The ballistic and diffusive regimes in the trajectory of the moving particle or aggregate is replicated by the fact that the chosen entity will move linearly over a distance of l_a before randomly changing direction under the influence of background gas. This is ensured by making a decision whether the particle or aggregate will keep moving in the same direction or assigned a new direction, determined by the probability P_r:,

$$P_r = \sigma / l_a \quad (10)$$

The center of mass of the selected aggregate is displaced by σ in the chosen direction. The move is then accepted or rejected based on an energy test, which compares the total energy due to magnetic interactions in the microstates before and after the move. The system follows the thermodynamics of canonical (NVT) ensemble. Hence, the acceptance probability (P_{NVT}) is:[4142]

$$P_{NVT} = \exp\left(-\frac{\Delta U}{k_B T}\right) \quad (11)$$

where $\Delta U = \sum_{final} U_{ij} - \sum_{initial} U_{ij}$, is the difference in net pairwise interaction potentials in the initial and the final states. Once the decision is made to accept the move, the non-dimensionalized time is incremented by $1/N_t$, where N_t is the total number of entities in the ensemble including both aggregates and isolated primary particles (monomers). The unit of time is given by the characteristic time-scale of m/ξ normalized

by the persistence length. When two lone primary particles or primary particles belonging to two different aggregates moves within a center to center distance of $< 1.1\sigma$, they are assumed to have collided and stuck irreversibly. The simulation is run till the number concentration of the monomers decreases to <10 % of the initial value. Periodic boundary conditions with minimum image convention has been considered throughout the simulation.

8.3.4 Stability analysis of Magnetic dipolar aggregates

The aggregation time-scales are estimated by the homogeneous monomer collision approximation of the Smoluchowski's equation, which is given by $n_1(t) = \frac{n_0}{1+n_0 Kt}$ where $n_1(t)$ is the number concentration of monomers at time *t*, n_0 is the initial number concentration of monomers and *K(1,1)* is the monomer collision kernel[36]. In the continuum regime, *K* is related to the medium viscosity (η), ~1.8x10^{-5} Pa-s for N_2, and temperature (T) as $K = 8k_BT/3\eta$ [8]. In free molecular regime, *K* is related to particle diameter (σ), density (ρ) and *T* by $K = 4\left(\frac{6\sigma k_B T}{\rho}\right)^{1/2}$ [43].

However, the attractive particle interaction introduced by the H-field enhances *K*, increasing the coagulation rate. Hence, a correction factor (*W*) have been derived (section S.2, supplemental) for both free molecular (W_{FM}) [31]and continuum (W_C) [8,44] regimes to estimate the coagulation kernel in the magnetic field (K_m), $K_m = KW$. The non-dimensionalized expressions of W_{FM} and W_C are given by:

$$W_{FM} = 2\int_0^\infty e^{-v^2} v^3 \left(1 + \frac{q}{2T'v^2}\right) dv \qquad (12)$$

$$W_C = \frac{1}{\int_1^\infty \frac{exp\left(-\frac{q}{2r_{ij}^3 T'}\right)}{r_{ij}^2} dr_{ij}}$$

where $T' = k_B T / k_B T_0$ is the non-dimensionalized parameter for thermal energy, v is the non-dimensionalized velocity, $q = \frac{p^2}{4\pi\mu_0 \sigma^3 k_B T_0}$, as shown in section 2.2 is a non-dimensional measure of the magnetic interaction energy. The non-dimensionalized form of transition regime *K* derived by more recent mean first passage time regression studies [25,31], is a function of the diffusive Knudsen number (Kn_D). Accounting for the magnetic field enhancement correction in Kn_D, $Kn_D = \frac{\sqrt{2k_B T m_p} W_C}{6\pi\eta\sigma^2 W_{FM}}$, the enhanced transition regime kernel can be estimated [31] (section S.2, supplemental). The corrected kernel, K_m has been used to estimate the half-life of the monomer concentration, to draw comparison between the theoretical and simulated coagulation time-scales, which is compared with the magnetic domain relaxation and H-field oscillation time-scales to determine the conditions for which the simulation is applicable. All theoretical estimations have been done using material properties of Fe for the particle and N_2 for the medium.

8.4 Results and discussions

8.4.1 Aggregate shape transition with H field

The aggregation of non-interacting or weakly-interacting nanoparticles in the aerosol phase formed by diffusion limited cluster aggregation (DLCA), leads to the

formation of aggregates of universal fractal dimension, D_f ~1.8. However, the presence of sufficiently strong inter-particle interactions can change the aggregation rate and assembly process leading to an altered fractal dimension. In our case I are applying a strong external magnetic field. Figure 8-2(a) shows visual representations of aggregates formed by primary particles of size $\sigma = 10\ nm$ at *T=1500 K*, in absence and presence of H-field. In absence of an external H-field typical DLCA aggregate of D_f ~1.7 is obtained. In the presence of H-field of strength 450 kA/m, induced magnetic dipole moments of the primary particles, influence the aggregation process, and low dimensional (D_f ~1.5) aggregates are obtained. When stronger H-fields (650 kA/m) are applied, the increased induced dipole strength leads to the formation of linear, chain-like 1-D aggregates.

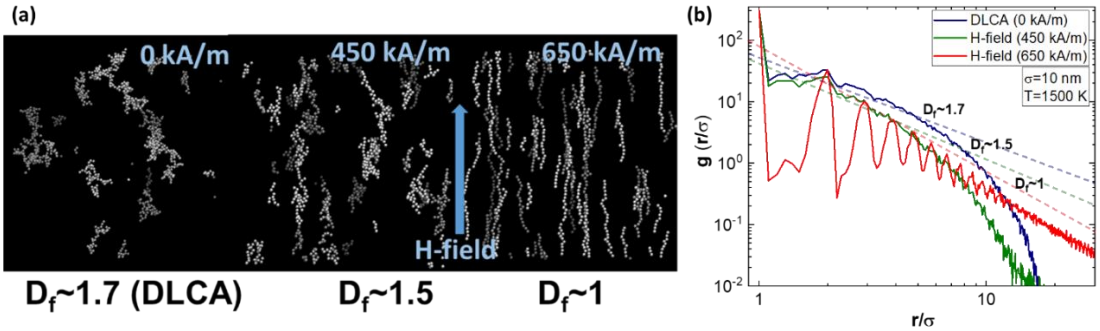

Figure 8-2 Visual representation of DLCA aggregates (in absence of H-field), low dimensional aggregates and linear chain-like aggregates in presence of H-field~450 kA/m and 650 kA/m respectively, (b) Pair-correlation function of DLCA aggregates with D_f*~1.7* (in absence of H-field), low dimensional aggregates with D_f*~1.5* (H-field~450 kA/m) and linear aggregates with D_f*~1* (H-field~650 kA/m) having peak and valley features, for ferromagnetic primary particles of size 10 nm at 1500 K.

Figure 8-2(b) shows the intra-cluster pair correlation function $g(r/\sigma)$ averaged over all the aggregates formed in the ensemble in presence and absence of the H-field. The D_f is estimated from the scaling law of $g\left(\frac{r}{\sigma}\right) \sim \left(\frac{r}{\sigma}\right)^{3-D_f}$. The typical feature of the pair

correlation function of DLCA aggregates in a log-scale consists of the highest peak at $r = \sigma$ due to occupied nearest neighbor sites, followed by a peak at $r = 2\sigma$, as only those second nearest neighbor sites are occupied which lie along the same linear direction as that of the first occupied nearest neighbor. This feature suggests a shape that has lower dimensionality than 2. A linearly decreasing trend follows the second peak and is used to estimate the D_f. The linear trend is terminated by a sharply decreasing cut-off region which follows the trend $\sim\exp\left(-\frac{r}{R_g}^{\gamma}\right)$, R_g being the radius of gyration and γ~2-2.5 (supplemental Figure S2), as also observed by several studies[37,45,46]. In Figure 8-2(b), the pair-correlation function of the aggregates formed in absence of the H-field has all the features as that of typical DLCA, with the estimated $D_f \sim 1.7$. In the presence of 450 kA/m H-field the slope of the linear scaling region increases due to a smaller D_f ~1.5,whereas in presence of stronger 650 kA/m H-field, the pair-correlation function has some additional peaks and valleys features, with an estimated $D_f \sim 1$. The peaks and valleys are at integral multiples of particle diameter (σ),and signifies that all the occupied neighboring sites lie along the same linear direction which in-turn signifies the formation of linear chain-like 1D structures. The peak values of straight linear chains of spheres exactly follows the power law, and the cut-off region arising due to dissimilar lengths follows the trend $e^{-r^{\gamma}}$ (supplemental, Figure S3 and S4).

The fact that the linear structures are also aligned along the direction of H-field suggests that aggregate growth has been favored only in a unique direction, as the attractive potential is strongest at the terminal edges of the aggregates whereas the repulsive potential is strongest at the lateral edges. Hence, from both the visual representation, and the pair-

correlation function it can be said that both the dimensionality and the directionality of growth of ferromagnetic particles can be tuned by applying an external H-field. However, significant high magnitude of magnetic dipole interactions are required to overpower the random Brownian fluctuations. Since, the magnetic interactions depend on σ and H, whereas the Brownian fluctuations are dependent on σ and T, it is essential to study the manner in which the combination of these variables affect the overall aggregation process, analysis of which is done in the subsequent sections.

8.4.2 Aggregate shape transition with temperature for a constant H-field

Figure 8-3(a) shows the visual representation of aggregates formed by primary particles of size $\sigma = 10\,nm$, in an applied H-field strength of *450 kA/m*, at different temperatures 300-1500 K. From Figure 8-3(a) it is evident that the aligned and linear aggregate growth is most prevalent at lower temperatures (300-500 K), where Brownian dynamics are slower. Figure 8-3(b) shows that the pair-correlation function loses the peak and valley features above 500 K, consistent with the structure images. However, the aggregates obtained at 1000 K ($D_f \sim 1.2$) and 1500 K ($D_f \sim 1.5$) are low dimensional compared to DLCA aggregates ($D_f \sim 1.7$) obtained in the absence of field.

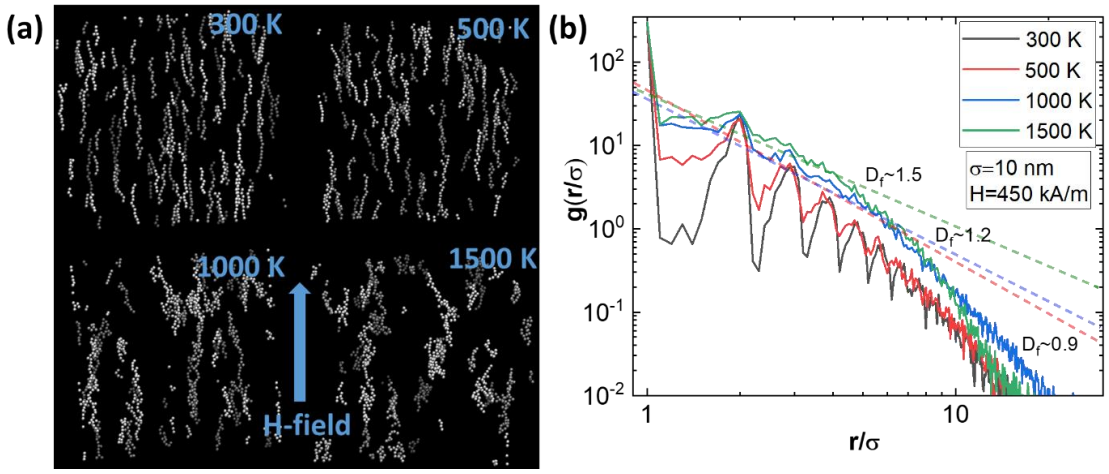

Figure 8-3 Visual representation (a) and pair-correlation function (b) of aggregates formed by ferromagnetic primary particles of size 10 nm in presence of H-field (450 kA/m) at different temperatures (300-1500 K). The linearity in the visual representation and the peak-valley features in the pair-correlation function are only retained till 500 K.

Even though the fractal dimension is changed at higher temperature, according to Figure 8-3 (a) the alignment with the H-field is still retained. This is because the growth is initiated with occupancy of the nearest neighboring sites, which involves strong dipolar interactions responsible for growth in the direction of H-field. However, the r^{-3}, decaying interaction strength, might not be enough to influence the collisions at further neighboring sites.

8.4.3 Threshold field intensity for directed linear assembly

As the assembly into linear aggregates is dependent on primary particle size and temperature, I evaluate the threshold H-field strength required for successful assembly. Figure 8-4 shows the threshold H-field strength required for successful assembly for different primary particle sizes at different temperatures. The field strengths at which more than 4 peaks at integral multiples of the monomer diameter, appear in the pair-correlation

functions, are considered to be the threshold. The required threshold decreases with increase in particle size. However, temperature only affects the lower particle sizes which follow ballistic trajectory. Hence, temperature only affects the aggregation in the ballistic regime, while size affects both ballistic and diffusive regimes. In the ballistic limit of the free-molecular regime, a strong external force is required to influence the trajectories of particles having very high persistence lengths. The directional repulsive interactions at the lateral edges ($\theta > 0\ or < \pi$) of the aggregates are most important for the formation of linear chains. In a simple 1-D model of one monomer approaching another monomer, with mean velocity $\sqrt{\frac{k_B T}{m_p}}$ along a direction perpendicular to the applied magnetic field ($\theta = \frac{\pi}{2}$), the condition $\frac{F_H}{m_p} \geq \sqrt{\frac{k_B T}{m_p}} \frac{\xi}{m_p} \frac{\sigma}{l_0}$ should hold, for the repulsive force of one monomer to negatively accelerate the approaching monomer to a stationary state, at a minimum separation of σ (supplemental,S.4). The field equivalent to generate the minimum repulsive force to satisfy the above condition, is the threshold field required for the linear assembly. Deriving F_H from 1-D version of eqn(7), one can arrive at the equation $\frac{H_{th}\sigma^{1.5}}{T^{0.5}} = C$, where H_{th} is the threshold H-field,and C is a constant (supplemental, S.4). This approximately explains the trend observed in Figure 8-4 as well as the negative slope of ~-1.7-1.9 in the logarithmic version of Figure 8-4 (supplemental, Figure S1)

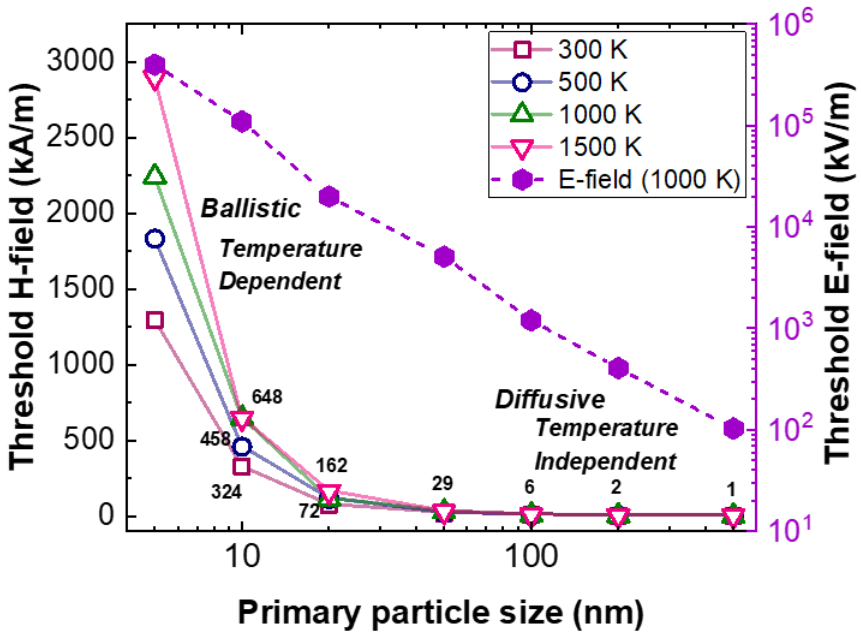

Figure 8-4 Threshold H-field required for linear assembly (D_f~1) for different primary particle sizes (5-500 nm) and at different temperatures (300-500 K). Threshold E-field for the same assembly for same primary particle sizes at 1000 K has been shown for comparison. Ballistic trajectory contributes to the temperature dependence.

For a comparison, a case of the threshold electric field (E-field) required for assembly of pre-aligned electric dipoles in ferroelectric particles at 1000 K, obtained by doing simulations in the same manner (details in supplemental, section S.5), has also been presented. It is evident that the threshold E-fields required for successful assembly of primary particle sizes <100 nm are beyond practicality, as the required fields exceed the breakdown field strength of air and most inert gases (~3000 kV/m)[47].

8.4.4 Coagulation time scales and kernel homogeneity

To understand growth kinetics the simulation was initiated with a number concentration of ~4x10^{21}/m^3 monomers. The monomer concentration was tracked and the simulation time-steps converted to real time by the scaling discussed in section 2.2. Figure 8-5(a) shows the depression in monomer ($\sigma = 10\ nm$) concentration with increasing time for different H-field strengths at 1500 K. The strong attractive forces due to the H-field, increases the coagulation rate, and this effect is observed even for field strengths below the threshold field strength required for assembly. The inset of Figure 8-5(a) shows the decreasing half-life ($t_{1/2}$) of the monomer concentration with increasing H-field strengths, resulting from the enhanced coagulation rates.

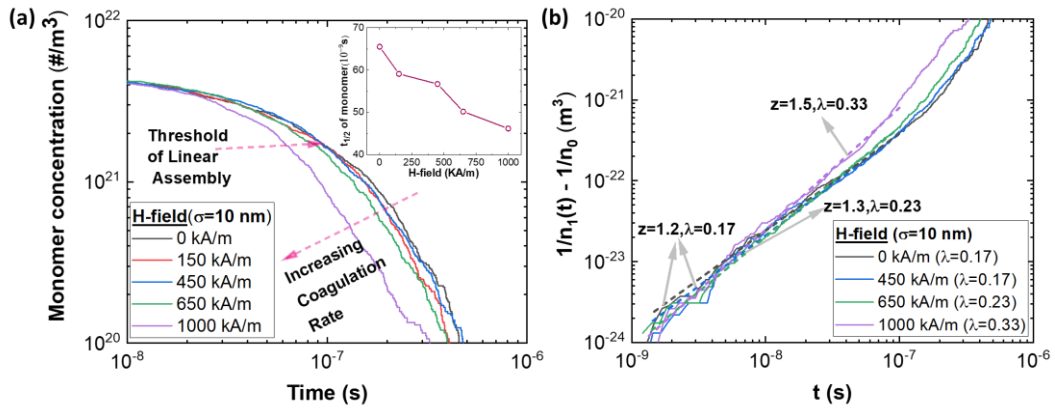

Figure 8-5 (a) Monomer (10 nm) concentration with time from the simulation at 1500 K. Rate of decrease in monomer concentration increases with H-field strength. Inset shows the half-lives ($t_{1/2}$) of the monomers decreases with increase in H-field strength. (b) Estimation of the homogeneity of the coagulation kernel (λ), which increases with increase in for the applied H-field strength.

The coagulation of fractal aggregates follows $\frac{1}{n_1(t)} - \frac{1}{n_0} = Kt^z$, where $z = \frac{1}{1-\lambda}$, λ being the homogeneity of the coagulation kernel [23]. Figure 8-5(b) shows the log-log plot of this equation at various applied field strengths, where z and λ, have been estimated from

the slope of the linear trend upto 10^{-7} s. z decreases whereas λ increases, with an increase in H-field strength.

8.4.5 Magnetization vs coagulation rates of linear assembly of ferromagnetic and superparamagnetic particles

The simulation starts with the assumption that all the primary particles are pre-magnetized with a net magnetic anisotropy in the form of dipoles, either in parallel ($\theta = 0$) or anti-parallel ($\theta = \pi$) to the applied H-field, typically known as the discrete-orientation approximation [48]. For static, ferromagnetic particles, at temperatures below the Curie point, this approximation holds true when a sufficiently high H-field is applied such that the thermal fluctuation energy ($k_B T$) is negligible compared to the demagnetization potential energy ($2pHcos\theta$)[49]. The demagnetization potential associated with the required threshold fields (Figure 8-4) at different temperatures, are orders of magnitude higher than the respective thermal energy (Table S1). In the case of an oscillating H-field, this approximation implies that the oscillation frequency of the dipoles will be equal to that of the field. However, for ferromagnetic particles undergoing Brownian dynamics at temperatures below the Curie point, the discrete-orientation approximation will hold true only if the period of oscillation of the dipoles (i.e.H-field), is faster than coagulation.

At temperatures above the Curie point or at weaker H-fields, the demagnetization potential will be comparable or less than the thermal energy. In this case, the approximation will still apply for sub-50 nm ferromagnetic particles which are nominally single domain and hence exhibit superparamagnetism[50], only if the demagnetization time-

scales are small compared to both H-field period [48] and coagulation time-scales. The net magnetic anisotropy or dipole needs to relax to a de-aligned state (zero-energy) from an aligned state (lowest energy), faster than the rate of change of the H-field, in order to keep the dipole always in an equilibrium alignment with the field. For superparamagnetic particles undergoing Brownian dynamics, the fast relaxation can be caused by either intra-particle domain relaxation by electronic spin exchange which can be estimated from the the Néel relaxation time (τ_s) [51,52] or domain relaxation by external Brownian rotation. The Brownian rotational time-scales (τ_B) have been estimated by considering ballistic and diffusive rotations in free-molecular and transition regimes (supplemental, S6). The net domain relaxation time scale is the harmonic mean of the Néel relaxation and the Brownian rotational relaxation time-scales, as given by $\tau_{net} = \frac{\tau_s \tau_B}{\tau_s + \tau_B}$ [53]. The values estimated for each of these time-scales have been presented in Tables: S3-S6.

To estimate the theoretical coagulation time-scales, the Smoluchowski's coagulation kernel has been corrected for both free molecular and transition regimes as described in section 2.3, and the theoretical $t_{1/2}$ has been estimated using the corrected kernel. Figure 8-6(a) shows the enhancement factors, and $t_{1/2}$ values estimated from the corrected theoretical kernel, at different applied field strengths, for 10 nm particles at 300 K (transition) and 1500 K (free molecular). The $t_{1/2}$ values estimated from theory at 1500 K, approximately has the same order of magnitude, compared to the $t_{1/2}$ values estimated from the simulation at 1500 K (Inset,5(a)). The approximate match between the theoretical and computational $t_{1/2}$, and the estimation of interaction dependent coagulation rates in

both regimes, enables us to use the theoretical equation to estimate the coagulation time-scales of an ensemble of monomers, with practical aerosol phase number concentrations of 10^{14}-10^{18}/m^3 [8].

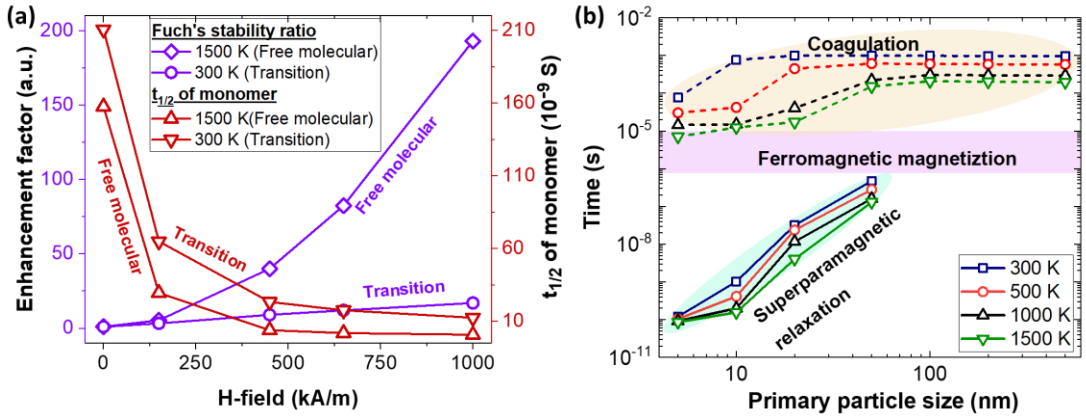

Figure 8-6 (a) Enhancement factor and comparison between theoretically estimated monomer half-lives ($t_{1/2}$) of free-molecular (1500 K) and transition regime (300 K). (b) Comparison between time-scales of superparamagnetic domain relaxation, ferromagnetic magnetization (H-field oscillation) and coagulation, for primary particle number concentration (10^{18}/m^3), for different primary particle sizes (5-500 nm) and different temperatures (300-1500 K).

Figure 8-6(b) shows the comparison between time-scales of superparamagnetic domain relaxation, ferromagnetic magnetization (H-field oscillation) and coagulation for different primary particle sizes, at different temperatures. For this comparison, the coagulation time-scales have been estimated theoretically for a practical aerosol number concentration of 10^{18}/m^3. As commonly applied H-fields have oscillation time-period (10^5-10^6 Hz) smaller than the coagulation time-scales, the discrete-orientation approximation will be consistent for all particle sizes below Curie temperature, at these frequencies. For sub-50 nm primary particle sizes, time-scales of superparamagnetic relaxation are shorter by orders of magnitude compared to the standard time period of oscillation of the H-field.

This implies that sub-50 nm particles will always be in an equilibrium alignment with the field, and will follow the oscillation of the field, at any field strength and temperature. Also, since both the relaxation time and the time period of oscillation is shorter by orders of magnitude compared to the coagulation time-scales, the discrete-orientation approximation will be consistent for the super-paramagnetic particles at all sizes and temperatures.

As discussed in section 3.3, the threshold H-fields required for linear assembly of primary particle sizes $\geq 10\ nm$, are practically achievable at temperatures between 300-1500 K. Hence, if the applied field is higher than the threshold field, all ferromagnetic particles can be linearly assembled at temperatures below their respective Curie points. Above, the Curie point, only super-paramagnetic particles in the size range 10-50 nm can be assembled. Table 7-1 shows the summary of the design parameters applicable to linearly assemble Fe, Ni and Co, which show both ferromagnetism and superparamagnetism.

Table 8-1 Design parameters required for the linear assembly of Fe, Co and Ni

Material	**Curie point** [54] **(K)**	**H-field Frequency (Hz) /strength (kA/m)**	**Ferromagnetic assembly**		**Superparamagnetic assembly**	
			Size (nm)	**T (K)**	**Size (nm)**	**T (K)**
Fe	1043	10^6-10^5/10-10^3	10-500	300-1043	10-50	>1043
Co	1400	10^6-10^5/10-10^3	10-500	300-1400	10-50	>1400
Ni	627	10^6-10^5/10-10^3	10-500	300-627	10-50	>627

Alloys of Fe, Co and Ni with para-magnetic metals such as Al, Cu, Pd etc. also shows ferromagnetic and super-paramagnetic behavior[55–58]. Hence, para-magnetic metal

particles like Al, Cu, Pd etc. when alloyed with Fe, Co and Ni can also be linearly assembled with an external H-field. Pulsed laser ablation, flame synthesis, chemical vapor deposition[1], inert gas condensation [59] are some of the most common aerosol routes to synthesize both monometallic and alloyed metal particles. Using the parameters represented in Table 7-1, one can design a magnetic coil in the vicinity of the substrates or chambers used in these synthesis procedures, to apply an oscillating magnetic field of desired strength, to direct the assembly of magnetic, metal and alloyed-metal nanoparticles.

8.5 Conclusion

Cluster-cluster aggregation simulations, typically used to understand aggregation and assembly processes in colloidal systems[15,17,34,46,60–63], have been employed through a hybrid Monte Carlo method, to demonstrate that externally applied magnetic fields can be used to direct the assembly of aerosol nanoparticles of ferromagnetic materials (Fe, Co, Ni etc), in both free-molecular and transition regimes. Application of an external field (electric or magnetic) induces a net magnetic dipole moment, within ferromagnetic (or ferroelectric) particles, which interact with each other through directional attraction and repulsion, ultimately leading to the growth of linear chain-like aggregates, as shown by several studies in the continuum regime[18]. However, in aerosol systems where the free-molecular and transition regimes are also simulated, a significant structure transition from D_f~1.8 have not been found earlier[23,25,37,45]. The simulations performed in this study indicate that magnetic dipolar interactions induced by external H-field can be used to cause such structure transition from the universal D_f~1.8 to D_f~1, which have been also found in our experimental study [22]. By performing simulations for different particle sizes 5-500 nm and

different temperature 300-1500 K, I find that the threshold H-field strength required for the linear assembly is both particle size and temperature dependent in the size range 5-50 nm. The threshold H-fields required for 10-100 nm particles are practically achievable, whereas the corresponding E-field threshold will be beyond breakdown strength of air. Given that the applied H-field is higher than the threshold, through analysis of the coagulation and magnetization time-scales, I show that primary particle sizes <50 nm will be magnetized and hence linearly assembled, at all temperatures. The results published in this work will be useful to material designers working on scalable fabrication of metal and alloyed metal nanocomposites in gas phase, with tunable micro-structural features, enabling possibilities for density, mechanical, and optical property modulation in the final materials of interest.

8.6 References

(1) Swihart, M. T. Vapor-Phase Synthesis of Nanoparticles. *Current Opinion in Colloid and Interface Science*. 2003. https://doi.org/10.1016/S1359-0294(03)00007-4.

(2) Ullmann, M.; Friedlander, S. K.; Schmidt-Ott, A. Nanoparticle Formation by Laser Ablation. *Journal of Nanoparticle Research* **2002**. https://doi.org/10.1023/A:1022840924336.

(3) Franklin, A. D.; Luisier, M.; Han, S. J.; Tulevski, G.; Breslin, C. M.; Gignac, L.; Lundstrom, M. S.; Haensch, W. Sub-10 Nm Carbon Nanotube Transistor. *Nano Lett* **2012**. https://doi.org/10.1021/nl203701g.

(4) Kelesidis, G. A.; Goudeli, E.; Pratsinis, S. E. Flame Synthesis of Functional Nanostructured Materials and Devices: Surface Growth and Aggregation. *Proceedings of the Combustion Institute* **2017**. https://doi.org/10.1016/j.proci.2016.08.078.

(5) Zhong, L.; Kwok, T.; Mangolini, L. Spray Pyrolysis of Yolk-Shell Particles and Their Use for Anodes in Lithium-Ion Batteries. *Electrochem commun* **2015**. https://doi.org/10.1016/j.elecom.2015.02.004.

(6) Yang, Y.; Romano, M.; Feng, G.; Wang, X.; Wu, T.; Holdren, S.; Zachariah, M. R. Growth of Sub-5 Nm Metal Nanoclusters in Polymer Melt Aerosol Droplets. *Langmuir* **2018**, *34* (2), 585–594. https://doi.org/10.1021/acs.langmuir.7b02900.

(7) Yang, Y.; Ghildiyal, P.; Zachariah, M. R. Thermal Shock Synthesis of Metal Nanoclusters within On-the-Fly Graphene Particles. *Langmuir* **2019**. https://doi.org/10.1021/acs.langmuir.8b03532.

(8) Friedlander, S. Smoke, Dust and Haze. Fundamentals of Aerosol Behaviour. **1977**. https://doi.org/10.1016/0004-6981(79)90129-x.

(9) Goddard, E. D. Surfactants and Interfacial Phenomena. *Colloids and Surfaces* **1989**. https://doi.org/10.1016/0166-6622(89)80030-7.

(10) Hamaker, H. C. The London-van Der Waals Attraction between Spherical Particles. *Physica* **1937**. https://doi.org/10.1016/S0031-8914(37)80203-7.

(11) Mountain, R. D.; Mulholland, G. W. Light Scattering from Simulated Smoke Agglomerates. *Langmuir* **1988**, *4* (6), 1321–1326. https://doi.org/10.1021/la00084a021.

(12) Gopalakrishnan, R.; Meredith, M. J.; Larriba-Andaluz, C.; Hogan, C. J. Brownian Dynamics Determination of the Bipolar Steady State Charge Distribution on Spheres and

Non-Spheres in the Transition Regime. *J Aerosol Sci* **2013**. https://doi.org/10.1016/j.jaerosci.2013.04.007.

(13) Gopalakrishnan, R.; Thajudeen, T.; Ouyang, H.; Hogan, C. J. The Unipolar Diffusion Charging of Arbitrary Shaped Aerosol Particles. *J Aerosol Sci* **2013**. https://doi.org/10.1016/j.jaerosci.2013.06.002.

(14) Gopalakrishnan, R.; Hogan, C. J. Coulomb-Influenced Collisions in Aerosols and Dusty Plasmas. *Phys Rev E Stat Nonlin Soft Matter Phys* **2012**. https://doi.org/10.1103/PhysRevE.85.026410.

(15) Mors, P. M.; Botet, R.; Jullien, R. Cluster-Cluster Aggregation with Dipolar Interactions. *J Phys A Math Gen* **1987**, *20* (15), L975–L980. https://doi.org/10.1088/0305-4470/20/15/008.

(16) Ku, J. G.; Liu, X. Y.; Chen, H. H.; Deng, R. D.; Yan, Q. X. Interaction between Two Magnetic Dipoles in a Uniform Magnetic Field. *AIP Adv* **2016**, *6* (2). https://doi.org/10.1063/1.4941750.

(17) Tan, Z. J.; Zou, X. W.; Zhang, W. B.; Jin, Z. Z. Structure Transition in Cluster-Cluster Aggregation under External Fields. *Phys Rev E Stat Phys Plasmas Fluids Relat Interdiscip Topics* **2000**. https://doi.org/10.1103/PhysRevE.62.734.

(18) Helgesen, G.; Skjeltorp, A. T.; Mors, P. M.; Botet, R.; Jullien, R. Aggregation of Magnetic Microspheres: Experiments and Simulations. *Phys Rev Lett* **1988**, *61* (15), 1736–1739. https://doi.org/10.1103/PhysRevLett.61.1736.

(19) Johnson, S. G.; Villeneuve, P. R.; Fan, S.; Joannopoulos, J. D. Linear Waveguides in Photonic-Crystal Slabs. *Phys Rev B Condens Matter Mater Phys* **2000**. https://doi.org/10.1103/PhysRevB.62.8212.

(20) Cintra, E. R.; Ferreira, F. S.; Santos Junior, J. L.; Campello, J. C.; Socolovsky, L. M.; Lima, E. M.; Bakuzis, A. F. Nanoparticle Agglomerates in Magnetoliposomes. *Nanotechnology* **2009**. https://doi.org/10.1088/0957-4484/20/4/045103.

(21) Li, Z.; Wang, M.; Zhang, X.; Wang, D.; Xu, W.; Yin, Y. Magnetic Assembly of Nanocubes for Orientation-Dependent Photonic Responses. *Nano Lett* **2019**. https://doi.org/10.1021/acs.nanolett.9b02984.

(22) Ghildiyal, P.; Biswas, P.; Steven, H.; Mulholland, G. W.; Yang, Y.; Abbaschian, R.; Zachariah, M. R. Magnetic-Field Directed Vapor-Phase Assembly of Low Fractal Dimension Metal Nanostructures: Experiment and Theory (Under Review). *Journal of Physical Chemistry Letters* **2021**.

(23) Heinson, W. R.; Pierce, F.; Sorensen, C. M.; Chakrabarti, A. Crossover from Ballistic to Epstein Diffusion in the Free-Molecular Regime. *Aerosol Science and Technology* **2014**, *48* (7), 738–746. https://doi.org/10.1080/02786826.2014.922677.

(24) Thajudeen, T.; Deshmukh, S.; Hogan, C. J. Langevin Simulation of Aggregate Formation in the Transition Regime. *Aerosol Science and Technology* **2015**. https://doi.org/10.1080/02786826.2015.1008971.

(25) Gopalakrishnan, R.; Hogan, C. J. Determination of the Transition Regime Collision Kernel from Mean First Passage Times. *Aerosol Science and Technology* **2011**. https://doi.org/10.1080/02786826.2011.601775.

(26) Gopalakrishnan, R.; Thajudeen, T.; Hogan, C. J. Collision Limited Reaction Rates for Arbitrarily Shaped Particles across the Entire Diffusive Knudsen Number Range. *Journal of Chemical Physics* **2011**. https://doi.org/10.1063/1.3617251.

(27) Hunt, B.; Thajudeen, T.; Hogan, C. J. The Single-Fiber Collision Rate and Filtration Efficiency for Nanoparticles i: The First-Passage Time Calculation Approach. *Aerosol Science and Technology* **2014**. https://doi.org/10.1080/02786826.2014.938798.

(28) Thajudeen, T.; Hunt, B.; Hogan, C. J. The Single-Fiber Collision Rate and Filtration Efficiency for Nanoparticles Ii: Extension to Arbitrary-Shaped Particles. *Aerosol Science and Technology* **2014**. https://doi.org/10.1080/02786826.2014.938799.

(29) Lindquist, G. J.; Pui, D. Y. H.; Hogan, C. J. Porous Particulate Film Deposition in the Transition Regime. *J Aerosol Sci* **2014**. https://doi.org/10.1016/j.jaerosci.2014.03.007.

(30) Chahl, H. S.; Gopalakrishnan, R. High Potential, near Free Molecular Regime Coulombic Collisions in Aerosols and Dusty Plasmas. *Aerosol Science and Technology* **2019**. https://doi.org/10.1080/02786826.2019.1614522.

(31) Ouyang, H.; Gopalakrishnan, R.; Hogan, C. J. Nanoparticle Collisions in the Gas Phase in the Presence of Singular Contact Potentials. *Journal of Chemical Physics* **2012**. https://doi.org/10.1063/1.4742064.

(32) Li, L.; Gopalakrishnan, R. An Experimentally Validated Model of Diffusion Charging of Arbitrary Shaped Aerosol Particles. *J Aerosol Sci* **2021**. https://doi.org/10.1016/j.jaerosci.2020.105678.

(33) Li, L.; Chahl, H. S.; Gopalakrishnan, R. Comparison of the Predictions of Langevin Dynamics-Based Diffusion Charging Collision Kernel Models with Canonical Experiments. *J Aerosol Sci* **2020**. https://doi.org/10.1016/j.jaerosci.2019.105481.

(34) Jungblut, S.; Joswig, J. O.; Eychmüller, A. Diffusion-Limited Cluster Aggregation: Impact of Rotational Diffusion. *Journal of Physical Chemistry C* **2019**, *123* (1), 950–954. https://doi.org/10.1021/acs.jpcc.8b10805.

(35) Bian, X.; Kim, C.; Karniadakis, G. E. 111 Years of Brownian Motion. *Soft Matter* **2016**, *12* (30), 6331–6346. https://doi.org/10.1039/c6sm01153e.

(36) Mulholland, G. W.; Mountain, R. D.; Samson, R. J.; Ernst, M. H. Cluster Size Distribution for Free Molecular Agglomeration. *Energy and Fuels* **1988**, *2* (4), 481–486. https://doi.org/10.1021/ef00010a014.

(37) Sorensen, C. M. The Mobility of Fractal Aggregates: A Review. *Aerosol Science and Technology*. 2011. https://doi.org/10.1080/02786826.2011.560909.

(38) Yensen, T. D. What Is the Magnetic Permeability of Iron? *J Franklin Inst* **1928**. https://doi.org/10.1016/S0016-0032(28)90558-X.

(39) Wait, G. R. Magnetic Permeability of Iron and Magnetite in High Frequency Alternating Fields. *Physical Review* **1927**. https://doi.org/10.1103/PhysRev.29.566.

(40) Koskela, P.; Teirikangas, M.; Alastalo, A.; Forsman, J.; Juuti, J.; Tapper, U.; Auvinen, A.; Seppä, H.; Jantunen, H.; Jokiniemi, J. Synthesis of Cobalt Nanoparticles to Enhance Magnetic Permeability of Metal-Polymer Composites. *Advanced Powder Technology* **2011**. https://doi.org/10.1016/j.apt.2010.09.010.

(41) Frenkel, D.; Smit, B. Monte Carlo Simulations in Various Ensembles. In *Understanding Molecular Simulation*; 2002. https://doi.org/10.1016/b978-012267351-1/50007-9.

(42) Moinuddin, M.; Biswas, P.; Tripathy, M. The Effect of Surface Roughness on the Phase Behavior of Colloidal Particles. *Journal of Chemical Physics* **2020**, *152* (4). https://doi.org/10.1063/1.5136080.

(43) Mountain, R. D.; Mulholland, G. W.; Baum, H. Simulation of Aerosol Agglomeration in the Free Molecular and Continuum Flow Regimes. *J Colloid Interface Sci* **1986**, *114* (1), 67–81. https://doi.org/10.1016/0021-9797(86)90241-9.

(44) Mellema, M.; Van Opheusden, J. H. J.; Van Vliet, T. Relating Colloidal Particle Interactions to Gel Structure Using Brownian Dynamics Simulations and the Fuchs Stability Ratio. *Journal of Chemical Physics* **1999**. https://doi.org/10.1063/1.479956.

(45) Sorensen, C. M. Light Scattering by Fractal Aggregates: A Review. *Aerosol Science and Technology* **2001**. https://doi.org/10.1080/02786820117868.

(46) Lattuada, M.; Wu, H.; Morbidelli, M. A Simple Model for the Structure of Fractal Aggregates. *J Colloid Interface Sci* **2003**, *268* (1), 106–120. https://doi.org/10.1016/j.jcis.2003.07.027.

(47) Abdel-Salam, M.; Anis, H.; El-Morshedy, A.; Radwan, R.; Abdel-Salam, M. Electrical Breakdown of Gases. In *High-Voltage Engineering*; 2018. https://doi.org/10.1201/9781482290035-4.

(48) Brown, W. F. Thermal Fluctuations of a Single-Domain Particle. *Physical Review* **1963**. https://doi.org/10.1103/PhysRev.130.1677.

(49) Jiles, D. C.; Atherton, D. L. Theory of Ferromagnetic Hysteresis. *J Magn Magn Mater* **1986**. https://doi.org/10.1016/0304-8853(86)90066-1.

(50) Marghussian, V. Magnetic Properties of Nano-Glass Ceramics. In *Nano-Glass Ceramics*; 2015. https://doi.org/10.1016/b978-0-323-35386-1.00004-9.

(51) Ota, S.; Takemura, Y. Characterization of Néel and Brownian Relaxations Isolated from Complex Dynamics Influenced by Dipole Interactions in Magnetic Nanoparticles. *Journal of Physical Chemistry C* **2019**, *123* (47), 28859–28866. https://doi.org/10.1021/acs.jpcc.9b06790.

(52) Dieckhoff, J.; Eberbeck, D.; Schilling, M.; Ludwig, F. Magnetic-Field Dependence of Brownian and Néel Relaxation Times. *J Appl Phys* **2016**, *119* (4). https://doi.org/10.1063/1.4940724.

(53) Deissler, R. J.; Wu, Y.; Martens, M. A. Dependence of Brownian and Néel Relaxation Times on Magnetic Field Strength. *Med Phys* **2014**, *41* (1). https://doi.org/10.1118/1.4837216.

(54) Kittel, C. Introduction to Solid State Physics, 8th Edition. *Wiley & Sons, New York, NY* **2004**.

(55) Kulkarni, R.; Murty, B. S.; Srinivas, V. Study of Microstructure and Magnetic Properties of AlNiCo(CuFe) High Entropy Alloy. *Journal of Alloys and Compounds*. 2018. https://doi.org/10.1016/j.jallcom.2018.02.275.

(56) Vrtnik, S.; Guo, S.; Sheikh, S.; Jelen, A.; Koželj, P.; Luzar, J.; Kocjan, A.; Jagličić, Z.; Meden, A.; Guim, H.; Kim, H. J.; Dolinšek, J. Magnetism of CoCrFeNiZrx Eutectic High-Entropy Alloys. *Intermetallics (Barking)* **2018**. https://doi.org/10.1016/j.intermet.2017.11.017.

(57) Nazir, R.; Mazhar, M.; Akhtar, M. J.; Raza Shah, M.; Khan, N. A.; Nadeem, M.; Siddique, M.; Mehmood, M.; Butt, N. M. Superparamagnetic Bimetallic Iron-Palladium

Nanoalloy: Synthesis and Characterization. *Nanotechnology* **2008**. https://doi.org/10.1088/0957-4484/19/18/185608.

(58) Vondrova, M.; Klimczuk, T.; Miller, V. L.; Kirby, B. W.; Yao, N.; Cava, R. J.; Bocarsly, A. B. Supported Superparamagnetic Pd/Co Alloy Nanoparticles Prepared from a Silica/Cyanogel Co-Gel. *Chemistry of Materials*. 2005. https://doi.org/10.1021/cm051244r.

(59) Maisels, A.; Kruis, F. E.; Fissan, H.; Rellinghaus, B.; Zähres, H. Synthesis of Tailored Composite Nanoparticles in the Gas Phase. *Appl Phys Lett* **2000**. https://doi.org/10.1063/1.1335843.

(60) Lazzari, S.; Nicoud, L.; Jaquet, B.; Lattuada, M.; Morbidelli, M. Fractal-like Structures in Colloid Science. *Adv Colloid Interface Sci* **2016**, *235*, 1–13. https://doi.org/10.1016/j.cis.2016.05.002.

(61) Jungblut, S.; Joswig, J. O.; Eychmüller, A. Diffusion- and Reaction-Limited Cluster Aggregation Revisited. *Physical Chemistry Chemical Physics* **2019**, *21* (10), 5723–5729. https://doi.org/10.1039/c9cp00549h.

(62) Kogler, F.; Velev, O. D.; Hall, C. K.; Klapp, S. H. L. Generic Model for Tunable Colloidal Aggregation in Multidirectional Fields. *Soft Matter* **2015**, *11* (37), 7356–7366. https://doi.org/10.1039/c5sm01103e.

(63) Kim, S.; Lee, K. S.; Zachariah, M. R.; Lee, D. Three-Dimensional off-Lattice Monte Carlo Simulations on a Direct Relation between Experimental Process Parameters and Fractal Dimension of Colloidal Aggregates. *J Colloid Interface Sci* **2010**, *344* (2), 353–361. https://doi.org/10.1016/j.jcis.2010.01.008.

8.7 Supporting information

S.1 Solution of mean square displacement from Langevin equation

The eqn below governs the Langevin dynamics of an entity in an ensemble of magnetic dipoles as represented by eqn(1) of main text:

$$m\frac{d^2x}{dt^2} = -\xi\frac{dx}{dt} + \tilde{F}(t) + F_H \tag{1}$$

The derivation is carried out using a similar procedure described in [1]. Neglecting F_H (described in section 2.1, main text), multiplying x on both sides of eqn(1) gives eqn (S2)

$$\frac{m}{2}2x\frac{d^2x}{dt^2} = -\xi x\frac{dx}{dt} + \left(\tilde{F}(t)\right)x \tag{S2}$$

Using the transformations $\frac{dx^2}{dt} = \frac{2xdx}{dt}$ and $\frac{d^2x^2}{dt^2} = 2\left(\frac{dx}{dt}\right)^2 + 2x(\frac{d^2x}{dt^2})$ I arrive at eqn (S3)

$$\frac{m}{2}\frac{d^2x^2}{dt^2} - m\left(\frac{dx}{dt}\right)^2 = -\frac{\xi}{2}\frac{dx^2}{dt} + \left(\tilde{F}(t)\right)x \tag{S3}$$

Putting $\left(\frac{dx}{dt}\right)^2 = v^2$ (velocity), and taking ensemble average on both sides gives eqn(S4),

$$\frac{m}{2}\frac{d^2\langle x^2\rangle}{dt^2} - m\langle v\rangle^2 = -\frac{\xi}{2}\frac{d\langle x^2\rangle}{dt} + \langle\left(\tilde{F}(t)\right)x\rangle \tag{S4}$$

Using equipartition $m\langle v\rangle^2 = k_BT$ and as $\langle\left(\tilde{F}(t)\right)x\rangle = 0$, I get eqn (S5)

$$\frac{m}{2}\frac{d^2\langle x^2\rangle}{dt^2} - k_BT = -\frac{\xi}{2}\frac{d\langle x^2\rangle}{dt} \tag{S5}$$

Solution to eqn (S5) will be (S6)

$$\frac{d\langle x^2\rangle}{dt} = \frac{2k_BT}{\xi}\left(1 - e^{-\frac{\xi t}{m}}\right) \qquad (S6)$$

Solution to eqn S6 will be eqn (2) in the main text

$$\langle x^2(t)\rangle = \frac{2k_BT}{\xi}\left(t - \frac{m}{\xi} + \frac{m}{\xi}e^{-\frac{\xi t}{m}}\right) \qquad (2)$$

S.2 Smoluchowski eqn and coagulation kernel [2]

The Smoluchowski coagulation eqn for homogeneous monomer kernel is given by eqn S(7)

$$\frac{dn_1}{dt} = -n_1^2 K(1,1) \qquad (S8)$$

The solution to which is given by $n_1(t) = \frac{n_0}{1+n_0K(1,1)t}$, which is used in the main text.

S.3 Correction to the free molecular coagulation kernel for accounting magnetic interactions

The correction is performed by introducing a correction factor in terms of a multiplier as $K_{corrected} = KW$, where W is the enhancement factor.

The enhancement factor for accounting inter-particle forces in both free-molecular and continuum regime is given by eqn (S10a and b) [3–5]

$$W_C = \frac{1}{\left(r_{pi} + r_{pj}\right)\int_{r_{pi}+r_{pj}}^{\infty} \frac{\exp\left(\frac{U_{ij}}{k_BT}\right)}{r^2}} \qquad (S10a)$$

$$W_{FM} = 2\int_0^{\infty} e^{-v^2} v^3 b_{crit}^2(v)dv \qquad (S10b)$$

Where $U_{ij}$the inter-particle interaction is potential given by eqn (7) in the main text and r is the magnitude of the radial distance vector. W_C is basically the reciprocal of the Fuch's

stability ratio. b_{crit} in eqn(S10b) is obtained from b, $b = r_m\sqrt{1 + \frac{|U_{ij}(r_m)|}{k_B T v^2}}$ when r_m is real and $r_m \leq 1$. Considering only collision of monomers, $r_{pi} = r_{pj} = \frac{\sigma}{2}$. When the average interactions for all the possible orientation of the radial distance vector with H-field are considered, the $\cos^2\theta$ term becomes ⅓, which makes $U_{ij} = -\frac{p^2}{8\pi\mu_0|\vec{r}_{ij}|^3}$. The thermal energy in the denominator of the exponential term can be non-dimensionalized by $T' = k_B T / k_B T_0$ and the non-dimensionalized form of U_{ij} as already shown in the main-text is $U_{ij} = \frac{q(1-3\cos^2\theta)}{r_{ij}^3}$ where $q = \frac{p^2}{4\pi\mu_0\sigma^3 k_B T_0}$. The length scales are non-dimensionalized by the monomer diameter σ. Hence, the non-dimensionalized orientation averaged expression of the interaction potential term is $U_{ij} = -\frac{q}{2r_{ij}^3}$. When $r_{ij} = r_m = 1$, $b_{crit}(v) = \sqrt{1 + \frac{q}{2kTv^2}}$. Substituting these non-dimensionalized forms in eqn (S10) gives eqn (12) of the main text.

The transition regime coagulation kernel is more complex. The expression for transition regime kernel has been derived by the Hogan group by first passage regression studies [3,4]. The dimensionless kernel considering only monomer collision is represented by eqn(S11)

$$H = \frac{K_T m W_C}{f\sigma^3 W_{FM}^2} \tag{S11}$$

Where K_T is the dimensional transition kernel. The diffusive Knudsen number on accounting the field induced enhancement is given by $Kn_D = \frac{\sqrt{2k_B T m_p} W_C}{6\pi\eta\sigma^2 W_{FM}}$. H is a function of Kn_D as represented in eqn(S12)

$$H = \frac{4\pi Kn_D^2 + C_1 Kn_D^3 + \sqrt{8\pi} C_2 Kn_D^4}{1 + C_3 Kn_D + C_4 Kn_D^2 + C_2 Kn_D^3} \quad \text{(S12)}$$

Where $C_1 = 25.836; C_2 = 11.211; C_3 = 3.502; C_4 = 7.211$

The transition kernel has been estimated from these equations and the enhancement factor (Figure 8-6(a)) has been evaluated by dividing the kernel in presence of field by the kernel in absence.

S.4 Simplistic 1-D model of repulsive interaction between two monomers with the line of approach parallel to the applied H-field

Considering only the repulsive (+ve) term in 1D (x-direction) version of eqn(7) one arrives at $U_{ij} = \frac{p^2}{4\pi\mu_0 x^3}$. Taking derivative of this with respect to x/σ, one will get the force on one of the monomers, $F_H = \frac{3p^2}{4\pi\mu_0 x^4}$. Time taken by monomer to move by persistence length (l_0) is m/ξ. Hence, time taken to move one monomer diameter (σ) is given by $t = \frac{\sigma}{l_0}\frac{m}{\xi}$. The acceleration required to be produced by the repulsive force F_H in order to negatively accelerate the approaching monomer from $v = \sqrt{\frac{k_B T}{m_p}}$ to $v = 0$ within a time t is given by $\frac{F_H}{m} = \frac{\sqrt{\frac{k_B T}{m_p}}}{t}$. Substituting t, one arrives at the critical condition, $\frac{F_H}{m_p} = \sqrt{\frac{k_B T}{m_p}}\frac{\xi}{m_p}\frac{\sigma}{l_0}$. Assuming a distance of 1 monomer diameter between the monomers $x = \sigma$, and using $p = \alpha H^2 \sigma^3$ from main text, one can arrive at $\frac{H_{th}\sigma^{1.5}}{T^{0.5}} = C(constant)$

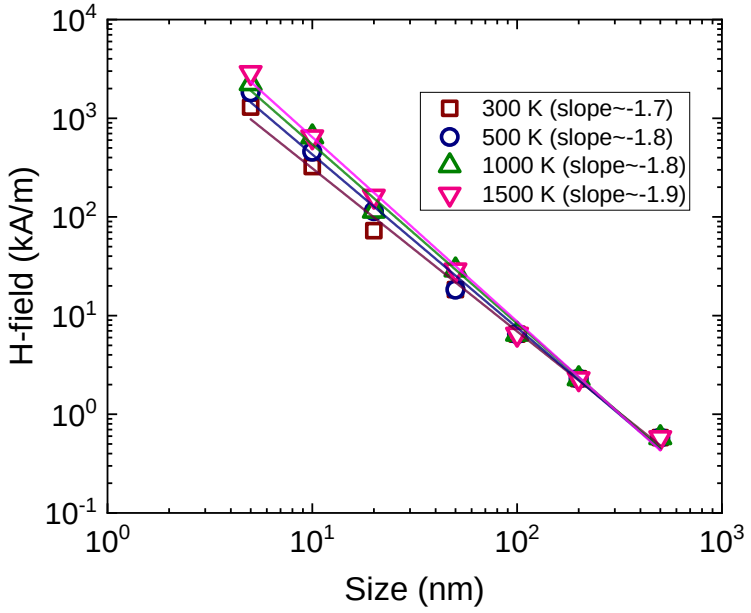

FigureS1 Log-log plot of threshold H-field with different primary particles sizes at various temperatures have a slope of ~1.7-1.9.

S.5 Analogous simulations for electric dipoles in electric field

The electric dipolar analogue of eqn (7) in the main text is given by eqn (S13)[6][7]

$$U_{ij} = \frac{p^2(1 - 3\cos^2\theta)}{4\pi\varepsilon_0 \left|\vec{\boldsymbol{r}}_{\boldsymbol{ij}}\right|^{\mathbf{3}}} \tag{S13}$$

Where ε_0 is the permittivity of free space, and that of eqn (8) is given by (S14)[6]

$$\alpha = 4\pi\varepsilon_0 \left(\frac{\varepsilon_r - 1}{\varepsilon_r + 2}\right) \tag{S 14}$$

Assuming ε_r>>1, the case of a highly ferroelectric material, I have performed the same simulations for an ensemble of electric dipoles, selected results from which have been represented in Figure 8-4 of main text.

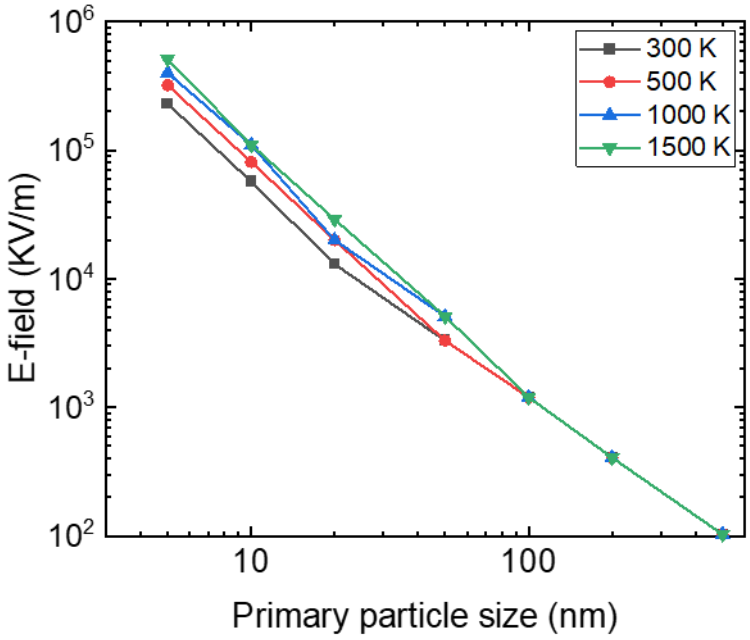

FigureS2 Threshold E-field required for linear assembly of primary particles having a net electric dipole moment aligned towards the E-field, for different sizes and temperatures.

Table. S1 *Field strengths at which demagnetization potential is equivalent to thermal energy*

Size (m)	H (kA/m) 300 K	H (kA/m) 500 K	H (kA/m) 1000 K	H (kA/m) 1500 K
5.00E-09	22.9	29.5	41.8	51.1
1.00E-08	8.08	10.4	14.8	18.1
2.00E-08	2.86	3.69	5.22	6.39
5.00E-08	0.7	0.9	1.32	1.62
1.00E-07	0.3	0.3	0.5	0.6
2.00E-07	0.1	0.2	0.2	0.2
5.00E-07	0.02	0.03	0.04	0.05

S.6 Estimation of Néel and **Brownian rotation times in different limits and regimes**

Néel relaxation time: The characteristic time-scale for the intra-particle domain relaxation can be estimated from the Néel relaxation time (τ_s) , $\tau_s = \tau_0 \, exp\left(\frac{\pi K \sigma^3}{6 k_B T}\right)$ where τ_0 is a proportionality constant ~10^{-10} s and K is the magneto-crystalline anisotropy which is a constant material property for ferromagnetic materials ~20,000 J/m^3.

Brownian relaxation time: The Brownian relaxation time-scales differ in various regimes. The translational Brownian relaxation time in the diffusive limit is obtained from the Einstein's relation $\langle r^2 \rangle = 6Dt$, D being the diffusivity as described in section 2.1, main

text. In the diffusive limit of transition regime, using $D = \frac{k_B T}{6\pi\eta(\frac{\sigma}{2})}$ and considering a mean displacement by half-monomer diameter, the characteristic time-scale for rotational Brownian relaxation is given by $\tau_{B_{diffT}} = \frac{\pi\eta\sigma^3}{4k_B T}$, where η is the viscosity of the N_2 gas medium (1.8×10^{-5} Pa-s). Similarly, in the diffusive limit of free molecular regime, using $D = \frac{k_B T}{\xi}$, I obtain the relaxation time-scale as $\tau_{B_{diffFM}} = \frac{\pi\delta P\sigma^4}{12k_B T\bar{v}}$, where $\bar{v} = \sqrt{\frac{3k_B T}{m_g}}$ [all parameters described in section 2.1, main text]. In the ballistic limit, the relaxation time-scale expression can be derived from the ballistic limit mean-square-displaced expression derived from Langevin equation as mention in section 2.1, main text. In this case, the relaxation time-scale is the time taken to rotate by π given an angular velocity, $\omega = \left(\frac{3k_B T}{I}\right)^{0.5}$, where *I* is the moment of inertia of a sphere. Hence, the ballistic limit time-scale expression derived in this manner is $\tau_{B_{bal}} = \sqrt{\frac{\pi I}{3k_B T}}$. The unified expression for Brownian rotational relaxation time-scale can be obtained by weighting the ballistic and diffusive limits by the monomer-size relative persistence length, as $\tau_B = \left(1 - \frac{\sigma}{l_0}\right)\tau_{B_{bal}} + \frac{\sigma}{l_0}\tau_{B_{diff}}$, where $\tau_{B_{diff}}$ can be either in free molecular ($\tau_{B_{diffFM}}$) or transition ($\tau_{B_{diffT}}$) regime depending on the size and temperature. The different time-scales are summarized in table S2.

Table S2. Summary of expressions of different time-scales

Relaxation time-scale	Expression
Néel relaxation time	$\tau_s = \tau_0 \, exp\left(\frac{\pi K \sigma^3}{6 k_B T}\right)$
Brownian rotation-diffusive (Transition)	$\tau_{B_{diffT}} = \frac{\pi \eta \sigma^3}{4 k_B T}$
Brownian rotation-diffusive (Free molecular)	$\tau_{B_{diffFM}} = \frac{\pi \delta P \sigma^4}{12 k_B T \bar{v}}$
Brownian rotation-Ballistic	$\tau_{B_{bal}} = \sqrt{\frac{\pi I}{3 k_B T}}$

Table S3: Estimated *Néel* relaxation times

Size (m)	τ_s(s) 300 K	τ_s(s) 500 K	τ_s(s) 1000 K	τ_s(s) 1500 K
5.00E-09	1.37E-10	1.21E-10	1.10E-10	1.07E-10
1.00E-08	1.25E-09	4.56E-10	2.14E-10	1.66E-10
2.00E-08	6.14E-02	1.87E-05	4.33E-08	5.72E-09
5.00E-08	2.07E+127	2.45E+72	1.57E+31	2.91E+17
1.00E-07	-	-	-	-
2.00E-07	-	-	-	-
5.00E-07	-	-	-	-

Blank values suggest computationally infinite numbers

Table S4: Estimated Brownian rotational time-scales in diffusive limits

Size (m)	$\tau_{B_{Diff}}$**(s) 300 K**	$\tau_{B_{Diff}}$**(s) 500 K**	$\tau_{B_{Diff}}$**(s) 1000 K**	$\tau_{B_{Diff}}$**(s) 1500 K**
5.00E-09	1.10E-11	5.12E-12	1.81E-12	9.85E-13
1.00E-08	3.79E-09	8.19E-11	2.90E-11	1.58E-11
2.00E-08	3.04E-08	1.82E-08	4.63E-10	2.52E-10
5.00E-08	4.74E-07	2.85E-07	1.42E-07	9.49E-08
1.00E-07	3.79E-06	2.28E-06	1.14E-06	7.59E-07
2.00E-07	3.04E-05	1.82E-05	9.11E-06	6.07E-06
5.00E-07	4.74E-04	2.85E-04	1.42E-04	9.49E-05

Table S5: Estimated Brownian rotational time-scales in ballistic limits

Size (m)	$\tau_{B_{Bal}}$(s) 300 K	$\tau_{B_{Bal}}$(s) 500 K	$\tau_{B_{Bal}}$(s) 1000 K	$\tau_{B_{Bal}}$(s) 1500 K
5.00E-09	1.02E-09	7.90E-10	5.59E-10	4.56E-10
1.00E-08	5.77E-09	4.47E-09	3.16E-09	2.58E-09
2.00E-08	3.26E-08	2.53E-08	1.79E-08	1.46E-08
5.00E-08	3.23E-07	2.50E-07	1.77E-07	1.44E-07
1.00E-07	1.82E-06	1.41E-06	9.99E-07	8.16E-07
2.00E-07	1.03E-05	7.99E-06	5.65E-06	4.62E-06
5.00E-07	1.02E-04	7.90E-05	5.59E-05	4.56E-05

Table S6: Estimated Net Brownian relaxation time-scale

Size (m)	τ_B(s) 300 K	τ_B(s) 500 K	τ_B(s) 1000 K	τ_B(s) 1500 K
5.00E-09	9.73E-10	7.68E-10	5.51E-10	4.52E-10
1.00E-08	5.51E-09	4.12E-09	3.04E-09	2.51E-09
2.00E-08	3.18E-08	2.37E-08	1.59E-08	1.35E-08
5.00E-08	4.74E-07	2.80E-07	1.62E-07	1.30E-07
1.00E-07	3.79E-06	2.28E-06	1.14E-06	7.69E-07
2.00E-07	3.04E-05	1.82E-05	9.11E-06	6.07E-06
5.00E-07	4.74E-04	2.85E-04	1.42E-04	9.49E-05

Table S7: Regimes of various size and temperatures

Size (m)	**300 K**	**500 K**	**1000 K**	**1500 K**
5.00E-09	F.M.	F.M.	F.M.	F.M.
1.00E-08	T	F.M.	F.M.	F.M.
2.00E-08	T	T	F.M.	F.M.
5.00E-08	T	T	T	T
1.00E-07	T	T	T	T
2.00E-07	T	T	T	T
5.00E-07	T	T	T	T

F.M. = free molecular, T=transition, Based on N_2 properties on the criteria Kn>20

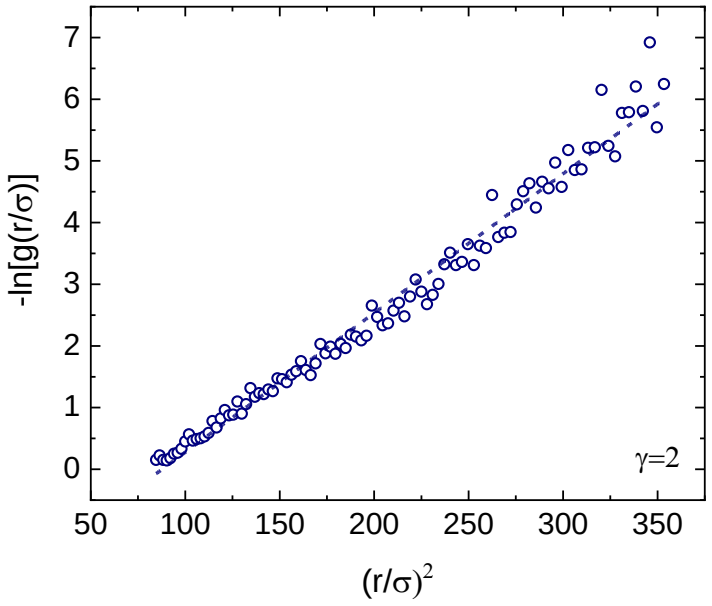

FigureS2 Cut-off region of the pair correlation of DLCA aggregates (D_f∼1.7) shows $\exp(-r^{\gamma})$ trend with $\gamma = 2$

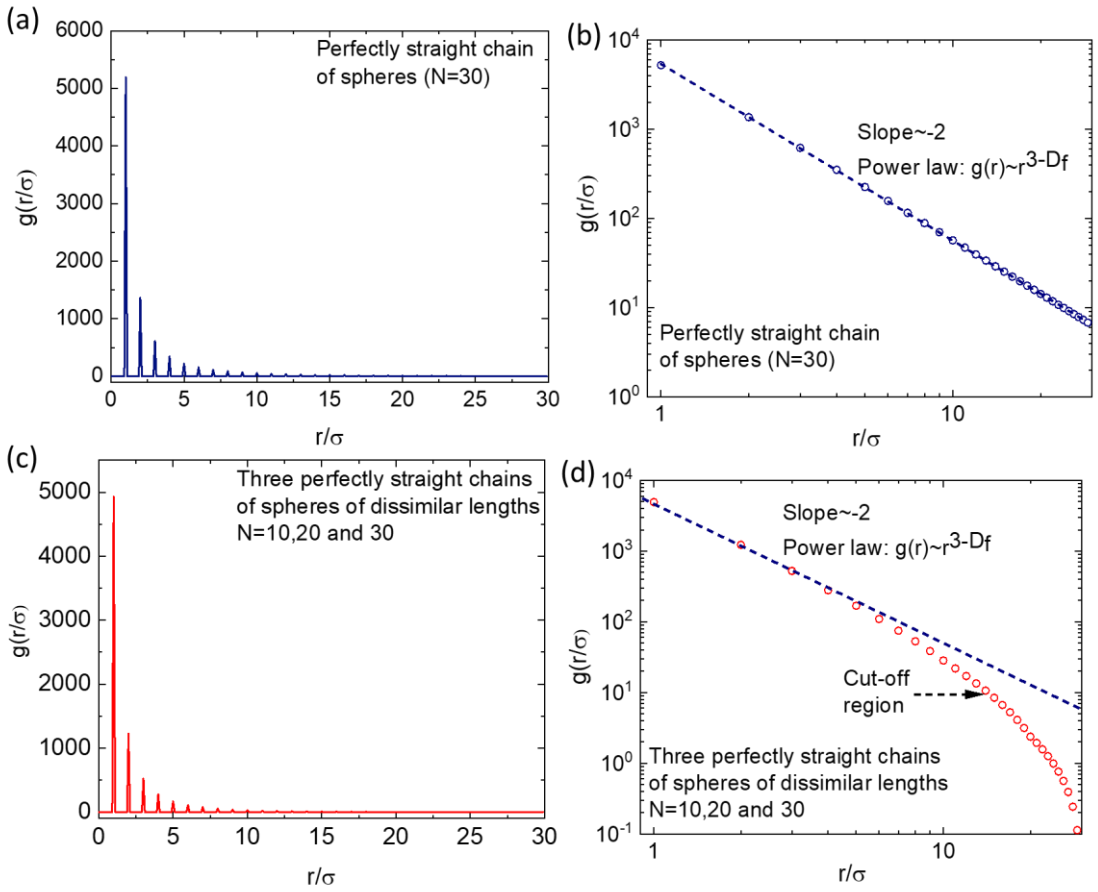

FigureS3 (a) Pair-correlation function of a straight chain of 30 spheres, (b) Integral peak values of the plot in FigureS3 (a) plotted in log-log scale, shows that power-law is followed till the end. (c) Average pair-correlation function of 3 straight chains of N=10, 20 and 30 spheres. (d) Integral peak values of plot in FigureS3(c), shows power law and cut-off behavior (analyzed further in FigureS4).

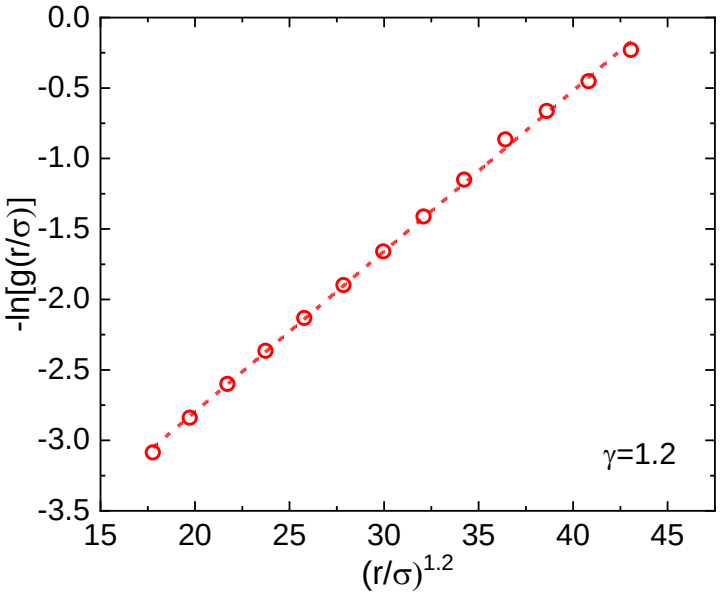

FigureS4 Cut-off region of average pair-correlation function of 3 straight chains of N=10, 20 and 30 spheres Figure S3 (c and d), shows $\exp(-r^{\gamma})$ trend with $\gamma = 1.2$

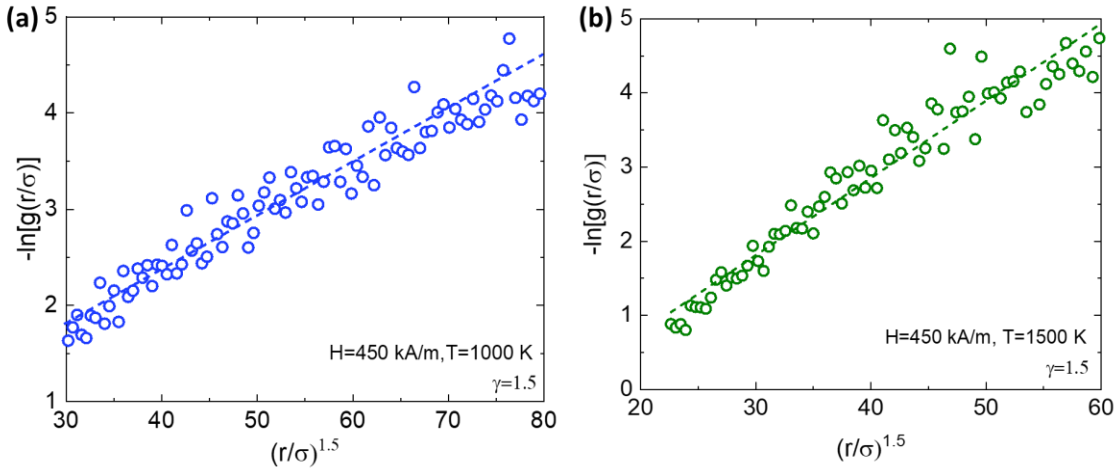

FigureS5 Cut-off region of pair-correlation function of 10 nm particles when H=450 kA/m and T=1000 K (a) and T=1500 K (b)

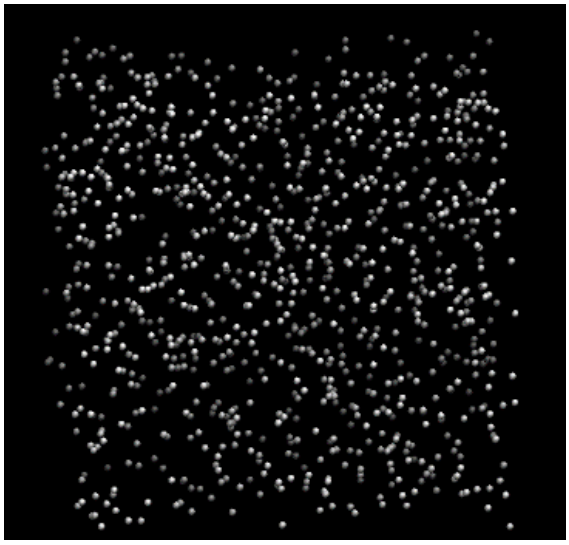

FigureS6 A representation of the initial configuration of randomly placed particles in a box

9 An Electrochemical Dead-man's Switch for Flammability of Liquid Fuels

9.1 Summary

One of the key features of liquid hydrocarbon fuels is that they are volatile, as combustion necessarily takes place in the gas phase [1–3]. Thus, to extinguish liquid fed combustion processes, removal of the oxidizing source (air) from the flame front is typically necessary. Here I demonstrate a new approach. I show that dynamic manipulation of the volatility of the liquid fuel can enable one to (a) store an involatile liquid as a non-flammable fuel (b) make it inflammable by increasing its volatility and (c) extinguishing its flame by decreasing its volatility. Room temperature ionic liquids (RTILs) are a special class of compounds with negligible vapor pressure, which causes them to be effectively non-flammable [4–7]. Herein, using an imidazolinium based model RTIL, I show that RTILs which are thermally stable and will not ignite, can be made flammable by application of a DC bias. I show that the electrolysis of the RTIL on application of the DC bias results in the volatilization of the RTIL into gas phase flammable species which can self-sustain a flame. Subsequently, an open circuit stops the volatilization of the RTIL, cutting off the supply of these gas phase fuel fragments to the flame, thereby leading to its extinction. This cycle can be repeated as often as desired. This approach presents a paradigm shift, offering the potential to make a 'safe fuel' and alternatively a simple electrochemically driven fuel metering scheme.

9.2 Introduction

Storage and transportation of all conventionally used liquid hydrocarbon fuels is associated with the potential of unintended fire and explosion.[1,8]. Liquid fuels, for example typical hydrocarbons, have high volatility at low temperatures, which also results in their low flash points[9–12]. High volatility is an inherent property of good fuels, as self-sustained combustion occurs when heat feedback from the flame volatilizes the fuel. Indeed, it is important to remember that liquid fuels do not combust in the liquid phase, rather they vaporize, and combustion occurs due to the rapid oxidation of the free fuel molecules in the vapor phase. Ignition is basically a method to volatilize enough fuel to the flash point so that the heat feedback from the flame can self-sustain the combustion[3,13,14]. Therefore, the typical way to extinguish a flame is to remove the oxygen source (air) from the flame front.

Here I pursue an alternative approach. Rather than removing the oxygen source, suppose I could dynamically manipulate the volatility of the liquid fuel, then in principle it should be possible to (a) store an involatile energetic liquid as non-flammable fuel (b) make it flammable by increasing its volatility and (c) extinguish its flame by decreasing its volatility. This approach, if realized, would offer the potential to make a 'safe fuel' or alternatively lay the foundation of a simple fuel metering scheme, which have never been realized for soft or condensed phase energetic materials.

Room temperature ionic liquids (RTIL) are a special class of compounds with negligible vapor pressure, which causes them to be non-flammable[6,7,15–17]. As such RTILs are often used as safe electrolytes for metal batteries[18]. Herein, using an imidazolinium based model

RTIL[19], I show that RTILs which are thermally stable and will not ignite can be made to be flammable by application of a DC bias, and subsequent open circuit leads to extinction of the flame.

9.3 Flammability On/Off Concept

The strategy to develop an electrochemical on/off control switch on flammability by leveraging the thermal insensitivity of room temperature ionic liquids (RTILs) is illustrated in Figure 9-1. Unlike other liquid fuels, RTILs do not ignite when exposed to thermal shock or when contacted with a flame owing to their insignificant vapor pressures. However, I show that a low external voltage can be applied to electrochemically decompose RTILs to reactive volatile species, which can ignite and sustain a flame.

For a specific demonstration I employ an imidazolinium based model RTIL[19.], which is thermally insensitive and cannot be ignited by hot-wire ignition even when subjected to extreme heating rates of 10^5 K/s, which is sufficient to thermally ignite most condensed phase fuels[20–24]. Additionally, I show that it is impossible to ignite even when in contact with a butane generated flame. However, when a voltage is applied across the RTIL, electrolysis of the RTIL results in its volatilization into flammable gas phase species, which can spontaneously ignite and combust. Continuous application of the voltage ensures continuous supply of reactive volatile fuel fragments to the flame, thereby leading to self-sustaining combustion. Withdrawing the voltage stops the volatilization of the RTIL, terminating the supply of the flammable species from the RTIL to the flame, thereby leading to the extinction of the flame. As the RTIL is thermally insensitive, the heat feedback from the flame is not able to generate significant vapor pressure from the fuel.

Hence, it can only ignite the flammable vapor phase species generated electrochemically and is unable to ignite the liquid RTIL. Leveraging this property, the vaporization and hence the flammability of the RTIL can be completely switched off by deactivating the electrochemical reactions through withdrawal of the voltage. Hence, I demonstrated that the flammability of the RTIL can be completely reversed at will by electrochemical means.

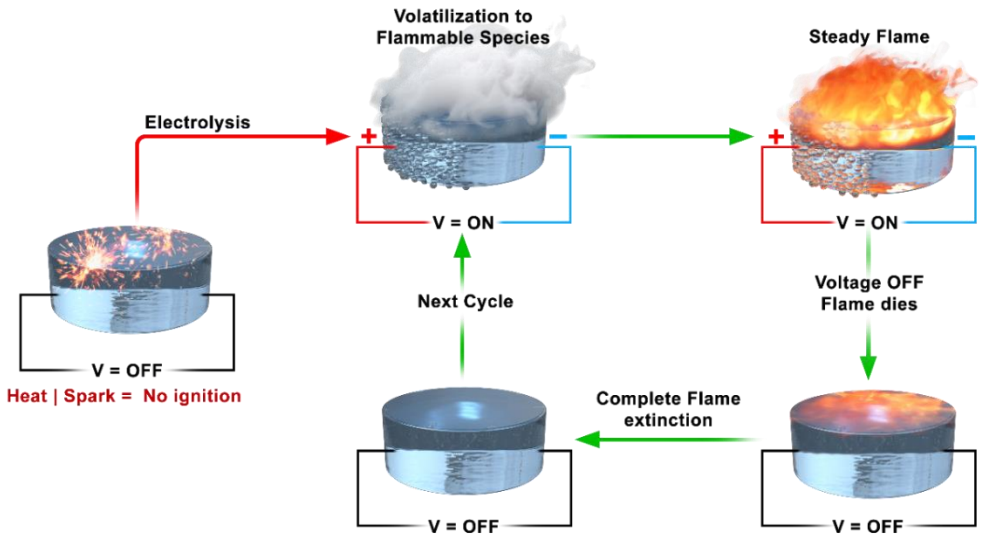

Figure 9-1 Concept of switching the flammability of RTILs via electrolysis. RTILs are inherently insensitive to thermal shock/spark, however they can be electrochemically volatilized to reactive flammable species which can ignite and self-sustain a flame. Turning off the voltage terminates the volatilization of the RTIL, thereby extinguishing the flame. This process can be repeated several times to sequentially meter energy from the RTIL.

9.4 Demonstration of activation/deactivation of flammability

As most common RTILs consist of imidazole-based cations, I have chosen 1-butyl 3-methyl imidazolinium perchlorate ($[BMIM]^+[ClO_4]^-$) as a model RTIL to demonstrate the concept of using electrochemistry to activate/deactivate the combustion and energy

generation processes from condensed phase fuels. $[BMIM]^+[ClO_4]^-$ have been synthesized by the hard acid soft base anion exchange by reacting dissolved precursors $[BMIM]^+[Cl]^-$ and $NaClO_4$ in ethanol, details of which can be found in the methods section. The solid residue of NaCl as a product of the reaction is removed by centrifugation and the ethanol is removed from the supernatant by vacuum drying to obtain $[BMIM]^+[ClO_4]^-$. ATR-FTIR spectra (Figure S1) confirms the presence of the ClO_4 groups in the synthesized $[BMIM]^+[ClO_4]^-$. XRD of the solid white residue shows that it is NaCl (Figure S2), thereby confirming the hard acid soft base ion exchange reaction has occurred successfully, resulting in the formation of $[BMIM]^+[ClO_4]^-$. Thermogravimetric analysis coupled with differential scanning calorimetry (TGA/DSC) measurements show that $[BMIM]^+[ClO_4]^-$ exothermically losses 80 % of its mass between ~523-610 K (Figure S3). A gradual mass loss is observed beyond ~610 K indicating the evaporation of the condensed phase product formed after its decomposition. Although it undergoes an exothermic decomposition, I demonstrate that it cannot be ignited thermally by hot-wire ignition at high heating rates (Figure S4) or by contacting a butane flame (Figure S5), thereby proving that it is thermally insensitive. This is probably due to its slow thermal decomposition rate or low flammability of the decomposition products.

However, as mentioned earlier, the combustion event of $[BMIM]^+[ClO_4]^-$ can be electrochemically activated/deactivated in multiple cycles as demonstrated in Figure 9-2. For performing the demonstration, $[BMIM]^+[ClO_4]^-$ liquid was electrochemically activated with two Pt wire electrodes (~75 μm diameter) as shown in the representative schematic (Figure 9-1). When the voltage (V=40 V) is applied, in the absence of an external igniter,

smoke and gas bubbles are generated only at the cathode as observed by high-speed optical and IR imaging (Figure S6). Figure 9-2 (a) and video SV1 shows that when a butane flame is held above the surface of the RTIL after turning on the voltage, the gaseous species released can be ignited. The flame height gradually grows and becomes constant indicating the ability of the gaseous species generated on electrolysis to undergo self-sustaining combustion. When the voltage is turned off, the flame height decreases and the flame is extinguished as the generation and supply of volatile flammable species to the flame is inhibited. The flame area from these images have been estimated by counting the number of bright pixels after excluding the frames containing the butane flame and the time-evolution of the normalized flame area has been represented in Figure 9-2(b) after moving-average smoothing, to corroborate the visual observations presented in Figure 9-2(a). This clearly demonstrates the aforementioned concept that the thermal energy generation from RTILs can be controlled, by sequentially dispensing and combusting volatile species from the condensed phase RTIL, which remains unaffected by the heat feedback from the flame. I used a voltage of 40 V for the demonstration purpose. Considering the electrochemical stability window of the RTILs[25,26] from voltametric measurements, any applied voltage above ~6 V will be able to electrolyze the given RTIL[19]. The effect of the voltage on the ignition delay can be addressed in future studies.

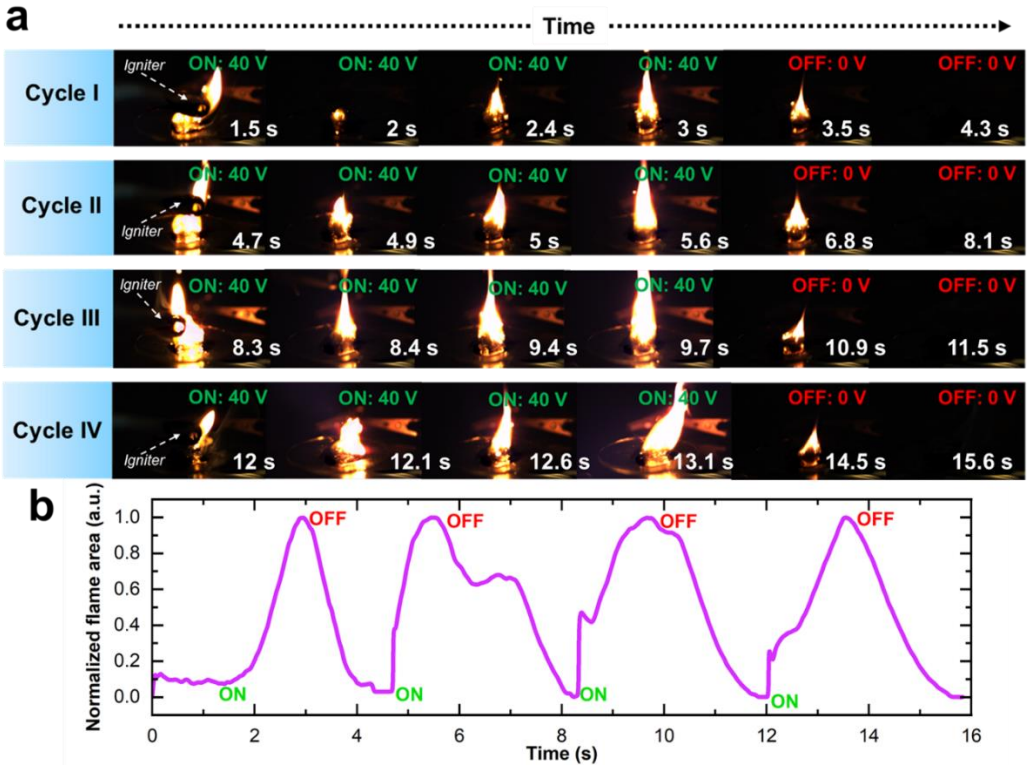

Figure 9-2 (a) High speed camera imaging of the electrochemical activation and deactivation of the combustion process of RTIL to demonstrate the concept presented in Figure 9-1. (b) Flame area as a function of time from the high-speed camera images showing that the energy generated from combustion of the RTIL can be sequentially controlled by turning on/off the applied voltage.

9.5 Mechanism of electrochemically dispensing reactive volatile species

The model RTIL, $[BMIM]^+[ClO_4]^-$, has been electrolyzed under vacuum and the evolving vapor and gas phase species have been directly sampled and analyzed by time-of-flight mass spectrometry[15]as explained in the methods section. The time-averaged mass spectra (Figure 9-3(a)) collected over ~100 ms by sampling at an interval of ~0.1 ms, shows the generation of 1-methyl 3-butyl imidazole-2-yl radical ($[BMIM]^\bullet$, m/z=139), 1-methyl imidazole-2-yl radical ($[MIM]^\bullet$, m/z=83) and butene (m/z=56).

The generation of these radicals can be explained by the cathodic reduction of the BMIM cation as shown in 9-3(b). On gaining an electron, the isomer of the BMIM cation having a methyl group attached to the N^+ forms $[BMIM]^\bullet$ whereas the other isomer with the butyl group attached to the N^+ results in the formation of $[MIM]^\bullet$ and butene. In order to verify this mechanism, I have also characterized other commercially available RTILs such as $[BMIM]^+[PF_6]^-$ and $[EMIM]^+[BF_4]^-$. The $[BMIM]^+[PF_6]^-$ shows both $[BMIM]^\bullet$ and $[MIM]^\bullet$ peaks (Figure S7), as observed in the case of $[BMIM]^+[ClO_4]^-$, indicating that the cathodic reaction of the BMIM-cation is independent of the anion attached to it. The $[EMIM]^+[BF_4]^-$ also shows $[EMIM]^\bullet$ and $[MIM]^\bullet$ peaks (Figure S7), indicating that the formation of imidazole-2-yl radicals by cathodic reduction is independent of the alkyl chain length attached to the N^+ of the BMIM-cation. This shows that the electrochemical reduction mechanism shown in Figure 9-3(b) can be generically applied to all imidazolinium based cations. The existence and the stability of these radicals have been also reported in previous studies[27–30].

Characteristic electron ionization mass spectra peaks (NIST standard reference database 69) of BF_3 and PF_5 gases appear in the obtained mass spectra of $[EMIM]^+[BF_4]^-$ and $[BMIM]^+[PF_6]^-$ respectively (Figure S7). This indicates that the $[BF_4]^-$ and $[PF_6]^-$ anions are oxidized at the anode to BF_3 and PF_5 respectively. No species from $[ClO_4]^-$ oxidation at the anode are observed in the mass spectra of $[BMIM]^+[ClO_4]^-$ (Figure 9-3(a), indicating that the species produced from $[ClO_4]^-$ oxidation reside in the condensed phase. Our aforementioned observation that the smoke and gas bubbles are only generated at the cathode (Figure S6), also implies that the oxidized products at the anode are retained in the

condensed phase. This can possibly happen when $[ClO_4]^-$ is oxidized to chlorate ($[ClO_3]^-$) and chlorite ($[ClO_2]^-$) ions[31–33].

Figure 9-3 (c) shows that $[BMIM]^\bullet$ can be sequentially dispensed by turning on/off the external voltage periodically. The volatility of the $[MIM]^\bullet$ (Figure S8) can also be manipulated in the same manner as that of $[BMIM]^\bullet$ by periodically controlling the external voltage. This corroborates with the temporal variation of the flame area on application and withdrawal of the DC bias (Figure 9-2). Hence, application of the DC bias on the RTIL generates volatile flammable species such as $[BMIM]^\bullet$, $[MIM]^\bullet$, and butene leading to a self-sustained flame, whereas an open circuit stops the volatilization of the RTIL into these species, thereby extinguishing the flame.

As discussed earlier, RTILs do not have a significant vapor pressure prior to the onset of their decomposition. Moreover, previous studies have reported that BMIM-based RTILs thermally decompose to 2-methyl imidazole which also has a low vapor pressure and a high boiling point[34,35]. The high decomposition temperature of the model RTIL and the high boiling point of its decomposition product collectively results in a low vaporization rate of its energetic components, thereby preventing it from undergoing self-propagating combustion when thermal energy is applied, making it thermally insensitive. In contrast, the application of a low external voltage, can spontaneously result in its vaporization in the form of $[BMIM]^\bullet$, $[MIM]^\bullet$, and butene. The absence of a thermal barrier results in an enhanced vaporization rate and the evolved gases when ignited by an external source, can undergo spontaneous combustion. Turning off the voltage immediately shuts off the generation of these species as shown in Figure 9-3(c), thereby extinguishing the flame

(Figure 9-1). Generally, thermal energy feedback from the flame spontaneously ignites the fuel to undergo self-sustaining combustion. In this case, the thermal energy feedback from the flame is unable to volatilize or decompose the fuel to flammable products and hence cannot facilitate self-propagating reactions. The combustion can be easily turned off electrochemically by leveraging on this feature.

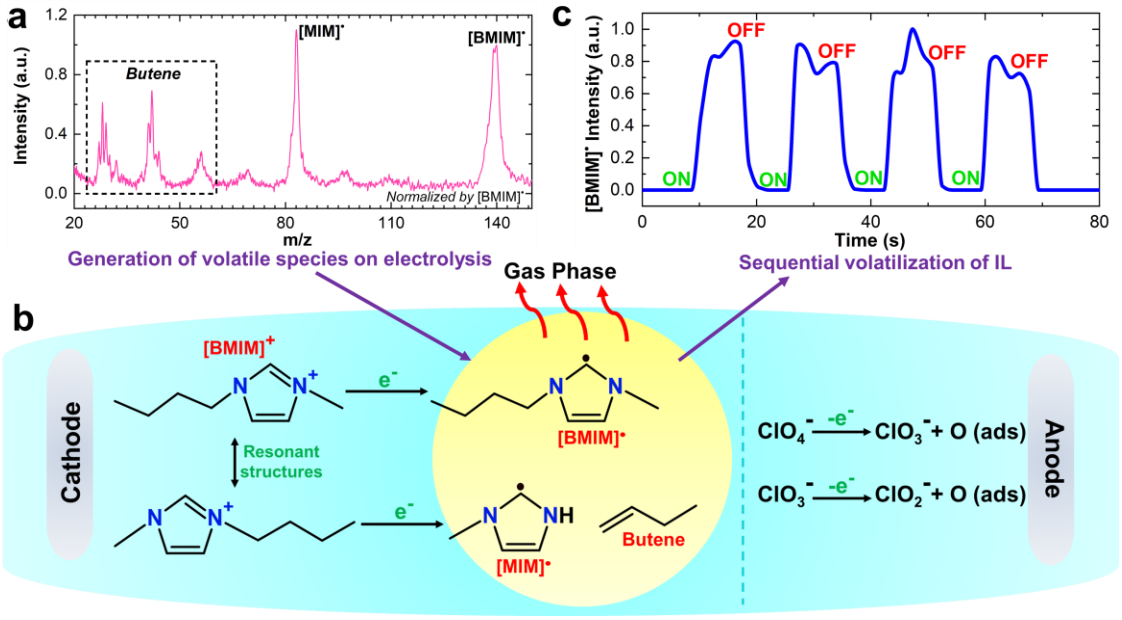

Figure 9-3 (a) Time-averaged electrochemical TOFMS spectra of $[BMIM]^+[ClO_4]^-$ showing the evolution of volatile species from the RTIL. (b) Electrochemical reduction mechanism of $[BMIM]^+$ to gas phase [BMIM]• and [MIM]• (c) Sequential volatilization of $[BMIM]^+[ClO_4]^-$ as inflammable [BMIM]•.

9.6 Discussion

In summary, I have demonstrated for the first time that the flammability of a liquid fuel can be reversed simply by applying and withdrawing a voltage across it. This approach does not therefore require any separation of fuel from oxidizer to manipulate flammability. In the current study, by using a model room temperature ionic liquid (RTIL) I have shown

that the energy generation from a liquid fuel can be controlled by electrolysis that effectively changes the RTIL from a involatile liquid to one containing volatile components. One can argue that the same can be achieved by electrolysis of water, as it generates H_2 as a fuel when electrolyzed. However, net energy cannot be extracted from combustion of H_2 generated from water electrolysis to form water itself, as reactant and product of the entire process is the same. Contrary to that, combustion of liquid hydrocarbons such as imidazolinium ionic liquids to CO_2, H_2O, and N_2 can generate ~20 kJ/g of energy according to the calculation shown in S.1, whereas the work performed to electrolyze it is ~0.8 kJ/g. Therefore, the energy output from the system is 25 times the electrochemical work performed, making this an attractive medium for thermal energy generation. Hence, it is more meritorious to apply this electrochemical switch to liquid hydrocarbon fuels than water, which gives no net energy output. These findings may bring in a paradigm shift by enabling the use of RTILs as safe fuels, energy generation from which can be controlled in a sequential manner. Moreover, this study lays the foundation of several fundamental studies which will focus on evaluation of the major degrees of freedom controlling the combustion energy release profile of these systems along with the characterization of their flame temperature and energy release rates.

9.7 References

1. Xu, C., Wu, S., Li, Y., Chu, S. & Wang, C. Explosion characteristics of hydrous bio-ethanol in oxygen-enriched air. *Fuel* **271**, 117604 (2020).

2. Venu, H., Raju, V. D. & Subramani, L. Combined effect of influence of nano additives, combustion chamber geometry and injection timing in a DI diesel engine fuelled with ternary (diesel-biodiesel-ethanol) blends. *Energy* **174**, 386–406 (2019).

3. Spalding, D. B. Combustion of Liquid Fuels. *Nature 1950 165:4187* **165**, 160–160 (1950).

4. Cao, Y. & Mu, T. Comprehensive investigation on the thermal stability of 66 ionic liquids by thermogravimetric analysis. *Ind Eng Chem Res* **53**, 8651–8664 (2014).
5. Earle, M. J. *et al.* The distillation and volatility of ionic liquids. *Nature 2005 439:7078* **439**, 831–834 (2006).

6. Chen, C. C., Liaw, H. J. & Chen, Y. N. Flammability characteristics of ionic liquid 1-Decyl-3-methylimidazolium bis(trifluoromethylsulfonyl)imide. *J Loss Prev Process Ind* **49**, 620–629 (2017).

7. Fox, D. M. *et al.* Flammability and Thermal Analysis Characterization of Imidazolium-Based Ionic Liquids. *Ind Eng Chem Res* **47**, 6327–6332 (2008).

8. Coronado, C. J. R. *et al.* Flammability limits: A review with emphasis on ethanol for aeronautical applications and description of the experimental procedure. *J Hazard Mater* **241–242**, 32–54 (2012).

9. Saldana, D. A., Starck, L., Mougin, P., Rousseau, B. & Creton, B. Prediction of Flash Points for Fuel Mixtures Using Machine Learning and a Novel Equation. (2013) doi:10.1021/ef4005362.

10. Aljaman, B. *et al.* A comprehensive neural network model for predicting flash point of oxygenated fuels using a functional group approach. *Fuel* **317**, 123428 (2022).

11. Al-Abdullah, M. H., Kalghatgi, G. T. & Babiker, H. Flash points and volatility characteristics of gasoline/diesel blends. *Fuel* **153**, 67–69 (2015).

12. Huang, Z. *et al.* A solvent-anchored non-flammable electrolyte. *Matter* (2022) doi:10.1016/J.MATT.2022.11.003.

13. Nakamura, M., Akamatsu, F., Kurose, R. & Katsuki, M. Combustion mechanism of liquid fuel spray in a gaseous flame. *Physics of Fluids* **17**, 123301 (2005).

14. Godsave, G. A. E. Combustion of Droplets in a Fuel Spray. *Nature 1949 164:4173* **164**, 708–709 (1949).

15. Bier, M. & Dietrich, S. Vapour pressure of ionic liquids. *http://dx.doi.org/10.1080/00268971003604609* **108**, 211–214 (2010).

16. Bara, J. E., Camper, D. E., Gin, D. L. & Noble, R. D. Room-Temperature ionic liquids and composite materials: Platform technologies for CO2 capture. *Acc Chem Res* **43**, 152–159 (2010).

17. Tokuda, H., Tsuzuki, S., Susan, M. A. B. H., Hayamizu, K. & Watanabe, M. How ionic are room-temperature ionic liquids? An indicator of the physicochemical properties. *Journal of Physical Chemistry B* **110**, 19593–19600 (2006).

18. Sun, H. *et al.* A safe and non-flammable sodium metal battery based on an ionic liquid electrolyte. *Nature Communications 2019 10:1* **10**, 1–11 (2019).

19. Wang, X. D., Wu, W. Y., Tu, G. F. & Jiang, K. X. Synthesis and physico-chemical properties of new green electrolyte 1-butyl-3-methylimidazolium perchlorate. *Transactions of Nonferrous Metals Society of China* **20**, 2032–2036 (2010).

20. Delisio, J. B. *et al.* Probing the Reaction Mechanism of Aluminum/Poly(vinylidene fluoride) Composites. *Journal of Physical Chemistry B* **120**, 5534–5542 (2016).

21. Guo, F., Kawaguchi, S., Hashimoto, N. & Fujita, O. Effect of pyrolysis kinetic parameters on the overload ignition of polymer insulated wires in microgravity. *Proceedings of the Combustion Institute* (2022) doi:10.1016/J.PROCI.2022.08.087.

22. Kim, J. H. *et al.* Effect of energetic polymer encapsulation for aluminum/potassium periodate-based composites on ignition sensitivity and combustion characteristics. *Chemical Engineering Journal* **444**, 136519 (2022).

23. Stathopoulos, P., Ninck, K. & von Rohr, P. R. Hot-wire ignition of ethanol–oxygen hydrothermal flames. *Combust Flame* **160**, 2386–2395 (2013).

24. Panagiotou, T. & Levendis, Y. A study on the combustion characteristics of PVC, poly(styrene), poly(ethylene), and poly(propylene) particles under high heating rates. *Combust Flame* **99**, 53–74 (1994).

25. Chen, M. *et al.* Adding salt to expand voltage window of humid ionic liquids. *Nature Communications 2020 11:1* **11**, 1–10 (2020).

26. Doblinger, S., Donati, T. J. & Silvester, D. S. Effect of Humidity and Impurities on the Electrochemical Window of Ionic Liquids and Its Implications for Electroanalysis. *Journal of Physical Chemistry C* **124**, 20309–20319 (2020).

27. Michez, R., Doneux, T., Buess-Herman, C. & Luhmer, M. NMR Study of the Reductive Decomposition of [BMIm][NTf2] at Gold Electrodes and Indirect Electrochemical Conversion of CO2. *ChemPhysChem* **18**, 2208–2216 (2017).

28. Xiao, L. & Johnson, K. E. Electrochemistry of 1-Butyl-3-methyl-1H-imidazolium Tetrafluoroborate Ionic Liquid. *J Electrochem Soc* **150**, E307 (2003).

29. Tian, Y. H., Goff, G. S., Runde, W. H. & Batista, E. R. Exploring electrochemical windows of room-temperature ionic liquids: A computational study. *Journal of Physical Chemistry B* **116**, 11943–11952 (2012).

30. Alwast, D., Schnaidt, J., Law, Y. T. & Behm, R. J. A Novel Approach for Differential Electrochemical Mass Spectrometry Studies on the Decomposition of Ionic Liquids. *Electrochim Acta* **197**, 290–299 (2016).

31. Miles, M. H. & Fletcher, A. N. The Electrochemical Reduction of Molten Perchlorate and Chlorate Salts. *J Electrochem Soc* **128**, 821–825 (1981).

32. Jung, Y. J., Baek, K. W., Oh, B. S. & Kang, J. W. An investigation of the formation of chlorate and perchlorate during electrolysis using Pt/Ti electrodes: The effects of pH and reactive oxygen species and the results of kinetic studies. *Water Res* **44**, 5345–5355 (2010).

33. Li, J. J. *et al.* Perchlorate reduction in microbial electrolysis cell with polyaniline modified cathode. *Bioresour Technol* **177**, 74–79 (2015).

34. Knorr, M., Icker, M., Efimova, A. & Schmidt, P. Reactivity of Ionic Liquids: Studies on Thermal Decomposition Behavior of 1-Butyl-3-methylimidazolium Tetrafluoroborate. *Thermochim Acta* **694**, 178786 (2020).

35. Efimova, A., Hubrig, G. & Schmidt, P. Thermal stability and crystallization behavior of imidazolium halide ionic liquids. *Thermochim Acta* **573**, 162–169 (2013).

9.8 Supporting information

Methods

Chemicals

$[BMIM]^+[Cl]^-$ (~98 %) solid powder (m.p. ~70 ^oC) were procured from Sigma Aldrich. $NaClO_4$ crystals and solvents such as ethanol and acetonitrile were obtained from Fischer scientific.

Synthesis of $[BMIM]^+[ClO_4]^-$

$[BMIM]^+[ClO_4]^-$ was synthesized by a hard acid soft base anion exchange reaction between $[BMIM]^+[Cl]^-$ with $NaClO_4$:

$$[BMIM]^+[Cl]^- + NaClO_4 \rightarrow [BMIM]^+[ClO_4]^- + NaCl$$

4 ml of a 1.4 M solution of $[BMIM]^+[Cl]^-$ in ethanol was added to 6 ml 0.96 M solution of $NaClO_4$ in ethanol to perform the above reaction. The resulting white precipitate of *NaCl* was centrifuged and separated. The liquid obtained after separation of the NaCl, was washed with acetonitrile as an antisolvent to precipitate trace amounts of dissolved NaCl. The white precipitate of NaCl was centrifuged and separated again. The liquid obtained after washing was dried in vacuum oven overnight to evaporate the ethanol and obtain $[BMIM]^+[ClO_4]^-$ as a room temperature ionic liquid.

Characterizations on the RTIL

ATR-FTIR characterizations have been performed using ThermoFisher Nicolet iS50R, for compositional analysis. X-ray Diffraction has been performed using PANalytical EMPYREAN (Cu Kα source, $\lambda = 1.54$ Å) to identify the composition of the

solid residue during the RTIL synthesis. Thermo-gravimetric analysis (TGA) was performed using Netzsch STA 449 F3.

Experiments for demonstrating on/off switching of flammability

For performing the combustion experiments under electrochemical stimulation, aliquots of the ionic liquid was placed in the center of the watch glass. Two Pt wire electrodes having a diameter of ~75 μm were immersed into the ionic liquids. The Pt wires were directly connected through copper alligator clips to the +-ve and -ve terminals of a DC power supply. A DC bias of ~40 V (maximum for the used power supply) was applied to electrolyze the ionic liquid. Then a butane flame generated by a commercial lighter was held above the surface of the RTIL placed on the watch glass, to ignite the volatile species released from the RTIL on electrolysis. After ignition of the gas phase species, the butane lighter was retracted from the surface of the RTIL, to allow the volatile species which are constantly generated under the DC bias, to self-sustain a flame. Once the flame was self-sustained, the DC bias was removed to create an open circuit to stop the generation of the volatile species and extinguish the flame. This process was repeated in several cycles. The high speed imaging was performed using a Phantom Miro 110 camera.

Electrochemical time of fight mass spectrometry of the RTIL for in-situ identification of the volatile species generated on its electrolysis

An assembly of aliquots of the RTIL placed on a glass slide with the ~75 μm diameter Pt wire electrodes immersed in it, connected to the terminals of the same DC power supply as described in the previous section, were inserted into the high vacuum ($\sim 10^{-9}$ atm) chamber of a time-of-flight mass spectrometer. The assembly was inserted right in

between the ion extractor plates of the time-of-flight assembly. The gas phase species generated on electrolysis where ionized by a ~70 eV electron gun and the positive ions were extracted and accelerated through the time-of-flight tube to be detected by the time-of-flight method. A parabolic calibration curve ($m/z=at^2+bt+c$) generated from a combination of standard samples such as SF_6 gas and vaporization/thermal decomposition of solid Bi_2O_3, CuO and I_2O_5m was used to identify the m/z values from the time-of-flight. For obtaining the average spectra, the DC bias was applied to the ionic liquid through the Pt electrodes. The volatile species generated was ionized and the positive ions were sampled and detected for 100 ms at every 0.1 ms by pulsing the voltage across the extractor plates. For demonstrating that the generation of the volatile species can be switched on/off through the DC bias, the mass spectra was obtained at every ~1.7 s intervals over a period of seconds. The data acquisition was performed with high frequency Teledyne Lecroy oscilloscope and the data analysis was performed through custom built MATLAB scripts.

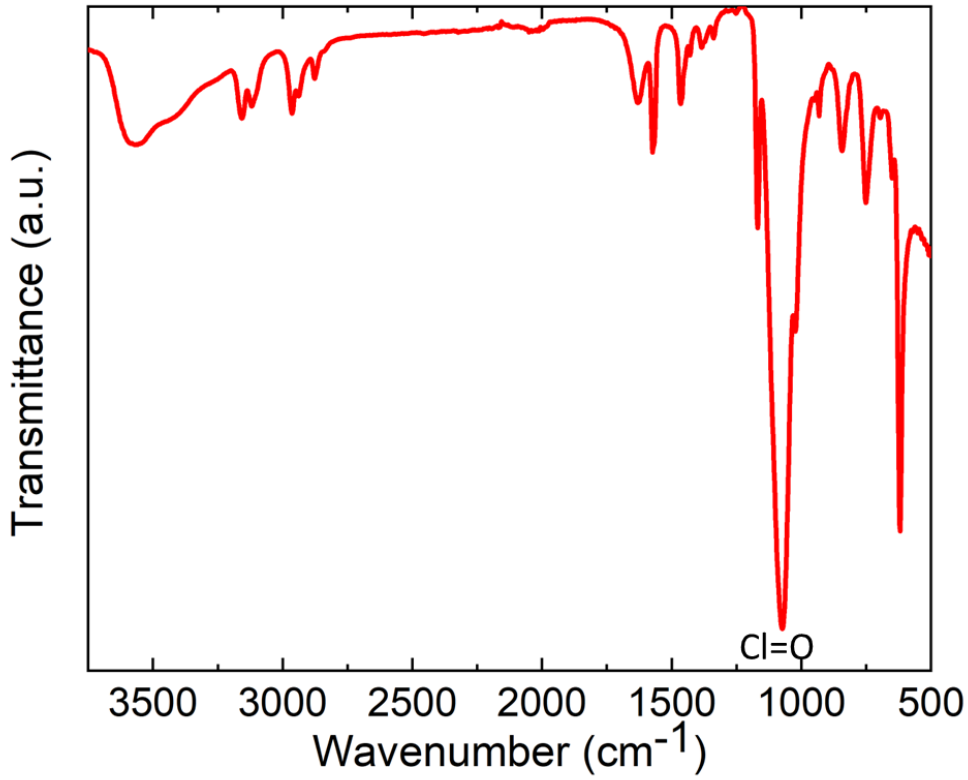

Figure S1 The peak around 1070 cm^{-1} can be attributed to the Cl=O groups. This indicates that the synthesized ionic liquid is $[BMIM]^+[ClO_4]^-$ as it has Cl=O bonds in its anion.

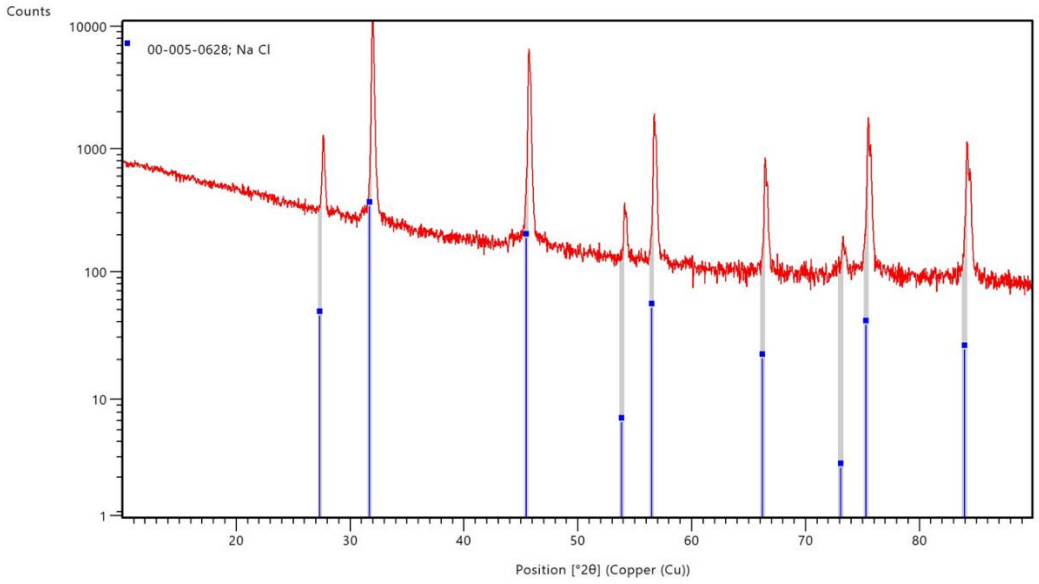

Figure S2 XRD of the solid precipitate formed after the hard acid soft base reaction between dissolved $[BMIM]^+[Cl]^-$ and $NaClO_4$ for $[BMIM]^+[ClO_4]^-$ synthesis : $[BMIM]^+[Cl]^{-1} + NaClO_4 = [BMIM]^+[ClO_4]^- + NaCl(s)$. The XRD peaks of the solid residue matches with the peaks for the standard reference peaks for NaCl. This confirms that the hard acid soft base reaction have occurred successfully and I have obtained $[BMIM]^+[ClO_4]^-$ in the liquid phase after separation of the solid residue.

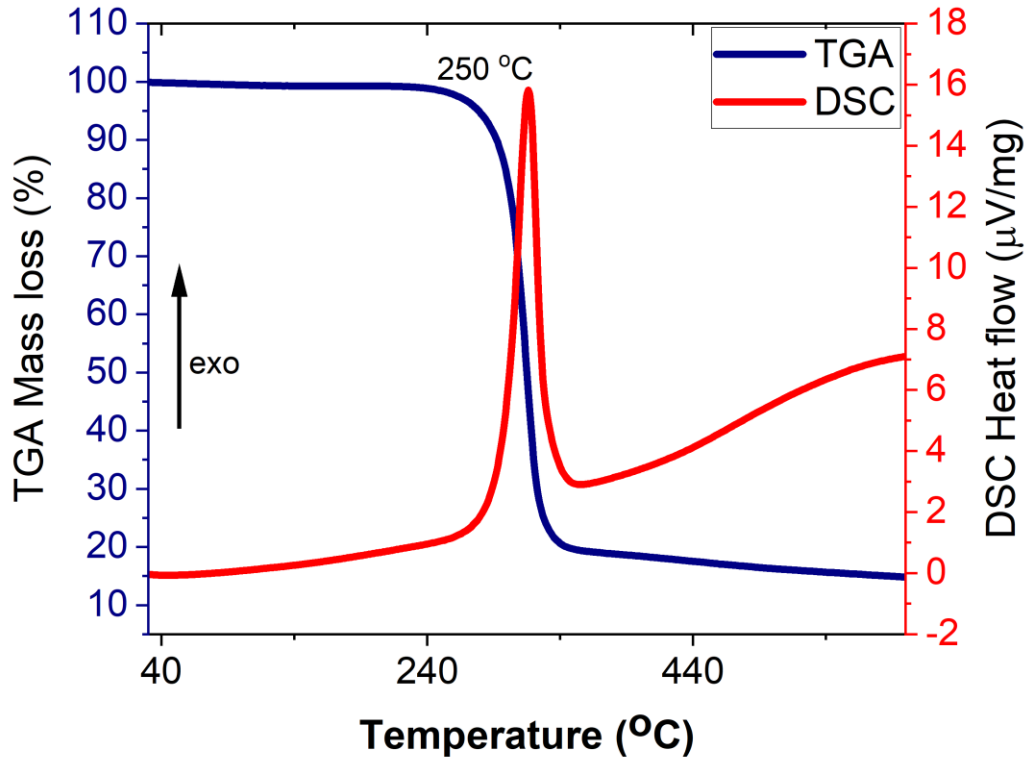

Figure S3 $[BMIM]^+[ClO_4]^-$ shows 80 % mass loss between 250-350 °C and the decomposition reaction is exothermic. No other endothermic peaks are observed prior to the decomposition temperature confirming indicating negligible vaporization of the RTIL on heating.

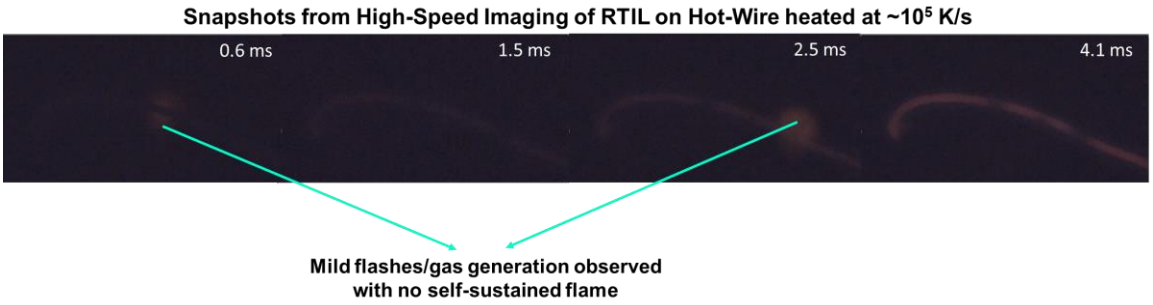

Figure S4 A film of the viscous RTIL ($[BMIM]^+[ClO_4]^-$), coated on wire and heated at ~10^5 K/s, shows mild flashes/gas generation. No self-sustained flame is observed. This implies that the RTIL is non-flammable.

Figure S5 Aliquot of the RTIL placed on a glass slide cannot be ignited by a butane flame. This indicates that the RTIL is thermally insensitive and non-flammable.

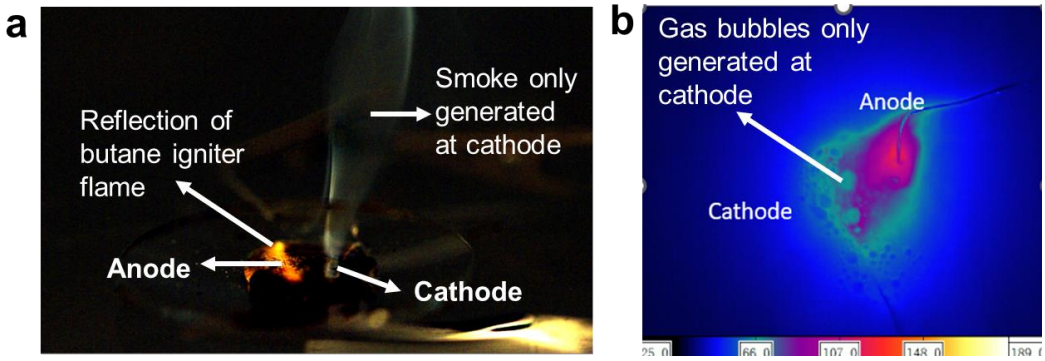

Figure S6 (a) High-speed optical camera image showing that smoke is only generated at the cathode when the DC bias is applied. The smoke is due to the condensation of the vapor phase species generated on electrolysis at the cathode possibly by the mechanism presented in Figure3(b). (b) High speed IR-camera imaging of the electrolysis process when the DC bias is applied. The gas bubbles are only generated at the cathode and there are insignificant number of gas bubbles near the anode. This again confirms our mechanism in Figure3(b), where I have mentioned that the cation $[BMIM]^+$ is reduced to gas phase species at the cathode, whereas the oxidized products of the anion ClO_4^- is retained in the condensed phase.

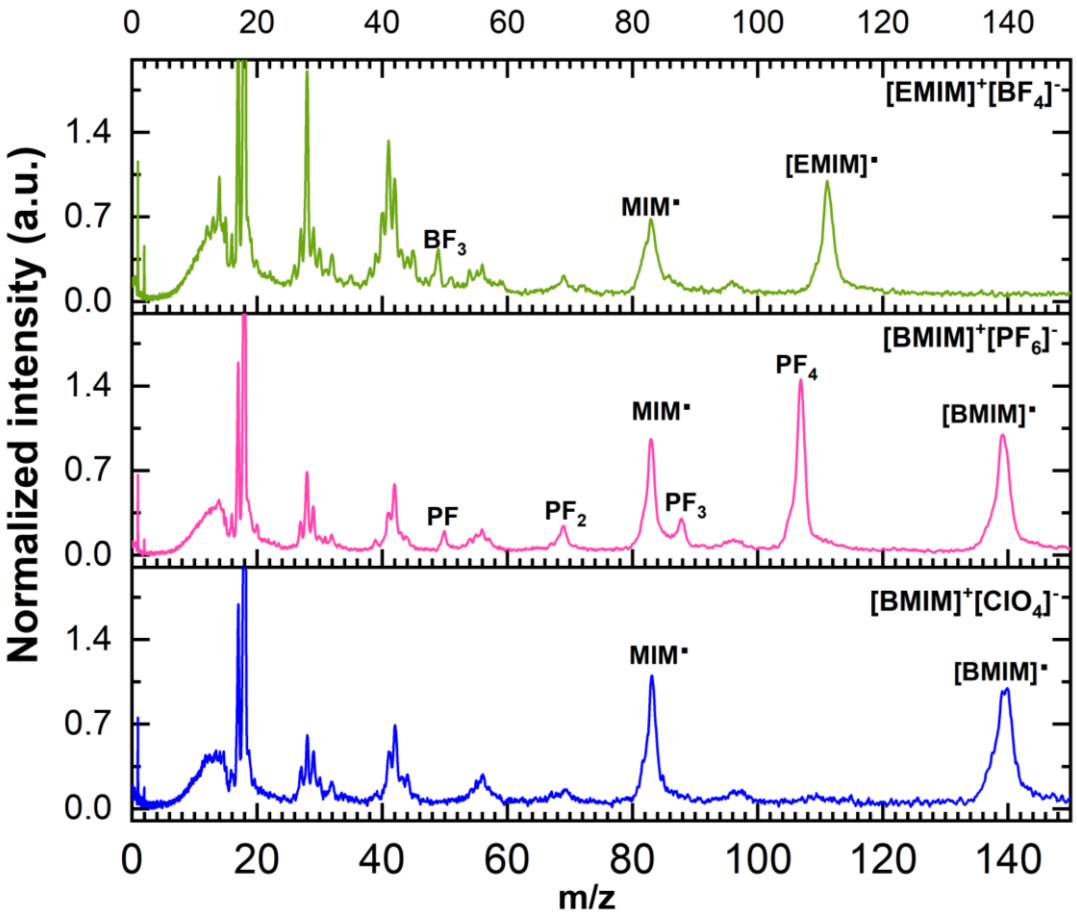

Figure S7 BMIM and EMIM cations form BMIM and EMIM radicals and butene following the mechanism suggested in Figure3 (b). This suggests that the reaction mechanism of the cation is independent of the chain length of the alkyl tail (butyl/ethyl) attached to the ring. No peaks from the anion is observed in case of $[BMIM]^+[ClO_4]^-$. $[BMIM]^+[PF_6]^-$ shows all the characteristic peaks of PF_5 gas (ionization mass spectra data from NIST webbook) . $[EMIM]^+[BF_4]^-$ also shows all the characteristic peaks of BF_3. Hence, the oxidation mechanism at the anode for these two cases can be explained by the following equations:

$$BF_4^- \rightarrow BF_3 + F_{ads} + e^-$$

$$PF_6^- \rightarrow PF_5 + F_{ads} + e^-$$

Since, the ClO_4^- do not show any gas phase species, its oxidized products are probably retained in the condensed phase as explained in Figure3(b).

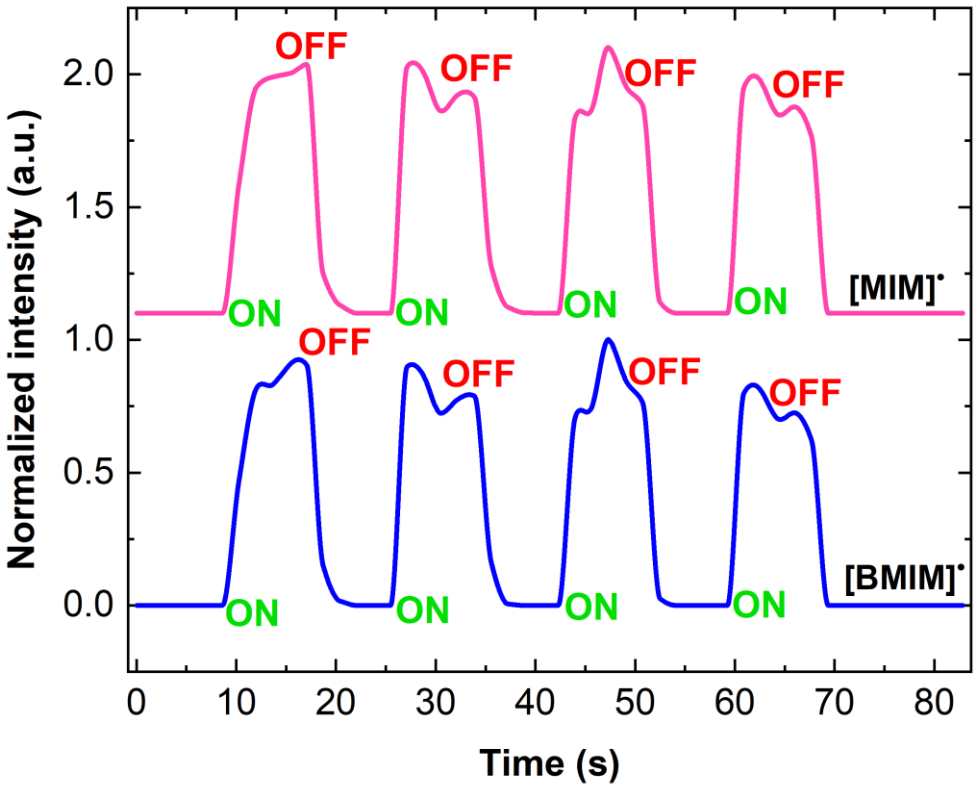

Figure S8 The MIM radical follows the same temporal trend as the BMIM radical when the applied DC bias is turned on/off. This implies that these volatile species can be generated at the same time by applying the DC bias and an open circuit stops their generation with similar delay times.

S.1 Calculation on enthalpy of combustion and electrochemical work performed

$[BMIM]^+[Anion]^- + O_2 \rightarrow 8\,CO_2 + 7.5H_2O + N_2$

The enthalpy of formation of both gas and liquid $[BMIM]^+[DCA]^-$ is available[1]. As the enthalpy of combustion majorly depends on the bulky fuel cation, I assume that the combustion enthalpy of BMIM based ionic liquids will be roughly similar.

$\Delta H_{f_{gas}} = 363.4$ kJ/mol;[1] $\Delta H_{f_{liquid}} = 206.2$ kJ/mol;[1] $\Delta H_{f_{CO_2}} = -393.5\ kJ/mol$ (NIST); $\Delta H_{H_2O} = -241\ kJ/mol$ (NIST)

From this, the combustion enthalpy of gas phase BMIM ionic liquid is -4592 kJ/mol and that of liquid phase is -4749 kJ/mol. However, on gravimetric basis both are approximately same ~20 kJ/g.

Cyclic voltammetry measurement on $[BMIM]^+[ClO_4]^-$ have reported[2] that the cathodic reaction $[BMIM]^+$ to BMIM radical occurs between -1.4-2 V, which is basically the work required to make the free energy of the system to be negative to obtain a spontaneous reaction. Hence, the electrochemical work required is Faraday constant times the voltage ~ 193 kJ/mol which is ~0.81 on a gravimetric basis.

1. Emel'yaneko N. V. et al., *J. Am. Chem. Soc.* 2007, 129, 3930-3937
2. Wang. X et al., Trans. Nonferrous Met. Soc. China 2010, 20, 2032-2036.

10 Microwave Absorption by Small Dielectric and Semi-conductor Coated Metal Particles

10.1 Summary

The presence of oxide coatings on conducting metal particles is often ignored in the calculations of microwave absorption. However, I find that the optical properties of the coatings play a significant role in enhancing or suppressing the absorption of electromagnetic energy. Here, I solve the Mie scattering equations numerically to separate and quantify the role of electric and magnetic field absorption from microwaves at 2.45 GHz by small metal spheres coated with dielectric or semi-conducting materials. The range of size and conductivities of the metal particles and the optical properties of the coatings are chosen for their practical importance. I also provide derive simple approximate expressions for the absorption per unit volume by coated spheres in the small particle limit which agrees very well with the exact Mie solution. I have demonstrated that for highly conducting particles coated with a material of low conductivity, the electric field absorption depends *only* on the optical properties, and the volume fraction of the coating. In contrast, magnetic field absorption depends only on the properties of the core which is the same as the bare metal. I find that the power absorbed by coated particles via the electric field is maximized when loss tangent, $tan\delta$~1. A key result of this study is that a thin layer of lossy coating (~15 % of the particle size) on highly conductive particles will significantly enhance (up to a factor of 10^5) both the power absorbed from the E-field and the total power absorbed.

10.2 Introduction

Microwave processing of materials encompasses a broad field of commercial importance including usage in chemical processes such as catalysis[1], material sintering[2] and combustion[3] as well as in biological diagnosis[4] and drug delivery[5]. Traditional heating processes heat from external conduction where the exterior is naturally hotter than the interior. However, microwaves heat by volumetric heating, which often leads to more uniform heating[6]. This behavior has immense significance in engineering chemical reactions [78], as in the instance of controlling exothermic reactions [910]. Beyond this, selective heating is often necessary in processing of material mixtures[11].

Microwaves are electromagnetic waves with frequency ranging from 300 MHz to 300 GHz out of which 2.45 GHz is widely used commercially. Hence, throughout this text microwaves will refer to 2.45 GHz frequency. To engineer new material processing technologies based on microwave heating, an understanding of the interaction of microwaves with materials based on their electromagnetic properties is necessary. The two most important electromagnetic properties of materials are the relative complex permittivity ($\varepsilon_r = \boldsymbol{\varepsilon}_r' + i\varepsilon_r''$) and the relative complex permeability ($\mu_r = \mu_r' + i\mu_r''$). Here $\varepsilon_r'$and $\mu_r'$are known as the dielectric constant and magnetic permeability respectively, whereas $\varepsilon_r''$and $\mu_r''$are known as the dielectric loss and magnetic loss respectively. Qualitatively, a higher dielectric loss tangent ($tan\delta = \varepsilon_r''/\varepsilon_r'$) and magnetic loss tangent ($tan\delta = \mu_r''/\mu_r'$), give a higher absorption of microwaves [12]. For non-magnetic particles, the relative complex permeability is considered to be 1.0 (same as free space value) as magnetic hysteresis losses are negligible. In this case, the dielectric loss,

which includes losses due to both oscillation of induced dipoles by the electric field and eddy current generated by the magnetic field [13], is a key parameter in determining the amount of electromagnetic energy absorbed by the particle.

Extensive research has been conducted on the interaction of microwaves with "good" dielectric materials, as most of the early microwave-based technologies have focused more on microwave propagation than microwave absorption[14]. However, the interaction of microwaves with lossy dielectric materials and metallic conductors are extremely important to understand microwave heating of these materials. Microwave heating of metal powders have wide application in a variety of fields such as activation of combustion reaction of energetic metal powders[15] and activation of metal nanoparticle catalyzed reactions [16]. Hence, a model to study the optimized conditions for heating of conducting metal particles with a dielectric or semiconductor coating, which is often the case, is extremely desirable.

Studies focusing on the exact solutions for spherical conducting particles[17] have showed the dominance of induced magnetic dipole absorption over induced electric dipole absorption by conducting spheres as the particle size increases from nanometers to micrometers. As such, metallic (non-magnetic) powders have peak absorption when placed at the magnetic field maximum [13]. Most metals naturally form a native oxide shell and this should be accounted for in any analysis, particularly when dealing with nanoparticles where the volume fraction of the oxide may be significant. This also leads one to consider applying coatings to metallic particles to moderate or enhance the optical interactions. One approach to understanding the role of a dielectric coating is to employ an effective-sphere

model which has been extensively applied in the visible region [18]. Studies of coating in the microwave region are limited [19] and thus warrant further attention.

The objective of this paper is to provide insights into the influence of the electrical properties and thickness of coatings on metal particles with various conductivities and sizes. The scope of this study is limited to using 2.45 GHz frequency due to its commercial prevalence. I employ an exact solution approach which enables one to separate and quantify the role of the electric (E-field) and magnetic field (H-field) on the effect of various coating on the absorption per volume as a function of the size and conductivity of the core particle. These examples maybe used as a baseline to explore the role of various coatings on the absorption of microwaves at 2.45 GHz by metal particles.

10.3 Modelling of absorption of microwaves by conducting particles

Absorption by a single spherical particle was calculated using Mie scattering theory. To standardize our calculations in terms of area irradiated and power delivered, I assume an area 1 m^2 is uniformly irradiated with an electromagnetic power deliverance of 1 W, which gives an incident intensity (I_0) of 1 W/m^2. In this study, particles of sizes ranging from the nanometer scale to the millimeter scale are considered, which is much smaller than the wavelength at 2.45 GHz (~12 cm). Our analysis is restricted to low volume fractions (i.e. 0.01 or less) as assumed by [17] removing the need for local field corrections. Hence, the scattered radiation can be neglected [17] and single particle approximation to compute the absorption of electromagnetic radiation using Mie theory is justified.

Computations have been performed for homogeneous conductive spheres and for coated spheres with a conductive core coated with a dielectric or semi-conductive coating.

Following the theory of prior works [17], the dielectric losses of the conductive core has been obtained from the respective conductivities (σ), ranging between 10^0-10^8 S/m, using the Drude model, from which the real component of the dielectric constant of the conductors are assumed to be null. This gives the relation between the relative complex permittivity and the conductivity, $\varepsilon_r = i\sigma/\omega\varepsilon_0$, where ω is the angular frequency of microwaves and ε_0 is the universal permittivity of free space. The values of ε_r for the dielectric or semi-conductive coatings can be expressed as $\varepsilon_r = \varepsilon_r'(1 + i\ tan\delta)$, where $tan\delta = \varepsilon_r"/\varepsilon_r'$ is the loss tangent as discussed in section 1. I will show later in this paper that for a fixed $tan\delta$, the effect of an increase in ε_2' is relatively small. I therefore assumed $\varepsilon_r' = 1$ and the loss tangents ($tan\delta$) are assumed to be in the range of 10^{-3}-10^0, for computation of the exact solutions. The values chosen for $tan\delta$ represents the optical properties for a range of materials which includes dielectrics and semi-conductors. For example, alumina has a $tan\delta$ of 10^{-3} whereas graphite has a $tan\delta$ of 10^{-1}[20]. All the materials considered are non-magnetic and hence the relative magnetic permeability (μ_r) has been assumed to be unity for all cases.

Absorption cross-sections (C_{abs}) for the homogeneous and coated spheres were computed using the BHMIE [21] and BHCOAT subroutines [21] . The product of the absorption cross-section with the incident intensity per unit volume of particle (V_p) gives the absorbed power density (P)[21] as expressed in eqn (1).

$$P = \frac{C_{abs} I_0}{V_p} \qquad (1)$$

10.4 Theory

10.4.1 Electric and magnetic dipole absorption by bare metal conductors

The Mie scattering theory for homogeneous spheres, relates the absorption cross-section of a single particle to the wavelength (λ) and Mie coefficients, a_n and b_n by eqn (2) [21].

$$C_{abs} = \frac{\lambda^2}{2\pi}\sum_{n=1}^{\infty}(2n+1)Re(a_n+b_n) - \frac{\lambda^2}{2\pi}\sum_{n=1}^{\infty}(2n+1)(|a_n|^2+|b_n|^2) \quad (2)$$

Here, Mie coefficients, a_n and b_n are functions of complex permittivity ($\varepsilon_r = \varepsilon_r' + i\varepsilon_r''$) and size parameter, $x = 2\pi r/\lambda$, as expressed in eqn (S1) in supplementary information, where *r* is the particle radius. The Mie coefficients have physical significance, where a_n is responsible for the E-field absorption and commonly known as the electric dipolar term, and b_n is responsible for the H-field absorption, commonly known as the magnetic dipolar term. The magnetic dipolar term accounts for the conduction losses due to the generation of eddy currents by the H-field of microwaves.

The first terms of the series for a_1 and b_1 are calculated from eqn (S1) and eqn (S2) in the supplementary information. In the limit $x \ll 1$, the terms with the lowest power of x are given by:

$$a_1 = -\frac{i2x^3}{3}\left(\frac{\varepsilon_r - 1}{\varepsilon_r + 2}\right)$$
$$b_1 = -\frac{ix^5}{45}\,(\varepsilon_r - 1) \tag{3}$$

For nanoparticles at microwave frequencies, these expressions provide good approximations to a_1 and b_1. From Eqs. (1-3), one obtains the following expression for the electric component of the power absorbed per volume:

$$P_E = \frac{18\pi}{\lambda}\frac{\varepsilon_r"}{(\varepsilon_r' + 2)^2 + \varepsilon"_r^2} I_0 \tag{4A}$$

One feature of this equation is that the volume specific power absorbed due to the E-field is independent of the particle radius (no x dependence). A second feature is that for $\varepsilon_r" \gg \varepsilon_r'$, which is the case for high conductivity metallic particles, the power absorbed is inversely proportional to the imaginary part of the relative permittivity and thus insensitive to ε_r', which is close to zero for high electrical conductors (e.g. metals).

The corresponding expression for the magnetic component of the power absorbed per volume is given by:

$$P_H = \frac{\pi x^2}{5\lambda}\varepsilon_r" I_0 \tag{4B}$$

Hence according to eqn (4A) and eqn (4B), for highly conducting particles (large ε_r"), the dependence on x^2 results in the domination of H-field power absorption over the E-field, with increasing x. However, if ε_r" has a moderately high value then, for small values of x, P_E which is independent of x, makes the volume specific power absorbed independent of the particle size.

10.4.2 Electric and magnetic dipole absorption by coated metallic spheres

I not turn to the more practical problem of coated metals, most usually through their native oxide. Spherical metallic conductors have been considered with a dielectric shell around them. The complex relative permittivity and the size parameter for the conducting core is ε_1 ($\varepsilon_1 = \varepsilon_1' + i\varepsilon_1$") and x respectively, and that of the dielectric shell is ε_2($\varepsilon_2 = \varepsilon_2' + i\varepsilon_2$") and y respectively, where $x = 2\pi r_c/\lambda$ and $y = 2\pi r/\lambda$ given that r_c is the radius of the core and r is the radius of the particle. For coated spheres, the C_{abs} remains the same as eqn (2), however the expressions for a_n and b_n are modified and expressed as a function of two additional terms A_n and B_n as shown in eqn (S3). A_n and B_n are dependent on the properties of the core, whereas a_n and b_n are dependent on the properties of the whole particle.

The first terms of the series, A_1 and B_1, are calculated from eqn (S3) and eqn (S2) for which $x \ll 1$ and thus only the terms with the lowest power of x are included. The expressions obtained for A_1 and B_1 are shown in eqn (5).

$$A_1 = \frac{2}{3}x^3\varepsilon_2^{3/2}\frac{\left(1-\frac{\varepsilon_2}{\varepsilon_1}\right)}{\left(1+\frac{2\varepsilon_2}{\varepsilon_1}\right)}$$

$$B_1 = \frac{1}{45} x^5 \varepsilon_1 \varepsilon_2^{3/2} (1 - \frac{\varepsilon_2}{\varepsilon_1}) \tag{5}$$

Substituting eqn (5) in the expression for a_1 and b_1 given in eqn (S3) one obtains eqn (6),

$$a_1 = -i\frac{2}{3} y^3 \left[\frac{(\varepsilon_2 - 1) + \frac{x^3}{y^3}(1 + 2\varepsilon_2)\frac{(1 - \frac{\varepsilon_2}{\varepsilon_1})}{(1 + \frac{2\varepsilon_2}{\varepsilon_1})}}{(\varepsilon_2 + 2) + \frac{x^3}{y^3}(2\varepsilon_2 - 2)\frac{(1 - \frac{\varepsilon_2}{\varepsilon_1})}{(1 + \frac{2\varepsilon_2}{\varepsilon_1})}}\right]$$

$$b_1 = \frac{i}{45}[(1 - \varepsilon_2)y^5 - (\varepsilon_1 - \varepsilon_2)x^5] \tag{6}$$

Considering the case where ε_1 is purely imaginary and $\varepsilon_1 \gg Im(\varepsilon_2)$. This would be the case for a highly conductive core, coated with a dielectric or semiconductor. One thus obtains eqn (7)

$$a_1 = -i\frac{2}{3} y^3 \left[\frac{(\varepsilon_2 - 1) + \frac{x^3}{y^3}(1 + 2\varepsilon_2)}{(\varepsilon_2 + 2) + \frac{x^3}{y^3}(2\varepsilon_2 - 2)}\right]$$

$$b_1 = -\frac{i}{45} x^5 \varepsilon_1 \tag{7}$$

While the expression of a_1 in eqn(7) is not valid in the limit $x = y$, it is valid provided $\varepsilon_1^{"}(1 - \frac{x^3}{y^3}) \geq 10^3$. This conditionality is obtained by comparing values of a_1

obtained from eqn(6) and eqn (7) and considering the limit in which these are equal up to the 4th decimal place with respect to both real and imaginary components. In a similar manner, I have found that the expression for b_1 in eqn (7) is valid provided $\varepsilon_1^{"}(x/y) \geq 10^3$. Rearranging eqn(7) to give: $a_1 = -\frac{2}{3} iy^3 (\frac{\varepsilon_2 - w}{\varepsilon_2 + 2w})$ where $w = \frac{1 - x^3/y^3}{1 + 2x^3/y^3}$. The volume specific power absorbed from the E-field for coated particles with this approximation is given by:

$$P_E(coat) = \frac{18\pi}{\lambda} \frac{w\varepsilon_2^{"}}{(\varepsilon_2' + 2w)^2 + \varepsilon_2^{"2}} I_0 \qquad (8A)$$

From eqn (8A), one can see that the contribution of the Electric field to the volume specific power absorbed, depends on ε_2 and x^3/y^3. This implies that the volume specific power dissipated from the E-field depends on the optical properties and volume fraction of the coating. For a fixed $tan\delta(\varepsilon_2"/\varepsilon_2')$ as considered in this paper, the effect of an increase in ε_2' is relatively small. For example, if $tan\delta = 10^{-2}$ with a coating thickness of 5 % of the diameter, the value of the power absorbed decreases by a factor of 7 as the value of ε_2' is increased from 1 to 10. Therefore, the assumption of $\varepsilon_2' = 1$ and $\varepsilon_2" = tan\delta$ (section 2) for computing the exact solution is justified.

The magnetic contribution to the power dissipated from the H-field is given by eqn (8B)

$$P_H(coat) = \frac{\pi x^2}{5\lambda} \varepsilon_1" I_0 \qquad (8B)$$

Thus, the power density absorbed by the particle from the H-field is independent of the properties of the coating in this limit and only proportional to the optical properties and the surface area of the core. Notice that equation 8B and 4B are actually the same in this case. Hence, for highly conducting particles, because of the dependence on x^2 as in eqn (8B) the H-field power absorption dominates via the core with increasing x. However, if ε_1" has a moderately high value then, for small values of x, P_E (coat) is independent of x while P_H (coat) is a function of x^2, which results in the domination of E-field absorption by the coating. Equations 5-8 represent new expressions that can be employed to rapidly calculate optical effects for coated particles in the MW region.

10.5 Results and Discussions

10.5.1 Absorption by bare metal particles

Absorbed power density from microwaves has been calculated for homogeneous spherical bare metal particles of different sizes having conductivity (σ) ranging from 10^0-10^8 S/m as shown in Figure 10-1 (a). Similar results have been also reported by [17], but has been presented here in order to bring context to the coated cases.

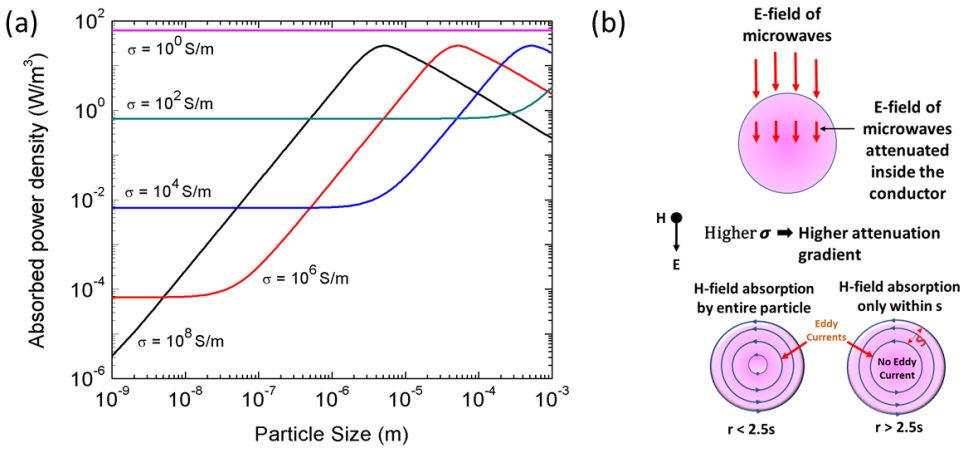

Figure 10-1 Microwave power density absorbed by bare metal particles of different sizes (diameters) with different conductivities. Particles with higher conductivity have lower E-field absorption but higher H-field absorption at smaller particle sizes. (b) Schematic showing E-field screening and eddy current path in metal particles smaller and larger than the skin depth.

In Figure 10-1(a), the region where volumetric power absorption is independent of particle size corresponds to E-field dominated absorption. The H-field absorption starts dominating at the point where the power absorption increases with increasing particle size. The particle-size transition from E to H field domination, occurs at smaller particle size as the conductivity (σ) or imaginary part of the relative permittivity increases. The E-field absorption is lower for particles with higher conductivities, a consequence of the partial screening (skin depth) of the E-field within a highly conducting particle [17] as seen in Figure 10-1(b).

In the region of H-field dominated absorption, for smaller particles the volume specific power absorbed (Figure 10-1 (a)) is proportional to surface area (x^2) as also explained by the approximate solution in eqn(4B) in small particle limit. The inverse dependence on particle size, for large particle sizes, is consistent with results given in [22]

for $x \ll 1$ and $\sqrt{\varepsilon_r}x \gg 1$. Full expression for b_1 is required to support this. The maximum in absorption depends on conductivity and is directly proportional to the skin depth (see Table S1); $r = 2.5s$, where s is the skin depth and r is the particle radius ($x = 2\pi r/\lambda$). This matches well with the interpretations in reference [23] who found a very similar radius dependence of the maxima as 2.41s. With further increases in particle size beyond this case, the absorption gradually decreases. The maximum value attained by the H-field power absorption is independent of σ. As shown in Figure 10-1(b), for particle sizes smaller than s, the eddy current generated by the H-field flows throughout the entire volume of the particles, flowing in the plane normal to the direction of the magnetic field and causing resistive energy dissipation. Eddy current power dissipation increases with an increase in particle size until $r = 2.5s$, after which the eddy current only flows within the skin depth (s), causing the power dissipation to be restricted only within this small region, such that H-field absorption decreases.

10.5.2 Absorption of E-field by coated metal particles

I now turn our attention to the coated particle problem. I present the results in a manner analogous to that shown for the pure conductors (Figure 10-1). Our particles are constructed whereby the coating thickness is 5 % of the total particle diameter. Figure 10-2(a) shows that the volume specific power absorbed from the E-field is independent of particle size and increases with $tan\delta$ of the coating ($tan\delta = \varepsilon_2"/\varepsilon_2'$) at a fixed conductivity.

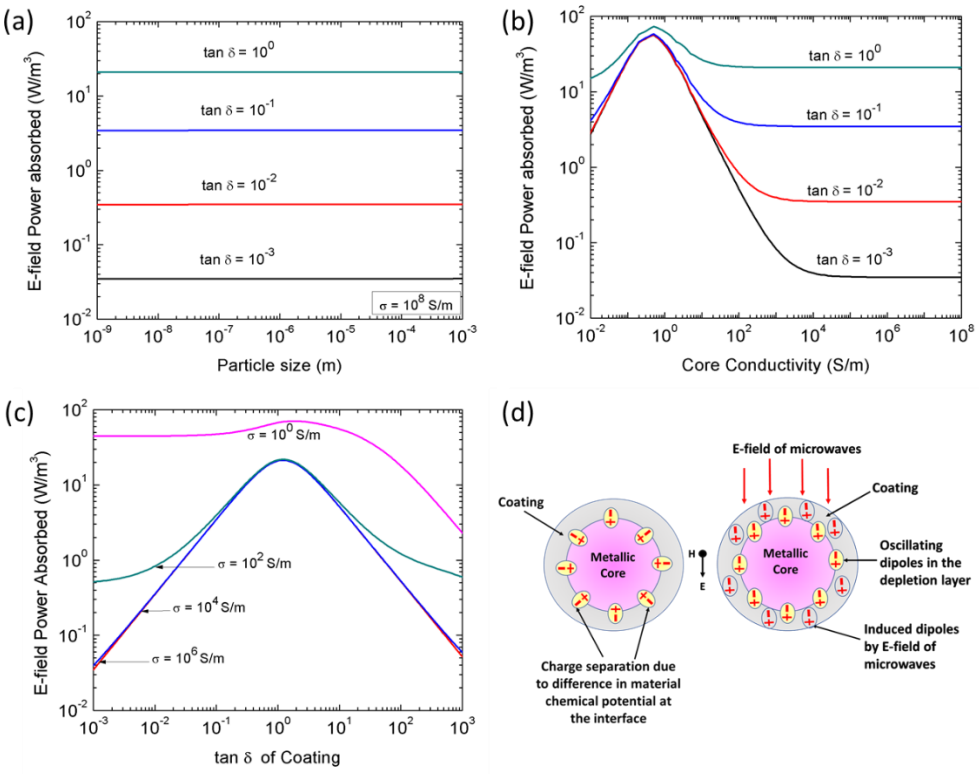

Figure 10-2 (a) E-field absorbed by conducting particles (σ=10^8 S/m) having coatings with different $tan\delta$ (coating), E-field absorbed by conducting particles as a function of different core conductivities having coatings with different $tan\delta$(c). (d) Schematic showing the role of inherent (interface) and induced (coating) dipoles in absorption of E-field of microwaves by coated metal particles.

Figure 10-2(b) shows the E-field absorbed by core-shell particles having different σ and$tan\delta$. The maximum power absorbed peaks at $\sigma = 0.5$ S/m which is $\sim 3\omega\varepsilon_0$, independent of $tan\delta$. The maxima in absorption in the case of bare metal particles is ~0.4 S/m as reported by [23] and implies that the presence of a coating does not affect the maxima of the absorption.

For conductivities in excess of 0.5 S/m, the E-field absorption gradually decreases and achieves a constant value, independent of conductivity of the core. This is the asymptotic region where the coating dominates and the core has no effect on absorption.

Eqn(7 & 8) are only dependent on the properties of the coating and hence these are applicable in this region.

Figure 10-2(c) shows the dependence of E-field absorbed on $tan\delta$ for coatings with σ ranging between 10^0-10^8 S/m. The absorption by the particles with different σ, peaks at the same $tan\delta$ of 1. When eqn (8A) is expressed in terms of $tan\delta$ by replacing $\varepsilon_2"/\varepsilon_1'$ with $tan\delta$ and assuming $\varepsilon_1' = 1$, the following equation is obtained:

$$P_E(coat) = \frac{18\pi}{\lambda} \frac{w\ tan\delta}{(1+2w)^2 + tan\delta^2} I_0 \qquad (9)$$

From eqn(9) i the peak absorption occurs when $tan\delta = 1 + 2w$ and since $0 < w < 1$, it can be said that the maxima is $tan\delta \sim 1$. The coating absorbs power from the E-field due to the oscillation of induced electric dipoles. The power absorbed by the coating increases with the increase in $tan\delta$ of the coating, and reaches a maximum at $tan\delta = 1$. This is because the increase in $tan\delta$ implies an increase in the polarizability of the medium resulting in higher power dissipation. However, with $tan\delta > 1$, the coating material itself behaves as a conductor, and this behaves as the case described in section 4.1, and the screening of the electric field within the coating results in the decrease in power absorption with increasing $tan\delta$. Figure 10-2(d) illustrates microwave absorption within the coating by induced dipoles and the depletion layer at the interface of the dielectric or semi-conductive coating and the conductive core driven by the chemical potential difference between the two materials. The presence of this depletion layer is well-known and previously analyzed in various studies [242526]. The absorption due to the oscillation of this

depletion layer has not been accounted in our calculations. Hence, our model may slightly underestimate the magnitude of power absorbed.

10.5.3 Significance of H-field absorption in coated metal particles

Absorption of the H-field and net effect of microwaves has been calculated for conductive metal particles of different sizes with conductivity (σ) ranging from 10^0-10^8 S/m, coated with dielectric and semi-conductive materials having loss tangents ($tan\delta$) ranging between 10^{-3}-10^0 S. The coating thickness has been assumed to be 5 % of the diameter of the particle, as with the previous case. Figure 10-3(a) shows the H-field absorbed by metal particles of different sizes and σ, with a coating of $tan\delta = 10^{-3}$, and I find similar results to that reported previously [18] and consistent with eqn (8B)

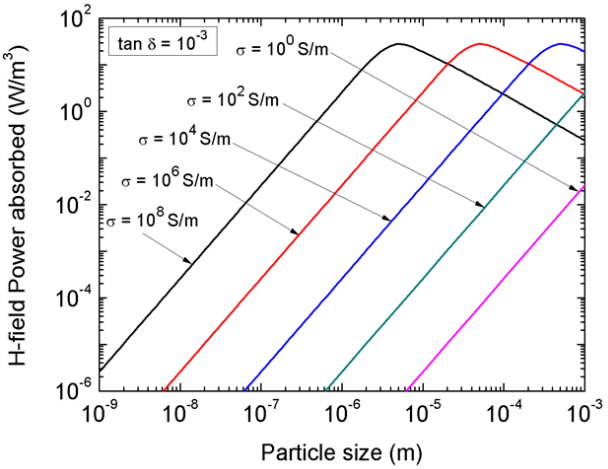

Figure 10-3 H-field absorbed by conducting particles of different sizes (diameters) and conductivities (σ) having a coating of $tan\delta = 10^{-3}$. The H-field absorption by the coated particles is the same as that of the core.

This is because the eddy currents can only be generated in the conductive metallic core. I have seen that the H-field absorption is independent of the $tan\delta$ of the coating and

have thereby chosen only one case with $tan\delta = 10^{-3}$ for representation. The maximum H-field absorption is still observed at $r = 2.5s$. The particles with higher σ, peak at lower particle sizes, similar to the case observed for bare metal particles.

10.5.4 Total power absorbed by coated metal particles

The total field absorbed from the microwaves have been computed for metal particles having σ of 10^8 S/m [Figure 10-4] with coatings of $tan\delta$ of 10^{-3} to 10^0. This is done to assess the relative importance of H vs. E fields as a function of particle size. Smaller particle sizes (nanometer range), show an increase in volume specific power absorption with increase in $tan\delta$ and is independent of particle size due to E-field domination of absorption by the coating. At higher particle sizes (micrometer range), however, the power absorbed increases for different $tan\delta$ and converges at a maximum at $r = 2.5s$; i.e the same as that for bare metals. For particle sizes beyond the maxima, absorption decreases. These trends show that at larger sizes H-field absorption by the core is the dominant factor.

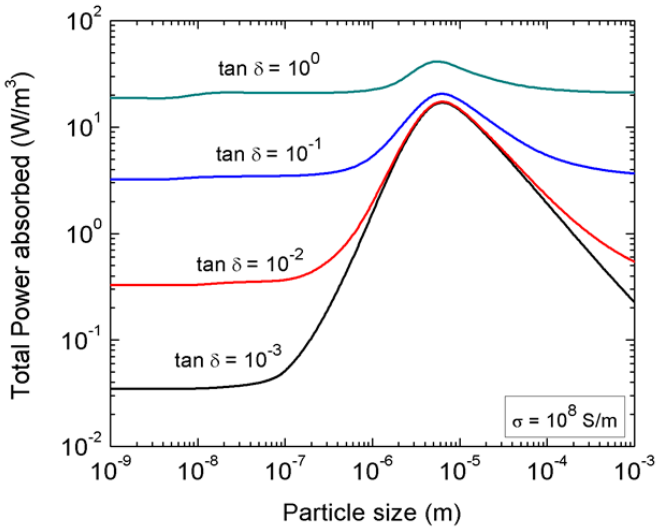

Figure 10-4 Total power absorbed by conducting particles of different sizes (diameters) with $\sigma = 10^8$ S/m, having coatings of $tan\delta$ ranging between 10^{-3}-10^0.

10.5.5 Dependence of absorption on the thickness of the coating

To assess the role of the coating thickness, I consider two different particle sizes, in the nano (10^{-8} m) and micro (10^{-6} m) range, and with two different coatings, $tan\delta = 10^{-3}$ (dielectric) and $tan\delta = 10^{-1}$(semi-conductive). Figure 10-5(a) and Figure 10-5(b) shows a very rapid increase in absorption for very small coating thicknesses regardless of particle size, with a dielectric coating ($tan\delta = 10^{-3}$). Increases as much as two orders of magnitude are observed for an increase in coating thickness of <15 %. I have already shown that E-field absorption dominates for both bare and coated metal nanoparticles (10^{-8} m). According to Figure 10-5(a), at a particle size of 10^{-8} m, the E-field absorption by the coating dominates that of the core, and hence the power absorption increases with increase in coating thickness until the coating thickness is ~15 % of the particle diameter. For the micron particle, as in Figure 10-5(b), at high conductivities ($\sigma = 10^8$ S/m) the bare particle

actually absorbs more than the coated due to the dominance of the H-field absorption. Only at lower conductivities does the coating enhance absorption due to the increasing importance of E-field absorption.

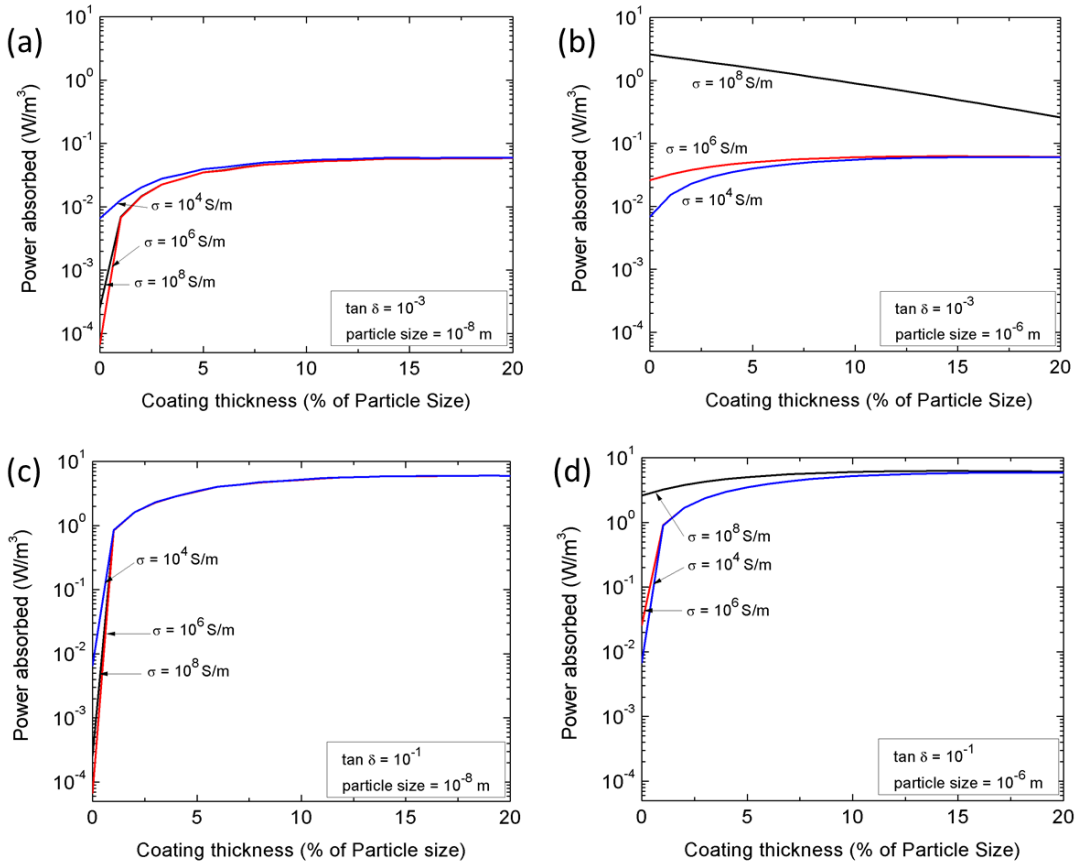

Figure 10-5 Power absorbed by conductive particles having different σ, with size (diameter) of 10^{-8} m and coating of $tan\delta = 10^{-3}$ (a), with size of 10^{-6} m and coating of $tan\delta = 10^{-3}$ (b), with size of 10^{-8} m and coating of $tan\delta = 10^{-1}$ (c) and with size of 10^{-6} m and coating of $tan\delta = 10^{-1}$ (d), with different coating thicknesses.

In a similar manner, Figure 10-5(c) and Figure 10-5(d) shows the case for a semi-conducting coating ($tan\delta = 10^{-1}$). For the nanoparticle (Figure 10-5(c)), the E-field absorbed by the coating is significantly higher than the core. Hence in these cases the

absorption increases drastically with increase in the coating thickness until the coating thickness is ~15 % of the particle size. At this coating thickness the absorption is significantly higher than the bare metal case as well as the case when the particles are coated with an inferior absorber of $tan\delta = 10^{-3}$. For the micron particle shown in Figure 10-5(d), absorption of H-field dominates when bare, but with increase in volume of the coating, the E-field absorption by the coating becomes more important.

In general, the results show that nanoparticle absorption is very sensitive to coating thickness and achieves a maximum at coatings of ~ 15%. Microparticles, in contrast, do not show quite the sensitivity to coatings, particularly if the coating is not a strong absorber or when the core is highly conductive.

Because of the potential interest in this finding, I also have plotted the ratio of the power absorbed by coated particles to power absorbed by bare particles for particles of various sizes and core conductivities (σ) to show the power enhancement in coated particles compared to the bare particles. Figure 10-6 represents this ratio (P_{coated}/P_{bare}) for particles of different sizes and conductivities, having a coating of $tan\delta = 10^{-1}$, with a thickness of 15 % of the particle size.

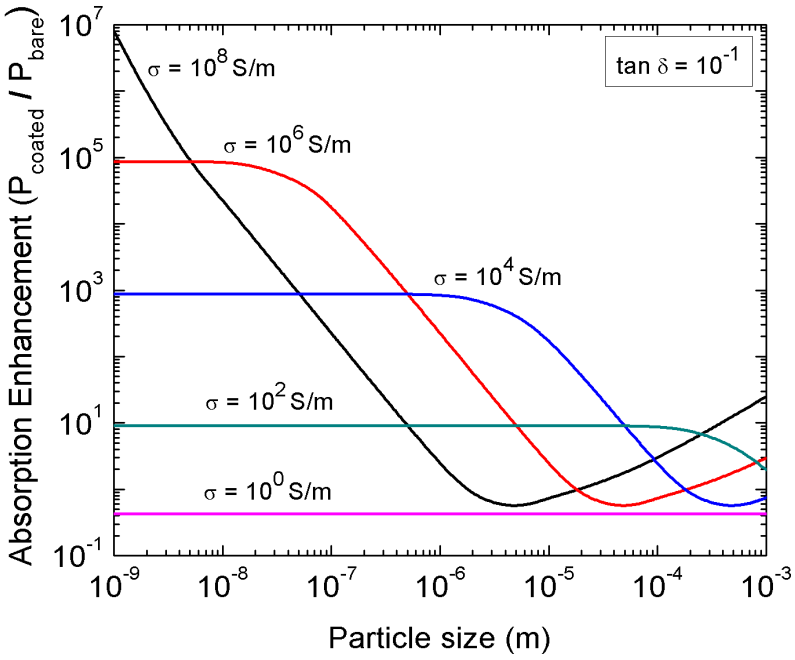

Figure 10-6 The absorption enhancement in coated particles compared to the bare particles of various sizes (diameters) and conductivities.

For σ = 10^{2}-10^{8} S/m, the ratio is very high for the smaller particles but decreases with increase in particle size because of the domination of the H-field absorption by the metallic core. The particles with σ = 10^{0} S/m are unaffected by the coating. Hence, the coating can increase the power absorption in the case of small and conducting particles but is not so effective for large particles. All of these results have been summarized in Table 9-1.

Table 10-1 Summary of absorption tendency and model equations for different domains of particle size and conductivity

Particle size (m)	σ = 10^0-10^2 S/m	σ = 10^4-10^6 S/m	σ = 10^8 S/m
10^{-9}-10^{-7} (nano)	Core (H-field) dominates **Eqn (8B)**	Coating (E-field) dominates* **Eqn (8A)**	Coating (E-field) dominates **Eqn (8A)**
10^{-6}-10^{-4} (micro)	Core (H-field) dominates **Eqn (8B)**	High loss Coatings (E-field) dominates **Eqn (8A)**	Core (H-field) dominates **Eqn (8B)**

**Domain of primary interest*

To establish the validity of our approximate solutions, I have compared the results for power absorbed from the E-field (P_E) i.e. eqn(8A) and power absorbed from H-field (P_M) i.e. eqn(8B) to the exact Mie solutions in Figure 10-7 for the case of a microparticle with a coating of $tan\delta = 10^{-1}$ and a core with σ = 10^6 S/m. The value of P_E increases by more than 4 orders of magnitude as one goes from the bare metal (0 % coating thickness) to all coating (100 % coating thickness). For thickness greater than 10^{-3} %, the volume specific power absorbed is a linear function of the coating thickness. However, for a coating thickness above ~10 %, both the approximate and exact solutions flatten out so the absorption is nearly constant as one approaches the case of 100% coating. The region where there is a discrepancy between the approximation and the exact result up to a factor of 2 is for very small coating thicknesses below ~10^{-4} %. The thickness of such a coating would be on the order of 1 % of the diameter of a hydrogen atom.

The approximate solution for P_M agrees with the exact solution so long as the coating thickness is less than 1.5 % of the particle size. However this latter consideration turns out to unimportant since for coatings greater than 1.5 % of the particle size, $P_E >> P_M$ in any case, and hence the breakdown of the approximate has no practical effect in

estimating the total power absorbed. Thus our approximate solutions are very robust as well as simple.

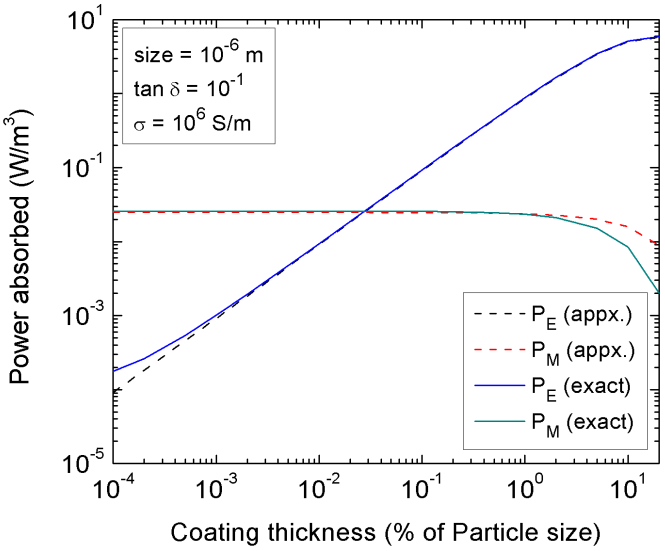

Figure 10-7 Comparison between approximate and exact Mie solutions of power absorbed from the E-field (P_E) and H-field (P_M) for a particle size (diameter) = 10^{-6} m with coating $tan\delta$ = 10^{-1} and core σ = 10^6 S/m

10.6 Experimental validation

This benchmarking model suggests that Ti nanoparticles with a TiO_2 will absorb ~100 times higher microwave power compared to that of Al based on the core and shell dielectric properties listed in Table S2. For experimental validation of this calculation, in a collaborative effort I have prepared directly ink-written composites of Ti and Al nanoparticle in PVDF matrix. When exposed to microwave radiation through needle monopole antenna, the Ti-particle laden film ignited locally in the region where microwave radiation is applied whereas the Al-particle laden film did not heat up and ignite (Figure 10-8). This suggests that the use of microwave radiation can be used for selective heating of localized regions in energetic composites[27].

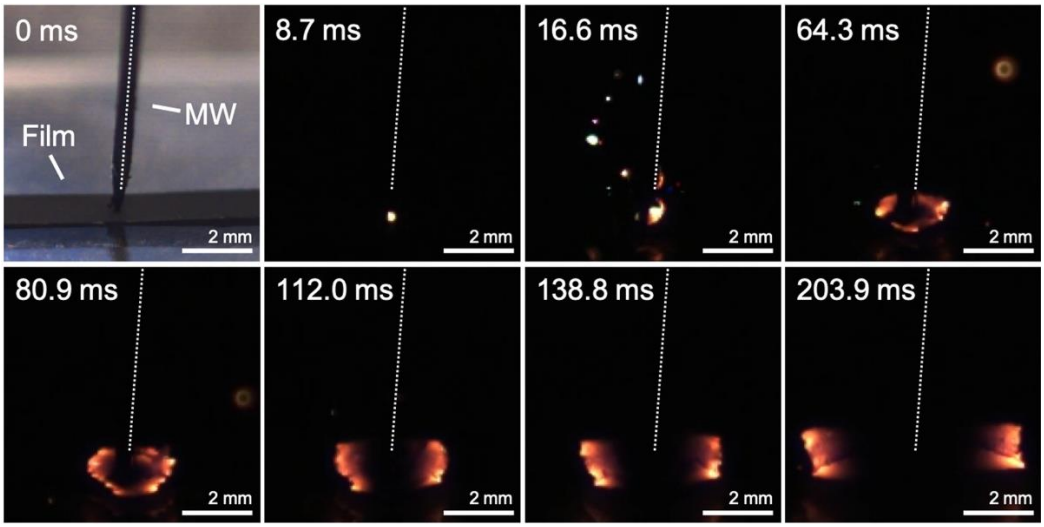

Figure 10-8 Ignition of Ti-PVDF films under microwave antenna (*Reproduced with permission from American Physical Society*).

The model also predicted that MnO2 as a microwave absorbing materials will be a good candidate to incorporate into energetic composites as microwave sensitizer cum oxidizer. The experimental validation of this have been presented in a collaborative publication[28].

10.7 Conclusions

In this work, I have obtained working formulas (eqn 5-8) validated on full Mie theory calculation for microwave absorption by conducting particles coated with a semi-conductive or dielectric coating in the small particle limit, for the condition $[\varepsilon_1" \gg \varepsilon_2"]$. The range in coating thickness and optical properties for which the formulas is valid was determined by comparing with the results using full Mie theory solutions for coated spheres. From these formulas I conclude that the E-field contribution to absorption depends

only on the optical properties, and the volume fraction of the coating. In fact, from the full solution I can also infer that for coating thicknesses greater than about 15 % of the particle size, absorption is equivalent to a sphere of the same size and with the same optical properties as the coating. The power absorbed from the H-field, depends only on the core properties, and is equivalent to that of the case of bare metals. The approximate solutions for E-field contribution to power absorbed agrees with the exact Mie solutions as long as the coating thickness is greater than 0.002 % of the particle size, whereas that for the H-field breaks down when coating thickness is greater than 1.5 % of the particle size, but is unimportant a thicker coating in any case.

The full solution is also being presented to show the cases where the condition $[\varepsilon_1" \gg \varepsilon_2"]$ is not satisfied. The peak value of P_E by the coated metal particles have been found when core conductivity, $\sigma \sim 3\omega\varepsilon_0$ and coating $tan\delta \sim 1$. I have shown that the presence of a thin layer (~15 % of particle size) of absorbing coating can drastically enhance the absorption of nanoparticles by a factor of ~10^5 compared to bare metal particles. The effect of the coating is more pronounced for the nanoparticles, whereas microparticles are not so sensitive to the coating particularly when the coating is an inferior absorber or when the core is highly conductive. The large enhancement in case of the nanoparticles, suggests that materials scientists working with nanoparticles focus more on E-field absorbing coatings rather than focusing on the H-field absorption.

Finally I note that existing effective medium theories [18] that use volume average optical properties to solve for non-homogeneous materials such as coated spheres, are mostly based on the electrostatic approximation employing an effective complex

permittivity (ε_r), while ignoring the permeability (μ_r). While this approximation may be adequate for nanoparticles, this work demonstrates that to adequately describe the absorption of microparticles; i.e. accounting for H-field absorption thorough the effective complex permeability would require development of new effective medium theories.

10.8 References

(1) Haneishi, N.; Tsubaki, S.; Abe, E.; Maitani, M. M.; Suzuki, E. ichi; Fujii, S.; Fukushima, J.; Takizawa, H.; Wada, Y. Enhancement of Fixed-Bed Flow Reactions under Microwave Irradiation by Local Heating at the Vicinal Contact Points of Catalyst Particles. *Scientific Reports* **2019**, *9* (1), 1–12. https://doi.org/10.1038/s41598-018-35988-y.

(2) Mishra, P.; Sethi, G.; Upadhyaya, A. Modeling of Microwave Heating of Particulate Metals. *Metallurgical and Materials Transactions B: Process Metallurgy and Materials Processing Science* **2006**, *37* (5), 839–845. https://doi.org/10.1007/s11663-006-0066-z.

(3) Stockman, E. S.; Zaidi, S. H.; Miles, R. B.; Carter, C. D.; Ryan, M. D. Measurements of Combustion Properties in a Microwave Enhanced Flame. *Combustion and Flame* **2009**, *156* (7), 1453–1461. https://doi.org/10.1016/j.combustflame.2009.02.006.

(4) Wang, L. Microwave Sensors for Breast Cancer Detection. *Sensors (Switzerland)* **2018**, *18* (2), 1–17. https://doi.org/10.3390/s18020655.

(5) Larrañeta, E.; Lutton, R. E. M.; Brady, A. J.; Vicente-Pérez, E. M.; Woolfson, A. D.; Thakur, R. R. S.; Donnelly, R. F. Microwave-Assisted Preparation of Hydrogel-Forming Microneedle Arrays for Transdermal Drug Delivery Applications. *Macromolecular Materials and Engineering* **2015**, *300* (6), 586–595. https://doi.org/10.1002/mame.201500016.

(6) Dolande, J.; Datta, A. Temperature Profiles in Microwave Heating of Solids: A Systematic Study. *Journal of Microwave Power and Electromagnetic Energy* **1993**, *28* (2), 58–67. https://doi.org/10.1080/08327823.1993.11688206.

(7) Gerbec, J. A.; Magana, D.; Washington, A.; Strouse, G. F. Microwave-Enhanced Reaction Rates for Nanoparticle Synthesis. *Journal of the American Chemical Society* **2005**, *127* (45), 15791–15800. https://doi.org/10.1021/ja052463g.

(8) Dudley, G. B.; Richert, R.; Stiegman, A. E. On the Existence of and Mechanism for Microwave-Specific Reaction Rate Enhancement. *Chemical Science* **2015**, *6* (4), 2144–2152. https://doi.org/10.1039/c4sc03372h.

(9) Barkley, S. J.; Kindem, D. K.; Zhu, K.; Michael, J. B.; Sippel, T. Dynamic Control of Composite Solid Propellant Flame Spread through Microwave Eddy Current Heating of Propellant-Embedded Antennas. *AIAA Scitech 2019 Forum* **2019**, No. January. https://doi.org/10.2514/6.2019-1239.
(10) Mirzaei, A.; Neri, G. Microwave-Assisted Synthesis of Metal Oxide Nanostructures for Gas Sensing Application: A Review. *Sensors and Actuators, B: Chemical*. 2016. https://doi.org/10.1016/j.snb.2016.06.114.

(11) Kitchen, H. J.; Vallance, S. R.; Kennedy, J. L.; Tapia-Ruiz, N.; Carassiti, L.; Harrison, A.; Whittaker, A. G.; Drysdale, T. D.; Kingman, S. W.; Gregory, D. H. Modern Microwave Methods in Solid-State Inorganic Materials Chemistry: From Fundamentals to Manufacturing. *Chemical Reviews* **2014**, *114* (2), 1170–1206. https://doi.org/10.1021/cr4002353.

(12) Gong, C.; Zhang, J.; Yan, C.; Cheng, X.; Zhang, J.; Yu, L.; Jin, Z.; Zhang, Z. Synthesis and Microwave Electromagnetic Properties of Nanosized Titanium Nitride. *Journal of Materials Chemistry* **2012**, *22* (8), 3370–3376. https://doi.org/10.1039/c1jm13509k.

(13) Ignatenko, M.; Tanaka, M.; Sato, M. Absorption of Microwave Energy by a Spherical Nonmagnetic Metal Particle. *Japanese Journal of Applied Physics* **2009**, *48* (6). https://doi.org/10.1143/JJAP.48.067001.

(14) Dragoman, M.; Cismaru, A.; Aldrigo, M.; Radoi, A.; Dinescu, A.; Dragoman, D. MoS2thin Films as Electrically Tunable Materials for Microwave Applications. *Applied Physics Letters* **2015**, *107* (24). https://doi.org/10.1063/1.4938145.

(15) Meir, Y.; Jerby, E. Thermite Powder Ignition by Localized Microwaves. *Combustion and Flame* **2012**, *159* (7), 2474–2479. https://doi.org/10.1016/j.combustflame.2012.02.015.

(16) Gracia, J.; Escuin, M.; Mallada, R.; Navascues, N.; Santamaria, J. Nano-Heaters: New Insights on the Outstanding Deposition of Dielectric Energy on Perovskite Nanoparticles. *Nano Energy* **2016**, *20*, 20–28. https://doi.org/10.1016/j.nanoen.2015.11.040.

(17) Porch, A.; Slocombe, D.; Edwards, P. P. Microwave Absorption in Powders of Small Conducting Particles for Heating Applications. *Physical Chemistry Chemical Physics* **2013**, *15* (8), 2757–2763. https://doi.org/10.1039/c2cp43310a.

(18) Chettiar, U. K.; Engheta, N. Internal Homogenization: Effective Permittivity of a Coated Sphere. *Optics Express* **2012**, *20* (21), 22976. https://doi.org/10.1364/oe.20.022976.

(19) Rybakov, K. I.; Semenov, V. E.; Egorov, S. V.; Eremeev, A. G.; Plotnikov, I. V.; Bykov, Yu. V. Microwave Heating of Conductive Powder Materials. *Journal of Applied Physics* **2006**, *99* (2), 023506. https://doi.org/10.1063/1.2159078.
(20) Horikoshi, S.; Schiffmann, R. F.; Fukushima, J.; Serpone, N. *Microwave Chemical and Materials Processing: A Tutorial*; 2017. https://doi.org/10.1007/978-981-10-6466-1.

(21) Bohren, C. F.; Huffman, D. R. *Absorption and Scattering of Light by Small Particles. New York: Wiley*. https://doi.org/10.1002/9783527618156.

(22) van de Hulst, H. C. *Light Scattering by Small Particles*; John Wiley and Sons: New York, 1958. https://doi.org/10.1002/qj.49708436025.

(23) Porch, A.; Slocombe, D.; Edwards, P. P. Microwave Absorption in Powders of Small Conducting Particles for Heating Applications. *Physical Chemistry Chemical Physics* **2013**, *15* (8), 2757–2763. https://doi.org/10.1039/c2cp43310a.

(24) Henz, B. J.; Hawa, T.; Zachariah, M. R. On the Role of Built-in Electric Fields on the Ignition of Oxide Coated Nanoaluminum: Ion Mobility versus Fickian Diffusion. *Journal of Applied Physics* **2010**, *107* (2). https://doi.org/10.1063/1.3247579.

(25) Monch, W. On the Physics of Metal-Semiconductor Interfaces. *Reports on Progress in Physics* **1990**. https://doi.org/10.1088/0034-4885/53/3/001.

(26) Di Bartolomeo, A. Graphene Schottky Diodes: An Experimental Review of the Rectifying Graphene/Semiconductor Heterojunction. *Physics Reports*. 2016. https://doi.org/10.1016/j.physrep.2015.10.003.

(27) Kline D.J., Rehwoldt M.C., Turner C.J., Biswas P., Mulholland G.W., McDonnell S.M., Zachariah M.R. Spatially focused microwave ignition of metallized energetic materials. *Journal of Applied Physics* 2020, 127, 055901.

(28) Alibay Z. , Olsen D., Biswas P., England C., Xu F. Ghildiyal P., Zhou M., Zachariah M.R. Microwave Stimulation of Energetic Al-Based Nanoparticle Composites for Ignition Modulation. *ACS Applied Nanomaterials* 2022, 5, 2, 2460–2469.

10.9 Supporting information

Bohren and Huffman gives the Mie coefficients for homogeneous spheres as follows:

$$a_n = \frac{m\Psi_n(mx)\Psi_n'(x) - \Psi_n(x)\Psi_n'(mx)}{m\Psi_n(mx)\xi_n'(x) - \xi_n(x)\Psi_n'(mx)}$$
$$b_n = \frac{\Psi_n(mx)\Psi_n'(x) - m\Psi_n(x)\Psi_n'(mx)}{\Psi_n(mx)\xi_n'(x) - m\xi_n(x)\Psi_n'(mx)} \quad \text{(S1)}$$

where m = $\sqrt{\varepsilon_r}$

The expansions of these terms expressed as Ricatti-Bessel functions are given in eqn (S2) as follows:

$$\Psi_1(z) = \frac{z^2}{3} - \frac{z^4}{30} \qquad \Psi_1'(z) = \frac{2z}{3} - \frac{2z^3}{15}$$
$$\xi_1(z) = -\frac{i}{z} - \frac{iz}{2} + \frac{z^2}{3} \qquad \xi_1'(z) = \frac{i}{z^2} - \frac{i}{2} + \frac{2z}{3} \quad \text{(S2)}$$
$$\chi_1(z) = -\frac{1}{z} - \frac{z}{2} \qquad \chi_1'(z) = \frac{1}{z^2} - \frac{1}{2}$$

These are approximated representations by only including the significant lower powers of z.

The Mie coefficients for coated spheres are given in eqn (S3) as follows:

$$a_n = \frac{\Psi_n(y)[\Psi_n'(m_2y) - A_n\chi_n'(m_2y)] - m_2\Psi_n'(y)[\Psi_n(m_2y) - A_n\chi_n(m_2y)]}{\xi_n(y)[\Psi_n'(m_2y) - A_n\chi_n'(m_2y)] - m_2\xi_n'(y)[\Psi_n(m_2y) - A_n\chi_n(m_2y)]}$$
$$b_n = \frac{m_2\Psi_n(y)[\Psi_n'(m_2y) - B_n\chi_n'(m_2y)] - \Psi_n'(y)[\Psi_n(m_2y) - B_n\chi_n(m_2y)]}{m_2\xi_n(y)[\Psi_n'(m_2y) - B_n\chi_n'(m_2y)] - \xi_n'(y)[\Psi_n(m_2y) - B_n\chi_n(m_2y)]}$$
$$A_n = \frac{m_2\Psi_n(m_2x)\Psi_n'(m_1x) - m_1\Psi_n'(m_2x)\Psi_n(m_1x)}{m_2\chi_n(m_2x)\Psi_n'(m_1x) - m_1\chi_n'(m_2x)\Psi_n(m_1x)} \quad \text{(S3)}$$
$$B_n = \frac{m_2\Psi_n(m_1x)\Psi_n'(m_2x) - m_1\Psi_n(m_2x)\Psi_n'(m_1x)}{m_2\chi_n'(m_2x)\Psi_n(m_1x) - m_1\Psi_n'(m_1x)\chi_n(m_2x)}$$

Where $m_1 = \sqrt{\varepsilon_1} \quad and \;\; m_2 = \sqrt{\varepsilon_2}$

Table S1: The skin depth of materials with different conductivity

Conductivity ($\boldsymbol{\sigma}$) (S/m)	**Skin depth (S) (m)**
10^0	4.90×10^{-06}
10^2	4.90×10^{-05}
10^4	4.90×10^{-04}
10^6	4.90×10^{-03}
10^8	4.90×10^{-02}

The relation between the skin depth and the conductivity is given by $s = \frac{1}{\sqrt{\pi f \mu_r \mu_0 \sigma}}$ where f is the microwave frequency of 2.45 GHz, μ_r =1 for non-magnetic materials and μ_0 = $4\pi x10^{-7}$

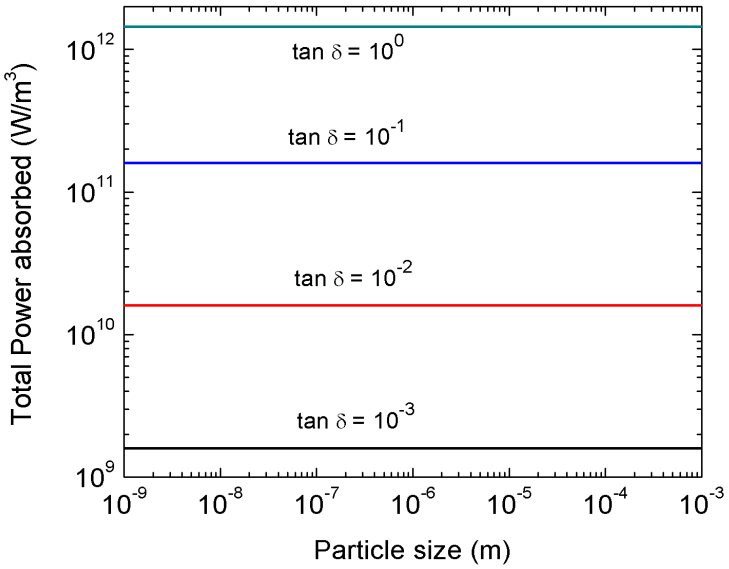

FigureS1 Microwave power absorbed by dielectric and semi-conductor materials with different optical properties

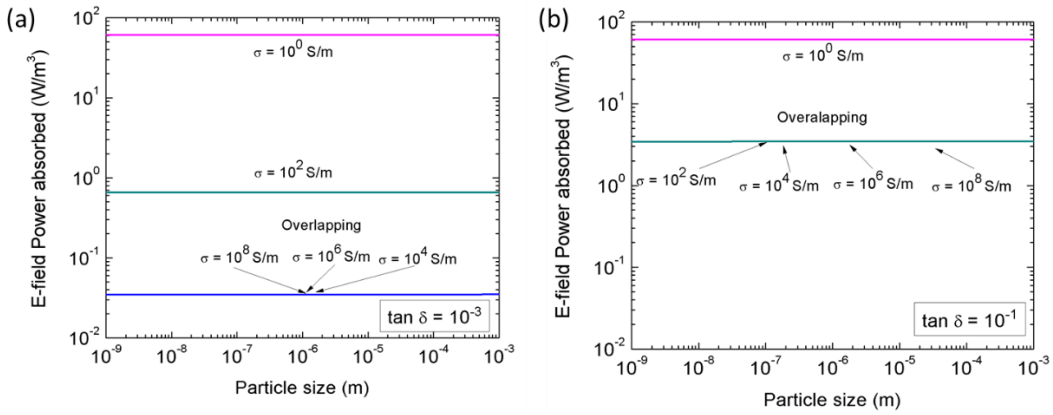

FigureS2 Power absorbed from the E-field of microwaves by particles of different sizes and conductivities with coating of $tan\delta$ = 10^{-3} (a) and $tan\delta$ = 10^{-1} (b). The properties of the coating dominates the power absorption, as particles with different conductivities absorb the same amount of power as the coating.

Table S1: Physical constants used for the complex dielectric constant and complex magnetic constants used in calculations to estimate the intensity fraction absorbed and the maximum temperature.

Material	$\tilde{\varepsilon}_r'$	$\tilde{\varepsilon}_r''$	μ′	μ″	***Source***
Al	*0*	*2.5 x 10^8*	1	0	[21], Azo Materials
Al_2O_3 (amorphous)	*9.8*	*1x 10^6*	1	0	[17]
Ti	*0*	*1.3 x 10^7*	1	0	[21], Azo Materials
TiO_2 (amorphous)	*33*	*10.4*	1	0	[34]
TiN	*15*	*4.2*	1	0	[33]

11 Summary and Future Work

11.1 Conclusions

The goal of this dissertation was to attain fundamental mechanistic insights into the thermally and electrochemically driven mass transfer processes and oxidation kinetics at reactive interfaces in condensed phase materials comprising of boron, aluminum, hydrogen, and imidazolinium ionic liquids for thermal energy generation required by propulsion systems. I have adopted solvent based, aerosol, and direct ink writing approaches to synthesize and fabricate functionalized nanoparticle, polymer nanocomposites, boron-hydrogen complex and imidazolinium ionic liquid based soft materials. I have exploited various characterization techniques such as in situ time-of-flight mass spectrometry, X-ray diffraction, scanning/transmission electron microscopy, spectroscopies (IR, NMR, Raman) and atomic force microscopy, as well as computation techniques such as density functional theory tight binding (DFTB), molecular dynamics, ensemble Monte Carlo, finite element method based simulations to study multiscale transport phenomena occurring at reactive interfaces in these materials. The following is the summary of the important conclusion of each chapter and my suggestions for future investigations.

Chapter 2-4 focuses on enhancing the combustion of boron. Chapter 2 and 3 is about selectively altering the decomposition of pathway to enable maximum energy extraction from ammonia borane which can potentially form gas phase boron and hydrogen. On external heating ammonia borane oligomerizes to higher molecular weight boron-nitrogen-hydrogen (BNH_x) clusters which impedes its rapid oxidation. Chapter 2

describes about a strategy to reroute the formation of the BNH_x clusters by using NH_4^+ ion based oxidizing salts where the N of the NH_4^+ ions competes with the ammonia group of ammonia borane (AB) in attacking the borane groups, which prevents the formation of the intermediate diammoniate of diborane / DADB ($[NH_3BH_2NH_3]^+[BH_4]^-$) by forming $[NH_3BH_2NH_3]^+$[oxidizing anion]$^-$ instead. The formation of the alternative intermediate inhibits the formation of BNH_x species and also results in fast and complete oxidation of AB. Chapter 3 presents about selectively altering the decomposition pathway of AB by placing it into polymer matrices with carbonyl groups. The carbonyl groups compete with the borane groups as centers of nucleophilic attack from the ammonia groups, which again prevents the formation of DADB and instead results in the lysis of the dative B-N bond of AB to generate NH_3 and B_2H_6, whereas the carbonyl and other functional groups of the polymer remain intact after AB decomposition, which implies that the carbonyl group has a catalytic effect on B-N bond dissociation of AB. B_2H_6 (diborane) has a lower autoignition temperature (~40 ^oC) than H_2 (~500 ^oC) and it spontaneously igniting in air on its release. Therefore it is attractive to be used as a fuel for air breathing jet propulsion, however its gas phase storage is difficult and dangerous. The discovery of this pathway enables AB to be used as a diborane storage material which can be activated to release diborane for energy generation when required. Chapter 4 mentions the mechanism of reduction of the oxide shell of particulate boron by reacting with metal vapors having lower free energy of oxidation than B. By performing a DFTB-MD simulation on the reaction of Mg vapor with a B_2O_3 surface, I have shown that the Mg gets oxidized on the surface forming mixed oxide phase, MgB_xO_y, the formation of which induces an overall tensile strain on the B_2O_3

surface. Additionally, I also found that the B at the interface shared by the developing MgB_xO_y phase and the pure B_2O_3 phase, gets reduced thereby developing dangling bonds, which can act as active centers for gas phase oxygen adsorption. The dangling bonds should enhance the rate of O_2 adsorption, and the tensile strain should increase the diffusion rate O from surface to the core thereby collectively enhancing oxidation rate of particulate B.

Chapter 5-7 presents findings about tuning the reactivity of widely used metallic fuel, Al and metal oxides (CuO, Fe_2O_3) by manipulating the microstructural features of their composites. Chapter 5 shows that the application of an in-situ thermochemical shock through decomposition of an explosive coated on the surface of Al nanoparticles, can induce tensile strain and non-uniformities at the Al/AlO_x interface. These non-uniformities facilitate the outward migration of Al-ions thereby resulting in condensed phase oxidation and ignition of Al nanoparticles, at temperatures lower than the usual oxidation/ignition onset. Chapter 6 shows that the reaction propagation rate in metal-metal oxide nanoparticulate composites can be controlled by controlling the mixing length between the fuel and oxidizer which can simply be achieved by direct ink writing of the particles in a laminate architecture. Increasing the thickness of the oxide layer increases the path length of oxygen diffusion thereby decreasing the flame propagation rate. Chapter 6 shows that the aggregate structure of superparamagnetic aerosol nanoparticles in free-molecular regime (small size and high temperature) can be tuned and altered from the Brownian diffusion controlled universal fractal dimension of diffusion limited cluster aggregates, by applying sufficiently strong electromagnetic fields, even when the ambient temperature is beyond the Curie point.

Chapters 8-9 focus on external stimuli driven control on the combustion of condensed phase materials. Safety is a major concern for high energy density materials, the storage and transportation of which in bulk amounts can lead to potential fire hazards. Chapter 8 presents a possible solution to this problem, by demonstrating that the volatility and the flammability of highly energy dense imidazolinium based ionic liquids can be dynamically manipulated simply by applying and removing a voltage bias. These ionic liquids have insignificant vapor pressure which makes them inflammable. I have shown that they can be electrolyzed to generate reactive gas phase imidazole free radicals which can participate in combustion and the flame can be subsequently extinguished at will simply by switching off the voltage used for the electrolysis, which stops the supply of the gas phase reactive species to the flame zone. This is a potentially seminal contribution which may advent the use of imidazolinium ionic liquids as 'safe' fuels with high energy density. There is considerable interest in using microwave frequencies to stimulate localized ignition in energetic materials, so that the combustion zone can be spatially confined. Chapter 9 presents a benchmarking model to estimate the microwave power absorption by metal, metal oxide, metal/metal oxide (core/shell) nanoparticles which are typically used as fuel or oxidizers in energetic composites. These calculations can be used to select microwave absorbers based on their dielectric properties and use them as sensitizers in energetic composites to enable spatially confined ignition. The model predicts that Ti nanoparticles, because of the favorable properties of the TiO_x oxide shell can absorb ~100 times higher microwave power than that of Al. This prediction has been proven by experimentally demonstrating that Ti nanoparticles can be ignited whereas Al

nanoparticles having roughly the same size and active fuel content cannot be ignited with same amount of microwave power.

Therefore, this dissertation has solved multiple challenges associated with chemical energy conversion from the perspective of high energy propulsion systems, opening new avenues for developing safe, economic, and energy efficient rotes for rocket and jet propulsion.

11.2 Recommendation for future work

11.2.1 In-operando experiments on propellant grains made from Ammonia borane/PMMA composites in counter air flow

The findings in chapter 3 have shown that ammonia borane (AB) when incorporated in PMMA matrix consisting of carbonyl groups, does not oligomerize to higher molecular weight boron-nitrogen-hydrogen clusters. Instead, AB in AB/PMMA composites decomposes releasing NH_3 and B_2H_6. In chapter 3 it has also been shown that B_2H_6 spontaneously ignites in air on its release from AB/PMMA composites, making it suitable for air breathing applications. Motivated by these findings I have fabricated ~1 mm thick free-standing sticks of AB/PMMA composites containing 25 and 75 wt. % of AB by direct ink writing and investigated their combustion under free-air as preliminary experiments. As shown in Figure 11-1 (a) and 11-1 (c), both 75 % and 25 % AB releases B_2H_6, combustion of which results in the green BO_2 emission. In both cases, the green emission from B_2H_6 combustion propagates along the stick indicating that the B_2H_6/air flame can self-sustain itself. However, the 75 % AB containing film leaves behind a residue whereas the 25 % film completely gasifies while burning. ATR-FTIR investigation of the

residue confirms that it majorly consists of B_2O_3 (Figure 11-1 (b)). However, from Figure 11-1 (c) it is clear that the B_2H_6 flame propagates ahead of the polymer and the polymer burns slowly, even after B_2H_6 is entirely combusted. This corroborates with the findings presented in chapter 3.

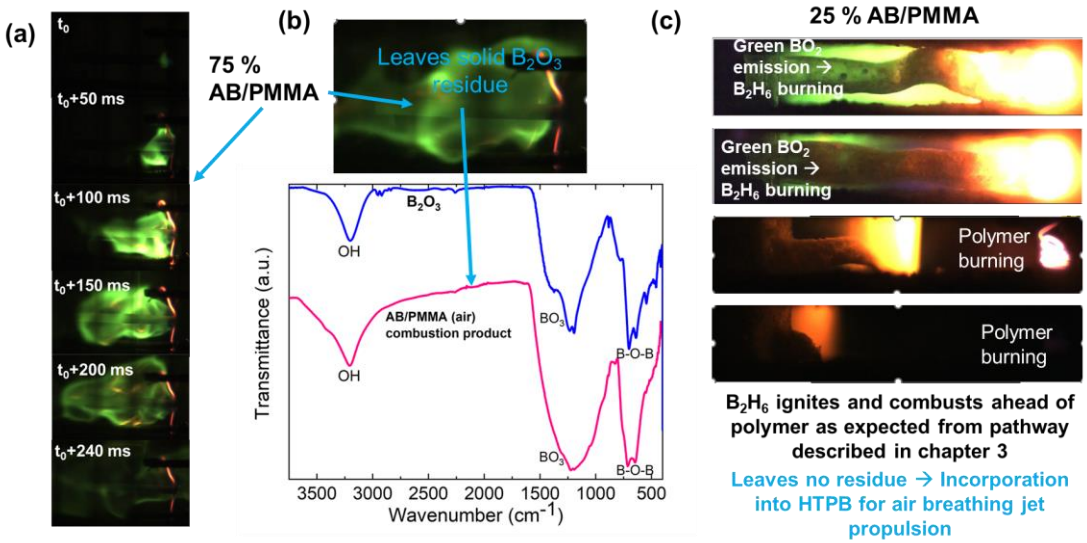

Figure 11-1 (a) Flame propagation in direct ink-written 75 % AB/PMMA composite. (b) ATR-FTIR on post-combustion residue of 75 % AB/PMMA composite in air. (c) Flame propagation in direct ink-written 25 % AB/PMMA composite which does not leave any residue.

From these preliminary experiments it can be inferred that high loading of AB in PMMA can leave behind a macroscale residue because of the formation and sintering of B_2O_3 whereas low AB loading possibly forms sub-micron B_2O_3 particles in the aerosol phase which gets dispersed in the atmosphere. Metals such as Al also suffer from sintering while combusting in air. Hence, AB/PMMA combustion in air needs to be compared with Al/PMMA combustion under *in operando* conditions with counter-air flow to evaluate the effect of sintering under realistic conditions. Also the performance of the AB/PMMA composite should be evaluated and compared with standard air breathing propellants such

as hydroxyl terminated polybutadiene (HTPB) under counter air flow, to justify its use for air-breathing applications. Additionally, there might be merit in incorporating AB/PMMA composite mesoparticles (chapter 3) into HTPB to enhance its burning characteristics in air.

11.2.2 Characterization of the electrochemical control on the flammability of gelled ionic liquids

Although chapter 8 presents a seminal contribution on electrochemically switching the flammability of room temperature ionic liquids, the findings are still at a preliminary stage and there is a scope of performing plethora of work to enable the use of this concept for actual propulsion systems. One of the primary directions to work on will be to investigate how does the flammability switching concept translates to systems where the ionic liquid exists as a gel. Currently the liquid state of the ionic liquid makes it incompatible to be used with solid state hybrid propellant composites. In order to incorporate it in the hybrid propellants, the ionic liquid needs to be gelled into a solid form either by incorporating it into polymer matrices as polymer electrolytes or by increasing its viscosity by addition of nanoparticles thereby forming nanofluid gels (Figure 11-2).

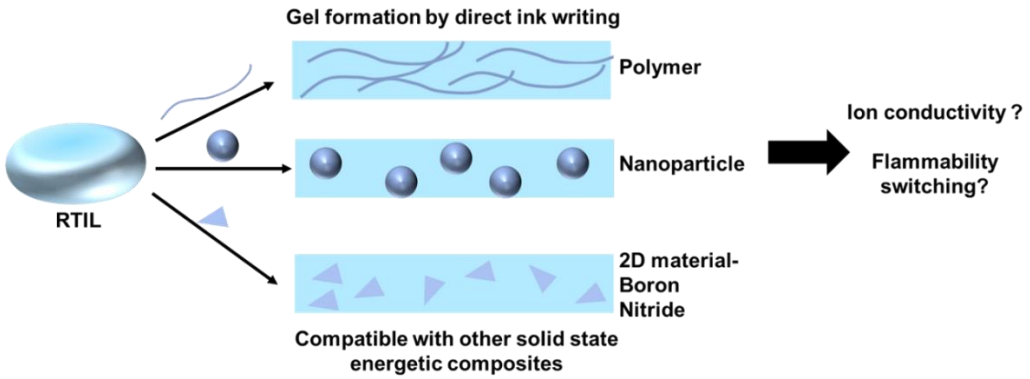

Figure 11-2 Direct ink writing of ionic liquids gels using polymer, nanoparticles and 2D materials at the gelling agent to address questions such as i) How much is the decrease in ion conductivity? ii) Will the concept of flammability switching still work for the gels?

Once the ionic liquid is confined in the solid state, its ionic conductivity will decrease. This will reduce its electrochemical reaction and volatilization rate. This will also impede its energy release rate through combustion. Hence, fundamental studies are required to identify the properties of polymer matrices that can facilitate the ionic conductivity and the electrochemical reaction of the imidazolinium cations. Moreover, as most polymers are flammable, the concept of extinguishing the combustion by stopping the generation of gas phase species through removal of the voltage bias, may fail with increasing polymer content. Another option might be to use nanoscale sheets of flame-retardant light 2-D materials such as boron nitride. A small wt. % addition of boron nitride might aid the gelation process and its flame-retardant characteristics will ensure that the combustion can be stopped on removal of the applied bias. Additionally, studies can be performed on the aging effects on the ionic liquid on interaction with the host materials (polymer, nanoparticle, boron nitride) and also evaluate the stability of the host materials post-electrolysis and combustion of the ionic liquids. Hence, there is a scope for performing

several fundamental studies on gelled composites of the ionic liquids. Moreover, the effect of electrode spacing and the applied voltage on the flame temperature, which is an indicator of the energy release rate of fuels, also needs to be studied. Tunability of the energy release rate by controlling the volatility through change of electrode spacing or applied voltage bias might increase the viability of this concept for practical applications.

11.2.3 Assembly of energetic nanoparticles via Ionic Liquid

Assembling fuel nanoparticles into less porous matrices is always advantageous to fabricate high energy density materials. Assembling methods involving polymers, which typically involves the dispersion of the nanoparticles in a dissolved solution of the polymers followed by solvent evaporation suffers from lack of porosity control as the polymer and nanoparticle phase may often phase separate. Room temperature ionic liquids (RTILs) being hydrophilic tends to wet metal oxide surfaces which are usually terminated by hydroxyl groups. Hence, energetic nanoparticle assembly via ionic liquids may potentially enable us to develop high energy density metal-metal oxide composites. Motivated by these I have performed some preliminary experiments to assemble unary (Al) and binary (Al and CuO) nanoparticles via RTIL using a reverse emulsion template based approach. When metal nanoparticles with the hydroxyl terminated oxide shells or metal oxides and ionic liquids dispersed/dissolved in aqueous solvents are added to a non-aqueous solvent, a water in oil emulsion develops. The ionic liquid and the metal oxide particles with hydrophilic surfaces tend to assemble and pack in the water phase, eventually forming dispersed colloidosomes. Then, spherical mesoscale particles which are an assembly of several nanoparticles and the ionic liquid can be obtained by the removal of

the oil phase by centrifugation and drying. Figure 11-3 shows the SEM images of Al/RTIL (a) and Al/CuO /RTIL (b) particles synthesized using this method. The metal oxide surfaces having lower dielectric constant than the aqueous solvent will have negative charges on their surface. This will attract ion-clusters having a net positive charge towards the metal oxide surface ensuring better wettability. The RTIL being smaller than the polymer chains and having strong affinity towards the metal oxide surface will tend to disperse the nanoparticles better than that of such assemblies formed in polymer matrices. Hence, these RTIL based composites will have less porosity and high energy density.

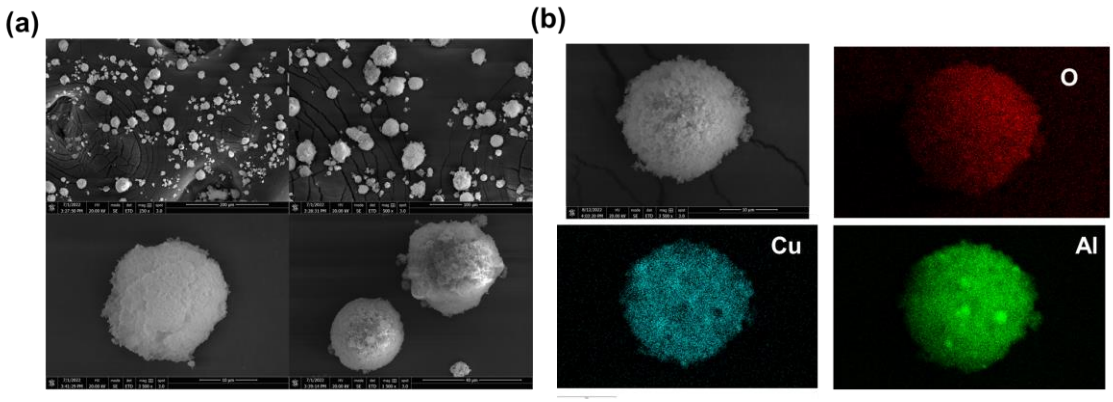

Figure 11-3 Al/RTIL composite particles (b) Al/CuO/RTIL composite particles assembled by reverse emulsion template.

Figure 11-4 shows the flame temperature of Al/RTIL composite particles where the ratio between the Al and RTIL is represented in terms of equivalence ratio assuming the ClO_4^- anion of the RTIL acts as an oxidizer for Al. However, the BMIM group is also a fuel and needs additional oxidizer to combust. Hence, as expected the flame temperature of the ionic liquid increases with increasing Al content which obviously is the better fuel in terms of energy density. These results should be compared with Al-polymer based composites. Additionally, the energetic performance of the Al/CuO/RTIL particles should

be evaluated and compared with Al/CuO/polymer particles, to understand the effect of porosity and energy density control on energetic performance.

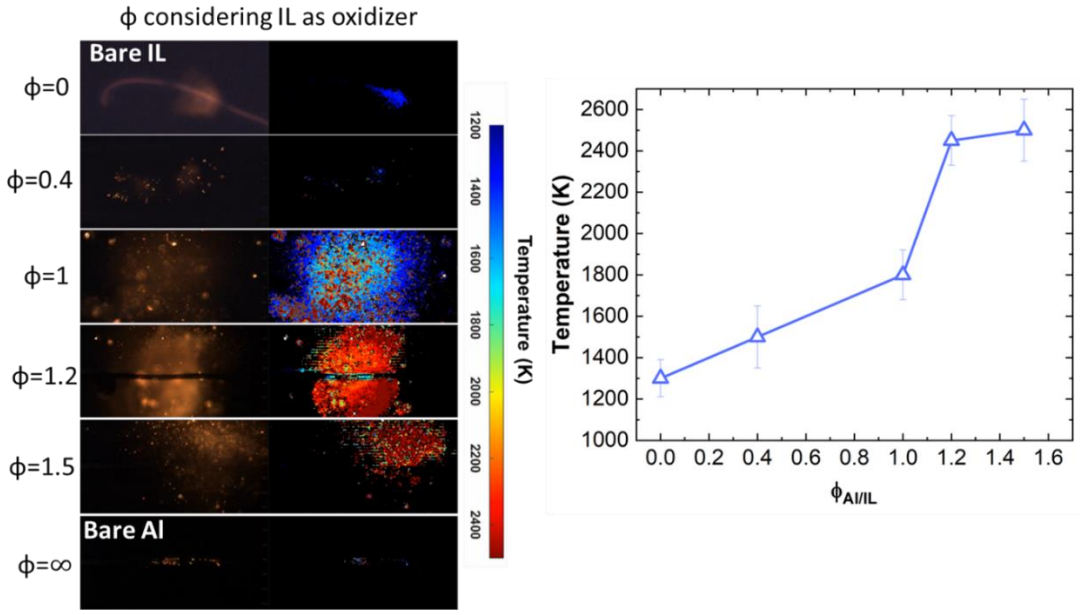

Figure 11-4 Color camera images and temperature maps of the flame of Al/RTIL composite particles with different Al content, ignited via hot wire.

11.2.4 Solid-state hydride or perchlorate salts in RTILs: Change in thermochemical and electrochemical pathways

As shown in Chapter 2 and 3, chemical hydrides like ammonia borane follow complex reaction pathways under varying conditions. The oligomerization of ammonia borane is stimulated by the formation of its dimeric intermediate (DADB) in molten phase which oligomerize further to form the higher molecular weight boron-nitrogen-hydrogen clusters. Dissolving ammonia borane in room temperature ionic liquids will trap separate molecules of ammonia borane or DADB in the ionic liquid matrix which may result in the alteration of its thermochemical reaction pathways, as it may prevent it from further oligomerization (Figure 11-5 (a)). Also, commonly used oxidizing salts such as $KClO_4$,

NH_4ClO_4, $LiClO_4$, KIO_3 etc. when dissolved in the RTIL will be trapped as separate ions. Therefore, their physical and thermochemical decomposition properties will change in the ionic liquid matrix (Figure 11-5 (b)). Moreover, the introduction of ions of dissimilar sizes will not only alter the electrochemical reaction pathways based on redox potential of the different ions but will also introduce vacancies/defects in the ionic liquid matrix. This may influence the mass transfer process associated with the electrochemical reactions (Figure 11-5 (c)). A mixture of room temperature ionic liquids may also be used to study this effect. The even dispersion of the salts in the ionic liquid might not be achieved by simply putting the solid salt in the ionic liquid. Rather, one needs to co-dissolve the solid salts and the RTIL in a common solvent and then remove the solvent to obtain the intended materials. Hence, there is a scope for performing fundamental interesting studies on dispersion/solution of solid-state salts in room temperature ionic liquids both from a thermochemical and electrochemical standpoint.

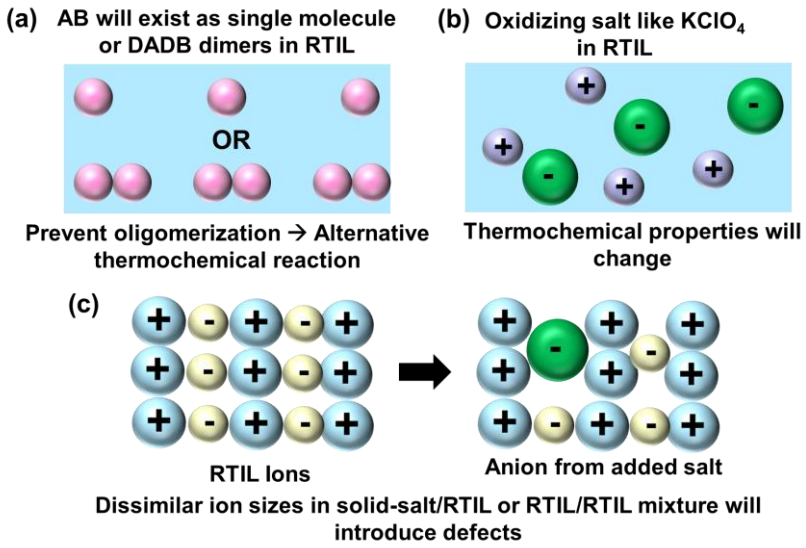

Figure 11-5 (a) AB trapped as single molecule or as dimers in RTIL will follow alternative thermochemical pathways (b) Oxidizing salts in RTIL will also have different thermochemical properties. (c) Dissimilar ion sizes in salt/RTIL and RTIL mixtures will introduce defects and influence ion conducting pathways, the effect of which on the electrochemical reaction of the RTIL needs to be investigated.

Appendices

A.1 DFTB input script

```
Parallel { UseOmpThreads = Yes}

Geometry = GenFormat {
 <<<"dftb.gen"
}


Driver = VelocityVerlet {
  Steps = 2000000
  TimeStep [fs] = 0.1
  MDRestartFrequency = 5
  MovedAtoms = !(1:40 81:120 161:200 241:280)
  KeepStationary = Yes
  Thermostat = NoseHoover {
    Temperature [Kelvin] = 2000.0
    CouplingStrength [cm^-1] = 3500
    ChainLength = 3
    Order=3
    IntegratorSteps=1
    #AdaptFillingTemp = Yes
  }
 # Velocities [angstrom/ps] {
  #<<<velocities_init.txt
  #}
}

Options = {
WriteChargesAsText=Yes
}

ParserOptions = { ParserVersion = 3}

Hamiltonian = DFTB {
  SCC = YES
  ChIMES {
  ParameterFile = "ChIMES_params.txt"
  }
  MaxSCCIterations = 2000
  Mixer = Broyden {
```

```
 MixingParameter = 0.1
  }
  Filling = Fermi {
  Temperature [Kelvin] = 2000.0
  }
  SlaterKosterFiles = Type2FileNames {
    Prefix = "/g/g20/zacharia/codes/SKF_files/chimes_1/"
    Separator = "-"
    Suffix = ".skf"
    LowerCaseTypeName = No
  }
PolynomialRepulsive = {
B-B = Yes
B-Mg = Yes
B-O = Yes
Mg-B = Yes
Mg-Mg = Yes
Mg-O = Yes
O-B = Yes
O-Mg = Yes
O-O = Yes
}
MaxAngularMomentum = {
   B = "p"
   Mg = "s"
   O = "p"
          }
KPointsAndWeights = SupercellFolding {
1  0  0
0  1  0
0  0  1
0.0  0.0  0.0
  }
}


Analysis {
  CalculateForces = Yes
}
```

A.2 DFTB restart input sample script

```
Parallel { UseOmpThreads = Yes}
```

```
Geometry = GenFormat {
 <<<"dftb.gen"
}


Driver = VelocityVerlet {
  Steps = 2000000
  TimeStep [fs] = 0.1
  MDRestartFrequency = 5
  MovedAtoms = !(1:40 81:120 161:200 241:280)
  KeepStationary = Yes
  Thermostat = NoseHoover {
    Temperature [Kelvin] = 2000.0
    CouplingStrength [cm^-1] = 3500
    ChainLength = 3
    Order=3
    IntegratorSteps=1
    Restart = {
     x = {0.3332833503E+01    0.2083619461E+02    0.1194522723E+03}
     v = { -0.5830152365E-05   -0.3585141506E-02    0.2155789460E-02}
     g = { -0.1671974474E-06   -0.6421413324E-05    0.6411431887E-05}
    }
  }
  Velocities [angstrom/ps] {
  <<<velocities.txt
  }
}

Options = {
WriteChargesAsText = Yes
ReadChargesAsText = Yes
}

ParserOptions = { ParserVersion = 3}

Hamiltonian = DFTB {
  SCC = YES
  ReadInitialCharges = YES
  ChIMES {
  ParameterFile = "ChIMES_params.txt"
  }
  MaxSCCIterations = 2000
  Mixer = Broyden {
 MixingParameter = 0.1
```

```
  }
  Filling = Fermi {
  Temperature [Kelvin] = 2000.0
  }
  SlaterKosterFiles = Type2FileNames {
    Prefix = "/g/g20/zacharia/codes/SKF_files/chimes_1/"
    Separator = "-"
    Suffix = ".skf"
    LowerCaseTypeName = No
  }
PolynomialRepulsive = {
B-B = Yes
B-Mg = Yes
B-O = Yes
Mg-B = Yes
Mg-Mg = Yes
Mg-O = Yes
O-B = Yes
O-Mg = Yes
O-O = Yes
}
MaxAngularMomentum = {
   B = "p"
   Mg = "s"
   O = "p"
          }
KPointsAndWeights = SupercellFolding {
1  0  0
0  1  0
0  0  1
0.0  0.0  0.0
  }
}


Analysis {
  CalculateForces = Yes
}
```

A.3 Velocities file

```
0.00000000      0.00000000      0.00000000
0.00000000      0.00000000      0.00000000
```

0.00000000 0.00000000 0.00000000
0.00000000 0.00000000 0.00000000
0.00000000 0.00000000 0.00000000
0.00000000 0.00000000 0.00000000
0.00000000 0.00000000 0.00000000
0.00000000 0.00000000 0.00000000
0.00000000 0.00000000 0.00000000
0.00000000 0.00000000 0.00000000
0.00000000 0.00000000 0.00000000
0.00000000 0.00000000 0.00000000
0.00000000 0.00000000 0.00000000
0.00000000 0.00000000 0.00000000
0.00000000 0.00000000 0.00000000
0.00000000 0.00000000 0.00000000
0.00000000 0.00000000 0.00000000
0.00000000 0.00000000 0.00000000
0.00000000 0.00000000 0.00000000
0.00000000 0.00000000 0.00000000
0.00000000 0.00000000 0.00000000
0.00000000 0.00000000 0.00000000
0.00000000 0.00000000 0.00000000
0.00000000 0.00000000 0.00000000
0.00000000 0.00000000 0.00000000
0.00000000 0.00000000 0.00000000
0.00000000 0.00000000 0.00000000
0.00000000 0.00000000 0.00000000
0.00000000 0.00000000 0.00000000
0.00000000 0.00000000 0.00000000
0.00000000 0.00000000 0.00000000
0.00000000 0.00000000 0.00000000
0.00000000 0.00000000 0.00000000
0.00000000 0.00000000 0.00000000
0.00000000 0.00000000 0.00000000
0.00000000 0.00000000 0.00000000
0.00000000 0.00000000 0.00000000
0.00000000 0.00000000 0.00000000
0.00000000 0.00000000 0.00000000
0.00000000 0.00000000 0.00000000
0.00000000 0.00000000 0.00000000
0.00000000 0.00000000 0.00000000
0.00000000 0.00000000 0.00000000
0.00000000 0.00000000 0.00000000
16.71744604 12.28165914 -29.72284100
-10.60967366 -7.45177595 -2.08402820
3.99930672 -22.82805165 14.07762914
10.22693080 -1.21849077 -10.00133753
23.32539797 -18.98365049 0.36023205
-0.07781588 12.29670029 -12.08651566

9.78600780 1.99453556 5.04784986
-2.77329208 8.75861639 -1.29341613
-9.52406505 -9.97940514 -13.70366990
10.54735054 -3.68643270 13.13782595
-19.23266014 -13.80131571 34.54740323
4.40389755 -5.07708272 -9.18326300
10.91331605 6.73354213 0.57118845
15.13293734 5.98110197 -7.71491870
-20.66852181 -5.45393606 9.44272202
-2.94480379 8.26988007 35.71136136
25.22825904 -12.45739761 -2.29227993
11.53499222 14.41808629 6.91206879
-2.27336176 5.09398709 16.01730639
-10.02753413 14.20430580 -5.99428936
-9.52428695 -12.35347791 -12.96258971
-27.29232668 -17.65805153 12.63112404
3.94151383 17.91708576 -3.85262369
-4.80909896 -41.48735190 -2.31628744
14.80856338 7.48153738 4.93568765
-14.84124956 6.74838297 -5.05794705
-7.87364185 19.36567588 15.59944923
4.74750217 -7.24969658 4.59832718
1.62719704 0.00495255 -7.04891394
14.03490375 3.90816637 -4.13486855
3.16943594 -6.41680173 -4.89306510
3.34265105 -12.68487995 -11.28040711
-3.38056925 5.29309635 -4.38030180
-19.50295390 13.30481139 19.50842970
-15.19093373 -5.17000849 1.21516048
-19.08358056 17.65516910 9.00891907
-9.68645860 -6.41743957 8.55735220
-4.25874388 10.18204479 -4.55186546
-0.74822512 -13.50110610 8.96942091
17.40034927 12.06076363 19.24111903
0.00000000 0.00000000 0.00000000
0.00000000 0.00000000 0.00000000
0.00000000 0.00000000 0.00000000
0.00000000 0.00000000 0.00000000
0.00000000 0.00000000 0.00000000
0.00000000 0.00000000 0.00000000
0.00000000 0.00000000 0.00000000
0.00000000 0.00000000 0.00000000
0.00000000 0.00000000 0.00000000
0.00000000 0.00000000 0.00000000

0.00000000 0.00000000 0.00000000
0.00000000 0.00000000 0.00000000
0.00000000 0.00000000 0.00000000
0.00000000 0.00000000 0.00000000
0.00000000 0.00000000 0.00000000
0.00000000 0.00000000 0.00000000
0.00000000 0.00000000 0.00000000
0.00000000 0.00000000 0.00000000
0.00000000 0.00000000 0.00000000
0.00000000 0.00000000 0.00000000
0.00000000 0.00000000 0.00000000
0.00000000 0.00000000 0.00000000
0.00000000 0.00000000 0.00000000
0.00000000 0.00000000 0.00000000
0.00000000 0.00000000 0.00000000
0.00000000 0.00000000 0.00000000
0.00000000 0.00000000 0.00000000
0.00000000 0.00000000 0.00000000
0.00000000 0.00000000 0.00000000
0.00000000 0.00000000 0.00000000
0.00000000 0.00000000 0.00000000
0.00000000 0.00000000 0.00000000
0.00000000 0.00000000 0.00000000
0.00000000 0.00000000 0.00000000
0.00000000 0.00000000 0.00000000
0.00000000 0.00000000 0.00000000
0.00000000 0.00000000 0.00000000
0.00000000 0.00000000 0.00000000
0.00000000 0.00000000 0.00000000
0.00000000 0.00000000 0.00000000
0.00000000 0.00000000 0.00000000
0.00000000 0.00000000 0.00000000
0.00000000 0.00000000 0.00000000
-2.84402633 6.72351769 -14.30039705
3.05616814 -4.09728068 7.81342232
-3.47712925 6.41725362 -7.11950567
-1.82240127 -19.56100334 2.48352115
31.04453274 22.94595570 -4.19976799
-8.36843988 -23.48491003 3.88279853
10.16641222 -4.34809952 -16.67506002
-6.32356707 2.89903177 11.36913329
13.32619472 -6.46213453 -13.51087766
-8.08666949 -0.28490904 3.39101058
-18.10108738 -21.44778727 6.04232501
5.66078351 -4.97215123 15.76874864
-1.89507500 -5.00677766 8.74274291
8.97452852 8.08326262 -1.55087201

-4.89715840 5.97027266 13.65765872
14.83284091 5.97049106 11.78038390
-5.62504094 8.50661431 0.85665038
-13.18206858 -6.12484130 -11.80573095
-11.68730480 -15.90542004 8.79106173
5.48668685 8.32627865 24.37174359
-0.82002120 -9.43258613 -7.73498405
6.62366276 0.89927831 -4.48031584
-3.60597189 0.04502362 15.08544353
18.39927765 -11.58837671 17.30210181
24.80561130 -6.84099210 -7.48741332
24.34470537 10.10716353 -21.60745778
-7.80747250 -2.30592836 -2.19564838
-9.10485496 1.78213447 10.26742248
6.44574583 -7.33005237 12.78329736
-9.08947138 -5.40980783 -12.79805119
6.90849361 -4.39572813 3.12495258
0.17856324 5.96096407 22.31226659
10.93596452 0.19802706 6.67418367
-10.11647098 2.03166703 1.25289072
-7.97103349 11.10110309 -2.21526740
6.35737560 -7.29806431 4.05247238
3.89478366 0.99021219 -3.17441716
1.30073324 4.33126508 -0.87114468
1.79188875 7.50811097 -9.59446793
11.09671158 12.14798895 0.07423839
0.00000000 0.00000000 0.00000000
0.00000000 0.00000000 0.00000000
0.00000000 0.00000000 0.00000000
0.00000000 0.00000000 0.00000000
0.00000000 0.00000000 0.00000000
0.00000000 0.00000000 0.00000000
0.00000000 0.00000000 0.00000000
0.00000000 0.00000000 0.00000000
0.00000000 0.00000000 0.00000000
0.00000000 0.00000000 0.00000000
0.00000000 0.00000000 0.00000000
0.00000000 0.00000000 0.00000000
0.00000000 0.00000000 0.00000000
0.00000000 0.00000000 0.00000000
0.00000000 0.00000000 0.00000000
0.00000000 0.00000000 0.00000000
0.00000000 0.00000000 0.00000000
0.00000000 0.00000000 0.00000000

0.00000000	0.00000000	0.00000000
0.00000000	0.00000000	0.00000000
0.00000000	0.00000000	0.00000000
0.00000000	0.00000000	0.00000000
0.00000000	0.00000000	0.00000000
0.00000000	0.00000000	0.00000000
0.00000000	0.00000000	0.00000000
0.00000000	0.00000000	0.00000000
0.00000000	0.00000000	0.00000000
0.00000000	0.00000000	0.00000000
0.00000000	0.00000000	0.00000000
0.00000000	0.00000000	0.00000000
0.00000000	0.00000000	0.00000000
0.00000000	0.00000000	0.00000000
0.00000000	0.00000000	0.00000000
0.00000000	0.00000000	0.00000000
0.00000000	0.00000000	0.00000000
0.00000000	0.00000000	0.00000000
0.00000000	0.00000000	0.00000000
0.00000000	0.00000000	0.00000000
0.00000000	0.00000000	0.00000000
-6.79194188	18.95321478	8.07484903
-21.46977737	4.96801159	13.50618203
21.39786697	8.65265163	-16.58913373
-2.05815303	-1.03632929	9.45300709
-2.91113607	4.96817913	-12.81423171
-18.25891105	9.97494537	8.80718629
-16.41295139	24.15581235	-13.05916454
-4.22272837	1.05565329	-4.89672851
4.07598606	-5.86118922	3.14420435
10.18333179	-6.12963836	11.78954905
-3.33302731	-11.36394059	1.06185891
15.50496849	-0.21713461	1.70116434
4.17574979	-6.13460008	-6.97041998
6.93881124	-0.87369091	4.39625227
12.50477182	13.02063939	1.60130780
12.58166972	35.42003697	2.35981948
-8.12576500	-14.59286923	-2.91824334
-14.54838991	-25.90350283	10.73983860
2.68753165	7.72976964	15.72458655
-7.90501037	-5.00116735	11.00506426
7.47325252	-8.97021568	-4.79181680
-9.97405920	8.41283300	-4.68788013

```
8.48907047     4.82141139     -0.18957315
20.16298683     -3.85498605     3.00916251
9.95576750     7.61755658     20.02829170
-17.87501857     2.74478615     1.59389915
-3.16671412     -6.21858556     13.16341814
12.44783682     8.40874439     -16.46175801
-6.40837547     2.45563213     -9.01146004
20.11935967     5.54606392     17.07013886
-6.91087120     7.26672185     2.61661300
5.20803397     -2.11707002     5.51122693
1.87664428     -12.33807577     1.46898301
14.17303137     -1.40846538     7.48695654
-7.68056808     -16.08294292     13.52591233
10.53653804     17.61230101     -0.22198071
15.96383588     -13.73242294     24.94804279
-17.16424254     -12.49612650     -20.19434823
-14.70911096     -15.50407684     0.32676414
-6.06617517     -9.02211701     -3.37811257
0.00000000     0.00000000     0.00000000
0.00000000     0.00000000     0.00000000
0.00000000     0.00000000     0.00000000
0.00000000     0.00000000     0.00000000
0.00000000     0.00000000     0.00000000
0.00000000     0.00000000     0.00000000
0.00000000     0.00000000     0.00000000
0.00000000     0.00000000     0.00000000
0.00000000     0.00000000     0.00000000
0.00000000     0.00000000     0.00000000
0.00000000     0.00000000     0.00000000
0.00000000     0.00000000     0.00000000
0.00000000     0.00000000     0.00000000
0.00000000     0.00000000     0.00000000
0.00000000     0.00000000     0.00000000
0.00000000     0.00000000     0.00000000
0.00000000     0.00000000     0.00000000
0.00000000     0.00000000     0.00000000
0.00000000     0.00000000     0.00000000
0.00000000     0.00000000     0.00000000
0.00000000     0.00000000     0.00000000
0.00000000     0.00000000     0.00000000
0.00000000     0.00000000     0.00000000
0.00000000     0.00000000     0.00000000
0.00000000     0.00000000     0.00000000
0.00000000     0.00000000     0.00000000
```

0.00000000 0.00000000 0.00000000
0.00000000 0.00000000 0.00000000
0.00000000 0.00000000 0.00000000
0.00000000 0.00000000 0.00000000
0.00000000 0.00000000 0.00000000
0.00000000 0.00000000 0.00000000
0.00000000 0.00000000 0.00000000
0.00000000 0.00000000 0.00000000
0.00000000 0.00000000 0.00000000
0.00000000 0.00000000 0.00000000
0.00000000 0.00000000 0.00000000
0.00000000 0.00000000 0.00000000
0.00000000 0.00000000 0.00000000
0.00000000 0.00000000 0.00000000
12.87441883 4.91041060 -31.09756715
1.73352989 -10.56686918 -2.98583594
-8.17612821 18.09564594 -3.22108605
4.19993662 -1.61300190 7.00170193
-17.45958294 3.30455167 17.78930603
8.62731133 -5.72286433 -16.07809780
2.62425793 -1.65670206 -4.51679678
-6.48110770 14.76315091 -9.94509795
9.61027240 5.31816506 -0.12339791
13.53543541 10.71661404 0.55879086
18.09477066 -3.84400326 2.06511656
-3.64120346 -19.44543957 24.48346057
-0.30217524 -15.50006620 -13.45891775
6.75779997 1.99165230 19.26410680
21.31378016 -16.41446299 -12.76250037
4.82241353 -6.49596214 9.45100979
-22.19879741 -0.21145153 9.20409815
19.51508361 6.14433108 16.87651552
1.54762412 -6.51713798 1.79183820
7.58605295 0.80583411 -5.07202676
-7.90228677 -9.65237292 -13.62543641
9.71685253 4.58896055 -11.43615826
6.55374344 5.14810997 4.43851803
-2.11385145 -4.96503727 5.15819562
6.14598454 10.64935508 1.75452117
3.08512099 -0.22743029 4.69340238
18.11634335 14.73282997 -9.27718323
5.09118327 -23.34467554 -7.62202879
9.70470639 4.58911132 13.79893996
-2.83357194 -4.97095466 9.60091199

2.92272794 -0.57422970 -5.70642775
12.54742409 -5.09203413 -13.34519021
8.78813630 -10.28690872 -3.86122048
-3.20302822 -15.46666100 -17.50121097
-7.32305912 9.65458979 -10.40761292
12.82511109 24.65464323 -7.70389095
-2.33891536 6.46574264 -0.55849204
-13.55724773 -11.63333730 6.30273208
-7.32443715 -4.45848634 -11.92989829
-4.01087900 2.15490530 -7.19459420
-6.88745965 -3.76943666 5.25216336
-8.20769955 -1.34942374 -5.12478887
-0.71779614 1.93202080 -4.06273306
-5.16113369 -11.31987972 -14.64956973
2.41370603 -1.54785438 -3.11449663
2.21560495 -3.03198179 1.84667549
-4.15991678 7.15256660 -7.13573069
-11.41749671 7.73162374 4.76544410
-13.68557900 -5.00743588 -2.43105417
10.60849912 0.61849536 -3.40144118
-7.86189501 3.54026209 1.78147025
9.70475036 9.92375493 5.82074870
-9.66276616 -8.14882452 -3.83973575
4.61771947 19.57086271 4.24511597
-6.63561996 1.96453276 -6.30995672
0.14215288 1.69401714 3.04612084
-0.13691332 -3.08711469 -7.06678805
-4.32496019 4.97385695 -7.52557481
1.06250704 -7.84035515 0.14770706
10.39572556 3.80641740 -16.29223827
-5.92638104 8.45102877 -0.25859127
-0.58955697 5.11233484 -3.00310703
-2.95600529 -0.48444051 -2.13252859
-7.35324251 5.41969607 -9.02459391
-2.52172706 3.09960624 -2.57504200
-4.64878869 7.46135045 4.07836063
1.85292765 6.17150828 5.05131214
-6.69374258 -0.73565627 -8.15579299
-4.52152031 11.06985957 1.07149912
-7.93207751 -1.78490304 -3.58600767
-16.32631377 8.33440838 2.11466884
-5.03681558 3.70242051 -1.98247583
2.92765251 0.65635028 -3.27829038
-5.47693932 -0.56415954 -9.49431063

-2.89633465 -3.50394755 -5.76452082
2.58203187 -0.33487560 -6.96690758
0.85971526 -3.40132250 -2.87483301
-0.46540256 2.70790132 -0.85931920
-4.68218208 4.72880084 -3.60554638
-4.98308746 6.27443602 -7.64918361

A.4 Initial Geometry File with Relaxed Surface (2000 K)

360 S
B O Mg

1	2	0.2084343343E+01	0.5078191330E+00	0.3033826250E+00
2	2	0.4299235731E+01	0.4344124690E+01	0.3033826250E+00
3	2	0.6514128384E+01	0.5078191330E+00	0.3033826250E+00
4	2	0.8729020772E+01	0.4344124690E+01	0.3033826250E+00
5	1	0.1363526018E+01	0.7015301417E+01	0.4418193910E+00
6	1	0.3578418406E+01	0.3178996029E+01	0.4418193910E+00
7	1	0.5793310793E+01	0.7015301417E+01	0.4418193910E+00
8	1	0.8008203181E+01	0.3178996029E+01	0.4418193910E+00
9	2	0.3498867100E+00	0.7068606101E+01	0.1348249889E+01
10	2	0.2564779097E+01	0.3232300260E+01	0.1348249889E+01
11	2	0.4779671219E+01	0.7068606101E+01	0.1348249889E+01
12	2	0.6994563607E+01	0.3232300260E+01	0.1348249889E+01
13	1	0.2104218237E+01	0.2327899597E+01	0.2254485132E+01
14	1	0.4319110492E+01	0.6164205438E+01	0.2254485132E+01
15	1	0.6534002879E+01	0.2327899597E+01	0.2254485132E+01
16	1	0.8748895267E+01	0.6164205438E+01	0.2254485132E+01
17	2	0.7347584160E+00	0.2286162441E+01	0.2392997127E+01
18	2	0.2949650803E+01	0.6122468290E+01	0.2392997127E+01
19	2	0.5164543457E+01	0.2286162441E+01	0.2392997127E+01
20	2	0.7379435844E+01	0.6122468290E+01	0.2392997127E+01
21	2	0.7347768970E+00	0.5388517040E+01	0.2999759465E+01
22	2	0.2949669284E+01	0.1552211537E+01	0.2999759465E+01
23	2	0.5164561406E+01	0.5388517040E+01	0.2999759465E+01
24	2	0.7379453794E+01	0.1552211537E+01	0.2999759465E+01
25	1	0.2104204115E+01	0.5346830654E+01	0.3138204918E+01
26	1	0.4319096502E+01	0.1510525143E+01	0.3138204918E+01
27	1	0.6533989156E+01	0.5346830654E+01	0.3138204918E+01
28	1	0.8748881543E+01	0.1510525143E+01	0.3138204918E+01
29	2	0.3499190830E+00	0.6060781220E+00	0.4044566012E+01
30	2	0.2564811568E+01	0.4442383794E+01	0.4044566012E+01
31	2	0.4779703955E+01	0.6060781220E+00	0.4044566012E+01
32	2	0.6994596343E+01	0.4442383794E+01	0.4044566012E+01
33	1	0.1363496977E+01	0.6594038980E+00	0.4950925625E+01

34	1	0.3578389364E+01	0.4495709516E+01	0.4950925625E+01
35	1	0.5793281752E+01	0.6594038980E+00	0.4950925625E+01
36	1	0.8008174139E+01	0.4495709516E+01	0.4950925625E+01
37	2	0.2084312184E+01	0.7166899510E+01	0.5089371079E+01
38	2	0.4299204572E+01	0.3330593891E+01	0.5089371079E+01
39	2	0.6514096702E+01	0.7166899510E+01	0.5089371079E+01
40	2	0.8728989090E+01	0.3330593891E+01	0.5089371079E+01
41	2	0.1743050021E+01	0.1268271020E+01	0.6101208672E+01
42	2	0.8296225290E+01	0.5478572452E+01	0.5821743185E+01
43	2	0.6081987996E+01	0.1624212634E+01	0.5649794462E+01
44	2	0.3304596362E+01	0.5586732896E+01	0.5564046999E+01
45	1	0.5193104818E+01	0.2637813813E+01	0.5434463910E+01
46	1	0.7112338090E+01	0.6954977178E+01	0.6573704659E+01
47	1	0.8866531510E+00	0.2844710626E+01	0.5946492305E+01
48	1	0.2578479766E+01	0.7084841604E+01	0.6119374859E+01
49	2	0.1323570431E+01	0.3649089346E+01	0.6918984075E+01
50	2	0.5068978784E+01	0.3707117938E+01	0.6934401926E+01
51	2	0.8342491095E+01	0.3122352400E+00	0.6262619791E+01
52	2	0.2729326065E+01	-0.1743378931E+00	0.7194516635E+01
53	1	0.6585306087E+01	0.3329090376E+00	0.7320403715E+01
54	1	0.2048563848E+01	0.5336609189E+00	0.7936117349E+01
55	1	0.4389009785E+01	0.4693709574E+01	0.7504019571E+01
56	1	0.1064254874E+01	0.4738205398E+01	0.8373224243E+01
57	2	0.7806747624E+01	0.1734105703E+01	0.7666964978E+01
58	2	0.2939496870E+01	0.2098027352E+01	0.8183730248E+01
59	2	0.1482078656E+01	0.6198090457E+01	0.7419402181E+01
60	2	0.5041204839E+01	0.6035649056E+01	0.8696487839E+01
61	2	0.2951351555E+01	0.4455918864E+01	0.8685158082E+01
62	2	0.7781589739E+01	0.4297264784E+01	0.8169800781E+01
63	2	0.6028928733E+01	0.8832450591E+00	0.8169474350E+01
64	2	0.7680603203E+00	0.1509737442E-01	0.7742762901E+01
65	1	0.2603263330E+01	0.3292599392E+01	0.8670029905E+01
66	1	0.5383969280E+01	0.7366618489E+01	0.8700476755E+01
67	1	0.7527291236E+01	0.2485045516E+01	0.8486246902E+01
68	1	0.1835292663E+01	0.7078626685E+01	0.8465151874E+01
69	2	0.1306339752E+01	0.7159526764E+01	0.9539226494E+01
70	2	0.4909920278E+01	0.7878042377E+01	0.9579622092E+01
71	2	0.8305834125E+00	0.3666174683E+01	0.9861211990E+01
72	2	0.6500612809E+01	0.2838315696E+01	0.9805981049E+01
73	1	0.5158437588E+00	0.2409901873E+01	0.9738913343E+01
74	1	0.7423672279E+01	0.1554184766E+01	0.1073672206E+02
75	1	0.4645593665E+01	0.8458487493E+01	0.1058559049E+02
76	1	0.8062779574E+01	0.5796995167E+01	0.9914416519E+01
77	2	0.5462853661E+01	0.8623742893E+01	0.1140262498E+02

78	2	0.7075842183E+01	0.5302737871E+01	0.1030665400E+02
79	2	0.3898279446E+00	0.1225873695E+01	0.9885153312E+01
80	2	0.7701377696E+01	0.2323704867E+01	0.1153005647E+02
81	2	0.1094391289E+02	0.5078191330E+00	0.3033826250E+00
82	2	0.1315880528E+02	0.4344124690E+01	0.3033826250E+00
83	2	0.1537369793E+02	0.5078191330E+00	0.3033826250E+00
84	2	0.1758859032E+02	0.4344124690E+01	0.3033826250E+00
85	1	0.1022309557E+02	0.7015301417E+01	0.4418193910E+00
86	1	0.1243798796E+02	0.3178996029E+01	0.4418193910E+00
87	1	0.1465288034E+02	0.7015301417E+01	0.4418193910E+00
88	1	0.1686777273E+02	0.3178996029E+01	0.4418193910E+00
89	2	0.9209456260E+01	0.7068606101E+01	0.1348249889E+01
90	2	0.1142434865E+02	0.3232300260E+01	0.1348249889E+01
91	2	0.1363924077E+02	0.7068606101E+01	0.1348249889E+01
92	2	0.1585413316E+02	0.3232300260E+01	0.1348249889E+01
93	1	0.1096378779E+02	0.2327899597E+01	0.2254485132E+01
94	1	0.1317868004E+02	0.6164205438E+01	0.2254485132E+01
95	1	0.1539357243E+02	0.2327899597E+01	0.2254485132E+01
96	1	0.1760846482E+02	0.6164205438E+01	0.2254485132E+01
97	2	0.9594327966E+01	0.2286162441E+01	0.2392997127E+01
98	2	0.1180922035E+02	0.6122468290E+01	0.2392997127E+01
99	2	0.1402411301E+02	0.2286162441E+01	0.2392997127E+01
100	2	0.1623900539E+02	0.6122468290E+01	0.2392997127E+01
101	2	0.9594346447E+01	0.5388517040E+01	0.2999759465E+01
102	2	0.1180923883E+02	0.1552211537E+01	0.2999759465E+01
103	2	0.1402413096E+02	0.5388517040E+01	0.2999759465E+01
104	2	0.1623902334E+02	0.1552211537E+01	0.2999759465E+01
105	1	0.1096377366E+02	0.5346830654E+01	0.3138204918E+01
106	1	0.1317866605E+02	0.1510525143E+01	0.3138204918E+01
107	1	0.1539355871E+02	0.5346830654E+01	0.3138204918E+01
108	1	0.1760845109E+02	0.1510525143E+01	0.3138204918E+01
109	2	0.9209488633E+01	0.6060781220E+00	0.4044566012E+01
110	2	0.1142438112E+02	0.4442383794E+01	0.4044566012E+01
111	2	0.1363927351E+02	0.6060781220E+00	0.4044566012E+01
112	2	0.1585416589E+02	0.4442383794E+01	0.4044566012E+01
113	1	0.1022306653E+02	0.6594038980E+00	0.4950925625E+01
114	1	0.1243795891E+02	0.4495709516E+01	0.4950925625E+01
115	1	0.1465285130E+02	0.6594038980E+00	0.4950925625E+01
116	1	0.1686774369E+02	0.4495709516E+01	0.4950925625E+01
117	2	0.1094388173E+02	0.7166899510E+01	0.5089371079E+01
118	2	0.1315877412E+02	0.3330593891E+01	0.5089371079E+01
119	2	0.1537366625E+02	0.7166899510E+01	0.5089371079E+01
120	2	0.1758855864E+02	0.3330593891E+01	0.5089371079E+01
121	2	0.1042810356E+02	0.1541087819E+01	0.5726011453E+01

122	2	0.1664372634E+02	0.5625219247E+01	0.5543923964E+01
123	2	0.1396027346E+02	0.1516297333E+01	0.6760409733E+01
124	2	0.1228834708E+02	0.5384055161E+01	0.6117902514E+01
125	1	0.1303235428E+02	0.2089145995E+01	0.6362711686E+01
126	1	0.1555235722E+02	0.6061961753E+01	0.5487621093E+01
127	1	0.8913766400E+01	0.2359869563E+01	0.6214152393E+01
128	1	0.1156828451E+02	0.7134734696E+01	0.6077529718E+01
129	2	0.9785788524E+01	0.3346464952E+01	0.7533979649E+01
130	2	0.1388566302E+02	0.3368657638E+01	0.7578281080E+01
131	2	0.1632004189E+02	0.6649596721E+00	0.6469882394E+01
132	2	0.1207616961E+02	-0.1538065094E+00	0.7017061926E+01
133	1	0.1532112229E+02	0.7840337693E+00	0.8190663951E+01
134	1	0.1178632500E+02	-0.3474566966E+00	0.8085542352E+01
135	1	0.1316802381E+02	0.4236771799E+01	0.7935233953E+01
136	1	0.9293309342E+01	0.4661514276E+01	0.7043593979E+01
137	2	0.1576978475E+02	0.1849687836E+01	0.8549782305E+01
138	2	0.1169185102E+02	0.1598324490E+01	0.7974020338E+01
139	2	0.9610999834E+01	0.5590383940E+01	0.8323229236E+01
140	2	0.1465568978E+02	0.5677907739E+01	0.7261008168E+01
141	2	0.1246788609E+02	0.3582275088E+01	0.9577244193E+01
142	2	0.1697866347E+02	0.4733967976E+01	0.7986209082E+01
143	2	0.1527478668E+02	-0.3526429255E+00	0.7895632079E+01
144	2	0.1099687910E+02	-0.1330161864E+01	0.8289840656E+01
145	1	0.1243757972E+02	0.2018282970E+01	0.8819581020E+01
146	1	0.1421373056E+02	0.6051481148E+01	0.8344452600E+01
147	1	0.1567379253E+02	0.3944449664E+01	0.8245744474E+01
148	1	0.9441708131E+01	0.6762435582E+01	0.8617498354E+01
149	2	0.8654389035E+01	0.6975983256E+01	0.9451013616E+01
150	2	0.1322964192E+02	0.5979451752E+01	0.9092848365E+01
151	2	0.1084358625E+02	0.1562659536E+01	0.9846741608E+01
152	2	0.1490717783E+02	0.4143579546E+01	0.9165743518E+01
153	1	0.1041471512E+02	0.2466580243E+01	0.9211780969E+01
154	1	0.1429707597E+02	0.4358379786E+01	0.1021839890E+02
155	1	0.1228551277E+02	0.5768962373E+01	0.9796945876E+01
156	1	0.1898788010E+02	0.8513868811E+01	0.9746327206E+01
157	2	0.1147594483E+02	0.5644105795E+01	0.1061446535E+02
158	2	0.1848293071E+02	0.9541402830E+01	0.9360269332E+01
159	2	0.9056581878E+01	0.2491314387E+01	0.9458219483E+01
160	2	0.1382345669E+02	0.4814703382E+01	0.1118817192E+02
161	2	0.2084343343E+01	0.8180430370E+01	0.3033826250E+00
162	2	0.4299235731E+01	0.1201673593E+02	0.3033826250E+00
163	2	0.6514128384E+01	0.8180430370E+01	0.3033826250E+00
164	2	0.8729020772E+01	0.1201673593E+02	0.3033826250E+00
165	1	0.1363526018E+01	0.1468791265E+02	0.4418193910E+00

166	1	0.3578418406E+01	0.1085160727E+02	0.4418193910E+00
167	1	0.5793310793E+01	0.1468791265E+02	0.4418193910E+00
168	1	0.8008203181E+01	0.1085160727E+02	0.4418193910E+00
169	2	0.3498867100E+00	0.1474121734E+02	0.1348249889E+01
170	2	0.2564779097E+01	0.1090491150E+02	0.1348249889E+01
171	2	0.4779671219E+01	0.1474121734E+02	0.1348249889E+01
172	2	0.6994563607E+01	0.1090491150E+02	0.1348249889E+01
173	1	0.2104218237E+01	0.1000051083E+02	0.2254485132E+01
174	1	0.4319110492E+01	0.1383681667E+02	0.2254485132E+01
175	1	0.6534002879E+01	0.1000051083E+02	0.2254485132E+01
176	1	0.8748895267E+01	0.1383681667E+02	0.2254485132E+01
177	2	0.7347584160E+00	0.9958773678E+01	0.2392997127E+01
178	2	0.2949650803E+01	0.1379507953E+02	0.2392997127E+01
179	2	0.5164543457E+01	0.9958773678E+01	0.2392997127E+01
180	2	0.7379435844E+01	0.1379507953E+02	0.2392997127E+01
181	2	0.7347768970E+00	0.1306112828E+02	0.2999759465E+01
182	2	0.2949669284E+01	0.9224822774E+01	0.2999759465E+01
183	2	0.5164561406E+01	0.1306112828E+02	0.2999759465E+01
184	2	0.7379453794E+01	0.9224822774E+01	0.2999759465E+01
185	1	0.2104204115E+01	0.1301944189E+02	0.3138204918E+01
186	1	0.4319096502E+01	0.9183136380E+01	0.3138204918E+01
187	1	0.6533989156E+01	0.1301944189E+02	0.3138204918E+01
188	1	0.8748881543E+01	0.9183136380E+01	0.3138204918E+01
189	2	0.3499190830E+00	0.8278689359E+01	0.4044566012E+01
190	2	0.2564811568E+01	0.1211499503E+02	0.4044566012E+01
191	2	0.4779703955E+01	0.8278689359E+01	0.4044566012E+01
192	2	0.6994596343E+01	0.1211499503E+02	0.4044566012E+01
193	1	0.1363496977E+01	0.8332015135E+01	0.4950925625E+01
194	1	0.3578389364E+01	0.1216832075E+02	0.4950925625E+01
195	1	0.5793281752E+01	0.8332015135E+01	0.4950925625E+01
196	1	0.8008174139E+01	0.1216832075E+02	0.4950925625E+01
197	2	0.2084312184E+01	0.1483951075E+02	0.5089371079E+01
198	2	0.4299204572E+01	0.1100320513E+02	0.5089371079E+01
199	2	0.6514096702E+01	0.1483951075E+02	0.5089371079E+01
200	2	0.8728989090E+01	0.1100320513E+02	0.5089371079E+01
201	2	0.1788214221E+01	0.8937858858E+01	0.6023154435E+01
202	2	0.8644147509E+01	0.1379778726E+02	0.5473359367E+01
203	2	0.6610127911E+01	0.9972212126E+01	0.5522101578E+01
204	2	0.3389304918E+01	0.1329536216E+02	0.5481692993E+01
205	1	0.5971159046E+01	0.1176159958E+02	0.5457465022E+01
206	1	0.7859271242E+01	0.1553897325E+02	0.5216408318E+01
207	1	0.9061233525E+00	0.1027733944E+02	0.5686124469E+01
208	1	0.2311880677E+01	0.1459874261E+02	0.6241751817E+01
209	2	0.1743491413E+01	0.1112521901E+02	0.6463291672E+01

210	2	0.6575977583E+01	0.1254906450E+02	0.6240887472E+01
211	2	0.8007821992E+01	0.7592394023E+01	0.6969752834E+01
212	2	0.4376365613E+01	0.8054813007E+01	0.6212160623E+01
213	1	0.7610603614E+01	0.8295248831E+01	0.8111095868E+01
214	1	0.3735146977E+01	0.8481467513E+01	0.7235172891E+01
215	1	0.4905447550E+01	0.1273593962E+02	0.7033964778E+01
216	1	0.2984016051E+00	0.1215843512E+02	0.7066817430E+01
217	2	0.8221532390E+01	0.9344607444E+01	0.8060636688E+01
218	2	0.3634387176E+01	0.9503078270E+01	0.8002313247E+01
219	2	0.1864466829E+01	0.1338311075E+02	0.7623041865E+01
220	2	0.5262115556E+01	0.1430113813E+02	0.8001464678E+01
221	2	0.4331581176E+01	0.1162469922E+02	0.7037316271E+01
222	2	0.8294850553E+01	0.1138756509E+02	0.7909953216E+01
223	2	0.6477698841E+01	0.7865714596E+01	0.8252879070E+01
224	2	0.3079339684E+01	0.7551801817E+01	0.7806548348E+01
225	1	0.3156219978E+01	0.1050600705E+02	0.7520980799E+01
226	1	0.4738127224E+01	0.1586213138E+02	0.8300747118E+01
227	1	0.7479403420E+01	0.1040946292E+02	0.8196382325E+01
228	1	0.8838229272E+00	0.1410845097E+02	0.7752245788E+01
229	2	-0.6791220969E-01	0.1352789923E+02	0.8416624537E+01
230	2	0.4651984826E+01	0.1566024675E+02	0.9641950038E+01
231	2	0.2577234149E+01	0.1147076352E+02	0.9045483379E+01
232	2	0.6619590592E+01	0.1013157718E+02	0.9087365882E+01
233	1	0.2905112163E+01	0.1040728593E+02	0.9623377309E+01
234	1	0.6945532973E+01	0.9254115318E+01	0.9896621453E+01
235	1	0.5450942874E+01	0.1628503415E+02	0.1025784255E+02
236	1	0.9815509011E+01	0.1325257431E+02	0.9847229694E+01
237	2	0.6479142143E+01	0.1582606861E+02	0.1049842427E+02
238	2	0.9906987706E+01	0.1251355008E+02	0.1078026669E+02
239	2	0.3036896196E+01	0.9516061556E+01	0.1042064011E+02
240	2	0.7775370138E+01	0.8558264573E+01	0.1036289455E+02
241	2	0.1094391289E+02	0.8180430370E+01	0.3033826250E+00
242	2	0.1315880528E+02	0.1201673593E+02	0.3033826250E+00
243	2	0.1537369793E+02	0.8180430370E+01	0.3033826250E+00
244	2	0.1758859032E+02	0.1201673593E+02	0.3033826250E+00
245	1	0.1022309557E+02	0.1468791265E+02	0.4418193910E+00
246	1	0.1243798796E+02	0.1085160727E+02	0.4418193910E+00
247	1	0.1465288034E+02	0.1468791265E+02	0.4418193910E+00
248	1	0.1686777273E+02	0.1085160727E+02	0.4418193910E+00
249	2	0.9209456260E+01	0.1474121734E+02	0.1348249889E+01
250	2	0.1142434865E+02	0.1090491150E+02	0.1348249889E+01
251	2	0.1363924077E+02	0.1474121734E+02	0.1348249889E+01
252	2	0.1585413316E+02	0.1090491150E+02	0.1348249889E+01
253	1	0.1096378779E+02	0.1000051083E+02	0.2254485132E+01

254	1	0.1317868004E+02	0.1383681667E+02	0.2254485132E+01
255	1	0.1539357243E+02	0.1000051083E+02	0.2254485132E+01
256	1	0.1760846482E+02	0.1383681667E+02	0.2254485132E+01
257	2	0.9594327966E+01	0.9958773678E+01	0.2392997127E+01
258	2	0.1180922035E+02	0.1379507953E+02	0.2392997127E+01
259	2	0.1402411301E+02	0.9958773678E+01	0.2392997127E+01
260	2	0.1623900539E+02	0.1379507953E+02	0.2392997127E+01
261	2	0.9594346447E+01	0.1306112828E+02	0.2999759465E+01
262	2	0.1180923883E+02	0.9224822774E+01	0.2999759465E+01
263	2	0.1402413096E+02	0.1306112828E+02	0.2999759465E+01
264	2	0.1623902334E+02	0.9224822774E+01	0.2999759465E+01
265	1	0.1096377366E+02	0.1301944189E+02	0.3138204918E+01
266	1	0.1317866605E+02	0.9183136380E+01	0.3138204918E+01
267	1	0.1539355871E+02	0.1301944189E+02	0.3138204918E+01
268	1	0.1760845109E+02	0.9183136380E+01	0.3138204918E+01
269	2	0.9209488633E+01	0.8278689359E+01	0.4044566012E+01
270	2	0.1142438112E+02	0.1211499503E+02	0.4044566012E+01
271	2	0.1363927351E+02	0.8278689359E+01	0.4044566012E+01
272	2	0.1585416589E+02	0.1211499503E+02	0.4044566012E+01
273	1	0.1022306653E+02	0.8332015135E+01	0.4950925625E+01
274	1	0.1243795891E+02	0.1216832075E+02	0.4950925625E+01
275	1	0.1465285130E+02	0.8332015135E+01	0.4950925625E+01
276	1	0.1686774369E+02	0.1216832075E+02	0.4950925625E+01
277	2	0.1094388173E+02	0.1483951075E+02	0.5089371079E+01
278	2	0.1315877412E+02	0.1100320513E+02	0.5089371079E+01
279	2	0.1537366625E+02	0.1483951075E+02	0.5089371079E+01
280	2	0.1758855864E+02	0.1100320513E+02	0.5089371079E+01
281	2	0.9732605371E+01	0.9152756801E+01	0.5831942466E+01
282	2	0.1709844891E+02	0.1315089686E+02	0.5869179685E+01
283	2	0.1438074770E+02	0.9036354214E+01	0.6019145714E+01
284	2	0.1212298484E+02	0.1248829315E+02	0.6094812370E+01
285	1	0.1354718486E+02	0.1085719847E+02	0.6191050665E+01
286	1	0.1610578006E+02	0.1488768010E+02	0.6010349171E+01
287	1	0.8843250832E+01	0.9879123376E+01	0.5510030887E+01
288	1	0.1117315292E+02	0.1414151282E+02	0.6376162290E+01
289	2	0.1000399543E+02	0.1099839511E+02	0.6669726352E+01
290	2	0.1468232189E+02	0.1092888132E+02	0.6698448942E+01
291	2	0.1678859720E+02	0.7128255707E+01	0.6915940590E+01
292	2	0.1195911528E+02	0.8268227248E+01	0.6492380047E+01
293	1	0.1494936779E+02	0.7735676879E+01	0.7311206944E+01
294	1	0.1229257277E+02	0.8663094048E+01	0.8300390847E+01
295	1	0.1349009141E+02	0.1163154550E+02	0.8168868178E+01
296	1	0.9433137171E+01	0.1111800514E+02	0.7731063816E+01
297	2	0.1539031936E+02	0.9221232092E+01	0.8415990628E+01

298	2	0.1293956945E+02	0.9631564455E+01	0.9046405139E+01
299	2	0.1016672836E+02	0.1304979881E+02	0.6570441500E+01
300	2	0.1342378526E+02	0.1337978144E+02	0.8237992998E+01
301	2	0.1211901904E+02	0.1145966431E+02	0.9418599144E+01
302	2	0.1700904742E+02	0.1184195494E+02	0.7436398035E+01
303	2	0.1447355429E+02	0.7406713599E+01	0.8317185362E+01
304	2	0.1114565195E+02	0.7444209938E+01	0.8828869312E+01
305	1	0.1219454229E+02	0.1024255138E+02	0.9710474349E+01
306	1	0.1424200880E+02	0.1428845832E+02	0.8222058629E+01
307	1	0.1563488489E+02	0.1056635463E+02	0.7786649884E+01
308	1	0.1016299006E+02	0.1312404813E+02	0.7761611894E+01
309	2	0.9425144742E+01	0.1281280316E+02	0.8824945616E+01
310	2	0.1332341938E+02	0.1553197789E+02	0.9401486367E+01
311	2	0.1195892129E+02	0.1017928728E+02	0.1104467821E+02
312	2	0.1485873757E+02	0.1145615414E+02	0.9275109332E+01
313	1	0.1262906688E+02	0.1089441236E+02	0.1166984405E+02
314	1	0.1463325051E+02	0.1015481220E+02	0.9949960775E+01
315	1	0.1323084160E+02	0.1443584105E+02	0.1009637631E+02
316	1	0.1721173085E+02	0.1479985086E+02	0.9195032148E+01
317	2	0.1290595728E+02	0.1369569445E+02	0.1107719163E+02
318	2	0.1658549344E+02	0.1522550624E+02	0.1006765869E+02
319	2	0.1310900655E+02	0.1021030969E+02	0.1289140910E+02
320	2	0.1394662025E+02	0.9736062364E+01	0.1082377956E+02
321	3	0.5974609898E+01	-0.1070257732E+01	0.9523315059E+01
322	3	0.9144972981E+01	0.7793269954E+01	0.1419598370E+02
323	3	0.1356314584E+01	0.9338550401E+01	0.1742345931E+02
324	3	0.5920743229E+01	0.2980376300E+01	0.1131511257E+02
325	3	0.1210771024E+02	0.6622571906E+01	0.1461279292E+02
326	3	0.1815876918E+02	0.1472798289E+00	0.1656684379E+02
327	3	0.9261506953E+01	0.1273127683E+02	0.1471093533E+02
328	3	0.2934066835E+01	0.2217440583E+01	0.1375948880E+02
329	3	0.1893602677E+02	0.1452847391E+02	0.1367158266E+02
330	3	0.1487140382E+02	0.1104148402E+02	0.1188417160E+02
331	3	0.1475283859E+02	0.6526080023E+01	0.1483782799E+02
332	3	0.1196338915E+02	0.8989512086E+01	0.1255299797E+02
333	3	0.4326004252E+01	0.1315284762E+02	0.1427513170E+02
334	3	0.9596372978E+01	0.2119132787E+01	0.1123716061E+02
335	3	0.1572767342E+01	0.5908578760E+01	0.1473412065E+02
336	3	-0.4255400151E+00	0.8710589155E+01	0.1285038753E+02
337	3	0.8726681131E+01	0.1133989265E+02	0.9776785020E+01
338	3	0.6419782105E+01	0.7161614517E+01	0.1059949991E+02
339	3	-0.1116561746E+01	0.9944323315E+01	0.1509176867E+02
340	3	0.7959379094E+01	0.3519321060E+01	0.1007600569E+02
341	3	0.1369913540E+02	0.9179223607E+01	0.1840402925E+02

```
342  3    0.1719995187E+02   -0.4343838627E+00    0.1955180486E+02
343  3    0.5728367715E+01   -0.1124059899E+01    0.2102899158E+02
344  3    0.1498677188E+02    0.5419594571E+00    0.1984131429E+02
345  3    0.1296457510E+02    0.1310213019E+02    0.1615652248E+02
346  3    0.6441538852E+01    0.7866509449E+01    0.2010779341E+02
347  3    0.1623228590E+02    0.4977882076E+01    0.1824748211E+02
348  3    0.2621076848E+01    0.1252972743E+02    0.1724229483E+02
349  3    0.4412913019E+01    0.8603591405E+01    0.1744126527E+02
350  3    0.5584260855E+01    0.1151482765E+02    0.1887569625E+02
351  3    0.1680765532E+02    0.3342303169E+01    0.1650267273E+02
352  3    0.1216834419E+02    0.4568608469E+01    0.1810982298E+02
353  3    0.3940080452E+01    0.2567220973E+01    0.1773819281E+02
354  3    0.1112646482E+02    0.3676905490E+01    0.1607280266E+02
355  3    0.1173854311E+02    0.1191616485E+02    0.1915448609E+02
356  3    0.8891612522E+01    0.8048829465E+01    0.1762741770E+02
357  3    0.1344552754E+02    0.1647527454E+02    0.1680738229E+02
358  3    0.7780593912E+01    0.2830016491E+01    0.1885945194E+02
359  3    0.4081768409E+01    0.6012537405E+01    0.1758853593E+02
360  3    0.1468335413E+01    0.1126538578E+02    0.2028320525E+02
  0.0000000000E+00   0.0000000000E+00   0.0000000000E+00
  0.1771913910E+02   0.0000000000E+00   0.0000000000E+00
  0.0000000000E+00   0.1534522247E+02   0.0000000000E+00
  0.0000000000E+00   0.0000000000E+00   0.2426739311E+02
```

A.5 Initial geometry file for 0 K B_2O_3 surface

```
320  S
 B O
   1  2   0.2084343343E+01   0.5078191330E+00   0.3033826250E+00
   2  2   0.4299235731E+01   0.4344124690E+01   0.3033826250E+00
   3  2   0.6514128384E+01   0.5078191330E+00   0.3033826250E+00
   4  2   0.8729020772E+01   0.4344124690E+01   0.3033826250E+00
   5  1   0.1363526018E+01   0.7015301417E+01   0.4418193910E+00
   6  1   0.3578418406E+01   0.3178996029E+01   0.4418193910E+00
   7  1   0.5793310793E+01   0.7015301417E+01   0.4418193910E+00
   8  1   0.8008203181E+01   0.3178996029E+01   0.4418193910E+00
   9  2   0.3498867100E+00   0.7068606101E+01   0.1348249889E+01
  10  2   0.2564779097E+01   0.3232300260E+01   0.1348249889E+01
  11  2   0.4779671219E+01   0.7068606101E+01   0.1348249889E+01
  12  2   0.6994563607E+01   0.3232300260E+01   0.1348249889E+01
  13  1   0.2104218237E+01   0.2327899597E+01   0.2254485132E+01
  14  1   0.4319110492E+01   0.6164205438E+01   0.2254485132E+01
  15  1   0.6534002879E+01   0.2327899597E+01   0.2254485132E+01
```

16	1	0.8748895267E+01	0.6164205438E+01	0.2254485132E+01
17	2	0.7347584160E+00	0.2286162441E+01	0.2392997127E+01
18	2	0.2949650803E+01	0.6122468290E+01	0.2392997127E+01
19	2	0.5164543457E+01	0.2286162441E+01	0.2392997127E+01
20	2	0.7379435844E+01	0.6122468290E+01	0.2392997127E+01
21	2	0.7347768970E+00	0.5388517040E+01	0.2999759465E+01
22	2	0.2949669284E+01	0.1552211537E+01	0.2999759465E+01
23	2	0.5164561406E+01	0.5388517040E+01	0.2999759465E+01
24	2	0.7379453794E+01	0.1552211537E+01	0.2999759465E+01
25	1	0.2104204115E+01	0.5346830654E+01	0.3138204918E+01
26	1	0.4319096502E+01	0.1510525143E+01	0.3138204918E+01
27	1	0.6533989156E+01	0.5346830654E+01	0.3138204918E+01
28	1	0.8748881543E+01	0.1510525143E+01	0.3138204918E+01
29	2	0.3499190830E+00	0.6060781220E+00	0.4044566012E+01
30	2	0.2564811568E+01	0.4442383794E+01	0.4044566012E+01
31	2	0.4779703955E+01	0.6060781220E+00	0.4044566012E+01
32	2	0.6994596343E+01	0.4442383794E+01	0.4044566012E+01
33	1	0.1363496977E+01	0.6594038980E+00	0.4950925625E+01
34	1	0.3578389364E+01	0.4495709516E+01	0.4950925625E+01
35	1	0.5793281752E+01	0.6594038980E+00	0.4950925625E+01
36	1	0.8008174139E+01	0.4495709516E+01	0.4950925625E+01
37	2	0.2084312184E+01	0.7166899510E+01	0.5089371079E+01
38	2	0.4299204572E+01	0.3330593891E+01	0.5089371079E+01
39	2	0.6514096702E+01	0.7166899510E+01	0.5089371079E+01
40	2	0.8728989090E+01	0.3330593891E+01	0.5089371079E+01
41	2	0.1821464668E+01	0.1545937326E+01	0.5892725414E+01
42	2	0.8196380202E+01	0.5426388371E+01	0.6083305913E+01
43	2	0.6169736163E+01	0.1693269311E+01	0.5567406816E+01
44	2	0.3506445868E+01	0.5730570853E+01	0.5307063880E+01
45	1	0.5261123908E+01	0.2942021035E+01	0.5877318793E+01
46	1	0.7199530571E+01	0.7071801447E+01	0.6604805678E+01
47	1	0.1166543081E+01	0.3071111836E+01	0.6337512361E+01
48	1	0.2723311237E+01	0.7185107610E+01	0.6062276127E+01
49	2	0.1730819348E+01	0.3610143353E+01	0.7468238794E+01
50	2	0.5432153263E+01	0.3730894469E+01	0.6969197154E+01
51	2	0.8188729653E+01	0.3449197039E+00	0.6265531843E+01
52	2	0.4134219973E+01	0.2670539918E+00	0.7013698442E+01
53	1	0.7246917766E+01	0.1241783913E+01	0.7333998842E+01
54	1	0.2676685133E+01	0.8403107282E+00	0.8015239114E+01
55	1	0.4808864871E+01	0.4556625051E+01	0.8021859078E+01
56	1	0.1566262554E+01	0.4952983751E+01	0.8844964001E+01
57	2	0.8617479371E+01	0.1834607668E+01	0.7571168818E+01
58	2	0.3709102904E+01	0.2316364104E+01	0.8494944288E+01
59	2	0.2063202352E+01	0.6150427659E+01	0.7528407344E+01

60	2	0.5386992615E+01	0.5850342895E+01	0.7781222273E+01
61	2	0.3434164994E+01	0.4608407886E+01	0.9170307280E+01
62	2	0.8312169247E+01	0.4409065676E+01	0.8344004062E+01
63	2	0.6637918499E+01	0.7774384111E+00	0.8322879116E+01
64	2	0.1634738255E+01	0.1011587730E+00	0.8488800635E+01
65	1	0.3180179995E+01	0.3130525254E+01	0.9187146161E+01
66	1	0.5543272310E+01	0.6863255518E+01	0.8543225201E+01
67	1	0.8010877288E+01	0.2774755093E+01	0.9020385239E+01
68	1	0.2214129509E+01	0.7302429021E+01	0.8428331876E+01
69	2	0.1459419048E+01	0.7278240639E+01	0.9480081720E+01
70	2	0.5040160329E+01	0.6795475481E+01	0.9544004222E+01
71	2	0.2041816423E+01	0.3011633104E+01	0.1010844539E+02
72	2	0.7025504072E+01	0.3370289399E+01	0.1035563909E+02
73	1	0.1219823690E+01	0.2147903545E+01	0.1053034288E+02
74	1	0.5897338934E+01	0.3602832485E+01	0.1109072474E+02
75	1	0.4566264734E+01	0.6995790280E+01	0.1070860200E+02
76	1	0.8772172025E+01	0.5865005507E+01	0.9912011043E+01
77	2	0.3718518935E+01	0.7118093971E+01	0.1164075486E+02
78	2	0.9659073270E+01	0.5324359942E+01	0.1041928498E+02
79	2	0.6512874195E+00	0.1051256654E+01	0.1075710098E+02
80	2	0.4961312376E+01	0.4089991999E+01	0.1181649309E+02
81	2	0.1094391289E+02	0.5078191330E+00	0.3033826250E+00
82	2	0.1315880528E+02	0.4344124690E+01	0.3033826250E+00
83	2	0.1537369793E+02	0.5078191330E+00	0.3033826250E+00
84	2	0.1758859032E+02	0.4344124690E+01	0.3033826250E+00
85	1	0.1022309557E+02	0.7015301417E+01	0.4418193910E+00
86	1	0.1243798796E+02	0.3178996029E+01	0.4418193910E+00
87	1	0.1465288034E+02	0.7015301417E+01	0.4418193910E+00
88	1	0.1686777273E+02	0.3178996029E+01	0.4418193910E+00
89	2	0.9209456260E+01	0.7068606101E+01	0.1348249889E+01
90	2	0.1142434865E+02	0.3232300260E+01	0.1348249889E+01
91	2	0.1363924077E+02	0.7068606101E+01	0.1348249889E+01
92	2	0.1585413316E+02	0.3232300260E+01	0.1348249889E+01
93	1	0.1096378779E+02	0.2327899597E+01	0.2254485132E+01
94	1	0.1317868004E+02	0.6164205438E+01	0.2254485132E+01
95	1	0.1539357243E+02	0.2327899597E+01	0.2254485132E+01
96	1	0.1760846482E+02	0.6164205438E+01	0.2254485132E+01
97	2	0.9594327966E+01	0.2286162441E+01	0.2392997127E+01
98	2	0.1180922035E+02	0.6122468290E+01	0.2392997127E+01
99	2	0.1402411301E+02	0.2286162441E+01	0.2392997127E+01
100	2	0.1623900539E+02	0.6122468290E+01	0.2392997127E+01
101	2	0.9594346447E+01	0.5388517040E+01	0.2999759465E+01
102	2	0.1180923883E+02	0.1552211537E+01	0.2999759465E+01
103	2	0.1402413096E+02	0.5388517040E+01	0.2999759465E+01

104	2	0.1623902334E+02	0.1552211537E+01	0.2999759465E+01
105	1	0.1096377366E+02	0.5346830654E+01	0.3138204918E+01
106	1	0.1317866605E+02	0.1510525143E+01	0.3138204918E+01
107	1	0.1539355871E+02	0.5346830654E+01	0.3138204918E+01
108	1	0.1760845109E+02	0.1510525143E+01	0.3138204918E+01
109	2	0.9209488633E+01	0.6060781220E+00	0.4044566012E+01
110	2	0.1142438112E+02	0.4442383794E+01	0.4044566012E+01
111	2	0.1363927351E+02	0.6060781220E+00	0.4044566012E+01
112	2	0.1585416589E+02	0.4442383794E+01	0.4044566012E+01
113	1	0.1022306653E+02	0.6594038980E+00	0.4950925625E+01
114	1	0.1243795891E+02	0.4495709516E+01	0.4950925625E+01
115	1	0.1465285130E+02	0.6594038980E+00	0.4950925625E+01
116	1	0.1686774369E+02	0.4495709516E+01	0.4950925625E+01
117	2	0.1094388173E+02	0.7166899510E+01	0.5089371079E+01
118	2	0.1315877412E+02	0.3330593891E+01	0.5089371079E+01
119	2	0.1537366625E+02	0.7166899510E+01	0.5089371079E+01
120	2	0.1758855864E+02	0.3330593891E+01	0.5089371079E+01
121	2	0.1054810822E+02	0.1825499216E+01	0.5646575491E+01
122	2	0.1713157473E+02	0.5750298254E+01	0.5574283090E+01
123	2	0.1478670714E+02	0.2244578755E+01	0.6022633887E+01
124	2	0.1288848291E+02	0.5718590349E+01	0.5899097490E+01
125	1	0.1373862863E+02	0.2772088519E+01	0.6125382206E+01
126	1	0.1615586395E+02	0.6385818052E+01	0.5514558349E+01
127	1	0.1004291696E+02	0.3170524749E+01	0.5585362176E+01
128	1	0.1197486324E+02	0.6900657181E+01	0.5963340273E+01
129	2	0.1034167622E+02	0.3785156456E+01	0.6762521356E+01
130	2	0.1489827517E+02	0.3531240532E+01	0.7571490517E+01
131	2	0.1636340525E+02	0.8632882845E-01	0.6753740272E+01
132	2	0.1267382957E+02	-0.1999211387E-02	0.6746181715E+01
133	1	0.1614051616E+02	0.8634258159E+00	0.8076311681E+01
134	1	0.1227031624E+02	0.1127250800E+00	0.7815306655E+01
135	1	0.1433729218E+02	0.4546890015E+01	0.7935448664E+01
136	1	0.9247376532E+01	0.4757886594E+01	0.7669018502E+01
137	2	0.1678585081E+02	0.2024345679E+01	0.8470938053E+01
138	2	0.1291853038E+02	0.1783215710E+01	0.7668785144E+01
139	2	0.9638652062E+01	0.5919750452E+01	0.7973894176E+01
140	2	0.1521213179E+02	0.6091778790E+01	0.7247295572E+01
141	2	0.1331420390E+02	0.4263600347E+01	0.9079453490E+01
142	2	0.1752194733E+02	0.5131200836E+01	0.8378670835E+01
143	2	0.1520838595E+02	0.1103204131E+00	0.8551082300E+01
144	2	0.1135221175E+02	-0.6755652626E+00	0.8166099815E+01
145	1	0.1294639234E+02	0.2640150745E+01	0.8498724936E+01
146	1	0.1479613876E+02	0.6583976272E+01	0.8328533170E+01
147	1	0.1660998568E+02	0.3869462227E+01	0.8753111510E+01

148	1	0.9652845291E+01	0.7101769952E+01	0.8429632423E+01
149	2	0.8822639498E+01	0.6987661306E+01	0.9514463742E+01
150	2	0.1377964961E+02	0.6335887254E+01	0.9062547550E+01
151	2	0.1188585324E+02	0.2205985323E+01	0.9848080692E+01
152	2	0.1599281571E+02	0.3975001701E+01	0.9737608489E+01
153	1	0.1068572705E+02	0.2587338453E+01	0.9586720203E+01
154	1	0.1586096788E+02	0.3605340269E+01	0.1112912079E+02
155	1	0.1332685191E+02	0.6571622259E+01	0.1027491423E+02
156	1	0.1851587558E+02	0.7620875490E+01	0.1055602191E+02
157	2	0.1225621451E+02	0.7012929261E+01	0.1066446571E+02
158	2	0.1763179680E+02	0.7577490590E+01	0.1135436073E+02
159	2	0.9520896614E+01	0.2747050498E+01	0.9827637172E+01
160	2	0.1532755464E+02	0.3658732052E+01	0.1221013263E+02
161	2	0.2084343343E+01	0.8180430370E+01	0.3033826250E+00
162	2	0.4299235731E+01	0.1201673593E+02	0.3033826250E+00
163	2	0.6514128384E+01	0.8180430370E+01	0.3033826250E+00
164	2	0.8729020772E+01	0.1201673593E+02	0.3033826250E+00
165	1	0.1363526018E+01	0.1468791265E+02	0.4418193910E+00
166	1	0.3578418406E+01	0.1085160727E+02	0.4418193910E+00
167	1	0.5793310793E+01	0.1468791265E+02	0.4418193910E+00
168	1	0.8008203181E+01	0.1085160727E+02	0.4418193910E+00
169	2	0.3498867100E+00	0.1474121734E+02	0.1348249889E+01
170	2	0.2564779097E+01	0.1090491150E+02	0.1348249889E+01
171	2	0.4779671219E+01	0.1474121734E+02	0.1348249889E+01
172	2	0.6994563607E+01	0.1090491150E+02	0.1348249889E+01
173	1	0.2104218237E+01	0.1000051083E+02	0.2254485132E+01
174	1	0.4319110492E+01	0.1383681667E+02	0.2254485132E+01
175	1	0.6534002879E+01	0.1000051083E+02	0.2254485132E+01
176	1	0.8748895267E+01	0.1383681667E+02	0.2254485132E+01
177	2	0.7347584160E+00	0.9958773678E+01	0.2392997127E+01
178	2	0.2949650803E+01	0.1379507953E+02	0.2392997127E+01
179	2	0.5164543457E+01	0.9958773678E+01	0.2392997127E+01
180	2	0.7379435844E+01	0.1379507953E+02	0.2392997127E+01
181	2	0.7347768970E+00	0.1306112828E+02	0.2999759465E+01
182	2	0.2949669284E+01	0.9224822774E+01	0.2999759465E+01
183	2	0.5164561406E+01	0.1306112828E+02	0.2999759465E+01
184	2	0.7379453794E+01	0.9224822774E+01	0.2999759465E+01
185	1	0.2104204115E+01	0.1301944189E+02	0.3138204918E+01
186	1	0.4319096502E+01	0.9183136380E+01	0.3138204918E+01
187	1	0.6533989156E+01	0.1301944189E+02	0.3138204918E+01
188	1	0.8748881543E+01	0.9183136380E+01	0.3138204918E+01
189	2	0.3499190830E+00	0.8278689359E+01	0.4044566012E+01
190	2	0.2564811568E+01	0.1211499503E+02	0.4044566012E+01
191	2	0.4779703955E+01	0.8278689359E+01	0.4044566012E+01

192	2	0.6994596343E+01	0.1211499503E+02	0.4044566012E+01
193	1	0.1363496977E+01	0.8332015135E+01	0.4950925625E+01
194	1	0.3578389364E+01	0.1216832075E+02	0.4950925625E+01
195	1	0.5793281752E+01	0.8332015135E+01	0.4950925625E+01
196	1	0.8008174139E+01	0.1216832075E+02	0.4950925625E+01
197	2	0.2084312184E+01	0.1483951075E+02	0.5089371079E+01
198	2	0.4299204572E+01	0.1100320513E+02	0.5089371079E+01
199	2	0.6514096702E+01	0.1483951075E+02	0.5089371079E+01
200	2	0.8728989090E+01	0.1100320513E+02	0.5089371079E+01
201	2	0.2100255268E+01	0.9127734572E+01	0.5645061598E+01
202	2	0.8486735907E+01	0.1382649954E+02	0.5457220476E+01
203	2	0.6599191950E+01	0.9908178829E+01	0.5451728608E+01
204	2	0.3429319820E+01	0.1336422115E+02	0.5422973345E+01
205	1	0.5961399831E+01	0.1165223295E+02	0.5393571227E+01
206	1	0.7858484335E+01	0.1558968223E+02	0.5166735585E+01
207	1	0.7617928534E+00	0.1026153230E+02	0.5677325741E+01
208	1	0.3330653539E+01	0.1501359338E+02	0.5920882222E+01
209	2	0.1076273798E+01	0.1070734702E+02	0.6995470602E+01
210	2	0.6647530269E+01	0.1226413644E+02	0.6319056924E+01
211	2	0.8009119501E+01	0.7778782347E+01	0.7079165303E+01
212	2	0.4366218804E+01	0.8034731752E+01	0.6184422894E+01
213	1	0.7542510155E+01	0.8349661853E+01	0.8271159225E+01
214	1	0.3738474422E+01	0.8878337802E+01	0.6924928533E+01
215	1	0.5972080814E+01	0.1269019349E+02	0.7284465559E+01
216	1	0.9907671394E-01	0.1210391850E+02	0.7316612287E+01
217	2	0.8249258464E+01	0.9293650118E+01	0.8463707061E+01
218	2	0.4520488711E+01	0.9745878914E+01	0.7634132130E+01
219	2	0.1378386715E+01	0.1332247743E+02	0.7106064173E+01
220	2	0.5981581386E+01	0.1398025046E+02	0.7911860612E+01
221	2	0.4870878322E+01	0.1229712148E+02	0.8050141267E+01
222	2	0.8657784488E+01	0.1198048101E+02	0.8926041917E+01
223	2	0.6415086623E+01	0.7788014333E+01	0.8386567232E+01
224	2	0.2976693269E+01	0.8384244598E+01	0.7787435367E+01
225	1	0.3898085285E+01	0.1061927814E+02	0.8132841002E+01
226	1	0.5806278718E+01	0.1496182194E+02	0.8409610939E+01
227	1	0.7645680985E+01	0.1040109991E+02	0.8782098247E+01
228	1	0.1129957513E+01	0.1418139350E+02	0.8198267572E+01
229	2	0.3714289086E+00	0.1370784903E+02	0.9150174457E+01
230	2	0.5124484925E+01	0.1502620641E+02	0.9451967161E+01
231	2	0.2607127672E+01	0.1144906662E+02	0.9017689567E+01
232	2	0.6550584809E+01	0.1001505000E+02	0.9393200949E+01
233	1	0.2631258007E+01	0.1044628281E+02	0.9893368536E+01
234	1	0.6682564977E+01	0.9020339615E+01	0.1009039537E+02
235	1	0.4290243668E+01	0.1457666284E+02	0.1022765845E+02

236	1	0.9554910530E+01	0.1480873625E+02	0.9328274662E+01
237	2	0.3429417610E+01	0.1463197301E+02	0.1112742122E+02
238	2	0.9117362416E+01	0.1540940766E+02	0.1023914991E+02
239	2	0.2403106427E+01	0.9621682690E+01	0.1088818187E+02
240	2	0.6394117154E+01	0.8457957373E+01	0.1117780359E+02
241	2	0.1094391289E+02	0.8180430370E+01	0.3033826250E+00
242	2	0.1315880528E+02	0.1201673593E+02	0.3033826250E+00
243	2	0.1537369793E+02	0.8180430370E+01	0.3033826250E+00
244	2	0.1758859032E+02	0.1201673593E+02	0.3033826250E+00
245	1	0.1022309557E+02	0.1468791265E+02	0.4418193910E+00
246	1	0.1243798796E+02	0.1085160727E+02	0.4418193910E+00
247	1	0.1465288034E+02	0.1468791265E+02	0.4418193910E+00
248	1	0.1686777273E+02	0.1085160727E+02	0.4418193910E+00
249	2	0.9209456260E+01	0.1474121734E+02	0.1348249889E+01
250	2	0.1142434865E+02	0.1090491150E+02	0.1348249889E+01
251	2	0.1363924077E+02	0.1474121734E+02	0.1348249889E+01
252	2	0.1585413316E+02	0.1090491150E+02	0.1348249889E+01
253	1	0.1096378779E+02	0.1000051083E+02	0.2254485132E+01
254	1	0.1317868004E+02	0.1383681667E+02	0.2254485132E+01
255	1	0.1539357243E+02	0.1000051083E+02	0.2254485132E+01
256	1	0.1760846482E+02	0.1383681667E+02	0.2254485132E+01
257	2	0.9594327966E+01	0.9958773678E+01	0.2392997127E+01
258	2	0.1180922035E+02	0.1379507953E+02	0.2392997127E+01
259	2	0.1402411301E+02	0.9958773678E+01	0.2392997127E+01
260	2	0.1623900539E+02	0.1379507953E+02	0.2392997127E+01
261	2	0.9594346447E+01	0.1306112828E+02	0.2999759465E+01
262	2	0.1180923883E+02	0.9224822774E+01	0.2999759465E+01
263	2	0.1402413096E+02	0.1306112828E+02	0.2999759465E+01
264	2	0.1623902334E+02	0.9224822774E+01	0.2999759465E+01
265	1	0.1096377366E+02	0.1301944189E+02	0.3138204918E+01
266	1	0.1317866605E+02	0.9183136380E+01	0.3138204918E+01
267	1	0.1539355871E+02	0.1301944189E+02	0.3138204918E+01
268	1	0.1760845109E+02	0.9183136380E+01	0.3138204918E+01
269	2	0.9209488633E+01	0.8278689359E+01	0.4044566012E+01
270	2	0.1142438112E+02	0.1211499503E+02	0.4044566012E+01
271	2	0.1363927351E+02	0.8278689359E+01	0.4044566012E+01
272	2	0.1585416589E+02	0.1211499503E+02	0.4044566012E+01
273	1	0.1022306653E+02	0.8332015135E+01	0.4950925625E+01
274	1	0.1243795891E+02	0.1216832075E+02	0.4950925625E+01
275	1	0.1465285130E+02	0.8332015135E+01	0.4950925625E+01
276	1	0.1686774369E+02	0.1216832075E+02	0.4950925625E+01
277	2	0.1094388173E+02	0.1483951075E+02	0.5089371079E+01
278	2	0.1315877412E+02	0.1100320513E+02	0.5089371079E+01
279	2	0.1537366625E+02	0.1483951075E+02	0.5089371079E+01

280	2	0.1758855864E+02	0.1100320513E+02	0.5089371079E+01
281	2	0.1016229438E+02	0.9552616184E+01	0.5382522750E+01
282	2	0.1668311703E+02	0.1289826125E+02	0.6070388031E+01
283	2	0.1474311697E+02	0.9318758062E+01	0.5972621889E+01
284	2	0.1239491937E+02	0.1328595437E+02	0.5433081080E+01
285	1	0.1408632182E+02	0.1060051501E+02	0.6077257395E+01
286	1	0.1598494376E+02	0.1460652424E+02	0.6163996319E+01
287	1	0.9008858311E+01	0.9974298440E+01	0.5443328378E+01
288	1	0.1169075080E+02	0.1432710851E+02	0.6273419648E+01
289	2	0.9388974524E+01	0.1111049920E+02	0.6995639620E+01
290	2	0.1476814220E+02	0.1138905997E+02	0.6838545027E+01
291	2	0.1720096593E+02	0.7549435820E+01	0.6527031612E+01
292	2	0.1223737295E+02	0.7846050252E+01	0.6898889401E+01
293	1	0.1561816046E+02	0.8155747019E+01	0.7190622207E+01
294	1	0.1184646574E+02	0.8719466709E+01	0.7848567038E+01
295	1	0.1368282729E+02	0.1149200957E+02	0.8013613900E+01
296	1	0.9289561548E+01	0.1197138671E+02	0.7917447049E+01
297	2	0.1634334218E+02	0.9587207963E+01	0.8052961966E+01
298	2	0.1230230246E+02	0.9795176664E+01	0.8179928923E+01
299	2	0.1068770092E+02	0.1336812936E+02	0.6640795802E+01
300	2	0.1421052328E+02	0.1331959182E+02	0.8286050908E+01
301	2	0.1219644364E+02	0.1178404118E+02	0.8799074422E+01
302	2	0.1653385581E+02	0.1210216984E+02	0.8556765225E+01
303	2	0.1522857998E+02	0.7889904038E+01	0.8228327174E+01
304	2	0.1072420814E+02	0.8014476629E+01	0.8607375280E+01
305	1	0.1155156756E+02	0.1064108201E+02	0.8845588332E+01
306	1	0.1421980307E+02	0.1451461006E+02	0.8906179610E+01
307	1	0.1598545061E+02	0.1069628723E+02	0.8120472265E+01
308	1	0.1056103884E+02	0.1369944581E+02	0.7814629782E+01
309	2	0.9575961184E+01	0.1377908696E+02	0.8702924253E+01
310	2	0.1362973470E+02	0.1492945680E+02	0.1011404559E+02
311	2	0.1079378920E+02	0.1052743431E+02	0.1000992226E+02
312	2	0.1451290400E+02	0.1057797146E+02	0.9235889321E+01
313	1	0.1020141291E+02	0.1001567864E+02	0.1101024555E+02
314	1	0.1361296469E+02	0.1009601955E+02	0.1011621663E+02
315	1	0.1279170433E+02	0.1463239386E+02	0.1109279459E+02
316	1	0.1782654715E+02	0.1498974075E+02	0.1051724224E+02
317	2	0.1178806366E+02	0.1461478931E+02	0.1184795829E+02
318	2	0.1673983242E+02	0.1458812112E+02	0.1109099890E+02
319	2	0.9334975691E+01	0.9733825017E+01	0.1179633740E+02
320	2	0.1319719605E+02	0.9836039140E+01	0.1121294846E+02

0.0000000000E+00	0.0000000000E+00	0.0000000000E+00
0.1771913910E+02	0.0000000000E+00	0.0000000000E+00
0.0000000000E+00	0.1534522247E+02	0.0000000000E+00

0.0000000000E+00 0.0000000000E+00 0.2426739311E+02

A.6 CHIMES parameters

! Date 2022-08-19
!
! Number of equations = 7920
! DLARS code for LASSO used
! DLARS alpha = 1.0000e-04
! Reading output from prior DLARS calculation
! RMS force error = 8.8150e+00
! max abs variable = 2.2975e+03
! number of fitting vars = 828
! Bayesian Information Criterion = 4.1908e+04
!
USECOUL: false
FITCOUL: false
USE3BCH: true
USE4BCH: false

PAIRTYP: CHEBYSHEV 24 12 0 -1 1

ATOM TYPES: 3

# TYPEIDX #	# ATM_TYP #	# ATMCHRG #	# ATMMASS #
0	B	0	10.811
1	O	0	15.999
2	Mg	0	24.305

ATOM PAIRS: 6

# PAIRIDX #	# ATM_TY1 #	# ATM_TY1 #	# S_MINIM #	# S_MAXIM #	# CHBDIST #	# MORSE_LAMBDA #
0	B	B	1.9	4	MORSE	1.5
1	O	O	1.9	4	MORSE	1.21
2	Mg	Mg	1.9	4	MORSE	2.85
3	B	O	0.9	4	MORSE	1.4
4	B	Mg	1.5	4	MORSE	2.5
5	O	Mg	1.5	4	MORSE	1.82

FCUT TYPE: TERSOFF 0.95

PAIR CHEBYSHEV PENALTY DIST: 0.15
PAIR CHEBYSHEV PENALTY SCALING: 1.0E5

PAIR CHEBYSHEV CUBIC SCALING: 1.0

SPECIAL 3B S_MAXIM: SPECIFIC 10
BBBBBB BB BB BB 4.00000 4.00000 4.00000
BBBOBO BB BO BO 4.00000 4.00000 4.00000
BBBMgBMg BB BMg BMg 4.00000 4.00000 4.00000
BOBOOO BO BO OO 4.00000 4.00000 4.00000
BOBMgOMg BMg BO OMg 4.00000 4.00000 4.00000
BMgBMgMgMg BMg BMg MgMg 4.00000 4.00000 4.00000
OOOOOO OO OO OO 4.00000 4.00000 4.00000
OOOMgOMg OMg OMg OO 4.00000 4.00000 4.00000
OMgOMgMgMg MgMg OMg OMg 4.00000 4.00000 4.00000
MgMgMgMgMgMg MgMg MgMg MgMg 4.00000 4.00000 4.00000

ATOM PAIR TRIPLETS: 10
ATOM PAIR QUADRUPLETS: 0

PAIR CHEBYSHEV PARAMS

PAIRTYPE PARAMS: 0 B B

 0 0.0000000000000e+00
 1 0.0000000000000e+00
 2 0.0000000000000e+00
 3 1.8463071668600e+01
 4 -8.6541111126990e+00
 5 1.2125464485290e+01
 6 0.0000000000000e+00
 7 0.0000000000000e+00
 8 0.0000000000000e+00
 9 0.0000000000000e+00
10 6.8194988836820e+00
11 -4.6598121262300e+00
12 0.0000000000000e+00
13 -1.8631477322980e+01
14 7.7786944129210e+00
15 0.0000000000000e+00
16 1.6349482127850e+01
17 -6.5451908446080e+00
18 0.0000000000000e+00
19 -1.8582714688020e+01
20 -1.1129594695550e+01
21 -1.4535974648070e+01
22 -4.3828551827050e+00

23 -4.0818413535600e+00

PAIRTYPE PARAMS: 1 O O

0 1.4241494537730e+00
1 -2.1270132580870e+01
2 0.0000000000000e+00
3 0.0000000000000e+00
4 0.0000000000000e+00
5 5.1934494729700e+00
6 -1.4125319559880e+01
7 0.0000000000000e+00
8 -6.2463255556420e+00
9 1.8495395284380e+01
10 -6.5011914296290e+00
11 2.3239269626560e+01
12 0.0000000000000e+00
13 1.8896130469520e+01
14 -9.5534414017370e+00
15 6.0689427237770e+00
16 -1.2295639000180e+01
17 4.3564921630550e-01
18 -1.0019845561810e+01
19 0.0000000000000e+00
20 -4.1152222334130e+00
21 8.2734289805440e-01
22 -1.2275449146880e+00
23 7.4129409047260e-01

PAIRTYPE PARAMS: 2 Mg Mg

0 0.0000000000000e+00
1 0.0000000000000e+00
2 0.0000000000000e+00
3 0.0000000000000e+00
4 0.0000000000000e+00
5 0.0000000000000e+00
6 9.5586550043510e+01
7 -4.2688806749750e+00
8 0.0000000000000e+00
9 0.0000000000000e+00
10 0.0000000000000e+00
11 0.0000000000000e+00
12 0.0000000000000e+00

13 0.0000000000000e+00
14 0.0000000000000e+00
15 0.0000000000000e+00
16 0.0000000000000e+00
17 6.4376592109900e+01
18 -1.2827585668500e+01
19 0.0000000000000e+00
20 0.0000000000000e+00
21 0.0000000000000e+00
22 0.0000000000000e+00
23 3.6087686007110e+01

PAIRTYPE PARAMS: 3 B O

0 0.0000000000000e+00
1 -5.1974983062920e+00
2 -3.8314136100120e+00
3 0.0000000000000e+00
4 4.8732003411720e+00
5 1.5458538845140e+01
6 -9.4224195405600e-03
7 -9.4050759484660e+00
8 0.0000000000000e+00
9 0.0000000000000e+00
10 1.2946617302690e-01
11 -5.8746659132280e+00
12 7.7496217311210e+00
13 0.0000000000000e+00
14 -2.1047895092410e-01
15 9.9482554998740e-01
16 1.7357695761330e+00
17 -2.0025195029980e+00
18 3.6581125480920e-03
19 0.0000000000000e+00
20 -5.7352584201210e-01
21 -5.1863229459420e-01
22 3.3473511329040e-01
23 -4.1752765001880e-01

PAIRTYPE PARAMS: 4 B Mg

0 0.0000000000000e+00
1 0.0000000000000e+00
2 2.7746242792910e+01

3 -3.3895394052140e+01
4 0.0000000000000e+00
5 4.7313012508210e+00
6 -9.9779755882930e+00
7 2.4323308453070e+00
8 -1.7263017914760e+01
9 7.3140645245760e-01
10 1.8900299974990e+00
11 -2.1282338462960e+00
12 -5.9212888420000e-01
13 0.0000000000000e+00
14 0.0000000000000e+00
15 6.1594692427280e-01
16 -2.1752846989090e+00
17 1.6657892203860e+00
18 -1.1170779134370e+00
19 -9.0526600853030e-01
20 -9.0553952310730e-01
21 1.1477833112350e+00
22 -5.7891330606530e-01
23 -7.4723269014510e-01

PAIRTYPE PARAMS: 5 O Mg

0 -5.6817428266570e+01
1 2.4450986193090e+01
2 3.0866501772320e+01
3 -9.1657270178470e+00
4 7.2349236931180e+00
5 0.0000000000000e+00
6 0.0000000000000e+00
7 -1.9167743406680e+00
8 -1.4669904357270e-01
9 0.0000000000000e+00
10 -1.4825059399130e+00
11 4.1579630826410e+00
12 -7.4361189319120e-01
13 5.4233807256750e+00
14 0.0000000000000e+00
15 3.0417236058770e+00
16 1.2990398799580e+00
17 2.6685683512110e+00
18 5.2574185561920e-02
19 2.5496532838040e+00

20 0.0000000000000e+00
21 1.7186194439180e+00
22 -6.8446983248740e-01
23 8.2929408043350e-01

TRIPLET CHEBYSHEV PARAMS

TRIPLETTYPE PARAMS:
INDEX: 0 ATOMS: B B B
PAIRS: BB BB BB UNIQUE: -1 TOTAL: 102
index | powers | equiv index | param index | parameter
---
0 0 4 9 198 35 -5.8729691787650e+00
1 4 0 9 198 35 -5.8729691787650e+00
2 0 9 4 198 35 -5.8729691787650e+00
3 9 0 4 198 35 -5.8729691787650e+00
4 4 9 0 198 35 -5.8729691787650e+00
5 9 4 0 198 35 -5.8729691787650e+00
6 0 6 9 270 48 5.1641193470090e+01
7 6 0 9 270 48 5.1641193470090e+01
8 0 9 6 270 48 5.1641193470090e+01
9 9 0 6 270 48 5.1641193470090e+01
10 6 9 0 270 48 5.1641193470090e+01
11 9 6 0 270 48 5.1641193470090e+01
12 0 7 8 291 52 6.1733199843080e+00
13 7 0 8 291 52 6.1733199843080e+00
14 0 8 7 291 52 6.1733199843080e+00
15 8 0 7 291 52 6.1733199843080e+00
16 7 8 0 291 52 6.1733199843080e+00
17 8 7 0 291 52 6.1733199843080e+00
18 0 8 10 324 58 4.8524123843510e+01
19 8 0 10 324 58 4.8524123843510e+01
20 0 10 8 324 58 4.8524123843510e+01
21 10 0 8 324 58 4.8524123843510e+01
22 8 10 0 324 58 4.8524123843510e+01
23 10 8 0 324 58 4.8524123843510e+01
24 0 8 11 330 59 -2.1263683080760e+01
25 8 0 11 330 59 -2.1263683080760e+01
26 0 11 8 330 59 -2.1263683080760e+01
27 11 0 8 330 59 -2.1263683080760e+01
28 8 11 0 330 59 -2.1263683080760e+01
29 11 8 0 330 59 -2.1263683080760e+01
30 0 9 11 345 62 8.8452592271460e+00
31 9 0 11 345 62 8.8452592271460e+00

32 0 11 9 345 62 8.8452592271460e+00
33 11 0 9 345 62 8.8452592271460e+00
34 9 11 0 345 62 8.8452592271460e+00
35 11 9 0 345 62 8.8452592271460e+00
36 1 3 11 496 95 6.1869762225570e+01
37 3 1 11 496 95 6.1869762225570e+01
38 1 11 3 496 95 6.1869762225570e+01
39 11 1 3 496 95 6.1869762225570e+01
40 3 11 1 496 95 6.1869762225570e+01
41 11 3 1 496 95 6.1869762225570e+01
42 2 4 10 806 157 -8.5293628090720e+01
43 4 2 10 806 157 -8.5293628090720e+01
44 2 10 4 806 157 -8.5293628090720e+01
45 10 2 4 806 157 -8.5293628090720e+01
46 4 10 2 806 157 -8.5293628090720e+01
47 10 4 2 806 157 -8.5293628090720e+01
48 3 4 6 999 198 -2.1964949548360e+02
49 4 3 6 999 198 -2.1964949548360e+02
50 3 6 4 999 198 -2.1964949548360e+02
51 6 3 4 999 198 -2.1964949548360e+02
52 4 6 3 999 198 -2.1964949548360e+02
53 6 4 3 999 198 -2.1964949548360e+02
54 3 9 11 1164 228 7.8627717392790e+00
55 9 3 11 1164 228 7.8627717392790e+00
56 3 11 9 1164 228 7.8627717392790e+00
57 11 3 9 1164 228 7.8627717392790e+00
58 9 11 3 1164 228 7.8627717392790e+00
59 11 9 3 1164 228 7.8627717392790e+00
60 4 6 8 1252 249 -2.4710010996030e+00
61 6 4 8 1252 249 -2.4710010996030e+00
62 4 8 6 1252 249 -2.4710010996030e+00
63 8 4 6 1252 249 -2.4710010996030e+00
64 6 8 4 1252 249 -2.4710010996030e+00
65 8 6 4 1252 249 -2.4710010996030e+00
66 4 10 11 1342 266 1.3129798440440e+01
67 10 4 11 1342 266 1.3129798440440e+01
68 4 11 10 1342 266 1.3129798440440e+01
69 11 4 10 1342 266 1.3129798440440e+01
70 10 11 4 1342 266 1.3129798440440e+01
71 11 10 4 1342 266 1.3129798440440e+01
72 6 8 11 1536 310 2.1529543232380e+01
73 8 6 11 1536 310 2.1529543232380e+01
74 6 11 8 1536 310 2.1529543232380e+01
75 11 6 8 1536 310 2.1529543232380e+01

76 8 11 6 1536 310 2.1529543232380e+01
77 11 8 6 1536 310 2.1529543232380e+01
78 6 9 10 1545 312 1.6208966509060e+01
79 9 6 10 1545 312 1.6208966509060e+01
80 6 10 9 1545 312 1.6208966509060e+01
81 10 6 9 1545 312 1.6208966509060e+01
82 9 10 6 1545 312 1.6208966509060e+01
83 10 9 6 1545 312 1.6208966509060e+01
84 7 9 10 1606 327 -4.3111921589700e+00
85 9 7 10 1606 327 -4.3111921589700e+00
86 7 10 9 1606 327 -4.3111921589700e+00
87 10 7 9 1606 327 -4.3111921589700e+00
88 9 10 7 1606 327 -4.3111921589700e+00
89 10 9 7 1606 327 -4.3111921589700e+00
90 8 10 10 1655 339 4.8405167830200e+01
91 10 8 10 1655 339 4.8405167830200e+01
92 10 10 8 1655 339 4.8405167830200e+01
93 8 10 11 1658 340 1.9019265187400e+00
94 10 8 11 1658 340 1.9019265187400e+00
95 8 11 10 1658 340 1.9019265187400e+00
96 11 8 10 1658 340 1.9019265187400e+00
97 10 11 8 1658 340 1.9019265187400e+00
98 11 10 8 1658 340 1.9019265187400e+00
99 9 11 11 1683 347 -9.5119578403250e+00
100 11 9 11 1683 347 -9.5119578403250e+00
101 11 11 9 1683 347 -9.5119578403250e+00

TRIPLETTYPE PARAMS:
  INDEX: 1 ATOMS: B B O
PAIRS: BB BO BO UNIQUE: -1 TOTAL: 355
  index | powers | equiv index | param index | parameter
  ---
0 0 1 2 1 1 7.0213091775860e+01
1 0 2 1 1 1 7.0213091775860e+01
2 0 1 3 3 2 3.3549744143860e+01
3 0 3 1 3 2 3.3549744143860e+01
4 0 1 9 15 8 3.5595320389740e+01
5 0 9 1 15 8 3.5595320389740e+01
6 0 2 3 22 12 -3.7571661818100e+01
7 0 3 2 22 12 -3.7571661818100e+01
8 0 2 6 28 15 7.5641787851110e+01
9 0 6 2 28 15 7.5641787851110e+01
10 0 2 7 30 16 3.2038727897550e+01
11 0 7 2 30 16 3.2038727897550e+01

12 0 2 9 34 18 -2.8986380703510e+01
13 0 9 2 34 18 -2.8986380703510e+01
14 0 2 11 38 20 -5.2641307638920e+00
15 0 11 2 38 20 -5.2641307638920e+00
16 0 3 5 43 23 -1.8133136572390e+01
17 0 5 3 43 23 -1.8133136572390e+01
18 0 3 7 47 25 -6.6038393514250e+00
19 0 7 3 47 25 -6.6038393514250e+00
20 0 3 8 49 26 1.6366178760340e+01
21 0 8 3 49 26 1.6366178760340e+01
22 0 3 10 53 28 1.1733082694700e+01
23 0 10 3 53 28 1.1733082694700e+01
24 0 4 10 68 36 -7.5482153930020e+00
25 0 10 4 68 36 -7.5482153930020e+00
26 0 4 11 70 37 1.7131694403630e+01
27 0 11 4 70 37 1.7131694403630e+01
28 0 5 11 83 44 -1.2921344315400e+01
29 0 11 5 83 44 -1.2921344315400e+01
30 0 6 8 88 47 -1.1382796827370e+01
31 0 8 6 88 47 -1.1382796827370e+01
32 0 6 11 94 50 2.9913901468110e+00
33 0 11 6 94 50 2.9913901468110e+00
34 0 7 8 97 52 6.6959940163430e+01
35 0 8 7 97 52 6.6959940163430e+01
36 0 8 10 108 58 -3.6939027179850e+00
37 0 10 8 108 58 -3.6939027179850e+00
38 0 9 10 113 61 4.2470499661450e+00
39 0 10 9 113 61 4.2470499661450e+00
40 0 9 11 115 62 -1.1026939918060e+01
41 0 11 9 115 62 -1.1026939918060e+01
42 0 10 11 118 64 -3.0104048638270e+00
43 0 11 10 118 64 -3.0104048638270e+00
44 0 11 11 120 65 -2.0692077487080e+00
45 1 8 10 251 135 1.9768674293510e+00
46 1 10 8 251 135 1.9768674293510e+00
47 1 8 11 253 136 -7.0072085095590e-01
48 1 11 8 253 136 -7.0072085095590e-01
49 2 0 3 268 145 8.7606962571110e+00
50 2 3 0 268 145 8.7606962571110e+00
51 2 0 6 274 148 2.1570329126160e+01
52 2 6 0 274 148 2.1570329126160e+01
53 2 0 7 276 149 -4.9979182319250e+01
54 2 7 0 276 149 -4.9979182319250e+01
55 2 0 10 282 152 5.1053399883950e+00

56 2 10 0 282 152 5.1053399883950e+00
57 2 3 5 329 177 1.4540388385310e+01
58 2 5 3 329 177 1.4540388385310e+01
59 2 3 7 333 179 3.7716580737820e+01
60 2 7 3 333 179 3.7716580737820e+01
61 2 3 8 335 180 -3.1983234533460e+01
62 2 8 3 335 180 -3.1983234533460e+01
63 2 3 11 341 183 9.8295920829270e+00
64 2 11 3 341 183 9.8295920829270e+00
65 2 4 9 352 189 1.9094623463450e+01
66 2 9 4 352 189 1.9094623463450e+01
67 2 7 9 385 207 -2.5554073303870e+01
68 2 9 7 385 207 -2.5554073303870e+01
69 2 8 8 391 210 3.1670658337700e+01
70 2 8 9 392 211 -2.1523339630210e+01
71 2 9 8 392 211 -2.1523339630210e+01
72 3 0 5 415 224 6.3062534411760e+00
73 3 5 0 415 224 6.3062534411760e+00
74 3 0 8 421 227 -1.7305358250410e+01
75 3 8 0 421 227 -1.7305358250410e+01
76 3 0 9 423 228 2.5421259880210e+00
77 3 9 0 423 228 2.5421259880210e+00
78 3 3 11 484 260 1.9973066942030e+00
79 3 11 3 484 260 1.9973066942030e+00
80 3 4 6 489 263 -1.8288227046580e+01
81 3 6 4 489 263 -1.8288227046580e+01
82 3 4 9 495 266 -2.4615748386260e+01
83 3 9 4 495 266 -2.4615748386260e+01
84 3 6 7 515 277 8.8477243645630e+00
85 3 7 6 515 277 8.8477243645630e+00
86 3 6 8 517 278 -5.6391866389370e+00
87 3 8 6 517 278 -5.6391866389370e+00
88 3 6 11 523 281 -5.9491190236130e+00
89 3 11 6 523 281 -5.9491190236130e+00
90 3 8 11 539 290 1.0846125772740e+00
91 3 11 8 539 290 1.0846125772740e+00
92 3 10 10 546 294 6.2656579893400e+00
93 3 10 11 547 295 -7.9963953284310e+00
94 3 11 10 547 295 -7.9963953284310e+00
95 4 4 6 632 340 1.5400994775820e+01
96 4 6 4 632 340 1.5400994775820e+01
97 4 4 10 640 344 -1.7524655358080e+01
98 4 10 4 640 344 -1.7524655358080e+01
99 4 6 6 657 353 -1.2485551551980e+00

100 4 6 9 662 356 -3.7113556034470e+00
101 4 9 6 662 356 -3.7113556034470e+00
102 4 7 11 675 363 2.2217965197640e+01
103 4 11 7 675 363 2.2217965197640e+01
104 4 8 8 677 364 -4.0093232763380e+01
105 4 8 11 682 367 -7.4365827443300e+00
106 4 11 8 682 367 -7.4365827443300e+00
107 4 11 11 692 373 -3.6091662528600e-01
108 5 0 7 705 380 -3.4398383906010e+01
109 5 7 0 705 380 -3.4398383906010e+01
110 5 0 9 709 382 -1.6447955553780e+01
111 5 9 0 709 382 -1.6447955553780e+01
112 5 1 3 718 387 -1.9414454122420e+01
113 5 3 1 718 387 -1.9414454122420e+01
114 5 2 6 743 400 -2.8500499975100e+01
115 5 6 2 743 400 -2.8500499975100e+01
116 5 3 8 764 411 -5.0129339255520e+00
117 5 8 3 764 411 -5.0129339255520e+00
118 5 4 6 775 417 1.0658205004860e+01
119 5 6 4 775 417 1.0658205004860e+01
120 5 4 11 785 422 -2.7439883369360e+00
121 5 11 4 785 422 -2.7439883369360e+00
122 5 6 10 807 434 -6.7346179507480e+00
123 5 10 6 807 434 -6.7346179507480e+00
124 5 6 11 809 435 1.5519842644810e+01
125 5 11 6 809 435 1.5519842644810e+01
126 5 8 10 823 443 3.4773251513420e-01
127 5 10 8 823 443 3.4773251513420e-01
128 5 10 10 832 448 -5.6738629116950e-01
129 6 0 6 846 456 -2.9207430900560e+00
130 6 6 0 846 456 -2.9207430900560e+00
131 6 0 8 850 458 5.9654398357280e+00
132 6 8 0 850 458 5.9654398357280e+00
133 6 0 9 852 459 4.1829530499920e+00
134 6 9 0 852 459 4.1829530499920e+00
135 6 1 2 859 463 1.4452159559830e+01
136 6 2 1 859 463 1.4452159559830e+01
137 6 2 2 879 473 -4.9612911791880e+01
138 6 2 8 890 479 -2.0117935878520e+01
139 6 8 2 890 479 -2.0117935878520e+01
140 6 3 5 901 485 -1.7306252738490e+00
141 6 5 3 901 485 -1.7306252738490e+00
142 6 3 7 905 487 8.6811655369260e+00
143 6 7 3 905 487 8.6811655369260e+00

144 6 4 8 922 496 1.0745598532690e+01
145 6 8 4 922 496 1.0745598532690e+01
146 6 4 9 924 497 -2.9416828156870e+01
147 6 9 4 924 497 -2.9416828156870e+01
148 6 5 6 931 501 -1.4311273087310e+00
149 6 6 5 931 501 -1.4311273087310e+00
150 6 6 8 946 509 -1.2710039690650e+01
151 6 8 6 946 509 -1.2710039690650e+01
152 6 6 11 952 512 2.3700578846240e+01
153 6 11 6 952 512 2.3700578846240e+01
154 6 7 8 955 514 -6.8259367546070e+00
155 6 8 7 955 514 -6.8259367546070e+00
156 6 7 11 961 517 -1.0224914461660e+01
157 6 11 7 961 517 -1.0224914461660e+01
158 6 8 11 968 521 2.0904335851250e+01
159 6 11 8 968 521 2.0904335851250e+01
160 6 9 10 971 523 -1.2576676549860e+01
161 6 10 9 971 523 -1.2576676549860e+01
162 6 10 10 975 525 1.2404815123920e+01
163 7 0 3 983 530 9.4787777019010e+00
164 7 3 0 983 530 9.4787777019010e+00
165 7 1 9 1016 547 -2.1895179305480e+01
166 7 9 1 1016 547 -2.1895179305480e+01
167 7 4 10 1069 575 -1.0080416356860e+01
168 7 10 4 1069 575 -1.0080416356860e+01
169 7 5 10 1082 582 -2.0750688134460e+01
170 7 10 5 1082 582 -2.0750688134460e+01
171 7 5 11 1084 583 3.8195051606630e+01
172 7 11 5 1084 583 3.8195051606630e+01
173 7 7 8 1098 591 1.9286723781140e+01
174 7 8 7 1098 591 1.9286723781140e+01
175 7 7 9 1100 592 -3.5475734915340e+00
176 7 9 7 1100 592 -3.5475734915340e+00
177 7 7 10 1102 593 1.3410055692160e+00
178 7 10 7 1102 593 1.3410055692160e+00
179 7 8 9 1107 596 -1.1470774040300e+00
180 7 9 8 1107 596 -1.1470774040300e+00
181 7 8 11 1111 598 -3.2769238036650e-01
182 7 11 8 1111 598 -3.2769238036650e-01
183 7 9 9 1113 599 4.6652213195030e+00
184 7 11 11 1121 604 1.3264703426960e+01
185 8 1 9 1159 624 6.4098728813070e+00
186 8 9 1 1159 624 6.4098728813070e+00
187 8 2 7 1174 632 3.2406353049840e+01

188 8 7 2 1174 632 3.2406353049840e+01
189 8 2 10 1180 635 -3.1482167354360e+00
190 8 10 2 1180 635 -3.1482167354360e+00
191 8 3 7 1191 641 -4.2182119973200e+00
192 8 7 3 1191 641 -4.2182119973200e+00
193 8 4 10 1212 652 4.2487268240940e+00
194 8 10 4 1212 652 4.2487268240940e+00
195 8 6 9 1234 664 1.6209846228450e+01
196 8 9 6 1234 664 1.6209846228450e+01
197 8 6 11 1238 666 -5.4490563761220e+00
198 8 11 6 1238 666 -5.4490563761220e+00
199 8 7 9 1243 669 2.8182292819960e+01
200 8 9 7 1243 669 2.8182292819960e+01
201 8 7 10 1245 670 -2.0794700357570e+01
202 8 10 7 1245 670 -2.0794700357570e+01
203 8 8 9 1250 673 5.2063156208000e+00
204 8 9 8 1250 673 5.2063156208000e+00
205 8 8 11 1254 675 -2.6532415042080e+00
206 8 11 8 1254 675 -2.6532415042080e+00
207 8 9 9 1256 676 -5.8583563189190e+00
208 8 10 11 1262 680 -3.5238964677620e-01
209 8 11 10 1262 680 -3.5238964677620e-01
210 9 0 2 1267 683 1.7102851846850e+01
211 9 2 0 1267 683 1.7102851846850e+01
212 9 0 4 1271 685 -1.9287370223630e+01
213 9 4 0 1271 685 -1.9287370223630e+01
214 9 0 7 1277 688 1.1307196857320e+00
215 9 7 0 1277 688 1.1307196857320e+00
216 9 0 11 1285 692 2.2484368217770e+01
217 9 11 0 1285 692 2.2484368217770e+01
218 9 1 7 1298 699 -1.0984204536270e+01
219 9 7 1 1298 699 -1.0984204536270e+01
220 9 2 10 1323 712 2.7929750279080e+01
221 9 10 2 1323 712 2.7929750279080e+01
222 9 2 11 1325 713 -6.1723732133530e-01
223 9 11 2 1325 713 -6.1723732133530e-01
224 9 3 5 1330 716 -5.6110908522100e+00
225 9 5 3 1330 716 -5.6110908522100e+00
226 9 3 11 1342 722 2.5913604994020e+00
227 9 11 3 1342 722 2.5913604994020e+00
228 9 4 6 1347 725 1.2651684962420e+01
229 9 6 4 1347 725 1.2651684962420e+01
230 9 4 9 1353 728 4.2214273306260e+00
231 9 9 4 1353 728 4.2214273306260e+00

232 9 4 10 1355 729 -1.1264450247370e+00
233 9 10 4 1355 729 -1.1264450247370e+00
234 9 6 7 1373 739 1.8089414304890e+01
235 9 7 6 1373 739 1.8089414304890e+01
236 9 6 8 1375 740 -3.7471934587380e+00
237 9 8 6 1375 740 -3.7471934587380e+00
238 9 6 10 1379 742 1.2273330882680e+01
239 9 10 6 1379 742 1.2273330882680e+01
240 9 7 9 1386 746 -5.1724125812340e+00
241 9 9 7 1386 746 -5.1724125812340e+00
242 9 7 10 1388 747 8.9822001181160e+00
243 9 10 7 1388 747 8.9822001181160e+00
244 9 7 11 1390 748 -2.3230343741770e+01
245 9 11 7 1390 748 -2.3230343741770e+01
246 9 8 10 1395 751 -2.9959038132210e+00
247 9 10 8 1395 751 -2.9959038132210e+00
248 9 10 11 1405 757 9.7283620754440e+00
249 9 11 10 1405 757 9.7283620754440e+00
250 9 11 11 1407 758 -1.1928686486040e+01
251 10 0 2 1410 760 -1.9036923366130e+01
252 10 2 0 1410 760 -1.9036923366130e+01
253 10 0 5 1416 763 1.6522650578690e+00
254 10 5 0 1416 763 1.6522650578690e+00
255 10 0 8 1422 766 -1.7649040166130e+01
256 10 8 0 1422 766 -1.7649040166130e+01
257 10 0 9 1424 767 -1.7623733308030e+01
258 10 9 0 1424 767 -1.7623733308030e+01
259 10 0 11 1428 769 -1.1358692820740e+01
260 10 11 0 1428 769 -1.1358692820740e+01
261 10 1 4 1435 773 2.2123359739310e+01
262 10 4 1 1435 773 2.2123359739310e+01
263 10 1 5 1437 774 -7.8150745252300e-01
264 10 5 1 1437 774 -7.8150745252300e-01
265 10 1 9 1445 778 6.2502580295040e+00
266 10 9 1 1445 778 6.2502580295040e+00
267 10 2 11 1468 790 3.5282045332760e+00
268 10 11 2 1468 790 3.5282045332760e+00
269 10 3 6 1475 794 -1.3505580469970e+00
270 10 6 3 1475 794 -1.3505580469970e+00
271 10 3 7 1477 795 8.3613373442610e+00
272 10 7 3 1477 795 8.3613373442610e+00
273 10 3 9 1481 797 -1.2972163139920e+01
274 10 9 3 1481 797 -1.2972163139920e+01
275 10 4 6 1490 802 1.0588584936010e+01

276 10 6 4 1490 802 1.0588584936010e+01
277 10 4 9 1496 805 1.5968668023340e+00
278 10 9 4 1496 805 1.5968668023340e+00
279 10 4 10 1498 806 6.4005190508420e+00
280 10 10 4 1498 806 6.4005190508420e+00
281 10 4 11 1500 807 1.1093963456450e+01
282 10 11 4 1500 807 1.1093963456450e+01
283 10 5 6 1503 809 2.3788567057470e+00
284 10 6 5 1503 809 2.3788567057470e+00
285 10 5 7 1505 810 -1.1229084528080e+01
286 10 7 5 1505 810 -1.1229084528080e+01
287 10 5 11 1513 814 1.1998310137860e+01
288 10 11 5 1513 814 1.1998310137860e+01
289 10 7 10 1531 824 -2.4293309109930e+00
290 10 10 7 1531 824 -2.4293309109930e+00
291 10 7 11 1533 825 1.2180178531000e+01
292 10 11 7 1533 825 1.2180178531000e+01
293 10 8 10 1538 828 1.9321145935790e+01
294 10 10 8 1538 828 1.9321145935790e+01
295 10 9 9 1542 830 -1.1643147815260e+01
296 10 9 10 1543 831 9.1105166542210e+00
297 10 10 9 1543 831 9.1105166542210e+00
298 10 10 10 1547 833 9.3691899305680e+00
299 10 10 11 1548 834 1.2868059796190e+01
300 10 11 10 1548 834 1.2868059796190e+01
301 11 0 1 1551 836 -1.9186051606000e+01
302 11 1 0 1551 836 -1.9186051606000e+01
303 11 0 6 1561 841 2.3108960939260e+01
304 11 6 0 1561 841 2.3108960939260e+01
305 11 1 2 1574 848 2.9631984193910e+01
306 11 2 1 1574 848 2.9631984193910e+01
307 11 1 6 1582 852 -1.9050765600190e+01
308 11 6 1 1582 852 -1.9050765600190e+01
309 11 1 10 1590 856 -1.1631192211260e+01
310 11 10 1 1590 856 -1.1631192211260e+01
311 11 1 11 1592 857 3.7975023740800e+00
312 11 11 1 1592 857 3.7975023740800e+00
313 11 2 8 1605 864 -1.2758482467520e+01
314 11 8 2 1605 864 -1.2758482467520e+01
315 11 3 4 1614 869 -5.7512815794590e+00
316 11 4 3 1614 869 -5.7512815794590e+00
317 11 3 8 1622 873 1.9000559222360e+01
318 11 8 3 1622 873 1.9000559222360e+01
319 11 3 9 1624 874 -1.9642036337200e+00

320 11 9 3 1624 874 -1.9642036337200e+00
321 11 3 10 1626 875 1.3846635913250e+00
322 11 10 3 1626 875 1.3846635913250e+00
323 11 3 11 1628 876 -2.3148537473480e+00
324 11 11 3 1628 876 -2.3148537473480e+00
325 11 4 7 1635 880 -7.1667088047680e+00
326 11 7 4 1635 880 -7.1667088047680e+00
327 11 4 9 1639 882 5.2068575313890e+00
328 11 9 4 1639 882 5.2068575313890e+00
329 11 5 5 1645 885 -1.6831345225610e+01
330 11 5 7 1648 887 1.1790358771130e+01
331 11 7 5 1648 887 1.1790358771130e+01
332 11 5 8 1650 888 1.5634673538860e+00
333 11 8 5 1650 888 1.5634673538860e+00
334 11 5 9 1652 889 -3.8378397535380e+00
335 11 9 5 1652 889 -3.8378397535380e+00
336 11 5 11 1656 891 -3.4709060087040e-01
337 11 11 5 1656 891 -3.4709060087040e-01
338 11 6 8 1661 894 7.3754860064040e-01
339 11 8 6 1661 894 7.3754860064040e-01
340 11 7 8 1670 899 -3.3788588413250e+00
341 11 8 7 1670 899 -3.3788588413250e+00
342 11 7 9 1672 900 5.4585770374720e+00
343 11 9 7 1672 900 5.4585770374720e+00
344 11 7 10 1674 901 -1.4514013433100e+01
345 11 10 7 1674 901 -1.4514013433100e+01
346 11 8 9 1679 904 -1.3713312842470e+01
347 11 9 8 1679 904 -1.3713312842470e+01
348 11 9 9 1685 907 7.2140671929790e+00
349 11 9 10 1686 908 -2.0676187500840e+01
350 11 10 9 1686 908 -2.0676187500840e+01
351 11 9 11 1688 909 1.1425581883140e+01
352 11 11 9 1688 909 1.1425581883140e+01
353 11 10 11 1691 911 2.2333533087950e+00
354 11 11 10 1691 911 2.2333533087950e+00

TRIPLETTYPE PARAMS:
  INDEX: 2 ATOMS: B B Mg
PAIRS: BB BMg BMg UNIQUE: -1 TOTAL: 0
   index | powers | equiv index | param index | parameter

TRIPLETTYPE PARAMS:
  INDEX: 3 ATOMS: B O O

PAIRS: BO BO OO UNIQUE: -1 TOTAL: 443

index	powers	equiv index	param index	parameter
0	0 1 10 18	9	4.0069549080000e-01	
1	1 0 10 18	9	4.0069549080000e-01	
2	0 2 7 34	17	-9.5687569984110e+00	
3	2 0 7 34	17	-9.5687569984110e+00	
4	0 2 10 40	20	-8.0130141068740e+00	
5	2 0 10 40	20	-8.0130141068740e+00	
6	0 3 6 54	27	5.4154190738130e+01	
7	3 0 6 54	27	5.4154190738130e+01	
8	0 3 9 60	30	1.3042084083050e+01	
9	3 0 9 60	30	1.3042084083050e+01	
10	0 3 10 62	31	2.4755071018160e+00	
11	3 0 10 62	31	2.4755071018160e+00	
12	0 4 2 68	34	3.1056467597590e+01	
13	4 0 2 68	34	3.1056467597590e+01	
14	0 4 5 74	37	-1.5902280073210e+01	
15	4 0 5 74	37	-1.5902280073210e+01	
16	0 5 2 90	45	-1.2625468987210e+01	
17	5 0 2 90	45	-1.2625468987210e+01	
18	0 5 3 92	46	-2.0323016495320e+01	
19	5 0 3 92	46	-2.0323016495320e+01	
20	0 5 6 98	49	6.4840882093830e+00	
21	5 0 6 98	49	6.4840882093830e+00	
22	0 5 9 104	52	-1.2589798338960e+01	
23	5 0 9 104	52	-1.2589798338960e+01	
24	0 6 3 114	57	2.2978904619690e+01	
25	6 0 3 114	57	2.2978904619690e+01	
26	0 6 6 120	60	-3.0772759863020e+00	
27	6 0 6 120	60	-3.0772759863020e+00	
28	0 6 9 126	63	-1.7456473915810e+00	
29	6 0 9 126	63	-1.7456473915810e+00	
30	0 6 11 130	65	8.6303967710760e+00	
31	6 0 11 130	65	8.6303967710760e+00	
32	0 7 2 134	67	-1.2658397572200e+01	
33	7 0 2 134	67	-1.2658397572200e+01	
34	0 7 3 136	68	-1.3335958261920e+01	
35	7 0 3 136	68	-1.3335958261920e+01	
36	0 7 5 140	70	5.3189468334890e+01	
37	7 0 5 140	70	5.3189468334890e+01	
38	0 7 11 152	76	5.1282937507850e+00	
39	7 0 11 152	76	5.1282937507850e+00	
40	0 8 3 158	79	3.4682727744390e+01	

41 8 0 3 158 79 3.4682727744390e+01
42 0 8 6 164 82 8.7581611519020e+00
43 8 0 6 164 82 8.7581611519020e+00
44 0 8 10 172 86 -8.7735218923140e-01
45 8 0 10 172 86 -8.7735218923140e-01
46 0 8 11 174 87 -3.5947945513710e+00
47 8 0 11 174 87 -3.5947945513710e+00
48 0 9 4 182 91 2.6183869146030e+01
49 9 0 4 182 91 2.6183869146030e+01
50 0 9 7 188 94 7.5614658663790e+00
51 9 0 7 188 94 7.5614658663790e+00
52 0 9 9 192 96 1.1479570736220e+01
53 9 0 9 192 96 1.1479570736220e+01
54 0 10 2 200 100 8.5163650024970e+00
55 10 0 2 200 100 8.5163650024970e+00
56 0 10 5 206 103 -7.4331414867060e+00
57 10 0 5 206 103 -7.4331414867060e+00
58 0 10 9 214 107 -4.0144990766200e+00
59 10 0 9 214 107 -4.0144990766200e+00
60 0 10 11 218 109 -6.0808211825930e+00
61 10 0 11 218 109 -6.0808211825930e+00
62 0 11 2 222 111 -1.5274748312740e+01
63 11 0 2 222 111 -1.5274748312740e+01
64 0 11 6 230 115 -1.1845937526460e+01
65 11 0 6 230 115 -1.1845937526460e+01
66 0 11 10 238 119 1.7234439827510e+00
67 11 0 10 238 119 1.7234439827510e+00
68 0 11 11 240 120 6.4282564057460e-01
69 11 0 11 240 120 6.4282564057460e-01
70 1 2 6 266 139 -5.3977759012990e+01
71 2 1 6 266 139 -5.3977759012990e+01
72 1 2 10 274 143 -1.9351079779430e+00
73 2 1 10 274 143 -1.9351079779430e+00
74 1 3 5 288 150 5.4295949456330e+01
75 3 1 5 288 150 5.4295949456330e+01
76 1 3 10 298 155 -7.0739334219140e+00
77 3 1 10 298 155 -7.0739334219140e+00
78 1 4 11 324 168 1.5782715036600e+01
79 4 1 11 324 168 1.5782715036600e+01
80 1 6 0 350 181 -4.4390933040740e+01
81 6 1 0 350 181 -4.4390933040740e+01
82 1 6 5 360 186 -1.1405742836690e+01
83 6 1 5 360 186 -1.1405742836690e+01
84 1 6 6 362 187 3.8700191569710e-01

85 6 1 6 362 187 3.8700191569710e-01
86 1 6 9 368 190 1.2693464876070e+01
87 6 1 9 368 190 1.2693464876070e+01
88 1 6 10 370 191 -1.3305526990670e+00
89 6 1 10 370 191 -1.3305526990670e+00
90 1 7 4 382 197 1.5076135280990e+01
91 7 1 4 382 197 1.5076135280990e+01
92 1 7 5 384 198 -4.8100482372920e+00
93 7 1 5 384 198 -4.8100482372920e+00
94 1 7 11 396 204 -3.8480222178600e+00
95 7 1 11 396 204 -3.8480222178600e+00
96 1 8 8 414 213 3.1101041242890e+01
97 8 1 8 414 213 3.1101041242890e+01
98 1 8 10 418 215 -1.8948955904470e+01
99 8 1 10 418 215 -1.8948955904470e+01
100 1 9 4 430 221 -1.5737449836270e+01
101 9 1 4 430 221 -1.5737449836270e+01
102 1 9 8 438 225 1.7772506388530e+01
103 9 1 8 438 225 1.7772506388530e+01
104 1 9 11 444 228 1.8970521709210e+00
105 9 1 11 444 228 1.8970521709210e+00
106 1 10 2 450 231 -8.7901008967280e+00
107 10 1 2 450 231 -8.7901008967280e+00
108 1 11 0 470 241 -7.5747388208050e+00
109 11 1 0 470 241 -7.5747388208050e+00
110 1 11 2 474 243 1.4772672397710e+01
111 11 1 2 474 243 1.4772672397710e+01
112 1 11 5 480 246 1.3163451045900e+01
113 11 1 5 480 246 1.3163451045900e+01
114 1 11 10 490 251 -3.9310863915780e+00
115 11 1 10 490 251 -3.9310863915780e+00
116 2 3 8 522 273 -8.4786244991390e+00
117 3 2 8 522 273 -8.4786244991390e+00
118 2 4 10 550 287 -7.3601908804690e+00
119 4 2 10 550 287 -7.3601908804690e+00
120 2 4 11 552 288 -7.9070522806460e+00
121 4 2 11 552 288 -7.9070522806460e+00
122 2 5 10 574 299 -1.6927047248030e+01
123 5 2 10 574 299 -1.6927047248030e+01
124 2 6 2 582 303 -1.1231673614860e+01
125 6 2 2 582 303 -1.1231673614860e+01
126 2 6 3 584 304 -1.9398285793980e+01
127 6 2 3 584 304 -1.9398285793980e+01
128 2 7 0 602 313 3.2151405191980e+01

129 7 2 0 602 313 3.2151405191980e+01
130 2 7 1 604 314 -2.8943789498320e+01
131 7 2 1 604 314 -2.8943789498320e+01
132 2 7 5 612 318 7.6341858881250e+01
133 7 2 5 612 318 7.6341858881250e+01
134 2 7 6 614 319 -4.5343520308650e+00
135 7 2 6 614 319 -4.5343520308650e+00
136 2 7 8 618 321 2.0591882270680e+01
137 7 2 8 618 321 2.0591882270680e+01
138 2 8 5 636 330 -6.8306839049220e+00
139 8 2 5 636 330 -6.8306839049220e+00
140 2 8 8 642 333 -4.8093782106470e-01
141 8 2 8 642 333 -4.8093782106470e-01
142 2 8 9 644 334 1.1585815456570e+01
143 8 2 9 644 334 1.1585815456570e+01
144 2 8 10 646 335 1.0794139284340e-02
145 8 2 10 646 335 1.0794139284340e-02
146 2 8 11 648 336 7.6615403564180e+00
147 8 2 11 648 336 7.6615403564180e+00
148 2 9 0 650 337 -1.6068141658810e+01
149 9 2 0 650 337 -1.6068141658810e+01
150 2 10 4 682 353 -1.4427361793170e+01
151 10 2 4 682 353 -1.4427361793170e+01
152 2 10 8 690 357 -5.4419668407460e-01
153 10 2 8 690 357 -5.4419668407460e-01
154 2 10 9 692 358 6.2452849950510e+00
155 10 2 9 692 358 6.2452849950510e+00
156 2 10 11 696 360 7.5023331715110e+00
157 10 2 11 696 360 7.5023331715110e+00
158 2 11 5 708 366 -8.4198082217090e+00
159 11 2 5 708 366 -8.4198082217090e+00
160 2 11 8 714 369 9.6889931229790e-01
161 11 2 8 714 369 9.6889931229790e-01
162 2 11 9 716 370 -1.2150698664100e+01
163 11 2 9 716 370 -1.2150698664100e+01
164 3 3 11 733 384 -7.8247082187450e+00
165 3 4 0 734 385 1.0766696372100e+01
166 4 3 0 734 385 1.0766696372100e+01
167 3 4 4 742 389 -3.2726821647740e+01
168 4 3 4 742 389 -3.2726821647740e+01
169 3 4 5 744 390 3.0267523952310e+01
170 4 3 5 744 390 3.0267523952310e+01
171 3 4 9 752 394 -8.8259719355280e+00
172 4 3 9 752 394 -8.8259719355280e+00

173 3 5 0 758 397 -1.0471284941030e+01
174 5 3 0 758 397 -1.0471284941030e+01
175 3 5 3 764 400 4.4880237647640e+00
176 5 3 3 764 400 4.4880237647640e+00
177 3 5 10 778 407 1.0285803968710e+01
178 5 3 10 778 407 1.0285803968710e+01
179 3 6 4 790 413 1.8745546573470e+01
180 6 3 4 790 413 1.8745546573470e+01
181 3 6 8 798 417 -1.3069803801830e+01
182 6 3 8 798 417 -1.3069803801830e+01
183 3 7 0 806 421 -5.5767262997200e+00
184 7 3 0 806 421 -5.5767262997200e+00
185 3 7 2 810 423 1.2252814011850e+01
186 7 3 2 810 423 1.2252814011850e+01
187 3 7 8 822 429 -5.8991961227990e+00
188 7 3 8 822 429 -5.8991961227990e+00
189 3 7 10 826 431 -1.1193420163790e+00
190 7 3 10 826 431 -1.1193420163790e+00
191 3 8 8 846 441 1.2349430561960e+01
192 8 3 8 846 441 1.2349430561960e+01
193 3 9 5 864 450 2.4320323910530e+01
194 9 3 5 864 450 2.4320323910530e+01
195 3 10 3 884 460 4.8923279503370e+00
196 10 3 3 884 460 4.8923279503370e+00
197 3 10 7 892 464 1.1925060159550e+00
198 10 3 7 892 464 1.1925060159550e+00
199 3 10 8 894 465 1.1177608786550e+01
200 10 3 8 894 465 1.1177608786550e+01
201 3 10 9 896 466 3.1198196738890e+00
202 10 3 9 896 466 3.1198196738890e+00
203 3 10 11 900 468 -6.6350742525910e+00
204 10 3 11 900 468 -6.6350742525910e+00
205 3 11 2 906 471 -5.8067893214210e+00
206 11 3 2 906 471 -5.8067893214210e+00
207 3 11 6 914 475 2.8199734735810e+01
208 11 3 6 914 475 2.8199734735810e+01
209 3 11 7 916 476 -2.2082792676500e+01
210 11 3 7 916 476 -2.2082792676500e+01
211 3 11 8 918 477 1.1488787490930e+01
212 11 3 8 918 477 1.1488787490930e+01
213 3 11 10 922 479 5.0933173251330e+00
214 11 3 10 922 479 5.0933173251330e+00
215 4 4 4 930 485 2.1939414097440e+01
216 4 5 4 946 497 -2.9514590898190e+01

217 5 4 4 946 497 -2.9514590898190e+01
218 4 5 7 952 500 8.8385157511200e-01
219 5 4 7 952 500 8.8385157511200e-01
220 4 5 8 954 501 1.5355063277240e+01
221 5 4 8 954 501 1.5355063277240e+01
222 4 6 3 968 508 2.0796489204960e+01
223 6 4 3 968 508 2.0796489204960e+01
224 4 6 10 982 515 -2.6816790378800e+01
225 6 4 10 982 515 -2.6816790378800e+01
226 4 6 11 984 516 8.6683459365840e-01
227 6 4 11 984 516 8.6683459365840e-01
228 4 7 5 996 522 2.0088264121650e+01
229 7 4 5 996 522 2.0088264121650e+01
230 4 7 7 1000 524 -1.3884461491480e+01
231 7 4 7 1000 524 -1.3884461491480e+01
232 4 7 10 1006 527 1.0039926397390e+01
233 7 4 10 1006 527 1.0039926397390e+01
234 4 8 2 1014 531 1.2797355874720e-01
235 8 4 2 1014 531 1.2797355874720e-01
236 4 8 6 1022 535 8.5729824486190e+00
237 8 4 6 1022 535 8.5729824486190e+00
238 4 8 9 1028 538 2.2190111079040e+00
239 8 4 9 1028 538 2.2190111079040e+00
240 4 9 0 1034 541 -4.5023132694730e+01
241 9 4 0 1034 541 -4.5023132694730e+01
242 4 9 5 1044 546 -1.9462290659300e+01
243 9 4 5 1044 546 -1.9462290659300e+01
244 4 9 10 1054 551 -4.1710509615200e+00
245 9 4 10 1054 551 -4.1710509615200e+00
246 4 9 11 1056 552 -1.0390348200910e+01
247 9 4 11 1056 552 -1.0390348200910e+01
248 4 10 0 1058 553 6.4760549950160e+00
249 10 4 0 1058 553 6.4760549950160e+00
250 4 10 1 1060 554 3.4948195347880e+00
251 10 4 1 1060 554 3.4948195347880e+00
252 4 10 2 1062 555 -6.0673107653680e-02
253 10 4 2 1062 555 -6.0673107653680e-02
254 4 10 6 1070 559 -3.7218699344920e-02
255 10 4 6 1070 559 -3.7218699344920e-02
256 4 11 0 1082 565 -3.0914332586470e+00
257 11 4 0 1082 565 -3.0914332586470e+00
258 4 11 6 1094 571 -1.1399510120890e+00
259 11 4 6 1094 571 -1.1399510120890e+00
260 5 5 6 1112 583 1.9689891744500e+00

261 5 7 5 1152 606 -2.7828485520070e+01
262 7 5 5 1152 606 -2.7828485520070e+01
263 5 7 11 1164 612 -2.6586616133830e+00
264 7 5 11 1164 612 -2.6586616133830e+00
265 5 8 9 1184 622 -8.4910322024930e+00
266 8 5 9 1184 622 -8.4910322024930e+00
267 5 8 11 1188 624 5.2962320980210e+00
268 8 5 11 1188 624 5.2962320980210e+00
269 5 9 5 1200 630 4.2443655824280e+01
270 9 5 5 1200 630 4.2443655824280e+01
271 5 9 6 1202 631 -5.4612775897340e+00
272 9 5 6 1202 631 -5.4612775897340e+00
273 5 9 9 1208 634 -2.0982944503840e+01
274 9 5 9 1208 634 -2.0982944503840e+01
275 5 9 11 1212 636 3.3326489136710e+00
276 9 5 11 1212 636 3.3326489136710e+00
277 5 10 2 1218 639 1.0352342042530e+01
278 10 5 2 1218 639 1.0352342042530e+01
279 5 10 7 1228 644 -1.9334979974570e+00
280 10 5 7 1228 644 -1.9334979974570e+00
281 5 10 9 1232 646 1.1944311355530e+01
282 10 5 9 1232 646 1.1944311355530e+01
283 5 10 10 1234 647 2.6025967625960e+00
284 10 5 10 1234 647 2.6025967625960e+00
285 5 10 11 1236 648 1.3095178209270e+01
286 10 5 11 1236 648 1.3095178209270e+01
287 5 11 3 1244 652 -8.0187501475870e+00
288 11 5 3 1244 652 -8.0187501475870e+00
289 5 11 7 1252 656 1.9413403437380e+01
290 11 5 7 1252 656 1.9413403437380e+01
291 5 11 8 1254 657 -1.4889980857160e+01
292 11 5 8 1254 657 -1.4889980857160e+01
293 5 11 11 1260 660 -3.7797382307280e+00
294 11 5 11 1260 660 -3.7797382307280e+00
295 6 7 4 1282 677 2.2106485457240e-01
296 7 6 4 1282 677 2.2106485457240e-01
297 6 7 11 1296 684 -3.8435936870160e+00
298 7 6 11 1296 684 -3.8435936870160e+00
299 6 8 0 1298 685 -4.2447445079690e+00
300 8 6 0 1298 685 -4.2447445079690e+00
301 6 9 3 1328 700 2.4274079541950e+00
302 9 6 3 1328 700 2.4274079541950e+00
303 6 9 4 1330 701 -2.0412193354620e+01
304 9 6 4 1330 701 -2.0412193354620e+01

305 6 9 5 1332 702 -1.0818570332420e+01
306 9 6 5 1332 702 -1.0818570332420e+01
307 6 9 9 1340 706 8.4748752745120e+00
308 9 6 9 1340 706 8.4748752745120e+00
309 6 9 10 1342 707 1.8842079505120e+01
310 9 6 10 1342 707 1.8842079505120e+01
311 6 9 11 1344 708 -3.2506696511840e-01
312 9 6 11 1344 708 -3.2506696511840e-01
313 6 10 4 1354 713 7.1518209738990e+00
314 10 6 4 1354 713 7.1518209738990e+00
315 6 10 9 1364 718 -1.3206347040740e+01
316 10 6 9 1364 718 -1.3206347040740e+01
317 6 10 10 1366 719 -7.1872014874070e+00
318 10 6 10 1366 719 -7.1872014874070e+00
319 6 10 11 1368 720 -1.4074574195420e+01
320 10 6 11 1368 720 -1.4074574195420e+01
321 6 11 0 1370 721 1.2991887940090e+01
322 11 6 0 1370 721 1.2991887940090e+01
323 6 11 7 1384 728 5.6601760060130e+00
324 11 6 7 1384 728 5.6601760060130e+00
325 6 11 8 1386 729 -3.2690248042510e+00
326 11 6 8 1386 729 -3.2690248042510e+00
327 6 11 9 1388 730 -7.9519253131060e+00
328 11 6 9 1388 730 -7.9519253131060e+00
329 7 8 5 1416 750 -1.2843976881900e+01
330 8 7 5 1416 750 -1.2843976881900e+01
331 7 8 8 1422 753 -3.6851614254480e+01
332 8 7 8 1422 753 -3.6851614254480e+01
333 7 8 9 1424 754 1.9403788744480e+01
334 8 7 9 1424 754 1.9403788744480e+01
335 7 8 10 1426 755 -1.7525358778770e+01
336 8 7 10 1426 755 -1.7525358778770e+01
337 7 8 11 1428 756 -1.4754911535540e-01
338 8 7 11 1428 756 -1.4754911535540e-01
339 7 9 2 1434 759 -4.5734705706360e+00
340 9 7 2 1434 759 -4.5734705706360e+00
341 7 9 3 1436 760 -1.1659437447320e+01
342 9 7 3 1436 760 -1.1659437447320e+01
343 7 9 4 1438 761 8.1815818245510e+00
344 9 7 4 1438 761 8.1815818245510e+00
345 7 9 9 1448 766 4.8896007569500e+00
346 9 7 9 1448 766 4.8896007569500e+00
347 7 9 10 1450 767 -7.2692398831620e+00
348 9 7 10 1450 767 -7.2692398831620e+00

349 7 10 0 1454 769 3.9994842763890e+00
350 10 7 0 1454 769 3.9994842763890e+00
351 7 10 3 1460 772 6.0327767991500e+00
352 10 7 3 1460 772 6.0327767991500e+00
353 7 10 5 1464 774 1.0180568909780e+01
354 10 7 5 1464 774 1.0180568909780e+01
355 7 10 9 1472 778 -3.9850557266960e-01
356 10 7 9 1472 778 -3.9850557266960e-01
357 7 10 10 1474 779 6.5973174779190e+00
358 10 7 10 1474 779 6.5973174779190e+00
359 7 11 0 1478 781 9.9746087682230e+00
360 11 7 0 1478 781 9.9746087682230e+00
361 7 11 3 1484 784 3.6257226954680e+00
362 11 7 3 1484 784 3.6257226954680e+00
363 7 11 6 1490 787 -9.3086062647530e+00
364 11 7 6 1490 787 -9.3086062647530e+00
365 7 11 10 1498 791 2.5994442669700e+00
366 11 7 10 1498 791 2.5994442669700e+00
367 7 11 11 1500 792 -2.2770183990170e+00
368 11 7 11 1500 792 -2.2770183990170e+00
369 8 8 0 1502 793 4.9573180548310e+00
370 8 8 9 1511 802 -5.6681250310090e+00
371 8 9 2 1518 807 1.2302810292860e+01
372 9 8 2 1518 807 1.2302810292860e+01
373 8 9 11 1536 816 5.4578286600750e+00
374 9 8 11 1536 816 5.4578286600750e+00
375 8 10 0 1538 817 -1.4012029353450e+00
376 10 8 0 1538 817 -1.4012029353450e+00
377 8 10 7 1552 824 3.6460890937160e+00
378 10 8 7 1552 824 3.6460890937160e+00
379 8 10 8 1554 825 -7.1028604224860e+00
380 10 8 8 1554 825 -7.1028604224860e+00
381 8 11 4 1570 833 -3.8535802569500e+00
382 11 8 4 1570 833 -3.8535802569500e+00
383 8 11 5 1572 834 4.5709634359760e+00
384 11 8 5 1572 834 4.5709634359760e+00
385 8 11 8 1578 837 2.1110057818980e+01
386 11 8 8 1578 837 2.1110057818980e+01
387 8 11 9 1580 838 -1.7579049724590e+01
388 11 8 9 1580 838 -1.7579049724590e+01
389 8 11 10 1582 839 6.1815578653210e+00
390 11 8 10 1582 839 6.1815578653210e+00
391 9 9 7 1593 848 -2.1559103283390e+01
392 9 9 9 1595 850 -4.9262141746970e+00

393 9 9 10 1596 851 8.4820133814200e+00
394 9 9 11 1597 852 8.6519602808130e+00
395 9 10 0 1598 853 2.8513397983840e-01
396 10 9 0 1598 853 2.8513397983840e-01
397 9 10 3 1604 856 -2.2089561158760e+01
398 10 9 3 1604 856 -2.2089561158760e+01
399 9 10 6 1610 859 -1.4471139813410e+01
400 10 9 6 1610 859 -1.4471139813410e+01
401 9 10 9 1616 862 -2.9389591677630e+00
402 10 9 9 1616 862 -2.9389591677630e+00
403 9 11 0 1622 865 -6.5869660340380e+00
404 11 9 0 1622 865 -6.5869660340380e+00
405 9 11 4 1630 869 1.2819282970770e+01
406 11 9 4 1630 869 1.2819282970770e+01
407 9 11 5 1632 870 -1.4595376771130e+01
408 11 9 5 1632 870 -1.4595376771130e+01
409 9 11 8 1638 873 -1.1445560322700e+01
410 11 9 8 1638 873 -1.1445560322700e+01
411 9 11 10 1642 875 -8.8938674668370e+00
412 11 9 10 1642 875 -8.8938674668370e+00
413 9 11 11 1644 876 4.0549920328910e+00
414 11 9 11 1644 876 4.0549920328910e+00
415 10 10 4 1650 881 -1.7664473583950e+00
416 10 10 7 1653 884 3.0215821573340e+01
417 10 10 8 1654 885 -8.4372588640750e+00
418 10 10 9 1655 886 1.9288014361210e+01
419 10 10 10 1656 887 3.2724960796730e-01
420 10 10 11 1657 888 6.4504524529220e-01
421 10 11 1 1660 890 1.6152298516860e+01
422 11 10 1 1660 890 1.6152298516860e+01
423 10 11 2 1662 891 -3.1779333689100e+00
424 11 10 2 1662 891 -3.1779333689100e+00
425 10 11 4 1666 893 1.3651606664950e+01
426 11 10 4 1666 893 1.3651606664950e+01
427 10 11 5 1668 894 -2.3881506260100e+00
428 11 10 5 1668 894 -2.3881506260100e+00
429 10 11 6 1670 895 1.2760800188180e+00
430 11 10 6 1670 895 1.2760800188180e+00
431 10 11 7 1672 896 -4.5472237164220e+00
432 11 10 7 1672 896 -4.5472237164220e+00
433 10 11 10 1678 899 -3.3357022498960e-01
434 11 10 10 1678 899 -3.3357022498960e-01
435 10 11 11 1680 900 4.7061381305990e+00
436 11 10 11 1680 900 4.7061381305990e+00

437 11 11 0 1682 901 -5.8064793217300e+00
438 11 11 2 1684 903 4.1606096262220e+00
439 11 11 3 1685 904 1.0970647228240e+01
440 11 11 8 1690 909 7.7039888578920e+00
441 11 11 9 1691 910 -5.8452918628560e+00
442 11 11 10 1692 911 -1.9107904033570e+00

TRIPLETTYPE PARAMS:
  INDEX: 4 ATOMS: B Mg O
PAIRS: BMg BO OMg UNIQUE: -1 TOTAL: 174
   index | powers | equiv index | param index | parameter
  ----
0 0 3 9 30 30 -5.3640600091190e+00
1 0 4 6 38 38 -5.7311128185450e+00
2 0 4 8 40 40 4.9576941241080e+00
3 0 4 10 42 42 -5.2130608413920e+00
4 0 5 10 53 53 4.3055284631260e-01
5 0 6 8 62 62 -4.3958801738810e+00
6 0 7 2 67 67 -4.5738831715700e+01
7 0 7 3 68 68 -1.3554377413560e+01
8 0 7 4 69 69 5.9456655161280e+00
9 0 7 9 74 74 7.5805003773850e+00
10 0 7 10 75 75 -3.9342746027220e+00
11 0 7 11 76 76 -3.4652647544980e+00
12 0 8 4 80 80 -1.2808024880560e+01
13 0 8 6 82 82 8.9979754421350e+00
14 0 8 9 85 85 -1.1676165364030e+01
15 0 10 3 101 101 -1.1864473679060e+01
16 0 10 6 104 104 -1.0825227206210e+01
17 0 11 11 120 120 2.5652055935090e+00
18 1 0 10 130 130 1.4258569431640e+01
19 1 7 0 204 204 -6.9100173476950e+01
20 1 10 8 248 248 -7.9509634858490e+00
21 2 0 4 267 267 1.7560566662360e+00
22 2 4 5 316 316 -1.8017220517060e+02
23 2 6 0 335 335 3.7468460903020e+01
24 2 6 9 344 344 -4.7566302865770e+00
25 2 7 4 351 351 -2.6510712215460e+01
26 2 9 1 372 372 1.7940908066660e+00
27 2 10 10 393 393 5.6321444299630e+00
28 3 0 8 414 414 -1.4337609712090e+00
29 3 4 4 458 458 5.7230518606730e+01
30 3 4 6 460 460 -7.4300224381200e+00
31 3 4 11 465 465 -1.7196557390160e+01

32 3 7 2 492 492 -1.1773423301400e+00
33 3 8 1 503 503 1.1693459929820e+01
34 3 8 10 512 512 2.0015239193490e-01
35 3 9 6 520 520 -1.8742641499790e+01
36 3 10 1 527 527 -1.6891744111810e+01
37 3 11 3 541 541 5.4201864061030e+00
38 4 0 7 556 556 -3.2972540480110e+01
39 4 0 8 557 557 2.9057124544170e+01
40 4 0 11 560 560 1.7227695765900e+00
41 4 5 11 620 620 3.0824878193640e+01
42 4 6 9 630 630 4.7091099219850e+01
43 4 6 10 631 631 -1.8627288026440e+00
44 4 7 0 633 633 -3.5152188686570e+01
45 4 7 7 640 640 3.6327180101170e+01
46 4 8 0 645 645 2.2195307526250e+01
47 4 9 1 658 658 -2.4289824393240e+01
48 4 9 9 666 666 -1.6383315232480e+01
49 4 9 10 667 667 2.4552197572440e+00
50 4 10 6 675 675 -3.4976334582020e+00
51 4 11 4 685 685 1.1541179972750e+01
52 4 11 5 686 686 -1.9152008560570e+00
53 4 11 6 687 687 -6.5014249574700e+00
54 4 11 9 690 690 7.1526315584470e-01
55 4 11 10 691 691 -1.3573123538990e+01
56 5 0 8 700 700 1.2117099824600e+01
57 5 0 10 702 702 -8.2189177184140e+00
58 5 3 0 728 728 -1.2024382966230e+01
59 5 3 4 732 732 9.7468372374130e+01
60 5 3 8 736 736 -7.7912374166370e-01
61 5 3 11 739 739 -1.0869837812850e+00
62 5 4 11 751 751 1.7456851937100e+00
63 5 6 0 764 764 1.8081594118000e+01
64 5 7 0 776 776 3.6829907795010e+01
65 5 7 4 780 780 -4.0448222119740e+01
66 5 8 0 788 788 -3.1724353970440e+01
67 5 11 4 828 828 9.1717247301570e+00
68 6 3 4 875 875 -6.5949276116210e+00
69 6 4 2 885 885 -3.0047466362630e+01
70 6 4 4 887 887 4.2474822042340e+01
71 6 4 5 888 888 1.6574038934610e+01
72 6 4 10 893 893 -1.0764861206590e+01
73 6 7 4 923 923 4.7067707698260e+01
74 6 8 5 936 936 -1.3614005620610e+01
75 6 8 10 941 941 1.0783991510450e+01

76 7 0 8 986 986 -1.2498992642890e+01
77 7 3 3 1017 1017 1.7605088998970e+01
78 7 3 9 1023 1023 -2.2959904806920e+01
79 7 5 9 1047 1047 2.1249501041940e+01
80 7 5 10 1048 1048 -5.8649730628520e-01
81 7 6 3 1053 1053 -4.2598298915920e+01
82 7 6 4 1054 1054 2.1155643856720e+01
83 7 6 8 1058 1058 -3.3311545461900e+01
84 7 7 1 1063 1063 1.8024213891460e+01
85 7 7 5 1067 1067 -2.7805383777070e+00
86 7 7 6 1068 1068 1.2690090269280e+01
87 7 8 5 1079 1079 3.1146187199530e+00
88 7 8 9 1083 1083 -1.3531426884560e+00
89 7 10 9 1107 1107 8.6983085644440e+00
90 7 10 10 1108 1108 -1.8047402474590e+01
91 7 11 10 1120 1120 -2.3953990348820e+01
92 7 11 11 1121 1121 -5.4548734685110e+00
93 8 3 9 1166 1166 7.7376278312230e+01
94 8 3 10 1167 1167 -5.9432751347850e+00
95 8 4 0 1169 1169 -5.3834672995220e+00
96 8 5 11 1192 1192 -1.8486338314250e+01
97 8 6 9 1202 1202 -1.7701179022640e+01
98 8 7 0 1205 1205 5.2854071014720e+00
99 8 7 5 1210 1210 1.3067705072400e+01
100 8 7 6 1211 1211 -8.5983680144690e+00
101 8 7 8 1213 1213 1.5370826376050e-01
102 8 7 9 1214 1214 -1.8015347067230e+00
103 8 8 4 1221 1221 6.6601994665540e-01
104 8 8 10 1227 1227 -6.4341457726100e+00
105 8 8 11 1228 1228 1.9071850090310e+01
106 8 9 6 1235 1235 1.6013786848820e+00
107 8 9 9 1238 1238 3.1985790070230e+00
108 8 10 7 1248 1248 -4.9034072870960e+00
109 8 10 8 1249 1249 -2.7523280059060e+00
110 8 10 9 1250 1250 4.5671276747220e+00
111 8 11 2 1255 1255 4.7774942351670e-01
112 8 11 5 1258 1258 -1.2632579151030e+01
113 8 11 11 1264 1264 -2.2054458557590e+00
114 9 0 3 1267 1267 1.6716042947500e+01
115 9 0 4 1268 1268 -6.7330889231490e+00
116 9 2 7 1295 1295 7.3926171003400e+01
117 9 3 0 1300 1300 -5.7555182070660e+00
118 9 3 4 1304 1304 2.5390588944960e+00
119 9 3 7 1307 1307 2.6561563754540e+01

120 9 3 8 1308 1308 -4.2257523593100e+01
121 9 3 11 1311 1311 -9.0841469771710e-01
122 9 4 2 1314 1314 -1.3510163286610e+01
123 9 5 9 1333 1333 -1.5543111665070e+00
124 9 6 3 1339 1339 1.5620425647440e+01
125 9 6 10 1346 1346 -1.3698909635590e+01
126 9 7 9 1357 1357 2.0170017882830e+01
127 9 10 5 1389 1389 1.4832360020530e+01
128 9 10 8 1392 1392 1.1333028980810e+01
129 9 10 9 1393 1393 -1.1687150069590e+01
130 9 11 4 1400 1400 5.7326171097190e+00
131 9 11 7 1403 1403 -1.1635072444610e+01
132 9 11 11 1407 1407 7.2107541025490e-01
133 10 0 3 1410 1410 -1.8863968100240e+01
134 10 3 7 1450 1450 -2.8871941553520e+01
135 10 3 8 1451 1451 3.9480598426840e+00
136 10 4 4 1459 1459 -2.1738010640420e+01
137 10 6 2 1481 1481 -8.9283396837240e+00
138 10 6 4 1483 1483 8.1106568043430e+00
139 10 6 5 1484 1484 -4.5788617284460e+00
140 10 6 8 1487 1487 -1.7982966906850e+01
141 10 6 9 1488 1488 9.6140454290990e+00
142 10 6 11 1490 1490 1.0724678644570e+01
143 10 7 0 1491 1491 -1.0612853612970e+01
144 10 7 5 1496 1496 -3.7225795550450e+00
145 10 7 10 1501 1501 1.0733767546870e+01
146 10 8 8 1511 1511 3.9324716997950e+01
147 10 8 9 1512 1512 -8.5098822581330e-01
148 10 10 10 1537 1537 -1.0171466516650e+01
149 10 10 11 1538 1538 -1.0599738100280e+01
150 10 11 3 1542 1542 -1.6116152914030e+01
151 10 11 6 1545 1545 1.4501790053830e+01
152 10 11 9 1548 1548 7.6356164135230e+00
153 10 11 10 1549 1549 -1.7513998747020e+01
154 11 0 3 1553 1553 -1.5923182693980e+01
155 11 3 0 1586 1586 6.8929700307060e+00
156 11 3 8 1594 1594 7.5962790599610e-01
157 11 4 9 1607 1607 2.0833467983150e+01
158 11 4 11 1609 1609 -1.4275625407890e+01
159 11 6 10 1632 1632 5.8908174394760e+00
160 11 7 10 1644 1644 1.1100401569930e+00
161 11 7 11 1645 1645 -1.0328673667830e+01
162 11 8 6 1652 1652 6.2137020236840e+00
163 11 8 9 1655 1655 -1.1398818280060e+00

164 11 8 11 1657 1657 1.7180553266730e+01
165 11 9 9 1667 1667 4.2931395760030e+00
166 11 10 0 1670 1670 -4.5172155129570e+00
167 11 10 3 1673 1673 -5.1132667692100e+00
168 11 10 6 1676 1676 -9.0198380094880e-02
169 11 10 10 1680 1680 -1.0909567975200e+01
170 11 10 11 1681 1681 5.0058197586700e+00
171 11 11 2 1684 1684 1.9854037520300e+00
172 11 11 6 1688 1688 -1.9457890566670e+01
173 11 11 7 1689 1689 1.0869828875060e+01

TRIPLETTYPE PARAMS:
  INDEX: 5 ATOMS: B Mg Mg
PAIRS: BMg BMg MgMg UNIQUE: -1 TOTAL: 0
   index | powers | equiv index | param index | parameter

TRIPLETTYPE PARAMS:
  INDEX: 6 ATOMS: O O O
PAIRS: OO OO OO UNIQUE: -1 TOTAL: 461
   index | powers | equiv index | param index | parameter
  ---
0 0 1 3 9 2 1.0904749716780e+01
1 1 0 3 9 2 1.0904749716780e+01
2 0 3 1 9 2 1.0904749716780e+01
3 3 0 1 9 2 1.0904749716780e+01
4 1 3 0 9 2 1.0904749716780e+01
5 3 1 0 9 2 1.0904749716780e+01
6 0 1 11 57 10 5.5736385439950e+00
7 1 0 11 57 10 5.5736385439950e+00
8 0 11 1 57 10 5.5736385439950e+00
9 11 0 1 57 10 5.5736385439950e+00
10 1 11 0 57 10 5.5736385439950e+00
11 11 1 0 57 10 5.5736385439950e+00
12 0 2 2 63 11 6.8803593165120e+00
13 2 0 2 63 11 6.8803593165120e+00
14 2 2 0 63 11 6.8803593165120e+00
15 0 2 3 66 12 -1.2360166343090e+01
16 2 0 3 66 12 -1.2360166343090e+01
17 0 3 2 66 12 -1.2360166343090e+01
18 3 0 2 66 12 -1.2360166343090e+01
19 2 3 0 66 12 -1.2360166343090e+01
20 3 2 0 66 12 -1.2360166343090e+01
21 0 2 9 102 18 -1.7672076005130e+01

22 2 0 9 102 18 -1.7672076005130e+01
23 0 9 2 102 18 -1.7672076005130e+01
24 9 0 2 102 18 -1.7672076005130e+01
25 2 9 0 102 18 -1.7672076005130e+01
26 9 2 0 102 18 -1.7672076005130e+01
27 0 2 10 108 19 9.6050303891980e+00
28 2 0 10 108 19 9.6050303891980e+00
29 0 10 2 108 19 9.6050303891980e+00
30 10 0 2 108 19 9.6050303891980e+00
31 2 10 0 108 19 9.6050303891980e+00
32 10 2 0 108 19 9.6050303891980e+00
33 0 3 5 129 23 1.2876753928550e+01
34 3 0 5 129 23 1.2876753928550e+01
35 0 5 3 129 23 1.2876753928550e+01
36 5 0 3 129 23 1.2876753928550e+01
37 3 5 0 129 23 1.2876753928550e+01
38 5 3 0 129 23 1.2876753928550e+01
39 0 3 10 159 28 -6.9997218909470e+00
40 3 0 10 159 28 -6.9997218909470e+00
41 0 10 3 159 28 -6.9997218909470e+00
42 10 0 3 159 28 -6.9997218909470e+00
43 3 10 0 159 28 -6.9997218909470e+00
44 10 3 0 159 28 -6.9997218909470e+00
45 0 4 8 192 34 -4.0703682130970e+01
46 4 0 8 192 34 -4.0703682130970e+01
47 0 8 4 192 34 -4.0703682130970e+01
48 8 0 4 192 34 -4.0703682130970e+01
49 4 8 0 192 34 -4.0703682130970e+01
50 8 4 0 192 34 -4.0703682130970e+01
51 0 4 9 198 35 3.9890816455700e+00
52 4 0 9 198 35 3.9890816455700e+00
53 0 9 4 198 35 3.9890816455700e+00
54 9 0 4 198 35 3.9890816455700e+00
55 4 9 0 198 35 3.9890816455700e+00
56 9 4 0 198 35 3.9890816455700e+00
57 0 5 7 225 40 -1.2431500896060e+01
58 5 0 7 225 40 -1.2431500896060e+01
59 0 7 5 225 40 -1.2431500896060e+01
60 7 0 5 225 40 -1.2431500896060e+01
61 5 7 0 225 40 -1.2431500896060e+01
62 7 5 0 225 40 -1.2431500896060e+01
63 0 5 11 249 44 -1.2979991870700e+00
64 5 0 11 249 44 -1.2979991870700e+00
65 0 11 5 249 44 -1.2979991870700e+00

66 11 0 5 249 44 -1.2979991870700e+00
67 5 11 0 249 44 -1.2979991870700e+00
68 11 5 0 249 44 -1.2979991870700e+00
69 0 6 6 255 45 1.6401753566900e+01
70 6 0 6 255 45 1.6401753566900e+01
71 6 6 0 255 45 1.6401753566900e+01
72 0 6 9 270 48 -1.0211116877350e+01
73 6 0 9 270 48 -1.0211116877350e+01
74 0 9 6 270 48 -1.0211116877350e+01
75 9 0 6 270 48 -1.0211116877350e+01
76 6 9 0 270 48 -1.0211116877350e+01
77 9 6 0 270 48 -1.0211116877350e+01
78 0 7 9 297 53 -2.6533892909920e+00
79 7 0 9 297 53 -2.6533892909920e+00
80 0 9 7 297 53 -2.6533892909920e+00
81 9 0 7 297 53 -2.6533892909920e+00
82 7 9 0 297 53 -2.6533892909920e+00
83 9 7 0 297 53 -2.6533892909920e+00
84 0 7 10 303 54 2.6254056145030e+00
85 7 0 10 303 54 2.6254056145030e+00
86 0 10 7 303 54 2.6254056145030e+00
87 10 0 7 303 54 2.6254056145030e+00
88 7 10 0 303 54 2.6254056145030e+00
89 10 7 0 303 54 2.6254056145030e+00
90 0 8 10 324 58 -3.8725907383700e+00
91 8 0 10 324 58 -3.8725907383700e+00
92 0 10 8 324 58 -3.8725907383700e+00
93 10 0 8 324 58 -3.8725907383700e+00
94 8 10 0 324 58 -3.8725907383700e+00
95 10 8 0 324 58 -3.8725907383700e+00
96 0 8 11 330 59 2.5976340115790e+00
97 8 0 11 330 59 2.5976340115790e+00
98 0 11 8 330 59 2.5976340115790e+00
99 11 0 8 330 59 2.5976340115790e+00
100 8 11 0 330 59 2.5976340115790e+00
101 11 8 0 330 59 2.5976340115790e+00
102 0 9 11 345 62 3.2415393447980e+00
103 9 0 11 345 62 3.2415393447980e+00
104 0 11 9 345 62 3.2415393447980e+00
105 11 0 9 345 62 3.2415393447980e+00
106 9 11 0 345 62 3.2415393447980e+00
107 11 9 0 345 62 3.2415393447980e+00
108 0 10 11 354 64 -6.5881403151540e-01
109 10 0 11 354 64 -6.5881403151540e-01

110 0 11 10 354 64 -6.5881403151540e-01
111 11 0 10 354 64 -6.5881403151540e-01
112 10 11 0 354 64 -6.5881403151540e-01
113 11 10 0 354 64 -6.5881403151540e-01
114 1 3 8 478 92 -1.5543837083590e-01
115 3 1 8 478 92 -1.5543837083590e-01
116 1 8 3 478 92 -1.5543837083590e-01
117 8 1 3 478 92 -1.5543837083590e-01
118 3 8 1 478 92 -1.5543837083590e-01
119 8 3 1 478 92 -1.5543837083590e-01
120 1 5 9 568 108 -1.1912526034480e+01
121 5 1 9 568 108 -1.1912526034480e+01
122 1 9 5 568 108 -1.1912526034480e+01
123 9 1 5 568 108 -1.1912526034480e+01
124 5 9 1 568 108 -1.1912526034480e+01
125 9 5 1 568 108 -1.1912526034480e+01
126 1 7 9 628 119 1.5183236156770e+01
127 7 1 9 628 119 1.5183236156770e+01
128 1 9 7 628 119 1.5183236156770e+01
129 9 1 7 628 119 1.5183236156770e+01
130 7 9 1 628 119 1.5183236156770e+01
131 9 7 1 628 119 1.5183236156770e+01
132 1 7 10 634 120 -2.4199151854070e+01
133 7 1 10 634 120 -2.4199151854070e+01
134 1 10 7 634 120 -2.4199151854070e+01
135 10 1 7 634 120 -2.4199151854070e+01
136 7 10 1 634 120 -2.4199151854070e+01
137 10 7 1 634 120 -2.4199151854070e+01
138 1 8 10 655 124 3.2544983681350e+00
139 8 1 10 655 124 3.2544983681350e+00
140 1 10 8 655 124 3.2544983681350e+00
141 10 1 8 655 124 3.2544983681350e+00
142 8 10 1 655 124 3.2544983681350e+00
143 10 8 1 655 124 3.2544983681350e+00
144 1 9 11 676 128 -5.6397502725000e+00
145 9 1 11 676 128 -5.6397502725000e+00
146 1 11 9 676 128 -5.6397502725000e+00
147 11 1 9 676 128 -5.6397502725000e+00
148 9 11 1 676 128 -5.6397502725000e+00
149 11 9 1 676 128 -5.6397502725000e+00
150 2 2 11 719 141 8.7784076435790e+00
151 2 11 2 719 141 8.7784076435790e+00
152 11 2 2 719 141 8.7784076435790e+00
153 2 3 9 755 148 -7.7353933387460e+00

154 3 2 9 755 148 -7.7353933387460e+00
155 2 9 3 755 148 -7.7353933387460e+00
156 9 2 3 755 148 -7.7353933387460e+00
157 3 9 2 755 148 -7.7353933387460e+00
158 9 3 2 755 148 -7.7353933387460e+00
159 2 4 6 782 153 1.6728259264470e+01
160 4 2 6 782 153 1.6728259264470e+01
161 2 6 4 782 153 1.6728259264470e+01
162 6 2 4 782 153 1.6728259264470e+01
163 4 6 2 782 153 1.6728259264470e+01
164 6 4 2 782 153 1.6728259264470e+01
165 2 4 7 788 154 -6.3618771030230e+01
166 4 2 7 788 154 -6.3618771030230e+01
167 2 7 4 788 154 -6.3618771030230e+01
168 7 2 4 788 154 -6.3618771030230e+01
169 4 7 2 788 154 -6.3618771030230e+01
170 7 4 2 788 154 -6.3618771030230e+01
171 2 5 8 833 162 -1.1881235358070e+01
172 5 2 8 833 162 -1.1881235358070e+01
173 2 8 5 833 162 -1.1881235358070e+01
174 8 2 5 833 162 -1.1881235358070e+01
175 5 8 2 833 162 -1.1881235358070e+01
176 8 5 2 833 162 -1.1881235358070e+01
177 2 5 9 839 163 1.6346880604590e+01
178 5 2 9 839 163 1.6346880604590e+01
179 2 9 5 839 163 1.6346880604590e+01
180 9 2 5 839 163 1.6346880604590e+01
181 5 9 2 839 163 1.6346880604590e+01
182 9 5 2 839 163 1.6346880604590e+01
183 2 8 11 932 180 4.4247016558930e+00
184 8 2 11 932 180 4.4247016558930e+00
185 2 11 8 932 180 4.4247016558930e+00
186 11 2 8 932 180 4.4247016558930e+00
187 8 11 2 932 180 4.4247016558930e+00
188 11 8 2 932 180 4.4247016558930e+00
189 2 10 11 956 185 -2.2205914648990e+00
190 10 2 11 956 185 -2.2205914648990e+00
191 2 11 10 956 185 -2.2205914648990e+00
192 11 2 10 956 185 -2.2205914648990e+00
193 10 11 2 956 185 -2.2205914648990e+00
194 11 10 2 956 185 -2.2205914648990e+00
195 3 3 5 969 189 -1.3536639301370e+01
196 3 5 3 969 189 -1.3536639301370e+01
197 5 3 3 969 189 -1.3536639301370e+01

198 3 3 7 975 191 -7.9179343733270e+00
199 3 7 3 975 191 -7.9179343733270e+00
200 7 3 3 975 191 -7.9179343733270e+00
201 3 3 11 987 195 -5.0955302481690e-01
202 3 11 3 987 195 -5.0955302481690e-01
203 11 3 3 987 195 -5.0955302481690e-01
204 3 4 6 999 198 -1.8465757902030e+01
205 4 3 6 999 198 -1.8465757902030e+01
206 3 6 4 999 198 -1.8465757902030e+01
207 6 3 4 999 198 -1.8465757902030e+01
208 4 6 3 999 198 -1.8465757902030e+01
209 6 4 3 999 198 -1.8465757902030e+01
210 3 4 7 1005 199 3.0044343766370e+01
211 4 3 7 1005 199 3.0044343766370e+01
212 3 7 4 1005 199 3.0044343766370e+01
213 7 3 4 1005 199 3.0044343766370e+01
214 4 7 3 1005 199 3.0044343766370e+01
215 7 4 3 1005 199 3.0044343766370e+01
216 3 4 10 1023 202 -1.2608234500170e+01
217 4 3 10 1023 202 -1.2608234500170e+01
218 3 10 4 1023 202 -1.2608234500170e+01
219 10 3 4 1023 202 -1.2608234500170e+01
220 4 10 3 1023 202 -1.2608234500170e+01
221 10 4 3 1023 202 -1.2608234500170e+01
222 3 4 11 1029 203 1.3477635269960e+01
223 4 3 11 1029 203 1.3477635269960e+01
224 3 11 4 1029 203 1.3477635269960e+01
225 11 3 4 1029 203 1.3477635269960e+01
226 4 11 3 1029 203 1.3477635269960e+01
227 11 4 3 1029 203 1.3477635269960e+01
228 3 5 11 1068 210 4.3163880407830e-01
229 5 3 11 1068 210 4.3163880407830e-01
230 3 11 5 1068 210 4.3163880407830e-01
231 11 3 5 1068 210 4.3163880407830e-01
232 5 11 3 1068 210 4.3163880407830e-01
233 11 5 3 1068 210 4.3163880407830e-01
234 3 7 8 1110 218 -4.1808557397930e+00
235 7 3 8 1110 218 -4.1808557397930e+00
236 3 8 7 1110 218 -4.1808557397930e+00
237 8 3 7 1110 218 -4.1808557397930e+00
238 7 8 3 1110 218 -4.1808557397930e+00
239 8 7 3 1110 218 -4.1808557397930e+00
240 3 7 11 1128 221 -9.8124842497710e+00
241 7 3 11 1128 221 -9.8124842497710e+00

242 3 11 7 1128 221 -9.8124842497710e+00
243 11 3 7 1128 221 -9.8124842497710e+00
244 7 11 3 1128 221 -9.8124842497710e+00
245 11 7 3 1128 221 -9.8124842497710e+00
246 4 5 7 1213 242 -1.4060047392800e+01
247 5 4 7 1213 242 -1.4060047392800e+01
248 4 7 5 1213 242 -1.4060047392800e+01
249 7 4 5 1213 242 -1.4060047392800e+01
250 5 7 4 1213 242 -1.4060047392800e+01
251 7 5 4 1213 242 -1.4060047392800e+01
252 4 5 8 1219 243 2.3794754976740e+01
253 5 4 8 1219 243 2.3794754976740e+01
254 4 8 5 1219 243 2.3794754976740e+01
255 8 4 5 1219 243 2.3794754976740e+01
256 5 8 4 1219 243 2.3794754976740e+01
257 8 5 4 1219 243 2.3794754976740e+01
258 4 5 9 1225 244 -4.8128931217480e+00
259 5 4 9 1225 244 -4.8128931217480e+00
260 4 9 5 1225 244 -4.8128931217480e+00
261 9 4 5 1225 244 -4.8128931217480e+00
262 5 9 4 1225 244 -4.8128931217480e+00
263 9 5 4 1225 244 -4.8128931217480e+00
264 4 6 7 1246 248 2.6215554175810e+01
265 6 4 7 1246 248 2.6215554175810e+01
266 4 7 6 1246 248 2.6215554175810e+01
267 7 4 6 1246 248 2.6215554175810e+01
268 6 7 4 1246 248 2.6215554175810e+01
269 7 6 4 1246 248 2.6215554175810e+01
270 4 6 8 1252 249 6.7873364135350e+00
271 6 4 8 1252 249 6.7873364135350e+00
272 4 8 6 1252 249 6.7873364135350e+00
273 8 4 6 1252 249 6.7873364135350e+00
274 6 8 4 1252 249 6.7873364135350e+00
275 8 6 4 1252 249 6.7873364135350e+00
276 4 6 10 1264 251 -2.3584315986870e-01
277 6 4 10 1264 251 -2.3584315986870e-01
278 4 10 6 1264 251 -2.3584315986870e-01
279 10 4 6 1264 251 -2.3584315986870e-01
280 6 10 4 1264 251 -2.3584315986870e-01
281 10 6 4 1264 251 -2.3584315986870e-01
282 4 7 10 1291 256 -6.6626365685170e+00
283 7 4 10 1291 256 -6.6626365685170e+00
284 4 10 7 1291 256 -6.6626365685170e+00
285 10 4 7 1291 256 -6.6626365685170e+00

286 7 10 4 1291 256 -6.6626365685170e+00
287 10 7 4 1291 256 -6.6626365685170e+00
288 4 8 9 1306 259 -4.8446110217840e+00
289 8 4 9 1306 259 -4.8446110217840e+00
290 4 9 8 1306 259 -4.8446110217840e+00
291 9 4 8 1306 259 -4.8446110217840e+00
292 8 9 4 1306 259 -4.8446110217840e+00
293 9 8 4 1306 259 -4.8446110217840e+00
294 4 9 9 1324 262 3.4300571620970e+00
295 9 4 9 1324 262 3.4300571620970e+00
296 9 9 4 1324 262 3.4300571620970e+00
297 4 9 10 1327 263 3.3795001196790e+00
298 9 4 10 1327 263 3.3795001196790e+00
299 4 10 9 1327 263 3.3795001196790e+00
300 10 4 9 1327 263 3.3795001196790e+00
301 9 10 4 1327 263 3.3795001196790e+00
302 10 9 4 1327 263 3.3795001196790e+00
303 4 10 10 1339 265 2.4912358620470e-01
304 10 4 10 1339 265 2.4912358620470e-01
305 10 10 4 1339 265 2.4912358620470e-01
306 4 10 11 1342 266 7.6605621035340e-01
307 10 4 11 1342 266 7.6605621035340e-01
308 4 11 10 1342 266 7.6605621035340e-01
309 11 4 10 1342 266 7.6605621035340e-01
310 10 11 4 1342 266 7.6605621035340e-01
311 11 10 4 1342 266 7.6605621035340e-01
312 4 11 11 1348 267 6.2686293372540e+00
313 11 4 11 1348 267 6.2686293372540e+00
314 11 11 4 1348 267 6.2686293372540e+00
315 5 6 7 1373 276 6.7873289191320e+00
316 6 5 7 1373 276 6.7873289191320e+00
317 5 7 6 1373 276 6.7873289191320e+00
318 7 5 6 1373 276 6.7873289191320e+00
319 6 7 5 1373 276 6.7873289191320e+00
320 7 6 5 1373 276 6.7873289191320e+00
321 5 6 10 1391 279 2.3679867211740e+01
322 6 5 10 1391 279 2.3679867211740e+01
323 5 10 6 1391 279 2.3679867211740e+01
324 10 5 6 1391 279 2.3679867211740e+01
325 6 10 5 1391 279 2.3679867211740e+01
326 10 6 5 1391 279 2.3679867211740e+01
327 5 6 11 1397 280 -1.4255224505330e+01
328 6 5 11 1397 280 -1.4255224505330e+01
329 5 11 6 1397 280 -1.4255224505330e+01

330 11 5 6 1397 280 -1.4255224505330e+01
331 6 11 5 1397 280 -1.4255224505330e+01
332 11 6 5 1397 280 -1.4255224505330e+01
333 5 7 8 1406 282 3.3620406020010e+01
334 7 5 8 1406 282 3.3620406020010e+01
335 5 8 7 1406 282 3.3620406020010e+01
336 8 5 7 1406 282 3.3620406020010e+01
337 7 8 5 1406 282 3.3620406020010e+01
338 8 7 5 1406 282 3.3620406020010e+01
339 5 7 10 1418 284 1.8852016617890e+01
340 7 5 10 1418 284 1.8852016617890e+01
341 5 10 7 1418 284 1.8852016617890e+01
342 10 5 7 1418 284 1.8852016617890e+01
343 7 10 5 1418 284 1.8852016617890e+01
344 10 7 5 1418 284 1.8852016617890e+01
345 5 8 8 1430 286 -2.2949792858080e+01
346 8 5 8 1430 286 -2.2949792858080e+01
347 8 8 5 1430 286 -2.2949792858080e+01
348 5 8 9 1433 287 1.9904096734560e+01
349 8 5 9 1433 287 1.9904096734560e+01
350 5 9 8 1433 287 1.9904096734560e+01
351 9 5 8 1433 287 1.9904096734560e+01
352 8 9 5 1433 287 1.9904096734560e+01
353 9 8 5 1433 287 1.9904096734560e+01
354 5 9 11 1460 292 5.3618505842700e+00
355 9 5 11 1460 292 5.3618505842700e+00
356 5 11 9 1460 292 5.3618505842700e+00
357 11 5 9 1460 292 5.3618505842700e+00
358 9 11 5 1460 292 5.3618505842700e+00
359 11 9 5 1460 292 5.3618505842700e+00
360 5 10 11 1469 294 -5.6553618397690e+00
361 10 5 11 1469 294 -5.6553618397690e+00
362 5 11 10 1469 294 -5.6553618397690e+00
363 11 5 10 1469 294 -5.6553618397690e+00
364 10 11 5 1469 294 -5.6553618397690e+00
365 11 10 5 1469 294 -5.6553618397690e+00
366 5 11 11 1475 295 -7.3785034082160e-01
367 11 5 11 1475 295 -7.3785034082160e-01
368 11 11 5 1475 295 -7.3785034082160e-01
369 6 6 11 1491 301 4.1432498926200e-01
370 6 11 6 1491 301 4.1432498926200e-01
371 11 6 6 1491 301 4.1432498926200e-01
372 6 7 9 1503 304 1.4653908391820e+01
373 7 6 9 1503 304 1.4653908391820e+01

374 6 9 7 1503 304 1.4653908391820e+01
375 9 6 7 1503 304 1.4653908391820e+01
376 7 9 6 1503 304 1.4653908391820e+01
377 9 7 6 1503 304 1.4653908391820e+01
378 6 8 8 1521 307 -3.4577112936040e+00
379 8 6 8 1521 307 -3.4577112936040e+00
380 8 8 6 1521 307 -3.4577112936040e+00
381 6 8 9 1524 308 2.5130233164480e+00
382 8 6 9 1524 308 2.5130233164480e+00
383 6 9 8 1524 308 2.5130233164480e+00
384 9 6 8 1524 308 2.5130233164480e+00
385 8 9 6 1524 308 2.5130233164480e+00
386 9 8 6 1524 308 2.5130233164480e+00
387 6 8 10 1530 309 -2.8054999675930e-01
388 8 6 10 1530 309 -2.8054999675930e-01
389 6 10 8 1530 309 -2.8054999675930e-01
390 10 6 8 1530 309 -2.8054999675930e-01
391 8 10 6 1530 309 -2.8054999675930e-01
392 10 8 6 1530 309 -2.8054999675930e-01
393 6 9 11 1551 313 -5.3000502364670e+00
394 9 6 11 1551 313 -5.3000502364670e+00
395 6 11 9 1551 313 -5.3000502364670e+00
396 11 6 9 1551 313 -5.3000502364670e+00
397 9 11 6 1551 313 -5.3000502364670e+00
398 11 9 6 1551 313 -5.3000502364670e+00
399 6 10 10 1557 314 -2.8349388192250e-01
400 10 6 10 1557 314 -2.8349388192250e-01
401 10 10 6 1557 314 -2.8349388192250e-01
402 7 7 8 1570 318 -2.9467726294880e+01
403 7 8 7 1570 318 -2.9467726294880e+01
404 8 7 7 1570 318 -2.9467726294880e+01
405 7 7 9 1573 319 -4.4742205857380e+00
406 7 9 7 1573 319 -4.4742205857380e+00
407 9 7 7 1573 319 -4.4742205857380e+00
408 7 8 8 1582 322 2.2490181344460e+01
409 8 7 8 1582 322 2.2490181344460e+01
410 8 8 7 1582 322 2.2490181344460e+01
411 7 8 11 1597 325 2.4358262186520e+00
412 8 7 11 1597 325 2.4358262186520e+00
413 7 11 8 1597 325 2.4358262186520e+00
414 11 7 8 1597 325 2.4358262186520e+00
415 8 11 7 1597 325 2.4358262186520e+00
416 11 8 7 1597 325 2.4358262186520e+00
417 7 9 10 1606 327 -3.4624098571730e-01

418 9 7 10 1606 327 -3.4624098571730e-01
419 7 10 9 1606 327 -3.4624098571730e-01
420 10 7 9 1606 327 -3.4624098571730e-01
421 9 10 7 1606 327 -3.4624098571730e-01
422 10 9 7 1606 327 -3.4624098571730e-01
423 7 9 11 1612 328 1.7695093584610e+00
424 9 7 11 1612 328 1.7695093584610e+00
425 7 11 9 1612 328 1.7695093584610e+00
426 11 7 9 1612 328 1.7695093584610e+00
427 9 11 7 1612 328 1.7695093584610e+00
428 11 9 7 1612 328 1.7695093584610e+00
429 7 10 10 1618 329 1.6116060024060e+00
430 10 7 10 1618 329 1.6116060024060e+00
431 10 10 7 1618 329 1.6116060024060e+00
432 7 11 11 1627 331 -3.3191210132280e+00
433 11 7 11 1627 331 -3.3191210132280e+00
434 11 11 7 1627 331 -3.3191210132280e+00
435 8 9 10 1643 337 -1.0592246834050e+01
436 9 8 10 1643 337 -1.0592246834050e+01
437 8 10 9 1643 337 -1.0592246834050e+01
438 10 8 9 1643 337 -1.0592246834050e+01
439 9 10 8 1643 337 -1.0592246834050e+01
440 10 9 8 1643 337 -1.0592246834050e+01
441 9 9 10 1668 343 3.6770463752820e+00
442 9 10 9 1668 343 3.6770463752820e+00
443 10 9 9 1668 343 3.6770463752820e+00
444 9 9 11 1671 344 -3.4892514551620e-01
445 9 11 9 1671 344 -3.4892514551620e-01
446 11 9 9 1671 344 -3.4892514551620e-01
447 9 10 10 1674 345 -1.9892752806570e+00
448 10 9 10 1674 345 -1.9892752806570e+00
449 10 10 9 1674 345 -1.9892752806570e+00
450 9 10 11 1677 346 1.1718552150620e+00
451 10 9 11 1677 346 1.1718552150620e+00
452 9 11 10 1677 346 1.1718552150620e+00
453 11 9 10 1677 346 1.1718552150620e+00
454 10 11 9 1677 346 1.1718552150620e+00
455 11 10 9 1677 346 1.1718552150620e+00
456 10 10 10 1686 348 -9.6363060191070e-01
457 10 10 11 1687 349 4.9973049517600e+00
458 10 11 10 1687 349 4.9973049517600e+00
459 11 10 10 1687 349 4.9973049517600e+00
460 11 11 11 1693 351 2.9997484807510e+00

TRIPLETTYPE PARAMS:
  INDEX: 7 ATOMS: Mg O O
PAIRS: OMg OMg OO UNIQUE: -1 TOTAL: 67
    index | powers | equiv index | param index | parameter
  ----
0 0 2 4 28 14 -3.2657011297450e+01
1 2 0 4 28 14 -3.2657011297450e+01
2 0 2 11 42 21 3.1794499191960e+00
3 2 0 11 42 21 3.1794499191960e+00
4 0 8 6 164 82 -1.8361859515890e+01
5 8 0 6 164 82 -1.8361859515890e+01
6 0 8 9 170 85 2.2350747588280e+01
7 8 0 9 170 85 2.2350747588280e+01
8 0 9 4 182 91 -1.7775529188790e+01
9 9 0 4 182 91 -1.7775529188790e+01
10 0 10 10 216 108 1.1735422670100e+01
11 10 0 10 216 108 1.1735422670100e+01
12 0 10 11 218 109 1.2039697582920e+01
13 10 0 11 218 109 1.2039697582920e+01
14 0 11 10 238 119 -1.8998035207820e+01
15 11 0 10 238 119 -1.8998035207820e+01
16 0 11 11 240 120 1.6273687868700e+01
17 11 0 11 240 120 1.6273687868700e+01
18 2 11 11 720 372 -1.2544327195210e+01
19 11 2 11 720 372 -1.2544327195210e+01
20 3 6 10 802 419 3.1667427507150e+01
21 6 3 10 802 419 3.1667427507150e+01
22 3 10 9 896 466 -3.5312193120390e+01
23 10 3 9 896 466 -3.5312193120390e+01
24 3 11 4 910 473 5.2869335401050e+00
25 11 3 4 910 473 5.2869335401050e+00
26 4 8 0 1010 529 2.2416950092250e+00
27 8 4 0 1010 529 2.2416950092250e+00
28 4 10 3 1064 556 3.2126766893430e+01
29 10 4 3 1064 556 3.2126766893430e+01
30 5 7 7 1156 608 -1.3652003157140e+01
31 7 5 7 1156 608 -1.3652003157140e+01
32 5 9 11 1212 636 -5.7831094967010e+00
33 9 5 11 1212 636 -5.7831094967010e+00
34 5 11 9 1256 658 -1.2373259854810e+01
35 11 5 9 1256 658 -1.2373259854810e+01
36 5 11 11 1260 660 2.5796969408420e-01
37 11 5 11 1260 660 2.5796969408420e-01
38 6 7 0 1274 673 1.2357883095520e+01

39 7 6 0 1274 673 1.2357883095520e+01
40 6 8 4 1306 689 -4.0456766934720e+01
41 8 6 4 1306 689 -4.0456766934720e+01
42 6 8 6 1310 691 8.8625478802250e+00
43 8 6 6 1310 691 8.8625478802250e+00
44 6 8 7 1312 692 6.2921755902180e+00
45 8 6 7 1312 692 6.2921755902180e+00
46 6 9 6 1334 703 -1.0784259583990e+02
47 9 6 6 1334 703 -1.0784259583990e+02
48 6 10 10 1366 719 -6.7667222944420e+00
49 10 6 10 1366 719 -6.7667222944420e+00
50 7 9 0 1430 757 2.6204210848090e+00
51 9 7 0 1430 757 2.6204210848090e+00
52 7 9 7 1444 764 2.4273242503900e+01
53 9 7 7 1444 764 2.4273242503900e+01
54 8 10 0 1538 817 -2.5119486475190e+00
55 10 8 0 1538 817 -2.5119486475190e+00
56 9 11 9 1640 874 1.4107956365950e+01
57 11 9 9 1640 874 1.4107956365950e+01
58 9 11 11 1644 876 -1.5206723793210e+01
59 11 9 11 1644 876 -1.5206723793210e+01
60 10 10 9 1655 886 -3.0823258857640e-01
61 10 11 3 1664 892 -1.4142718756210e+01
62 11 10 3 1664 892 -1.4142718756210e+01
63 10 11 10 1678 899 1.1275639225250e+01
64 11 10 10 1678 899 1.1275639225250e+01
65 10 11 11 1680 900 1.8018458764480e+01
66 11 10 11 1680 900 1.8018458764480e+01

TRIPLETTYPE PARAMS:
  INDEX: 8 ATOMS: Mg Mg O
PAIRS: MgMg OMg OMg UNIQUE: -1 TOTAL: 0
    index | powers | equiv index | param index | parameter

TRIPLETTYPE PARAMS:
  INDEX: 9 ATOMS: Mg Mg Mg
PAIRS: MgMg MgMg MgMg UNIQUE: -1 TOTAL: 0
    index | powers | equiv index | param index | parameter

QUADRUPLET CHEBYSHEV PARAMS

PAIRMAPS: 9
0 BB
4 BMg
3 BO
4 MgB
2 MgMg
5 MgO
3 OB
5 OMg
1 OO

TRIPMAPS: 27
0 BBBBBB
2 BBBMgBMg
1 BBBOBO
2 BMgBBBMg
2 BMgBMgBB
5 BMgBMgMgMg
4 BMgBOOMg
5 BMgMgMgBMg
4 BMgOMgBO
1 BOBBBO
4 BOBMgOMg
1 BOBOBB
3 BOBOOO
4 BOOMgBMg
3 BOOOBO
5 MgMgBMgBMg
9 MgMgMgMgMgMg
8 MgMgOMgOMg
4 OMgBMgBO
4 OMgBOBMg
8 OMgMgMgOMg
8 OMgOMgMgMg
7 OMgOMgOO
7 OMgOOOMg
3 OOBOBO
7 OOOMgOMg
6 OOOOOO

NO ENERGY OFFSETS: 3
ENERGY OFFSET 1   0.0000000000000e+00
ENERGY OFFSET 2   2.2975028414740e+03
ENERGY OFFSET 3   0.0000000000000e+00

ENDFILE

A.7 job_dftb.sh file

```
#!/bin/sh

#SBATCH -N 1
#SBATCH -J 1
#SBATCH -t 11:00:00
#SBATCH -p pbatch
#SBATCH -A cbronze

module load mkl

exe="/g/g20/zacharia/codes/dftbplus-21.2/_with_MPI/_install/bin/dftb+"
$exe > DFTB_output
```

A.8 MATLAB code to extract the assigned numbers of B, Mg and O atoms as array

```
% open the file
 %%%%parameters to be changed everytime
 filename=input("\nInput file name with extension:\n","s");
 fid=fopen(filename,'r');
 Niter=input("\nInput Number of iterations:\n"); %total no of MDiterations

 %%%will remain the same in most cases unless we change number of atoms or
 %%%printfrequency
 Numatoms=input("\n Number of atoms: \n");
 Nline=Numatoms+2; %% no. of lines in each MDiter considering first two
 %lines are blank and rest contains coordinate and vel info
 Iterint=5;  %saving frequency or RestartFrequency in DFTB+ now set to 5
 totallines=((Niter/Iterint)+1)*Nline;  %1 accounts for t=0

 %set linenum to the desired line number that you want to import
% linenum = [83:83:161850];
 % use '%s' if you want to read in the entire line or use '%f' if you want to read only the
first numeric value
% for i=1:length(linenum)
    %%C(i,:) = textscan(fid,'%s %f %f %f %f %f %f %f',1,'delimiter','\n',
'headerlines',linenum(i)-1);
    %fseek(fid,0,'bof');
 %end
%formatSpec = '%s %f %f %f %f %f %f %f' ;
```

```
%A = fscanf(fid,formatSpec);
tlines=cell(0,1);

n=0;
iter=0;
for i=1:1:totallines %161850
   %tlines{end+1,1}=fgetl(fid);
   n=n+1;
   if n==1 || n==2
      dump=fgetl(fid);

   else
     %tlines{end+1,1}=fgetl(fid);
     m=fgetl(fid);
     A1=extractAfter(m,5);
     A2(n-2,:)=str2num(A1);
   end
   if mod(i,Nline)==0
      iter=iter+1;
      C(iter)={A2};
      n=0;
   end
end
%%%reading and storing the atom type first column
fseek(fid,0,'bof');
%Atype=(Nline-2,1);
for i=1:1:Nline %161850
   %tlines{end+1,1}=fgetl(fid);

   if i==1 || i==2
      dump=fgetl(fid);

   else
     %tlines{end+1,1}=fgetl(fid);
     m=fgetl(fid);
     Atype1=extractBefore(m,6);
     Atype(i-2)=extractAfter(Atype1,4); %store type of atom Atype(5) with return the
fifth atom element
   end
end
o1=0;
m1=0;
b1=0;
for i=1:length(Atype)
```

```
   if strcmp(Atype(i),'O')==1
      o1=o1+1;
      oxygenno(o1)=i;
   end
   if strcmp(Atype(i),'B')==1
      b1=b1+1;
      boronno(b1)=i;
   end
   if strcmp(Atype(i),'g')==1   %%%added to test and also if we add more mg later
      m1=m1+1;
      mgno(m1)=i;
   end
end
```

A.9 MATLAB code for RDF run after code in A8

```
lasttimestep=(Niter/5)+1;
timearr=[1:1:lasttimestep];
Lx=0.1771913910E+02;%8.859569550;
Ly=0.1534522247E+02; %7.672611237;
Lz=12.5; %24.267393110;
L=(Lx*Ly*Lz)^(1/3);%10;
dr=0.2;
rhobo=320/(L^3);
rhomgo=200/(L^3);
rhomgb=136/(L^3);
rbysigma=[dr:dr:(0.5*L)];
rcutoffbo=1.5;
Numberofbins=floor(0.5*L/dr);
mgsolid=[321,324,330,332,334,337,338,340];
gboronoxygen=zeros(1,Numberofbins);
gmgoxygen=zeros(1,Numberofbins);
gmgboron=zeros(1,Numberofbins);
initialvel=C{1};
for i=1:length(boronno)

    for j=1:length(oxygenno)
        dx=initialvel(oxygenno(j),1)-initialvel(boronno(i),1);
      %%%PBC only
         if dx>0.5*Lx
            dx = dx - Lx;
         elseif dx<-0.5*Lx
            dx = dx + Lx;
```

```
        end
        dy=initialvel(oxygenno(j),2)-initialvel(boronno(i),2);
      %%%PBC only
        if dy>0.5*Ly
          dy = dy - Ly;
        elseif dy<-0.5*Ly
          dy = dy + Ly;
        end
        dz=initialvel(oxygenno(j),3)-initialvel(boronno(i),3);
        %%%PBC only
      %   if(dz>0.5*L)
       %{dz = dz - L;}
      %else if(dz<-0.5*L)
       %{dz = dz + L;}
        rijsq=(dx)^2+(dy)^2+(dz)^2;
        rij=sqrt(rijsq);
        if rijsq<(L/2)^2
          gboronoxygen(floor(rij/dr))=gboronoxygen(floor(rij/dr))+2;


       end
      end

end
 for k=1:1:Numberofbins
      gboronoxygen(k)=gboronoxygen(k)/(4*pi*(((k+1)^3)-(k^3))*(dr^3))/3;
      %gboronoxygen(i,k)=gboronoxygen(i,k)/(rhobo*(Nboron+Noxygen));
      gboronoxygen(k)=gboronoxygen(k)/((rhobo)*320);
 end

 for i=1:length(mgsolid)

    for j=1:length(oxygenno)
       dx=initialvel(oxygenno(j),1)-initialvel(mgsolid(i),1);
      %%%PBC only
        if dx>0.5*Lx
          dx = dx - Lx;
        elseif dx<-0.5*Lx
          dx = dx + Lx;
        end
        dy=initialvel(oxygenno(j),2)-initialvel(mgsolid(i),2);
      %%%PBC only
        if dy>0.5*Ly
          dy = dy - Ly;
```

```
        elseif dy<-0.5*Ly
          dy = dy + Ly;
        end
        dz=initialvel(oxygenno(j),3)-initialvel(mgsolid(i),3);
        %%%PBC only
      %   if(dz>0.5*L)
       %{dz = dz - L;}
      %else if(dz<-0.5*L)
       %{dz = dz + L;}
        rijsq=(dx)^2+(dy)^2+(dz)^2;
        rij=sqrt(rijsq);
        if rijsq<(L/2)^2
          gmgoxygen(floor(rij/dr))=gmgoxygen(floor(rij/dr))+2;


       end
      end

end
 for k=1:1:Numberofbins
      gmgoxygen(k)=gmgoxygen(k)/(4*pi*(((k+1)^3)-(k^3))*(dr^3))/3;
      %gboronoxygen(i,k)=gboronoxygen(i,k)/(rhobo*(Nboron+Noxygen));
      gmgoxygen(k)=gmgoxygen(k)/((rhomgo)*200);
 end

 for i=1:length(mgsolid)

    for j=1:length(boronno)
       dx=initialvel(boronno(j),1)-initialvel(mgsolid(i),1);
      %%%PBC only
        if dx>0.5*Lx
          dx = dx - Lx;
        elseif dx<-0.5*Lx
          dx = dx + Lx;
        end
        dy=initialvel(boronno(j),2)-initialvel(mgsolid(i),2);
      %%%PBC only
        if dy>0.5*Ly
          dy = dy - Ly;
        elseif dy<-0.5*Ly
          dy = dy + Ly;
        end
        dz=initialvel(boronno(j),3)-initialvel(mgsolid(i),3);
        %%%PBC only
```

```
%   if(dz>0.5*L)
  %{dz = dz - L;}
%else if(dz<-0.5*L)
  %{dz = dz + L;}
    rijsq=(dx)^2+(dy)^2+(dz)^2;
    rij=sqrt(rijsq);
    if rijsq<(L/2)^2
      gmgboron(floor(rij/dr))=gmgboron(floor(rij/dr))+2;


   end
  end

end
 for k=1:1:Numberofbins
      gmgboron(k)=gmgboron(k)/(4*pi*(((k+1)^3)-(k^3))*(dr^3))/3;
      %gboronoxygen(i,k)=gboronoxygen(i,k)/(rhobo*(Nboron+Noxygen));
      gmgboron(k)=gmgboron(k)/((rhomgo)*136);
 end
figure(1)
 plot(rbysigma,gboronoxygen,'b','LineWidth',2);
 figure(2)
 plot(rbysigma,gmgoxygen,'b','LineWidth',2);
 figure(3)
 plot(rbysigma,gmgboron,'b','LineWidth',2);
gboronoxygen=gboronoxygen';
rbysigma=rbysigma';
gmgoxygen=gmgoxygen';
gmgboron=gmgboron';
```

A.10 MATLAB code to track O-B bond distance and Mulliken Charge as neighboring to Mg

```
lasttimestep=(Niter/5)+1;
timearr=[1:1:lasttimestep];
Lx=0.1771913910E+02;%8.859569550;
Ly=0.1534522247E+02; %7.672611237;
Lz=24.267393110;
rcutoffbo=1.5;
% for i=1:length(boronno)
%     counter=0;
%     for j=1:length(oxygenno)
%         dx=initialvel(oxygenno(j),1)-initialvel(boronno(i),1);
```

```
%       %%%PBC only
%          if dx>0.5*Lx
%            dx = dx - Lx;
%          elseif dx<-0.5*Lx
%            dx = dx + Lx;
%          end
%          dy=initialvel(oxygenno(j),2)-initialvel(boronno(i),2);
%       %%%PBC only
%          if dy>0.5*Ly
%            dy = dy - Ly;
%          elseif dy<-0.5*Ly
%            dy = dy + Ly;
%          end
%          dz=initialvel(oxygenno(j),3)-initialvel(boronno(i),3);
%          %%%PBC only
%       %   if(dz>0.5*L)
%         %{dz = dz - L;}
%       %else if(dz<-0.5*L)
%         %{dz = dz + L;}
%          rijsq=(dx)^2+(dy)^2+(dz)^2;
%          rij=sqrt(rijsq);
%          if rijsq<(rcutoffbo)^2
%            %gboronoxygen(floor(rij/dr))=gboronoxygen(floor(rij/dr))+1;
%            counter=counter+1;
%            noattched(i)=counter;
%            oattached(i,counter)=oxygenno(j);
%            %boronneigh(j,counter)=boronno(l);
%          end
%       end
%
% end
%oxygenno=omovedtowardsmg
for i=1:lasttimestep
   coordinates=C{i};
   counter3=0;
   for j=1:length(omovedtowardsmg)
      counter2=0;
      chargesum=0;
      sumrij=0;
      for k=1:length(battached(1,:))
        if battached(j,k)==0
           break;
        end
        counter2=counter2+1;
```

```
          dx=coordinates(omovedtowardsmg(j),1)-coordinates(battached(j,k),1);
           if dx>0.5*Lx
             dx = dx - Lx;
          elseif dx<-0.5*Lx
             dx = dx + Lx;
          end
          dy=coordinates(omovedtowardsmg(j),2)-coordinates(battached(j,k),2);
           if dy>0.5*Ly
             dy = dy - Ly;
          elseif dy<-0.5*Ly
             dy = dy + Ly;
          end
          dz=coordinates(omovedtowardsmg(j),3)-coordinates(battached(j,k),3);
          rijsq=(dx)^2+(dy)^2+(dz)^2;
          rij=sqrt(rijsq);
          charge=3-coordinates(battached(j,k),4);
          %bobonddist(i,j)=rij;
%            rijmax(counter2)=rij;
          sumrij=sumrij+rij;
          chargesum=chargesum+charge;
        end
         if counter2==0
            obbonddist(i,j)=0;
            bcharge(i,j)=0;
            counter3=counter3+1;
         else
            obbonddist(i,j)=sumrij/counter2;
            bcharge(i,j)=chargesum/counter2;
         end

    end
end
for i=1:lasttimestep
    avgobbondist(i)=max(obbonddist(i,:));%sum(bobonddist(i,:))/(length(boronno));
    avgbcharge(i)=min(bcharge(i,:));
end
time=[1:1:lasttimestep].*5*0.1;
figure(1)
plot(time,avgobbondist,'b','LineWidth',2);
avgobbondist=avgobbondist';
figure(2)

plot(time,avgbcharge,'b','LineWidth',2);
avgobbondist=avgobbondist';
```

```
avgbcharge=avgbcharge';
```

Publications

(1) **Biswas, P.**; Ghildiyal, P.; Kwon, H.; Wang, H.; Alibay, Z.; Xu, F.; Wang, Y.; Wong, B. M.; Zachariah, M. R. Rerouting Pathways of Solid-State Ammonia Borane Energy Release. *The Journal of Physical Chemistry C* **2021**, *126* (1), 48–57.

(2) **Biswas, P.**; Wang, Y.; Herrera, S.; Ghildiyal, P.; Zachariah, M. R. Catalytic Cleavage of the Dative Bond of Ammonia Borane by Polymeric Carbonyl Groups for Enhanced Energy Generation. *Chemistry of Materials* **2022**, *35*, 963.

(3) **Biswas, P.**; Xu, F.; Ghildiyal, P.; Zachariah, M. R. In-Situ Thermochemical Shock-Induced Stress at the Metal/Oxide Interface Enhances Reactivity of Aluminum Nanoparticles. *ACS Applied Materials and Interfaces* **2022**, *14* (23), 26782–26790.

(4) Wang, H.; **Biswas, P. (co-first author)**; Zachariah, M. R. Direct Imaging and Simulation of the Interface Reaction of Metal/Metal Oxide Nanoparticle Laminates. *The Journal of Physical Chemistry C* **2022**, *126* (20), 8684–8691.

(5) **Biswas, P.**; Ghildiyal, P.; Mulholland, G. W.; Zachariah, M. R. Modelling and Simulation of Field Directed Linear Assembly of Aerosol Particles. *Journal of Colloids and Interface Science* **2021**, *592*, 195–204.

(6) **Biswas, P.**; Mulholland, G. W.; Rehwoldt, M. C.; Kline, D. J.; Zachariah, M. R. Microwave Absorption by Small Dielectric and Semi-Conductor Coated Metal Particles. *Journal of Quantitative Spectroscopy and Radiative Transfer* **2020**, 247, 106938.

(7) **Biswas, P.**; Wang, Y.; Hagen, E.; Zachariah, M. R. An Electrochemical Dead-man's Switch for Flammability of Liquid Fuels (*Nature Communications-under review*)

(8) **Biswas, P.**; Pham, C. H.; Zachariah, M. R. Magnesium Induced Strain and Immobilized Radical Generation on Boron Oxide Surface Enhances Oxidation Rate of Boron Particles: A DFTB-MD Study (*Langmuir-under review*)